NATO Science for Peace and Security Series - C:
Environmental Security

Disposal of Dangerous Chemicals in Urban Areas and Mega Cities

Role of Oxides and Acids of Nitrogen in Atmospheric Chemistry

Edited by
Ian Barnes
Krzysztof J. Rudziński

Springer

NATO OTAN

This publication is supported by:

The NATO Science for Peace and Security Programme

Disposal of Dangerous Chemicals in Urban Areas and Mega Cities

NATO Science for Peace and Security Series

This Series presents the results of scientific meetings supported under the NATO Programme: Science for Peace and Security (SPS).

The NATO SPS Programme supports meetings in the following Key Priority areas: (1) Defence Against Terrorism; (2) Countering other Threats to Security and (3) NATO, Partner and Mediterranean Dialogue Country Priorities. The types of meeting supported are generally "Advanced Study Institutes" and "Advanced Research Workshops". The NATO SPS Series collects together the results of these meetings. The meetings are co-organized by scientists from NATO countries and scientists from NATO's "Partner" or "Mediterranean Dialogue" countries. The observations and recommendations made at the meetings, as well as the contents of the volumes in the Series, reflect those of participants and contributors only; they should not necessarily be regarded as reflecting NATO views or policy.

Advanced Study Institutes (ASI) are high-level tutorial courses to convey the latest developments in a subject to an advanced-level audience

Advanced Research Workshops (ARW) are expert meetings where an intense but informal exchange of views at the frontiers of a subject aims at identifying directions for future action

Following a transformation of the programme in 2006 the Series has been re-named and re-organised. Recent volumes on topics not related to security, which result from meetings supported under the programme earlier, may be found in the NATO Science Series.

The Series is published by IOS Press, Amsterdam, and Springer, Dordrecht, in conjunction with the NATO Emerging Security Challenges Division.

Sub-Series

A.	Chemistry and Biology	Springer
B.	Physics and Biophysics	Springer
C.	Environmental Security	Springer
D.	Information and Communication Security	IOS Press
E.	Human and Societal Dynamics	IOS Press

http://www.nato.int/science
http://www.springer.com
http://www.iospress.nl

Series C: Environmental Security

Disposal of Dangerous Chemicals in Urban Areas and Mega Cities

Role of Oxides and Acids of Nitrogen in Atmospheric Chemistry

edited by

Ian Barnes
University of Wuppertal
FB C – Department of Physical Chemistry
Wuppertal, Germany

and

Krzysztof J. Rudziński
Institute of Physical Chemistry of the PAS
Warsaw, Poland

Published in Cooperation with NATO Emerging Security Challenges Division

Proceedings of the NATO Advanced Research Workshop on
Disposal of Dangerous Chemicals in Urban Areas and Mega Cities
Gdansk, Poland
9–13 October 2011

Library of Congress Control Number: 2012943344

ISBN 978-94-007-5036-4 (PB)
ISBN 978-94-007-5033-3 (HB)
ISBN 978-94-007-5034-0 (e-book)
DOI 10.1007/978-94-007-5034-0

Published by Springer,
P.O. Box 17, 3300 AA Dordrecht, The Netherlands.

www.springer.com

Printed on acid-free paper

Preface

The NATO Advanced Research Work "Disposal of Dangerous Chemicals in Urban Areas and Mega Cities" took place in Gdańsk, Poland, 9–13 October 2011 and was attended by 39 participants from ten countries. The major aim of the workshop was to look at the present state of knowledge on the role of oxides and acids of nitrogen in oxidant radical formation and cycling and consequently the oxidation capacity of the atmosphere in general and urban areas and mega cities in particular.

Oxides and acids of nitrogen play an important role in regulating the atmospheric levels of the OH radical which is the main imitator of the degradation of chemicals in the atmosphere. The workshop gave a comprehensive overview on the methods used to measure nitrogen (NO_2) and nitrous acid (HONO) in the troposphere and difficulties associated with certain techniques were highlighted. Reports from recent field measurements using very sensitive HONO instruments served to show the growing recognition among the scientific community that photolysis of HONO is a much more important daytime OH radical than previously thought. Presentations on the state of the art in OH and HO_2 radical atmospheric measurement methods were an important topic of the workshop and recently recognised difficulties, in particular with HO_2 radicals, were highlighted.

Our present understanding of the gas, aqueous and particulate/aerosol phase atmospheric degradation chemistry of chemicals under different NO_x environments was presented and discussed in great detail. The potential importance of photo-enhanced reactions on surfaces and particles was highlighted at the meeting through the presentation of recent research. This is an area that is currently finding many applications for the removal of chemicals from the atmosphere, e.g. through photocatalytic remediation processes.

Examples of measurements of NO_x and chemicals in the atmosphere were presented for rural and urban environments and also megacities such as Cairo in conjunction with modelling studies which attempt to simulate the field observations using state-of-the art knowledge on the chemistry and radical levels. These examples helped to highlight some of the more important gaps in our knowledge on the degradation of chemicals in the atmosphere, e.g. large uncertainties in different steps of the degradation routes, missing sources for the important OH radical

precursor HONO, and very importantly an inadequate knowledge of OH/HO_2 radical recycling in the degradation of chemicals. Modelling the impact of megacities on air quality and climate is associated with many difficulties and unknowns. These were concisely presented at the workshop along with new approaches to this immense problem which are being applied within, for example, the EU FP7 project MEGAPOLI.

The workshop has played an important role in collecting together most aspects of the current state of knowledge on the role of oxides and acids of nitrogen in the atmospheric degradation of chemicals from the viewpoint of measurement, chemistry and modelling. The manuscripts presented here in the proceedings reflect the presentations given at the workshop. PDFs of the presentations are available online or can be obtained upon request from barnes@uni-wuppertal.de

Ian Barnes, Ali Shakour and Krzysztof Rudzinski (worship organisers), April 2012.

Group photograph showing most of the participants at the NATO ARW held in the Novotel, Gdańsk, Poland, 9–13 October 2011

Acknowledgements

The ARW was kindly financed by the following organizations for the workshop conveners are extremely grateful:

NATO Scientific and Environmental Affairs Division, Brussels
http://www.nato.int/science/index.html

The EC 6th Framework Programme, EUROCHAMP project "support for Infrastructures – Integrated Infrastructure Initiative"
http://www.eurochamp.org/

Contents

List of Participants

Nasser M. Abdel-Latif Air Pollution Department, National Research Centre, Dokki, Cairo, Egypt

Nadia Mohamed Eltayeb Aly Air Pollution Department, National Research Centre, Cairo, Egypt

Abdel Hamed A. Awad Air Pollution Department, National Research Centre, Cairo, Egypt

Karl-Heinz Becker Physikalische Chemie, Bergische Universität Wuppertal, Wuppertal, Germany

Mykola M. Biliaiev Department of Fluid Dynamics, Railway Transport University, Dnipropetrovsk, Ukraine

William J. Bloss School of Geography, Earth & Environmental Sciences, University of Birmingham, Birmingham, UK

Steven S. Brown Chemical Sciences Division, NOAA Earth System Research Laboratory, Boulder, CO USA

Tim Butler Institute for Advanced Sustainability Studies, Potsdam, Germany

Magda Claeys Department of Pharmaceutical Sciences, University of Antwerp, Antwerp, Belgium

Teimuraz Davitashvili I.Vekua Institute of Applied Mathematics, Tbilisi State University, Tbilisi, Georgia

Valerie Derpmann FB C – Physical & Theoretical Chemistry, University of Wuppertal, Wuppertal, Germany

Mohammed Abd El-Samea Ali El-Hashmey Air Pollution Department, National Research Centre, Cairo, Egypt

Yasin Elshorbany Department of Atmospheric Chemistry, Max Planck Institute for Chemistry, Mainz, Germany

Atef Mohamed Ali Fathy Air Pollution Department, National Research Centre, Cairo, Egypt

Christa Fittschen Physicochimie des Processus de Combustion et de l'Atmosphère, USTL, Villeneuve d'Ascq, France

Christian George Institut de Recherches sur la Catalyse et l'Environnement de Lyon (IRCELYON), UMR5256 CNRS-Université LYON, Villeurbanne Cedex, France

Dwayne Heard School of Chemistry, University of Leeds, Leeds, UK

Yoshiteru Iinuma Leibniz-Institut für Troposphärenforschung, Leipzig, Germany

Solvejg Jørgensen Department of Chemistry, University of Copenhagen, Copenhagen, Denmark

Mykola M. Kharytonov Department of Soil Science and Ecology, Dnipropetrovsk State Agrarian University, Dnipropetrovsk, Ukraine

Railway Transport University, Dnipropetrovsk, Ukraine

Rashid A. Khaydarov Uzbekistan Academy of Sciences, Institute of Nuclear Physics, Tashkent, Uzbekistan

Sonja Klee FB C – Department of Physical Chemistry, University of Wuppertal, Wuppertal, Germany

Jörg Kleffmann Physikalische Chemie, Bergische Universität Wuppertal, Wuppertal, Germany

Adkhamjon Paiziev Institute of Electronics Uzbek Academy of Science, Tashkent, Uzbekistan

Kerri Pratt Department of Chemistry, Purdue University, Purdue, USA

Mila Ródenas UMH-Fundación CEAM, Paterna, Valencia, Spain

Krzysztof J. Rudziński Institute of Physical Chemistry PAS, Warszawa, Poland

Alia A. Shakour Air Pollution Department, National Research Center, Dokki, Cairo, Egypt

Jochen Stutz Department of Atmospheric and Oceanic Sciences, University of California Los Angeles, Los Angeles, CA USA

Hang Su Biogeochemistry Department, Max Plank Institute for Chemistry, Mainz, Germany

Rafal Szmigielski Laboratory of Environmental Chemistry, Institute of Physical Chemistry, Polish Academy of Sciences (PAS), Warsaw, Poland

Yana Virolainen Department of Atmospheric Physics, Saint-Petersburg State University, St. Petersburg-Petrodvorets, Russia

Bernhard Vogel Institute for Meteorology and Climate Research, Karlsruhe Institute of Technology, Karlsruhe, Germany

Timothy J. Wallington Ford Motor Company, Dearborn, MI USA

Department of Atmospheric, Oceanic and Space Sciences, University of Michigan, Ann Arbor, MI USA

Peter Wiesen Physikalische Chemie, Bergische Universität Wuppertal, Wuppertal, Germany

Xianliang Zhou Wadsworth Center, New York State Department of Health, and School of Public Health, State University of New York, Albany, NY USA

Tong Zhu State Key Laboratory for Environmental Simulation and Pollution Control, College of Environmental Sciences, Peking University, Beijing, China

Chapter 1
Field Observations of Daytime HONO Chemistry and Its Impact on the OH Radical Budget

Jochen Stutz, Kam Weng Wong, and Catalina Tsai

Abstract Measurements of daytime nitrous acid (HONO) are reviewed and possible daytime sources of HONO are discussed. The importance of the observed daytime HONO mixing ratios for the HOx budget in urban and rural environments is assessed and recommendation for future work are given.

Keywords Nitrous Acid • Daytime radical chemistry • Heterogeneous chemistry

1.1 Introduction

The formation of nitrous acid, HONO, during the day has received considerable attention in recent years due to its potential impact on the chemistry of hydroxyl radicals, OH, in the lower troposphere. It is well known that the photolysis of HONO accumulated throughout the night:

$$HONO + h\nu \xrightarrow{\lambda<400\,\mathrm{nm}} OH + NO \qquad (1.R1)$$

is a significant, and often the dominant, source of OH-radicals in the early morning, when other primary HO_x ($OH + HO_2$) sources, such as ozone and HCHO photolysis, are still weak [3, 4]. HONO mixing ratios typically decrease after sunrise, and for many years it has been assumed that HONO reaches a photo-stationary state, $[HONO]_{ss}$, between its photolysis (1.R1), the gas-phase formation from NO and OH (1.R2), and its reaction with OH (1.R3):

$$NO + OH \rightarrow HONO \qquad (1.R2)$$

$$HONO + OH \rightarrow NO_2 + H_2O \qquad (1.R3)$$

J. Stutz (✉) • K.W. Wong • C. Tsai
Department of Atmospheric and Oceanic Sciences, University of California Los Angeles, 7127 Math Sciences, Los Angeles, CA 90095-1565, USA
e-mail: jochen@atmos.ucla.edu

I. Barnes and K.J. Rudziński (eds.), *Disposal of Dangerous Chemicals in Urban Areas and Mega Cities*, NATO Science for Peace and Security Series C: Environmental Security,
DOI 10.1007/978-94-007-5034-0_1,

$$[HONO]_{ss} = \frac{k_2[NO][OH]}{J_{HONO} + k_3[OH]} \quad (1.1)$$

However, atmospheric observations in recent years have found daytime HONO mixing ratios of up to 100–300 ppt, that considerably exceeded the expected $[HONO]_{ss}$ (e.g. [1, 19, 30, 47]).

Urban daytime HONO mixing ratios are generally found to be highest in the morning and to decrease throughout the day, or to show a minimum at noon [2–4, 11, 39]. Remote and semi-rural HONO mixing ratios were found to peak at noontime [1, 44] or showed similar diurnal profiles as in urban areas [18, 30, 47]. Most of these observations were performed at one altitude, often within the lowest 10–20 m from the surface, and information on the vertical distribution of daytime HONO is still sparse. Significant vertical HONO gradients were not observed in a semi-rural area in Germany on a 190 m high tower [18] or in the lowest 25 m of a forest [29], while Villena et al. [39] found higher daytime HONO mixing ratios at 6 m compared to 53 m altitude in an urban area in Chile. Negative HONO vertical gradients were also observed by aircraft in the lowest 2,500 m of the atmosphere in northern Michigan [43], while airborne measurements of HONO in the lowest 1,000 m above the ground in Germany showed no vertical gradients [15].

The observed daytime HONO mixing ratios are expected to impact the HO_x budget in urban and rural areas [2, 19, 22, 27, 47]. Previous analyses have attributed up to 55% of the total primary OH formation to HONO photolysis [1, 3, 5, 11, 19, 23]. Nevertheless, the magnitude and impact of daytime HONO on the OH budget is still not well established. The observation of vertical HONO profiles implies that the OH formation from HONO photolysis could be altitude dependent, but little effort to investigate this effect and its impact on the tropospheric OH budget has been made.

To address the questions of the vertical distribution of HONO, its daytime formation, and the impact on OH, we have performed observations of HONO vertical concentration profiles with long-path Differential Optical Absorption Spectroscopy (LP-DOAS) in Houston, Texas, USA, in spring 2009. Here we will use these observations to identify possible sources of HONO during the day. In addition, the altitude dependence of primary OH formation by HONO photolysis, and its contribution relative to those from ozone, and HCHO photolysis, will be discussed.

1.2 Daytime Chemistry of HONO

The presence of HONO mixing ratios above the simple photo-stationary state during the day has now been firmly established. Nevertheless, the exact mixing ratios are still under discussion due to the difficulty of accurately measuring HONO, as well as a still sparse dataset on daytime HONO in different environments.

The source(s) of daytime HONO also remain elusive. It is, however, clear that the non-photolytic conversion of NO_2 on humid surfaces, which is believed to be responsible for the nocturnal accumulation of HONO [13, 35, 41], is too slow to explain the observed daytime HONO mixing ratios [17]. Consequently a number of new HONO formation pathways have been proposed. Following atmospheric and laboratory observations most of these mechanisms have in common that they require solar radiation [14, 21, 31, 47].

Two gas-phase mechanisms have been proposed: The photolysis of *ortho*-nitrophenols [7] leads to the formation of HONO with a rate that is linearly dependent on the *ortho*-nitrophenol concentration and the actinic flux. HONO formation through the formation of photo-excited NO_2, NO_2^*, followed by its reaction with water vapor is expected to be proportional to the actinic flux, NO_2 concentrations, and water vapor concentrations. The rate and branching ratio of the $NO_2^* + H_2O$ reaction is currently uncertain [8, 9, 21]. Only at the higher rate reported by Li et al. [21] is this mechanism important [12].

Two different heterogeneous mechanisms are currently under discussion. The first is based on the photo-enhanced conversion of NO_2 on organic surface films. Laboratory studies found that the conversion of NO_2 to HONO on aromatic hydrocarbon films, such as phenols and aromatic ketones, was accelerated by 1–2 orders of magnitude upon irradiation with UV light (300–420 nm) compared to the dark reaction [14]. A similar enhancement was found on humic acid (HA) surfaces [31]. To explain these observations a mechanism forming HONO through the reaction of NO_2 with photolytically activated reductive centers (A^{red}) has been proposed [31]. The formation of HONO on these surfaces was found to be first order in NO_2 for low to semi-polluted conditions and linearly dependent on irradiance in the spectral range from 300 to 700 nm (see Eq. 1.2).

$$\frac{d[HONO]}{dt} \propto surface\ area\ concentration \times [NO_2] \times Irradiance \tag{1.2}$$

The second heterogeneous HONO formation mechanism is the photolysis of surface adsorbed nitric acid (HNO_3), which has been suggested based on a number of field measurements in remote areas [6, 10, 16, 47] and a glass sample manifold experiment [45, 46]. Further evidence for this mechanism was recently presented by Zhou et al. [48]. The formation of HONO is expected to be proportional to UV solar irradiance and the amount of the surface adsorbed HNO_3.

These mechanisms can occur either on surfaces at the ground or on aerosols. Stemmler et al. [32] suggests that the humic acid pathway is unimportant on aerosols. However, other similar HONO formation processes on aerosols, or the photolysis of aerosol nitric acid cannot be excluded. The main difference between the ground surface and aerosol pathways is their dependence on solar radiation. While surface processes should be proportional to solar irradiance (Eq. 1.2), aerosol processes should be proportional to the actinic flux.

Su et al. [37] recently proposed that soil nitrite was also a strong source of daytime HONO. HONO soil emissions did not depend on gas-phase NO_2, but rather

on soil nitrite, which, by itself, was dependent on soil acidity and temperature. Finally, it should be noted that direct emission is also a possible source of daytime HONO in urban areas [20, 25]. This source would solely depend on temporal traffic patterns and correlate, through co-emission, with NO_x ($NO + NO_2$).

1.3 Spectroscopic Observation of Daytime HONO

Observations of daytime HONO, NO_2, O_3 and HCHO were performed using LP-DOAS [26] in April and May 2009, in Houston, Texas, USA. The LP-DOAS telescope was set up on the roof of a 70 m high building on the campus of the University of Houston. The telescope sequentially sent light from a Xe-arc lamp onto three arrays of retroreflectors, which were mounted at different altitudes (20 m, 130 m and 300 m agl) on buildings in downtown Houston (Fig. 1.1). The light returning from the retroreflectors was detected by a spectrometer-detector combination in the wavelength interval from 300 to 380 nm, as described in detail in Wong et al. [42]. Spectral retrieval of NO_2, HONO, O_3 and HCHO concentrations was achieved using the DOAS method (see [3, 36] for details), using literature absorption cross section of the different trace gases [24, 34, 38, 40]. The mixing ratio errors reported here were derived by the retrieval routine and are 1σ statistical uncertainties [33, 42]. The detection limit of path averaged HONO mixing ratios was in the range of 10–30 ppt. Figure 1.2 shows that daytime HONO was clearly identified spectroscopically in Houston. Path-averaged mixing ratios of the lower and middle light paths are

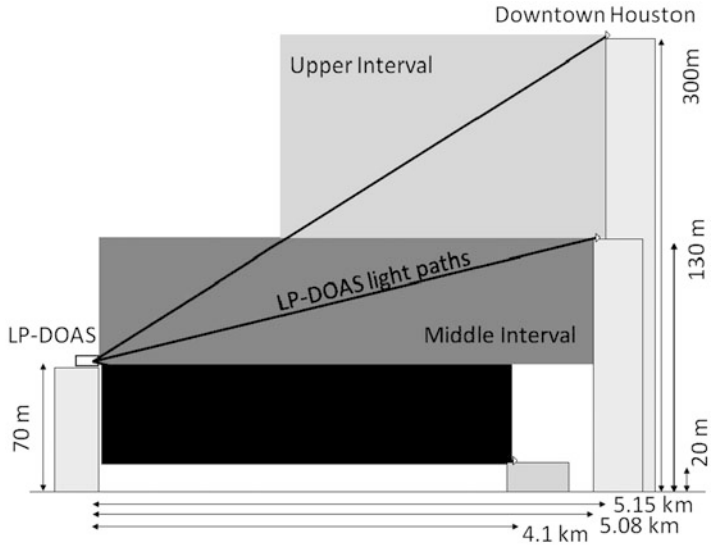

Fig. 1.1 Setup of LP-DOAS instrument in Houston, TX

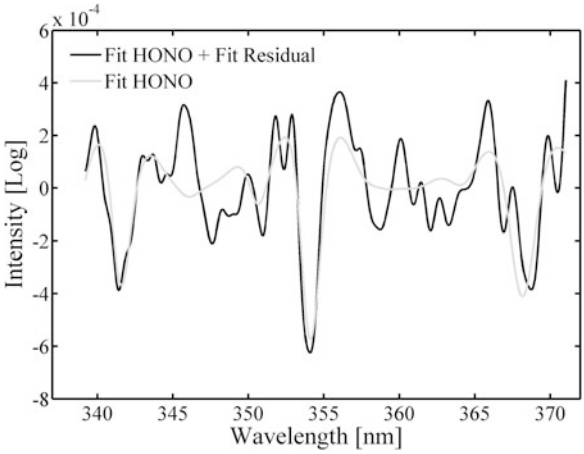

Fig. 1.2 Comparison of a HONO reference spectrum (*gray line*) with the retrieved HONO signal (*black line*), i.e. the HONO absorption together with unexplained spectral structures [42]. A HONO mixing ratio of 0.139 ± 0.013 ppb was clearly identified in the spectrum

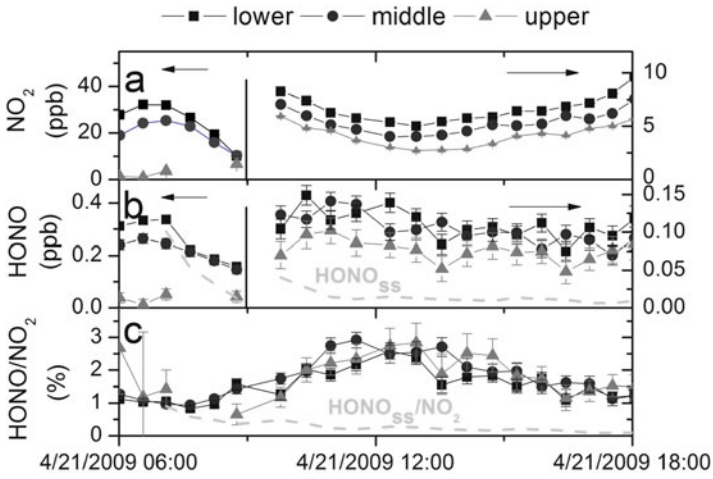

Fig. 1.3 $[NO_2]$, [HONO], and $[HONO]/[NO_2]$ for a sunny day (21 April 2009) in Houston, TX (Adapted from Wong et al. [42])

representative for the respective height intervals: (20–70 m and 70–130 m). The mixing ratio in the upper height interval (130–300 m) was calculated by subtracting the scaled mixing ratios of the middle light path from the upper light path.

Figure 1.3 shows NO_2 and HONO mixing ratios in the three height intervals during a sunny April day in Houston. Clear vertical gradients with higher mixing ratios in the lower height interval were found for both species. The diurnal cycle of NO_2 showed a minimum at noon, while HONO mixing ratios displayed a slow decrease throughout the day. The HONO behavior is similar to that observed in other urban studies [2, 11, 39]. The $[HONO]/[NO_2]$ ratio, which can be used as a parameter to analyze HONO formation, shows a clear maximum around noon. This is in

agreement with previous observations, which found this behavior to correlate with NO_2 photolysis and thus is indicative of a photolytic HONO source [2, 11, 39]. Our observations show no statistically significant vertical profile in [HONO]/[NO_2], in contrast to previous reports that sometimes found larger [HONO]/[NO_2] ratios aloft [39].

1.4 Daytime HONO Sources

Using observations of [OH], [NO] and HONO photolysis frequencies, J_{HONO}, we calculated $[HONO]_{ss}$ following Eq. 1.1 [42]. A comparison with the observations shows that the observed HONO mixing ratios exceeded this value considerably during the day (Fig. 1.3), confirming previous reports of an unknown source of HONO during the day (e.g. [17, 30]).

Using a pseudo steady state approach between the various HONO formation and loss pathways we can calculated the strength of the unknown HONO source, $P_{unknown}$:

$$P_{unknown} = J_{HONO}[HONO] + k_3[HONO][OH] - k_2[NO][OH] - emission \quad (1.3)$$

Emission rates previously determined in Houston [41] were used in this calculation. A comparison between the HONO loss rate and $P_{unknown}$ shows that $P_{unknown}$ is the dominant source term for daytime HONO (Fig. 1.4a). The difference between loss and $P_{unknown}$ in the morning can be explained by traffic emissions and the OH + NO pathway, which is higher in the morning, due to elevated NO levels in Houston.

$P_{unknown}$ shows a clear asymmetry throughout the day, with higher levels in the morning than the afternoon. Considering that many daytime HONO formation mechanisms assume a dependence on [NO_2], one of the likely HONO precursors, we normalized $P_{unknown}$ to [NO_2]: $P_{unknown}^{*} = P_{unknown}/[NO_2]$. $P_{unknown}^{*}$ shows a symmetric diurnal profile that varies with actinic flux and/or solar irradiance (courtesy of B. Lefer, N. Grossman, U. Houston). This result, which was observed on other sunny days in Houston, supports the conclusion that the formation of daytime HONO involves NO_2 (Eq. 1.2), or a species that shows the same diurnal profile as NO_2.

Figure 1.4b also shows the observed NO_2 photolysis frequencies and the visible solar irradiance. It is clear from these observations that, while these two quantities are related, they have a different diurnal profile. Through a correlation analysis of the dependence of $P_{unknown}^{*}$ on these two parameters one can gain insight on daytime HONO formation, i.e. ground vs. gas-phase/aerosol. We performed this analysis for $P_{unknown}^{*}$ in the lower and middle height interval on the four cloud free days during the Houston experiment. The range of correlations of $P_{unknown}^{*}$ with NO_2 was $R^2 = 0.58$–0.89 with an average $R_{avg}^2 = 0.76$, while the correlation coefficient with visible solar irradiance (400–700 nm) was in the range of $R^2 = 0.65$–0.96 with an average of $R_{avg}^2 = 0.85$ and that of UV solar irradiation (286.5–363 nm) was in

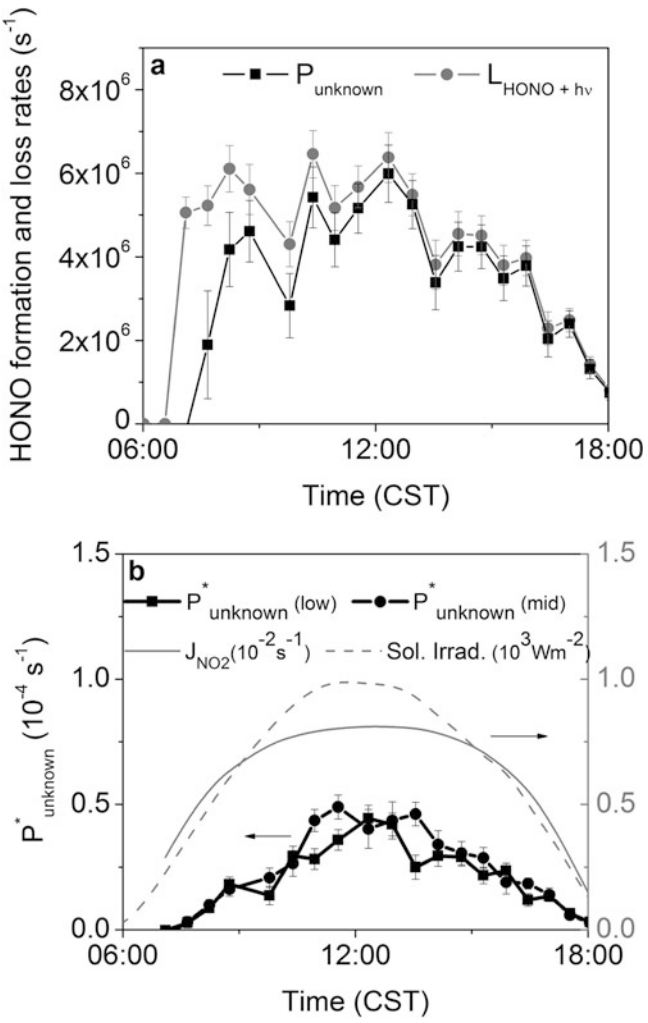

Fig. 1.4 Analysis of HONO observations on 21 April 2009. (**a**) Comparison of photolytic HONO loss with the rate of the unknown HONO source, $P_{unknown}$. (**b**) Normalized unknown HONO source rate, $P_{unknown}^{*}$, in the lower and middle height intervals (*left* y-axis), and NO_2 photolysis frequency and solar irradiance (*right* y-axis) (Adapted from Wong et al. [42])

the range of $R^2 = 0.70–0.97$ with an average of $R_{avg}^2 = 0.87$ (see [42] for details). These values indicate that $P_{unknown}^{*}$ correlates better with solar irradiance than the actinic flux, implying that HONO is predominately formed at the ground [42]. The difference between UV and solar irradiance is not statistically significant and no conclusion can be drawn on the wavelength dependence of the formation process.

A second line of argument against a conversion of NO_2 to HONO in the gas-phase or on the aerosol can be made using the [HONO]/[NO_2] ratio. We will use the well justified assumption that the HONO loss during the day is dominated by its

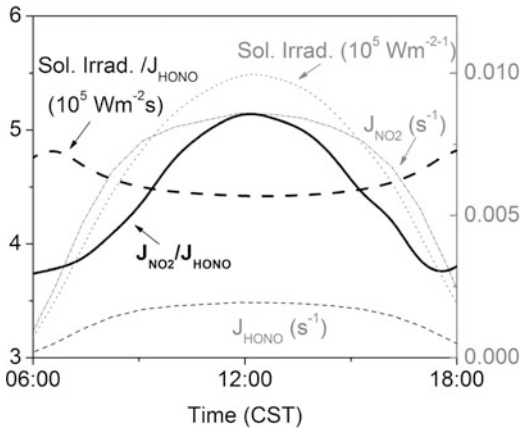

Fig. 1.5 Visible solar irradiance, J_{NO2}, J_{HONO} (*right* y-axis) and the ratios of solar irradiance/J_{NO2} and J_{NO2}/J_{HONO} (*left* y-axis) on a sunny day in Houston (Adapted from Wong et al. [42])

photolysis. As we have shown above the source of HONO in Houston depends on the NO_2 concentration and on either solar irradiance or the actinic flux, which we will for simplicity call J_{source}. As shown above all other potential factors influencing the photolytic HONO source are minor compared to NO_2 and J_{source} in Houston, and are here summarized in a constant. We can now perform a pseudo steady state calculation to determine the function dependence of [HONO]/[NO_2].

$$\frac{d[HONO]}{dt} = J_{source} \times [NO_2] \times \text{const.} - J_{HONO} \times [HONO] = 0 \qquad (1.4)$$

$$\frac{[HONO]}{NO_2} \propto \frac{J_{source}}{J_{HONO}} \qquad (1.5)$$

From this simple argument one can see that [HONO]/[NO_2] should depend on the ratio between the radiation term in the HONO formation and HONO photolysis. Using observed HONO and NO_2 photolysis frequencies and solar irradiance (Fig. 1.5) one can now apply Eq. 1.5 and compare the calculated diurnal profile of [HONO]/[NO_2] to the observations (Fig. 1.3).

In the case that the HONO source depends on the actinic flux, here J_{NO2} is used as a proxy, the calculated [HONO]/[NO_2] diurnal profile is fairly constant with a slight minimum at noon. This is in contrast to the observations, which showed a clear maximum of [HONO]/[NO_2] at noon (Fig. 1.3). The calculated diurnal profile can be explained by the fact that both, the HONO source and loss rate depend on the actinic flux and thus this dependence mostly cancels out. Consequently [HONO]/[NO_2] is fairly constant throughout the day, or, depending on the wavelength dependence of the photolytic source, has a slight minimum at noon. On the other hand, if the HONO source is linked to solar irradiance Eq. 1.5 results in a maximum of solar irradiance/J_{HONO} and thus a maximum of [HONO]/[NO_2] at noon (Fig. 1.5), in agreement with the observations (Fig. 1.3). This argument thus also leads to the conclusion that HONO formation is most likely occurring at the ground rather than in the gas-phase or on aerosols.

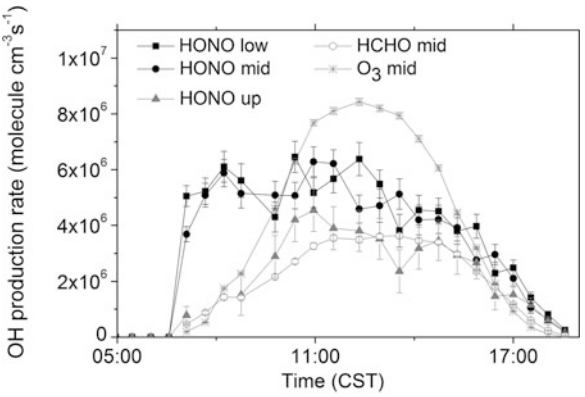

Fig. 1.6 OH formation rates from HONO, O_3, and HCHO photolysis on 21 April 2009, in Houston, TX. Rates from HONO photolysis are shown in all the altitude intervals

1.5 OH-Radical Formation Profiles from HONO Photolysis

HONO mixing ratios showed clear vertical profiles in Houston (Fig. 1.3). As a consequence one would expect that the OH formation rate from HONO photolysis should also be altitude dependent. To illustrate this point we performed calculations of the OH formation rate from HONO photolysis based on our LP-DOAS observations in the three height intervals and direct measurements of the HONO photolysis frequency (Fig. 1.6). The back reaction of OH + NO → HONO was not considered in this calculation, as it has only a minor impact on the HONO budget. For comparison we also calculated the OH formation rate from ozone photolysis to $O(^1D)$ followed by its reaction with water vapor, based on LP-DOAS ozone observations (not shown) and direct measurements of $J_{O3 \rightarrow O1D}$ and water (courtesy of N. Grossberg and B. Lefer, University of Houston). Ozone showed only a small vertical gradient during the day and thus only the results of this calculation for the middle height interval is shown in Fig. 1.6. We also considered the photolysis of HCHO to HO_2 followed by the reaction of $HO_2 + NO \rightarrow OH + NO_2$ as a primary OH source, assuming that the conversion of HO_2 to OH is fast in the polluted atmosphere of Houston, where NO is always present at high concentrations. HCHO mixing ratios by the LP-DOAS instrument (not shown) and observations of J_{HCHO} were used in this calculation. As in the case of ozone, no strong vertical profiles of HCHO were observed during the day. Thus only the OH production rate from HCHO photolysis for the middle light path is in Fig. 1.6.

HONO photolysis dominates in the lowest and middle light path in the morning over O_3 and HCHO photolysis (Fig. 1.6). This result is in agreement with previous observations of the contribution of early morning HONO photolysis to the OH budget, which were all performed close to the surface (for example [3, 4]). In contrast, HONO photolysis is less important as an OH source above 130 m altitude, where it is approximately of the same magnitude as the photolysis of ozone and HCHO. After 10:00 CST ozone photolysis becomes the dominant primary OH source in all height intervals. However, both HCHO and HONO photolysis continue to contribute significantly to primary OH formation. Below 130 m altitude

HONO photolysis is more important than HCHO as an OH precursor, while both processes are about equal in importance aloft. It is interesting to note that HONO photolysis again becomes the dominant OH source in the late afternoon.

These results confirm that OH formation from HONO photolysis is altitude dependent, in particular in the morning. The morning behavior can be explained by considering the meteorology during the morning transition from a stable to a well-mixed boundary layer. It is well known that HONO accumulates in the nocturnal boundary layer, showing very strong vertical HONO concentration gradients [41]. The break-up of the nocturnal boundary layer by solar heating typically occurs a few hours after sunrise, i.e. around 10:00 CST in our case. In the period between sunrise and the nocturnal boundary layer break-up, photolysis of HONO is occurring while vertical mixing remains inhibited. Consequently HONO levels near the surface remain high, mostly due to HONO left over from the previous night and due to the enhanced HONO formation caused by high NO_2 near the surface. HONO levels aloft are low as nocturnal HONO, [NO_2], and the available surface area for heterogeneous chemistry are small. Since photolysis frequencies do not show a vertical profile in the lowest atmosphere, the strong HONO vertical profiles in the morning thus lead to altitude dependent OH formation. As soon as the boundary layer is more efficiently mixed, the HONO profile and the OH formation profile becomes weaker. It should be noted that the mechanism that maintains the observed HONO profile throughout the day is currently under investigation.

1.6 Conclusions and Recommendations for Future Work

Despite the now well established presence of HONO mixing ratios significantly above the simple photo-stationary state between OH, NO and HONO, many aspects of daytime HONO chemistry remain poorly understood. Here we presented open-air LP-DOAS observations of daytime HONO in Houston, Texas, USA. Our HONO observations are similar to those from previous studies [1, 2, 11, 19, 28–30, 39, 43, 45], but fall on the lower end of reported mixing ratios. A comparison of our observations with pseudo steady state HONO mixing ratios confirms that a strong daytime source of HONO is present in the urban atmosphere (see for example Kleffmann [17, 42]). A detailed analysis of our observations leads to the following conclusions:

- The strong daytime HONO source identified in our observations is correlated to NO_2 concentrations. It thus appears that the HONO formation mechanism involves NO_2 or other species that shows a diurnal behavior very similar to NO_2.
- Our results strongly suggest that daytime HONO formation in urban areas occurs at the surface. This conclusion is supported by two different lines of argument. First, the NO_2-normalized daytime HONO formation rate correlates better with solar irradiance than with J_{NO2}, which served as a proxy for the actinic flux. Second, observed [HONO]/[NO_2] ratios show a diurnal profile with a maximum at noon, which can be explained if the formation depends on solar irradiance,

rather than on the actinic flux. Our arguments seem to contradict the proposed gas-phase HONO formation through the reaction of photo-excited NO_2^* with water vapor [21] or photolysis of *ortho*-nitrophenols [7] as an important HONO source in urban areas.

- HONO photolysis contributes significantly to primary OH formation in Houston in the lowest 300 m of the atmosphere. The morning peak in primary OH formation due to the photolysis of HONO accumulated throughout the night [41], is restricted to the lowest 130 m of the atmosphere, which has an impact on the significance of the morning photolysis of nocturnal HONO. The morning behavior can be explained by considering that the break-up of the nocturnal boundary layer occurs a few hours after sunrise, while photolysis starts at sunrise when the boundary layer is still stratified.

A number of open questions on the sources and consequences of daytime HONO remain to be answered. While it has now been established that a significant photolytic daytime source of HONO is present in many environments [17], the exact mechanism of HONO formation is still under discussion. More targeted investigations of the dependence of the photolytic daytime source on environmental parameters are needed. This includes a better understanding of dependence on NO_2 or the identification of other precursors in the atmosphere. The impact of the characteristics and composition of the reactive surfaces and/or films on surfaces needs to be better understood. In particular, the question whether the surfaces investigated in the laboratory are truly representative for surfaces found in the atmosphere needs to be addressed. The dependence of HONO formation on solar irradiance and its wavelength dependence also deserve further attention. The question of a daytime HONO volume source, gas-phase or on aerosols, requires further investigation, as it could be significant in the upper daytime boundary layer and in the free troposphere, where ground surface chemistry has little or no influence. Ultimately, a detailed mechanistic understanding of daytime HONO formation on a molecular level is highly desirable. In light of more and better observations of daytime HONO, as well as the emerging understanding of the altitude dependence of OH formation, more detailed studies on the impact of this OH source on tropospheric chemistry in polluted and remote areas are needed.

Acknowledgement We would like to thank all participants of the 2009 Study of Houston Atmospheric Radical Precursor (SHARP) experiment, and in particular B. Lefer, J. Flynn, and N. Grossberg from the University of Houston, for the use of their data. This work was funded by the State of Texas through the Texas Commission of Environmental Quality, the Houston Advanced Research Center, and the Air Quality Research Program of the University of Texas. Funding was also provided by a National Science Foundation (NSF) Career Award (ATM-0348674).

References

1. Acker K, Möller D, Wieprecht W, Meixner F, Bohn B, Gilge S, Plass-Dulmer C, Berresheim H (2006) Strong daytime production of OH from HNO_2 at a rural mountain site. Geophys Res Lett 33:L02809. doi:10.1029/2005GL024643

2. Acker K, Febo A, Trick S, Perrino C, Bruno P, Wiesen P, Möller D, Wieprecht W, Auel R, Guisto M, Geyer A, Platt U, Allegrini I (2006) Nitrous acid in the urban area of Rome. Atmos Environ 40:3123–3133
3. Alicke B, Platt U, Stutz J (2002) Impact of nitrous acid photolysis on the total hydroxyl radical budget during the Limitation of Oxidant Production/Pianura Padana Produzione di Ozono study in Milan. J Geophys Res 107:8196. doi:10.1029/2000JD000075
4. Alicke B, Geyer A, Hofzumahaus A, Holland F, Konrad S, Pätz H-W, Schäfer J, Stutz J, Volz-Thomas A, Platt U (2003) OH formation by HONO photolysis during the BERLIOZ experiment. J Geophys Res 108:8247. doi:10.1029/2001JD000579
5. Aumont B, Chervier F, Laval S (2003) Contribution of HONO sources to the NO_x/HO_x/O_3 chemistry in the polluted boundary layer. Atmos Environ 37:487–498
6. Beine HJ, Dominé F, Simpson W, Honrath RE, Sparapani R, Zhou X, King M (2002) Snowpile and chamber experiments during the Polar Sunrise Experiment, Alert 2000: exploration of nitrogen chemistry. Atmos Environ 36:2707–2719
7. Bejan I, Abd El Aal Y, Barnes I, Benter T, Bohn B, Wiesen P, Kleffmann J (2006) The photolysis of ortho-nitrophenols: a new gas phase source of HONO. Phys Chem Chem Phys 8:2028–2035
8. Carr S, Heard D, Blitz M (2009) Comment on "Atmospheric hydroxyl radical production from electronically excited NO_2 and H_2O". Science 324:5925. doi:10.1126/science.1166669
9. Crowley J, Carl S (1997) OH formation in the photoexcitation of NO_2 beyond the dissociation threshold in the presence of water vapor. J Phys Chem A 101:4178–4184. doi:10.1021/jp970319e
10. Dibb JE, Arsenault M, Peterson MC, Honrath RE (2002) Fast nitrogen oxide photochemistry in Summit, Greenland snow. Atmos Environ 36:2501–2511
11. Elshorbany YF, Kurtenbach R, Wiesen P, Lissi E, Rubio M, Villena G, Gramsch E, Rickard AR, Pilling M, Kleffmann J (2009) Oxidation capacity of the city air of Santiago, Chile. Atmos Chem Phys 9:2257–2273. doi:10.5194/acp-9-2257-2009
12. Ensberg JJ, Carreras-Sospedra M, Dabdub D (2010) Impacts of electronically photo-excited NO_2 on air pollution in the South Coast Air Basin of California. Atmos Chem Phys 10:1171–1181. doi:10.5194/acp-10-11771-2010
13. Finlayson-Pitts BJ, Wingen LM, Sumner AL, Syomin D, Ramazan KA (2003) The heterogeneous hydrolysis of NO_2 in laboratory systems and in outdoor and indoor atmospheres: an integrated mechanism. Phys Chem Chem Phys 5:223–242
14. George C, Strekowski RS, Kleffmann J, Stemmler K, Ammann M (2005) Photoenhanced uptake of gaseous NO_2 on solid organic compounds: a photochemical source of HONO? Faraday Discuss 130:195–210
15. Häseler R, Brauers T, Holland F, Wahner A (2009) Development and application of a new mobile LOPAP instrument for the measurement of HONO altitude profiles in the planetary boundary layer. Atmos Meas Tech Discuss 2:2027–2054. doi:10.5194/amtd-2-2027-2009
16. He Y, Zhou X, Hou J, Gao H, Bertman S (2006) Importance of dew in controlling the air-surface exchange of HONO in rural forested environments. Geophys Res Lett 33:L02813. doi:10.1029/2005GL024348
17. Kleffmann J (2007) Daytime sources of nitrous acid (HONO) in the atmospheric boundary layer. Chem Phys Chem 8:1137–1144
18. Kleffmann J, Kurtenbach R, Lörzer J, Wiesen P, Kalthoff N, Vogel B, Vogel H (2003) Measured and simulated vertical profiles of nitrous acid – part I: field measurements. Atmos Environ 37:2949–2955
19. Kleffmann J, Gavriloaiei T, Hofzumahaus A, Holland F, Koppmann R, Rupp L, Schlosser E, Siese M, Wahner A (2005) Daytime formation of nitrous acid: a major source of OH radicals in a forest. Geophys Res Lett 32:L05818. doi:10.1029/2005GL022524
20. Kurtenbach R, Becker K, Gomes J, Kleffmann J, Lorzer J, Spittler M, Wiesen P, Ackermann R, Geyer A, Platt U (2001) Investigations of emissions and heterogeneous formation of HONO in a road traffic tunnel. Atmos Environ 35:3385–3394

21. Li S, Mattews J, Sinba A (2008) Atmospheric hydroxyl radical production from electronically excited NO_2 and H_2O. Science 319:1657–1660
22. Li G, Lei W, Zavala M, Volkamer R, Dusanter S, Stevens P, Molina LT (2010) Impacts of HONO sources on the photochemistry in Mexico City during the MCMA-2006/MILAGO Campaign. Atmos Chem Phys 10:6551–6567. doi:10.5194/acp-10-6551-2010
23. Mao J, Ren X, Chen S, Brune WH, Chen Z, Martinez M, Harder H, Lefer B, Rappenglück B, Flynn J, Leuchner M (2010) Atmospheric oxidation capacity in the summer of Houston 2006: comparison with summer measurements in other metropolitan studies. Atmos Environ 44:4107–4115. doi:10.1016/j.atmosenv.2009.01.013
24. Meller R, Moorgat GK (2000) Temperature dependence of absorption cross sections of formaldehyde between 223 and 323 K in the wavelength range 225–375 nm. J Geosphys Res 105:7089–7101
25. Pitts J, Biermann H, Winer A, Tuazon E (1984) Spectroscopic identification and measurement of gaseous nitrous-acid in dilute auto exhaust. Atmos Environ 18:847–854
26. Platt U, Stutz J (2008) Differential optical absorption spectroscopy: principles and applications. Springer, Berlin/Heidelberg, pp 1–597, doi:10.1007/978-3-540-75776-4
27. Ren X, Harder H, Martinez M, Lesher RL, Oliger A, Simpas JB, Brune WH, Schwab JJ, Demerjian KL, He Y, Zhou X, Gao H (2003) OH and HO_2 chemistry in the urban atmosphere of New York City. Atmos Environ 37:3639–3651
28. Ren X, Gao H, Zhou X, Crounse JD, Wennberg PO, Browne EC, LaFranchi BW, Cohen RC, McKay M, Goldstein AH, Mao J (2010) Measurement of atmospheric nitrous acid at Blodgett Forest during BEARPEX2007. Atmos Chem Phys 10:6283–6294. doi:10.5194/acp-10-6283-2010
29. Sörgel M, Trebs I, Serafimovich A, Moravek A, Held A, Zetzsch C (2011) Simultaneous HONO measurements in and above a forest canopy: influence of turbulent exchange on mixing ratio differences. Atmos Chem Phys 11:841–855. doi:10.5194/acp- 11-841-2011
30. Sörgel M, Regelin E, Bozem H, Diesch J-M, Drewnick F, Fischer H, Harder H, Held A, Hosaynali-Beygi Z, Martinez M, Zetzsch C (2011) Quantification of the unknown HONO daytime source and its relation to NO_2. Atmos Chem Phys 11:10433–10447. doi:10.5194/acp-11-10433-2011
31. Stemmler K, Ammann M, Donders C, Kleffmann J, George C (2006) Photosensitized reduction of nitrogen dioxide on humic acid as a source of nitrous acid. Nature 440:195–198. doi:10.1038/nature04603
32. Stemmler K, Ndour M, Elshorbany Y, Kleffmann J, D'Anna B, George C, Bohn B, Ammann M (2007) Light induced conversion of nitrogen dioxide into nitrous acid on submicron humic acid aerosol. Atmos Chem Phys 7:4237–4248. doi:10.5194/acp-7-4237-2007
33. Stutz J, Platt U (1997) Improving long-path differential optical absorption spectroscopy with a quartz-fiber mode mixer. Appl Opt 36:1105–1115
34. Stutz J, Kim E, Platt U, Bruno P, Perrino C, Febo A (2000) UV-visible absorption cross sections of nitrous acid. J Geophys Res 105:14585–14592
35. Stutz J, Alicke B, Ackermann R, Geyer A, Wang S, White A, Williams E, Spicer C, Fast J (2004) Relative humidity dependence of HONO chemistry in urban areas. J Geophys Res 109: D03307. doi:10.1029/2003JD004135, 2004
36. Stutz J, Oh H-J, Whitlow S, Anderson C, Dibb JE, Flynn J, Rappenglück B, Lefer B (2010) Simultaneous DOAS and mist-chamber IC measurements of HONO in Houston, TX. Atmos Environ 44:4090–4098. doi:10.1016/j.atmosenv.2009.02.003
37. Su H, Cheng Y, Oswald R, Behrendt T, Trebs I, Meixner F, Andreae M, Cheng P, Zhang Y, Pöschl U (2011) Soil nitrite as a source of atmospheric HONO and OH radicals. Science 333:1616–1618. doi:10.1126/science.1207687
38. Vandaele A, Hermans C, Fally S, Carleer M, Colin R, Merienne M, Jenouvrier A, Coquart B (2002) High-resolution Fourier transform measurement of the NO_2 visible and near-infrared absorption cross sections: temperature and pressure effects. J Geophys Res 107:4348. doi:10.1029/2001JD000971

39. Villena G, Kleffmann J, Kurtenbach R, Wiesen P, Lissi E, Rubio M, Croxatto G, Rappenglück B (2011) Vertical gradients of HONO, NO_x and O_3 in Santiago de Chile. Atmos Environ 45:3867–3873. doi:10.1016/j.atmosenv.2011.01.073
40. Voigt S, Orphal J, Bogumil K, Burrows JP (2001) The temperature dependence (203-293 K) of the absorption cross sections of O_3 in the 230-850 nm region measured by Fourier-transform spectroscopy. J Photochem Photobiol A 143:1–9
41. Wong KW, Oh H-J, Lefer BL, Rappenglück B, Stutz J (2011) Vertical profiles of nitrous acid in the nocturnal urban atmosphere of Houston, TX. Atmos Chem Phys 11:3595–3609. doi:10.5194/acp-11-3595-2011
42. Wong KW, Tsai C, Lefer B, Haman C, Grossberg N, Brune WH, Ren X, Luke W, Stutz J (2012) Daytime HONO vertical gradients during SHARP 2009 in Houston, TX. Atmos Chem Phys 12:635–652. doi:10.5194/acp-12-635-2012
43. Zhang N, Zhou X, Shepson PB, Gao H, Alaghmand M, Stirm B (2009) Aircraft measurements of HONO vertical profiles over a forested region. Geophys Res Lett 36:L15820. doi:10.1029/2009GL038999
44. Zhou X, Beine HJ, Honrath RE, Fuentes JD, Simpson W, Shepson PB, Bottenheim J (2001) Snowpack photochemical production as a source for HONO in the Arctic boundary layer in springtime. Geophys Res Lett 28:4087–4090
45. Zhou X, He Y, Huang G, Thornberry TD, Carroll MA, Bertman SB (2002) Photochemical production of nitrous acid on glass sample manifold surface. Geophys Res Lett 29:1681. doi:10.1029/2002GL015080
46. Zhou X, Gao H, He Y, Huang G, Bertman SB, Civerolo K, Schwab J (2003) Nitric acid photolysis on surfaces in low-NO_x environments: significant atmospheric implications. Geophys Res Lett 30:2217. doi:10.1029/2003GL018620
47. Zhou X, Huang G, Civerolo K, Royxgowdhury U, Demerjian KL (2007) Summertime observations of HONO, HCHO, and O_3 at the summit of Whiteface Mountain, New York. J Geophys Res 112:D08311. doi:10.1029/2006JD007256
48. Zhou X, Zhang N, TerAvest M, Tang D, Hou J, Bertman S, Alaghmand M, Shepson PA, Carroll MA, Griffith S, Dusanter S, Stevens P (2011) Nitric acid photolysis on forest canopy surface as a source for tropospheric nitrous acid. Nat Geosci 4:440–443. doi:10.1038/NGEO1164

Chapter 2
NO_2 Measurement Techniques: Pitfalls and New Developments

Jörg Kleffmann, Guillermo Villena Tapia, Iustinian Bejan, Ralf Kurtenbach, and Peter Wiesen

Abstract Reliable measurements of atmospheric trace gases are necessary for both, a better understanding of the chemical processes occurring in the atmosphere, and for the validation of model predictions. Nitrogen dioxide (NO_2) is a toxic gas and is thus a regulated air pollutant. Besides, it is of major importance for the oxidation capacity of the atmosphere and plays a pivotal role in the formation of ozone and acid precipitation. Detection of NO_2 is a difficult task since many of the different commercial techniques used are affected by interferences. The chemiluminescence instruments that are used for indirect NO_2 detection in monitoring networks and smog chambers use either molybdenum or photolytic converters and are affected by either positive (NO_y) or negative interferences (radical formation in the photolytic converter). Erroneous conclusions on NO_2 can be drawn if these interferences are not taken into consideration. In the present study, NO_2 measurements in the urban atmosphere, in a road traffic tunnel and in a smog-chamber using different commercial techniques, i.e. chemiluminescence instruments with molybdenum or photolytic converters, a luminol based instrument and a new NO_2-LOPAP, were compared with spectroscopic techniques, i.e. DOAS and FTIR. Interferences of the different instruments observed during atmospheric measurements were partly characterised in more detail in the smog chamber experiments. Whereas all the commercial instruments showed strong interferences, excellent agreement was obtained between a new NO_2-LOPAP instrument and the FTIR technique for the measurements performed in the smog chamber.

Keywords Nitrogen dioxide • Chemiluminescence • Luminol • LOPAP

J. Kleffmann (✉) • G.V. Tapia • I. Bejan • R. Kurtenbach • P. Wiesen
Physikalische Chemie, Bergische Universität Wuppertal, Gauss Strasse 20, Wuppertal 42119, Germany
e-mail: kleffman@uni-wuppertal.de

I. Barnes and K.J. Rudziński (eds.), *Disposal of Dangerous Chemicals in Urban Areas and Mega Cities*, NATO Science for Peace and Security Series C: Environmental Security,
DOI 10.1007/978-94-007-5034-0_2,

2.1 Introduction

Despite their relatively low concentration, nitrogen oxides ($NO_x = NO + NO_2$) play a crucial role in tropospheric chemistry. NO_2 affects the oxidation capacity of the atmosphere through its direct participation in the formation of ozone (O_3) and nitrous acid (HONO), which through their photolysis, are major sources of the OH radical, the detergent of the atmosphere. In addition, by its reaction with the OH radical, NO_2 also limits radical concentrations in the polluted atmosphere. NO_2 contributes to acid precipitation and formation of other atmospheric oxidants such as the nitrate radical (NO_3) [2, 7, 18].

Many direct or indirect techniques have been developed for measuring NO_2 in the laboratory and/or in the field. Spectroscopic methods, for example, Differential Optical Absorption Spectroscopy (DOAS), Laser Induced Fluorescence (LIF), Cavity Ring Down Spectroscopy (CRDS) and Resonance Enhanced MultiPhoton Ionisation (REMPI), have been used for selective NO_2 detection ([19] and references therein). Although some of the methods have very low detections limits (e.g. REMPI, LIF), most techniques require considerable operational expertise, are expensive and have complex system components.

Thus, the most widely used technique, and at the same time the reference method recommended by the US EPA [3] and by European legislation [5] for the measurement of NO_2 in monitoring networks is the chemiluminescence technique. This method involves the reduction of NO_2 to NO using heated (300–350 °C) molybdenum (Mo) surfaces:

$$Mo + 3\ NO_2 \rightarrow MoO_3 + 3\ NO, \tag{2.R1}$$

followed by the gas-phase reaction between NO and O_3 (2.R2) forming an electronically excited NO_2^* molecule that emits light (2.R3), which is proportional to the NO concentration [8, 14].

$$NO + O_3 \rightarrow NO_2^* + O_2 \tag{2.R2}$$

$$NO_2^* \rightarrow NO_2 + h\nu \tag{2.R3}$$

Photolytic conversion of NO_2 to NO (2.R4), using either Xenon lamps or UV emitting diodes ("blue light converters"), followed by detection of the chemiluminescence from the reaction of NO with O_3 are also used (2.R3) [12, 15, 16]:

$$NO_2 + h\nu \rightarrow NO + O(^3P). \tag{2.R4}$$

Another commonly used technique is the luminol-chemiluminescence method, which employs the reaction between NO_2 and an alkaline solution of luminol resulting in light emission [21].

In the present study, the performances of different commercial NO_2 instruments and a new NO_2-LOPAP (Long Path Absorption Photometer; [19]) were intercompared

with those of spectroscopic techniques using measurements made in the urban atmosphere, in a road traffic tunnel and in a smog chamber in order to better understand the sources and nature of the interferences affecting the different methods typically employed.

2.2 Experimental

2.2.1 Chemiluminescence Instrument with Molybdenum Converter/(Mo-CLD)

During an intercomparison in Santiago de Chile a TELEDYNE model 200 E (hereafter: *TELEDYNE Mo*), and in a street canyon campaign in Wuppertal (Germany) an Ansyco AC31M (hereafter: *Ansyco Mo*) were used, both with molybdenum converters. Details of the instruments are explained elsewhere [20].

2.2.2 Photolytic Conversion/Chemiluminescence Detection (PC-CLD)

The ECO Physics "CLD 770 Al ppt" (hereafter: *ECO*) detects NO_2 using a photolytic converter (PLC 760) operated with a Xenon lamp (300 W, 320–420 nm, 2.R4) and is explained elsewhere [20]. In the Ansyco AC31M (hereafter: *Ansyco blue light*) a homemade "blue light converter" (6 UV LEDs, 395 $\pm$ 10 nm, converter efficiency of 52%) is used for NO_2 conversion (see [20]).

2.2.3 LMA3D

In the Unisearch LMA 3D instrument (hereafter: *Luminol*) NO_2 is detected by using a specially formulated luminol (5-amino-2,3-dihydro-1,4-phthalazinedione) solution. Details are explained elsewhere [20].

2.2.4 NO_2-LOPAP Instrument

The NO_2-LOPAP instrument (hereafter: *LOPAP*) was recently developed at the University of Wuppertal in co-operation with QUMA Elektronik and Analytik GmbH. The instrument is based on the light absorption of an azodye formed by the Saltzman reaction [17]. The instrument is described in detail elsewhere [19].

2.3 Results

2.3.1 Intercomparison in the Urban Atmosphere

Figure 2.1a shows the campaign averaged diurnal profiles of NO_2 obtained by DOAS and a chemiluminescence instrument with molybdenum converter (TELEDYNE Mo) from a 2-week field campaign in 2005 in Santiago de Chile [4]. There is a clear difference between the results from both instruments with lower concentrations of the DOAS compared to the chemiluminescence instrument. While during the night, both data sets differ by only ~5–10 ppbv, the TELEDYNE Mo shows positive interferences of up to ~25 ppbv during daytime. On a relative basis, the chemiluminescence instrument overestimates NO_2 by up to a factor of four during daytime (see Fig. 2.1a) using the average campaign data. Interestingly, the positive interferences of the TELEDYNE Mo correlate quite well with the concentration of ozone (see Fig. 2.1b). Ozone may be used as an indicator for the photo-chemical activity of the atmosphere. Since most interfering NO_y species, such as nitric acid (HNO_3), peroxyacetyl nitrate (PAN), and organic nitrates ($RONO_2$), are photo-chemically formed during daytime the observed differences are due to NO_y interferences of the chemiluminescence instrument. Even after subtraction of the interferences due to PAN and HONO, significant, not quantified NO_y-interferences, which correlated well with the concentration of ozone, were observed (see Fig. 2.1b).

2.3.2 Intercomparison in a Road Traffic Tunnel

Figure 2.2 shows the diurnal variation of NO and NO_2 concentrations in the Kiesberg tunnel during a campaign in 1999 [13], in which a chemiluminescence instrument with photolytic NO_2 converter (ECO) was compared with a DOAS instrument. Both NO_2 data sets exhibit excellent agreement for measurements at low pollution levels during night-time (see Fig. 2.2 0:00–4:00 LT). However, with the onset of elevated volumes of traffic through the tunnel, the NO_2 measurements of the ECO instrument exhibited strong negative interferences. Remarkable are the artificial negative concentrations measured by the ECO Physics instrument during the early night at high pollution levels as indicated by the high NO concentrations also shown in Fig. 2.2. The reasons for the negative NO_2 concentrations were completely unclear at that time, but had been also observed in laboratory studies [1, 10]. It was only later that experiments in a smog chamber (see below) gave some insight as to the reasons for this phenomenon. High exhaust gas levels, which contain large quantities of photo-labile VOCs, e.g. carbonyls, cause the formation of peroxy radicals (HO_2, RO_2) in the photolytic converter, which reduce NO only in the NO_x channel of the instrument. In the tunnel, the NO_x level results almost exclusively from local direct vehicle emissions, which contain high quantities of NO (typically >90% at that time). Thus, when more NO is reacting with peroxy radicals in the photolytic converter compared to the low NO_2 present in the sample,

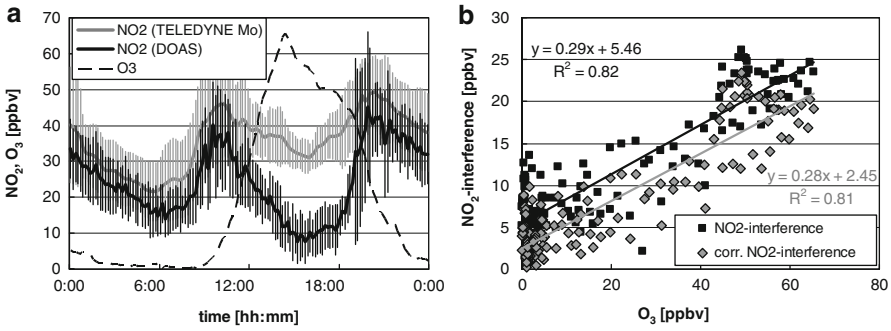

Fig. 2.1 (**a**) Campaign averaged NO_2 and O_3 diurnal profiles in Santiago de Chile, 2005 [4]. The spectroscopic DOAS technique was used as a reference in this campaign. (**b**) Correlation of the NO_2-interference of the chemiluminescence instrument (i.e. difference TELEDYNE-Mo – DOAS) with the ozone concentration. In addition, the NO_2-interference, which was corrected for the HONO and PAN interferences of the chemiluminescence instrument, is also shown ("corr. NO_2-interference")

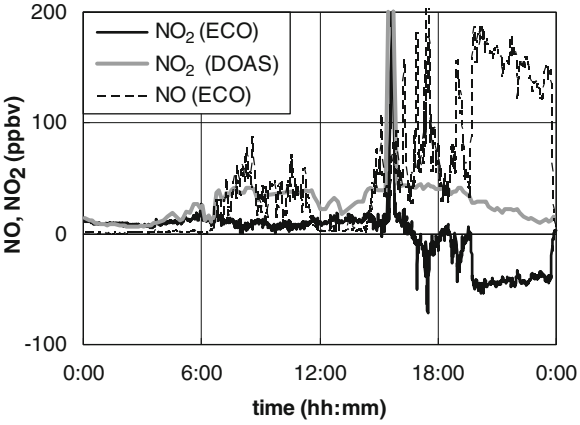

Fig. 2.2 NO and NO_2 diurnal profiles measured with DOAS and ECO instruments in a tunnel study [13]. The spectroscopic DOAS technique was used as a reference for NO_2 in this campaign

the NO level in the NO_x channel is lower than the NO level actually in the sample, and artificial negative concentrations result. Since these interferences, which are explained in more detail below, are caused by highly non-linear reactions, these interferences cannot be corrected. Thus, only the DOAS NO_2 data was used in the 1999 campaign [13]. Based on these results, chemiluminescence instruments with photolytic converter should not be used for studies at high pollution level, i.e. in the polluted urban atmosphere and in smog-chambers (see below).

2.3.3 Intercomparison in a Street Canyon

To demonstrate, that the negative interferences observed for photolytic converters can also be of importance in the open urban atmosphere, two chemiluminescence

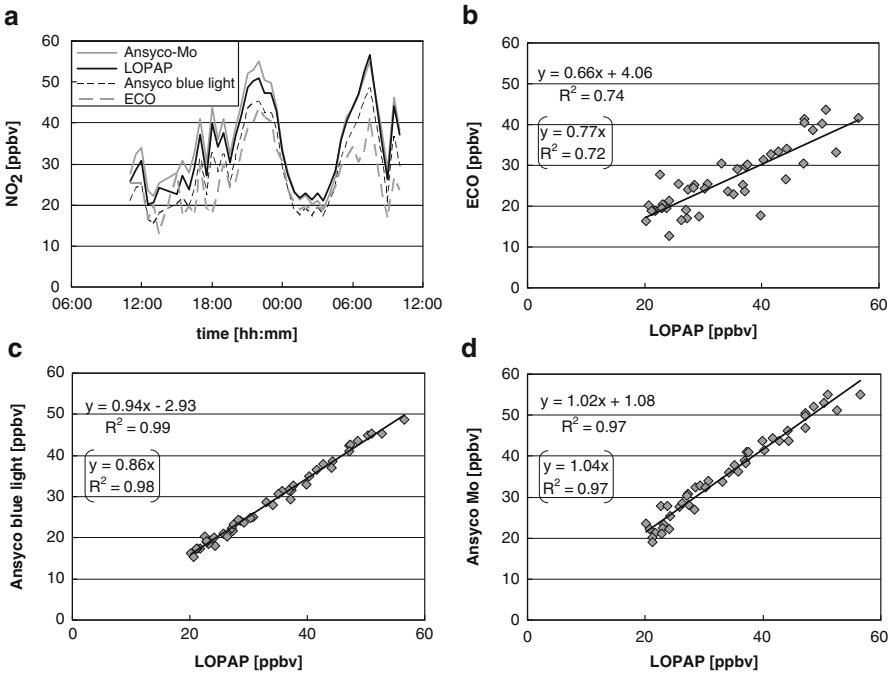

Fig. 2.3 (**a**) NO_2 concentrations measured by different instruments in a street canyon; (**b–d**) correlation plots of the different chemiluminescence instruments against the LOPAP data, which was used as reference here (see text). For the correlation equations given in brackets the intercept was forced to zero

instruments (ECO and Ansyco blue light) were compared with the LOPAP instrument in a street canyon in Wuppertal for 2 days [20]. In addition, this intercomparison was also aimed to quantify typical positive interferences of the molybdenum converter instrument (Ansyco Mo) which is routinely used at that site. The LOPAP instrument was used as reference caused by the excellent agreement with the FTIR technique under complex conditions in a smog chamber, for which the other instruments showed strong interferences (see Sect. 3.4). All instruments were calibrated by the same calibration mixtures to ensure that the differences observed were only caused by interferences and the precision errors.

For the early night and during the morning rush hour, higher NO_2 levels were observed (see Fig. 2.3a), for which the differences between the instruments were largest. In contrast, during late night-time when the NO_2 levels were lower, better agreement was obtained. For more quantitative evaluation the 30 min average data of all chemiluminescence instruments were plotted against the corresponding LOPAP data. As expected, both instruments with photolytic converters showed smaller NO_2 levels compared to the LOPAP, which was more distinct for the ECO Physics with Xenon lamp converter (ca. 30% deviation) compared to the Ansyco with blue light converter (ca. 10% deviation, see Fig. 2.3b, c). While the correlation

of Ansyco to the LOPAP was excellent ($r^2 = 0.99$), a lower correlation was observed for the ECO Physics ($r^2 = 0.72$), which is caused by the one channel design of this instrument, for which fast variations of the trace gas levels lead to artificial noise. The higher negative interferences of the ECO Physics are explained by the broader spectral range of the Xenon lamp converter compared to the blue light converter, for which much more photo-labile species will form interfering peroxy radicals (for details, see Sect. 3.4). Thus, although the extent of the negative interferences of the photolytic converters was much lower compared to the tunnel measurements and no negative NO_2 data was obtained, the NO_2 concentration was still significantly underestimated in the open atmosphere.

In contrast, for the chemiluminescence instrument with molybdenum converter (Ansyco Mo) slightly higher concentrations compared to the LOPAP were observed (see Fig. 2.3d). However, the small differences of ca. 3% were close to the precision errors of both instruments. Such small differences can only be explained by the absence of significant NO_y species, which is in contrast to the results from Santiago de Chile. However, since the measurements in the street canyon were close to the main NO_x emission source, it can be expected that only emitted NO_y species play an important role here. In contrast, the data shown in Sect. 3.1 was collected at an urban background site on the open campus of the University of Santiago de Chile, for which secondary photochemical formation of NO_y species is more important, also with respect to the much higher photochemical activity in Santiago de Chile compared to Germany. The slightly higher NO_2 levels from the chemiluminescence instrument compared to the LOPAP can be well explained by NO_y emissions from vehicles, for which mainly nitrous acid (HONO) is expected. Since the typical emission ratio of HONO is ~1% of NO_x [13], and since the average NO_x concentration was ca. two times higher than NO_2 during the intercomparison, a positive interferences by HONO of only ~2% is expected for the molybdenum converter instrument.

The results from the street canyon show that chemiluminescence instruments with molybdenum converters can provide even more accurate NO_2 data compared to instruments with photolytic converters under certain condition, i.e. for measurements close to emission sources, e.g. in kerbside or tunnel studies. For example, if only two chemiluminescence instruments with molybdenum and photolytic converter were used in the street canyon (e.g. ECO and Ansyco Mo), the differences would have been explained by the well known interferences from the molybdenum converter and not by the yet unknown but more important negative interferences of photolytic converters.

2.3.4 Intercomparison in a Smog Chamber

To better understand the negative interferences mentioned above and to validate the recently developed NO_2-LOPAP instrument, an intercomparison campaign with four NO_2 analysers (ECO, Ansyco blue-light, Luminol, LOPAP) and the FTIR technique was conducted under complex photo-smog conditions in a 1080 *l* smog

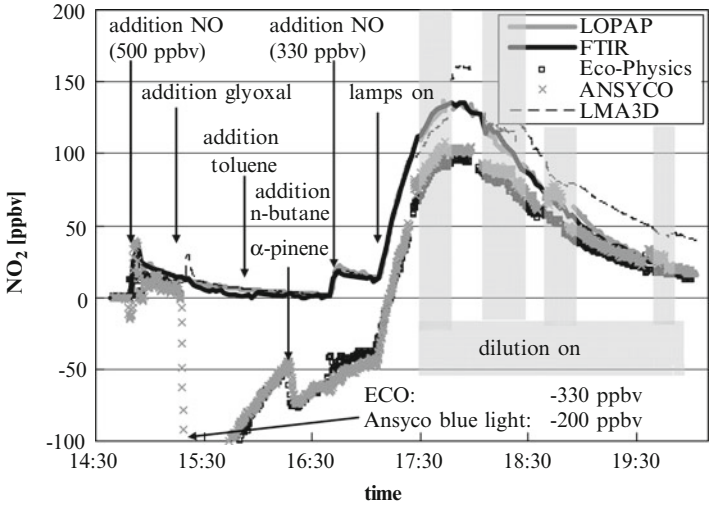

Fig. 2.4 Intercomparison of three commercial NO_2 instruments and the new NO_2-LOPAP instrument with FTIR spectrometry during a complex photo-smog experiment. The *grey shaded* area indicate the periods, when the sample air of all the external instruments was diluted with synthetic air by factors of between 1.2 and 3.5, which was considered for the concentration calculations

chamber [20]. The spectroscopic FTIR technique was used as a reference in these measurements, since sampling artefacts can be ruled out for this non-intrusive method. Details of this campaign are explained elsewhere [20].

An example of a photo-smog experiment is shown in Fig. 2.4, in which a complex volatile organic compound (VOC)/NO_x mixture was irradiated with UV/VIS light. In the experiment, NO (500 ppbv) with ~6% impurities of NO_2, glyoxal (1.1 ppmv), toluene (0.64 ppmv), *n*-butane (0.56 ppmv) and α-pinene (0.43 ppmv) were introduced sequentially into a dark chamber. Before the lamps were switched on, a second NO injection (330 ppbv) was made to compensate for the dilution of the mixture caused by the sample flow to the external instruments. The radical initiated degradation of the VOCs leads to the formation of O_3 and peroxy radicals (HO_2, RO_2), and further reaction with NO results in increasing levels of NO_2 in this photo-smog mixture. When the reaction mixture was irradiated, the sample flow to all the external instruments was diluted by accurately known factors, of between 1.2 and 3.5, for certain periods to check for the linearity of the interferences affecting the different instruments (see grey shaded area in Fig. 2.4). Theoretically, the concentrations calculated in the smog chamber should not depend on the dilution ratio, when corrected for. In contrast to the external instruments, the FTIR measurements were not affected by the dilution tests. Since hundreds of products including potential interfering photo-oxidants, like PAN, are formed during the irradiation, this complex photo-smog experiment is a good test to validate a new instrument under conditions that are even more complex and with higher pollution levels compared to the atmosphere.

Whereas excellent agreement was obtained between the NO_2 measurements made with the LOPAP and FTIR techniques, substantial deviations were observed for the other NO_2 instruments used (Fig. 2.4). For the luminol instrument lower NO_2 concentrations could be initially observed when adding high (500 ppbv) NO concentrations (Fig. 2.4, first addition of NO). This is due to the quenching of the chemiluminescence of the luminol by NO, which decreases the sensitivity of the instrument [11]. This phenomenon was also observed for high concentrations of nitroaromatic species in another recent study [1]. Since the quenching efficiency of different trace gases is not well known, the luminol technique should not be used for smog-chamber experiments, at least when ppmv levels of trace gases are used.

Deviations also arose for the luminol instrument in comparison with the FTIR during the photo-smog period. In contrast to the Ansyco blue light and ECO instruments, the luminol technique suffered from positive interferences during the course of the photo-smog experiment, which may be explained by photo-chemical formation of ozone and different PAN (peroxyacylnitrates) like species [6]. Under the very alkaline sampling conditions prevailing in the luminol instrument, it is well known that PAN and other peroxyacylnitrates decompose [9]. The observed positive interferences of the luminol technique showed a clear non-linear behaviour, which decreased with increasing dilution of the sample (see Fig. 2.4, dilution on). In contrast, for interferences, which increase linearly with the concentration of the interfering species, the dilution tests should not affect the calculated concentrations in the chamber.

For both of the chemiluminescence instruments with photolytic converters (ECO and Ansyco blue light) strong negative interferences were observed when adding glyoxal to the chamber. As in the tunnel study mentioned before, artificial negative concentrations were registered for the ECO and Ansyco blue light instruments reaching −330 and −200 ppbv, respectively (see Fig. 2.4). To understand these negative interferences the photo-chemistry of glyoxal has to be considered, which produces formyl radicals (HCO) at wavelengths <420 nm:

$$(HCO)_2 + h\nu \rightarrow 2HCO, \tag{2.R5}$$

which further react with molecular oxygen leading to the formation of HO_2 radicals:

$$HCO + O_2 \rightarrow HO_2 + CO. \tag{2.R6}$$

It is well known that peroxy radicals (HO_2, RO_2) efficiently convert NO into NO_2:

$$HO_2(RO_2) + NO \rightarrow OH\ (RO) + NO_2. \tag{2.R7}$$

For the high glyoxal concentrations used, the NO concentration in the NO_x channels of both instruments is significantly reduced via reaction (2.R7). The apparent negative concentrations can be explained with the low NO_2/NO_x ratio at the beginning of the experiment and the high loss of NO through reaction (2.R7). This results in the measured NO concentration without converter (NO channel) being greater than that with converter (NO_x channel).

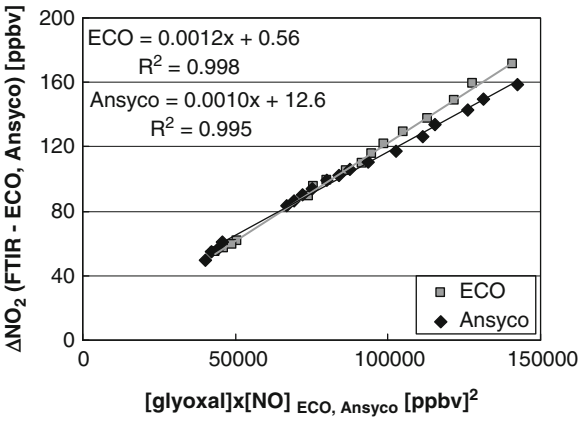

Fig. 2.5 Correlation of the negative interferences of the ECO Physics and the Ansyco blue light against the product [glyoxal] × [NO]

To confirm the explanation of the negative interferences observed in the photo-smog experiment, the deviation of both instruments compared to the FTIR data during the dark period was plotted against the product of [NO] × [glyoxal] (see Fig. 2.5). Highly linear correlations were obtained for both chemiluminescence instruments. Reactions (2.R5) and (2.R6) follow first-order and pseudo first-order kinetics, respectively. In addition, HO_2 self reactions are no of significant importance caused by the high NO levels present. Thus, it can be expected that the HO_2 concentration in the converter will scale linearly with glyoxal. In this case the negative interference, which is explained here by NO loss through reaction (2.R7), follows second order kinetics and will be proportional to [NO] × [HO_2] and [NO] × [glyoxal], as observed (see Fig. 2.5). As a consequence of these non-linear negative interferences, the NO_2 level given by both instruments was not observed to increase during the second addition of NO at ~16:50 local time (LT) (see Fig. 2.4), in contrast to the other instruments, for which the impurities of NO_2 in the NO could be correctly quantified. This is caused by the increasing NO level leading to increasing negative interferences by reaction (2.R7), which compensates the increased NO_2 level in the chamber.

Another interesting feature of the intercomparison was the enhancement of the negative interferences of both chemiluminescence instruments after the addition of *n*-butane and α-pinene (see Fig. 2.4). Both VOCs do not photolyse in the spectral range of both photolytic converters and thus, will themselves not form the peroxy radicals necessary to convert NO by reaction (2.R7). However, since OH radicals are formed from glyoxal photolysis via reactions (2.R5, 2.R6, and 2.R7), peroxy radicals (RO_2) will be formed by the OH initiated degradation of *n*-butane and α-pinene ("R-H"):

$$R - H + OH \rightarrow R + H_2O, \tag{2.R8}$$

$$R + O_2 \rightarrow RO_2. \tag{2.R9}$$

The RO_2 radicals will further reduce the NO level in the photolytic converter by reaction (2.R7). Hence, photo-induced radical chemistry, well known from atmospheric chemistry textbooks, takes place in the photolytic converters, depending on the admitted VOCs, so that NO_2 data using these instruments are inaccurate for highly polluted conditions such as can prevail in street canyons, tunnels and smog chambers. However, because of the second order reaction kinetics, these negative interferences are not expected to be of significant importance in the less polluted atmosphere (see for example, Fig. 2.2, 0:00–4:00 LT, and [19]).

During the course of the experiment a continuous reduction of the negative interferences of the chemiluminescence instruments with photolytic converter (Ansyco blue light und ECO) was observed. This is due to the continuous dilution of the reaction mixture which results from the addition of synthetic air to replenish the gas sample flow to the external instruments and the second order reaction kinetics of the interferences (see above). The non-linear behaviour of these interferences was also reflected by the data in instances where the reaction mixture was diluted for the external instruments leading to decreases in the interferences (see Fig. 2.4, Ansyco blue light and ECO: dilution on).

Generally, negative interferences were larger for the ECO compared to the Ansyco blue light instrument. This can be explained by the broader spectral range (290–420 nm) of the Xenon lamp used in the photolytic converter of the ECO instrument compared to the blue light converter ($\lambda_{max} = 395 \pm 10$ nm), which is optimised for the photolysis of only NO_2. In addition, the residence time in the blue-light converter is much shorter compared to the Xenon lamp converter. Thus, in the case of the ECO instrument, more photons are absorbed by glyoxal in the photolytic converter leading to higher radical yields. In addition, caused by the different spectral range applied, it can be expected that in the atmosphere, photolysis of more photo-labile species will lead to larger radical production in a photolytic converter containing a Xenon lamp compared to one using a blue light converter, which was confirmed by the results from the study in the street canyon (see Sect. 3.3). Thus, if photolytic converters are used for the chemiluminescence technique, it is recommended to use blue light converters, although these instruments will still suffer from negative interferences for high pollution levels (see Figs. 2.3 and 2.4).

In contrast to the chemiluminescence instruments the LOPAP instrument showed excellent agreement with the FTIR technique (see Fig. 2.4) with an average deviation of 4% (see Fig. 2.6). Lower concentrations were observed for the FTIR technique compared to the LOPAP instrument only while adding glyoxal (Fig. 2.4). However, since glyoxal does not react with NO_2 in the dark and since the LOPAP signal remained unchanged in the presence of glyoxal, this difference can be explained by optical interference of the FTIR instrument resulting from the overlap of absorption bands from glyoxal and NO_2. These interferences accounted for max. Five ppbv, which is close to the precision of the FTIR instrument. In addition, the optical interference decreased with time because of the continuous dilution of the reaction mixture and thus, did not influence the accuracy of the FTIR during the photo-smog phase of the experiment.

In addition to the general good agreement with the FTIR technique, no changes of the corrected measurement signal of the LOPAP instrument occurred during the

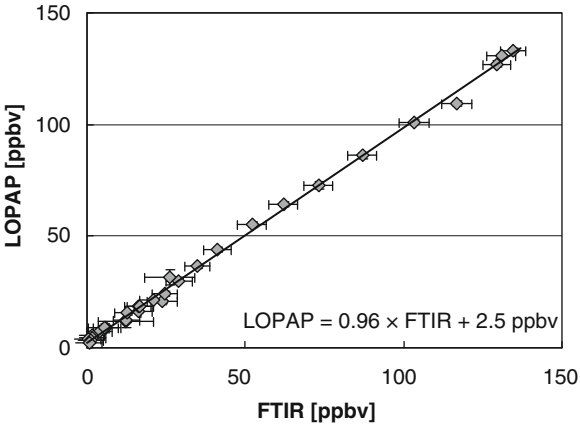

Fig. 2.6 Correlation of all LOPAP and FTIR NO_2 data during the complex photo-smog experiment, shown in Fig. 2.4. The error bars only represent the precision of both instruments

dilution tests. Accordingly, significant interference can be excluded for the LOPAP instrument even for this very complex reaction mixture. Furthermore, since no interferences were observed in channel 2 of the instrument neither during the smog-chamber experiments, nor in the atmosphere [19], an even simpler one-channel set-up could be used in the future. In conclusion, the new LOPAP is not only suitable for atmospheric applications [19] but also for complex smog-chamber experiments, for which chemiluminescence instruments have severe problems.

2.4 Atmospheric Implication

In the present study, commercial NO_2 chemiluminescence instruments have shown strong interferences compared to spectroscopic techniques under certain conditions. Accordingly, if data from these instruments are used, e.g. in chemical models, model-measurement deviation may be also caused by the uncertainties in the NO_2 measurement data. Therefore, critical evaluation of the data from each type of NO_2 instrument for any measurement condition is required. For example, at urban kerbside stations for which chemiluminescence instruments are generally used, the NO_2 level may be strongly underestimated if instruments with photolytic converters are used, whereas it will be overestimated for those using molybdenum converters. Whereas the positive interferences of molybdenum converters by NO_y species are a well known problem, the negative interferences of photolytic converters have not yet been discussed in the literature in detail. If an intercomparison of these two types of instruments is carried out under heavily polluted atmospheric conditions; one might argue that instruments with photolytic converter would provide better data than those with molybdenum converter. However, under these conditions, the negative deviations of the photolytic converters can be even much stronger than the positive interferences by the NO_y species for the molybdenum converters (see Sect. 3.3).

On the other hand, for urban background, rural or remote measurement stations the NO_y and PAN fractions can be significant compared to the NO_2 level, for which the luminol technique and the chemiluminescence instruments with molybdenum converters would be more affected. Thus, the use of selective NO_2 instruments, like for example DOAS, LIF, cavity ring down or the new NO_2-LOPAP technique, are recommended for the detection of NO_2 in the atmosphere.

2.5 Conclusions

In the present study, NO_2 measurements performed with different techniques, i.e. chemiluminescence instruments with molybdenum or photolytic converters, a luminol based instrument and a new NO_2-LOPAP were compared with spectroscopic techniques, i.e. DOAS and FTIR, in the urban atmosphere, a road traffic tunnel and a smog-chamber. Strong positive interferences for a chemiluminescence instrument with molybdenum converter were observed under typical photo-smog conditions in the urban atmosphere of Santiago de Chile. This has been explained by interferences caused by photochemically formed NO_y species, leading to an overestimation of daytime NO_2 levels by up to a factor of four. In contrast, strong negative interferences, even with artificial negative NO_2 concentrations, were observed for a chemiluminescence instrument with photolytic converter in a road traffic tunnel. These interferences are explained by the photolysis of VOCs in the photolytic converter and consecutive peroxy radical reactions with NO. This was confirmed by smog-chamber experiments, where the addition of glyoxal also resulted in strong negative interferences. Under heavily polluted conditions close to emission sources, these negative interferences can be even more important compared to the positive NO_y interferences of molybdenum converter instruments. Whereas all the commercial instruments showed strong deviations compared to the spectroscopic FTIR technique in the smog chamber, excellent agreement between a new NO_2-LOPAP instrument and the FTIR technique was obtained. Since the NO_2-LOPAP instrument is in addition much more sensitive (DL = 2 pptv) compared to commercial chemiluminescence instruments, its use is recommended for the simple, sensitive and selective detection of NO_2 in the atmosphere.

Acknowledgement The authors would like to thank the German Environment Foundation (Deutsche Bundesstiftung Umwelt – DBU, Contract No. 24171) for financial and QUMA Elektronik and Analytik GmbH, Wuppertal, Germany, for continuous technical support during the development of the NO_2-LOPAP instrument.

References

1. Bejan I, Abd El Aal Y, Barnes I, Benter T, Bohn B, Wiesen P, Kleffmann J (2006) The photolysis of ortho-nitrophenols: a new gas phase source of HONO. Phys Chem Chem Phys 8:2028–2035
2. Crutzen PJ (1979) The role of NO and NO_2 in the chemistry of the troposphere and stratosphere. Annu Rev Earth Planet Sci 7:443–472
3. Demerjian KL (2000) A review of national monitoring networks in North America. Atmos Environ 34:1861–1884
4. Elshorbany YF, Kurtenbach R, Wiesen P, Lissi E, Rubio M, Villena G, Gramsch E, Rickard AR, Pilling MJ, Kleffmann J (2009) Oxidation capacity of the city air of Santiago, Chile. Atmos Chem Phys 9:2257–2273
5. European Standard, EN 14211 (2005) Ambient air quality – standard method for the measurement of the concentration of nitrogen dioxide and nitrogen monoxide by chemiluminescence, VDI/DIN-Handbuch Reinhaltung der Luft im VDI und DIN-Normenausschluss KRdL, 2005
6. Fehsenfeld FC, Drummond JW, Roychowdhury UK, Galvin PJ, Williams EJ, Buhr MP, Parrish DD, Hübler G, Langford AO, Calvert JG, Ridley BA, Grahek F, Heikes BG, Kok GL, Shetter JD, Walega JG, Elsworth CM, Norton RB, Fahey DW, Murphy PC, Hovermale C, Mohnen VA, Demerjian KL, Mackay GI, Schiff HI (1990) Intercomparison of NO_2 measurement techniques. J Geophys Res 95(D4):3579–3597
7. Finlayson-Pitts BJ, Pitts JN Jr (2000) Chemistry of the upper and lower atmosphere: theory, experiments and applications. Academic, New York
8. Fontjin A, Sabadell AJ, Ronco RJ (1970) Homogeneous chemiluminescence measurement of nitric oxide with ozone. Anal Chem 42:575–579
9. Frenzel A, Kutsuna S, Takeuchi K, Ibusuki T (2000) Solubility and reactivity of peroxyacetyl nitrate (PAN) in dilute aqueous solutions and in sulphuric acid. Atmos Environ 34:3641–3644
10. Kleffmann J, Heland J, Kurtenbach R, Lörzer JC, Wiesen P, Ammann M, Gutzwiller L, Rodenas García M, Pons M, Wirtz K, Scheer V, Vogt R (2001) HONO emissions from a diesel engine. In: Proceedings of the 94th annual conference and exhibition of the Journal of the Air & Waste Management Association, paper 239
11. Kleffmann J, Benter T, Wiesen P (2004) Heterogeneous reaction of nitric acid with nitric oxide on glass surfaces under simulated atmospheric conditions. J Phys Chem A 108:5793–5799
12. Kley D, McFarland M (1980) Chemiluminescence detector for NO and NO_2. Atmos Tech 12:63–69
13. Kurtenbach R, Becker KH, Gomes JAG, Kleffmann J, Lörzer JC, Spittler M, Wiesen P, Ackermann R, Geyer A, Platt U (2001) Investigation of emissions and heterogeneous formation of HONO in a road traffic tunnel. Atmos Environ 35:3385–3394
14. Ridley BA, Howlett LC (1974) An instrument for nitric oxide measurements in the stratosphere. Rev Sci Instrum 45:742–746
15. Ryerson TB, Williams EJ, Fehsenfeld FC (2000) An efficient photolysis system for fast-response NO_2 measurements. J Geophys Res 105:26447–26461
16. Sadanaga Y, Fukumori Y, Kobashi T, Nagata M, Takenaka N, Bandow H (2010) Development of a selective light-emitting diode photolytic NO_2 converter for continuously measuring NO_2 in the atmosphere. Anal Chem 82:9234–9239
17. Saltzman BE (1954) Colorimetric microdetermination of nitrogen dioxide in the atmosphere. Anal Chem 26:1949–1955
18. Seinfeld JH, Pandis SN (2006) Atmospheric chemistry and physics: from air pollution to climate change, 2nd edn. Wiley, Hoboken
19. Villena G, Bejan I, Kurtenbach R, Wiesen P, Kleffmann J (2011) Development of a new long path absorption photometer (LOPAP) instrument for the sensitive detection of NO_2 in the atmosphere. Atmos Meas Tech 4:1663–1676
20. Villena G, Bejan I, Kurtenbach R, Wiesen P, Kleffmann J (2012) Interferences of commercial NO_2 instruments in the urban atmosphere and in a smog-chamber. Atmos Meas Tech 5:149–159
21. Wendel GJ, Stedman DH, Cantrell CA (1983) Luminol-based nitrogen dioxide detector. Anal Chem 55:937–940

Chapter 3
An Overview of Measurement Techniques for Atmospheric Nitrous Acid

Xianliang Zhou

Abstract An overview is given of all the spectroscopic and wet chemical used for atmospheric measurements of nitrous acid. The measurement precision and difficulties associated with the techniques are discussed.

Keywords Nitrous Acid • HONO • Techniques • Measurement • Atmosphere

3.1 Introduction

It has been known for quite some time that photolysis of nitrous acid (HONO) is an important early morning source for hydroxyl radicals (OH) [8, 17, 38, 41]. Many recent field measurements further indicate that HONO also exists at significant levels during the day in the atmospheric boundary layer, up to several parts per billion by volume (ppbv) in urban atmosphere [2, 10, 28, 29, 45, 46, 60] and to several hundred parts per trillion by volume (pptv) in rural atmosphere [3, 18, 21, 24, 25, 66, 69–71]. Under solar radiation, HONO undergoes fast photolysis (3.R1) and becomes an important or even a major OH source in both urban and rural environments:

$$\mathrm{HONO} + h\nu \rightarrow \mathrm{OH} + \mathrm{NO}. \qquad (3.\mathrm{R1})$$

Since OH is responsible for the removal of primary pollutants in the atmosphere, and plays a crucial role in the formation of secondary pollutants, such as O_3 and aerosol [15], HONO, as a major OH precursor, may play an important role in the atmospheric chemistry. As a result, interest in HONO chemistry has dramatically increased in the two past decades, and a large variety of techniques have been developed for atmospheric HONO measurement.

X. Zhou (✉)
Wadsworth Center, New York State Department of Health, and School of Public Health, State University of New York, Albany, NY 12201, USA
e-mail: zhoux@wadsworth.org

I. Barnes and K.J. Rudziński (eds.), *Disposal of Dangerous Chemicals in Urban Areas and Mega Cities*, NATO Science for Peace and Security Series C: Environmental Security,
DOI 10.1007/978-94-007-5034-0_3,

This paper is to provide an overview of HONO measurement techniques currently available in the literature, with a brief discussion of advantages, disadvantages and characteristics of each method. To better organize the discussion, these techniques are divided into three main categories: direct optical spectroscopic techniques, indirect spectroscopic techniques, and wet chemical techniques.

3.2 Direct Optical Spectroscopic Techniques

Measurements using the direct optical spectroscopic techniques, except the cavity ring-down spectroscopy, are based on Beer-Lambert's absorption law: the amount of light absorbed is proportionally related to the number of gas molecules in the light's path. The identification and quantification of HONO are made by fitting the characteristic absorption spectra in either the IR region (e.g., TDLAS) or in the UV region (e.g., DOAS). If the HONO absorption cross sections are accurately established in the characteristic bands or lines, HONO concentrations may be retrieved directly from the absorption spectra without calibration. Fourier transform infrared (FTIR) spectroscopy is a direct optical method and has been used in the laboratory for HONO measurement. However, its detection limit of tens of ppbv is not low enough for ambient application; the technique will not be discussed here.

3.2.1 DOAS

Among the spectroscopic techniques for HONO measurement, the most established is differential optical absorption spectroscopy (DOAS). In fact, the first unequivocal detection of HONO in the atmosphere was made by Perner and Platt [38] using long-path DOAS (LP-DOAS). Detailed descriptions of principles and applications of the DOAS technique can be found in a recent book by Platt and Stutz [43]. Most DOAS systems for HONO measurement are so called active DOAS, which uses broad-band light sources, such as Xe arc lamp. It is also possible to use the sun or scattered sunlight as light source, which is called passive DOAS (e.g., multi-axis DOAS, or MAX-DOAS). The typical length of the light path in the atmosphere ranges from several hundred meters to more than ten kilometers in LP-DOAS. The absorption signal is separated into two parts: the low-frequency broadband signal, caused by Mie scattering, instrument effects and turbulences, and the high-frequency narrowband cross section, considered as characteristic absorption lines or bands of trace gases. HONO's narrow-band absorption features between 340 and 370 nm are used in absorption spectral fitting to retrieve the path-averaged HONO concentration, based on Beer-Lambert's law. The detection limit of DOAS is usually around 100 pptv for a time resolution of 5–15 min; as low as 16 pptv can be achieved [55]. The LP-DOAS can also provide vertical HONO concentration profile information by collecting light absorption spectra from multiple retro-reflectors located at different heights [53, 55, 62, 63]. Furthermore, DOAS allows

for the simultaneous spectral fitting and detection of HONO and other species, including NO_2, O_3 and HCHO [43]. The long absorption path utilized in the traditional LP-DOAS systems may provide high measurement sensitivity, but it becomes a disadvantage when small spatial variations in the atmosphere are of interest. Multi-reflection cell (White cell) can then be used to achieve sufficient light-path length over a short distance of open space (MR-DOAS) [5], which is widely adopted in photochemical chambers (such as EUPHORE chamber in Valencia, Spain, and SAPHIR chamber in Jülich, Germany). MR-DOAS can also provide "*in situ*" HONO measurement data, which is useful for intercomparison with other techniques.

The DOAS technique has been widely used in HONO measurements, mostly in the urban and semi-rural environments [2, 4–6, 17, 38, 41, 44, 53–55, 62, 63]. Since the HONO concentration is retrieved from HONO characteristic absorption spectra without any sampling procedures, the obtained HONO concentration is free of artifacts commonly associated with sampling procedures, and thus considered to be "absolute". For this reason, DOAS is often used as a reference during HONO method intercomparisons. While the capability of measuring several species simultaneously is an advantage of DOAS, the presence of multiple absorption bands of multiple species at high concentrations, especially NO_2, may introduce significant uncertainty for HONO concentration retrieval [26].

3.2.2 IBBCEAS

In incoherent broad band cavity-enhanced absorption spectroscopy (IBBCEAS), a high power UV-LED [16, 64] or a short-arc xenon lamp [14] is used as the light source. The light is trapped between two highly reflecting dielectric mirrors, resulting in a long effective absorption path length, up to several km. The optical cavity can be placed in a closed chamber [14, 16] or in the open air [64]. The absorption coefficient of the gas mixture inside the cavity is determined using the following equation [16]:

$$\alpha(\lambda) = \frac{1}{L}\left(\frac{I_0}{I} - 1\right)(1 - R) \tag{3.E1}$$

where $\alpha(\lambda)$ is the absorption coefficient of the sample, R is the mirror reflectivity, L is the separation of the mirrors and I_0 and I are, respectively, the intensities of light transmitted by the cavity in the absence and presence of the absorbing species. Similar to DOAS, data retrieval involves absorption spectral fittings for absorbing species, such as HONO and NO_2:

$$\alpha(\lambda) = n_{\mathrm{HONO}}\sigma_{\mathrm{HONO}}(\lambda) + n_{\mathrm{NO_2}}\sigma_{\mathrm{NO_2}}(\lambda) + a\lambda + b \tag{3.E2}$$

where n_{HONO} and n_{NO2} are the number densities and σ_{HONO} and σ_{NO2} are the absorption cross-sections of HONO and NO_2, respectively. The technique offers

a detection limit of 130 pptv for HONO and 380 pptv for NO_2 with a 10-min integration time [16], or ~430 pptv for HONO and ~1 ppbv for NO_2 with an acquisition time of 90 s [64]. While the technique is very promising with good sensitivity and time resolution, no application to ambient HONO measurement has been reported yet in the literature.

3.2.3 TDLS

Tunable diode laser spectroscopy (TDLS) [32, 50] and its variation, tunable infrared laser differential absorption spectroscopy (TILDAS) using continuous-wave mode quantum cascade lasers (cw-QCLs) [30, 31], belong to high-resolution infrared spectroscopy. A multi-pass cell is used to achieve a long light absorption path (e.g., ~150 m adsorption path in Li et al. [32]). Ambient air is sampled through an inlet into a multi-pass cell into which the IR light from a laser device is directed. The absorption spectra at a strong HONO absorption feature (e.g., centered at 1713.5111 cm^{-1}, Li et al. [32]) are used to derive HONO concentrations with a spectral fitting software. The detection limit of ~200 pptv has been estimated with an integration time of 1 s [32]. Compact systems have been developed using thermo-electrically cooled quantum cascade lasers [30, 31]. TDLS has been successfully used for HONO measurements in indoor air [32], ambient air [30], and in aircraft exhausts [31]. Since air sampling is a necessary step in TDLS in HONO measurement, caution should be taken to prevent or minimize secondary HONO formation on inlet or cell walls.

3.2.4 CRDS

Cavity ring-down spectroscopy (CRDS) is another cavity-enhanced spectroscopic technique, but it is based on the measurement of the decay rate, instead of the magnitude, of light absorption at a strong HONO absorption wavelength (e.g., 354.2 nm) through the sample [61]. Tunable laser pulses (in nanoseconds) are injected into an optical cavity with two highly reflective mirrors ($R > 99.9\%$) and the trapped light makes ~1,000 round trips in the cavity; the absorption signal decay rate, $1/\tau$, is measured. HONO concentration can then be derived from the following relationship (3.E3):

$$\sigma n = \frac{1}{c}\left(\frac{1}{\tau} - \frac{1}{\tau_0}\right), \tag{3.E3}$$

where σ is the absorption cross section, n is the number density of HONO in the light path, and $1/\tau_o$ is the background decay rate attributed to the mirror

transmission loss and scattering loss. The detection limit was estimated to be ~5 ppbv with a sampling time of 15 s in the laboratory using pure HONO standard; and it is possible to further lower the detection limit to ~0.1 ppbv with upgraded optics and longer cavity [61]. However, no field application has been reported yet. Since air sampling is a necessary step in CRDS in HONO measurement, caution should be taken to prevent or minimize secondary HONO formation on inlet or cell walls.

3.3 Indirect Spectroscopic Techniques

Several indirect spectroscopic techniques have been developed for ambient HONO measurement. In these techniques, HONO is converted into a product that can be quantified by a highly sensitive spectroscopic technique. The detection limits of indirect spectroscopic techniques are generally lower than those of direct spectroscopic techniques. It should be pointed out that the following techniques are not absolute methods like direct optical spectroscopic techniques discussed above, and thus system calibrations are necessary. Furthermore, since air sampling is a necessary step in HONO measurement by these methods, caution should be taken to prevent or minimize secondary HONO formation on inlet or cell walls.

3.3.1 CIMS

In chemical ionization mass spectrometry (CIMS), neutral HONO molecule is chemically ionized by a reagent ion to yield a product ion, for example, through fluoride ion transfer reaction (3.R2) by CF_3O^- to form an ionic adduct $HF{\bullet}NO_2^-$ [47]:

$$CF_3O^- + HONO \rightarrow HF \bullet NO_2^- + CF_2O \quad (3.R2)$$

or through a negative proton transfer reaction (3.R3) by $CH_3C(O)O^-$ to form a NO_2^- ion [48, 59]:

$$HONO + CH_3C(O)O^- \rightarrow NO_2^- + CH_3C(O)OH \quad (3.R3)$$

The product ions are analyzed by a MS analyzer. High sensitivity (detection limit ~10–25 pptv) and excellent time resolution (~1 s) have been achieved [47, 48]. The CIMS technique has been used for ambient HONO measurement in a rural forested site [47] and for the measurements HONO and other species emitted from biomass fires [48, 59].

3.3.2 PF/LIF

The photo-fragmentation/laser induced florescence (PF/LIF) technique was first developed more than 20 years ago by Rogers and Davis [49], and recently modified and improved by Liao et al. [33]. HONO molecule was first photo-fragmented by a laser to produce NO and OH:

$$\mathrm{HONO} + h\nu\ (355\ \mathrm{nm}) \rightarrow \mathrm{OH} + \mathrm{NO} \tag{3.R4}$$

The produced OH is quantified by laser induced fluorescence at an excitation wavelength of 282 nm and an emission wavelength of 309 nm. The PF/LIF offers high sensitivity and good time resolution, with a detection limit of ~15 pptv a time resolution of 1 min [33, 34], and has been successfully deployed to measure HONO concentration at the South Pole Station [34]. However, uncertainty may be as high as $\sim$ 35%, due to the generation of artificial OH signals by photolysis of potential atmospheric species (e.g., H_2O_2, HNO_3, CH_2O, HO_2NO_2) [33].

3.3.3 TDC

In thermal dissociation chemiluminescence (TDC) technique, the HONO molecule is first thermally dissociated at high temperature (>650 °C) to NO and OH:

$$\mathrm{HONO} + \mathrm{heat}\ (>650^{\circ}\mathrm{C}) \rightarrow \mathrm{NO} + \mathrm{OH} \tag{3.R5}$$

The thermal dissociation was found to be quantitative [37]. The produced NO is then quantified by a commercial chemiluminescence NO analyzer. The sensitivity of the method is determined by the NO analyzer used, ~50 pptv. Laboratory tests have showed that measurements are affected in predictable ways by some atmospheric species, such as NO_2, peroxy nitrates, alkyl nitrates, HNO_3, O_3 and H_2O; thus potential interference from these species need to be taken into account when applying this technique for ambient HONO measurement. No field application of this technique has been reported yet.

3.4 Wet Chemical Techniques

Compared to the gas-phase spectroscopic techniques described above, the wet chemical techniques are usually simpler and less expensive, and often provide higher sensitivities, with detection limit in the lower pptv or even sub pptv levels. To measure atmospheric HONO using these techniques, gaseous HONO is first collected from ambient air and converted to an aqueous solution, using a variety of sampling devices, such as annular denuder, wet denuders, mist chamber, and coil sampler. The collected nitrite in the solution is then quantified using a variety of

analytical methods, such as ion chromatography (IC), chemiluminescence, fluorescence, HPLC, and spectrophotometry. Ambient HONO concentration is calculated based on the detected nitrite amount along with the information of air sampling volume (or flow rate), collection solution volume (or flow rate), sample collection efficiency, temperature and pressure. The sampling procedures may introduce unintended artifacts, such as heterogeneous formation of HONO from other NO_y species on inlet and sampler surfaces, especially at the presence of some reactive organic and inorganic species. Steps must be taken to eliminate, minimize or correct for the potential interferences when using the wet chemical techniques described below for the HONO measurement.

3.4.1 Annular Denuder-IC

The dry diffusion denuder technique for HONO sampling was first deployed by Ferm and Sjödin [13]; several types of denuders, most notably annular denuders, have then been designed, tested and used (e.g., [11, 12, 27, 39, 40]). The sampling of HONO by dry diffusion denuders is based on the diffusion and adsorption of gaseous HONO onto the Na_2CO_3-coated wall surface to form nitrite. The nitrite collected on the denuder surfaces is then extracted and analyzed by analytical techniques, mostly ion chromatography. The sensitivity of the method depends on the volume of air processed; a detection limit of low pptv may be achieved if a large amount of air is sampled (e.g., [7, 40]).

Laboratory and field tests showed that while the denuder sampling technique achieves high collection efficiency for HONO ($\geq$95%), it suffers from both positive interference, mainly from PAN and NO_2 that undergo heterogeneous reactions on alkaline surfaces to form nitrite, and negative interference from O_3 that oxidizes nitrite to nitrate (e.g., [11–13, 27, 39]). Attempts have been made to correct or to minimize the interfering artifacts. For example, corrections can be made for the positive artifacts with a second Na_2CO_3-coated annular denuder. Even taking these corrective measures, one still needs to be cautious in evaluating and interpreting the collected data using this technique, since some interference factors may still not be corrected for. Furthermore, sampling time using annular denuder is usually quite long, from hours to days. Thus it is not suitable to study short-term variation of HONO in the atmosphere.

3.4.2 Wet Denuder

There are several designs of wed denuders available for sampling HONO and other water solution species, including wet effluent diffusion denuder (WEDD, either cylindrical or parallel-plate) [36, 52, 58, 65], air dragged aqua-membrane denuder (ADAMD) [56], and rotating wet annular denuder (RWAN) [1, 57]. All the

wet denuder samplers offer good collection efficiency, >95%, and allow for the separation of gaseous HONO from aerosol nitrite.

The WEDD is the most commonly used wet denuder for HONO measurement. It is set up vertically; ambient air is pulled upward through the denuder tube from the bottom opening, and the absorbing solution (typically purified water) is continuously pumped into the tube at the top to produce a thin aqueous film on the inner wall surface as the solution flows downward under the gravity. The absorbing solution film collects gaseous HONO based on HONO's high solubility in water and the solution is aspirated at the bottom of the denuder tube by a pump for analysis for nitrite. Ion chromatography has been deployed most frequently to analyzed nitrite and some other acidic species collected by the WEDD [1–3, 36, 52, 58, 65], achieving a low-pptv detection limit. The sample integration time is mostly determined by the run time of IC, in the order of 5–30 min. Recently, a flow-injection/chemiluminescence technique has been developed and used with the WEDD for HONO measurement [35]. The collected nitrite in the solution is oxidized by H_2O_2 to form peroxynitrous acid under the acidic condition; a chemiluminescent light is emitted and detected when the peroxynitrite reacts with luminal under the basic condition. The detection limit is about 15 pptv with a time resolution of 70 s.

The ADAMD is also set up vertically, and the absorbing solution is continuously pumped into the denuder tube at the bottom. A thin aqueous film is formed on the denuder inner wall surface when the solution is dragged upward by the sample air flow, and effectively collects gaseous HONO from ambient air into the solution phase [56]. The collected nitrite reacts with 2,3-diaminonaphthalene (DAN) in an acidic solution to produce 1-naphthotriazole. The formed 1-naphthotriazole is a fluorescent compound under an alkaline condition, and is detected with a flow injection/fluorescence technique, at an excitation wavelength of 360 nm and an emission wavelength of 405 nm [56]. The detection limit is about 8 pptv with a time resolution of 2 min.

The RWAN is set up horizontally; the absorbing solution, typically a diluted basic solution, such as 0.5 mM K_2CO_3 [1] or 0.1 mM $NaHCO_3$ [57], is continuously pumped into the denuder at the rear end away from the air inlet and out of the denuder at the front end near the air inlet. The rotating denuder tube spreads the absorbing solution as a thin film on the denuder inner wall surface. Air is pulled through the denuder at high flow rate (up to 30 L min^{-1}), and the solution film effectively absorbs gaseous HONO. The collected nitrite is quantified by IC, achieving a detection limit of as low as 12 pptv [57]. The sample integration time is mostly determined by the run time of IC, in the order of 5–60 min.

3.4.3 Mist Chamber-IC

Mist chambers have been successfully used for sampling HONO and other water soluble species (e.g., [9, 55]). The scrubbing solution (typically purified water) is nebulized into fine mist by the high-flow of ambient air drawn into the chamber.

The fine water droplets effectively collect gaseous HONO from the gas phase and is refluxed in the chamber with a hydrophobic Teflon filter mounted at the top of chamber to prevent the water droplets from escaping. The solution is withdrawn for nitrite analysis after a sampling interval, from 5 to 30 min depending on ambient HONO levels, by ion chromatography. A sub to low pptv detection limit has been achieved [9, 55]. Since mist chamber can collect both soluble gaseous species and aerosol particles at high efficiency, a filter is usually used to remove aerosol particles from the air stream before entering the chamber.

3.4.4 Coil Sampler

A coil sampler typically consists of an inlet T for introducing sample air and scrubbing solution, a coil section for scrubbing gaseous HONO from gas into liquid, and an enlarged tube section for gas-liquid separation. The sampling of HONO from the gas phase into the scrubbing solution may be based either on high effective solubility HONO in an aqueous solution at neutral pH [20, 68] or on fast reaction of HONO with a reagent in the scrubbing solution [19], resulting in a quantitative collection efficiency. HONO measurement may be accomplished by coupling coil sampler with a variety of analytical techniques, such as DNPH derivatization/HPLC [68], and azo dye derivatization-HPLC [20], azo dye derivatization and long-path absorption photometry [18, 19, 23, 67, 71].

In the long-path absorption photometric (LOPAP) technique described in Heland et al. [19] and Kleffmann et al. [23, 26], gaseous HONO is collected with a stripping solution containing 60 mM sulfanilamide (SA) in 1 M HCl. The gaseous HONO in the ambient air reacts instantly with SA at high acidity to form a diazonium ion in the sampling coil. After sample collection, the diazonium ion in the stripping solution reacts with N-(1-naphthyl) ethylenediamine dihydrochloride (NED) to form a highly light-absorbing azo dye, which is detected by a long-path absorption photometer at 540 nm. The use of long-path flow cell (also called liquid waveguide capillary cell, LWCC) greatly enhances the detection sensitivity of absorbance spectrophotometry, by 2 orders of magnitude compared to that using a conventional cuvette. The detection limit is about 1 pptv with a time resolution of 1.5–4 min. The most unique feature in this LOPAP technique is that two coil samplers in series are used: The first coil samples almost all the HONO but only a small fraction of any interfering species such as NO_x and PAN; the second coil samples about the same amount of the interfering species but almost no HONO. By subtracting the concentration signal of the second coil from that of the first coil, potential interferences are removed, and the obtained HONO concentration should be close to the true value. Indeed, later laboratory and field studies suggest that such a correction by the second coil signal effectively eliminates the potential interferences [22, 23, 26], and intercomparisons with DOAS technique have resulted in excellent agreements [26]. The LOPAP technique has been developed into a compact instrument and commercialized by QUMA Elektronik & Analytik GmbH (http://www.quma.de/home.htm), and is widely used for the measurement of atmospheric HONO.

An evolving series of HONO measurement techniques have been developed in the author's group in Wadsworth Center, based on coil sampling with 1-mM phosphate buffer solution (pH ~ 7) or purified water as the scrubbing solution. [18, 20, 67, 68, 71]. In our first method described in Zhou et al. [68], the collected nitrite is derivatized with 2,4-dinitrophenolhydrazine (DNPH) to form highly UV-absorbing 2,4-dinitrophenolazide (DNPA). The DPHA derivative is then separated from DNPH and hydrazones by C18 reverse-phase HPLC, and is detected at 309 nm by an UV-visible detector. In our next technique described in Huang et al. [20], the collected nitrite is derivatized with SA and NED to form azo dye, which is then pre-concentrated on a C-18 pre-column and quantified by C18 reverse-phase HPLC with a UV-visible detector at 540 nm. The detection limits of both HPLC-based methods are 1 pptv with a time resolution of 5 min [2, 20, 68–70]. In the next development, the HPLC system is replaced by a flow-injection system with a long-path absorption photometer [18, 66]. This modification has achieved the same detection limit of ~1 pptv and time resolution of 5 min, but eliminated the use of organic solvents needed for HPLC elution. Potential interferences from reactive species, such as NO, NO_2, PAN, O_3, HNO_3, and HCHO have been studied in the laboratory and found to be negligible. Further field tests using a Na_2CO_3-coated denuder demonstrated that interference artifact signals from gaseous and particulate species were <3 pptv at a clean low-NO_x rural site at Whiteface Mountain, NY, and accounted for a maximum of 8% of total HONO signal during the day at a urban site in Albany, NY [20].

In our most recent modification (Fig. 3.1), the coil sampler alternately samples ambient air (20 min) and "zero-HONO" air (10 min) in a 30-min measurement cycle, controlled by a 3-way solenoid valve. The "zero-HONO" air was generated by pulling ambient air through a Na_2CO_3-coated annular denuder in which HONO, and acidic gases were removed while other atmospheric constituents, including NO_x, aerosol particles and other neutral NO_y species, were allowed to pass through. Interference from these atmospheric species was removed and corrected for by subtracting the "zero-HONO" air signal from the ambient air signal [67, 71]. The "zero-HONO" background signal exhibits a distinctive diurnal variation: staying low and relatively stable during the night and reaching a maximum plateau in the afternoon (Fig. 3.2). The variation in the background signal may reflect the changes in interference intensity from atmospheric species as well as the instrument baseline drift mainly caused by temperature changes. The detection limit was 1 pptv with a time resolution of better than 2 min.

3.5 Summary

Table 3.1 summarizes the techniques discussed in this presentation, including their detection limit (DL), time resolution (RT), and applications in laboratory or in field measurements, with some additional comments. Some direct optical spectroscopic techniques can provide positive HONO identification and are capable of quantifying ambient HONO concentrations without calibrations. In general, however,

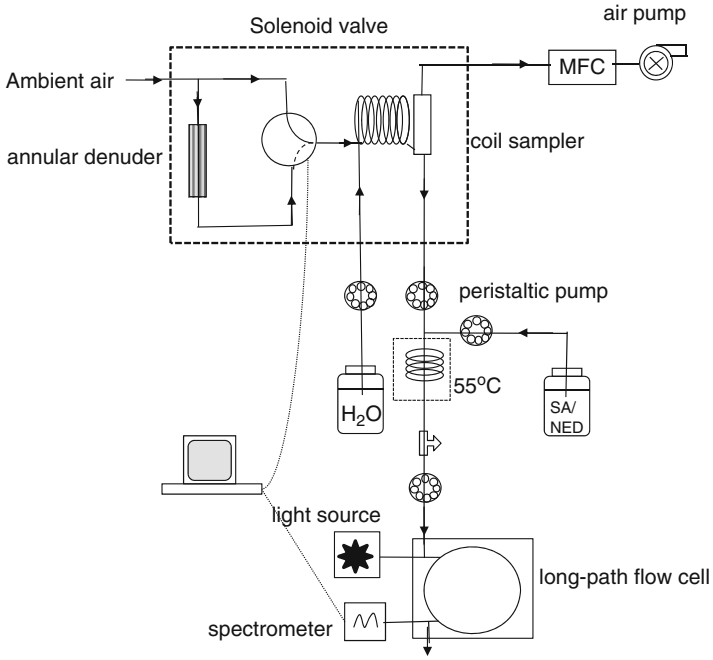

Fig. 3.1 A schematic diagram of a HONO measurement system

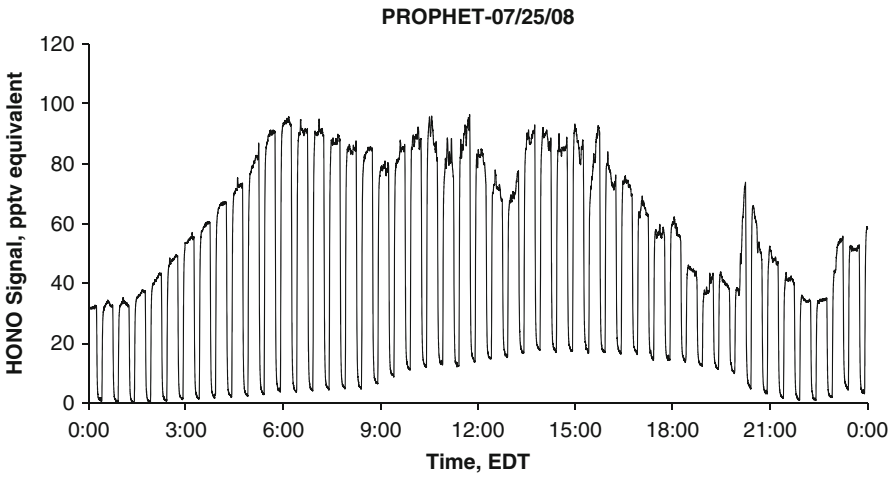

Fig. 3.2 An example of raw collected at 0.3 HZ during a 24-h period on July 25, 2008. The system was run in a measurement cycle with 20-min ambient air (*upper contour*) and 10 min zero-HONO air (*lower contour*)

Table 3.1 Overview summary of techniques for atmospheric HONO measurement

Technique	DL (pptv)	TR (min)	Applications Lab	Applications Field	Comments
Direct optical spectroscopic techniques					
LP-DOAS	16	5–15	No	Yes	Established, well characterized
MR-DOAS	84	5–15	Yes	Yes	Established, well characterized
IBBCEAS	130 430	10 1.5	Yes	No	Promising, but no field tested yet, intercomparison needed
TDLS	200	0.017	Yes	Yes	Intercomparison needed
CRDS	5,000	0.25	Yes	No	Not field tested yet
Indirect spectroscopic techniques					
CIMS	~10	~0.01	Yes	Yes	Intercomparison needed
PF/LIF	15	1	Yes	Yes	Intercomparison needed
TDC	50	1	Yes	No	Under development
Wet chemical techniques					
Annular denuder-IC	~10	>60	Yes	Yes	Interferences reported, intercomparison needed
WEDD-IC	~10	5–30	Yes	Yes	Intercomparison needed
WEDD-chemiluminescence	15	1	Yes	Yes	Intercomparison needed
ADAMD-IC	8	2	Yes	Yes	Intercomparison needed
RWAN-fluorescence	12	5–60	Yes	Yes	Intercomparison needed
Mist chamber-IC	1–5	5–30	Yes	Yes	Intercomparison needed
Coil-HPLC	~1	5	Yes	Yes	Intercomparison needed
Coil-LOPAP (Wadsworth)	~1	1–5	Yes	Yes	Interference corrected, intercomparison needed
LOPAP (Wuppertal)	~1	1.5–4	Yes	Yes	Well characterized, interference corrected

the indirect techniques are more sensitive than the direct optical spectroscopic techniques; and the wet chemical techniques are significantly cheaper and are simpler to operate than the spectroscopic techniques.

Secondary HONO formation is known to occur on the walls of inlets and sampling devices and is a major interference concern in HONO measurement when air sampling is involved. With increasing applications of wet chemical techniques, it is critically important to validate these techniques, and to quantify and/or correct for potential interferences. It is an effective validation procedure to intercompare different techniques based on different working principles; the FIONA (Formal Intercomparison of Observations of Nitrous Acid) campaign is such an example, as discussed by [49] in this volume. HONO measurement in the clean rural and remote regions is still a great challenge, and is conducted using mostly wet chemical techniques. Intercomparison is therefore urgently needed to validate these techniques under clean conditions.

Acknowledgement This work s supported by the National Science Foundation (NSF), ATM-0632548.

References

1. Acker K, Spindler G, Brüggemann E (2004) Nitrous and nitric acid measurements during the NTERCOMP2000 campaign in Melpitz. Atmos Environ 38:6497–6505
2. Acker K, Febo A, Trick S, Perrino C, Bruno P, Wiesen P, Möller D, Wieprecht W, Auel R, Giusto M, Geyer A, Platt U, Allegrini I (2006) Nitrous acid in the urban area of Rome. Atmos Environ 40:3123–3133
3. Acker K, Möller D, Wieprecht W, Meixner F, Bohn B, Gilge S, Plass-Dülmer C, Berresheim H (2006) Strong daytime production of OH from HNO_2 at rural mountain site. Geophys Res Lett 33. doi:10.1029/2005GL024643
4. Alicke B, Platt U, Stutz J (2002) Impact of nitrous acid photolysis on the total hydroxyl radical budget during the Limitation of Oxidant Production/Pianura Padana Produzione di Ozono study in Milan. J Geophys Res 107. doi:10.1029/2000JD000075
5. Alicke B, Geyer A, Hofzumahaus A, Holland F, Konrad S, Patz HW, Schafer J, Stutz J, Volz-Thomas A, Platt U (2003) OH formation by HONO photolysis during the BERLIOZ experiment. J Geophys Res 108. doi:10.1029/2001JD000579
6. Andres-Hernandez MD, Notholt J, Hjorth J, Schrems O (1996) A DOAS study on the origin of nitrous acid at urban and non-urban sites. Atmos Environ 30:175–180
7. Beine HJ, Allegrini I, Sparapani R, Ianniello A, Valentini F (2001) Three years of springtime trace gas and particle measurements at Ny-Ålesund, Svalbard. Atmos Environ 35:645–3658
8. Calvert JG, Yarwood G, Dunker AM (1994) An evaluation of the mechanism of nitrous acid formation in the urban atmosphere. Res Chem Intermed 20:463–502
9. Dibb JE, Huey LG, Slusher DL, Tanner DJ (2004) Soluble reactive nitrogen oxides at South Pole during ISCAT 2000. Atmos Environ 38:5399–5409
10. Elshorbany YF, Kleffmann J, Kurtenbach R, Lissi E, Rubio M, Villena G, Gramsch E, Rickard AR, Pilling MJ, Wiesen P (2010) Seasonal dependence of the oxidation capacity of the city of Santiago de Chile. Atmos Environ 44:5383–5394
11. Febo A, Perrino C, Cortiello M (1993) A denuder technique for the measurement of nitrous acid in urban atmospheres. Atmos Environ 27:1721–1728
12. Febo A, Perrino C, Gherardi M, Sarapani R (1995) Evaluation of a high-purity and high stability continuous generation system for nitrous acid. Environ Sci Technol 29:2390–2395
13. Ferm M, Sjödin A (1985) A sodium carbonate coated denuder for determination of nitrous acid in the atmosphere. Atmos Environ 19:979–983
14. Fiedler SE, Hese A, Ruth AA (2003) Incoherent broad-band cavity enhanced absorption spectroscopy. Chem Phys Lett 371:284–294
15. Finlayson-Pitts BJ, Pitts JN Jr (2000) Chemistry of the upper and lower atmosphere: theory, experiments, and applications. Academic, San Diego
16. Gherman T, Vebables DS, Vaughan S, Orphal J, Ruth AA (2008) Incoherent broadband cavity-enhanced absorption spectroscopy in the near-ultraviolet: application to HONO and NO_2. Environ Sci Technol 42:890–895
17. Harris GW, Carter WPL, Winer AM, Pitts JN Jr, Platt U, Perner D (1982) Observations of nitrous acid in the Los Angeles atmosphere and the implications for the ozone-precursor relationships. Environ Sci Technol 16:414–419
18. He YX, Zhou JH, Bertman S (2006) Importance of dew in controlling air-surface exchange of HONO in rural forested environments. Geophys Res Lett 33. doi:10.1029/2005GL024348
19. Heland J, Kleffmann J, Kurtenbach R, Wiesen P (2001) A new instrument to measure gaseous nitrous acid (HONO) in the atmosphere. Envrion Sci Technol 35:3207–3212
20. Huang G, Zhou X, Deng G, Qiao H, Civerolo K (2002) Measurements of atmospheric nitrous acid and nitric acid. Atmos Environ 36:2225–2235
21. Kleffmann J (2007) Daytime sources of nitrous acid (HONO) in the atmospheric boundary layer. Chem Phys Chem 8:1137–1144
22. Kleffmann J, Wiesen P (2008) Quantification of interferences of wet chemical HONO LOPAP measurements under simulated polar conditions. Atmos Chem Phys 8:6813–6822

23. Kleffmann J, Heland J, Kurtenbach R, Lörzer JC, Wiesen P (2002) A new instrument (LOPAP) for the detection of nitrous acid (HONO). Environ Sci Pollut Res 9:48–54
24. Kleffmann J, Kurtenbach R, Lorzer J, Wiesen P, Kalthoff N, Vogel B, Vogel H (2003) Measured and simulated vertical profiles of nitrous acid – part I: field measurements. Atmos Environ 37:2949–2955
25. Kleffmann J, Gavriloaiei T, Hofzumahaus A, Holland F, Koppmann R, Rupp L, Schlosser E, Siese M, Wahner A (2005) Daytime formation of nitrous acid: a major source of OH radicals in a forest. Geophys Res Lett 32. doi:10.1029/2005GL022524
26. Kleffmann J, Lörzer JC, Wiesen P, Kern C, Trick S, Volkamer R, Rodenas M, Wirtz K (2006) Intercomparisons of the DOAS and LOPAP techniques for the detection of nitrous acid (HONO) in the atmosphere. Atmos Environ 40:3640–3652
27. Koutrakis P, Wolfson JM, Slater JL, Brauer M, Spengler JD, Stevens KR, Stone CL (1988) Evaluation of an annular denuder/filter pack system to collect acidic aerosols and gases. Environ Sci Technol 22:1463–1468
28. Lammel G, Cape JN (1996) Nitrous acid and nitrite in the atmosphere. Chem Soc Rev 25:361–369
29. Lammel G, Perner D (1988) The atmospheric aerosol as a source of nitrous acid in the polluted atmosphere. J Aerosol Sci 19:1199–1202
30. Lee BH, Wood EC, Zahniser MS, McManus JB, Nelson DD, Herndon SC, Santoni GW, Wofsy SC, Munger JW (2011) Simultaneous measurements of atmospheric HONO and NO_2 via absorption spectroscopy using tunable mid-infrared continuous-wave quantum cascade lasers. Appl Phys B 102:417–423
31. Lee BH, Santoni GW, Wood EC, Herndon SC, Miake-Lye RC, Zahniser MS, Wofsy SC, Munger JW (2011) Measurements of nitrous acid in commercial aircraft exhaust at the Alternative Aviation Fuel Experiment. Environ Sci Technol 45:7648–7654
32. Li YQ, Schwab JJ, Demerjian KL (2008) Fast time response measurements of gaseous nitrous acid using a tunable diode laser absorption spectrometer: HONO emission source from vehicle exhausts. Geophys Res Lett 35. doi:10.1029/2007GL031218
33. Liao W, Hecobian A, Mastromarino J, Tan D (2006) Development of a photo-fragmentation/laser-induced fluorescence measurement of atmospheric nitrous acid. Atmos Environ 40:17–26
34. Liao W, Case AT, Mastromarino J, Tan D, Dibb JE (2006) Observations of HONO by laser-induced fluorescence at the South Pole during ANTCI 2003. Geophys Res Lett 33:L09810. doi:10.1029/2005GL025470
35. Mikuška P, Motyka K, Večeřa Z (2008) Determination of nitrous acid in air using wet effluent diffusion denuder–FIA technique. Talanta 77:635–641
36. Neftel A, Blatter A, Hesterberg R, Staffelbach T (1996) Measurements of concentration gradients of HNO_2 and HNO_3 over a semi-natural ecosystem. Atmos Environ 30:3017–3025
37. Pérez IM, Wooldridgea PJ, Cohen RC (2007) Laboratory evaluation of a novel thermal dissociation chemiluminescence method for in situ detection of nitrous acid. Atmos Environ 41:3993–4001
38. Perner D, Platt U (1979) Detection of nitrous acid in the atmosphere by differential optical absorption. Geophys Res Lett 6:917–920
39. Perrino C, De Santis F, Febo A (1990) Criteria for the choice of a denuder sampling technique devoted to the measurement of atmospheric nitrous and nitric acids. Atmos Environ 24:617–727
40. Perrino C, Ramirez D, Allegrini I (2001) Monitoring acidic air pollutants near Rome by means of diffusion lines: development of a specific quality control procedure. Atmos Environ 35:331–341
41. Pitts JN, Biermann HW, Winer AM, Tuazon EC, M (1984) Spectroscopic identification and measurement of gaseous nitrous acid in dilute auto exhaust. Atmos Environ 18:847–854
42. Pitts JN Jr, Bierman HW, Atkinson A, Winer AM (1994) Atmospheric implications of simultaneous nighttime measurements of NO_3 radicals and HONO. Geophys Res Lett 11:557–560

43. Platt U, Stutz J (2008) Differential optical absorption spectroscopy: principles and applications. Springer, Heidelberg
44. Reisinger AR (2000) Observations of HNO_2 in the polluted winter atmosphere: possible heterogeneous production on aerosols. Atmos Environ 34:3865–3874
45. Ren X, Harder H, Martinez M, Lesher RL, Oliger A, Simpas JB, Brune WH, Schwab JJ, Demerjian KL, He Y, Zhou X, Gao H (2003) H OH and HO_2 chemistry in the urban atmosphere of New York City. Atmos Environ 37:3639–3651
46. Ren X, Brune WH, Mao J, Mitchell MJ, Lesher RL, Simpas JB, Metcalf AR, Schwab JJ, Cai C, Li Y, Demerjian KL, Felton HD, Boynton G, Adams A, Perry J, He Y, Zhou X, Hou J (2006) Behavior of OH and HO_2 in the winter atmosphere in New York city. Atmos Environ 40: S252–S263
47. Ren X, Gao H, Zhou X, Crounse JD, Wennberg PO, Browne EC, LaFranchi BW, Cohen RC, McKay M, Goldstein AH, Mao J (2010) Measurement of atmospheric nitrous acid at Blodgett Forest during BEARPEX2007. Atmos Chem Phys 10:6283–6894
48. Roberts JM, Veres P, Warneke C, Neuman JA, Washenfelder RA, Brown SS, Baasandorj M, Burkholder JB, Burling IR, Johnson TJ, Yokelson RJ, de Gouw J (2010) Measurement of HONO, HNCO, and other inorganic acids by negative-ion proton-transfer chemical-ionization mass spectrometry (NI-PT-CIMS): application to biomass burning emissions. Atmos Meas Tech 3:981–990
49. Ródenas M, Muñoz A, Alacreu F, Brauers T, Dorn H.-P, Kleffmann J, Bloss W (2012) Assessment of HONO measurements: The FIONA campaign at EUPHORE. In: Barnes I, and Rudziński KJ (eds). Disposal of Dangerous Chemicals in Urban Areas and Mega Cities, NATO Science for Peace and Security Series C: Environmental Security. Springer Science+Business Media Dordrecht, pp 45–58. doi:10.1007/978-94-007-5034-0_4
50. Rodgers M, Davis DD (1989) A UV-photofragmentation/laser-induced fluorescence sensor for the atmospheric detection of HONO. Environ Sci Technol 23:1106–1112
51. Schiller CL, Locquiao S, Johnson TJ, Harris GW (2001) Atmospheric measurements of HONO by tunable diode laser absorption spectroscopy. J Atmos Chem 40:275–293
52. Simon PK, Dasgupta PK (1993) Wet effluent denuder coupled liquid/ion chromatography systems: annular and parallel plate denuders. Anal Chem 65:1134–1139
53. Stutz J, Alicke B, Neftel A (2002) Nitrous acid formation in the urban atmosphere: gradient measurements of NO_2 and HONO over grass in Milan, Italy. J Geophys Res 107. doi:10.1029/2001JD000390
54. Stutz J, Alicke B, Ackermann R, Geyer A, Wang S, White AB, Williams EJ, Spicer CW, Fast JD (2004) Relative humidity dependence of HONO chemistry in urban areas. J Geophys Res 109:D03307. doi:10.1029/2003JD004135
55. Stutz J, Oha H-J, Whitlow SI, Anderson C, Dibb JE, Flynn JH, Rappenglück B, Lefer B (2010) Simultaneous DOAS and mist-chamber IC measurements of HONO in Houston, TX. Atmos Environ 44:4090–4098
56. Takenaka NH, Terada Y, Oro MH, Yoshikawa H, Okitsu K, Bandow H (2004) A new method for the measurement of trace amounts of HONO in the atmosphere using an air-ragged aqua-membrane-type denuder and fluorescence detection. Analyst 129:1130–1136
57. Trebs I, Meixner FX, Slanina J, Otjes R, Jongejan P, Andreae MO (2004) Real-time measurements of ammonia, acidic trace gases and water-soluble inorganic aerosol species at a rural site in the Amazon Basin. Atmos Chem Phys 4:967–987
58. Večeřa Z, Dasgupta PK (1991) Measurement of atmospheric nitric and nitrous acids with a wet effluent diffusion denuder and low-pressure ion chromatography-postcolumn reaction detection. Anal Chem 63:2210–2216
59. Veres P, Roberts JM, Burling IR, Warneke C, de Gouw J, Yokelson RJ (2010) Measurements of gas phase inorganic and organic acids from biomass fires by negative-ion proton-transfer chemical-ionization mass spectrometry. J Geophys Res 115:D23302. doi:10.1029/2010JD014033
60. Villena G, Kleffmann J, Kurtenbach R, Wiesen P, Lissi E, Rubio MA, Croxatto G, Rappenglück B (2011) Vertical gradients of HONO, NO_x and O_3 in Santiago de Chile. Atmos Environ 45:3867–3873

61. Wang L, Zhang J (2000) Detection of nitrous acid by cavity ring-down spectroscopy. Environ Sci Technol 34:4221–4227
62. Wong KW, Oh H-J, Lefer B, Rappenglück B, Stutz J (2011) Vertical profiles of nitrous acid in the nocturnal urban atmosphere of Houston, TX. Atmos Chem Phys 11:3595–3609
63. Wong KW, Tsai C, Lefer B, Haman C, Grossberg N, Brune WH, Ren X, Luke W, Stutz J (2011) Daytime HONO vertical gradients during SHARP 2009 in Houston, TX. Atmos Chem Phys Discuss 11:24365–24411
64. Wu T, Chen W, Fertein E, Cazier F, Dewaele D, Gao X (2011) Development of an open-path incoherent broadband cavity-enhanced spectroscopy based instrument for simultaneous measurement of HONO and NO_2 in ambient air. Appl Phys B. doi:10.1007/s00340-011-4818-3
65. Zellweger C, Amman M, Hofer P, Baltensperger U (1999) NO_y speciation with a combined wet effluent diffusion denuder-aerosol collector coupled to ion chromatography. Atmos Environ 33:1131–1140
66. Zhang N, Zhou X, Shepson PB, Gao H, Alaghmand M, Stirm B (2009) Aircraft measurement of HONO vertical profiles over a forested region. Geophys Res Lett 36:L15820. doi:10.1029/2009GL038999
67. Zhang N, Zhou X, Bertman X, Alaghmand M, Shepson PB, and Carroll MA (2012) Measurements of ambient HONO and vertical HONO flux above a Northern Michigan forest Canopy. Atmos Chem Phys Discuss 12:7273–7304
68. Zhou X, Qiao H, Deng G, Civerolo K (1999) A method for atmospheric HONO based on DNPH derivatization and HPLC analysis. Environ Sci Technol 33:3672–3679
69. Zhou X, Civerolo K, Dai H, Huang G, Schwab J, Demerjian K (2002) Summertime nitrous acid chemistry in the atmospheric boundary layer at a rural site in New York State. J Geophys Res 107. doi:10.1029/2001JD001539
70. Zhou X, Huang G, Civerolo K, Roychowdhury U, Demerjian KL (2007) Summertime observations of HONO, HCHO, and O_3 at the summit of Whiteface Mountain, New York. J Geophys Res 112. doi:10.1029/2006JD007256
71. Zhou X, Zhang N, TerAvest M, Tang D, Hou J, Bertman S, Alaghmand M, Shepson PB, Carroll MA, Griffith S, Dusanter S, Stevens PS (2011) Nitric acid photolysis on forest canopy surface as a tropospheric nitrous acid source. Nat Geosci 4. doi:10.1038/NGEO1164

Chapter 4
Assessment of HONO Measurements: The FIONA Campaign at EUPHORE

Mila Ródenas, Amalia Muñoz, Francisco Alacreu, Theo Brauers, Hans-Peter Dorn, Jörg Kleffmann, and William Bloss

Abstract HONO is an important source of OH-radicals, the major oxidant in the atmosphere during daytime that participates in ozone formation and can lead to photo-smog. Nevertheless, there are still many open questions about its formation and role as a source of OH-radicals. A better knowledge of HONO processes is highly desirable for the improvement of air pollution models, many of which do not currently include heterogeneous HONO production mechanisms. One reason for the uncertainties in the atmospheric role of HONO is the difficulty in measuring this species.

To elucidate both aspects – chemical and instrumental issues – a HONO intercomparison campaign was carried out at the EUPHORE simulation chambers within the framework of the EUROCHAMP-2 project, in May 2010. EUPHORE provided a large and well-mixed gas volume for the simultaneous operation of multiple instruments under well controlled, realistic conditions. Ten experiments were carried out to simulate typical urban and semi-rural conditions and to address the following topics: (i) intercomparison of the different techniques, (ii) study of interferences (aerosols, nitrates, nitrites, NO_2, etc.) and (iii) HONO sources (nitrophenols, vehicle emissions, ambient air, etc.). The first three experiments were part of an open-informal intercomparison while the rest of the intercomparison experiments were conducted under formally blind conditions with an external referee. The extensive participant list included the majority of groups working in

M. Ródenas (✉) • A. Muñoz • F. Alacreu
UMH-Fundación CEAM, Charles R. Darwin, 14. Parque Tecnológico, Paterna, Valencia, Spain
e-mail: milaceam@hotmail.com; mila@ceam.es

T. Brauers • H.-P. Dorn
Forschungszentrum Jülich, Jülich ICG-2, Germany

J. Kleffmann
Department of Physical Chemistry, Univerity of Wuppertal, Wuppertal, Germany

W. Bloss
Department of Chemistry, University of Birmingham, Birmingham, UK

I. Barnes and K.J. Rudziński (eds.), *Disposal of Dangerous Chemicals in Urban Areas and Mega Cities*, NATO Science for Peace and Security Series C: Environmental Security,
DOI 10.1007/978-94-007-5034-0_4,

this area globally, running simultaneously 18 techniques/instruments that covered nearly the whole range of techniques capable of measuring HONO. These included spectroscopic and chemical instruments.

In this work, an overview of the campaign in terms of participants, instruments aim of the experiments, etc. is presented, as well as the results of a selected open experiment.

Keywords HONO • FIONA • Intercomparison • Simulation chambers • EUPHORE

4.1 Introduction

It is generally accepted that nitrous acid (HONO), which accumulates during the night in the planetary boundary layer, is of great importance in atmospheric chemistry since it is an important source of the OH radical, the primary oxidant in the atmosphere, through the reaction:

$$\mathrm{HONO} + h\nu(300 - 390\ \mathrm{nm}) \rightarrow \mathrm{OH} + \mathrm{NO} \tag{4.1}$$

OH radicals initiate the formation of photo-oxidants like ozone in the so-called photo-smog in polluted areas. In addition, HONO is an important indoor pollutant that can react with secondary and tertiary amines resulting in nitrosamines [29]. Although this is not an important sink of atmospheric HONO, its implications for human health may be substantial since nitrosamines are known to be carcinogenic.

Nevertheless, the sources and sinks of atmospheric HONO are not well defined or are not completely understood. The photolysis of HONO (Eq. 4.1) was historically considered to be of importance as an OH source only in the early morning [2], but recent studies have indicated a very high contribution of HONO to OH throughout the day, which could account for up to 60% of the direct OH radical production. The high contribution was initially proposed by [17, 38, 43], and later confirmed in field campaigns [1, 13, 18], and is explained by photochemical sources. In any case, the mechanisms leading to such strong HONO sources are still the subject of ongoing debate (e.g. [34, 43]).

In addition, direct emission by combustion processes, e.g. traffic emissions, only contribute partly to the HONO levels found in the atmosphere [20], while gas-phase reactions do not explain night-time HONO formation [7]. Several studies have proposed that HONO is formed through the conversion of NO_2 on humid surfaces due to heterogeneous processes [21]. Formation on the surface of particles or on the ground has been proposed [13, 28, 31, 32, 37], however, from simultaneous gradient measurements of HONO, NO_x and particles [17] night-time formation on ground surfaces seems to dominate over particle sources. In addition, there are still many open questions concerning the importance of HONO as a source of OH radicals, and its production rates during the night and day. This means that only simplified HONO production mechanisms are included in chemical air pollution models so far. Therefore, a better understanding of the HONO chemistry is highly desirable as it will help to understand the formation of photo-smog, it will impact pollution models and very likely influence environmental policies.

One of the reasons for the uncertainties faced in our understanding of the HONO processes is the difficulty to measure it quantitatively. In fact, field and chamber studies have shown large differences in the HONO concentrations provided by distinct instruments [4, 24]. Many techniques have been developed for HONO detection, ranging from spectroscopic to chemical, but some of the instruments used are compromised by interferences or are limited in terms of poor detection limits, sampling procedures, etc.

Chemical instruments normally show better detection limits and precisions than spectroscopic techniques, but may suffer from artifacts caused by chemical interferences. Most of them are based on the detection of the nitrite ion after adsorption of HONO onto a solid surface (dry denuder) or onto humid or aqueous surfaces (e.g. wet denuders, [25], mist-chambers (MC), [1, 7, 9]). One of the latest chemical methods introduced is the Long Path Absorption Photometer (LOPAP) technique [14] which has been successfully used in recent years in field campaigns, e.g. in SHARP [42] and in chamber experiments [19]. Among the spectroscopic techniques, Differential Optical Absorption Spectroscopy, DOAS, has been shown over recent decades to be a very reliable direct method [30, 35], where the detection of HONO is achieved by quantifying its absorption in the UV region. This absolute technique requires long optical path-lengths to reach suitable detection limits. This limitation has been solved recently by the newly developed Broadband Cavity-Enhanced Absorption Spectroscopy method, BBCEAS, [5, 11, 36], and other spectroscopic techniques like Tunable Diode Laser Spectroscopy, TDL, [22], Photofragmentation-Laser Induced Fluorescence, PF-LIF, [24], etc., which has proven to be very sensitive, but is not yet widely used or has to be further validated.

Therefore, there is an urgent need to evaluate the different techniques under controlled conditions through intercomparisons and validation exercises. The FIONA campaign was an excellent platform to simulate scenarios that would allow a better understanding of the role of HONO in the oxidation capacity of the atmosphere and characterization of instrument interferences under quasi-realistic conditions. The EUPHORE facility has already successfully hosted HONO-related campaigns, e.g., LOPAP vs. DOAS HONO intercomparisons in 2001 and 2004 [19] or the DIFUSO project [40], with studies of HONO emission indices and HONO formation on soot surfaces and thus, it was an excellent platform to carry out the proposed studies.

4.2 Experimental

The experiments of the campaign were conducted within the framework of the EUROCHAMP-2 project at the EUPHORE photoreactors between 3 and 28 May 2010. The facilities have been described in detail elsewhere [6, 26] and only specific information directly related to the present work is provided here.

These outdoor chambers consist of two half spherical bags (FEP foil), each one of approximately 200 m^3, integrated into the UMH-CEAM Foundation building in Valencia, Spain. The FEP foil is practically an inert material, highly transparent

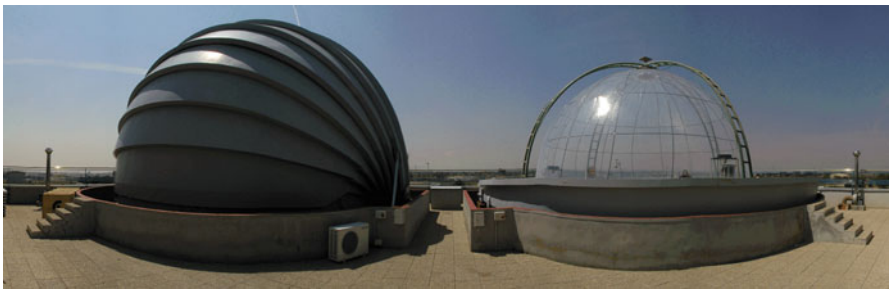

Fig. 4.1 Photochemical reaction chambers (EUPHORE)

to sunlight, with a transmission higher than 80% of the solar radiation in the wavelength range 280–640 nm, relevant for photochemical tropospheric processes. A retractable steel housing surrounds the chamber, and it is used to control the time of exposure to sunlight. The floor of the chamber is made of aluminium panels also covered with FEP foil, and has a specially designed cooling system to compensate for the heating caused by the solar radiation, maintaining ambient temperatures. Two mixing fans placed on the ground allow the recirculation of the air mass facilitating the homogeneity of the temperature as well as of the gas mixture. The inlet ports for the reagents and for sampling by the various analytical instruments are located on the floor of the chambers. During the experiments, the chamber is filled to atmospheric pressure with dry purified air. A pressure sensor (Air-DB-VOC) records the pressure, while the temperature and humidity are continuously recorded by using PT-100 thermocouples and a dew-point mirror system (Waltz TS-2), respectively. The NO_2 photolysis rate (JNO_2) was measured with a filter radiometer (Fig. 4.1).

Several measuring systems are integrated at EUPHORE to monitor precursor species and products. The facility is equipped with optical and chromatographic instrumentation and with different monitors and particle systems. In addition to the instruments available at EUPHORE to measure HONO, the techniques used during the FIONA campaign were: Laser Induced Fluorescence (LIF), to measure OH and HO_2 radicals, which provides valuable information for the study of photo-oxidation processes and of ozone formation, Gas Chromatography (GC-ECD) to measure peroxyacetyl nitrate, ozone monitor (non-dispersive UV photometer monitor, Monitor Labs 9810), HCHO monitor (AL-4001, Aero-Laser), NO_x analyser (ECO- Physics CLD 770 with a photolytic converter) used to measure NO, NO_2 and NO_x, CO monitor (TE48C) and Scanning Mobility Particle Sizer – SMPS (3080, TSI) to measure the particulate size distribution of aerosols. Volatile organic compounds (VOCs) were characterized by using a Fourier Transform Infrared system with MCT detector (Magna 550, Nicolet) coupled to a White-type multi-reflection system located in the chamber. FTIR spectra were collected with a system configuration of 616 m optical path length, a spectral resolution of 1 cm^{-1} and a sampling time of 5 min. SF_6 data were also used to characterize the chamber dilution by following the SF_6 concentration decay by means of FTIR. All these

techniques enable the characterization of the chemical reactions taking place during the experiments. On the other hand, they allow the understanding and quantification of the interferences due to compounds introduced in the chamber to test their impact on the HONO measurements by the different instruments.

4.3 HONO Measurements: Instruments

The experiments were supported by the EUROCHAMP-2 project, within the Transnational Activities created with the aim of promoting a better integration of simulation chambers to study atmospheric processes as well as to facilitate the exchange of expertise by the users. In fact, nearly 50 people from eight different countries participated in the experiments, belonging to 18 institutions. Therefore, the extensive participant list included the majority of groups and scientists working in this area globally, indicating the high relevance of FIONA.

Most types of instruments capable of measuring HONO were used in the campaign. These included spectroscopic and chemical instruments. Spectroscopic techniques are those where HONO is detected by spectroscopic features directly in the gas-phase (e.g. DOAS, TDL, Cavity Ring-Down Spectroscopy (CRDS), etc.) or after photolysis or ionisation (e.g. LIF, CIMS). Under the generic name of chemical instruments, we consider those where HONO is detected after chemical conversion to e.g. nitrite, an azo dye, etc. on humid surfaces (e.g. DNPH-cartridges, dry denuders) or aqueous surfaces (e.g. wet denuders, stripping coil instruments, mist chamber, LOPAP, etc.).

Among the spectroscopic techniques used during the FIONA campaign, UV absorption based techniques were used: DOAS and three different BBCEAS were deployed; one of them (U. College Cork/FZ Jülich) with the cavity placed directly in the simulation chamber, and two of them (U. College Cork and by U. Leicester) placed in the platform below the chamber from which the air samples were taken through sampling lines. Furthermore, a Fourier Transform Infra-red (FTIR) was used (CEAM Foundation), based on IR absorption. Other spectroscopic methods used were Chemical Ionization Mass Spectrometry (CIMS by German Aerospace Center-DLR) and Photo Fragmentation Laser-Induced Fluorescence (PF-LIF by Georgia Institute of Technology).

Regarding chemical techniques, five LOPAP monitors were used during the campaign with differences with respect to configuration and location of the instruments in the chamber (F. CEAM, U. Wuppertal, FZ Jülich, U. Houston and CNRS-ICARE). Other techniques used were: a MIST Chamber Ion Chromatography (MC/IC by U. New Hampshire); a Luminol chemilumines-cence based with wet denuder monitor (Institute of Analytical Chemistry of Brno); two instruments based on coil acid derivatization using HPLC (LISA: NITROMAC) and long path flow cell spectrometry (Wadsworth Center: SUNY); sodium carbonate denuders (IVL-Swedish Environmental Research Institute) and a Liquid Chromatography-Mass Spectrometer (LC-MS by CEAM Foundation). Further details on the instruments

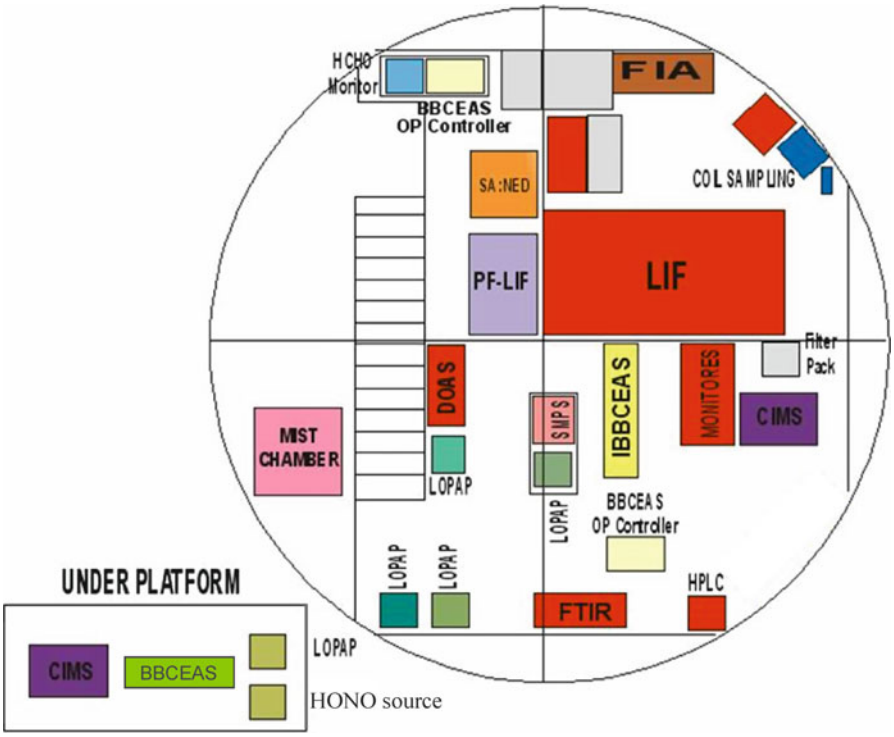

Fig. 4.2 Instrument locations on the platform below the EUPHORE chamber and in the lab floor below

and on the experiments during the FIONA campaign can be found in [27]. Figure 4.2 shows a schematic of the instrument locations during the campaign on the platform, i.e., below the simulation chamber, to which they were connected through sampling lines and flanges. Instruments under the platform are also shown. The optical set-up of the in situ techniques (DOAS, FTIR and Open-BBCEAS) installed inside the chamber, are not shown here.

The variety of techniques in the FIONA campaign required the design of experiments with conditions that allowed all the instruments to measure simultaneously. Thus, scenarios were simulated, which resulted in HONO concentrations that were measurable by all the instruments. Table 4.1 shows the different groups attending the campaign and the corresponding instruments deployed, together with the typical concentration ranges and detection limits. As observed, the sampling time of the instruments varied from seconds to 10 min, though most of the instruments with higher temporal resolution averaged their data to 1 min of sampling. On the other hand, detection limits varied from a few ppt to 2 ppb for the FTIR. In addition, the range of concentrations detectable by the instruments was from a few ppt up to hundreds of ppb. Urban HONO levels can vary widely depending on the atmospheric conditions. Daytime concentrations are low; averaged minimum values lower than 0.1 ppb have been reported [16, 39]. On the other hand, observations

Table 4.1 Instruments used to measure HONO during the FIONA campaign

Institution	Instrument	Location	Ranges	Det. Limit
UCC (Ireland)	OPIBBCEAS	Chamber	0.2–100 ppb	0.2 ppb
FZJ Jülich (Germany)	(Open-path IBBCEAS)			
UCC (Ireland)	IBBCEAS	Platform/ Lab-Floor	0.5–100 ppb	0.5 ppb
U. Leicester (UK)	BBCEAS	Platform	>100 ppt	100 ppt
Georgia Tech (USA)	PF-LIF	Platform	0–2 ppb	1 ppt
CEAM (Spain)	DOAS	Chamber	0.4–200 ppb	0.4 ppb
CEAM (Spain)	FTIR	Chamber	1.5–2,000 ppb	1.5 ppb
U. Houston (USA)	LOPAP	Chamber[a]	2 ppt–200 ppb	2 ppt
BUW (Germany)	LOPAP	Lab-Floor[a]	5 ppt–200 ppb	5 ppt
CNRS-ICARE (France)	LOPAP	Chamber[a]	2 ppt–200 ppb	2 ppt
U. Jiüich (Germany)	LOPAP	Chamber[a]	2 ppt–200 ppb	2 ppt
CEAM (Spain)	LOPAP	Chamber[a]	5 ppt–150 ppb	5 ppt
LISA (France)	NITROMAC	Chamber	5 ppt–35 ppb	5 ppt
DLR (Germany)	CIMS	Lab-Floor	15 ppt–20 ppb	15 ppt
U. New Hampshire, Durham (USA)	MC/IC	Platform	1 ppt–several ppb	1 ppt
Inst Analytical Chem (Czech Rep)	DENUDER (Wet denuder + chemiluminescent monitor)	Platform	15 ppt–45 ppb	15 ppt
Wadsworth Center and SUNY (USA)	CALPAS (Coil/azo dye deny/long-path flow cell spectrometry with denuder)	Platform	3 ppt–20 ppb	3 ppt
CEAM (Spain)	LC-MS (DNPH cartridges)	Platform	100 ppt–few ppb	100 ppt
Swedish Environ Res Inst (Sweden)	Filter pack denuders	Chamber	–	–

[a] Refers to the location of the sampling unit

follow a trend that shows averaged values of 0.3–3.5 ppb during the night [10, 23] and 0.07–2 ppb during the day [3, 31], with maximum HONO peaks up to 15 ppb reached before sunrise [11, 41]. Taking these data as well as the characteristics of the instruments participating in the campaign into account, urban and semi-rural sites were simulated.

4.4 Chamber Experiments

As stated above, the aim of the FIONA campaign was to intercompare HONO measurements by different instruments with the emphasis on both the chemistry of the atmosphere and the interferences of the methodologies involved. Therefore, the experiments were designed on the basis of studying the behaviour of the methodologies under different conditions as well as the HONO chemistry according to the following topics:

1. Intercomparison of the techniques for different scenarios simulated throughout the campaign. In particular, comparisons were also made using added unknown amounts of HONO into the chamber or by dilution of the initial concentration of HONO to get various lower concentration levels.
2. Characterization of potential interferences under different conditions (aerosols, nitrites, or/inorganic nitrates, NO_2, O_3, aerosols, aromatics, peroxides, NO_2 + SO_2 and small aldehydes).
3. Study of identified HONO sources (nitrophenols, vehicle emissions, etc). With this purpose, simulations of semi-rural and urban sites were done:

   - HONO mixing ratios: 0.5–15 ppb
   - Diesel engine exhaust
   - Ambient air
   - Photochemical processes

The campaign was divided into two parts. The first experiments were part of an open-informal intercomparison, where the participants could exchange and discuss their results with the aim of improving their instruments and checking them after the special set-up performed to be adapted to the chamber. They also allowed the detection and solution of potential problems prior to starting the second part of the campaign, i.e., the formal blind intercomparison. In these experiments, the groups were not allowed to share their results with the other participants and the data were directly inspected by an external referee.

For a better dissemination of data, the results of the experiments will be freely accessible at the EUROCHAMP webpage www.eurochamp.org upon registration and after data exploitation by the campaign participants. Raw data will be provided in the specific EUROCHAMP text format (edf). More information on the FIONA campaign can be found at http://euphore.es/fiona/fiona.html.

4.5 Results and Discussion

The experiment shown here was performed on 18 May 2010. An unknown amount of HONO was introduced in the clean and dry chamber through a stream of purified air. HONO was obtained by the addition of a 1.5% solution of $NaNO_2$, (Fluka) to a 30% solution of H_2SO_4 (Scharlab), while continuously flushing the resulting gas

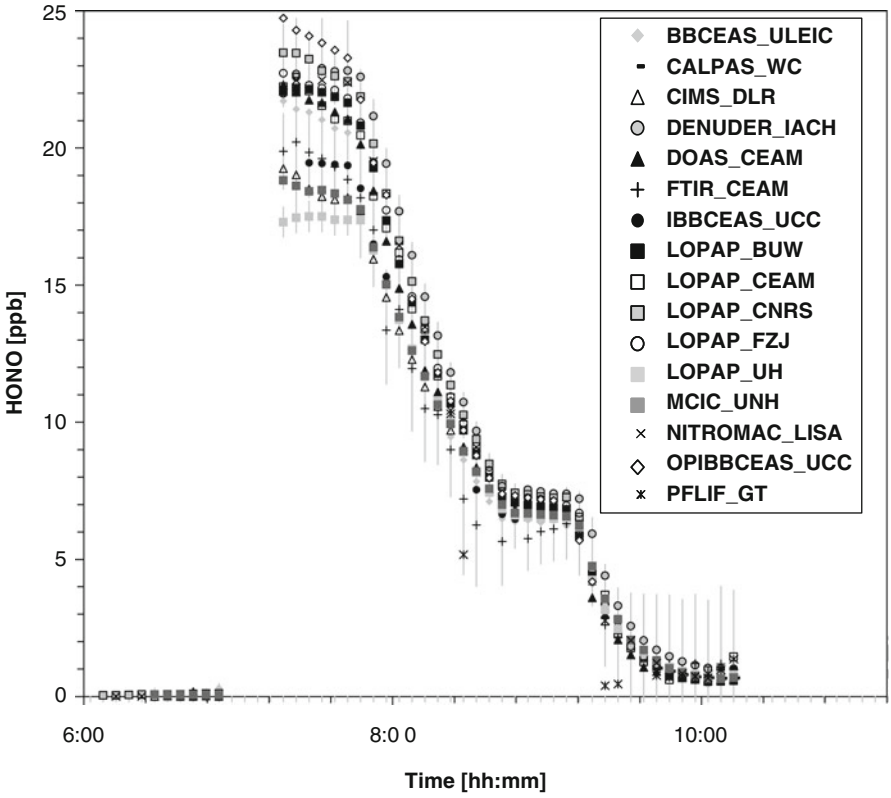

Fig. 4.3 Temporal HONO concentration profile. Chamber was flushed at 7:52 and opened at 9:12

phase products into the chamber (10 $l \cdot min^{-1}$). This generation method also produces NO and NO_2, with a typical HONO/NO_x ratio of 1:1. The aim of the experiment was to perform simultaneous HONO measurements at different concentration levels. After the addition of HONO to the chamber (*ca.* 22 ppb), the gas mixture was allowed to remain there for measurements for 30 min. The concentration was then decreased to by *ca.* 7 ppb by dilution of the air mixture by introducing clean air. Instruments measured also at this concentration for 30 min before the chamber was exposed to the sunlight which caused the HONO concentration to decrease to *ca.* 0.6 ppb.

Figure 4.3 shows the HONO profile observed by the different instruments. For the high concentrations (not representative of atmospheric conditions) during the first part of the experiment some of the instruments may have shown non-linearities or saturation. However, these high values have not yet been reported in the atmosphere, neither at semi-rural nor urban conditions, which were the object of study of the FIONA campaign.

Figure 4.4 shows the regressions of the HONO data from the different instruments presented in Fig. 4.3 against the DOAS data, which was adopted as a common basis for comparison.

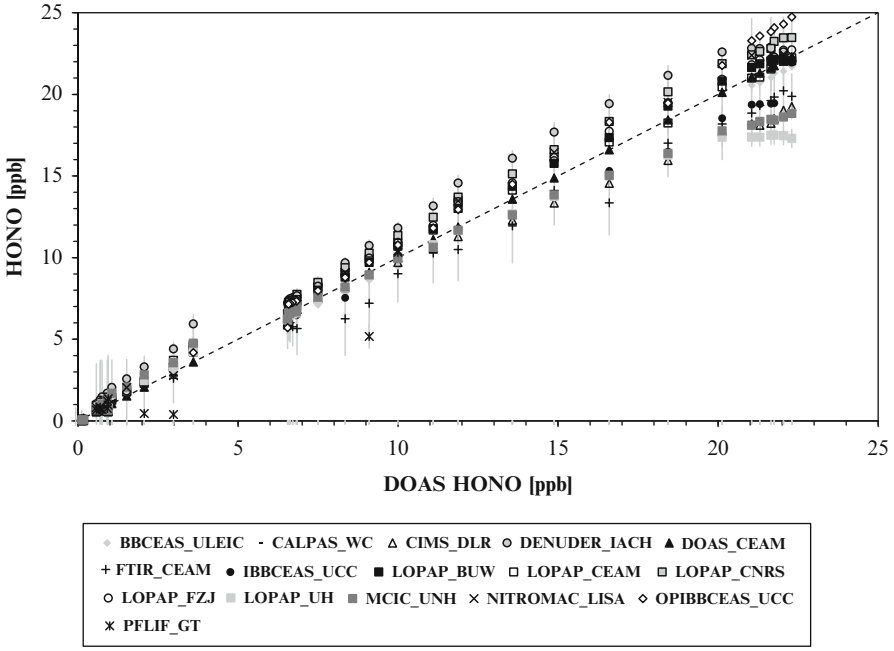

Fig. 4.4 HONO concentrations measured by the instruments vs. HONO retrieved using DOAS

Table 4.2 Regression of HONO data from the different instruments vs. the DOAS data

Y = bx + a	b	a	R^2
BBCEAS_ULEIC	0.928	0.141	0.996
CALPAS_WC	1.094	0.034	0.870
CIMS_DLR	0.950	0.258	0.995
DENUDER_IACH	1.064	0.726	0.983
FTIR_CEAM	0.864	0.193	0.966
IBBCEAS_UCC	0.924	0.326	0.983
LOPAP_BUW	1.047	0.061	0.996
LOPAP_CEAM	1.051	0.174	0.992
LOPAP_CNRS	1.106	0.068	0.997
LOPAP_FZJ	1.072	0.095	0.997
LOPAP_UH	0.933	0.411	0.997
MCIC_UNH	0.950	0.354	0.992
NITROMAC_LISA	1.041	0.145	0.996
OPIBBCEAS_UCC	1.058	0.023	0.963
PFLIF_GT	0.824	−0.312	0.837

The coefficients of the corresponding regression curves for this experiment calculated for concentrations below 15 ppb are shown in Table 4.2.

As expected for this simple reaction mixture, there is a general good agreement among the techniques with regression factors near unity showing also high precision, while differences can be partly attributed to saturation of some instruments at

high concentrations. In fact, the MC/IC, was configured to measure at lower values. PF-LIF could have suffered from misalignments since the adaptation of the instrument to the chamber was initially complicated during the first days.

Another reason for the differences could possibly be calibration issues. In addition, it must be also considered that DOAS has been used as reference in the regressions here, and, although it shows high accuracy as stated above, it has a lower precision than other techniques (see Table 4.1), which could worsen the R^2 factor because concentrations close to its detection limit are included in the data set. FTIR shows a high detection limit, resulting in a poorer regression curve.

4.6 Conclusions

During the international FIONA campaign almost all types of instruments used to detect HONO in the atmosphere were simultaneous intercompared under atmospheric conditions for the first time. A set of experiments was carried out at the EUPHORE chambers to test a wide range of scenarios, simulating urban and semi-rural environments, under well controlled conditions. Interferences and chemical issues were addressed. Complex mixtures studied within the campaign, showed deviations for some measurements under given circumstances, which will be studied further. Nevertheless, the first results of the experiments showed good agreement among the techniques with generally good correlations. Exploitation of the FIONA results is still under development as work is ongoing.

Acknowledgments The authors wish to acknowledge the European Community's Seventh Framework Program under the grant agreement no. 228335 (Eurochamp2) through the TA E2-2009-12-29-0014 and E2-2010-02-15-0020.

The Instituto Universitario CEAM-UMH is partly supported by Generalitat Valenciana, and the projects GRACCIE (Consolider-Ingenio 2010) and FEEDBACKS (Prometeo – Generalitat Valenciana). EUPHORE instrumentation is partly funded by the Spanish Ministry of Science and Innovation, through INNPLANTA project: PCT-440000-2010-003

The FIONA Team

A. Muñoz[1], M. Ródenas[1], F. Alacreu[1], H-P. Dorn[2], T. Brauers[2], J. Kleffmann[3], P. Mikuška[5], Z. Večeřa[5], R. Häseler[2], C. Ye[2], A. Ruth[6], S. Dixneuf[6], D. Venables[6], S. Darby[6], J. Chen[6], E. Ashu-Ayem[6], Y. Elshorbany[3], C. Voigt[7], P. Jessberger[7], S. Kaufmann[7], D. Schäuble[7], A. Mellouki[8], M. Cazaunau[8], B. Grosselin[8], J.-F. Doussin[9], A. Colomb[9], V. Michoud[9], K. Miet[9], C. Afif[9], S. Ball[10], M. Daniels[10], I. Goodall[10], D. Tan[11], R. Stickel[11], A. Case[12], B. Rappenglück[13], G. Croxatto[13], J. Dibb[14], E. Scheuer[14], X. Zhou[15], M. Ferm[16], R. Varma[17], M. Pilling[18], E. Clemente[1], R. Porras[1], T. Vera[1], M. Vázquez[1], E. Borrás[1], J. Valero[1], W. Bloss[4].

[1]Instituto Universitario UMH – CEAM, Paterna, Valencia, Spain
[2]Forschungszentrum Jülich, Jülich, ICG-2, Germany
[3]Bergische Universität Wuppertal (BUW), Wuppertal, Germany
[4]University of Birmingham, Birmingham, UK
[5]Institute of Analytical Chemistry–Brno, Brno, Czech Republic
[6]University College Cork, Cork, Ireland

[7]German Aerospace Center – DLR, Bonn, Germany
[8]CNRS – ICARE, Orleans, France
[9]LISA, University Paris-12, Paris, France
[10]Univeristy of Leicester, Leicester, UK
[11]Georgia Technology, Atlanta, GA, USA
[12]University of Louisiana, Monroe, LA, USA
[13]University of Houston, Houston, TX, USA
[14]University of New Hampshire, Durham, NH, USA
[15]Wadsworth Center and SUNY Albany, NY, USA
[16]Swedish Environmental Research Institute, Göteborg, Sweden
[17]National Institute of Technology – NIT Calicut, Kerala, India
[18]University of Leeds, Leeds, UK

References

1. Acker K, Möller D, Wieprecht W, Meixner FX, Bohn B, Gilge S, Plass-Dülmer C, Berresheim H (2006) Strong daytime production of OH from HNO_2 at a rural mountain site. Geophys Res Lett 33(2):L02809
2. Alicke B, Platt U, Stutz J (2002) Impact of nitrous acid photolysis on the total hydroxyl radical budget during the Limitation of Oxidant Production/Pianura Padana Produzione di Ozono study in Milan. J Geophys Res 107(D22):8196
3. Alicke B, Geyer A, Hofzumahaus A, Holland F, Konrad S, Pätz H-W, Schäfer J, Stutz J, Volz-Thomas A, Platt U (2003) OH formation by HONO photolysis during the BERLIOZ experiment. J Geophys Res 108(D4):8247
4. Appel BR, Winer AM, Tokiwa Y, Biermann HW (1990) Comparison of atmospheric nitrous acid measurements by annular denuder and optical absorption systems. Atmos Environ 24 (A):611–616
5. Ball SM, Langridge JM, Jones RL (2004) Broadband cavity enhanced absorption spectroscopy using light emitting diodes. Chem Phys Lett 398:68–74
6. Becker KH (1996) The European photoreactor EUPHORE final report of the EC-project EUPHORE, contract EV5V-CT92-0059, Wuppertal
7. Calvert JG, Yarwood G, Dunker AM (1994) An evaluation of the mechanism of nitrous acid formation in the urban atmosphere. Res Chem Intermed 20:463–502
8. Dibb JE, Arsenault M, Peterson MC, Honrath RE (2002) Fast nitrogen oxide photochemistry in Summit, Greenland snow. Atmos Environ 36:2501–2511
9. Dibb JE, Huey LG, Slusher DL, Tanner DJ (2004) Soluble reactive nitrogen oxides at South Pole during ISCAT 2000. Atmos Environ 38:5399–5409
10. Elshorbany YF, Kurtenbach R, Wiesen P, Lissi E, Rubio M, Villena G, Gramsch E, Rickard AR, Pilling MJ, Kleffmann J (2009) Oxidation capacity of the city air of Santiago, Chile. Atmos Chem Phys 9:2257–2273
11. Elshorbany YF, Kleffmann J, Kurtenbach R, Lissi E, Rubio M, Villena G, Gramsch E, Rickard AR, Pilling MJ, Wiesen P (2010) Seasonal dependence of the oxidation capacity of the city of Santiago de Chile. Atmos Environ 44:5383–5394
12. Gherman T, Venables DS, Vaughan S, Orphal J, Ruth AA (2008) Incoherent broadband cavity-enhanced absorption spectroscopy in the near-ultraviolet: application to HONO and NO_2. Environ Sci Technol 42(3):890–895
13. Harrison RM, Kitto AMN (1994) Evidence for a surface source of atmospheric nitrous acid. Atmos Environ 28:1089–1094
14. Kleffmann J, Heland J, Kurtenbach R, Lörzer JC, Wiesen P (2002) A new instrument (LOPAP) for the detection of nitrous acid (HONO). Environ Sci Pollut Res 9:48–54

15. Kleffmann J (2007) Daytime sources of nitrous acid (HONO) in the atmospheric boundary layer. Chem Phys Chem 8:1137–1144
16. Kleffmann K, Wiesen P (2008) Technical note: quantification of interferences of wet chemical HONO LOPAP measurements under simulated polar conditions. Atmos Chem Phys 8:6813–6822
17. Kleffmann J, Kurtenbach R, Lörzer J, Wiesen P, Kalthoff N, Vogel B, Vogel H (2003) Measured and simulated vertical profiles of nitrous acid, part I: field measurements. Atmos Environ 37:2949–2955
18. Kleffmann J, Gavriloaiei T, Hofzumahaus A, Holland F, Koppmann R, Rupp L, Schlosser E, Siese M, Wahner A (2005) Daytime formation of nitrous acid: a major source of OH radicals in a forest. Geophys Res Lett 32:L05818
19. Kleffmann J, Lörzer JC, Wiesen P, Kern C, Trick S, Volkamer R, Rodenas M, Wirtz K (2006) Intercomparison of the DOAS and LOPAP techniques for the detection of nitrous acid (HONO). Atmos Environ 40:3640–3652
20. Kurtenbach R, Becker KH, Gomes JAG, Kleffmann J, Lörzer JC, Spittler M, Wiesen P, Ackermann R, Geyer A, Platt U (2001) Investigation of emissions and heterogeneous formation of HONO in a road traffic tunnel. Atmos Environ 35:3385–3394
21. Lammel G, Cape JN (1996) Nitrous acid and nitrite in the atmosphere. Chem Soc Rev 25:361–369
22. Li YQ, Schwab JJ, Demerjian KL (2008) Fast time response measurements of gaseous nitrous acid using a tunable diode laser absorption spectrometer: HONO emission source from vehicle exhausts. Geophys Res Lett 35(4):L04803
23. Li X, Brauers T, Häseler R, Bohn B, Hofzumahaus A, Holland F, Lu KD, Rohrer F, Hu M, Zeng LM, Zhang YH, Garland R, Su H, Nowak A, Takegawa N, Shao M, Wahner A (2011) Exploring the atmospheric chemistry of nitrous acid (HONO) at a rural site in Southern China. Atmos Chem Phys Discuss 11:27591–27635
24. Liao W, Case AT, Mastromarino J, Tan D, Dibb JE (2006) Observations of HONO by laser-induced fluorescence at the South Pole during ANTCI 2003. Geophys Res Lett 33(9):L09810
25. Mikuška P, Motyka K, Večeřa Z (2008) Determination of nitrous acid in air using wet effluent diffusion denuder – FIA technique. Talanta 77:635–641
26. Muñoz A, Vera T, Sidebottom H, Mellouki A, Borrás E, Ródenas M, Clemente E, Vazquez M (2011) Studies on the atmospheric degradation of Chlorpyrifos-methyl. Environ Sci Technol 45:1880–1886
27. Muñoz A, Ródenas M, Alacreu F, Dorn H-P, Brauers T, Kleffmann J, Mikuška P, Večeřa Z, Häseler R, Ye C, Ruth A, Dixneuf S, Venables D, Darby S, Chen J, Ashu-ayem E, Elshorbany Y, Voigt C, Jessberger P, Kaufmann S, Schäuble D, Mellouki A, Cazaunau M, Grosselin B, Doussin J-F, Colomb A, Michoud V, Miet K, Afif C, Ball S, Daniels M, Goodall I, Tan D, Stickel R, Case A, Rappenglück B, Croxatto G, Dibb J, Scheuer E, Zhou X, Ferm M, Varma R, Pilling M, Clemente E, Porras R, Vera T, Vázquez M, Borrás E, Valero J, Bloss W. Overview of the FIONA campaign, Final Report to the European Commission, 2012 (in preparation)
28. Notholt J, Hjorth J, Raes F, Schrems O (1992) Simultaneous long path field measurements of HNO_2, CH_2O and aerosol. Ber Bunsenges Phys Chem 3:290–293
29. Pitts JN Jr, Grosjean D, van Cauwenberghe K, Schmid JP, Fitz DR (1978) Photooxidation of aliphatic amines under simulated atmospheric conditions: formation of nitrosamines, nitramines, amides, and photochemical oxidant. Environ Sci Technol 12:946–953
30. Platt U, Perner D, Harris GW, Winer AM, Pitts JN (1980) Observations of nitrous acid in an urban atmosphere by differential optical absorption. Nature 285:312–314
31. Qin M, Xie P, Su H, Gu J, Peng F, Li S, Zeng L, Liu J, Liu W, Zhang Y (2009) An observational study of the HONO–NO_2 coupling at an urban site in Guangzhou City, South China. Atmos Environ 43:5731–5742
32. Reisinger AR (2000) Observation of HNO_2 in the polluted winter atmosphere: possible heterogeneous production on aerosols. Atmos Environ 34:3865–3874

33. Schimang R, Folkers A, Kleffmann J, Kleist E, Miebach M, Wildt J (2006) Uptake of gaseous nitrous acid (HONO) by several plant species. Atmos Environ 40:1324–1335
34. Stemmler K, Ammann M, Dondors C, Kleffmann J, George C (2006) Photosensitized reduction of nitrogen dioxide on humic acid as a source of nitrous acid. Nature 440:195–198
35. Stutz J, Oh H-J, Whitlow SI, Anderson C, Dibb JE, Flynn JH, Rappenglück B, Lefer B (2010) Simultaneous DOAS and mist-chamber IC measurements of HONO in Houston, TX. Atmos Environ 44:4090–4098
36. Varma RM, Venables DS, Ruth AA, Heitmann U, Schlosser E, Dixneuf S (2009) Long optical cavities for open-path monitoring of atmospheric trace gases and aerosol extinction. Appl Opt 48(4):B159–B171
37. Veitel H (2002) Vertical profiles of NO_2 and HONO in the boundary layer. Dissertation, Universität Heidelberg
38. Vogel B, Vogel H, Kleffmann J, Kurtenbach R (2003) Measured and simulated vertical profiles of nitrous acid, part II: model simulations and indications for a photolytic source. Atmos Environ 37:2957–2966
39. Wentzell JJB, Schiller CL, Harris GW (2010) Measurements of HONO during BAQS-Met. Atmos Chem Phys 10:12285–12293
40. Wiessen P (2000) DIFUSO: diesel fuel and soot – fuel formulation and its atmospheric implications. Final report of the EC project, Wuppertal
41. Winer AM, Biermann HW (1994) Long pathlength differential optical absorption spectroscopy (DOAS) measurements of gaseous HONO, NO_2 and HCHO in the California South Coast Air Basin. Res Chem Intermed 20:423–445
42. Wong KW, Oh H-J, Lefer BL, Rappenglück B, Stutz J (2011) Vertical profiles of nitrous acid in the nocturnal urban atmosphere of Houston, TX. Atmos Chem Phys 11:3595–3609
43. Zhou X, Civerolo K, Dai H, Huang G, Schwab J, Demerjian K (2002) Summertime nitrous acid chemistry in the atmospheric boundary layer at a rural site in New York State. J Geophys Res 107(D21):4590

Chapter 5
State of the Art OH and HO_2 Radical Measurement Techniques: An Update

Dwayne Heard

Abstract The methods used for atmospheric measurements of OH and HO_2 radicals are reviewed. Focus is given to advances in the measurement technology, instrument design and calibration for OH and HO_2 measurements and a summary of results from some recent intercomparison studies, in particular, the HOxCOMP campaign are presented.

Keywords Radicals • Oxidation • Photochemistry • FAGE • CIMS • Interferences

5.1 Introduction

Free-radicals mediate virtually all of the oxidative chemistry in the atmosphere, being responsible for the transformation of primary emissions into secondary pollutants such as NO_2, O_3 and particulates. Radicals control the lifetime of climate gases (e.g. CH_4), the budget of O_3 in all parts of the atmosphere, and the production of acidic species. Understanding the behaviour of free-radicals in the atmosphere is of paramount importance in understanding the lifetime and hence spatial scales of pollutant transport. Predictive models for future air quality and climate change contain complex chemical schemes, and the measurement of free-radicals in the present atmosphere constitutes the best validation of these schemes through comparison with model predictions. The lifetime of free-radicals is short, and in general, their budgets are controlled only by *in situ* chemistry, and not by transport processes, and hence the chemistry can be studied by field-measurements at a single point in order to constrain zero-dimensional models. In summary, free-radicals are the instigators of all chemistry that impacts climate and air quality, and are ideal targets for atmospheric models. They are short-lived (seconds), and hence their concentrations are not influenced by their transport, only by the local *in situ* chemistry.

D. Heard (✉)
School of Chemistry, University of Leeds, Leeds LS2 9JT, UK
e-mail: D.E.Heard@leeds.ac.uk

I. Barnes and K.J. Rudziński (eds.), *Disposal of Dangerous Chemicals in Urban Areas and Mega Cities*, NATO Science for Peace and Security Series C: Environmental Security,
DOI 10.1007/978-94-007-5034-0_5,

The hydroxyl radical, OH, removes the majority of trace gases emitted into the atmosphere, including greenhouse gases and substances harmful to health, and initiates the formation of wide range of secondary species, for example ozone and secondary organic aerosol, two components of photochemical smog. The reaction of HO_2 and RO_2 radicals with NO represents the only tropospheric *in situ* source of ozone. There have now been a considerable number of field campaigns in which field measured concentrations of short-lived free-radicals have been compared with the results of zero-dimensional model simulations, highly constrained to the observed field data for longer-lived species (for older work see [15, 19] and references therein). The use of a zero-dimensional model with no spatial resolution is presumed adequate for model comparisons, since transport of such short-lived radical species does not contribute significantly to their local concentration.

In this paper, a summary and recent developments will be presented concerning two techniques that are currently used for the measurement of tropospheric OH and HO_2 radicals, namely laser-induced fluorescence at low-pressure, known as FAGE (Fluorescence Assay by Gas Expansion), and CIMS (Chemical Ionisation Mass Spectrometry). The emphasis will be on developments concerning FAGE. FAGE detects OH directly, whereas in the CIMS method it is first converted to H_2SO_4 which is then detected by mass spectrometry. HO_2 is not detected directly by either of the techniques, rather it is converted first to OH. Other methods have been developed for the direct detection of OH and HO_2 radicals, for example Differential Optical Absorption Spectroscopy (DOAS) and Matrix Isolation Electron Spin Resonance (MIESR). However, other than for comparison in chambers these will not be considered in this paper, as they are techniques that are no longer used for field measurements. Advances in technology, instrument design and calibration will be discussed for OH and HO_2 measurements, together with a summary of results from some recent intercomparison studies, in particular the HOxCOMP campaign [10, 31] performed in the SAPHIR (Simulation of Atmospheric PHotochemistry In a large Reaction Chamber) chamber at Forschungszentrum, Julich. Interferences are a potential problem shared by all field instruments, and recently there has been a reported interference for HO_2 measured using the FAGE technique [11], which will be discussed, together with potential interferences for OH which may be present under certain types of field conditions. A new method, which is able to partially speciating atmospheric peroxy radicals is also described, as detection is based on the FAGE technique following a pre-reactor which converts organic peroxy radicals into HO_2 which are then detected [8].

5.2 FAGE and CIMS Techniques Used for Field Measurement of Tropospheric OH and HO_2 Radicals

Field measurements of tropospheric OH and HO_2 radicals are extremely challenging, owing to their very low concentrations (OH ~ 10^6 molecule cm^{-3}; HO_2 ~10^8 molecule cm^{-3}), high reactivity and therefore short lifetime (τ(OH) ~0.01–1 s;

$\tau(HO_2)$ ~5–100 s), and their rapid loss rate onto surfaces of inlets. Both the FAGE and CIMS techniques have been described before (for representative references see [15]), and have enjoyed considerable success for field measurement of OH and HO_2. In the FAGE technique, OH radicals are measured by 308 nm laser-induced fluorescence (LIF) spectroscopy at low pressure and HO_2 is first converted to OH by the addition of NO prior to FAGE detection of the OH formed. Simultaneous measurements are possible *via* two independent detection cells, which depending on the design are either in series with a single sampling pinhole and the OH fluorescence cell closer to the sampling nozzle, or in parallel with two independent sampling pinholes, and allowing a different pressure in each cell. Delayed gated photon counting is used to detect fluorescence from OH and to discriminate from the more intense scattered light. Two types of high pulse-repetition frequency laser system are used, either a Nd: YAG pumped dye-laser, which is frequency doubled to generate 308 nm, or an all solid state Nd: YAG pumped titanium sapphire laser, which is frequency tripled to generate 308 nm. A typical detection limit for the FAGE technique is (2–5) $\times$ 10^5 and (5–10) $\times$ 10^5 molecule cm^{-3} for OH and HO_2, respectively, with an accuracy of ~20–30% [15].

In the CIMS technique OH is converted quantitatively to $H_2{}^{34}SO_4$ by the following reactions:

$$OH + {}^{34}SO_2 + M \rightarrow H^{34}SO_3 + M \tag{5.1}$$

$$H^{34}SO_3 + O_2 \rightarrow {}^{34}SO_3 + HO_2 \tag{5.2}$$

$${}^{34}SO_3 + H_2O + M \rightarrow H_2{}^{34}SO_4 + M \tag{5.3}$$

and $H_2{}^{34}SO_4$ is chemically ionised by the reaction:

$$NO_3{}^-.HNO_3 + H_2{}^{34}SO_4 \rightarrow H^{34}SO_4{}^-.HNO_3 + HNO_3 \tag{5.4}$$

The isotopically labelled ^{34}S is used to discriminate against naturally occurring $H_2{}^{32}SO_4$. The CIMS method is the most sensitive of all OH field instruments, with a detection limit of better than 10^5 molecule cm^{-3} [1, 7, 32].

There remains only one calibration method used in the field for the calibration of FAGE and CIMS instruments, the mercury pen-lamp photolysis of water vapour at 184.9 nm, which in the presence of air generates equal concentrations of OH and HO_2, which are given by:

$$[OH] = [HO_2] = [H_2O]\,\sigma_{H2O,184.9\,nm}\,\phi_{OH}\,F_{184.9\,nm}\,t \tag{5.E1}$$

where σ is the water vapour absorption cross-section, ϕ is the photodissociation quantum yield of OH from water vapour (=1), F is the photon flux of the lamp, all at 184.9 nm, and where t is the photolysis exposure time. The first three terms can be determined accurately, and there have been two approaches to measure the

product $F_{184.9\ nm}\ t$. One approach measures $F_{184.9\ nm}$ directly using a calibrated phototube, and t is calculated using the known flow properties of the calibration flow tube. The other approach is to use a chemical actinometer to determine the product, rather than each individually, and two have been developed involving the production and measurement of O_3 or NO initiated from O_2 and N_2O (added to the flow) photolysis, respectively, and which give the same value within errors.

All groups active in field measurements of OH and HO_2 rely on the photolysis of water vapour to calibrate their instruments, and although there is currently no evidence that there is a bias or other problem with this method, it is a concern that reliance for all absolute concentrations is given to a single method. Intercomparisons with the DOAS method, which does not rely on a calibration (only needing knowledge of spectroscopic constants which are well established in the laboratory), either in the field [17] or in chambers [30, 31], provides confidence in the calibration method. Indirect calibration has been achieved using the decay of a hydrocarbon for which the rate coefficient k_{OH+HC} is well established in the literature, with [HC] measured using GC-FID as function of time to give:

$$[OH] = \frac{(-d[HC]/dt)}{k_{OH+HC} \times [HC]} \tag{5.E2}$$

Such an approach has given good agreement with [OH] measured in chambers with instruments calibrated using the water photolysis method [2]. The calibration of instruments as a function of pressure, which varies during the operation of aircraft measurements, is difficult to achieve, but recently the HIRAC (Highly Instrumented Reactor for Atmospheric Chemistry) [13] chamber, which is constructed of stainless steel, has been used to generate OH radicals at a total pressure of 220–760 Torr. OH concentrations determined by HC decays agreed with those obtained using a FAGE instrument that had been previously calibrated using the water vapour technique at atmospheric pressure, but using sampling pinholes of different diameters to reproduce the necessary pressure within the fluorescence cell [23]. The generation of OH from a reaction of an alkene giving a known yield of OH can also been used to calibrate for OH [24], but is not currently used in the field. For HO_2, observing the rate of HO_2 decay from the second order self-reaction, and knowledge of the rate coefficient and any wall loss, k_{loss} enables $[HO_2]$ to be determined from solution of the following differential equation:

$$\frac{d[HO_2]}{dt} = -(k_{loss}[HO_2] + 2k_{HO2+HO2}[HO_2]^2) \tag{5.E3}$$

in order to calibrate instruments. This method has enjoyed success in chambers [23], but is not used in the field owing to the length of time required to observe the decay under realistic concentrations of HO_2.

5.3 HOxCOMP: A Recent Intercomparison at the SAPHIR Chamber

Intercomparisons between different field instruments measuring OH and/or HO_2 radicals are still uncommon, but represent one of the quality control mechanisms to probe any differences in instrument behaviour, calibration and susceptibility towards interferences [15]. The SAPHIR campaign in Julich is a highly-instrumented chamber equipped with the only operating long-path DOAS instrument with the capability of measuring atmospheric levels of OH. As DOAS requires no calibration, merely knowledge of the absorption cross-sections at the relevant temperature and pressure and the path length, it provides an absolute standard for OH. The HOxCOMP campaign, performed in 2005 [10, 31], provided both an out of chamber (ambient) and an in chamber formal-blind intercomparison for both OH and HO_2. One DOAS (in SAPHIR chamber only), 3 FAGE and 1 CIMS instruments from Germany and Japan were involved, and followed on from a successful previous OH intercomparison involving just the Julich group [30]. For OH the agreement is in general very good over a range of different levels of humidity, O_3, NO_2, and radiation (including under dark conditions) with gradients of the correlation plots ranging from 1.01 to 1.13. A CIMS instrument also participated in the ambient phase of the intercomparison, together with three LIF instruments, and correlation gradients of 1.06–1.69 were observed, which were sometimes outside the combined uncertainty limits.

Three FAGE instruments employing NO induced $HO_2 \rightarrow OH$ conversion participated in an HO_2 intercomparison, and here the agreement between instruments was more variable, with correlation slopes between 0.69 and 1.26 in the chamber and sometimes higher for ambient [10]. The agreement in the chamber was a function of the particular experiment, with better correlations when grouped by water vapour. There is an unknown factor related to water vapour which appears to give a bias for some instruments [10].

5.4 Partial Speciation of RO_2 and HO_2 Using a Variant of FAGE (ROxLIF)

Although one of the holy grails for atmospheric composition is the speciated field measurement of individual peroxy radicals, this has not yet been realised. The ROxLIF method is a fairly recent innovation which enables HO_2 and the sum of organic peroxy radicals to be measured separately [8], and with good sensitivity (~0.1 pptv detection limit in ~1 min). This provides additional information than provided by the peroxy radical chemical amplifier (PERCA) technique, although HO_2 and the sum of RO_2 has been measured separately using a CIMS detection method to measure OH via H_2SO_4 formation (ROXMAS: [14]; PerCIMS: [6]). Although upon addition of NO, conversion of RO_2 to RO is rapid (OH in the case of

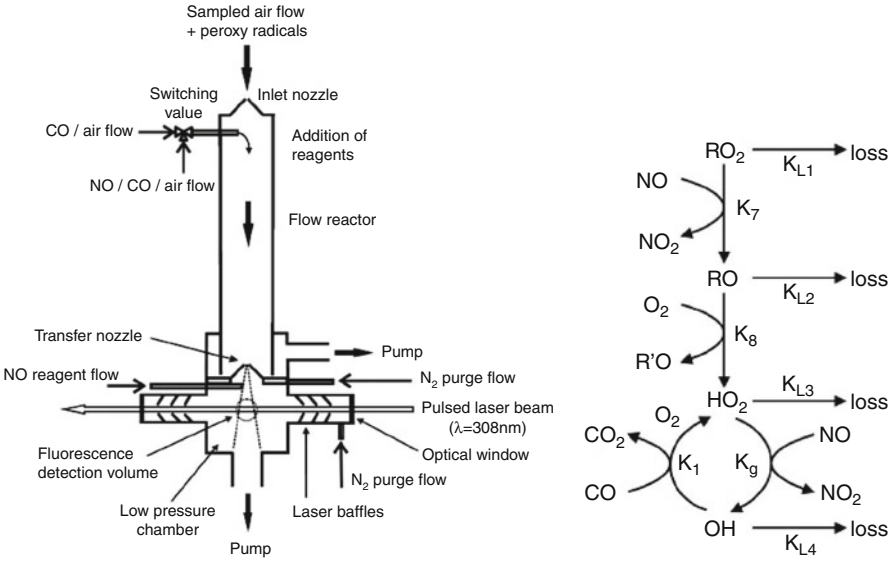

Fig. 5.1 Schematic diagram (*left*) of the ROxLIF instrument used to measure the sum of organic peroxy radicals. RO_2 is first converted to HO_2 in the flow reactor (25 hPa) through the addition of NO and CO via the chemical scheme shown on the *right hand panel*, and HO_2 is then detected in a FAGE fluorescence cell (Taken from Fuchs et al. [8])

HO_2), in a normal FAGE fluorescence cell, where the pressure is typically between 0.6 and 4 Torr, the rate of the reaction:

$$RO + O_2 \rightarrow R'CHO + HO_2 \tag{5.5}$$

is too slow to give significant conversion prior to the laser-probe volume where OH is detected, and so RO_2 does not constitute any of the signal measured as HO_2. This assumption, however, has recently been brought into question for larger R, and also when R contains an unsaturated or oxygenated functional group, as described below. Figure 5.1 shows the apparatus developed by Fuchs et al. [8] to measure RO_2 radicals, which is a modification of FAGE with a tubular pre-reactor into which ambient air is sampled via an expansion and NO and CO are added. The pre-reactor is connected to the FAGE fluorescence cell via a large pinhole (4 mm in diameter), where air undergoes a further, but modest expansion, and OH and HO_2 are detected (the latter via a second addition of NO).

The NO converts both HO_2 to OH, and RO_2 to RO, but as the pre-reactor is held at a considerably higher pressure (~30 Torr), the rate of reaction (5) is now high enough to give good conversion of RO to HO_2. However, the HO_2 formed is rapidly converted to OH, and due to the relatively long residence time in the pre-reactor to ensure that reaction (5) is complete, wall-losses of OH will be significant, leading to a very large loss of radicals before the second expansion, and concomitant loss in sensitivity. In a manner similar to PERCA, CO is added to convert OH and HO_2, and the relative flows and hence partial pressures of NO and CO are maintained

such that the lifetime of OH by reaction with CO is very short, and the HO_2 to OH ratio kept high, so wall losses are minimised (HO_2 is much less reactive on the walls). Hence the radicals are in the form of HO_2 when sampled a second time into the FAGE cell for detection as HO_2. This method has now been adopted by other groups, and has enjoyed success both in the field and in chamber studies. Although a larger number of NO_2 and CO_2 molecules will be formed, as in PERCA, it is HO_2 that is detected directly using the FAGE technique with excellent sensitivity.

Speciation between, OH, HO_2 and the sum of other peroxy radicals is achieved in the ROxLIF method via modulation of the two NO flows and the CO flow. With no NO or CO added in the pre-reactor, HO_2 and RO_2 survive the passage to the second pinhole, and enter into the FAGE fluorescence cell, where only OH is detected in the absence of added NO. The OH signal is very low as ambient OH is chemically or physically lost on the walls during the significant residence time in the pre-reactor. With NO added in the fluorescence cell HO_2, but not RO_2, is detected due to the very low pressure (but see section below on interferences), and if CO is added to the pre-reactor, the sum of OH and HO_2 can be measured. Finally with NO added as well to the pre-reactor the sum of OH, HO_2 and RO_2 is measured, and RO_2 can be obtained by subtraction. If the pre-reactor/fluorescence cell combination is calibrated for HO_2, then measurement of [HO_2] in a separate, independent FAGE cell will enable continuous subtraction of the contribution of HO_2 to the observed total signal from HO_2 and RO_2 in the RO_2 cell. By adding the relevant hydrocarbon to the calibration flow-reactor containing water vapour, a range of RO_2 species can be generated and used to calibrate the instrument. Fuchs et al. measured the relative sensitivity of their ROxLIF instrument for peroxy radicals derived from methane (1.00), ethane (0.91), propane (0.96), isobutane (0.59), ethene (0.98) and isoprene (1.21), with the value in brackets being relative to CH_3O_2. A disadvantage is that ROxLIF still does not distinguish between different organic peroxy radicals, so in order to compare with a model calculation, it is necessary first to multiply the model-derived concentration for each RO_2 by the relevant sensitivity factor in order to compare with the field measured value. However, the ratio [ΣRO_2]/[HO_2] from the same instrument still provides important, and novel information about the mechanisms for chemical oxidation. An intercomparison between ROxLIF and the matrix isolation electron spin resonance (MIESR) technique (no longer operated by Julich) for HO_2 and RO_2 gave good agreement, with correlation slopes of 0.98 and 1.02, respectively [9]. An older field intecomparison between a PerCIMS and FAGE instrument for HO_2 also gave good agreement [27].

5.5 Surprising Results from the Field Which Have Raised Questions

Measurements of OH and HO_2 radicals in and above forested regions at low NOx have proven difficult to reconcile with the calculations of constrained box-models with embedded chemical mechanisms which can be very detailed. Carslaw et al. [3]

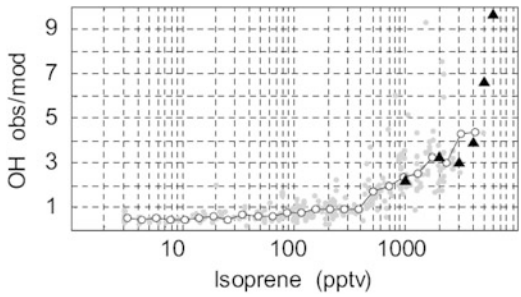

Fig. 5.2 Observed to modelled ratio of [OH] taken during INTEX-A for less than 1 km altitude (*open circles*) and from the ground during PROPHET (*solid triangles*) (Taken from Ren et al. [29])

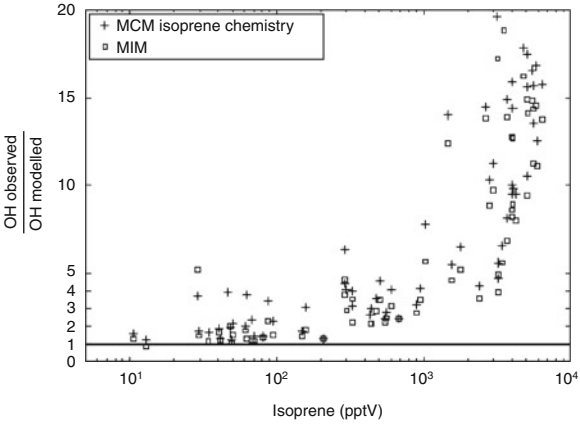

Fig. 5.3 Observed to modelled ratio of [OH] during the GABRIEL campaign over the Suriname rainforest as a function of isoprene concentration, for two different models (Taken from Kubistin et al. [20])

observed an OH_{obs}/OH_{mod} ratio of ~2 in a pine forest during the AEROBIC campaign in Northern Greece. During INTEX-A over the continental United States Ren et al. [29] reported OH_{obs}/OH_{mod} and $HO_{2,obs}/HO_{2,mod}$ ratios up to 8 and 5, respectively, with the ratio scaling roughly with the concentration of isoprene, as shown for OH in Fig. 5.2. Measurements in the boundary layer above the tropical rainforests of Suriname during the GABRIEL campaign [20] observed similar behaviour, with OH_{obs}/OH_{mod} as high as 15, as shown in Fig. 5.3. In these environments, which are characterised by a rich mix of biogenically derived BVOCs, it is difficult to adequately measure all the sinks for OH. Whalley et al. [37], using field measurements of OH reactivity to constrain the total rate of loss of OH, were able to show in a tropical rainforest in Malaysian Borneo during the OP-3 campaign that including all measured OH sources into a model gave a factor of ~10 underprediction compared with measured [OH], as shown in Fig. 5.4. Likewise, Stone et al. [33], using the very detailed *Master Chemical Mechanism*, reported a significant underprediction of [OH] using currently accepted mechanisms. Finally, as shown in Fig. 5.5, during low NOx periods near the Pearl River Delta in China during the PRIDE-PRD campaign, Hofzumahaus et al. [18], using a similar approach with measured [OH] and OH reactivity, reported a significant model underprediction.

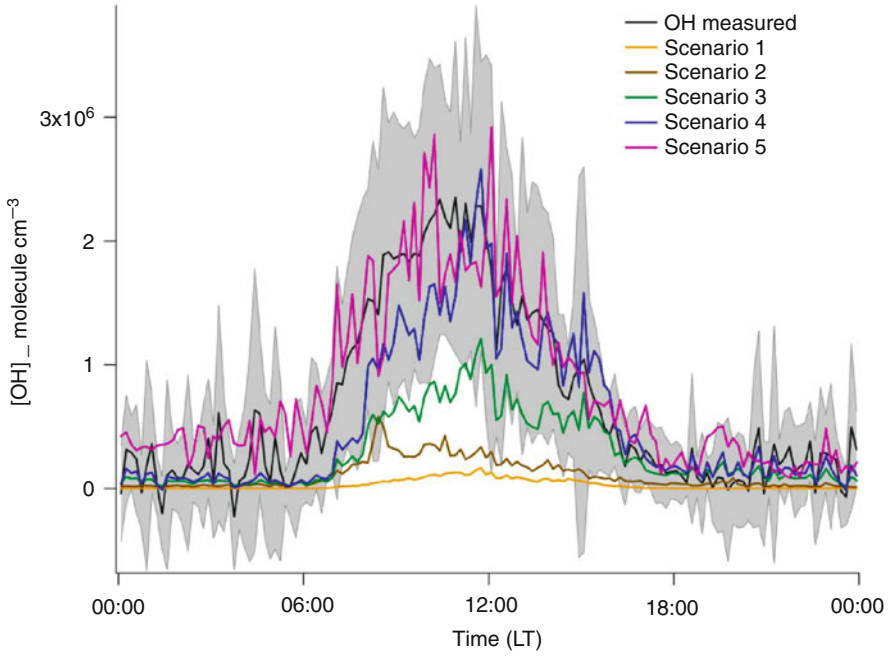

Fig. 5.4 Diurnal profile of measured OH concentrations during the OP-3 campaign in Borneo (*black line*) together with model calculations constrained by the measured OH reactivity and various source terms (Scenarios 1–5). Unless a significant OH recycling term during the oxidation of isoprene is included, the measured/modelled ratio of [OH] is high (Taken from Whalley et al. [37])

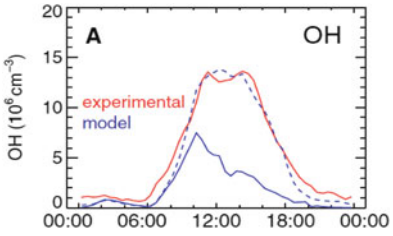

Fig. 5.5 Comparison of measured and modelled mean diurnal profiles of OH radicals during the Pearl River Campaign, China. The model used was the RACM, with the *dotted line* representing an extended RACM model with additional HO_2 and RO_2 recycling (Modified from Hofzumahaus et al. [18])

Recently, attention has been given to the photo-oxidation of hydroperoxy-aldehydes (HPALDS), a product of isoprene oxidation, which upon photolysis leads to the formation of OH, and which also reacts with OH, and inclusion of this chemistry buffering OH concentrations improves agreement between measurements and model calculations [35].

All of these results suggest a lack of understanding in our description of the chemistry taking place at these locations. There have been a number of theoretical, laboratory and chamber studies which have suggested new sources of OH from the oxidation of isoprene, and which can partially explain these findings. Discussion of this new chemistry is beyond the scope of this paper, yet remains a controversial topic with several groups striving to measure the rates of key reactions in the laboratory. Some aspects of this are covered in, for example, Taraborrelli et al. [35], Stone et al. [33], Peeters et al. [26], Crounse et al. [5] and papers therein.

5.6 HO_2 Interference from Alkene-Derived RO_2 Radicals

Ambient measurements of HO_2 have almost exclusively been made by chemical titration of HO_2 to OH by NO and the subsequent detection by FAGE of the OH radical using laser induced fluorescence (LIF) at low pressures (~1 Torr) [15]. Until recently it was assumed that higher peroxy radicals (RO_2) could not act as an HO_2 interference in LIF because although these species also react with NO to form an alkoxy radical (RO) at 1 Torr the subsequent reaction RO + O_2 to give HO_2 is too slow. Independent laboratory studies conducted at the University of Leeds, UK [16] and at the Forschungzentrum, Julich, Germany [11], however, have revealed that alkene-derived RO_2 radicals, longer chain alkane-derived RO_2 (>C3) and also RO_2 from methanol and aromatic species can be converted to HO_2 in the presence of NO in a LIF detection cell, via the mechanisms shown in Fig. 5.6 [11]. Heard et al. [16] showed that if allowed to proceed to completion by ensuring a long enough reaction time, the yields of HO_2 were found in the most part to agree with yields calculated using the *Master Chemical Mechanism* (http://mcm.leeds.ac.uk/MCM/) [16]. For ethene and isoprene derived RO_2 species, the relative sensitivity was found to be close to 100% with respect to that for HO_2. Ironically, it was during experiments designed to measure the HO_2 yield following the oxidation of OH by isoprene, that the interference in the detection of HO_2 due to alkene-derived RO_2 was discovered, as the reaction of OH with ethene appeared to generate HO_2, which it should not in the absence of NO [16]. Given these results, and the agreement with the MCM, it is perhaps surprising that it has taken the radical measurement community so long to appreciate that some RO_2 species may contribute some of the signal that has previously been assigned to HO_2, particularly in urban or forested environments. Using a clever isotope experiment, it was also demonstrated that the photolysis of water vapour at 185 nm generated equal concentrations of OH and HO_2, a critical assumption made by groups using this calibration method, but never explicitly demonstrated [11].

However, the interference will only be significant for field reported concentrations of HO_2 if the experimental configuration of the FAGE instrument being used is conductive to any conversion of RO_2 into HO_2 in the presence of NO. Experimental variables which vary considerably between different field instruments include the fluorescence cell pressure, the residence time of the sampled

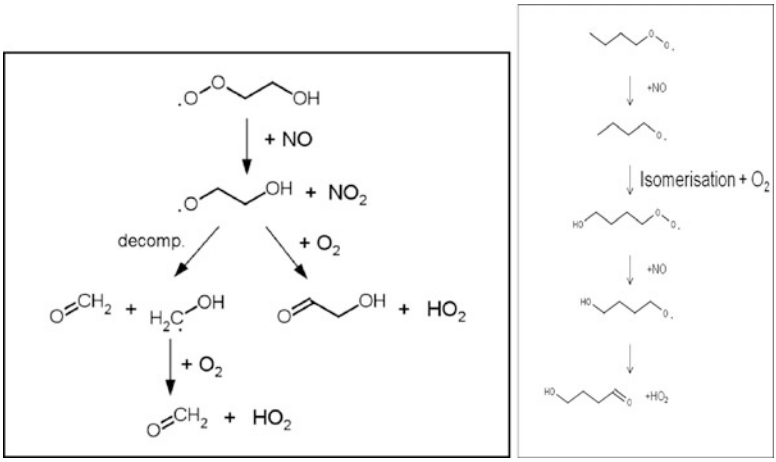

Fig. 5.6 Reaction scheme (*left*) which converts β-hydroxyalkyl peroxy radicals to HO_2 in the presence of NO (shown here for the ethene RO_2 radical) (Taken from Fuchs et al. [11]). The *right hand panel* shows how a C_4 alkoxy radical can isomerise and react with O_2 and eventually reform HO_2 (diagram courtesy of Dr. L. Whalley)

air in the fluorescence cell prior to laser excitation of OH (related to the pumping speed and geometry of the cell), the concentration of NO added to convert HO_2, details of the supersonic expansion which will determine the degree of mixing of NO into the ambient jet, the proximity of the walls to the sampled flow, and the volume from which fluorescence is imaged on to the detector (determined by whether a single or multi-pass laser excitation scheme is used). The percentage conversion of RO_2 into HO_2 will be influenced by these parameters. Fuchs et al. [11] demonstrated that by changing the inlet configuration of the FAGE cell (diameter of the sampling pinhole which changed the sample flow rate and hence the conversion reaction time), the interference was changed considerably.

Under the field operating conditions employed during the 2008 OP3 campaign that took place in the Borneo rainforest, the University of Leeds ground-based LIF instrument for HO_2 was not sensitive to detection of these RO_2 species, despite the presence of high concentrations of isoprene [16]. The large cell, low pressure and short residence time (due to large capacity pumps), coupled with relatively poor mixing of NO into the ambient air-stream for the titration of HO_2 to OH, minimised this potential interference, and $<10\%$ of $[HO_2]$ may be attributed to any interference from isoprene derived RO_2 for this setup. For the Leeds aircraft instrument [4], which utilises smaller fluorescence cells and a longer residence time, the interference was higher (40% for ethene compared to 12% for the ground configuration). Furthermore, the degree of interference could be reduced using a lower concentration of NO in the cell, as predicted using the model, and consistent with the results of Fuchs et al. [11]. Equipped with knowledge of this interference for HO_2 and the controlling parameters, it will be possible for practitioning groups to design the configuration and geometry of their FAGE sampling systems and cells to

minimise interferences from RO_2. Also, a cell that is not subject to interference from isoprene derived RO_2 species can be used to determine the yield of HO_2 radicals from the OH initiated oxidation of isoprene. Using the Leeds ground-based LIF detection cell coupled to a flow-tube, experiments to determine the time resolved yield of HO_2 radicals during the OH-initiated oxidation of isoprene have been conducted. OH was generated by photolysis of t-butyl-hydro-peroxide by 254 nm radiation from a Hg lamp in a dry air flow at variable positions along the flow-tube. Isoprene was then added downstream of the lamp. However, no HO_2 was observed on a ~1 s timescale, consistent with a smaller value of the isomerisation rate of the isoprene-RO_2 radical to generate HO_x reported by Crounse et al. [5], but not with the larger rate calculated by Peeters et al. [26].

5.7 Is There an Interference for OH Radicals During Field Measurements Using FAGE?

Earlier experiments performed in the laboratory by Ren et al. [28] reported negligible interferences for the detection of OH for a range of species, including H_2O_2, SO_2, HONO, HCHO and a range of VOCs with difference functional groups (alkanes, alkenes, alcohols, including isoprene). A small interference scaling with ozone and water vapour was observed, as reported by some other groups, but which can be corrected for. The usual method to determine the background signal in a FAGE instrument is to exploit the narrow spectral profile of a single rotational transition of OH, and move the laser wavelength away from the OH line and measure the sum of solar, cell-induced and Mie scattered light. However, in the recent BEARPEX study in a California forest using a FAGE instrument, Mao et al. [25] used an alternative method to determine the background, which does not involve changing the wavelength, rather injecting C_3F_6 into the sampled ambient air stream to remove ambient OH before it enters the instrument. Any remaining signal is the background, although a complication was that the addition of C_3F_6 just outside the sampling inlet also removed some of the additional OH generated inside the cell. Mao et al. found that the background using this method was considerably higher than using the spectral method, and showed that the additional background was due to OH radicals, and postulated that the OH was generated within the instrument from oxidation of an unidentified biogenic VOC. Evidence was provided to rule out laser-generation of OH within the cell. Allowing for this increased background gave measured OH concentrations that were ~40–50% of those determined using the spectral background method, and which agreed better with the calculations of a constrained box model [25].

The field site was within a Ponderosa pine plantation, and a key question is whether this type of interference has been seen previously by this and other FAGE instruments operating in other forested environments. For HO_2, the degree of interference was shown to be dependent upon instrument design [11, 16], and the

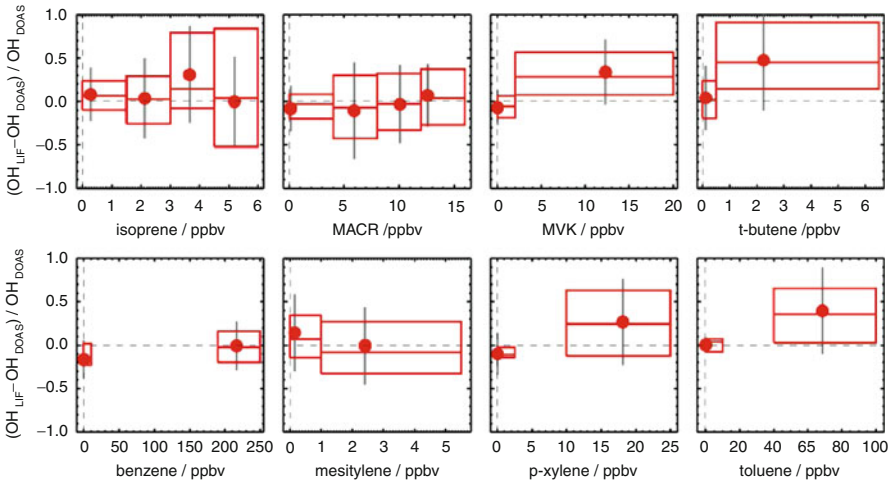

Fig. 5.7 Relative differences between DOAS and FAGE measured OH concentrations in the SAPHIR chamber as a function of various VOC concentrations. The *dots* are mean values (Taken from Fuchs et al. [12])

same may be true for any potential OH interferences. All FAGE groups should adopt the addition of C_3F_6 for some periods during fieldwork in all environments to determine the background, and compare this with the traditional spectral method, to see if there is an interference as reported by Mao et al. [25]. Laboratory experiments are also required which add a range of biogenic species and their oxidation products in order to try to observe a FAGE interference and identify its source. There is of course, no guarantee that the smoking-gun species is discovered.

A recent experiment utilising the SAPHIR chamber has compared OH concentrations measured by DOAS and FAGE under conditions of low NOx and in which significant concentrations of isoprene, methyl vinyl ketone (MVK), methacrolein (MACR) and aromatic compounds were added and were photochemically oxidised [12]. Conditions were chosen to replicate those in which significantly higher OH concentrations were measured in China compared with model predictions [18]. Over the entire set of experiments over 20 days, the linear regression of OH concentrations measured by FAGE compared to DOAS gave a slope of 1.02 ± 0.01 and an intercept of $(1.0 \pm 0.3) \times 10^5$ molecule cm^{-3}. These experiments provide strong evidence that the FAGE calibration is accurate, and as shown in Fig. 5.7, there are no significant interferences for isoprene, MACR and aromatics, although a small bias (with large uncertainties) was observed for MVK and toluene. Any differences between DOAS and LIF are far too small to explain the unexpectedly high OH concentrations seen in China [18]. Further evidence in support of the higher OH concentrations in a rainforest environment come from field measurements of HCHO using DOAS in Borneo during OP3, which can only be reproduced in a model using the measured OH levels, but not using modelled levels which are a factor of 10 lower [22].

5.8 Interferences for CIMS Instruments

In the case of CIMS, studies regarding interferences [34] have been much less studied compared to FAGE instruments. Tests include reactions that could compete with the reaction of SO_3 with H_2O (reaction (3)), the effect of H_2O vapour on the ion molecule chemistry involving $NO_3^-/HNO_3/H_2SO_4$ and potential wall losses. Excess propane is periodically added at the inlet (at the same injection point where SO_2 is added) in order to rapidly remove ambient OH (on a timescale that is much shorter than removal by SO_2) and enable a background signal to be determined. Also, the chemistry which generates H_2SO_4 from OH generates HO_2 in reaction (2), and this together with any HO_2 present in the ambient sample (typically HO_2 is 10–100 times more abundant than OH), could be recycled to HO_2, for example by reaction with NO or O_3 and lead to a positive bias for OH [1, 7]. Any OH produced by recycling from HO_2 (or indeed from any other mechanism) is prevented from reacting with SO_2 (and hence being detected) through removal by the addition of excess propane downstream of the injection position for SO_2 (sufficiently downstream so that all ambient OH reacts with SO_2 before it encounters propane). However, any species which can oxidise SO_2 to SO_3, but which is not removed by reaction with propane, will be detected as H_2SO_4, and will cause a positive bias to the OH measurements. Recently, Welz et al. [36] showed that the simplest Criegee intermediate, CH_2OO, reacts quickly with SO_2, and hence this is one candidate to give such an interference. A negative bias in the measured OH concentration could result from species present in ambient air reacting with OH once the air has been sampled by the CIMS inlet but before the SO_2 injection point – as these species will not be present in the calibration gas. As the transit time is short compared with the atmospheric lifetime of OH, only a small fraction of the OH would be lost in way, although this assumption may not be true if the OH reactivity is very high.

5.9 Implications for the Interpretation of Past Field Data and Future Outlook

In the case of HO_2, it is possible to provide a correction and account for the additional HO_2 concentration that derives from RO_2 radicals, using the following expression:

$$[HO_2^*] = [HO_2] + \sum_i (\alpha_{RO2,i} \times [RO_2]_i) \quad (5.E4)$$

where $[HO_2^*]$ is the HO_2 concentration in ambient air plus contribution from RO_2 interferences (the total measured quantity), $[HO_2]$ is the HO_2 concentration in ambient air (the desired quantity), $\alpha_{RO2,i}$ is the fraction of a given RO_2 species converted to HO_2, and subsequently OH in the detection cell, determined for the FAGE instrument in the laboratory, and $[RO_2]_i$ is the concentration of a given RO_2 in ambient air calculated using a box-model [21]. A significant disadvantage of this

method is that is relies on a model calculation for RO_2, as there are no field measurements of individual RO_2 species. However, this method does allow investigation of the difference between HO_2* and HO_2, which will depend on the mix of RO_2 at a particular location. For the Leeds aircraft FAGE instrument, which utilises smaller cells and for which α has been measured to be significant for some RO_2, the ratio $[HO_2^*]/[HO_2]$ was determined to only be 1.23 on average for the OP3 campaign over the Borneo rainforest, despite high concentrations of isoprene [33]. For other campaigns, for example AMMA [4], the value is much lower, 1.065. The correction to HO_2 is not likely here to change significantly any conclusions regarding the ability of the model to reproduce $[HO_2]$, although this has not been tested for urban environments. However, a far better strategy is to make sure that any future measurements of HO_2 are not subject to this interference, through judicious design of the instrument.

For OH, it is important for the community to know whether measurements reported in previous field campaigns are accurate, for example the unexpectedly high concentrations of OH observed mainly, but not exclusively, in forested environments. The implementation of any new chemistry that is developed to explain these findings may lead to erroneous results, for example in the calculation of the lifetime of CH_4 (an important greenhouse gas), if the field data upon which the development of the new chemistry is based, are wrong. Mao et al. [25] developed a different measurement strategy utilising a chemical background in order to examine interferences in their instrument set-up for a forest in California, but it is difficult to know if previous measurements during other campaigns are subject to the same type of interference. All groups should perform agreed laboratory experiments to investigate the presence or not of interferences, which may allow some understanding of whether corrections to previous data are required or not. However, if an interference is revealed, the concentration of the guilty species may not have been measured, but it may be possible to use a model to calculate its concentration. Certainly groups should adopt instrument designs and sampling procedures (for example to determine the background) which minimise the possibility of interferences. In addition, there need to be further intercomparisons for OH and HO_2 using different methods, for example FAGE and CIMS, under field conditions in environments that provide a range of potentially interfering species.

References

1. Berresheim H, Elste T, Plass-Dulmer C, Eisele FL, Tanner DJ (2000) Chemical ionization mass spectrometer for long-term measurements of atmospheric OH and H_2SO_4. Int J Mass Spectrom 202:91–109
2. Bloss WJ, Lee JD, Bloss C, Heard DE, Pilling MJ, Wirtz K, Martin-Reviejo M, Siese M (2004) Validation of the calibration of a laser-induced fluorescence instrument for the measurement of OH radicals in the atmosphere. Atmos Chem Phys 4:571–583
3. Carslaw N, Creasey DJ, Harrison D, Heard DE, Hunter MC, Jacobs PJ, Jenkin ME, Lee JD, Lewis AC, Pilling MJ, Saunders SM, Seakins PW (2001) OH and HO_2 radical chemistry in a forested region of north-western Greece. Atmos Environ 35:4725–4737

4. Commane R, Floquet C, Ingham T, Heard D, Stone D, Evans M (2011) Observations of OH and HO_2 over West Africa. Atmos Chem Phys 10:8783–8801
5. Crounse JD, Paulot F, Kjaergaard HG, Wennberg PO (2011) Peroxy radical isomerization in the oxidation of isoprene. Phys Chem Chem Phys 13:13607–13613
6. Edwards GD, Cantrell CA, Stephens S, Hill B, Goyea O, Shetter RE, Mauldin RL, Kosciuch E, Tanner DJ, Eisele FL (2003) Chemical ionization mass spectrometer instrument for the measurement of tropospheric HO_2 and RO_2. Anal Chem 75:5317–5327
7. Eisele FL (1995) New insights and questions resulting from recent ion-assisted OH measurements. J Atmos Sci 52:3337–3341
8. Fuchs H, Holland F, Hofzumahaus A (2008) Measurement of tropospheric RO_2 and HO_2 radicals by a laser-induced fluorescence instrument. Rev Sci Instrum 79:084104
9. Fuchs H, Brauers T, Häseler R, Holland F, Mihelcic D, Müsgen P, Rohrer F, Wegener R, Hofzumahaus A (2009) Intercomparison of peroxy radical measurements obtained at atmospheric conditions by laser-induced fluorescence and electron spin resonance spectroscopy. Atmos Meas Tech 2:55–64
10. Fuchs H, Brauers T, Dorn H-P, Harder H, Häseler R, Hofzumahaus A, Holland F, Kanaya Y, Kajii Y, Kubistin D, Lou S, Martinez M, Miyamoto K, Nishida S, Rudolf M, Schlosser E, Wahner A, Yoshino A, Schurath U (2010) Formal blind intercomparison of HO_2 measurements in the atmosphere simulation chamber SAPHIR during the HO_xComp campaign. Atmos Chem Phys 10:12233–12250
11. Fuchs H, Bohn B, Hofzumahaus A, Holland F, Lu KD, Nehr S, Rohrer F, Wahner A (2011) Detection of HO_2 by laser-induced fluorescence: calibration and interferences from RO_2 radicals. Atmos Meas Tech 4:1209–1225
12. Fuchs H, Dorn H-P, Bachner M, Bohn B, Brauers T, Gomm S, Hofzumahaus A, Holland F, Nehr S, Rohrer F, Tillmann R, Wahner A (2012) Comparison of OH concentration measurements by DOAS and LIF during SAPHIR chamber experiments at high OH reactivity and low NO concentration. Atmos Meas Tech Discuss 5:2077–2110
13. Glowacki DR, Goddard A, Hemavibool K, Malkin TL, Commane R, Anderson F, Bloss WJ, Heard DE, Ingham T, Pilling MJ, Seakins PW (2007) Design of and initial results from a Highly Instrumented Reactor for Atmospheric Chemistry (HIRAC). Atmos Chem Phys 7:5371–5390
14. Hanke M, Uecker J, Reiner T, Arnold F (2002) Atmospheric peroxy radicals: ROXMAS, a new mass-spectrometric methodology for speciated measurements of HO_2 and $\sum RO_2$ and first results. Int J Mass Spec 213:91–99
15. Heard DE, Pilling MJ (2003) Measurement of OH and HO_2 in the troposphere. Chem Rev 103:5163–5198
16. Heard DE, Whalley LK, Blitz MA, Seakins PW (2011) The sensitivity of laser induced fluorescence instruments at low pressure to RO_2 radicals and the use of this detection method to determine the yield of HO_2 during OH-initiated isoprene oxidation, Abstract A11I-04 presented at 2011 Fall Meeting, AGU, San Francisco, CA, 5–9 Dec 2011
17. Hofzumahaus A, Aschmutat U, Brandenburger U, Brauers T, Dorn H-P, Hausmann M, Hessling M, Holland F, Plass-Dülmer C, Ehhalt DH (1998) Intercomparison of tropospheric OH measurements by different laser techniques during the POPCORN campaign, 1994. J Atmos Chem 31:227–246
18. Hofzumahaus A, Rohrer F, Lu K, Bohn B, Brauers T, Chang CC, Fuchs H, Holland F, Kita K, Kondo Y, Li X, Lou S, Shao M, Zeng L, Wahner A, Zhang Y (2009) Amplified trace gas removal in the troposphere. Science 324:1702–1704
19. Kanaya Y, Akimoto H (2002) Direct measurements of HO_x radicals in the marine boundary layer: testing the current tropospheric chemistry mechanism. Chem Rec 2:199–211
20. Kubistin D, Harder H, Martinez M, Rudolf M, Sander R, Bozem H, Eerdekens G, Fischer H, Gurk C, Klupfel T, Konigstedt R, Parchatka U, Schiller CL, Stickler A, Taraborrelli D, Williams J, Lelieveld J (2010) Hydroxyl radicals in the tropical troposphere over the Suriname rainforest: comparison of measurements with the box model MECCA. Atmos Chem Phys 10:9705–9728
21. Lu KD, Rohrer, F, Holland F, Fuchs H, Bohn B, Brauers T, Chang CC, Häseler R, Hu M, Kita K, Kondo Y, Li X, Lou SR, Nehr S, Shao M, Zeng LM, Wahner A, Zhang YH, Hofzumahaus A (2012) Observation and modelling of OH and HO_2 concentrations in the

Pearl River Delta 2006: a missing OH source in a VOC rich atmosphere. Atmos Chem Phys 12:1541–1569
22. MacDonald SM, Oetjen H, Mahajan AS, Whalley LK, Edwards PM, Heard DE, Jones CE, Plane JMC (2012) DOAS measurements of formaldehyde and glyoxal above a South-East Asian tropical rainforest. Atmos Chem Phys Discuss 12:5903–5937
23. Malkin TL (2010) Detection of free-radicals and other species to investigate atmospheric chemistry in the HIRAC chamber. Ph.D. thesis, University of Leeds
24. Malkin TL, Goddard A, Heard DE, Seakins PW (2010) Measurements of OH and HO_2 yields from the gas phase ozonolysis of isoprene. Atmos Chem Phys 10:1441–1459
25. Mao J, Ren X, Brune WH, Van Duin DM, Cohen RC, Park J-H, Goldstein AH, Paulot F, Beaver MR, Crounse JD, Wennberg PO, DiGangi JP, Henry SB, Keutsch FN, Park C, Schade GW, Wolfe GM, Thornton JA (2012) Insights into hydroxyl measurements and atmospheric oxidation in a California forest. Atmos Chem Phys Discuss 12:6715–6744
26. Peeters J, Nguyen TL, Vereecken L (2009) HO_x radical regeneration in the oxidation of isoprene. Phys Chem Chem Phys 11:5935–5939
27. Ren X, Edwards GD, Cantrell CA, Lesher RL, Metcalf AR, Shirley T, Brune WH (2003) Intercomparison of peroxy radical measurements at a rural site using laser-induced fluorescence and Peroxy Radical Chemical Ionization Mass Spectrometer (PerCIMS) techniques. J Geophys Res 108:4605
28. Ren X, Harder H, Martinez M, Falona IC, Tan D, Lesher RL, Carlo PD, Simpas JB, Brune WH (2004) Interference testing for atmospheric HO_x measurements by laser-induced fluorescence. J Atmos Chem 47:169–190
29. Ren X, Olson JR, Crawford JH, Brune WH, Mao J, Long RB, Chen Z, Chen G, Avery MA, Sachse GW, Barrick JD, Diskin GS, Huey LG, Fried A, Cohen RC, Heikes B, Wennberg PO, Singh HB, Blake DR, Shetter RE (2008) HO_x chemistry during INTEX-A 2004: observation, model calculation, and comparison with previous studies. J Geophys Res 11(3):D05310. doi:10.1029/2007JD009166
30. Schlosser E, Bohn B, Brauers T, Dorn H-P, Fuchs H, Häseler R, Hofzumahaus A, Holland F, Rohrer F, Rupp LO, Siese M, Tillmann R, Wahner A (2007) Intercomparison of two hydroxyl radical measurement techniques at the atmosphere simulation chamber SAPHIR. J Atmos Chem 56:187–205
31. Schlosser E, Brauers T, Dorn H-P, Fuchs H, Häseler R, Hofzumahaus A, Holland F, Wahner A, Kanaya Y, Kajii Y, Miyamoto K, Nishida S, Watanabe K, Yoshino A, Kubistin D, Martinez M, Rudolf M, Harder H, Berresheim H, Elste T, Plass-Dülmer C, Stange G, Schurath U (2009) Formal blind intercomparison of OH measurements: results from the international campaign HOxComp. Atmos Chem Phys 9:7923–7948
32. Sjostedt SJ, Huey LG, Tanner DJ, Pieschl J, Chen G, Dibb JE, Lefer B, Hutterli MA, Beyersdorf AJ, Blake NJ, Blake DR, Sueper D, Ryerson T, Burkhart J, Stohl A (2007) Observations of hydroxyl and the sum of peroxy radicals at summit, Greenland during the 2003 summer field study. Atmos Environ 41:5122–5137
33. Stone D, Evans MJ, Edwards PM, Commane R, Ingham T, Rickard AR, Brookes DM, Hopkins J, Leigh RJ, Lewis AC, Monks PS, Oram D, Reeves CE, Stewart D, Heard DE (2011) Isoprene oxidation mechanisms: measurements and modelling of OH and HO_2 over a South-East Asian tropical rainforest during the OP3 field campaign. Atmos Chem Phys 11:6749–6771
34. Tanner DJ, Eisele FL (1995) Present OH measurement limits and associated uncertainties J Geophys Res 100(D2):2883–2892
35. Taraborrelli D, Lawrence MG, Crowley JN, Dillon TJ, Gromov S, Groß CBM, Vereecken L, Lelieveld J (2012) Hydroxyl radical buffered by isoprene oxidation over tropical forests. Nat Geosci 5:190–193
36. Welz O, Savee JD, Osborn DL, Vasu SS, Percival CJ, Shallcross DE (2012) Direct kinetic measurements of criegee intermediate (CH_2OO) formed by reaction of CH_2I with O_2. Science 335:204–207
37. Whalley LK, Edwards PM, Furneaux KL, Goddard A, Ingham T, Evans MJ, Stone D, Hopkins JR, Jones CE, Karunaharan A, Lee JD, Lewis AC, Monks PS, Moller SJ, Heard DE (2011) Quantifying the magnitude of a missing hydroxyl radical source in a tropical rainforest. Atmos Chem Phys 11:7223–7233

Chapter 6
HO_x and RO_x Radicals in Atmospheric Chemistry

Damien Amedro, Alexander E. Parker, Coralie Schoemaecker, Chaithanya Jain, Pranay Morajkar, Paul S. Monks, Koji Miyazaki, Yoshizumi Kajii, and Christa Fittschen

Abstract Work on the relevance of the reaction of excited NO_2 with water vapour as an atmospheric source of OH radicals is presented and measurement of absolute absorption cross sections of HONO in the near infrared are reported.

Keywords Excited NO_2, HONO • Selective HO_2 and RO_2 measurement • FAGE • cw-CRDS • PERCA

6.1 Introduction

New results concerning three different aspects of radical chemistry and quantification in the atmosphere have been presented during the workshop:

(a) the formation of OH radicals from the reaction of excited NO_2 with H_2O
(b) measurement of absolute absorption cross sections of HONO in the near infrared as a tool for quantifying HONO in laboratory studies
(c) the development of a new technique designed for selective measurement of HO_2 and RO_2 radicals.

6.1.1 The Formation of OH Radicals from a Reaction of Excited NO_2 with H_2O

6.1.1.1 Introduction

The hydroxyl radical, OH, is the principal oxidant in the atmosphere. It controls the removal of most of the trace gases (e.g. hydrocarbons, NO_2, VOC) and the

D. Amedro • A.E. Parker • C. Schoemaecker • C. Jain • P. Morajkar • P.S. Monks • K. Miyazaki • Y. Kajii • C. Fittschen (✉)
Physicochimie des Processus de Combustion et de l'Atmosphère, USTL, Cité Scientifique, Bâtiment C11, Villeneuve d'Ascq 59655, France
e-mail: christa.fittschen@univ-lille1.fr

I. Barnes and K.J. Rudziński (eds.), *Disposal of Dangerous Chemicals in Urban Areas and Mega Cities*, NATO Science for Peace and Security Series C: Environmental Security,
DOI 10.1007/978-94-007-5034-0_6,

characterization of its different sources is important towards the understanding of tropospheric chemistry. The main source of OH during daytime, is the reaction of $O(^1D)$, produced from the photolysis of O_3 ($\lambda < 340$ nm), with H_2O. A new potential source of atmospheric OH was recently proposed through the reaction of electronically excited NO_2 by visible light with H_2O via the following mechanism

$$NO_2 + h\nu(\lambda{>}420\text{ nm}) \rightarrow NO_2{}^* \tag{6.1}$$

$$NO_2{}^* + H_2O \rightarrow OH + HONO \tag{6.2}$$

The electronically excited NO_2 can also be deactivated through collisions with other molecules

$$NO_2{}^* + H_2O \rightarrow NO_2 + H_2O \tag{6.3a}$$

$$NO_2{}^* + N_2 \rightarrow NO_2 + N_2 \tag{6.3b}$$

$$NO_2{}^* + O_2 \rightarrow NO_2 + O_2 \tag{6.3c}$$

Li et al. [24] have studied the reaction by exciting NO_2 at low pressure in the 560–640 nm range in the presence of water vapour and using in-situ laser induced fluorescence to detect OH formation; both lasers had been focused in this study. They have reported a rate constant of 1.7×10^{-13} cm^3 s^{-1} for reaction (6.2) and have shown that the OH concentration depended linearly on the excitation energy, thus excluding a multi-photon absorption process. The upper limit for k_2/k_{3a}, i.e. the ratio between reactive and collisional quenching, obtained in their work was 1×10^{-3}. Wennberg and Dabdub [44] performed model calculations for polluted urban atmosphere to estimate the impact of the result from Li et al. [24]. Even though reaction (6.2) has a low yield (1×10^{-4}), i.e. the fraction of $NO_2{}^*$ that reacts with H_2O rather than being quenched through reactions 3, a significant increase in the O_3 concentration of up to 40% was obtained.

In a previous study, Crowley and Carl [9] observed OH formation below 450 nm following 2-photon absorption by NO_2 leading to $O(^1D)$ formation followed by the reaction with H_2O, but did not observe OH formation at 532 nm, where the 2-photon process is not sufficiently energetic to form $O(^1D)$, and they established an upper limit of 7×10^{-5}, more than one order of magnitude lower than the one reported by Li et al. [24].

The disagreement between the two studies and the possible major impact of this reaction on atmospheric chemistry lead to a new study by Carr et al. [7]. They failed to observe OH formation from the reaction of excited NO_2 with H_2O, now using an unfocused laser for excitation. The upper limit for k_2/k_{3a} calculated from their study was 6×10^{-5} at the 2σ level, in good agreement with Crowley and Carl [9]. They concluded that the OH formation observed by Li et al. [24] could be generated from a multi-photon process even though this possibility was ruled out by Li et al. They highlighted that the dependence of the OH signal on laser fluence, although linear, had a negative intercept which is in contradiction with a single photon absorption process. Li et al. [25] gave an answer to this comment, they mentioned that the negative intercept was likely due to an electronic offset and that the energy fluence used was higher in their study.

To conclude on whether this reaction is relevant to atmospheric chemistry, we studied the reaction using a laser photolysis cell using an unfocused and a focused excitation beam. The cell was coupled to detection of OH radicals by FAGE (Fluorescence Assay Detection by Gas Expansion).

6.1.1.2 Experimental Details

The University of Lille Fluorescence Assay by Gas Expansion (UL-FAGE) was used to detect OH radicals at 308 nm by Laser Induced Fluorescence (LIF) at low pressure (1.5 Torr). A photolysis flow tube was coupled to the FAGE cell in order to follow the OH decay (details on the experimental set-up can be found elsewhere [3, 4, 31, 32]). Gas is pumped continuously from the laser photolysis cell (held at 11 Torr, see below) through a small aperture (1 mm) into the FAGE detection cells (1.5 Torr) at a flow rate of 300 ccm STP using an Edwards GX6/100 L pump.

The excitation beam is generated by a dye laser (Quantel TDL50, Rhodamine 590), pumped by a frequency doubled YAG laser (Quantel YG 781 C) at a repetition rate of 2 Hz. For the excitation of NO_2, the dye laser beam has been used directly at 565 nm with pulse energies of 9–15 mJ pulse^{-1}, while for the relative calibration measurements a doubling crystal was introduced into the laser beam and O_3 was photolysed at 282.5 nm in the presence of H_2O with pulse energies of 3 mJ pulse^{-1}.

$$O_3 + h\nu \rightarrow O(^1D) + O_2 \tag{6.4}$$

$$O(^1D) + H_2O \rightarrow 2\ OH \tag{6.5}$$

6.1.2 Results and Discussion

In this paper only a brief summary of the results obtained in this study is given, more details can be found in Amedro et al. [3, 4]. The low yield of OH formation from reaction (6.2) along with the low time resolution of the set-up, due to the separation between radical generation and detection in our system [3, 4, 31, 32], obliged the experimental conditions to be chosen carefully in order to facilitate the detection of OH radicals. Therefore, measurements were made at low pressure (11 Torr Helium) with $[NO_2]_{max} = 2 \times 10^{14}$ cm^{-3} in order to decrease the decay of OH radicals through the strongly pressure dependent reaction of OH with NO_2.

Figure 6.1 shows the OH signals obtained from the calibration with O_3 at 282.5 nm (filled symbols) and from the reaction of excited NO_2 with H_2O at 565 nm (open symbols): the left graph (a) has been obtained using the unfocused laser, the right graph (b) using the focused laser. It can clearly be seen that under unfocused conditions the OH signal from O_3-photolysis is three to four times higher than in the focused case: this higher sensitivity (the same absolute number of OH radicals has been generated in both cases, only in different volumes) can be

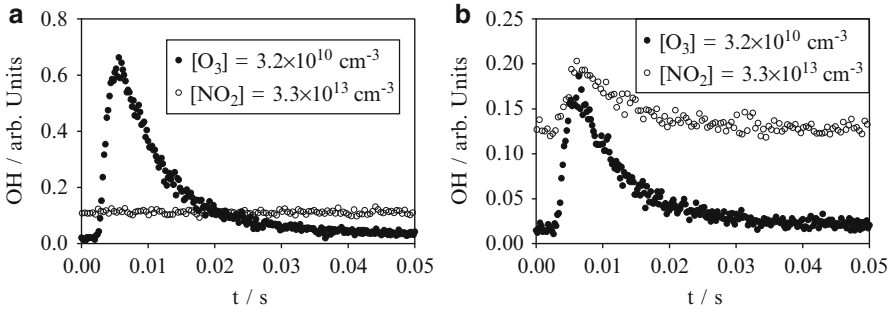

Fig. 6.1 Formation of OH radicals from O_3 (*closed symbols*, 3 mJ at 282.5 nm excitation) and NO_2 (*open symbols*, 15 mJ at 565 nm excitation): (**a**) unfocused excitation laser, (**b**) focused laser

explained through the fact that the OH radicals in the focused case need to travel further than in the unfocused case, hence the radicals will be more diluted before they arrive at the FAGE inlet. However, no OH formation was observed from the reaction of excited NO_2 with H_2O using the unfocused laser, while there is clear OH formation using the focused beam even though the sensitivity is three to four times lower in this focused laser configuration. This is a clear indication that the OH signal observed in our experiments originate from a multi-photon process and that single-photon absorption, used by Li et al. [24] to explain the formation of OH from the excited NO_2 reaction with H_2O, can be ruled out. From the absence of any OH-signal under unfocused conditions, and using the calibration obtained from the O_3 photolysis, an upper limit of 8×10^{-6} for k_2/k_{3a} can be estimated, in agreement with the results from Carr et al. [7] and Crowley and Carl [9].

From a comparison of the signal intensity observed under focused conditions (b) with the signal obtained from O_3 photolysis, an OH-yield of 3×10^{-5} can be calculated supposing a single photon process: this is at the same order of magnitude as Li et al. [24].

Experiments have been performed by varying the excitation energy: the left graph of Fig. 6.2 shows such signals with $[NO_2] = 6.8 \times 10^{13}$ cm^{-3}. The right graph shows the dependence of the maximum OH-signal with laser fluence: even though a linear dependence seems to exist, the linear regression (full line) does not pass through the origin and shows an intercept.

It is interesting to note that the same observation was also made by Li et al. [24]: they explained it as an electronic offset. In our experiment, we do not observe any offset, this is understandable as generation and detection of radicals are physically separated and also time delayed ($\Delta t \sim 2$ ms). Li et al. [24] proposed a mechanism involving two excited NO_2^* in order to explain the OH($v = 1$) they observed in their work:

$$NO_2^* + H_2O \rightarrow NO_2 + H_2O^* \tag{6.6}$$

$$NO_2^* + H_2O^* \rightarrow OH(v'' \geq 1) + HONO \tag{6.7}$$

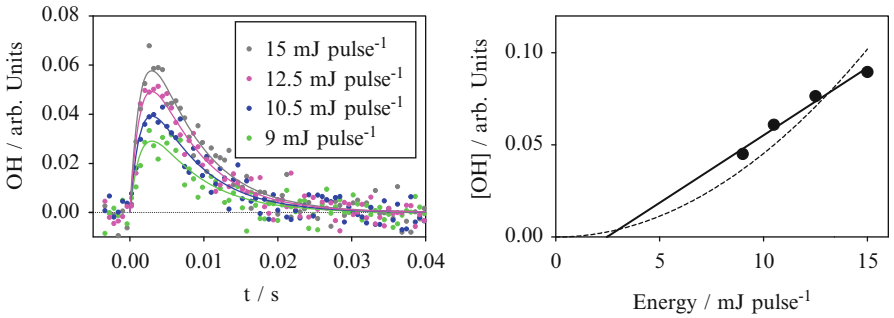

Fig. 6.2 *Left graph*: Formation of OH radicals at different pulse energies using $[NO_2] = 6.8 \times 10^{13}$ cm^{-3}, *right graph*: max. OH-signal as a function of pulse energy

As this mechanism would involve two excited NO_2^*, the OH signal should exhibit a squared dependence on the reactant concentration, $[NO_2]$, as well as on the laser fluence, as pointed out by Carr et al. [7]. The dashed line in Fig. 6.2 represents such a squared dependence of the OH-signal as function of the excitation beam: from this figure, however, such a dependence cannot be concluded; our accessible energy range was too small to draw any further conclusions.

6.1.2.1 Conclusion

In this work, we have shown that OH formation can be observed from the reaction of H_2O with NO_2, excited by multi-photon absorption at 565 nm. The compelling experiment in this work is that we observed OH radicals with a similar yield as Li et al. [24] when using similar conditions, i.e. a focused excitation beam, but we did not observe any OH when using an unfocused beam, even though the experiment is more sensitive in the latter case. Nevertheless, due to experimental constraints, conclusive information about the mechanism of the OH formation could not be drawn. The upper limit of the OH yield for reaction (6.2) compared to reaction (6.3a) was 8×10^{-6}. Consequentially, this reaction does not play any significant role under atmospheric conditions.

A detailed description of the results presented here can be found in Amedro et al. [3, 4].

6.1.3 Measurement of Absolute Absorption Cross Sections of HONO in the Near Infrared

6.1.3.1 Introduction

Nitrous acid (HONO) is an important chemical species in the atmosphere as well as in laboratory studies. In the atmosphere it is, especially in polluted areas, a major photochemical precursor for OH radicals in the early morning [43], but has also

been detected in remote areas such as the south pole [26]. HONO can be produced in a simple gas phase reaction between OH radicals and NO, but heterogeneous reactions seem to be more important and heterogeneous formation has been shown to occur on ice [16], but also on photocatalytic surfaces [23, 30]. In laboratory studies, it has been identified as an heterogeneously formed, important OH radical precursor in atmospheric simulation chambers [34], but also as a by-product in the photolysis of CH_3ONO [10], another important OH-radical precursor for chamber studies. HONO can also be an interesting OH-precursor for laser photolysis studies, because it generates OH radicals after 351 nm excimer photolysis, thus avoiding possible unwanted complications arising at shorter, but more commonly used wavelengths [2, 18].

HONO is often detected and quantified by spectroscopic methods: UV–VIS absorption using open path DOAS technique has been very successful for atmospheric measurements [33], but FTIR spectroscopy has also been used, especially in laboratory studies [22]. The qualitative absorption spectra of HONO have been studied by many authors in the UV–VIS and IR range (e.g. [13, 14, 36, 37, 45]). However, a major difficulty using spectroscopic detection methods for quantitative determination of HONO is the uncertainty linked to the absolute absorption cross sections: HONO exists in an equilibrium with other components such as NO, NO_2, HNO_3 and H_2O, and is a rather unstable molecule, decomposing easily through heterogeneous reactions. Therefore, determining the absolute concentration of HONO contained in an absorption cell is rather difficult. Febo et al. [11] have developed a method allowing the generation of stable HONO flows with very high purity, and this method has subsequently been used to determine absorption cross sections in the UV [38] and in the IR [5].

Cavity enhanced absorption spectroscopy is becoming more and more popular, especially in the near IR range, where cheap and reliable components such as DFB lasers and detectors are available. This makes this spectroscopic range attractive, because now the rather small absorption cross sections expected for overtone transitions occurring in this wavelength range can be compensated for by the high sensitivity of the cavity enhanced methods.

HONO is known to exist in equilibrium in two different forms, *trans*- and *cis*-HONO in a ratio of approximately 2 to 1 in favour of the *trans* form [42]. The rovibrational parameters of both isomers, including the $2\nu_1$ overtone of the OH stretch, have been published [13, 14]: the band centre of the $2\nu_1$ overtone of the *cis*-isomer has been located at around 6,665 cm^{-1}, but no individual absorption lines have been assigned in this wavelength range. The $2\nu_1$ overtone of the *cis*-isomer lies close to well-known and relatively intense $2\nu_1$ overtone features of the HO_2 radical [39, 41], an important intermediate in the oxidation of VOCs. The knowledge of absolute absorption cross sections for some HONO absorption lines in this wavelength range would allow for future, simultaneous measurements of HONO and HO_2 in laboratory studies.

Only one fairly indirect measurement of absorption cross sections for HONO is available in this range: Djehiche et al. [10] have detected HONO by cw-CRDS at 6,625.69 cm^{-1} as reaction product during the photolysis of CH_3ONO in a

simulation chamber at a total pressure of 40 Torr of air. Through simultaneous measurements of CH_2O and subsequent modelling they deduced the theoretical HONO concentration, postulating that it is formed in a reaction of OH radicals with the precursor CH_3ONO. From this fairly indirect approach they have estimated the absorption cross section for *cis*-HONO to $\sigma_{6625.69cm\text{-}1} = 4.2 \times 10^{-21}$ cm^2, assuming that only 1/3 of the formed HONO is in *cis*-configuration.

Here we present measurements of the HONO spectrum in the range 6,623.6–6,645.6 cm^{-1} as well as the determination of absolute absorption cross sections for selected lines using pulsed photolysis for the generating HONO.

6.1.3.2 Experimental Details

Experiments have been performed using laser photolysis coupled to detection by cw-CRDS: the experiment has been detailed in earlier publications [31, 32, 40] and will not be repeated here.

In order to overcome the uncertainty linked to the determination of the absolute concentrations, we have generated HONO by 248 nm photolysis of H_2O_2 in the presence of NO. Doing so, we can determine the absolute initial radical concentration by measuring HO_2 and OH profiles in the absence of NO, using the well-known absorption and broadening coefficients [17, 41]. From these measurements we can extract the initial OH radical concentration. Upon adding a known NO concentration to the reaction mixture, a simple model including well known rate constants, allows calculation of the yield of OH radicals that are converted to HONO and thus the absolute concentration of HONO, present in the reactor. Typical, time-resolved evolution of the ring-down time at a given wavelength is shown in the upper right graph of Fig. 6.3: at $t = 0$, H_2O_2 is photolysed and HONO is generated instantaneously on the time scale of the graph. the baseline is obtained from ring-down events having occurred before the laser pulse, while the absorption signal is obtained as extrapolation to $t = 0$ of the ring-down event occurring after the photolysis pulse. The absorbance α can than be calculated for each wavelength by the equation, given in the lower, right corner of Fig. 6.3.

6.1.3.3 Results and Discussion

The spectrum of HONO measured this way in the range 6,623.6–6,645.6 cm^{-1} is shown in Fig. 6.4 The absorption cross sections of six of the largest lines in this wavelength range, indicated with an arrow, have been measured with great care.

The absorption cross sections at 40 Torr of Helium for these lines are given in Table 6.1.

Pressure broadening is not negligible in this wavelength range, and the pressure broadening for the most intense line at 6,642.51 cm^{-1} has been measured for three different pressures in He and N_2 and the results are given in Table 6.2.

As can be seen in Fig. 6.4, the spectrum is very dense and the absorption does not decrease to 0 next to the absorption lines. Therefore, we have given in Table 6.2

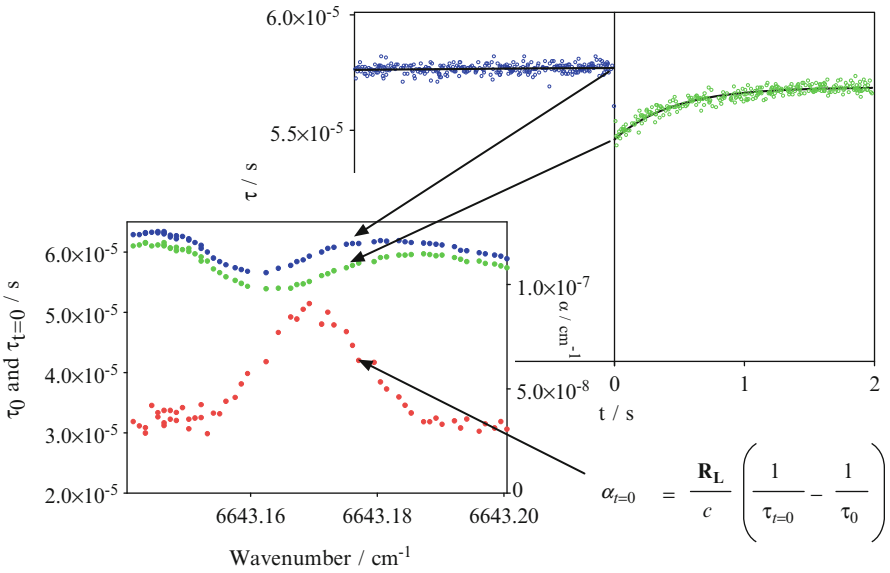

Fig. 6.3 *Upper right graph*: typical signal obtained at a given wavelength during photolysis of H_2O_2 in the presence of NO. *Lower left graph*: portion of the HONO absorption spectrum, extracted from the time resolved signals. *Lower, right corner*: common equation for calculation of absorbance α from ring-down times in absence and presence of absorbing species

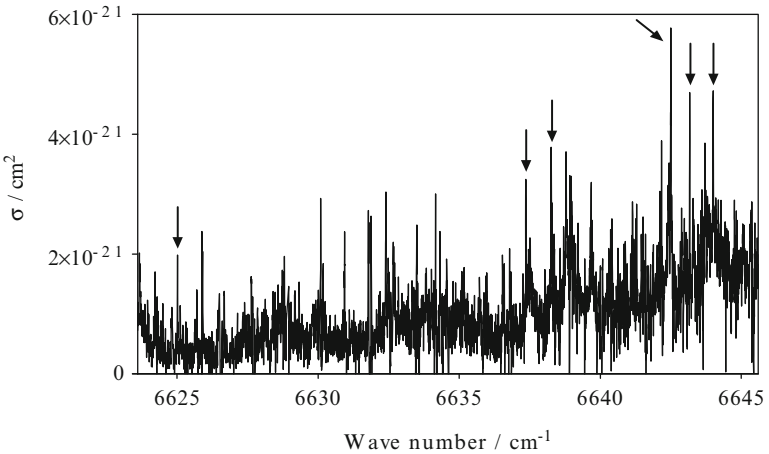

Fig. 6.4 Full spectrum of HONO accessible with the DFB diode, obtained by pulsed HONO generation and calibrated to the six individual absorption lines indicated by an *arrow*

also the absorption cross section just off the absorption line: this way, absolute HONO concentrations can still be obtained even in experiments, where it is not possible to measure the baseline in absence of HONO.

Table 6.1 Absorption cross sections σ of some selected HONO absorption lines in the near infrared region

Wavenumber/cm^{-1}	$\sigma/10^{-21}$ cm^2
6,625.01	1.6 ± 1.0
6,637.36	3.5 ± 1.6
6,638.26	3.8 ± 1.6
6,642.51	5.8 ± 2.2
6,643.17	4.2 ± 1.7
6,644.00	4.8 ± 1.9

Errors have been estimated from the signal-to-noise ratio ($\Delta\alpha = 1.5 \times 10^{-8}$ cm^{-1}) plus 30 % for other errors such as drift in H_2O_2 concentration, photolysis energy and uncertainties in the retrieval of the HONO concentration

Table 6.2 Pressure dependant absorption cross sections at the centre of the strongest line at 6,642.51 cm^{-1}

	He		N_2	
P/Torr	σ*	σ**	σ*	σ**
10	7.0 ± 2.6	1.8 ± 1.0	6.6 ± 2.5	1.8 ± 1.0
40	5.8 ± 2.2	2.1 ± 1.1	5.1 ± 2.0	2.3 ± 1.2
74	4.6 ± 1.8	2.3 ± 1.2	4.3 ± 1.8	2.4 ± 1.2

For practical purposes, the absorption cross section at 6,642.46 cm^{-1} is also given (see text)
ν = *: 6,642.51 cm^{-1} **: 6,642.46 cm^{-1}, all σ in 10^{-21} cm^2

6.1.3.4 Conclusion

The HONO spectrum has been measured in the wavelength range 6,623.6–6,645.6 cm^{-1} The strongest line in this wavelength range has been found at 6,642.51 cm^{-1} with $\sigma_{40\text{Torr He}} = (5.8 \pm 2.2) \times 10^{-21}$ cm^2. Using current cw-CRDS set-ups, HONO concentrations of as low as 2×10^{11} cm^{-3} (corresponding to $\alpha = 1 \times 10^{-9}$ cm^{-1}) can easily be quantified at 40 Torr He. Pressure broadening up to 74 Torr has been measured for the most intense line in He and N_2 as bath gas. The results show, that absorption spectroscopy in the near IR-range is not suitable for atmospheric measurements due to too small absorption cross section combined with strong pressure broadening and a very congested spectrum. However, it can provide an interesting tool for laboratory studies.

A detailed description of the results presented here can be found in [19].

6.1.4 Development of a New Technique for Selective Measurement of HO_2 and RO_2 Radicals

6.1.4.1 Introduction

Peroxy radicals RO_2 (with R = H or C_xH_y) play an important role in the photo-oxidation cycles of the troposphere. They are produced mainly via the atmospheric oxidation of hydrocarbons and carbon monoxide by OH radicals and subsequent

reactions with O_2. They can further react with NO to recycle OH radicals. This oxidation of NO through the reaction with peroxy radicals is an important source of tropospheric ozone, a major constituent of photochemical oxidants that is detrimental to human health and contributes to global warming. The concentration of tropospheric ozone has been significantly increased in recent years [1]. To understand the mechanism of this tropospheric ozone increase, precise and accurate measurements of ambient peroxy radical concentrations are essential.

Several methods have been developed for measuring atmospheric peroxy radicals and have recently been reviewed [12, 15, 35]. Peroxy radical chemical amplification (PERCA) is a method of measuring the total concentration of peroxy radicals, i.e. the sum of HO_2 and RO_2. In this method, peroxy radicals are converted in an inlet tube to higher concentrations of NO_2 via a chain amplification reaction by OH and HO_2 catalysed oxidation of NO to NO_2 and CO to CO_2 by the addition of high concentrations of NO and CO. The NO_2 product is then quantified by the appropriate measurement method. In order to obtain absolute concentrations, the chain length of the amplification has to be determined in calibration experiments, as well as the response of the NO_2 detector. Recent studies of PERCA have reported greater wall loss rate of HO_2 relative to RO_2. For example, Mihele et al. [27] reported a wall loss rate on a ¼ Teflon tube of 2.8 $\pm$ 0.2 s^{-1} for HO_2 and 0.8 $\pm$ 0.1 s^{-1} for both CH_3O_2 and $C_2H_5O_2$ radicals in dry condition. In this study, the HO_2 loss rate increased markedly with the relative humidity while the organic radicals didn't show any dependence.

The greater wall loss rate of HO_2 relative to RO_2 can be actively used to separate HO_2 and RO_2 during atmospheric measurements by predominantly denuding HO_2 prior to the PERCA inlet. This makes it possible to measure the concentration of RO_2 separately from the sum of HO_2 and RO_2, and therefore obtain the ambient concentrations of HO_2 and RO_2. It will no longer be necessary to deduce the concentration of the individual radical species from estimation of the ratio between HO_2 and RO_2 [6, 8].

Here we describe the development of a prototype instrument for the separate measurement of HO_2 and RO_2 by use of selective destruction of HO_2 prior to quantification by PERCA technique. Three different materials have been tested as the peroxy radical remover. Also, the dependence on initial radical concentration and on humidity on HO_2 and RO_2 removal efficiency was investigated for all materials.

6.1.4.2 Experimental Details

The experimental system is a further development of the PERCA system already described in detail by Sadanaga et al. [35]: to the original experiment consisting of (i) peroxy radical generator, (ii) chemical amplification reaction tube and (iii) LIF NO_2 detector, a (iv) removal cell for the selective removal of HO_2 radicals has been added in this new set-up.

(i) Peroxy radicals are generated as described by Kanaya et al. [20] through photolysis of either H_2O

$$H_2O + h\nu_{185nm} \rightarrow H + OH, \tag{6.8}$$

$$H + O_2 + M \rightarrow HO_2 + M. \tag{6.9}$$

or acetone

$$(CH_3)_2CO + h\nu_{185nm} \rightarrow 2CH_3 + CO, \tag{6.10}$$

$$CH_3 + O_2 + M \rightarrow CH_3O_2 + M. \tag{6.11}$$

(ii) The amplification system is based on Sadanaga et al. [35] and consists of a 300 mm long glass tube of 20 mm diameter. When used in the chemical amplification mode (PERCA mode), the flow from the radical generator was mixed with a NO/N_2 mixture and pure CO gas at the entrance of the reaction tube; flows were adjusted to obtain concentrations of NO and CO of 5 ppmV and 10% respectively. In order to measure the background NO_2 concentration (BG mode), CO was added at approximately 75 mm upstream from the inlet, leading to a distance of 225 mm between second addition point and radical detection point.

(iii) The NO_2 fluorescence detection system was essentially the same as the instrument described in an earlier work by Miyazaki et al. [28]. The pressure inside the fluorescence detection cell is reduced to ca. 2 Torr using a critical orifice (0.3 mm id) and an oil rotary pump (Ulvac, GVD-200A; 200 $l\ min^{-1}$) in order to minimize the collisional quenching of the excited NO_2 molecules by air. The second harmonic of the diode-laser-pumped solid-state pulsed Nd: YAG laser (Spectra-Physics, YHP70-106Q; 5 W, 10 kHz, 532 nm) is used for NO_2 excitation.

(iv) The removal cell consists of a tube and beads of the material. We have tested two different types of Teflons (PFA and PTFE) as well as glass. Cylindrical Teflon (PFA and PTFE) beads (Flon Industry, 2 dia. × 5 mm high) were packed into a 30 cm long 1/2 in. diameter Teflon tube. For testing glass, spherical glass beads (GL Science, 1 mm dia.) were packed into a 5 cm long 1/2 in. glass tube. For easy comparison, the length of the removal cell was adjusted to obtain a removal efficiency of approximately 90% for HO_2 radicals.

6.1.4.3 Results and Discussion

Figure 6.5 shows an example of the removal efficiency measurement: the upper part (a) of the figure illustrates the measurement of HO_2 radicals, while the lower part (b) is a typical example for CH_3O_2 radicals. In both cases, the signal differences

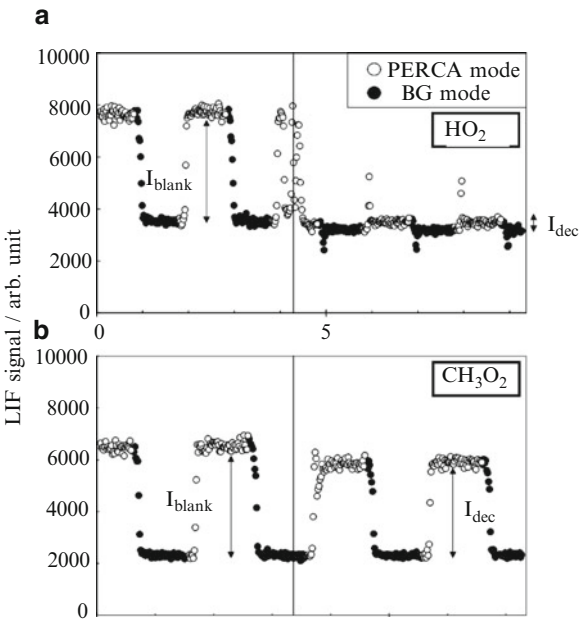

Fig. 6.5 An example of removal efficiency measurements showing PERCA/BG mode for both blank (*left side*) and removal (*right side*) mode. PERCA/BG mode are switched every minute. *Upper figure* (**a**) shows HO_2, *lower figure* (**b**) is RO_2

between PERCA and BG mode (I_{HO2}) is the HO_2 or CH_3O_2 concentration. The left part of each figure shows the HO_2/CH_3O_2 concentration after passing through the blank cell, while the right part of the graph shows the signal obtained after passing the gas mixture through the removal cell prior to entering the PERCA inlet, also in PERCA and BG mode. The connecting tubing in the blank cell path and in the removal cell path are made of the same materiel: the path in the blank cell (and therefore the residence time) is roughly ten times shorter than the tubing in the removal cell path. We, therefore, believe that radical loss is insignificant under our experimental conditions in this part of the experimental set-up and no correction need to be considered. The HO_2 concentrations for each blank or removal mode can be described as follows

$$[HO_2]_{dec} \text{ or} [HO_2]_{blank} = \frac{I_{HO2\_dec} \text{ or } I_{HO2\_blank}}{S_{HO2} \times C_{Humnid}} \tag{6.12}$$

where $[HO_2]_{dec}$ and $[HO_2]_{blank}$ indicates the concentration of HO_2 radicals in the removal and blank mode respectively and C_{Humid} indicates the correction coefficient for humidity.

Variation in the removal of HO_2 was evaluated by defining a removal efficiency factor α:

$$\alpha = 1 - \frac{I_{HO_2-dec}}{I_{HO2-blank}} \tag{6.13}$$

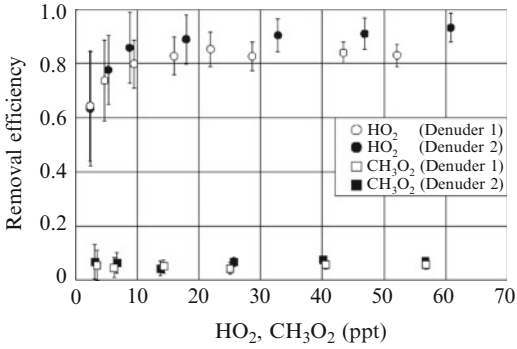

Fig. 6.6 Removal efficiency α for two different long denuders as a function of initial HO_2 and RO_2 concentration. Denuder 2 is twice as long as Denuder 1

$[HO_2]_{dec}$ and $[HO_2]_{blank}$ can be substituted by Eq.(6.2) and finally the removal efficiency α of HO_2 radicals is determined as follows:

$$\alpha = 1 - \frac{I_{HO2\_dec}}{I_{HO2\_blank}} \tag{6.14}$$

The removal efficiency of CH_3O_2 can be expressed the same way.

$$\beta = 1 - \frac{I_{CH3O2\_dec}}{I_{CH3O2\_blank}} \tag{6.15}$$

As can be seen in Fig. 6.5, the removal efficiency for HO_2 is much higher than for CH_3O_2. This has been observed for all materials and for all initial radical concentrations. It has been found, that the best material is glass bead, as for this material the removal efficiency was not dependant on the humidity. However, it turned out that the removal efficiency even for glass beads was concentration dependant, i.e. the efficiency decreases with decreasing concentration. Therefore we have tested removal cells with yet another material in order to achieve a high removal rate for HO_2 also under typical atmospheric conditions (≈10 ppt). Figure 6.6 shows the result for both, HO_2 and CH_3O_2 radicals. In these experiments, a honeycomb structure has been used as filling material, and it can be seen that the removal efficiency for HO_2 is still very high, even at typical atmospheric concentrations. The longer denuder cell leads to slightly higher removal efficiencies.

Preliminary measurements under real, atmospheric conditions have been performed in order to demonstrate the capabilities of this new instrument: Fig. 6.7 shows an example of the diurnal profile of HO_2 and RO_2 radical concentration. The average over 2 min has been plotted, and the full line represents the ten points moving average. Maximum noon time concentrations of 50 ppt for RO_2 and 25 ppt for HO_2 were observed. The concentrations of RO_2 and HO_2 were highly correlated, and HO_2 concentrations were obtained similar to those observed previously [21].

From this observation, we conclude that the new coupling of the denuder to a classical PERCA-LIF set-up for the selective removal of HO_2 radicals has a great potential to enhance the possibilities of existing PERCA set-ups.

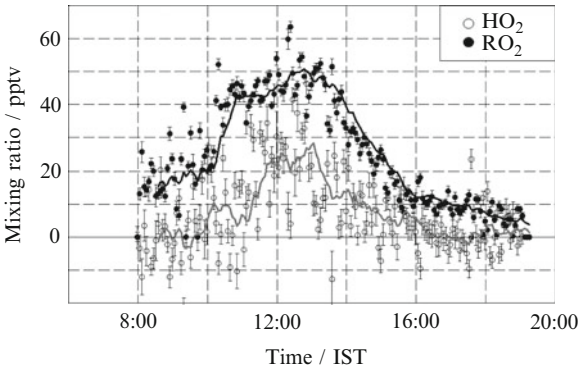

Fig. 6.7 In situ measurements of HO_2 and RO_2 radical concentrations with 1σ precision error bars. Each *solid line* indicates the ten points moving average data. The measurements were obtained on 23 July 2010 in Hachoji, Tokyo

6.1.4.4 Conclusion

We have demonstrated an improvement to the well-established PERCA technique allowing the selective measurement of HO_2 and RO_2 radicals. Advantage is taken of the difference in heterogeneous removal efficiency of HO_2 and RO_2. Different materials have been tested, and it has been found that glass is the most appropriate because the removal efficiency does not exhibit a pronounced dependence on water concentration. The efficiency for HO_2 depends also on the initial radical concentration, and in order to efficiently remove HO_2 even at low, ambient concentrations, a honeycomb structure offering a high surface area has shown a high efficiency, even under typical ambient HO_2 concentrations. A preliminary experiment on the roof of the laboratory near Tokyo has shown the high potential that this new method has compared to classical PERCA set-ups.

A detailed description of the results presented here can be found in Miyazaki et al. [29].

References

1. Akimoto H (2003) Global air quality and pollution. Science 302:1716–1719
2. Aluculesei A, Tomas A, Schoemaecker C, Fittschen C (2008) On the direct formation of HO_2 radicals after 248 nm irradiation of benzene C_6H_6 in the presence of O_2. Appl Phys B Laser Opt 92:379–385
3. Amedro D, Miyazaki K, Parker AE, Schoemaecker C, Fittschen C (2011) Atmospheric and kinetic studies of OH and HO_2 by the LIF technique. JES. doi:10.1016/S1001-0742(11)60723-7
4. Amedro D, Parker AE, Schoemaecker C, Fittschen C (2011) Direct observation of OH radicals after 565 nm multi-photon excitation of NO_2 in the presence of H_2O. Chem Phys Lett 513:12–16
5. Barney WS, Wingen LM, Lakin MJ, Brauers T, Stutz J, Finlayson-Pitts BJ (2000) Infrared absorption cross-section measurements for nitrous acid (HONO) at room temperature. J Phys Chem A 104:1692–1699

6. Cantrell CA, Shetter RE, Lind JA, McDaniel AH, Calvert JG, Parrish DD, Fehsenfeld FC, Buhr MP, Trainer M (1993) An improved chemical amplifier technique for peroxy radical measurements. J Geophys Res 98:2897–2909
7. Carr S, Heard DE, Blitz MA (2009) Comment on "atmospheric hydroxyl radical production from electronically excited NO_2 and H_2O". Science 324:336
8. Clemitshaw KC, Carpenter LJ, Penkett SA, Jenkin ME (1997) A calibrated peroxy radical chemical amplifier for ground-based tropospheric measurements. J Geophys Res 102:25405–25416
9. Crowley JN, Carl SA (1997) OH formation in the photoexcitation of NO_2 beyond the dissociation threshold in the presence of water vapor. J Phys Chem A 101:4178–4184
10. Djehiche M, Tomas A, Fittschen C, Coddeville P (2011) First direct detection of HONO in the reaction of methylnitrite (CH_3ONO) with OH radicals. Environ Sci Technol 45:608–614
11. Febo A, Perrino C, Gherardi M, Sparapani R (1995) Evaluation of a high-purity and high-stability continuous generation system for nitrous acid. Environ Sci Technol 29:2390–2395
12. Fuchs H, Holland F, Hofzumahaus A (2008) Measurement of tropospheric RO_2 and HO_2 radicals by a laser-induced fluorescence instrument. Rev Sci Instrum 79:084104
13. Guilmot JM, Godefroid M, Herman M (1993) Rovibrational parameters for trans-nitrous acid. J Mol Spectrosc 160:387–400
14. Guilmot JM, Melen F, Herman M (1993) Rovibrational parameters for cis-nitrous acid. J Mol Spectrosc 160:401–410
15. Heard DE, Pilling MJ (2003) Measurement of OH and HO_2 in the troposphere. Chem Rev 103:5163–5198
16. Hellebust S, Roddis T, Sodeau JR (2007) Potential role of the nitroacidium ion on HONO emissions from the snowpack. J Phys Chem A 111:1167–1171
17. Ibrahim N, Thiebaud J, Orphal J, Fittschen C (2007) Air-broadening coefficients of the HO_2 radical in the $2\nu_1$ band measured using cw-CRDS. J Mol Spectrosc 242:64–69
18. Jain C, Parker AE, Schoemaecker C, Fittschen C (2010) HO_2 formation from the photoexcitation of benzene/O_2 mixtures at 248 nm: an energy dependence study. Chemphyschem 11:3867–3873
19. Jain C, Morajkar P, Schoemaecker C, Viskolcz B, Fittschen C (2011) Measurement of absolute absorption cross sections for nitrous acid (HONO) in the near-infrared region by the continuous wave cavity ring-down spectroscopy (cw-CRDS) technique coupled to laser photolysis. J Phys Chem A 115:10720–10728
20. Kanaya Y, Sadanaga Y, Hirokawa J, Kajii Y, Akimoto H (2001) Development of a ground-based LIF instrument for measuring HO_x radicals: instrumentation and calibrations. J Atmos Chem 38:73–110
21. Kanaya Y, Cao R, Akimoto H, Fukuda M, Komazaki Y, Yokouchi Y, Koike M, Tanimoto H, Takegawa N, Kondo Y (2007) Urban photochemistry in central Tokyo: 1. Observed and modeled OH and HO_2 radical concentrations during the winter and summer of 2004. J Geophys Res 112:D21312
22. Karlsson RS, Ljungstrom EB (1996) Laboratory study of CINO hydrolysis. Environ Sci Technol 30:2008–2013
23. Langridge JM, Gustafsson RJ, Griffiths PT, Cox RA, Lambert RM, Jones RL (2009) Solar driven nitrous acid formation on building material surfaces containing titanium dioxide: a concern for air quality in urban areas? Atmos Environ 43:5128–5131
24. Li S, Matthews J, Sinha A (2008) Atmospheric hydroxyl radical production from electronically excited NO_2 and H_2O. Science 319:1657–1660
25. Li S, Matthews J, Sinha A (2009) Response to comment on "atmospheric hydroxyl radical production from electronically excited NO_2 and H_2O". Science 324:336c
26. Liao W, Case AT, Mastromarino J, Tan D, Dibb JE (2006) Observations of HONO by laser-induced fluorescence at the South Pole during ANTCI 2003. Geophys Res Lett 33:L09810

27. Mihele CM, Mozurkewich M, Hastie DR (1999) Radical loss in a chain reaction of CO and NO in the presence of water: implications for the radical amplifier and atmospheric chemistry. Int J Chem Kinet 31:145–152
28. Miyazaki K, Matsumoto J, Kato S, Kajii Y (2008) Development of atmospheric NO analyzer by using a laser-induced fluorescence NO_2 detector. Atmos Environ 42:7812–7820
29. Miyazaki K, Parker AE, Fittschen C, Monks PS, Kajii Y (2010) A new technique for the selective measurement of atmospheric peroxy radical concentrations of HO_2 and RO_2 using a denuding method. Atmos Meas Tech 3:1547–1554
30. Monge ME, D'Anna B, George C (2010) Nitrogen dioxide removal and nitrous acid formation on titanium oxide surfaces-an air quality remediation process? Phys Chem Chem Phys 12:8991–8998
31. Parker A, Amedro D, Schoemaecker C, Fittschen C (2011) OH reactivity measurements by FAGE. JEEM 10:107–114
32. Parker A, Jain C, Schoemaecker C, Szriftgiser P, Votava O, Fittschen C (2011) Simultaneous, time-resolved measurements of OH and HO_2 radicals by coupling of high repetition rate LIF and cw-CRDS techniques to a laser photolysis reactor and its application to the photolysis of H_2O_2. Appl Phys B Laser Opt 103:725–733
33. Perner D, Platt U (1979) Detection of nitrous acid in the atmosphere by differential optical absorption. Geophys Res Lett 6:917–920
34. Rohrer F, Bohn B, Brauers T, Bröning D, Johnen F-J, Wahner A, Kleffmann J (2005) Characterisation of the photolytic HONO-source in the atmosphere simulation chamber SAPHIR. Atmos Chem Phys 5:2189–2201
35. Sadanaga Y, Matsumoto J, Sakurai K, Isozaki R, Kato S, Nomaguchi T, Bandow H, Kajii Y (2004) Development of a measurement system of peroxy radicals using a chemical amplification/laser-induced fluorescence technique. Rev Sci Instrum 75:864–872
36. Sironneau V, Orphal J, Demaison J, Chelin P (2008) High-resolution infrared spectroscopy of trans- and cis-$H^{18}ON^{18}O$: equilibrium structures of the nitrous acid isomers. J Phys Chem A 112:10697–10702
37. Stockwell WR, Calvert JG (1978) The near ultraviolet absorption spectrum of gaseous HONO and N^2O^3. J Photochem 8:193–203
38. Stutz J, Kim ES, Platt U, Bruno P, Perrino C, Febo A (2000) UV-visible absorption cross sections of nitrous acid. J Geophys Res 105:14585–14592
39. Tang Y, Tyndall GS, Orlando JJ (2010) Spectroscopic and kinetic properties of HO_2 radicals and the enhancement of the HO_2 self reaction by CH_3OH and H_2O. J Phys Chem A 114:369–378
40. Thiebaud J, Fittschen C (2006) Near infrared cw-CRDS coupled to laser photolysis: spectroscopy and kinetics of the HO_2 radical. Appl Phys B Laser Opt 85:383–389
41. Thiebaud J, Crunaire S, Fittschen C (2007) Measurement of line strengths in the $2\nu_1$ band of the HO_2 radical using laser photolysis/continuous wave cavity ring down spectroscopy (cw-CRDS). J Phys Chem A 111:6959–6966
42. Varma R, Curl RF (1976) Study of the dinitrogen trioxide-water-nitrous acid equilibrium by intensity measurements in microwave spectroscopy. J Phys Chem 80:402–409
43. Volkamer R, Sheehy P, Molina LT, Molina MJ (2010) Oxidative capacity of the Mexico City atmosphere – part 1: a radical source perspective. Atmos Chem Phys 10:6969–6991
44. Wennberg PO, Dabdub D (2008) Rethinking ozone production. Science 319:1624–1625
45. Yamano D, Yabushita A, Kawasaki M, Perrin A (2010) Absorption spectrum of nitrous acid for the $\nu_1 + 2\nu_3$ band studied with continuous-wave cavity ring-down spectroscopy and theoretical calculations. J Quant Spectrosc Radiat Transf 111:45–51

Chapter 7
The Exchange of Soil Nitrite and Atmospheric HONO: A Missing Process in the Nitrogen Cycle and Atmospheric Chemistry

Hang Su, Yafang Cheng, and Ulrich Pöschl

Abstract An important nitrogen exchange process that has not been considered in the nitrogen cycle and atmospheric chemistry is presented. The exchange process suggests that soil nitrite can release HONO and explain the reported strength and diurnal variation of the missing HONO source that is necessary to explain field measurements.

Keywords Soil • Nitrite • Nitrogen cycle • OH radical • HONO

7.1 Atmospheric N(III): HONO

OH radicals represent an essential oxidizing species in the atmosphere [6]. As a major driven force of atmospheric oxidation reactions, OH is actively involved in the formation ozone, particulate matter, and acid rains. OH radicals are also known as an atmospheric detergent, which significantly contributes to the removal of air pollutants (e.g., all CH_4, 90% of CO and 80% of CH_3Cl) [25].

Nitrous acid (HONO) has been considered as one of the most important atmospheric odd nitrogen species. In the lower atmosphere, up to ~30% of the primary OH radical production is attributed to the photolysis of HONO (reaction 7.1).

$$\mathrm{HONO} + h\nu \rightarrow \mathrm{OH} + \mathrm{NO}\ (300\mathrm{nm} < \lambda < 405\ \mathrm{nm}) \tag{7.1}$$

Despite of its importance, the source of atmospheric HONO is still not fully understood. The well-recognized sources are the reaction of NO with OH radicals [22, 28] and HONO emissions from combustion processes [2, 17]. The sinks of HONO are the photolysis process during daytime and the wet/dry depositions. However, field measurements suggest that there is still a large missing source,

H. Su (✉) • Y. Cheng • U. Pöschl
Biogeochemistry Department, Max Plank Institute for Chemistry, Mainz 55020, Germany
e-mail: h.su@mpic.de

I. Barnes and K.J. Rudziński (eds.), *Disposal of Dangerous Chemicals in Urban Areas and Mega Cities*, NATO Science for Peace and Security Series C: Environmental Security,
DOI 10.1007/978-94-007-5034-0_7,

which produces more HONO (>10 times) than the sources aforementioned [15, 19, 26, 31]. A special feature of the missing source is that it is higher during daytime than during the night time [15, 19, 26, 31].

Heterogeneous reactions of NO_2 [3, 8] on aerosol surfaces have been suggested to account for the missing source [1, 14, 15, 30]. In the presence of light, enhanced HONO production was observed on several aerosol species, such as organics and soot particles [9, 21, 27]. The photo-enhanced mechanism provides an explanation to the correlation between the observed missing source and the sunlight intensity. However, due to low uptake coefficients for NO_2, HONO production on aerosol surfaces is not enough to explain the measured HONO production rates [21, 27]. Thus, the ground surface, especially the soil surface, has been suggested as a potential substrate for the production of N(III) in HONO from N(IV) in NO_2 [21, 27, 32].

7.2 Nitrogen Cycle and Soil N(III): NO_2^-

The dominant sources of N(III) in soil, however, are biological nitrification and denitrification processes [5], which produce nitrite ions (NO_2^-) from ammonium (by nitrifying microbes) as well as from nitrate (by denitrifying microbes). Though rarely considered in the atmospheric chemistry, soil nitrite has been recognized as an important compound in the nitrogen cycle. The nitrogen cycle is the process by which nitrogen is converted between its various chemical forms and transported between soil, ocean and atmosphere. The conversion processes (nitrification, denitrification and N fixation), known as the biogeochemistry of nitrogen (BIO), is primarily mediated by micro-organisms [5].

Our analysis suggests that N(III) production by BIO is much faster than that from heterogeneous reactions of NO_2 (CHEM). For terrestrial system, N(III) production by BIO seems to be of the same order as the total nitrogen input (N fixation, N deposition and even the fertilizer application) to the ground surfaces [10]. On the other hand, the NO_2 uptake on ground surfaces, i.e. NO_2 deposition, can be considered as an upper limit for N(III) production by CHEM. Since NO_2 deposition contribute only ~1% of the total N input to the terrestrial system (according to data of [5, 13]), N(III) production by BIO should overwhelm the production by CHEM.

7.3 Soil-Atmosphere Exchange of N(III)

After being produced, soil N(III) is actively involved in the soil-atmosphere nitrogen exchange. The emission of NO, N_2O and N_2 from soil are all mediated by nitrite [5]. However, until recently the emission of soil N(III) itself was rarely discussed [16, 31]. Since N(III) compounds are present in both soil and atmosphere, we suggest that there should be they are actively interacting with each other through the exchange processes as the other nitrogen compounds (Fig. 7.1).

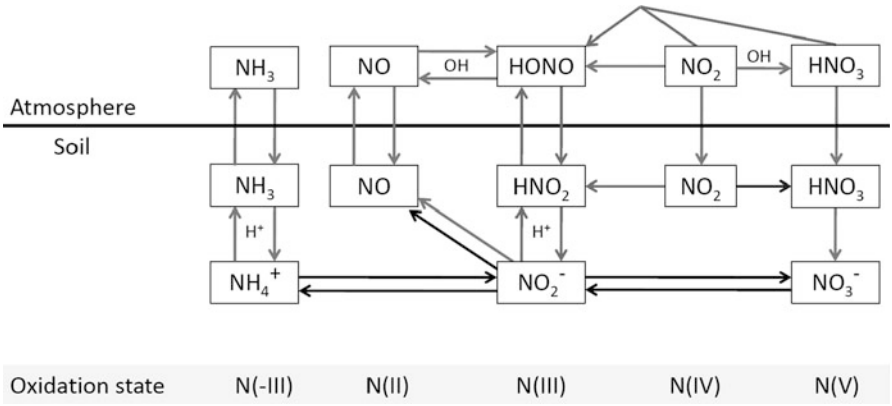

Fig. 7.1 Coupling of atmospheric HONO with soil nitrite (Reprinted from Su et al. [31], with permission from *Science*)

The production of soil nitrite doesn't necessarily lead to the HONO release. HONO may stay on soil or other kinds of surfaces, as its deposition on ground surfaces has been considered as an important sink of HONO [12]. There are ample evidences suggest that the HONO deposition/release is highly pH dependent. For example, basic and neutral surfaces are commonly used in the sampling of atmospheric HONO by denuder techniques [29, 30] and the surfaces of denuders need to be replaced/replenished when it becomes too acidic. Laboratory studies of NO_2 reactions on aerosol surfaces also found that the release of HONO depends on the pH of aerosol particles [27]. Besides, the nitrite accumulation in soil was also found to be favored by basic conditions ([31] and references therein).

The strong pH dependence suggests that the release/deposition of HONO might be controlled by the acid–base reaction and gas–liquid partitioning processes (reaction 7.2)

$$NO_2^-(aq) + H^+(aq) \Leftrightarrow HNO_2\,(aq) \Leftrightarrow HONO\,(g) \tag{7.2}$$

According to reaction (7.2), the direction of HONO exchange depends on the relative abundance of N(III) in the gas and aqueous phases. Ideally, under certain pair of soil pH and nitrite concentration, an equilibrium $[HONO]^*$ can be expected. When $[HONO]^*$ is higher than the actual gas-phase concentration, [HONO], nitrous acid will be released from the aqueous phase; otherwise, gaseous HONO will be deposited.

7.4 Experimental Evidence

We first analyzed data published in literature (in which both soil pH and nitrite concentrations are available) to estimate the equilibrium HONO concentration ($[HONO]^*$) according to reaction (7.2). $[HONO]^*$ in different types of soils vary

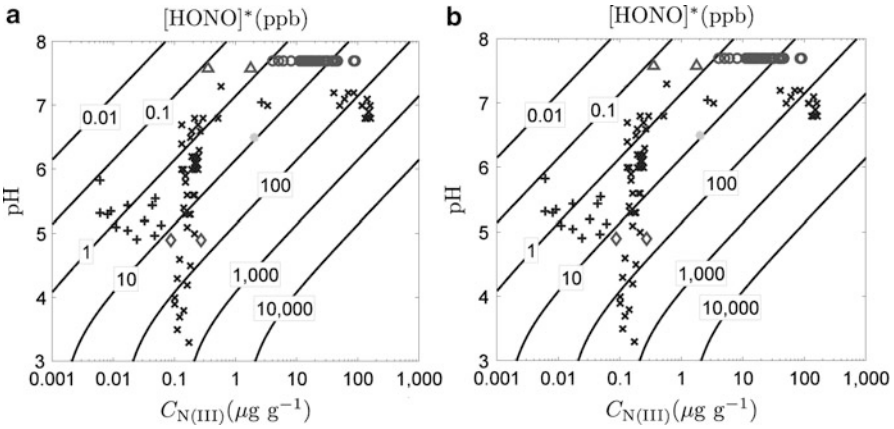

Fig. 7.2 $[HONO]^*$ and F_{max}. (**a**) Equilibrium gas phase HONO concentration, $[HONO]^*$; and (**b**) Maximum HONO release flux, F_{max}. The lines are logarithmic isopleths. The points represent data pairs of soil pH and $C_{N(III)}$ (in terms of mass of nitrogen) reported from field measurements, incubation experiments with ambient soil samples and from the chamber experiment in Su et al. [31] (Reprinted from Su et al. [31], with permission from *Science*)

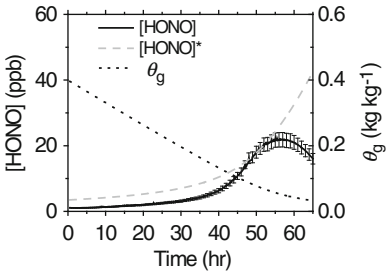

Fig. 7.3 Chamber measurement of HONO emissions from soil. [HONO], gas phase HONO concentration in the chamber exit (*solid line*); $[HONO]^*$, equilibrium HONO concentration (*dashed lines*); and θ_g, gravimetric soil water content (*dots*) (Reprinted from Su et al. [31] with permission from *Science*)

widely from ~0.1 ppb to ~600 ppb (Fig. 7.2). The atmospheric HONO concentrations observed in the planetary boundary layer vary from tens of parts per trillion in polar and forest regions [7, 24, 32] to several parts per billion in rural and urban areas [14, 18]. These field measurement results are within the range of $[HONO]^*$ values calculated for the available data pairs of soil pH and nitrite. Thus, the release of HONO from soil nitrite may indeed account for the missing source of HONO.

To test the validity of the proposed HONO release mechanism, we conducted a chamber experiment with real soil. [HONO] exhibited a strong increase from ~1 to ~22 ppb as the water content θg decreased because of soil water evaporation (Fig. 7.3), which is consistent with increasing CN(III) concentration in the soil water and increasing [HONO]* in the soil pore space. After reaching a maximum at $\theta g \approx 0.05$ kg kg^{-1}, [HONO] decreased slightly as θg further decreased. The

observed dependence of [HONO] on θg closely resembles the previously reported humidity dependence of nitric oxide (NO) emissions from soil [20]. This confirms the proposed relation between atmospheric HONO and soil nitrite, because the soil emissions of NO are known to be linked to soil nitrite as well [20].

Throughout the chamber experiment, the deviations between the observed gas-phase concentration [HONO] and the theoretical equilibrium concentration $[HONO]^*$ were less than a factor of 3 (Fig. 7.3), which is small compared with the large variability of ambient soil nitrite concentrations and pH ranging over multiple orders of magnitude (Fig. 7.2). The deviations can be attributed to the kinetic limitations of mass transfer and to non-ideal solution behavior (adsorption, Kelvin and solute interaction effects on gas/liquid partitioning [4]).

7.5 Soil Nitrite as a Source of HONO

To quantify the flux rate of HONO emissions from soil nitrite, we applied a standard formalism (Eq. 7.3) describing the atmosphere-soil exchange of trace gases as a function of the difference between the atmospheric concentration and the equilibrium concentration at the soil solution surface. The transfer velocity, v_t, depends primarily on meteorological and soil conditions, and over continents it is typically of the order of ~1 cm s^{-1} [25].

$$F = -v_t([HONO] - [HONO]^*) \tag{7.3}$$

In the observed range of soil pH, $C_{N(III)}$ and [HONO], F varies from ~1 ng m^{-2} s^{-1} up to ~3,000 ng m^{-2} s^{-1}. This range fully covers the range of surface fluxes corresponding to the strength of the missing HONO source reported from field measurements [15, 24, 30]. By considering the temperature dependence of the equilibriums in reaction (7.2), the HONO release from soil nitrite can also explain the characteristic diurnal course observed in field measurements [31].

7.6 Conclusions

In this study, we suggest an important nitrogen exchange process that has not been considered in the nitrogen cycle and atmospheric chemistry. The exchange process suggests that soil nitrite can release HONO and explain the reported strength and diurnal variation of the missing source. Fertilized soils with low pH appear to be particularly strong sources of HONO and OH. Due to enhanced fertilizer use and soil acidification in developing countries [11], the release of HONO from soil nitrite might strongly increase in the course of global change and affect the oxidizing capacity and composition of the atmosphere. Besides fertilization and intensified agricultural use of soils in populated environments, nitrite production and HONO release may also be important in natural environments, including forests and boreal soils, because of increasing nitrogen deposition [23] and the ubiquity of (de)

nitrifying microbes. In view of the potentially large impact on atmospheric chemistry and global environmental change, we recommend further studies of HONO release from soil nitrite and related processes in the biogeochemical cycling of nitrogen in both agricultural and natural environments.

References

1. Acker K, Moller D, Wieprecht W, Meixner FX, Bohn B, Gilge S, Plass-Dulmer C, Berresheim H (2006) Strong daytime production of OH from HNO_2 at a rural mountain site. Geophys Res Lett 3(3):L02809
2. Ackermann R (2000) Auswirkungen von Kraftfahrzeugemissionen in der urbanen Atmosphaere. Univerisity of Heidelberg, Heidelberg
3. Ammann M, Kalberer M, Jost DT, Tobler L, Roessler E, Piguet D, Gaeggeler HW, Baltensperger U (1998) Heterogeneous production of nitrous acid on soot in polluted air masses. Nature 395:157–160
4. Bohn HL, McNeal BL, O'Connor GA (2001) Soil chemistry, 2nd edn. Wiley, New York
5. Canfield DE, Glazer AN, Falkowski PG (2010) The evolution and future of earth's nitrogen cycle. Science 330:192–196
6. Crutzen PJ, Zimmermann PH (1991) The changing photochemistry of the troposphere. Tellus B 43:136–151
7. Dibb JE, Arsenault M, Peterson MC, Honrath RE (2002) Fast nitrogen oxide photochemistry in Summit, Greenland snow. Atmos Environ 3(6):2501
8. Finlayson-Pitts BJ, Wingen LM, Sumner AL, Syomin D, Ramazan KA (2003) The heterogeneous hydrolysis of NO_2 in laboratory systems and in outdoor and indoor atmospheres: an integrated mechanism. Phys Chem Chem Phys 5:223–242
9. George C, Strekowski RS, Kleffmann J, Stemmler K, Ammann M (2005) Photoenhanced uptake of gaseous NO_2 on solid organic compounds: a photochemical source of HONO? Faraday Discuss 130:195–210
10. Gruber N, Galloway JN (2008) An Earth-system perspective of the global nitrogen cycle. Nature 451:293–296
11. Guo JH, Liu XJ, Zhang Y, Shen JL, Han WX, Zhang WF, Christie P, Goulding KWT, Vitousek PM, Zhang FS (2010) Significant acidification in major Chinese croplands. Science 327:1008–1010
12. Harrison RM, Peak JD, Collins GM (1996) Tropospheric cycle of nitrous acid. J Geophys Res 101:14429–14440
13. Holland EA, Braswell BH, Sulzman J, Lamarque J-F (2005) Nitrogen deposition onto the United States and Western Europe: synthesis of observations and models. Ecol Appl 15:38–57
14. Kleffmann J (2007) Daytime sources of nitrous acid (HONO) in the atmospheric boundary layer. Chemphyschem 8:1137–1144
15. Kleffmann J, Gavriloaiei T, Hofzumahaus A, Holland F, Koppmann R, Rupp L, Schlosser E, Siese M, Wahner A (2005) Daytime formation of nitrous acid: a major source of OH radicals in a forest. Geophys Res Lett 3(2):L05818
16. Kubota M, Asami T (1985) Source of nitrous acid volatilized from upland soils. Soil Sci Plant Nutr 31:35–42
17. Kurtenbach R, Becker KH, Gomes JAG, Kleffmann J, Loerzer JC, Spittler M, Wiesen P, Ackermann R, Geyer A, Platt U (2001) Investigations of emissions and heterogeneous formation of HONO in a road traffic tunnel. Atmos Environ 35:3385–3394
18. Lammel G, Cape JN (1996) Nitrous acid and nitrite in the atmosphere. Chem Soc Rev 25:361–369

19. Li X, Brauers T, Häseler R, Bohn B, Fuchs H, Hofzumahaus A, Holland F, Lou S, Lu KD, Rohrer F, Hu M, Zeng LM, Zhang YH, Garland RM, Su H, Nowak A, Wiedensohler A, Takegawa N, Shao M, Wahner A (2012) Exploring the atmospheric chemistry of nitrous acid (HONO) at a rural site in Southern China. Atmos Chem Phys 12:1497–1513
20. Ludwig J, Meixner FX, Vogel B, Förstner J (2001) Soil-air exchange of nitric oxide: an overview of processes, environmental factors, and modeling studies. Biogeochemistry 52:225–257
21. Monge ME, D'Anna B, Mazri L, Giroir-Fendler A, Ammann M, Donaldson DJ, George C (2010) Light changes the atmospheric reactivity of soot. Proc Natl Acad Sci 107:6605–6609
22. Pagsberg P, Bjergbakke E, Ratajczak E, Sillesen A (1997) Kinetics of the gas phase reaction OH + NO(+M) $\rightarrow$ O(+M) and the determination of the UV absorption cross sections of HONO. Chem Phys Lett 272:383–390
23. Reay DS, Dentener F, Smith P, Grace J, Feely RA (2008) Global nitrogen deposition and carbon sinks. Nat Geosci 1:430–437
24. Ren X, Gao H, Zhou X, Crounse JD, Wennberg PO, Browne EC, LaFranchi BW, Cohen RC, McKay M, Goldstein AH, Mao J (2010) Measurement of atmospheric nitrous acid at Bodgett Forest during BEARPEX2007. Atmos Chem Phys 10:6283–6294
25. Seinfeld JH, Pandis SN (2006) Atmospheric chemistry and physics, from air pollution to climate change. Wiley, New York
26. Sörgel M, Regelin E, Bozem H, Diesch JM, Drewnick F, Fischer H, Harder H, Held A, Hosaynali-Beygi Z, Martinez M, Zetzsch C (2011) Quantification of the unknown HONO daytime source and its relation to NO_2. Atmos Chem Phys 11:10433–10447
27. Stemmler K, Ndour M, Elshorbany Y, Kleffmann J, D'Anna B, George C, Bohn B, Ammann M (2007) Light induced conversion of nitrogen dioxide into nitrous acid on submicron humic acid aerosol. Atmos Chem Phys 7:4237–4248
28. Stuhl F, Niki H (1972) Flash photochemical study of the reaction OH + NO + M using resonance fluorescent detection of OH. J Chem Phys 57:3677–3679
29. Su H, Cheng YF, Cheng P, Zhang YH, Dong S, Zeng LM, Wang X, Slanina J, Shao M, Wiedensohler A (2008) Observation of nighttime nitrous acid (HONO) formation at a non-urban site during PRIDE-PRD2004 in China. Atmos Environ 42:6219–6232
30. Su H, Cheng YF, Shao M, Gao DF, Yu ZY, Zeng LM, Slanina J, Zhang YH, Wiedensohler A (2008) Nitrous acid (HONO) and its daytime sources at a rural site during the 2004 PRIDE-PRD experiment in China. J Geophys Res 11(3):D14312
31. Su H, Cheng YF, Oswald R, Behrendt T, Trebs I, Meixner FX, Andreae MO, Cheng P, Zhang Y, Pöschl U (2011) Soil nitrite as a source of atmospheric HONO and OH radicals. Science 333:1616–1618
32. Zhang N, Zhou X, Shepson PB, Gao H, Alaghmand M, Stirm B (2009) Aircraft measurement of HONO vertical profiles over a forested region. Geophys Res Lett 3(6):L15820

Chapter 8
Nitrogen Oxides: Vehicle Emissions and Atmospheric Chemistry

Timothy J. Wallington, John R. Barker, and Lam Nguyen

Abstract An overview of vehicle emissions, ambient concentrations, and atmospheric chemistry of NO, NO_2, and N_2O is presented. We start with a discussion of air quality standards and trends in NO_2 levels. We then discuss the formation of nitrogen oxides in vehicle engines, technologies used to control emissions of nitrogen oxides, and the trends in vehicle emissions.

Keywords Nitrogen oxides • NO • NO_2 • Vehicles • Air pollution

8.1 Introduction

It is well recognized that emissions from vehicles can play an important role in the degradation of local air quality and contribute to radiative forcing of climate change. There are three different classes of vehicle emissions which contribute to local air pollution; hydrocarbons, nitrogen oxides, and particulate matter. The goal of the present paper is to provide an overview of the emissions of nitrogen oxides from vehicles and their atmospheric chemistry. There are three nitrogen oxides that are emitted from vehicles; NO, NO_2, and N_2O. Nitrogen monoxide (NO) and nitrogen dioxide (NO_2) are interconverted rapidly (typically on a time scale of minutes) in atmospheric processes and their chemistry is so interlinked that they are usually referred to together as NO_x ($NO + NO_2$). NO_x chemistry plays an important

T.J. Wallington (✉)
Ford Motor Company, Mail Drop RIC-2122, Dearborn Michigan 48121-2053, USA

Department of Atmospheric, Oceanic and Space Sciences, University of Michigan, Ann Arbor, MI 48109-2143, USA
e-mail: twalling@ford.com

J.R. Barker • L. Nguyen
Department of Atmospheric, Oceanic and Space Sciences, University of Michigan, Ann Arbor, MI 48109-2143, USA

I. Barnes and K.J. Rudziński (eds.), *Disposal of Dangerous Chemicals in Urban Areas and Mega Cities*, NATO Science for Peace and Security Series C: Environmental Security,
DOI 10.1007/978-94-007-5034-0_8,

role in the formation of local air pollution (smog). In stark contrast to NO_x, dinitrogen monoxide (N_2O) is inert to chemical and physical processes in the lower atmosphere, has an atmospheric lifetime of 114 years [19], and plays no role in local air quality. N_2O is a potent greenhouse gas although as we discuss in the present article the emissions from vehicles are small and only make a small contribution to radiative forcing of climate change.

The goal of the present paper is to provide an overview of nitrogen oxide emissions from vehicles and their atmospheric chemistry. We start with a discussion of air quality standards and trends in NO_2 levels. We then discuss the formation of nitrogen oxides in vehicle engines, technologies used to control emissions of nitrogen oxides, and the chemistry of nitrogen oxides after they have been emitted into the atmosphere. We highlight areas of current research interest and future research directions.

8.2 Air Quality Standards

Under the Clean Air Act the United States Environmental Protection Agency (USEPA) establishes air quality standards to protect public health and the environment [28]. USEPA has set national air quality standards for six common air pollutants. These are carbon monoxide, ozone, lead, particulate matter, sulfur dioxide, and nitrogen dioxide. Using a nationwide network of monitoring sites, EPA has reported ambient air quality trends for nitrogen dioxide (NO_2). Figure 8.1 shows the average annual NO_2 concentration measured in 81 monitoring sites across the U.S. As seen from Fig. 8.1, there has been a significant and steady trend

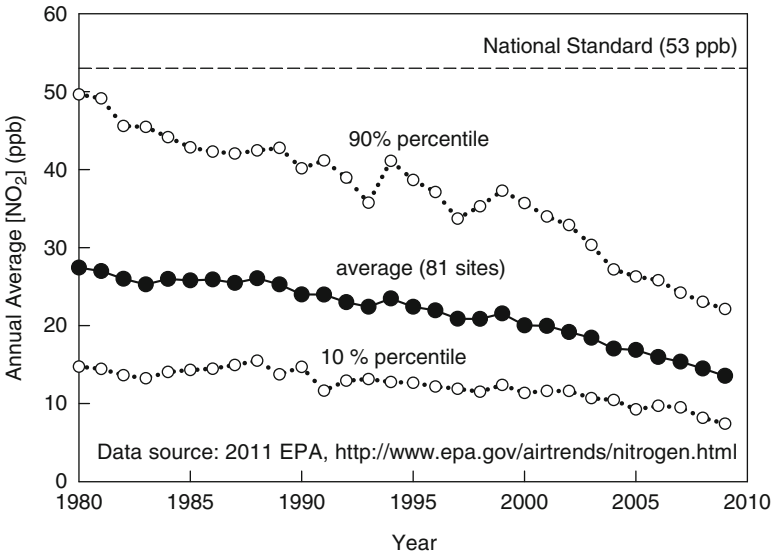

Fig. 8.1 Annual average NO_2 concentrations form 81 sites in the U.S. (average, 90th, and 10th percentile) (Data from USEPA [28])

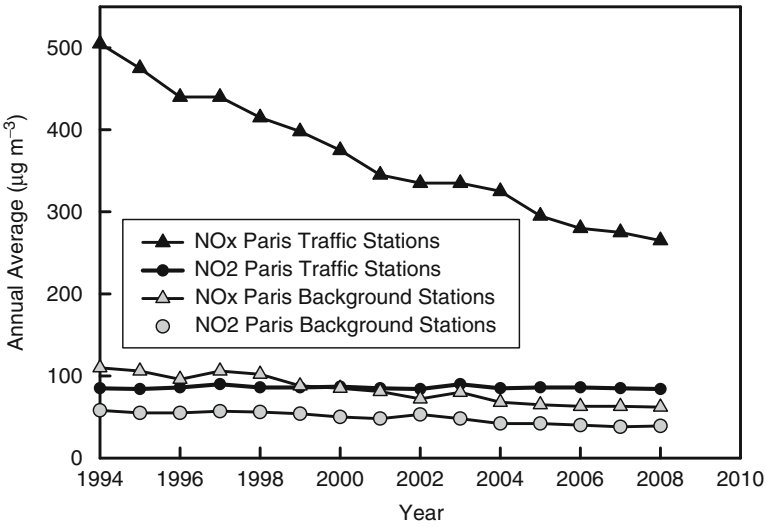

Fig. 8.2 Annual average NO_x (*triangles*) and NO_2 (*circles*) concentrations from traffic (*filled symbols*) and background (*grey symbols*) stations in Paris (Data were taken from Carslaw et al. [10])

of decreased NO_2 levels in air in the U.S. over the past 30 years. This trend reflects the success of emission control measures on mobile and stationary sources adopted since the enactment of the Clean Air Act in 1970.

USEPA set the annual average NO_2 standard of 53 ppb (102 µg/m^3) in 1971. USEPA reviewed the NO_2 standard in 1985 and 1996 and decided to retain the 53 ppb annual average standard. In 2010 EPA established a new 1-h NO_2 standard at 100 ppb (192 µg/m^3) and decided to retain the 53 ppb annual average standard. As seen from Fig. 8.1, the levels of NO_2 in air in the U.S. are typically substantially below the annual average standard.

The European Commission set a 1 h NO_2 limit value of 200 µg/m^3 (104 ppb) and http://ppdys1138/eHR-ESS/Login_Page.aspxannual NO_2 limit value of 40 µg/m^3 (21 ppb) effective in 2010. In China the 1 h NO_2 limit value is 240 µg/m^3 (125 ppb), daily NO_2 limit value is 120 µg/m^3 (63 ppb), and annual NO_2 limit value is 80 µg/m^3 (42 ppb) for cities. NO_x concentrations in European cities have declining significantly over the past few decades mainly as a result of reduced traffic emissions, however NO_2 concentrations in European cities over the past decade are declining slowly, or are showing little trend [10]. Figure 8.2 shows the trend in annual average concentrations of NOx and NO_2 reported by Carslaw et al. [10] from stations in Paris which are close to traffic emissions and stations which are located in what are considered urban background locations somewhat removed from the influence of direct emissions. The slower decrease in NO_2 concentrations than NO_x concentrations in Europe has been attributed to decreased overall NO_x levels in vehicle exhaust with a higher fraction of NO_2 within the exhaust [10]. The annual average NO_2 limit value in Europe of 40 µg/m^3 (21 ppb) effective in 2010 is approximately a factor of 2.5 times lower, and more difficult to achieve, than the US annual average NO_2 standard of 53 ppb.

8.3 Nitrogen Oxide Emissions from Vehicles

NO_x emissions from vehicles can be traced to oxidation of fuel-bound nitrogen and high temperature oxidation of atmospheric nitrogen in the combustion chamber [13, 18]. The chemistry associated with NO_x formation and treatment in vehicles has been discussed by Wallington et al. [30]. The vast majority of NO_x emissions come from oxidation of atmospheric nitrogen initiated via reaction with O atoms, $O + N_2 = NO + N$, followed by $N + O_2 = NO + O$, and $N + HO = NO + H$ [17]. This is known as the Zeldovich mechanism after its discoverer [34]. Oxygen atoms are produced by the unimolecular thermal decomposition of molecular oxygen, hence the formation of NO increases sharply with temperature.

There are two methods to reduce the emission of NO_x from vehicles. First, the engine design and operation can be chosen to minimize the formation of NO_x. Second, once formed the NO_x can be treated (reduced to N_2) in the exhaust system before leaving the tailpipe. Both approaches are used in modern engines. Reducing the burned gas temperature is an effective means to limit NO_x formation within the engine. One commonly employed strategy, termed exhaust gas recirculation (EGR), involves recirculating a fraction (5–10%) of the exhaust gas to the intake manifold. The dilution effect combined with replacement of air with the exhaust gases CO_2 and H_2O, which have higher heat capacities, leads to lower combustion temperatures and hence reduced NO formation.

Exhaust catalysts are highly effective devices used to reduce the engine-out hydrocarbon, CO, and NO_x emissions [14, 15, 20, 30]. Automotive catalytic converters on gasoline vehicles typically consist of one or more ceramic monolithic honeycomb substrates wrapped with a mounting material and contained in a metal can. The monolith surface is coated with alumina, other high surface area oxides such as ceria or zirconia, and precious metals such as Pt, Rh, and Pd. The precious metals provide catalytic reduction/oxidation of the pollutants in the exhaust gas, while the oxides can improve catalytic efficiency by storing and giving up oxygen as engine operating conditions change. These catalysts are very efficient after the catalyst has reached its optimum operating temperature (light-off). Oxidation catalysts were introduced in the mid-1970s to control HC and CO emissions. When more stringent NO_x control was mandated, a new type of catalyst was required that could oxidize CO and HC to CO_2 and H_2O while simultaneously reducing NO_x to N_2 and O_2. This type of catalyst is often called a "three-way" catalyst because it decreases the emissions of three important compounds, or classes of compounds: CO, HC, and NO_x. To meet the requirement of simultaneously oxidizing CO and HC while reducing NO_x, the engine must be operated at close to the stoichiometric air/fuel (A/F) ratio, requiring careful feedback control using an on-board exhaust gas sensor. The overall conversion efficiency is improved somewhat by causing the A/F ratio to oscillate by ~2–3% around the stoichiometric A/F ratio.

The primary regulated emissions from diesel engines are similar to those from gasoline engines (e.g. organics, CO, and NOx), but there are differences in degree. Exhaust CO and HC emissions are lower in diesel engines and can be converted to H_2O and CO_2 with an exhaust oxidation catalyst. Engine out NO_x levels are

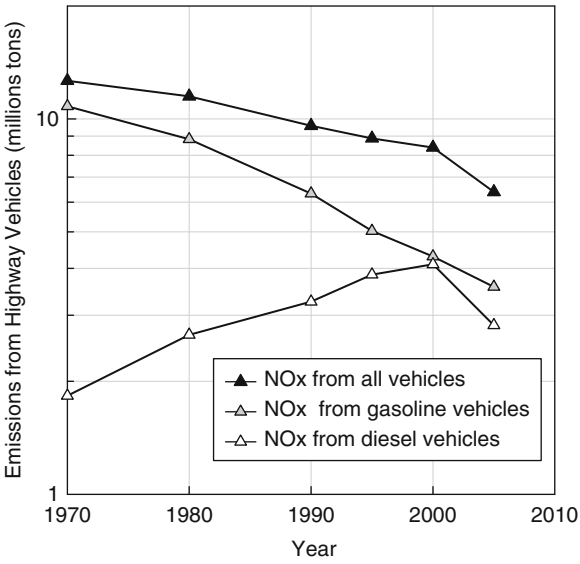

Fig. 8.3 Emissions from U.S. highway diesel (*open symbols*), gasoline (*grey symbols*) vehicles, and all vehicles (*filled symbols*) (Data were taken from Davis et al. [12])

lower for diesel engines than their stoichiometric gasoline counterparts reflecting the somewhat lower combustion temperatures in the diesel engine. However, tailpipe-out NO_x emissions can be higher from diesels reflecting difficulties in reducing NO_x to N_2 in the highly oxidizing environment of diesel exhaust which typically contains approximately 14% O_2.

Options for treating NO_x in diesel exhaust include Lean NOx Traps (LNT) and urea Selective Catalytic Reduction (SCR). LNTs trap and store NO_x in the form of nitrates on a base metal. When the trap is full the NO_x is released during a rich transient and then reduced using a Pd/Rh catalyst. LNTs tend to use a large amount of expensive precious metals, although the overall content has decreased in recent years. In urea SCR systems an aqueous solution of urea is injected into the exhaust stream. Urea undergoes thermal decomposition to give NH_3 which is then used to selectively reduce NO_x [21]. For SCR systems, the urea dosing system adds some cost which is offset by the use of a base metal catalyst. Most manufacturers, especially for medium- and heavy-duty vehicles, have adopted SCR strategies for NO_x control. As a result of the adoption of emission control technologies the emissions of NOx from highway vehicles in the U.S. is declining as shown in Fig. 8.3 [12, 32]. As the on-road vehicle fleet is replaced with vehicles equipped with modern emission control technologies, the progress indicated in Fig. 8.3 will continue and further reductions in NO_x emissions are expected over the coming decades. The progress made shown in Fig. 8.3 is even more impressive in light of the fact that the total vehicle miles travelled on U.S. highways increased by approximately a factor of 3 from 1970 to 2005 [12].

To estimate future emissions from road transportation the International Energy Agency (IEA) worked together with the World Business Council for Sustainable development (WBCSD) to develop a global transport spreadsheet model. The Sustainable Mobility Project (SMP) spreadsheet model is available from the WBCSD

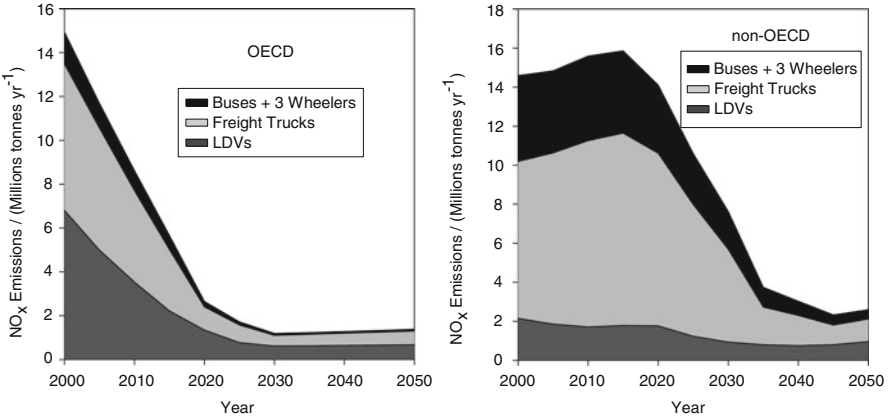

Fig. 8.4 Projected NO_x emissions from OECD (*left panel*) and non-OECD (*right panel*) countries in the SMP Reference Case [33]. The *bottom dark grey* section in *both panels* shows NO_x emissions from light-duty vehicles (passenger cars and trucks), the *middle light grey* section shows emissions from freight trucks and the *top black section* shows the combined emissions trends from buses and three wheelers (mopeds and motorcycles)

website (http://www.wbcsd.org) and provides a tool for projecting emissions associated with global transportation over the time period 2000–2050. Many of the world's leading automotive related companies were involved in developing the model: General Motors Corporation, Toyota Motor Corporation, Ford Motor Company, DaimlerChrysler AG, Honda Motor Company, Volkswagen AG, Nissan Motor Company, Renault SA, BP plc, Royal Dutch/Shell Group of Companies, Michelin, and Norsk Hydro ASA [33]. The reference case SMP model presents one possible set of future conditions, based on existing trends and including existing policies, population projections, income projections and expected availability of new technologies. In general, no major new policies are assumed to be implemented beyond those already implemented in 2003.

An exception was when there was clear evidence of "policy trajectories" such as future policy actions that are either explicit or implicit in other trends. For example, a clear trend was discernable in the developing world to adopt vehicle emissions standards similar to those already implemented in more developed nations. Figure 8.4 shows the projected decrease in NO_x emissions in the SMP model. The left panel gives the emissions from Organization of Economic Cooperation and Development, OECD, countries (Australia, Austria, Belgium, Canada, Czech Republic, Denmark, Finland, France, Germany, Greece, Hungary, Iceland, Ireland, Italy, Luxembourg, Mexico, The Netherlands, Norway, Japan, Korea, New Zealand, Poland, Portugal, Slovak Republic Sweden, Switzerland, United Kingdom, USA). The right panel gives the projected emissions from non-OECD countries. As shown in Fig. 8.4, substantial reductions in the emissions of NO_x are anticipated from the on-road global vehicle fleet over the coming decades. The projected decreases reflect the diffusion of modern emission control technology into the on-road fleet (approximately 10–15 year time lag) and comes despite a factor of approximately 2 projected increase in mobility delivered by light duty vehicles (1.5×10^{13} passenger km in 2000, 3.5×10^{13} passenger km in 2050) [33].

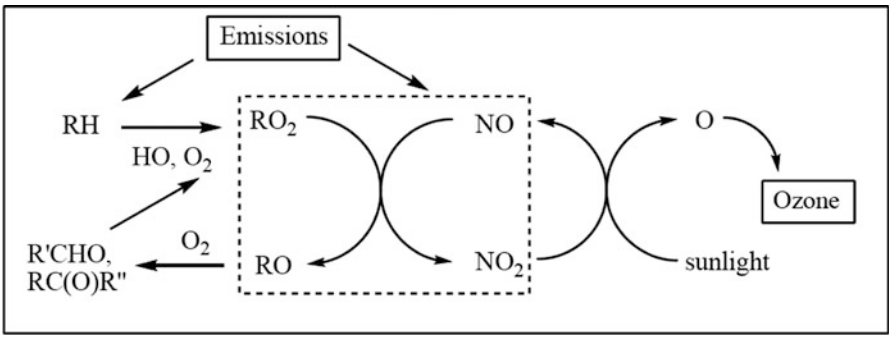

Fig. 8.5 Simplified mechanism for photochemical production of ozone illustrating the central importance of the RO_2 + NO reaction (*dashed box*)

In the process of reducing NO_x to N_2 in exhaust catalysts some N_2O is formed and escapes through the tailpipe. While N_2O is a potent greenhouse gas, its emission from vehicles is modest and it has a global warming impact which is only approximately 1–3% of that of CO_2 emitted from the on-road vehicle fleet [31].

8.4 Atmospheric Chemistry of Nitrogen Oxides

Nitrogen oxides play a central role in the reactions that lead to the photochemical formation of ozone in the lower atmosphere associated with urban air pollution. The chemistry is represented in a very simplified form in Fig. 8.5.

The chemistry is initiated by reaction of HO radicals with hydrocarbons (RH) to give alkyl radicals (R) which, in one atmosphere of air, add O_2 rapidly (within 10^{-7} s) to give peroxy radicals, RO_2. The dominant fate of RO_2 radicals in urban air is reaction with NO which occurs with a rate constant of the order of 1×10^{-11} cm^3 molecule^{-1} s^{-1} [3, 4] under ambient conditions (see Fig. 8.6). Typical NO levels in polluted urban air are 10–100 ppb and thus the lifetime of RO_2 radicals is approximately 0.1–1.0 s. Alkoxy radicals, RO, have an atmospheric lifetime typically of the order of 0.01–0.10 ms and undergo isomerization, decomposition via C–C bond scission, or reaction with O_2 to give carbonyl containing compounds which in turn can react with HO radicals to generate more peroxy radicals. The reaction of RO_2 (and HO_2 generated in the RO + O_2 reaction) with NO generates NO_2 which is a brown colored gas and absorbs at 400–450 nm. Photolysis of NO_2 gives O atoms and regenerates NO which reacts with more RO_2 radicals to form more NO_2. The NO_2 photolysis rate, J_{NO2}, in the lower atmosphere (troposphere) depends on the cloud cover and is typically in the range $(0.3–1) \times 10^{-2}$ s^{-1}, giving a lifetime of NO_2 of several minutes. In one atmosphere of air, O atoms add O_2 with an effective bimolecular rate constant of 1.5×10^{-14} cm^3 molecule^{-1} s^{-1}, $[O_2] = 5.2 \times 10^{18}$ cm^{-3}, and O atoms have a lifetime of 13 μs with respect to conversion into ozone.

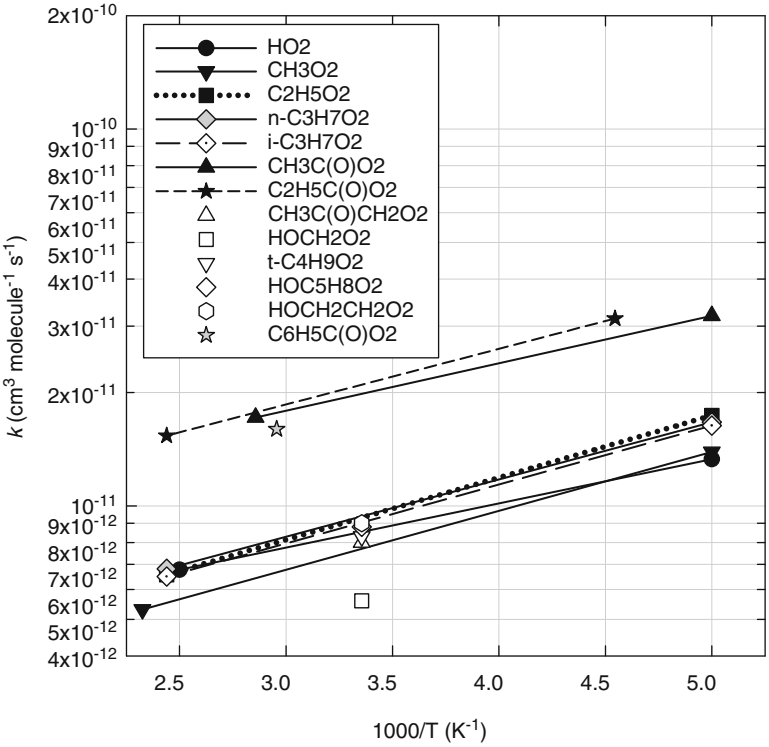

Fig. 8.6 Rate coefficients for reactions of selected peroxy (RO_2) and acyl peroxy ($RC(O)O_2$) radicals with NO recommended by IUPAC [3, 4]

Figure 8.5 does not include the processes that limit ozone formation, such as the formation of nitric acid and organic nitrates ($RONO_2$). The addition reaction of HO radicals with NO_2 gives HNO_3. Nitric acid does not participate in gas phase ozone forming reactions and is removed by wet and dry deposition. Formation of HNO_3 is a major loss mechanism for atmospheric NO_x and limits the formation of ozone. Organic nitrates, $RONO_2$, are formed as minor, but important products, in the reaction of RO_2 radicals with NO.

Acyl peroxy nitrates (e.g., $CH_3C(O)OONO_2$) are formed via the association reaction of NO_2 and acyl peroxy radicals (e.g., $CH_3C(O)O_2$). $RONO_2$ and $RC(O)OONO_2$ species tend to be less reactive than their parent hydrocarbons and serve as sinks for radicals and NO_x in urban air. Acyl peroxy nitrates such as $CH_3C(O)OONO_2$ commonly known as peroxyacetyl nitrate or PAN, $C_2H_5C(O)OONO_2$ commonly known as peroxy propionyl nitrate or PPN, and $C_6H_5C(O)OONO_2$ commonly known as peroxy benzoyl nitrate or PBzN are powerful lacrymators and are responsible for the eye irritation associated with air pollution. Concentrations of PAN in urban air typically exceed those of PPN and PBzN by factors of approximately 10 and 100, respectively, reflecting the source strengths of the corresponding aldehyde precursors.

As illustrated in Fig. 8.5, the reaction of RO_2 radicals with NO plays a central role in tropospheric ozone formation. Recognition of the importance of this reaction has led to a large number of experimental and computational studies which have provided a wealth of information. Figure 8.6 shows Arrhenius plots of the rate coefficients for reactions of RO_2 radicals (including HO_2) with NO determined in experimental studies as recommended by IUPAC [3, 4]. The kinetics of the reactions of simple alkyl peroxy radicals (e.g., HO_2, CH_3O_2, $C_2H_5O_2$, $C_3H_7O_2$, $CH_3C(O)O_2$) with NO are well established [3, 4, 24, 27, 29]. At 298 K the reactions of alkyl peroxy radicals (CH_3O_2, $C_2H_5O_2$, $C_3H_7O_2$) and acylperoxy radicals (e.g., $CH_3C(O)O_2$, $C_2H_5CO(O)_2$) proceed with rate coefficients of approximately 1×10^{-11} and 2×10^{-11} cm^3 $molecule^{-1}$ s^{-1}. The reactions display negative temperature dependencies (rates increase with decreasing temperature) indicating that the reactions proceed via a mechanism involving the formation of an adduct intermediate. The database for substituted peroxy radicals (e.g., oxygenated species such as $HOCH_2O_2$ and halogenated species such as CH_2ClO_2) is more limited and further work is needed to establish the kinetics of their reactions with NO.

Experimental and theoretical studies have shown that the RO_2 + NO reaction proceeds via a complicated mechanism which can be represented as:

$$RO_2 + NO \leftrightarrow ROONO^*$$

$$ROONO^* \rightarrow RO^* + NO_2$$

$$ROONO^* \rightarrow RONO_2{}^*$$

$$RONO_2{}^* + M \rightarrow RONO_2 + M$$

$$RO^* + M \rightarrow RO + M^*$$

$$RO^* \rightarrow \text{decomposition and/or isomerization}$$

$$RO \rightarrow \text{decomposition, isomerization, and/or reaction with } O_2$$

The yield of organic nitrates increases with size of the RO_2 radical, increasing total pressure, and decreasing temperature. The nitrate yield can be substantial for large peroxy radicals (e.g., approximately 20–30% for $C_8H_{17}O_2$ and $C_{10}H_{21}O_2$ [1, 2]) but is low for small peroxy radicals (e.g., <0.5% for CH_3O_2 [27]) in 760 Torr of air at 298 K. Empirical expressions have been developed to estimate nitrate yields [1] but our fundamental understanding of nitrate formation is limited.

The RO_2 + NO reaction has a substantial exothermicity and chemical activation in the nascent RO^* atmospheric reactivity [23]. For chemical activation to be significant three conditions need to be satisfied: (i) the lifetime of $ROONO^*$ must be long enough ($>10^{-12}$ s) to enable efficient intramolecular energy flow, but short enough ($<10^{-9}$ s) that collisions with the diluent gas do not remove a significant fraction of the $ROONO^*$ excitation (ii) the RO radical must possess a

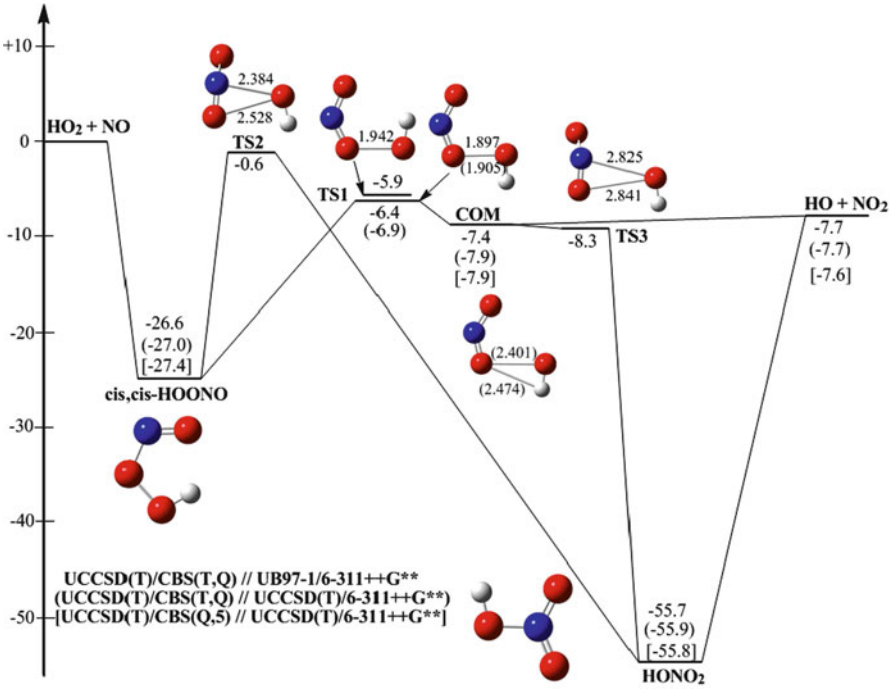

Fig. 8.7 Potential energy surface for the reactions initiated by HO_2 + NO [6]. Optimized geometries and energies (including zero point energy) were obtained using the levels of theory shown as abbreviations (Energies are expressed in units of kcal mol^{-1}; 1 kcal mol^{-1} = 4.184 kJ mol^{-1})

decomposition, or isomerization, pathway which has an activation barrier which is comparable to, or lower than, the excitation of the nascent RO^* radical and (iii) the overall rate of prompt decomposition of RO^* must be sufficiently fast (i.e., the A factor for decomposition must be sufficiently large) that collisions with the diluent gas do not remove a significant fraction of the RO^* excitation prior to "prompt" decomposition.

Numerous theoretical treatments of the RO_2 + NO reaction mechanism have been published. These include quantum chemical calculations [22, 26] of the structures and relative energies of the intermediates, as well as master equation [5, 16, 35, 36] and classical trajectory simulations [11, 25] of the chemical reactions. The $ROONO^* \rightarrow$ RONO2 isomerization step has posed particular theoretical challenges [9]. The general mechanism for the homologous RO_2 + NO reactions is currently believed to be analogous to that for HO_2 + NO, which is illustrated in Fig. 8.7. The initial reaction produces vibrationally excited cis,cis-HOONO, which can rapidly re-dissociate or pass through transition structure TS1 on the way to forming HO + NO_2 or $HONO_2$. The details of this process are not fully understood, because the quantum chemistry calculations for these species are very challenging. Moreover, dynamics calculations indicate that slow intramolecular vibrational energy redistribution may also play a role [25]. Transition structure TS2 is energetically accessible, but most of the reaction is believed to pass through TS1.

In calculations that are currently underway, high level quantum chemistry methods (i.e. UCCSD(T)/CBS(T,Q)//UB97-1/6-311++G**) generally support the calculations of Butovskaya et al., which were carried out at lower levels of theory [9]. The results suggest that after passing through TS1, the reaction encounters a very shallow well on the potential energy surface, where the reactive flux bifurcates: >99% of the reaction proceeds to form HO + NO_2, but a small fraction may instead proceed into the $HONO_2$ potential energy well, possibly explaining the reported experimental yields of $HONO_2$ [7–9]. Master equation simulations are being carried out to investigate these yields quantitatively [6]. Replacement of the H-atom by organic groups is expected to result in changes in relative energies, chemical lifetimes, and product branching ratios, as in previous studies.

8.5 Conclusions

While vehicles are a significant source of NO_x in urban areas, the emissions from vehicles are currently declining in the OECD countries and are expected to decline in non-OECD countries in the future (see Fig. 8.4). The decreased NO_x emissions from vehicles reflects improved emissions control technology in new vehicles and the replacement of older vehicles as they are retired from the on-road fleet. NO_x and NO_2 concentrations in U.S. cities have been declining over the past few decades. NO_x concentrations have been declining in European cities but there is little, or no, trend for NO_2 over the past decade. The reaction of peroxy radicals (RO_2) with NO plays a very important role in photochemical ozone production. As a result of a large number of experimental and computational studies the general features of the RO_2 + NO reactions are clear. For peroxy radicals derived from hydrocarbons: (i) kinetic data for reactions with NO appear to be indistinguishable, (ii) empirical methods to estimate nitrate yields are available, and (iii) chemical activation of RO radicals can be important. For peroxy radicals derived from oxygenated and halogenated organic compounds: (i) kinetic data for reactions with NO are scattered, (ii) nitrate yields appear to be very low and methods to estimate nitrate yields are not available, and (iii) chemical activation of RO radicals can be important. Further experimental work to better define the kinetics and nitrate yields in the reactions of peroxy radicals derived from oxygenated organics would be useful. Theoretical master equation calculations are currently being carried out on the HO_2 + NO reaction system, but addition simulations will be needed for representative RO_2 + NO systems.

Acknowledgements We thank Carolyn Hubbard, Christine Lambert, Rainer Vogt, and Wei Shen for helpful discussions.

References

1. Arey J, Aschmann SM, Kwok ESC, Atkinson R (2001) Alkyl nitrate, hydroxyalkyl nitrate, and hydroxycarbonyl formation from the NO_x-air photooxidations of C5-C8 n-alkanes. J Phys Chem A 105:1020–1027
2. Aschmann SM, Arey J, Atkinson R (2001) Atmospheric chemistry of three C10 alkanes. J Phys Chem A 105:7598–7606
3. Atkinson R, Baulch DL, Cox RA, Crowley JN, Hampson RF, Hynes RG, Jenkin ME, Rossi MJ, Troe J (2006) Evaluated kinetic and photochemical data for atmospheric chemistry: volume II – gas phase reactions of organic species. Atmos Chem Phys 6:3625–4055
4. Atkinson R, Baulch DL, Cox RA, Crowley JN, Hampson RF, Hynes RG, Jenkin ME, Rossi MJ, Troe J, Wallington TJ (2008) Evaluated kinetic and photochemical data for atmospheric chemistry: volume IV – gas phase reactions of organic halogen species. Atmos Chem Phys 8:4141–4496
5. Barker JR, Golden DM (2003) Master equation analysis of pressure-dependent atmospheric reactions. Chem Rev 103:4577–4591
6. Barker JR, Nguyen TL, Kumar TJD, Stanton JF (2012) Kinetics and mechanisms of the HO_2 + NO/OH + NO_2 reaction systems (in preparation)
7. Butkovskaya NI, Kukui A, Pouvesle N, Le Bras G (2005) Formation of nitric acid in the gas-phase HO_2 + NO reaction: effects of temperature and water vapor. J Phys Chem A 109:6509–6520
8. Butkovskaya NI, Kukui A, Le Bras G (2007) HNO_3 forming channel of the HO_2 + NO reaction as a function of pressure and temperature in the ranges of 72–600 torr and 223–323 K. J Phys Chem A 111:9047–9053
9. Butkovskaya NI, Rayez M-T, Rayez J-C, Kukui A, Le Bras G (2009) Water vapor effect on the HNO_3 yield in the HO_2 + NO reaction: experimental and theoretical evidence. J Phys Chem A 113:11327–11342
10. Carslaw DC, Beevers SD, Westmoreland E, Williams ML, Tate JE, Murrells T, Stedman J, Li Y, Grice S, Kent A, Tsagatakis I (2011) Trends in NO_x and NO_2 emissions and ambient measurements in the UK. Version: July 2011. DEFRA Report, http://uk-air.defra.gov.uk/reports/cat05/1108251149_110718_AQ0724_Final_report.pdf
11. Chen C, Shepler BC, Braams BJ, Bowman JM (2009) Quasiclassical trajectory calculations of the HO_2 + NO reaction on a global potential energy surface. Phys Chem Chem Phys 11:4722–4727
12. Davis SC, Diegel SW, Boundy RG (2010) Transportation energy data book. U.S. Department of Energy, Washington, DC
13. Dean AM, Bozzelli JW (2000) In: Gardiner WC Jr (ed) Gas-phase combustion chemistry. Springer, New York
14. Farrauto RJ, Heck RM (1999) Catalytic converters: state of the art and perspectives. Catalysis Today 51:351–360
15. Gandhi HS, Graham GW, McCabe RW (2003) Automotive exhaust catalysis. J Catalysis 216:433–442
16. Golden DM, Barker JR, Lohr LL (2003) Master equation models for the pressure- and temperature-dependent reactions HO + NO_2→$HONO_2$ and HO + NO_2 →HOONO. J Phys Chem A 107:11057–11071
17. Heywood JB (1988) Internal combustion engine fundamentals. McGraw-Hill, Inc., New York
18. Hill SC, Smoot LD (2000) Modeling of nitrogen oxides formation and destruction in combustion systems. Prog Energy Combust Sci 26:417–458
19. IPCC (2007) Climate change 2007: the physical science basis. Cambridge University Press, Cambridge
20. Khalek IA, Bougher TL, Merritt PM, Zielinska B (2011) Regulated and unregulated emissions from highway heavy-duty diesel engines complying with U.S. Environmental Protection Agency 2007 emissions standards. J Air Waste Manage Assoc 61:427–442

21. Koebel M, Elsener M, Kleemann M (2000) Urea-SCR: a promising technique to reduce NO_x emissions from automotive diesel engines. Catalysis Today 59:335–345
22. Lohr LL, Barker JR, Shroll RM (2003) Modeling the organic nitrate yields in the reaction of alkyl peroxy radicals with nitric oxide. I. Electronic structure calculations and thermochemistry. J Phys Chem A 107:7429–7433
23. Orlando JJ, Tyndall GS, Wallington TJ (2003) The atmospheric chemistry of alkoxy radicals. Chem Rev 103:4657–4689
24. Sander SP, Abbatt J, Barker JR, Burkholder JB, Friedl RR, Golden DM, Huie RE, Kolb CE, Kurylo MJ, Moortgat GK, Orkin VL, Wine PH (2011) Chemical kinetics and photochemical data for use in atmospheric studies, evaluation no. 17, pp 10–16 JPL Publication, Jet Propulsion Laboratory, Pasadena. http://jpldataeval.jpl.nasa.gov
25. Stimac PJ, Barker JR (2008) Non-RRKM dynamics in the CH_3O_2 + NO reaction system. J Phys Chem A 112:2553–2562
26. Sumathy R, Peyerimhoff SD (1997) An *ab initio* molecular orbital study of the potential energy surface of the HO_2 + NO reaction. J Chem Phys 107:1872–1880
27. Tyndall GS, Cox RA, Granier C, Lesclaux R, Moortgat GK, Pilling MJ, Ravishankara AR, Wallington TJ (2001) The atmospheric chemistry of small organic peroxy radicals. J Geophys Res 106:12157–12182
28. USEPA (2011) What are the six common air pollutants?. http://www.epa.gov/airquality/urbanair/
29. Wallington TJ, Dagaut P, Kurylo MJ (1992) UV absorption cross sections and reaction kinetics and mechanisms for peroxy radicals in the gas phase. Chem Rev 92:667–710
30. Wallington TJ, Kaiser EW, Farrell JT (2006) Automotive fuels and internal combustion engines: a chemical perspective. Chem Soc Rev 35:335–347
31. Wallington TJ, Sullivan JL, Hurley MD (2008) Emissions of CO_2, CO, NO_x, HC, PM, HFC-134a, N_2O and CH_4 from the global light duty vehicle fleet. Meteorol Z 17:109–116
32. Wallington TJ, Lambert CK, Ruona WC (2012) Diesel vehicles and sustainable mobility in the U.S. Energy Policy, in press, doi:10.1016/j.enpol.2011.11.068
33. World Business Council for Sustainable Development (2004) Mobility 2030: meeting the challenges to sustainability. ISBN: 2-940240-57-4, Geneva, Switzerland
34. Zeldovich J (1946) The oxidation of nitrogen in combustions and explosions. Acta Physicochimica URSS 21:577–628
35. Zhang JY, Donahue NM (2006) Constraining the mechanism and kinetics of OH + NO_2 and HO_2 + NO using the multiple-well master equation. J Phys Chem A 110:6898–6911
36. Zhang JY, Dransfield T, Donahue NM (2004) On the mechanism for nitrate formation via the peroxy radical plus NO reaction. J Phys Chem A 108:9082–9095

Chapter 9
Modeling Atmospheric HONO Concentrations on the Regional Scale

Bernhard Vogel and Heike Vogel

Abstract Mechanisms to simulate the formation of nitrous acid (HONO), an important OH radical source in the atmosphere, have been incorporated into numerical models. The results from the model simulations of HONO formation are compared with field measurements of HONO and conclusions are drawn regarding HONO formation mechanisms in the atmosphere and their representation in models.

Keywords Model • Regional scale • Nitrous acid

9.1 Introduction

Nitrous acid (HONO) is an important nitrogen compound of the atmosphere as it is involved in the OH budget. However, the formation of HONO is currently still not understood. Recent investigations have shown that numerical models that include only homogeneous gas phase reactions of HONO are not able to simulate the observed HONO concentrations. Even when direct emissions and heterogeneous reactions at surfaces are taken into account the concentrations of HONO are underestimated and some of the observed features are not represented by atmospheric models. Investigations of Vogel et al. [13] and Sarwar et al. [11] have shown that including a hypothetical photolytic source of HONO improves the model results considerably when compared with measurements. In this study we will present 1-D simulations of Vogel et al. [13] and recently performed 3-D simulations with the new model system COSMO-ART.

B. Vogel (✉) • H. Vogel
Institute for Meteorology and Climate Research, Karlsruhe Institute of Technology, Karlsruhe, Germany
e-mail: bernhard.vogel@kit.edu

I. Barnes and K.J. Rudziński (eds.), *Disposal of Dangerous Chemicals in Urban Areas and Mega Cities*, NATO Science for Peace and Security Series C: Environmental Security,
DOI 10.1007/978-94-007-5034-0_9,

9.2 The Model System

The model system COSMO-ART, where ART stands for **A**erosols and **R**eactive **T**race gases [14] is an enhanced model system to simulate the spatial and temporal distributions of reactive gaseous and particulate matter. It is used to quantify the feedback processes between aerosols and the state of the atmosphere on the continental to the regional scale with two-way interactions between different atmospheric processes. The meteorological driver is the operational weather forecast model COSMO [2] of the German Weather Service (DWD). In addition to MADEsoot the treatment of mineral dust, sea salt, and pollen bacteria was added to the aerosol module.

The advantage of COSMO-ART with respect to other models is that identical numerical schemes and parameterizations are used for identical physical processes as advection and turbulent diffusion. This avoids truncation errors and model inconsistencies. COSMO is verified operationally by DWD, the model system can be embedded by one way nesting into individual global scale models as the GME model of DWD or the IFS model of ECMWF. All components of the model system are coupled on line with time steps on the order of tenth of seconds. Nesting of COSMO-ART within COSMO-ART is possible. Typical horizontal grid sizes vary between 2.8 and 28 km.

The model system treats secondary aerosols as well as directly emitted components like soot, mineral dust, sea salt, volcanic ash and biological material. Secondary aerosol particles are formed from the gas phase. Therefore, a complete gas phase mechanism (RADMKA) is included in COSMO-ART. Modules for the emissions of biogenic precursors of aerosols, mineral dust, sea salt, biomass burning aerosol and pollen grains are included. For the treatment of secondary organic aerosol (SOA) chemistry the volatility basis set (VBS) was included. Wet scavenging and in-cloud chemistry are taken into account [7]. Processes as emissions, coagulation, condensation (including the explicit treatment of the soot aging; [9, 10]), deposition, washout and sedimentation are taken into account. In order to simulate the interaction of the aerosol particles with radiation and the feedback of this process with the atmospheric variables the optical properties of the simulated particles are parameterized based on detailed Mie-calculations [4]. New methods to calculate efficiently the photolysis frequencies and the radiative fluxes, based on the actual aerosol load and on the GRAALS radiation scheme, respectively, were developed and are implemented in COSMO-ART. To simulate the impact of the various aerosol particles on the cloud microphysics and precipitation COSMO-ART was coupled with the two-moment cloud microphysics scheme of Seifert and Beheng [12] by using comprehensive parameterisations for aerosol activation and ice nucleation [3].

9.3 Treatment of HONO

As regards HONO, the following gas phase reactions are taken into account:

$$\mathrm{NO} + \mathrm{OH} + \mathrm{M} \rightarrow \mathrm{HONO} + \mathrm{M} \qquad (9.\mathrm{R1})$$

This reaction is the most important gas phase source of HONO. For the rate constant of 9.R1, the recent IUPAC recommendation of 9.7 10^{-12} cm^{-6} s^{-1} [1] is used. During daytime, HONO is photolyzed:

$$HONO + h \cdot \nu \rightarrow NO + HO \tag{9.R2}$$

Since the highest HONO concentrations are reached during the night, it is obvious that there must be additional sources of HONO. Following the results of a tunnel study of Kurtenbach et al. [8], a direct HONO source is included in the lowest model layer proportional to the emissions of NO ($E_{HONO} = 0.008 \cdot E_{NO}$).

In addition, the following heterogeneous reaction [5] is included:

$$2 \cdot NO_2 + H_2O \rightarrow HONO + HNO_3 \tag{9.R3}$$

This heterogeneous reaction which was found to be of first order in $[NO_2]$ in laboratory studies is implemented with the following rate constant:

$$k_{het} = 3 \cdot 10^{-3}\, m\, min^{-1} \cdot S/V \tag{9.1}$$

S/V is the surface to volume ratio. This rate constant is based on a tunnel study [8] where an effective uptake coefficient for NO_2 of $\gamma_{NO2} = 10^{-6}$ was found on a tunnel surface. To take into account the heterogeneous production of HONO at aerosol surfaces, S/V in Eq. (9.1) is replaced by the simulated aerosol surface density. To consider the heterogeneous reactions directly on the ground, a source of HONO is introduced in the lowest model layer and it is assumed that the surface to volume ratio of this model layer is 0.1 m^{-1}. This is equivalent to an effective surface of 1.7 m^2 per geometric surface in this layer. Furthermore, we implemented a hypothetical photolytic source of HONO:

$$X + h \cdot \nu \rightarrow HONO + Y \tag{9.R4}$$

In the model this reaction is realized as an additional source of HONO at the surface:

$$E_{HONO} = A \cdot J_{NO2} \tag{9.2}$$

E_{HONO} is the rate of HONO formation by the photolytic source, A is a tuning parameter and J_{NO2} is the photolysis rate coefficient of NO_2. Actually, we do not know by which species X should be replaced in (9.R4). In our case we used the photolysis rate constant of NO_2. However, that does not mean that we think that NO_2 is the missing species. A is the product of the concentration of the unknown species X and an additional factor. In our study we assumed that A is constant with time and used that parameter for the tuning of our model.

9.4 Model Simulations

We used a hierarchy of model versions for a systematic investigation of the improved description of the processes involved in HONO formation and their influence on the photo-oxidant production. We carried out one-dimensional

simulations with KAMM/DRAIS including MADEsoot [13] to quantify the effects of different processes in a more systematic way. Then we performed three-dimensional simulations to investigate the effects of the individual processes important for HONO in the real atmosphere when transport processes and the spatial distribution of the sources and sinks of the gaseous and particulate trace constituents interact with the chemical processes. As HONO acts as an OH source it alters not only the gas phase concentrations but also the chemical composition of the aerosol particles.

9.5 1-D Simulations

Assuming horizontal homogeneous conditions we performed sensitivity runs for October 18, 2001. For the reference case (R) direct emissions of HONO and heterogeneous reactions at the aerosol surface and at the ground were taken into account together with the gas-phase reactions. For the cases E and S the direct emissions of HONO (E) and the heterogeneous reactions at the surface (S) were switched off, respectively. Figure 9.1 shows simulated daily cycles of HONO at 17 m above surface for the cases R, E, and S together with the observations taken at a tower at KIT. In case R the simulated nighttime concentrations are in reasonable agreement with the observations. After 9:00 CET the observations are underestimated. During daytime the simulated HONO concentrations are 30–50% lower than the observed ones. When the direct emissions of HONO are switched off (E), the HONO concentrations are reduced by 50% at maximum between 06:00 CET and 09:00 CET. Between 21:00 CET and 28:00 CET this difference reduces to 40% (Fig. 9.2, *left*). When the heterogeneous reactions are switched off (S) the early morning concentrations of HONO are reduced by 25% between 06:00 and 09:00 CET, and by 30% between 21:00 CET and 28:00 CET.

In all cases the simulated HONO concentrations during daytime do not differ too much but are 30–50% lower than the observations. This shows that there must be an additional strong HONO source during the day. Therefore an artificial photolytic HONO source (P) was introduced. Figure 9.2 (*right*) shows that we received a much better agreement between measured and simulated concentrations of HONO. Especially the decrease of HONO between 9:00 CET and 12:00 CET was simulated very well and the HONO concentrations around noon are comparable to the observed ones. The conclusions from this 1-D simulations are: During daytime the simulated HONO concentrations for the individual cases are much lower than the observed ones. The additional photolytic source of HONO gives much better results. Nighttime HONO concentration close to the surface is simulated quite well. HONO production on aerosols plays no role. Direct emissions of HONO and heterogeneous production of HONO at the ground contribute by the same amount to the sources of HONO during the night. Above 100 m larger differences for the HONO concentrations are found. Possible reasons are transport effects.

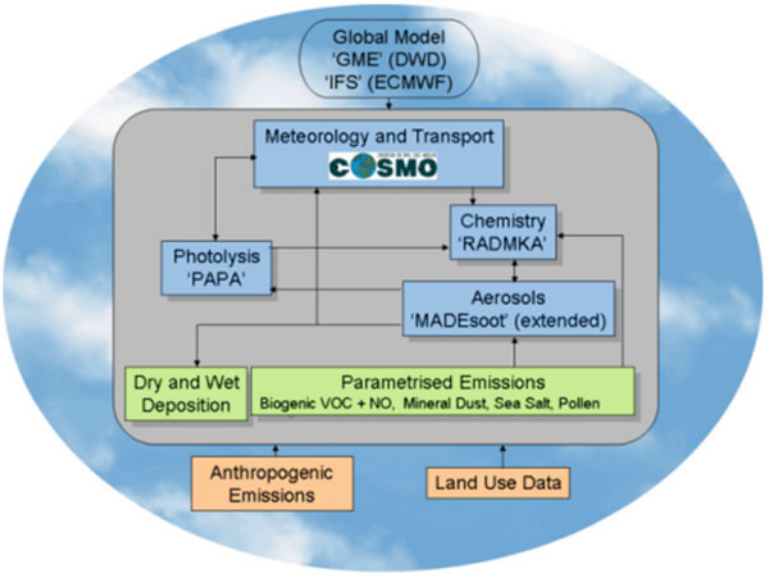

Fig. 9.1 The model system COSMO-ART

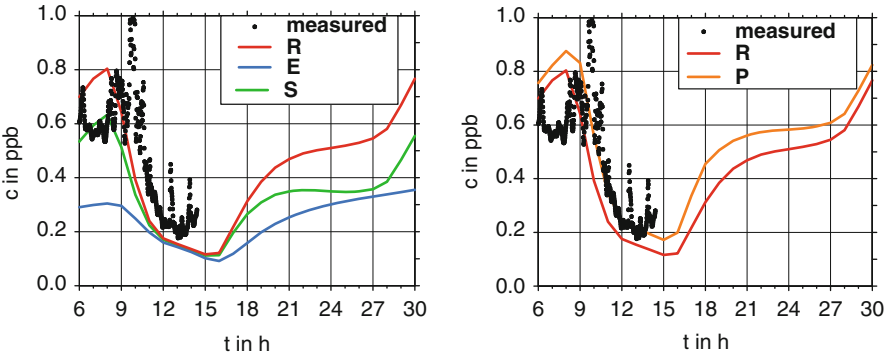

Fig. 9.2 Observed and simulated daily cycles of the HONO concentration at October 18, 2001. *R* reference case, *E* with HONO emissions, *S* the heterogeneous reaction at the surface, *P* with photolytic source. Hour 6 is identical to 6:00 CET at October 18, 2001

9.6 3-D Simulations

Simulations with the CMAQ modeling systems were carried out for the summer 2001 and compared with observations [11]. Taken into account only gas phase reactions gives to low HONO concentrations and show also a different diurnal cycle in comparison to the measurements. Adding the heterogeneous reaction of HONO at ground surfaces as well as at aerosol surfaces with a rate constant of

3×10^{-3} S/V m^{-1} (S/V is the ratio of surface area to volume of air) leads to much better agreement for the night. A major uncertainty is the estimation of the surface areas of the structures in urban environments. Zhou et al. [16] proposed a production of HONO and NO_2 during the day due to photolysis of adsorbed HNO_3. Implementing this source leads to a remarkable increase of the HONO concentration during the day. This implies the need of further investigation of this reaction.

Using COSMO-ART simulations were carried out for an ozone episode in June 2006. We performed five sensitivity runs. In the first run (Gas phase, Standard) gas phase reactions were taken into account only. The second run (E & het R) accounts for direct emissions of HONO and heterogeneous reactions (9.R3). With respect to the photolytic reaction we introduced two separate parameterizations. In the first case the photolytic source was switched on (Eq. 9.1 with $A = 2.5\ 10^{-4}$) when the actual HNO_3 concentration close to the surface was above 1 ppb over land (E & het R & P (const)). In the second one the photolytic source was switched on when the actual HNO_3 concentration close to the surface was above 1 ppb and the following equation was applied (E & het R & P (const)) to modulate the photolytic source according to the HNO_3 concentration in ppb.

$$E_{HONO} = A \cdot J_{NO2} \cdot [HNO3]/5 \tag{9.3}$$

Figure 9.3 shows as an example the horizontal distributions of NO_x, HONO (13 June, 6 UTC), HNO_3, and ozone (June 13, 2006, 13 UTC). Concerning NO_x and HONO a good correlation with the emission distribution can be recognized whereas for ozone and HNO_3 the highest concentrations can be also found in the western part of Germany and Northern Italy but the pattern are more homogeneous. Figure 9.4 gives the temporal development of the HONO concentrations at the grid point of the tower of KIT for the time interval June 10,–13, 2006. Again different sensitivity runs were performed. Even though horizontal transport processes were now taken into account the calculated HONO concentration is rather low if only gas phase reactions are considered. The implementation of a photolytic source over land areas leads to an increase of the HONO concentration. The blue curve in Fig. 9.4 shows the result for a constant source whereas the red line represents the case when the source is a function of the HNO_3 concentration. Remarkable differences between these two runs occur except of the 2nd day during the night. A similar behavior can be seen in Fig. 9.5, which shows the according ratio of HONO/NO_x.

Also in discussion is the question if the HONO concentration shows a distinct profile with height or not. Häsler et al. [6] analyzed Zeppelin measurements up to 1,000 m height and found almost no gradient of the mean HONO concentration. Zhang et al. [15] showed measured profile at different sites and found no clear behavior. Figure 9.5 gives the simulated concentrations profiles of HONO at different point of time. One can recognize a sharp gradient close to the surface and above a well-mixed layer with almost no gradient with height. The same feature can be found for the ratio HONO/NO_x.

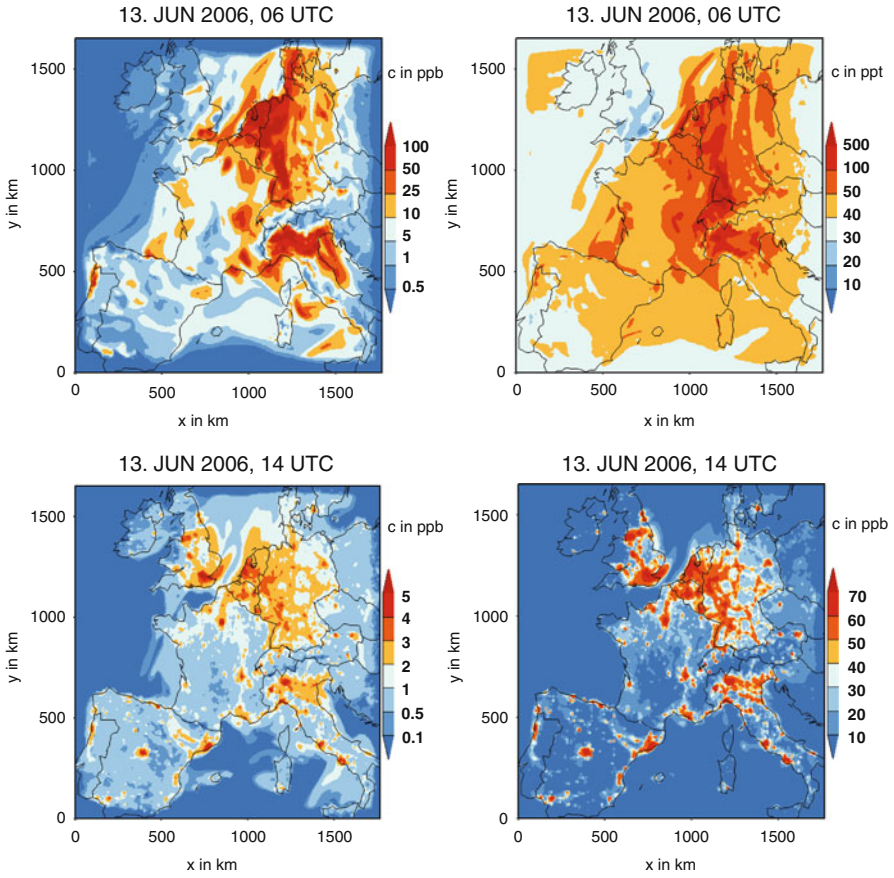

Fig. 9.3 Simulated horizontal distributions of NO_x, HONO, HNO_3, and O_3 at ~20 m above ground ((E & het R & P (const))

HONO is an important species in case of ozone formation especially in the early morning hours. Therefore it raises the question which changes can be found in the OH and also in the ozone concentrations when the additionally sources for HONO are included in the model run. Figure 9.7 shows the temporal development of OH and ozone for the sensitivity runs. The implementation of the HONO emissions and the heterogeneous reaction at the surface has no impact on the OH concentration. If the photolytic source is added an increase of the OH concentration of up to 30% during the day can be seen. In contrast to this finding no clear effect on the ozone concentration can be found. The higher HONO concentrations lead only to very small increase of the ozone concentration. Similar results were found by Sarwar et al. [11].

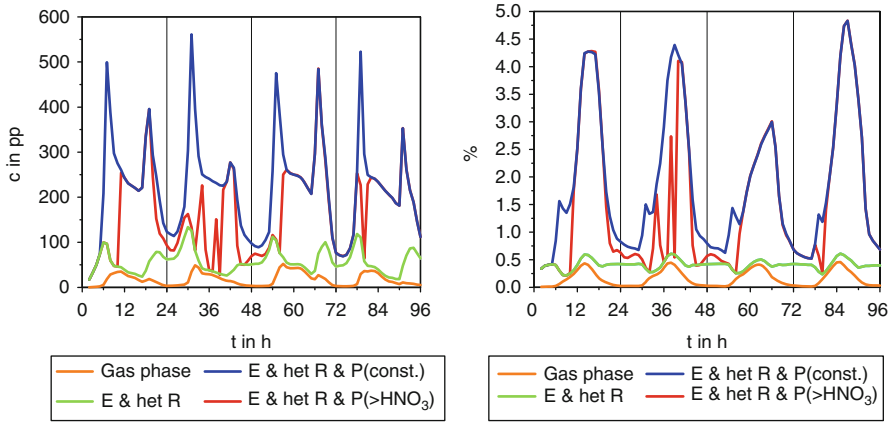

Fig. 9.4 Simulated daily cycles of the HONO concentration (*left*) and HONO/NO_x (*right*) at grid point Karlsruhe (June 10–13, 2006)

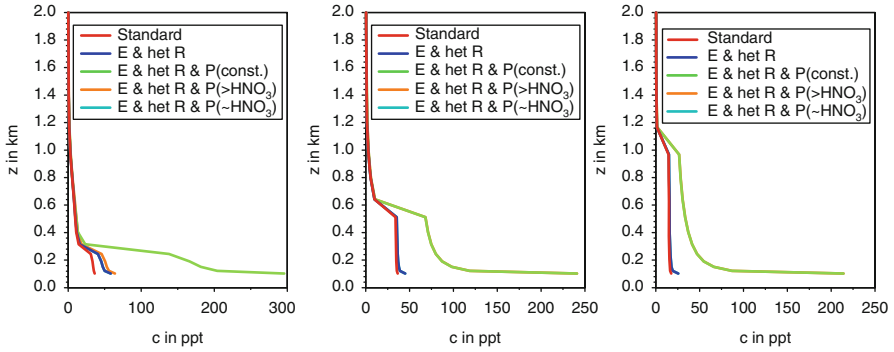

Fig. 9.5 Simulated vertical profiles of the HONO concentration at 8.00, 11:00 and 14:00 CET

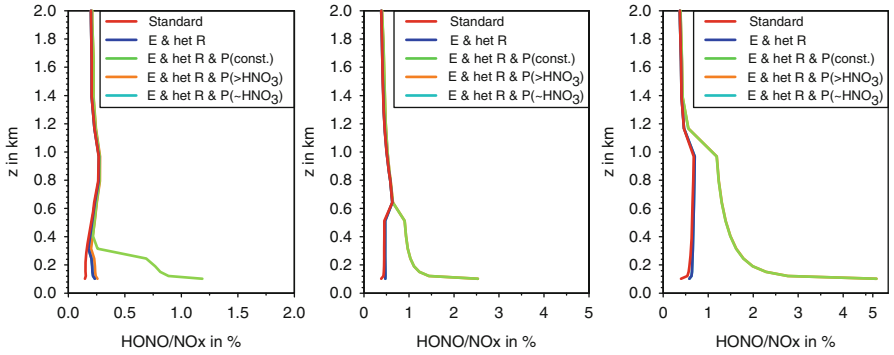

Fig. 9.6 Simulated vertical profiles of the HONO/NO_x at 8.00, 11:00 and 14:00 CET

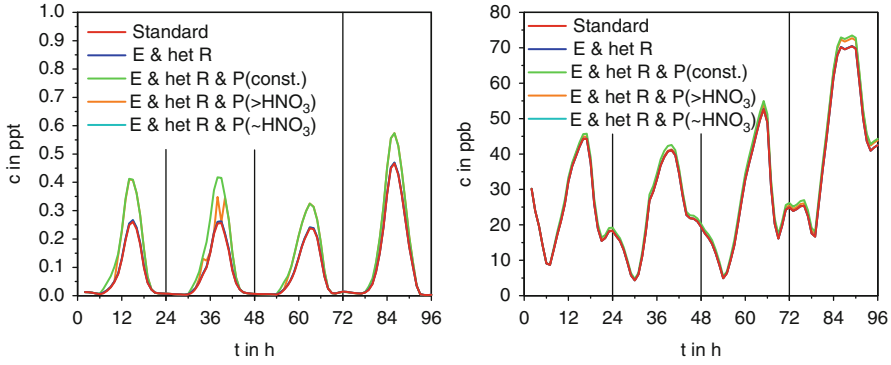

Fig. 9.7 Simulated daily cycles of OH (*left*) and O_3 (*right*) concentration at grid point Karlsruhe (June 10–13, 2006)

9.7 Conclusions

From the 1-D simulations we could see that during daytime the simulated HONO concentrations for the individual cases were much lower than the observed ones. Adding an additional photolytic source of HONO gives much better results. For the nighttime the HONO concentration close to the surface was simulated quite well. Direct emissions of HONO and heterogeneous production of HONO at the ground contribute by the same amount to the sources of HONO during the night. Above 100 m larger differences for the HONO concentrations are found.

The 3-D simulations showed also that introducing a daytime source proportional to radiation or surface temperature leads to HONO concentrations comparable to observed ones close to the surface. It is still not clear what kind of source this is. With respect to the vertical profiles the picture is still not clear. If HONO would be constant with height throughout the convective boundary layer a very strong source is missing. Concerning ozone our results show that even if we simulate HONO concentrations close to the observations the impact on ozone and also other species is smaller than one might expect.

References

1. Atkinson R, Baulch DL, Cox RA, Crowley JN, Hampson RF, Hynes RG, Jenkin ME, Rossi MJ, Troe J (2004) Evaluated kinetic and photochemical data for atmospheric chemistry: volume I gas phase reactions of Ox, HOx, NOx, and SOx, species, Atmos Chem Phys 4:1461–1738
2. Baldauf M, Seifert A, Foerstner J, Majewski D, Raschendorfer M, Reinhardt T (2011) Operational convective-scale numerical weather prediction with the COSMO model: description and sensitivities. Mon Weather Rev 139:3887–3905. doi:10.1175/MWR-D-10-05013.1, e-View, 2011. 31941, 31942

3. Bangert M, Kottmeier C, Vogel B, Vogel H (2011) Regional scale effects of the aerosol cloud interaction simulated with an online coupled comprehensive chemistry model. Atmos Chem Phys 11:4411–4423. doi:10.5194/acp-11-4411-2011
4. Geleyn J-F, Ritter B (1992) A comprehensive radiation scheme for numerical weather prediction models with potential applications in climate simulations. Mon Weather Rev 120:303–325
5. Harris GW, Carter WPL, Winer AM, Pitts JN Jr, Platt U, Perner D (1982) Observations of nitrous acid in the Los Angeles atmosphere and the implications for the ozone-precursor relationships. Environ Sci Technol 16:414–419
6. Häseler R, Brauers T, Holland F, Wahner A (2009) Development and application of a new mobile LOPAP instrument for the measurement of HONO altitude profiles in the planetary boundary layer. Atmos Meas Tech Discuss 2:2027–2054. doi:10.5194/amtd-2-2027-2009
7. Knote C, Brunner D, Vogel H, Allan J, Asmi A, Äijälä M, Carbone S, van der Gon HD, Jimenez JL, Kiendler-Scharr A, Mohr C, Poulain L, Prévôt ASH, Swietlicki E, Vogel B (2011) Towards an online-coupled chemistry-climate model: evaluation of trace gases and aerosols in COSMO-ART. Geosci Model Dev 4:1077–1102. doi:10.5194/gmd-4-1077-2011
8. Kurtenbach R, Becker K, Gomes J, Kleffmann J, Lorzer J, Spittler M, Wiesen P, Ackermann R, Geyer A, Platt U (2001) Investigations of emissions and heterogeneous formation of HONO in a road traffic tunnel. Atmos Environ 35:3385–3394
9. Riemer N, Vogel H, Vogel B, Schell B, Ackermann I, Kessler C, Hass H (2003) The impact of the heterogeneous hydrolysis of N_2O_5 on tropospheric chemistry and nitrate aerosol formation. J Geophys Res 108:4144. doi:10.1029/2002JD002436
10. Riemer N, Vogel H, Vogel B (2004) Soot aging time scales in polluted regions during day and night. Atmos Chem Phys 4:1885–1893, SRef-ID: 1680-7324/acp/2004-4-1885
11. Sarwar G, Roselle S, Mathur R, Appel W, Dennis RL, Vogel B (2008) A comparison of CMAQ HONO predictions with observations from the northeast oxidant and particle study. Atmos Environ 42:5760–5770. doi:10.1016/j.atmosenv.2007.12.065
12. Seifert A, Beheng KD (2006) A two-moment cloud microphysics parameterization for mixed-phase clouds. Part 1: model description. Meteorol Atmos Phys 92:45–66. doi:10.1007/s00703-005-0112-4. 31942, 31943, 31944, 31946, 31947
13. Vogel B, Vogel H, Kleffmann J, Kurtenbach R (2003) Measured and simulated vertical profiles of nitrous acid, part II – model simulations and indications for a photolytic source. Atmos Environ 37:2957–2966
14. Vogel B, Vogel H, Bäumer D, Bangert M, Lundgren K, Rinke R, Stanelle T (2009) The comprehensive model system COSMO-ART – radiative impact of aerosol on the state of the atmosphere on the regional scale. Atmos Chem Phys 9:8661–8680
15. Zhang N, Zhou X, Shepson PB, Gao H, Alaghmand M, Stirm B (2009) Aircraft measurements of HONO vertical profiles over a forested region. Geophys Res Lett 36:L15820. doi:10.1029/2009GL038999
16. Zhou X, Gao H, He Y, Huang G, Bertman S, Civerolo K, Schwab J (2003) Nitric acid photolysis on surfaces in low-NO_x environments: significant atmospheric implications. Geophys Res Lett 30(23):2217. doi:10.1029/2003GL018620

Chapter 10
Heterogeneous Atmospheric Chemistry of Nitrogen Oxides: New Insights from Recent Field Measurements

Steven S. Brown, Nicholas L. Wagner, William P. Dubé, and James M. Roberts

Abstract The heterogeneous chemistry of nitrogen oxides that occurs in the dark is important to both the overall budgets of reactive nitrogen in the atmosphere, as well as the formation of oxidants. Two of the most relevant processes include the conversion of NO_2 to HONO on ground surfaces and the uptake of N_2O_5 to produce either HNO_3 or $ClNO_2$ on aerosol surfaces. Results from recent field measurements that have investigated the latter process have demonstrated several important findings. First, the uptake of N_2O_5 is highly variable, and the uptake coefficient, $\gamma(N_2O_5)$, is often smaller than model parameterizations based on laboratory studies would suggest. Second, production of $ClNO_2$ is much more efficient than previously thought, and is formed in relatively high yields even at interior continental sites that are well removed from direct sources of sea spray. Finally, N_2O_5 uptake and $ClNO_2$ production both vary strongly with height in the nocturnal boundary layer, leading to significant complexity in this nighttime chemistry.

Keywords Heterogeneous uptake • Nighttime chemistry • Dinitrogen pentoxide • Nitryl chloride

10.1 Introduction

The chemistry of nitrogen oxides is central to the understanding of atmospheric oxidants. The photochemical cycling between NO and NO_2 (commonly referred to as NO_x) is the chemical source for ozone in the troposphere [11]. Oxidation of NO to NO_2 by O_3 and the subsequent photolysis of NO_2 back to NO and atomic oxygen produces a net null cycle. Reaction of NO with peroxy radicals (RO_2), derived

S.S. Brown (✉) • N.L. Wagner • W.P. Dubé • J.M. Roberts
Chemical Sciences Division, NOAA Earth System Research Laboratory, Boulder, CO 80305, USA
e-mail: Steven.S.Brown@noaa.gov

I. Barnes and K.J. Rudziński (eds.), *Disposal of Dangerous Chemicals in Urban Areas and Mega Cities*, NATO Science for Peace and Security Series C: Environmental Security,
DOI 10.1007/978-94-007-5034-0_10,

mainly from the photochemical oxidation of volatile organic compounds, perturbs this cycle and leads to net ozone production. This mechanism influences both air quality and climate. It is responsible for the production of large excess ozone in urban areas that is linked to health impacts [25]. Anthropogenic NO_x emission during the industrial era are also responsible for the increase in tropospheric ozone [22], the third most important greenhouse gas after carbon dioxide and methane [34].

Heterogeneous reactions of nitrogen oxides, such as the surface or aerosol uptake of NO_2 or N_2O_5, have also been understood for several decades as an important part of the overall nitrogen oxide budget [21]. As discussed below, they also exert a strong influence on tropospheric oxidants. Several of these processes occur during darkness – that is, they do not proceed to a significant extent in the presence of sunlight because of the photochemical instability of either the reaction products or their precursors. Two nighttime heterogeneous reactions discussed in this manuscript include nitrous acid production and dinitrogen pentoxide uptake. The latter is the major emphasis of this paper.

The nighttime conversion of NO_2 to nitrous acid (HONO) and can be an important radical source in urban areas [35]. Daytime production of HONO may also be an important radical source, but it remains poorly quantified due to uncertainty in the mechanism for sunlight-driven production (see, for example, George et al. [20]). Conversion of NO_2 to HONO is thought to occur primarily on the ground or other surface rather than in the aerosol phase, since the laboratory-measured uptake coefficients to aerosol are too small to explain observed nighttime HONO levels [6]. Vertically resolved HONO measurements typically show that it has a strong nighttime vertical gradient due to its source at ground level and its production in a stable nocturnal boundary layer [43]. Although HONO production is an important component of nighttime heterogeneous nitrogen oxide reactions, this paper does not discuss the topic in detail due in part to the many contributions dealing with this topic within the context of this workshop. Its description here does provide an important point of comparison to the nighttime heterogeneous reactions of NO_3 and N_2O_5, described below.

The second nighttime heterogeneous process is aerosol uptake of dinitrogen pentoxide, N_2O_5. This compound forms principally at night from the reversible addition of NO_3 with NO_2. Although homogeneous hydrolysis of N_2O_5 to nitric acid, HNO_3, is strongly favored thermodynamically, it is kinetically limited and is very slow as a gas phase reaction [41, 42]. The hydrolysis occurs readily in the aerosol phase, however, by the mechanism described in Sect. 10.2. Nitryl chloride arises from the heterogeneous reaction of N_2O_5 with aerosol phase chloride (Cl^-), a reaction that competes with N_2O_5 hydrolysis to produces nitric acid (or aerosol phase nitrate) [3, 18]. A key finding from recent field measurements is that nitryl chloride, $ClNO_2$, is present in surprisingly large concentrations in urban air masses across a wide range of environments [31, 37].

$$N_2O_5(g) + H_2O(l) \rightarrow 2HNO_3(g) \quad (10.R1)$$

$$N_2O_5(g) + Cl^-(aq) \rightarrow ClNO_2(g) + NO_3{}^-(aq) \quad (10.R2)$$

Because $ClNO_2$ does not have rapid sinks in the dark, it builds up overnight as reaction (10.R2) proceeds. It undergoes photolytic degradation after sunrise to produce atomic chlorine radicals and to regenerate NO_2.

$$ClNO_2 + h\,\nu \rightarrow NO_2 + Cl \tag{10.R3}$$

Production and loss of $ClNO_2$ is thus analogous to that of HONO in that it is a radical reservoir species that forms through nighttime heterogeneous nitrogen oxide reactions, and in that it influences next-day photochemistry through morning photolysis to produce both radicals and NO_x. Nighttime $ClNO_2$ formation differs substantially from that of HONO in that it proceeds mainly on the aerosol phase rather than on the ground surface. Because it also occurs at night when the atmosphere is poorly mixed, the nighttime distribution of both N_2O_5 and $ClNO_2$ are likely to differ from that of HONO. The vertical distributions of N_2O_5, $ClNO_2$ and HONO are important to understanding the influence nitrogen oxide heterogeneous chemistry over urban areas.

The remainder of this manuscript focuses primarily on recent advances in the understanding of N_2O_5 and $ClNO_2$, with comparisons to HONO formation where appropriate.

10.2 Tropospheric Chemistry of N_2O_5

Heterogeneous hydrolysis of N_2O_5 via reaction (10.1) has a large impact on both regional and global budgets for tropospheric NO_x. On the regional scale, the rate of overnight NO_x loss through this reaction influences next-day ozone formation as well as the formation of nitrate aerosol [13, 32], especially in winter [28]. The landmark study of Dentener and Crutzen [14] demonstrated the importance of N_2O_5 hydrolysis in regulating both the global burden of nitrogen oxides and oxidants. Their study showed a 50% reduction in global NO_x as a result of reaction (10.1), with an 80% reduction in the northern hemisphere during winter. The reaction decreased global modeled O_3 and OH by 9% each, with a 25% reduction in O_3 in the springtime northern mid-latitudes and subtropics. Subsequent studies have largely confirmed the importance of this reaction for NO_x and oxidants, although estimates for the impact have varied with assumptions about the efficiency of the reaction [1, 16, 17, 24, 27, 38, 39]. The impact of $ClNO_2$ formation has not been considered in regional or global models to date.

The earlier model studies on N_2O_5 hydrolysis [14, 24, 39] relied on the relatively simple assumption that the reaction proceeds with a constant aerosol uptake coefficient, $\gamma(N_2O_5) = 0.1$ [30]. In the limit where gas phase diffusion to the particle surface is negligible (valid for small particle sizes and small uptake coefficients), the first order loss rate coefficient for N_2O_5, k_{N2O5}, is proportional to the uptake coefficient.

$$k_{N_2O_5} = \frac{1}{4} c_{mean} S_A \gamma(N_2O_5) \tag{10.1}$$

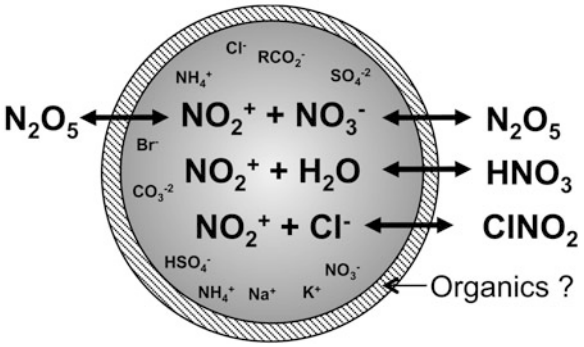

Fig. 10.1 Mechanism for the uptake of gas phase N_2O_5 to aerosol and its subsequent reaction. The figure shows N_2O_5 ionization and reaction with liquid water, solution phase NO_3^- and Cl^-, as well as the potential role of organics. See text for detailed description

Here c_{mean} is the gas-kinetic mean molecular speed of N_2O_5, and S_A is the aerosol surface area density (surface area per unit volume). As more recent laboratory data has become available (see, for example the review of [12] and references therein), models have incorporated the variability of $\gamma(N_2O_5)$ as a function of aerosol composition and relative humidity (RH). The task is difficult, however, since recent laboratory-derived $\gamma(N_2O_5)$ studies span a range of more than two orders of magnitude, from less than 10^{-4} on organic substrates to 0.04 on pure water droplets.

Figure 10.1 shows a simple mechanism for the heterogeneous uptake of N_2O_5 to the aerosol phase and illustrates some of the factors that regulate its efficiency and the branching between HNO_3 and $ClNO_2$. The initial step is solvation of N_2O_5 followed by ionization to NO_2^+ (aq) and NO_3^- (aq). While NO_3^- is a common anion that is stable in solution, NO_2^+ is reactive, and its fate determines both the reaction efficiency and the branching to different products. Indeed, NO_2^+ may not exist as a bare cation, but rather as a hydrate (i.e., $H_2O{\bullet}NO_2^+$) [4]. Thus the first step in the mechanism involving both N_2O_5 solvation and ionization is highly dependent on the availability of liquid water, which is the first and likely most important parameter determining the efficiency of N_2O_5 uptake. Liquid water also reacts directly with NO_2^+, leading to the irreversible production of aerosol phase nitrate or gas phase nitric acid.

A second parameter that influences the uptake efficiency is the presence of excess aerosol phase nitrate. The presence of this anion, derived either from N_2O_5 hydrolysis itself, or from daytime oxidation of nitrogen oxides, reverses the ionization process to regenerate gas phase N_2O_5 and effectively suppresses the uptake coefficient. Uptake coefficients on pure nitrate aerosol are approximately 1 order of magnitude smaller than on other inorganic salts at moderate RH, for example [41, 42]. A third parameter is the presence of aerosol phase chloride, which also competes with both NO_3^- and liquid water for reaction with NO_2^+. Competition between Cl^- and H_2O is the primary factor that influences the branching between HNO_3 and $ClNO_2$. Laboratory studies have shown that Cl^- reacts approximately 450 times more rapidly with NO_2^+ than H_2O [33], such that only a small amount of aerosol phase chloride is required to substantially increase the production of $ClNO_2$. Competition between Cl^- and NO_3^- for reaction with NO_2^+ can reverse the nitrate effect in aerosol that are rich in both chloride and nitrate, with Cl^- reacting approximately 30 times more rapidly than NO_3^- [4].

Finally, N_2O_5 uptake coefficients are strongly influenced by the presence of aerosol phase organics. Organics generally lead to suppression of N_2O_5 uptake, though the mechanism for this suppression remains unclear and likely depends on the type of organic. For example, organics may form coatings on inorganic particles that present a hydrophobic barrier through which N_2O_5 must diffuse in order to solvate and react with liquid water or other inorganic ions, as represented in Fig. 10.1 [19]. The organic component may also simply act to reduce the liquid water content of the aerosol phase, suppressing $\gamma(N_2O_5)$. While recent parameterizations for use in atmospheric models have successfully treated the laboratory data related to the inorganic composition and its relative humidity dependence [4, 13], the dependence of $\gamma(N_2O_5)$ on organic content is a somewhat more difficult problem (e.g., [5, 17]) that has not led to reproducible agreement between parameterizations and field observations of N_2O_5. The next sections describe some of the efforts toward characterization of N_2O_5 uptake coefficients and branching to HNO_3 and $ClNO_2$ from field measurements.

10.3 Uptake Coefficients of N_2O_5 from Aircraft Measurements

Recent measurements of N_2O_5 in ambient air during field intensives have allowed for the direct characterization of its heterogeneous chemistry and have provided tests for parameterizations used to represent this reaction in atmospheric models. There are now several methods for detection of NO_3 and N_2O_5 at part per trillion levels using *in-situ* instruments [12]. Our research group has developed instruments based on cavity ring-down spectroscopy, a high sensitivity optical detection method, using either pulsed or continuous-wave lasers at 662 nm, where NO_3 has a strong maximum in its absorption spectrum [15, 40]. The instruments detect NO_3 directly using a combination of optical absorption at 662 nm and zeroing via chemical titration with NO. Thermal dissociation of N_2O_5 in a second channel with a heated inlet provides a measurement of the sum of NO_3 and N_2O_5, with N_2O_5 determined by difference. This instrument has flown on the NOAA P-3 aircraft during three separate field campaigns in North America, as Fig. 10.2 shows. These include a 2004 study in New England, a 2006 study in Texas a 2010 study in California. Each included a series of nighttime flights that characterize the regional and vertical distribution of NO_3 and N_2O_5, their precursors and their major sinks. Data from these research flights have also provided quantitative determinations of N_2O_5 uptake coefficients.

The 2004 study in New England was the first airborne measurement of N_2O_5. Analysis of these data identified a large regional variability in the N_2O_5 uptake coefficient [8], as shown in Fig. 10.2b. Quantitative determinations of $\gamma(N_2O_5)$ were based on observations of NO_3, N_2O_5, their production rate from NO_2 and O_3, and aerosol surface area measured by a particle-counting instrument. The NO_3 production rate is simply the product of the rate coefficient, k, for the reaction of NO_2 with O_3 with the concentrations of these two species. The N_2O_5 lifetime is

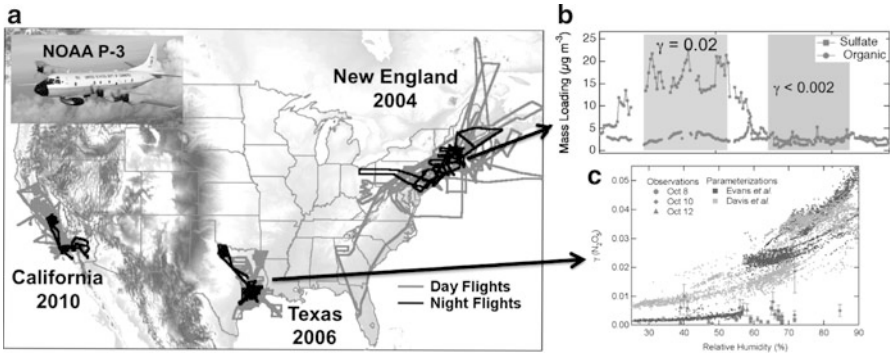

Fig. 10.2 (**a**) Map of aircraft campaigns of the NOAA P-3 that have included night flights and measurements of NO_3 and N_2O_5. (**b**) Variation in sulfate and organic aerosol from August 9–10, 2004 during the New England study. (**c**) Dependence of observed and parameterized N_2O_5 uptake coefficients on relative humidity during the Texas 2006 study

defined as the ratio of the N_2O_5 mixing ratio to this production rate and is a common measure of N_2O_5 reactivity [7].

$$P(NO_3) = k[O_3][NO_2] \tag{10.2}$$

$$\tau(N_2O_5) = N_2O_5/P(NO_3) \tag{10.3}$$

On the August 9–10 flight, nighttime levels of N_2O_5 over Ohio and Pennsylvania (the Ohio River Valley Area) were small even in the presence of large levels of NO_x and O_3, indicating that N_2O_5 had a steady-state lifetime of approximately 13 min. Downwind of New York City, by contrast, levels of N_2O_5 ranged to greater than 3 parts per billion, with a lifetime in excess of 6 h. Sulfate aerosol levels on were larger over the Ohio River Valley, which has large sulfur emission from coal-fired electric power generating plants in that region. Uptake coefficients for N_2O_5 on this highly acidic, sulfate-dominated aerosol were similar to those derived from laboratory studies on sulfate salts over moderate to high RH, with $\gamma(N_2O_5) = 0.02$. The area downwind of New York had a more neutral, mixed sulfate/organic aerosol, with $\gamma(N_2O_5) < 0.002$, more than an order of magnitude smaller. The suppression in $\gamma(N_2O_5)$ may have been related to reduced aerosol acidity (e.g., more neutralized aerosol containing a larger nitrate content), increased organic content relative to sulfate, RH (60–80% over the Ohio River Valley, 40–65% downwind of New York) or a combination of these factors. The principal conclusion related to N_2O_5 uptake coefficients from the 2004 study was that they are variable, and that the variability was linked to sulfate aerosol derived from coal sulfur emissions and its ratio to other aerosol components, such as organics.

Night flights during the 2006 Texas study provided determinations of $\gamma(N_2O_5)$ in the region around the urban area of Houston, Texas as well as a rural area of north Texas [10]. Comparison of the $\gamma(N_2O_5)$ derived from the aircraft observations to parameterizations for use in atmospheric models showed that the

parameterizations systematically over-estimated the observations, even though they explicitly included the effects of aerosol composition and RH. The parameterizations included Evans and Jacob [17], currently used in the GEOS-Chem global atmospheric chemical model, and Davis et al., [13], developed at the U.S. Environmental Protection Agency for use in regional air quality models. While the Evans parameterization explicitly included organic aerosol, it showed a steeper RH dependence than the observations, producing large over-estimates of $\gamma(N_2O_5)$ above 50% RH. The Davis parameterization did not include organic aerosol, and overestimated the observations over the entire RH range. Aerosols in Texas were composed of mixed sulfate/organic in which the sulfate was fully neutralized by ammonium. This aerosol type resembled that observed downwind of New York from the 2004 New England study.

Data from the 2010 study in California are still undergoing analysis to quantitatively determine the N_2O_5 uptake coefficients. The following section on $ClNO_2$ production will briefly discuss findings from that study, which identified a large variation in N_2O_5 reactivity with height above ground level within the nighttime boundary layer structure of the Los Angeles basin.

10.4 Wintertime N_2O_5 Measurements

Heterogeneous N_2O_5 uptake has a greater impact on NO_x and oxidant levels in winter than in summer. Colder temperature shift the equilibrium between NO_3 and N_2O_5 in favor of the latter, reduced wintertime biogenic emissions lead to smaller reactivity for NO_3, and reduced solar actinic flux and longer nights increase the importance of N_2O_5 reactions relative to photochemistry in the oxidation and removal of NO_x. Despite the importance of N_2O_5 in the wintertime, the database for characterization of its heterogeneous chemistry from ambient measurements is smaller in the winter season than in the summer. Simpson and coworkers have characterized N_2O_5 production and loss in the Arctic [2, 23], but there are few measurements at mid-latitudes. All of the aircraft measurements described in Sect. 10.3 occurred during warm season months, for example.

Figure 10.3 shows an example wintertime measurement from a recent study near Denver, CO, USA. Data are from a 300 m tower located approximately 30 km north of the urban center. The tower has a movable carriage on the outside that allows vertical profiling over the entire height of the tower approximately once every 10 min. A previous publication describes the measurement site and its use for nighttime vertical profiling [9]. Instruments for measurements of nitrogen oxides, halogen species, organic and inorganic acids and aerosol size distributions and composition were installed on the tower during a field intensive in February and March, 2011. Figure 10.3 shows a single vertical profile of O_3, NO_2, NO_3 production rate, $P(NO_3)$, N_2O_5, N_2O_5 lifetime and $\gamma(N_2O_5)$ derived from these measurements and the aerosol surface area density (not shown).

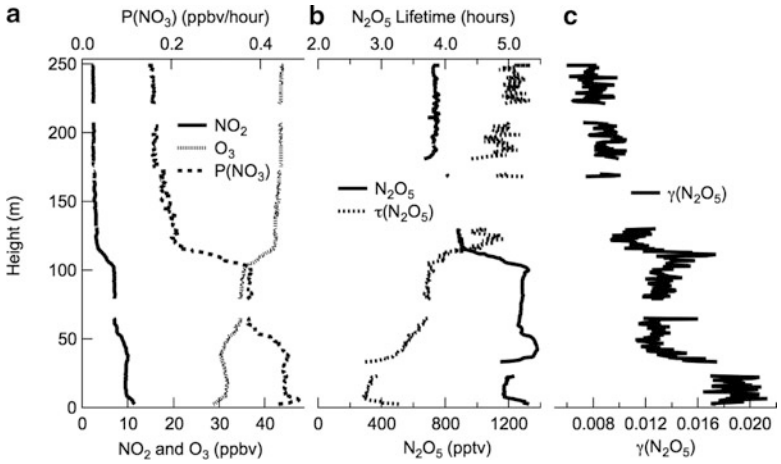

Fig. 10.3 The altitude (*left axis*) dependence of (**a**) NO_2, O_3 (*bottom axis*) and nitrate radical production rate, ($P(NO_3)$, *top axis*); (**b**) N_2O_5 (*bottom axis*) and N_2O_5 lifetime (*top axis*); and (**c**) N_2O_5 uptake coefficient derived from the measurements in the first two panels

Figure 10.3 shows large variations in the nighttime concentrations of N_2O_5 and its precursors over a small altitude range near the surface. This observation is consistent with previous understanding of the mixing of urban pollutants in a stable nocturnal boundary layer [36]. Figure 10.3 shows enhanced mixing ratios of NO_2 (~10 ppbv) below approximately 100 m, along with decreased mixing ratios of O_3, below 110 m, which is likely the top of the nocturnal boundary layer in this example. (Note that there is another slight increase in NO_2 near the bottom of the profile at approximately 10 m that likely represents a shallow surface layer [9].) The NO_3 production rate is high throughout the nocturnal boundary layer. The lifetime of N_2O_5 shows the opposite trend, varying from 2 h near the surface to 5 h at the top of the profile. Although the N_2O_5 lifetime is a common measure of reactivity, it is often only an upper limit to the reactivity (i.e., the lifetime from Eq. (10.3) is a lower limit to the actual lifetime of N_2O_5), especially under cold conditions [7]. The uptake coefficients shown in panel C are derived from Eq. (10.1), where $k(N_2O_5)$ is taken as the inverse of $\tau(N_2O_5)$; the calculation is verified by a box model analysis that considers the reaction time and the approach to steady state. The derived uptake coefficients have considerable uncertainty (more than a factor of 2 in this case), but the variation with height is likely to be at least qualitatively correct. In this example, near-surface $\gamma(N_2O_5)$ is large, near the value of 0.02 typical for organic salts. The value of $\gamma(N_2O_5)$ at the top of the profile is approximate a factor of two smaller. The aerosol composition for this profile (not shown) was mixed organic/inorganic, with the inorganic component dominated by ammonium nitrate. Further analysis on the entire data set from this campaign will examine the role of nitrate aerosol in suppression of $\gamma(N_2O_5)$ in wintertime. The example in Fig. 10.3 demonstrates that N_2O_5, its lifetime, and its uptake coefficient are variable as a function of height above surface level.

10.5 Nitryl Chloride Production

The recent discovery of unexpectedly large amounts of nitryl chloride in urban air at night has added a new dimension to the complexity of N_2O_5 heterogeneous chemistry. The demonstration of sensitive $ClNO_2$ detection in ambient air by chemical ionization mass spectrometry (CIMS) has enabled field investigations of this compound [26]. During a ship-based campaign along the U.S. Gulf Coast and the area near Houston, TX, Osthoff et al. [31] showed that $ClNO_2$ mixing ratios reached part per billion levels and that the yield of $ClNO_2$ from uptake of N_2O_5 was in the range 10–65% for the coastal environment in which the study took place. The study also demonstrated that the mass of $ClNO_2$ produced was much larger than the chloride mass present in the submicron aerosol, which accounts for the majority of the surface area on which N_2O_5 uptake occurs. The observation implied that a gas phase reservoir of HCl, in equilibrium with the aerosol phase, was required to sustain $ClNO_2$ production. The ultimate source of this chloride was thought to be acid displacement from supermicron sea salt, which contains a large chloride mass but presents a smaller surface area for heterogeneous reaction, at least relative to urban, submicron aerosol. Thornton et al. [37] demonstrated that $ClNO_2$ is also consistently present at hundreds of parts per trillion in the Denver urban plume in wintertime. Yields of $ClNO_2$ from that study ranged from 7 to 36%, indicating substantial $ClNO_2$ production even at an inland location, nearly 1,600 km from the nearest coastline. The source of this inland chloride was not clear from that study, although a similar requirement for a gas phase HCl reservoir was inferred from the relationship between gas phase $ClNO_2$ and aerosol phase chloride. A model estimate derived from a NO_x emission inventory, the fraction of this NO_x oxidized through N_2O_5, and the yield of $ClNO_2$ estimated from long-term monitoring network data of aerosol chloride, suggested that the atomic chlorine production from nighttime $ClNO_2$ production is 1.4–3.6 Tg y^{-1} in the continental U.S. and 8–22 Tg y^{-1} globally. Observations of $ClNO_2$ at a separate, mid-continental site in Calgary, Canada [29], are consistent with these conclusions and corroborate the widespread production of $ClNO_2$ in inland urban areas.

A prime uncertainty in the estimates of $ClNO_2$ production and its impacts is its vertical distribution. The initial field work on $ClNO_2$ was based on nighttime surface-level measurements, which are not necessarily representative of the entire vertical distribution of NO_x pollution within an urban-influenced, nighttime boundary layer. Figure 10.4 shows one example of vertically resolved measurements of both N_2O_5 and $ClNO_2$ from aircraft during the 2010 field study in California (see Fig. 10.2). The profile is from a missed approach of the P-3 to an airfield in the Los Angeles basin on May 31, 2010. The aircraft reached a minimum altitude of approximately 100 m above ground level, sufficient to probe the residual daytime boundary layer and part, but probably not all, of the nocturnal boundary layer. The maximum altitude on this profile extended above the residual layer and into the cleaner, free troposphere above it. The steep increases in potential temperature,

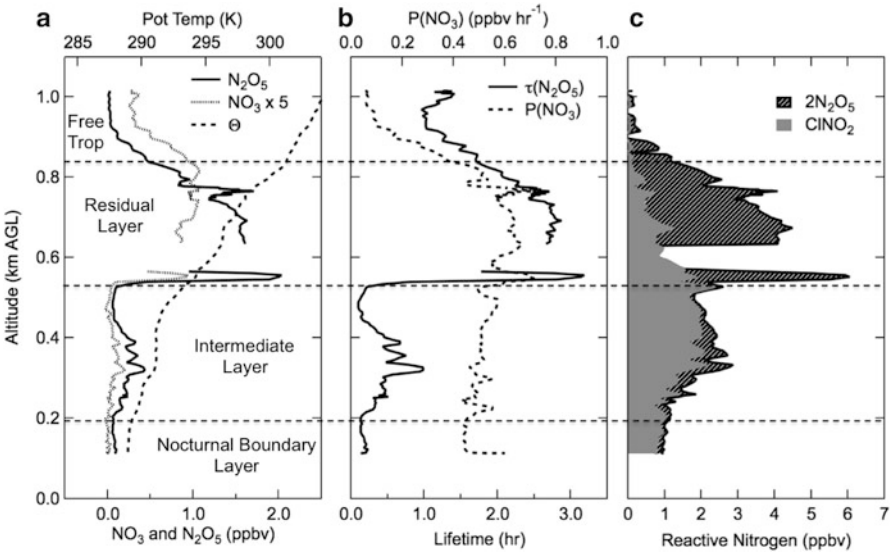

Fig. 10.4 Vertical profile from the NOAA P-3 aircraft over an airfield in the Los Angeles basin at 2:30 AM local time on May 31, 2010. (**a**) NO_3, N_2O_5 (*bottom axis*) and potential temperature, Θ (*top axis*). (**b**) NO_3 production rate, $P(NO_3)$ (*top axis*) and N_2O_5 lifetime, $\tau(N_2O_5)$ (*bottom axis*), as in Eqs. 10.2 and 10.3. (**c**) Mixing ratios of $ClNO_2$ and 2 × N_2O_5. The N_2O_5 is stacked on the $ClNO_2$ to show the sum of the nitrogen in the two species

Θ in panel A, with height define the multiple layer structures on this profile. These include the nocturnal boundary layer to approximately 100 m, an intermediate layer above it to approximately 500 m, the a residual daytime boundary layer to slightly above 800 m, and the cleaner free troposphere above. The NO_3 production rate in panel B is moderately large and relatively constant with height to the top of the residual layer. The NO_3 and N_2O_5 mixing ratios (Panel A) increase sharply at the interface to the residual layer, however, as does the N_2O_5 lifetime (Panel B). These observations indicate more efficient N_2O_5 uptake in the lower layers and a smaller uptake coefficient in the residual layer. Panel C shows the reactive nitrogen present as $ClNO_2$ and N_2O_5, where N_2O_5 has been multiplied by a factor of 2 since it contains two nitrogen atoms. In the lower layers, there is little N_2O_5 relative to $ClNO_2$, indicating both a high $ClNO_2$ yield and efficient N_2O_5 uptake. The residual layer, by contrast, has N_2O_5 in excess over $ClNO_2$, consistent with lower yields and slower uptake.

Like Houston, where the first ship-based $ClNO_2$ measurements took place, Los Angeles is a coastal city with a ready source of aerosol chloride from sea salt and a large source of urban NO_x. The Los Angeles basin also has frequent exceedences of U.S. national air quality standards for ozone pollution. Regeneration of NO_x and production of Cl radicals may be a contributing factor in this ozone production. Accurate models of the role of nighttime chemistry in next-day ozone in Los-Angeles

will require an understanding of the vertical distribution of both N_2O_5 and $ClNO_2$ to constrain the magnitude of the Cl and NO_x source as well as its distribution. The vertical variability in Fig. 10.4 illustrates the complexity of this problem, which will be the subject of ongoing analysis of data from the 2010 night flights in California.

10.6 Conclusions and Recommendations for Future Work

Recent field measurements of N_2O_5 and $ClNO_2$ have provided new insights into the nighttime heterogeneous chemistry of nitrogen oxides and its impact on reactive nitrogen and oxidants on both regional and global scales. Advances in analytical instrumentation for sensitive and accurate *in-situ* detection of these species have enabled these studies, which have led to several important conclusions. First, the efficiency of N_2O_5 uptake is highly variable, and the uptake coefficient to aerosol, $\gamma(N_2O_5)$ is frequently, though not exclusively, smaller than parameterizations designed for use in atmospheric models. The uptake coefficient is large on aerosol that is dominated by inorganic sulfate, and smaller on mixed organic/sulfate aerosol. Inorganic nitrate likely also serves to suppress N_2O_5 uptake, while chloride tends to counteract the nitrate effect and enhance uptake. Second, production of $ClNO_2$ from N_2O_5 heterogeneous uptake is surprisingly efficient, even in continental locations that are well removed from continental chloride sources. The reaction proceeds rapidly on the large aerosol surface area presented by submicron aerosol of urban origin containing only modest chloride content. The observations are consistent with a gas phase chloride reservoir in the form of HCl. Finally, vertically resolved measurements from aircraft and a tall tower have demonstrated that N_2O_5 uptake and $ClNO_2$ production may vary as a function of height above ground level within a stable nighttime boundary layer structure.

Field studies to date have only partially addressed the uncertainties in nighttime nitrogen oxide chemistry, and there are several outstanding issues for future work. First, these efforts should seek to expand the database for *in-situ* measurements of N_2O_5 and the dependence of its uptake on aerosol composition and relative humidity. Where possible, such studies should include vertical resolution to understand the variability throughout the boundary layer structure. Second, there is relatively little data available in the winter season, when N_2O_5 uptake is most important to nitrogen oxide and oxidant budgets, and when $ClNO_2$ production may provide a large source of atomic Cl radicals. Third, the database for $ClNO_2$ measurements remains quite sparse. A larger number of measurements across a wider range of environments and seasons is required to fully understand the influence of this compound in the recycling of NO_x and as a source of chlorine radicals. Finally, field studies should seek to understand the relative importance of nighttime radical reservoirs, such as $ClNO_2$ and HONO, which have similar characteristics but which likely have very different spatial distributions and production efficiencies in different environments. Their relative and absolute contributions to regional oxidation budgets remain uncertain.

References

1. Alexander B, Hastings MG, Allman DJ, Dachs J, Thornton JA, Kunasek SA (2009) Quantifying atmospheric nitrate formation pathways based on a global model of the oxygen isotopic composition of ($\Delta^{17}O$) of atmospheric nitrate. Atmos Chem Phys 9:5043–5056
2. Apodaca RL, Huff DM, Simpson WR (2008) The role of ice in N_2O_5 heterogeneous hydrolysis at high latitudes. Atmos Chem Phys 8:7451–7463
3. Behnke W, George C, Scheer V, Zetzsch C (1997) Production and decay of $ClNO_2$, from the reaction of gaseous N_2O_5 with NaCl solution: bulk and aerosol experiments. J Geophys Res Atmos 102:3795–3804
4. Bertram TH, Thornton JA (2009) Toward a general parameterization of N_2O_5 reactivity on aqueous particles: the competing effects of particle liquid water, nitrate and chloride. Atmos Chem Phys 9:8351–8363
5. Bertram TH, Thornton JA, Riedel TP, Middlebrook AM, Bahreini R, Bates TS, Quinn PK, Coffman DJ (2009) Direct observations of N_2O_5 reactivity on ambient aerosol particles. Geophys Res Lett 36:L19803
6. Bröske R, Kleffmann J, Wiesen P (2003) Heterogeneous conversion of NO_2 on secondary organic aerosol surfaces: a possible source of nitrous acid (HONO) in the atmosphere. Atmos Chem Phys 3:469–474
7. Brown SS, Stark H, Ravishankara AR (2003) Applicability of the steady-state approximation to the interpretation of atmospheric observations of NO_3 and N_2O_5. J Geophys Res 10(8): D174539
8. Brown SS, Ryerson TB, Wollny AG, Brock CA, Peltier R, Sullivan AP, Weber RJ, Dubé WP, Trainer M, Meagher JF, Fehsenfeld FC, Ravishankara AR (2006) Variability in nocturnal nitrogen oxide processing and its role in regional air quality. Science 311:67–70
9. Brown SS, Dubé WP, Osthoff HD, Wolfe DE, Angevine WM, Ravishankara AR (2007) High resolution vertical distributions of NO_3 and N_2O_5 through the nocturnal boundary layer. Atmos Chem Phys 7:139–149
10. Brown SS, Dubé WP, Fuchs H, Ryerson TB, Wollny AG, Brock CA, Bahreini R, Middlebrook AM, Neuman JA, Atlas E, Trainer M, Fehsenfeld FC, Ravishankara AR (2009) Reactive uptake coefficients for N_2O_5 determined from aircraft measurements during TexAQS 2006; comparison to current model parameterizations. J Geophys Res 114:D00F10
11. Chameides WL (1978) Photo-chemical role of tropospheric nitrogen oxides. Geophys Res Lett 5:17–20
12. Chang WL, Bhave PV, Brown SS, Riemer N, Stutz J, Dabdub D (2011) Heterogeneous atmospheric chemistry, ambient measurements, and model calculations of N_2O_5: a review. Aerosol Sci Technol 45:655–685
13. Davis JM, Bhave PM, Foley KM (2008) Parameterization of N_2O_5 reaction probabilities on the surface of particles containing ammonium, sulfate and nitrate. Atmos Chem Phys 8:5295–5311
14. Dentener FJ, Crutzen PJ (1993) Reaction of N_2O_5 on tropospheric aerosols: impact on the global distributions of NO_x, O_3, and OH. J Geophys Res 98:7149–7163
15. Dubé WP, Brown SS, Osthoff HD, Nunley MR, Ciciora SJ, Paris MW, McLaughlin RJ, Ravishankara AR (2006) Aircraft instrument for simultaneous, in-situ measurements of NO_3 and N_2O_5 via cavity ring-down spectroscopy. Rev Sci Instrum 7(7):034101
16. Emmerson KM, Evans MJ (2009) Comparison of tropospheric gas-phase chemistry schemes for use within global models. Atmos Chem Phys 9:1831–1845
17. Evans MJ, Jacob DJ (2005) Impact of new laboratory studies of N_2O_5 hydrolysis on global model budgets of tropospheric nitrogen oxides, ozone and OH. Geophys Res Lett 3(2):L09813
18. Finlayson-Pitts BJ, Ezell MJ, Pitts JNJ (1989) Formation of chemically active chlorine compounds by reactions of atmospheric NaCl particles with gaseous N_2O_5 and $ClONO_2$. Nature 337:241–244
19. Folkers M, Mentel TF, Wahner A (2003) Influence of an organic coating on the reactivity of aqueous aerosols probed by the heterogeneous hydrolysis of N_2O_5. Geophys Res Lett 3:L121644. doi:10.1029/2003GL017168

20. George C, Strekowski RS, Kleffmann J, Stemmler K, Ammann M (2005) Photoenhanced uptake of gaseous NO_2 on solid organic compounds: a photochemical source of HONO? Faraday Discuss 130:195–210
21. Heikes BG, Thompson AM (1983) Effects of heterogeneous processes on NO_3, HONO and HNO_3 chemistry in the troposphere. J Geophys Res 88:10883–10895
22. Horowitz L (2006) Past, present, and future concentrations of tropospheric ozone and aerosols: methodology, ozone evaluation, and sensitivity to aerosol wet removal. J Geophys Res 11(1):D22211. doi:10.1029/2005JD006937
23. Huff DM, Joyce PL, Fochesatto GJ, Simpson WR (2010) Deposition of dinitrogen pentoxide, N_2O_5, to the snowpack at high latitudes. Atmos Chem Phys 11:4929–4938
24. Jacob DJ (2000) Heterogeneous chemistry and tropospheric ozone. Atmos Environ 34:2131–2159
25. Jerrett M, Burnett RT, Pope CA, Ito K, Thurston G, Krewski D, Shi YL, Calle E, Thun M (2009) Long-term ozone exposure and mortality. N Engl J Med 360:1085–1095
26. Kercher JP, Riedel TP, Thornton JA (2009) Chlorine activation by N_2O_5: simultaneous, in-situ detection of $ClNO_2$ and N_2O_5 by chemical ionization mass spectrometry. Atmos Meas Tech 2:193–204
27. Macintyre HL, Evans MJ (2010) Sensitivity of a global model to the uptake of N_2O_5 by tropospheric aerosol. Atmos Chem Phys 10:7409–7414
28. Mathur R, Yu S, Kang D, Schere KL (2008) Assessment of the wintertime performance of developmental particulate matter forecasts with the Eta-Community Multiscale Air Quality modeling system. J Geophys Res 11(3):D02303
29. Mielke LH, Furgeson A, Osthoff HD (2011) Observation of $ClNO_2$ in a mid-continental urban environment. Environ Sci Technol 45:8889–8896
30. Mozurkewich M, Calvert JG (1988) Reaction probability of N_2O_5 on aqueous aerosols. J Geophys Res 93:15889–15896
31. Osthoff HD, Roberts JM, Ravishankara AR, Williams EJ, Lerner BM, Sommariva R, Bates TS, Coffman D, Quinn PK, Dibb JE, Stark H, Burkholder JB, Talukdar RK, Meagher JF, Fehsenfeld FC, Brown SS (2008) High levels of nitryl chloride in the polluted subtropical marine boundary layer. Nat Geosci 1:324–328
32. Riemer N, Vogel H, Vogel B, Schell B, Ackerman I, Kessler C, Hass H (2003) Impact of the heterogeneous hydrolysis of N_2O_5 on chemistry and nitrate aerosol formation in the lower troposphere under photosmog conditions. J Geophys Res 10(8):4144
33. Roberts JM, Osthoff HD, Brown SS, Ravishankara AR (2009) Laboratory studies of products of N_2O_5 uptake on Cl_- containing substrates. Geophys Res Lett 3(6):L20808
34. Solomon S, Qin D, Manning M, Chen Z, Marquis M, Averyt KB, Tignor M, Miller HL (2007) Climate change 2007: the physical science basis. contribution of Working Group I to the fourth assessment report of the Intergovernmental Panel on Climate Change. Summary for policy makers. Cambridge University Press, Cambridge
35. Stutz J, Alicke B, Neftel A (2002) Nitrous acid formation in the urban atmosphere: gradient measurements of NO_2 and HONO over grass in Milan, Italy. J Geophys Res Atmos 107:8192
36. Stutz J, Alicke B, Ackermann R, Geyer A, White AB, Williams E (2004) Vertical profiles of NO_3, N_2O_2, O_3, and NO_x in the nocturnal boundary layer: 1. Observations during the Texas Air Quality Study 2000. J Geophys Res 109:D12306
37. Thornton JA, Kercher JP, Riedel TP, Wagner NL, Cozic J, Holloway JS, Dubé WP, Wolfe GM, Quinn PK, Middlebrook AM, Alexander B, Brown SS (2010) A large atomic chlorine source inferred from mid-continental reactive nitrogen chemistry. Nature 464:271–274
38. Tie X, Brasseur G, Emmons L, Horowitz L, Kinnison D (2001) Effects of aerosols on tropopsheric oxidants: a global model study. J Geophys Res 106:22931–22964
39. Tie X, Emmons L, Horowitz L, Brasseur G, Ridley B, Atlas E, Stroud C, Hess P, Klonecki A, Madronich S, Talbot R, Dibb J (2003) Effect of sulfate aerosol on tropospheric NO_x and ozone budgets: model simulations and TOPSE evidence. J Geophys Res 10(8):8364

40. Wagner NL, Dubé WP, Washenfelder RA, Young CJ, Pollack IB, Ryerson TB, Brown SS (2011) Diode laser-based cavity ring-down instrument for NO_3, N_2O_5, NO, NO_2 and O_3 from aircraft. Atmos Meas Tech 4:1227–1240
41. Wahner A, Mentel TF, Sohn M (1998) Gas-phase reaction of N_2O_5 with water vapor: importance of heterogeneous hydrolysis of N_2O_5 and surface desorption of HNO_3 in a large teflon chamber. Geophys Res Lett 25:2169–2172
42. Wahner A, Mentel TF, Sohn M, Stier J (1998) Heterogeneous reaction of N_2O_5 on sodium nitrate aerosol. J Geophys Res Atmos 103:31103–31112
43. Wong KW, Oh HJ, Lefer BL, Rappenglück B, Stutz J (2011) Vertical profiles of nitrous acid in the nocturnal urban atmosphere of Houston, TX. Atmos Chem Phys 11:3595–3609

Chapter 11
VOC Degradation in the Atmosphere by Nanophotocatalysts

Rashid A. Khaydarov, Renat R. Khaydarov, Olga Gapurova, and N.K. Nasirova

Abstract The paper deals with a novel method for the destruction of VOCs in air. The method is based on usage of an aqueous colloidal solution of nanocarbon-metal oxides compositions in which titanium is chosen as the metal. The colloidal solution is sprayed in the air and under natural solar radiation the nanocomposition, as a photocatalyst, forms OH-radicals in the presence of water molecules from aqueous solution drops or natural moisture. Results of laboratory tests of the method conducted with benzene, toluene, trichloroethene (TCE), *cis*-dichloroethene and *trans*-dichloroethene (DCE) in a plexiglass box with dimensions of 2,000 × 1,000 × 1,000 mm are described. The concentrations of substances in the air in the experiments were within the range 1–15 mg/m^3, and the concentration of sprayed solution of nanophotocatalysts was about 0.1 g/m^3. The concentration of nanophotocatalysts in the colloidal solution was 100 mg/l, and the average size of the nanocompositions and aqueous solution drops were about 5 nm and 5 μm, respectively. The temperature of the air was 25°C and the air humidity was 7–15 g/m^3. The air in the box was irradiated with a 60 W UV lamp during 15 min, giving degradation efficiencies of 90–99% for all compositions. Two to three hours were necessary to reach this degradation efficiency with irradiation of the box by sunlight. Concentrations of secondary products from the VOC degradation process were below detectable levels.

Keywords Nanophotocatalyst • VOC • Sunlight • Nanoparticle • Nanotechnology

R.A. Khaydarov (✉) • R.R. Khaydarov • O. Gapurova • N.K. Nasirova
Uzbekistan Academy of Sciences, Institute of Nuclear Physics, Tashkent, Uzbekistan
e-mail: renat2@gmail.com

I. Barnes and K.J. Rudziński (eds.), *Disposal of Dangerous Chemicals in Urban Areas and Mega Cities*, NATO Science for Peace and Security Series C: Environmental Security,
DOI 10.1007/978-94-007-5034-0_11,

11.1 Introduction

It is well established that OH-radicals are responsible for the oxidation of most VOCs in the atmosphere and can form harmful photooxidants such as ozone and peroxyacetyl nitrate and also secondary organic aerosols [2, 4–8, 14, 18–21, 24, 25, 28–30]. However, there are many situations when fast removal of VOCs from the atmosphere is required, for instance, after accidents in industrial enterprises and research organizations, natural cataclysms, terrorist acts, etc. Moreover a number of countries around the world have the capability to use chemical weapons.

There are no effective methods for the purification of atmospheric air. Usually chemical methods are used for decontamination of polluted surfaces but not for air. As a result of chemical reaction less dangerous or harmless chemical substances are produced. Consumption of materials is very high because the concentration of chemicals must be more than the required stoichiometric ratio in order to guarantee the decontamination process. This paper describes a new technology for destruction of organic substances present in the atmosphere, which is based on the usage of nanocarbon-metal compositions (NCMC) as nanophotocatalysts.

11.2 Principle of the Method

The principle of the method is based on the destruction of organic substances by nanophotocatalysts (NPC) dispersed in air. The NPC under natural ultraviolet radiation form OH-radicals in the presence of water molecules and the radicals degrade organic substances. In brief, the photocatalytic reactions of an aqueous NPC suspension system can be described as follows [27]:

$$\mathrm{NPC} + h\nu \rightarrow \mathrm{NPC} + {e^-}_{CB} + {h^+}_{VB} \tag{11.1}$$

$${h^+}_{VB} + \mathrm{OH^-(surface)} \rightarrow \mathrm{OH^\bullet} \tag{11.2}$$

$${h^+}_{VB} + \mathrm{H_2O} \rightarrow \mathrm{OH^\bullet} + \mathrm{H^+} \tag{11.3}$$

$${e^-}_{CB} + \mathrm{O_2} \rightarrow {O^-}_2 \tag{11.4}$$

$${e^-}_{CB} + {h^+}_{VB} \rightarrow \mathrm{heat} \tag{11.5}$$

where hν is the UV irradiation, ${h_{VB}}^+$ is valence-band hole, and ${e_{CB}}^-$ is a conduction-band electron. It is known that active oxygen and radical species existing in the presence of oxygen and water take part in the oxidation-reduction reaction and destroy organic molecules.

The NPC must be harmless, their concentration in air must be lower than permissible level, and nanoparticles must form agglomerates during the required time, i.e. they must form safe ordinary particles. Many semiconductive metal compounds are used as photocatalysts and the best known among them being TiO_2. Usually photocatalysts are applied on a carrier or plates [1, 11, 15, 16, 22, 26, 31] and cannot

be used for dispersions in air. That is why it is necessary to develop a new type of nanophotocatalyst which can meet all above listed requirements.

It is well known that nanocomposites combine the properties of two or more different materials with the possibility of novel mechanical, physical or chemical behavior arising [3]. Nanocomposites of conjugated materials and metal nanoparticles are prepared from different metals, different types of conjugated polymers and oligomer linkers. Another type of nanoscale materials are nanocomposites of carbon nanoparticles and polymers. Indeed, for example, electrolytically generated nanocarbon colloids (NCC) have functional groups such as carbonyl, hydroxyl and carboxyl groups formed on the surface of carbon nanoparticles [10, 12, 17, 23]. These nanocomposites can be modified by attaching different cations. On the other hand, most polymers can react with different ions and molecules and also participate in the modification of nanocomposites, for example, like nanocarbon–polymer nanocomposites (NCPC) prepared with electrolytically generated NCC and polyethylenimine PEI [13]. A similar method can be used to prepare nanocarbon-metal nanocomposites (NCMC) as the nanophotocatalysts.

11.3 Materials and Equipment

Nanocarbon-metal nanocomposites with titanium as the metal NCMC (Ti) were prepared by the electrochemical method. The process was based on the use of a two-electrode device in which one electrode was made of a high-density isotropic graphite OEG4 (Russia) and the second electrode was made of titanium plate. The electrodes were immersed in a plastic electrolytic cell filled with 0.025 M H_2SO_4 as the electrolyte. The process of device operation involved two repeatable consecutive steps: (1) the electrolysis during 2–10 min when Ti-electrode was as an anode, (2) the electrolysis during 2–5 min when carbon electrode was as an anode.

The size and the shape of nanoparticles were determined with transmission electron microscopy (TEM) (LEO-912-OMEGA, Carl Zeiss, Germany). The concentrations of Ti in the solutions were determined by neutron activation analysis by irradiating samples of air filters in the Nuclear Reactor of the Institute of Nuclear Physics (Tashkent, Uzbekistan). A Ge(Li) detector with a resolution of about 1.9 keV at 1.33 MeV and a 4096-channel analyzer were used for detection of gamma-ray quanta. The area under the γ-peak of the radionuclide ^{51}Ti (half-life $T_{1/2} = 5.8$ min, energy of the γ-peak $E_\gamma = 0.319$ MeV) was measured to determine the concentrations of Ti.

A schematic diagram of the experimental system is shown in Fig. 11.1. The box with dimensions of 2,000 × 1,000 × 1,000 mm was made of plexiglass and contains a 60 W UV lamp (DB-60, Russia), a fan (VN-2, Russia) to mix the air, and thermometer and humidity meters inside. For preparation of the necessary gas mixtures for the experiments in the box benzene, toluene, TCE and DCE were purchased from Ximreaktivinvest Ltd., Uzbekistan. The appropriate volumes of these liquids were injected into the box by syringe. Colloidal solutions of nanophotocatalysts were dispersed in the box by air humidifier UV-2 (Russia).

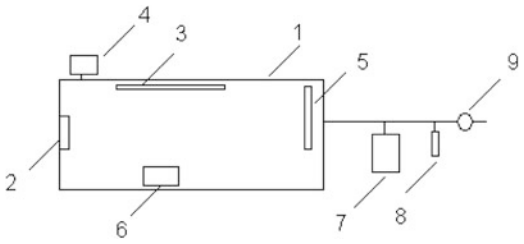

Fig. 11.1 Scheme of the experimental system: *1*-experimental box, *2*-electric fan, *3*-UV-lamp, *4*-syringe, *6*-nanophotocatalyst colloidal solution disperser, *7*-gas sampling bag, *8*-flow meter, *9*-pump

The concentration changes of the substances were initially monitored as a function of the reaction time after injection them into the box in order to determine the loss of the substances due to adsorption on inside surfaces of the box and the devices in the box. The influence of UV radiation on concentrations of test chemical substances was then monitored by Gas Chromatography Cvet-2 (Russia).

11.4 Results and Discussions

Experiments have shown that the yield of NCMC (Ti) in the electrolysis process depends on the voltage V between the electrodes and the pH of the solution. Figure 11.2 shows that the yield dC_{Ti}/dt of Ti 6 min after beginning the electrolysis process, where C_{Ti} is the concentration of Ti in the electrolyte, which increases with increasing voltage between the electrodes up to 12–13 V but then decreases slowly again. This behavior is explained by formation of three-valence titanium on the surface of the Ti-electrode; the electrode becomes blue in color. Figure 11.3 demonstrates the dependence of dC_{Ti}/dt on the concentration of H_2SO_4 in the solution 6 min after beginning the electrolysis process. When the pH of the electrolyte approaches the neutral value three-valence titanium is formed on the surface of the Ti electrode.

During the first stage of the electrolysis process when Ti-electrode is the anode, electric current between electrodes is about 3–4 mA/cm^2. In the second stage after changing the polarity electric current increases up to 180–200 mA/cm^2 in about 0.1–0.2 s. During the first stage oxygen is released on the titanium anode, titanium oxides and sulfates are formed on the surface and titanium ions left the anode are oxidized by oxygen near the surface of anode in the solution or react with NCC which have carboxyl groups as the active groups. The thin semiconductor layer formed on the surface of the titanium electrode has high resistance and electric current between electrodes is small, about 3–4 mA/cm^2. At the same time the negatively charged carbon nanoparticles go away from the graphite cathode and the functional groups such as carbonyl (>C = O), hydroxyl (−OH), and carboxyl (−COOH) groups are formed on the surface of carbon particles.

During the second stage oxidation process is occurred at the carbon anode. The magnitude of repulsion forces formed between the stacked layers of graphite gets larger than that of the Van der Waals attraction forces between the layers, creating a condition for the formation of carbon nanoparticles when polarity of the

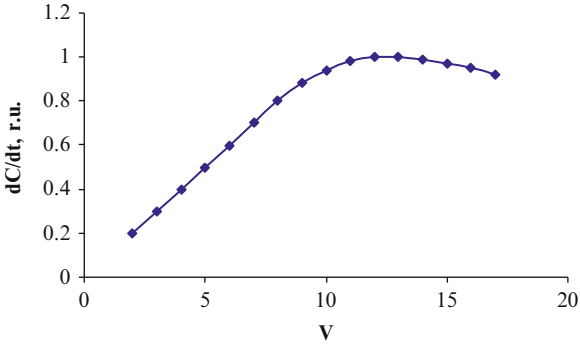

Fig. 11.2 Yield of titanium 6 min after beginning the electrolysis process versus electrolysis voltage

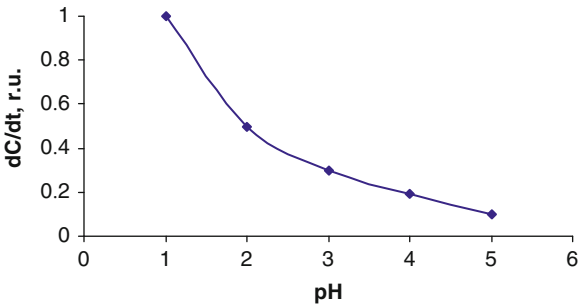

Fig. 11.3 Yield of titanium 6 min after beginning the electrolysis process versus the pH of the solution

electrode is changed. The surface of the titanium cathode is cleaned from the oxides and the electric current between the electrodes increases up to 180–200 mA/cm^2. Titanium ions and charged particles of titanium oxide interact with carbon nanoparticles and form NCMC (Ti). Oxygen adsorbed on the surface of the particles forms –Ti(OH)–O–Ti(OH)–, which can help the photogenerated holes h^+ to change into $OH^\bullet$ free radical. Otherwise, the oxidization activity of $OH^\bullet$ is the strongest in aqueous solution. A typical TEM micrograph of NCMC (Ti) is given in Fig. 11.4 and shows that nanoparticles have a spherical morphology. Measurements of particles sizes have shown that the average dimension of the nanoparticles is 6 ± 2 nm.

Investigations of VOC decompositions were performed at an air temperature in the box of 25°C and humidities of 30 and 60%. Experiments have shown that the concentration of NCMC (Ti) in the box decreases gradually during 10 min from an initial value of 0.1 g/m^3 to 0.05–0.06 g/m^3 because of adsorption of solution drops on the walls of the box and devices. Additional portions of NCMC (Ti) solution were injected into the box every 10 min to maintain its concentration at an average value of 0.08–0.1 g/m^3 or about 8–10 μg/m^3 of NCMC (Ti). These injections also gradually increase the air humidity in the box. Changes of humidity during 10–15 min is inessential but absolute humidity increases from 7 to 9 g/m^3 or from 14 to 16 g/m^3 during 3 h with initial relative humidities of 30 or 60% respectively. Figures 11.5 and 11.6 demonstrate the changes in photocatalyst concentration and air humidity in the box as functions of time during the experiments described above.

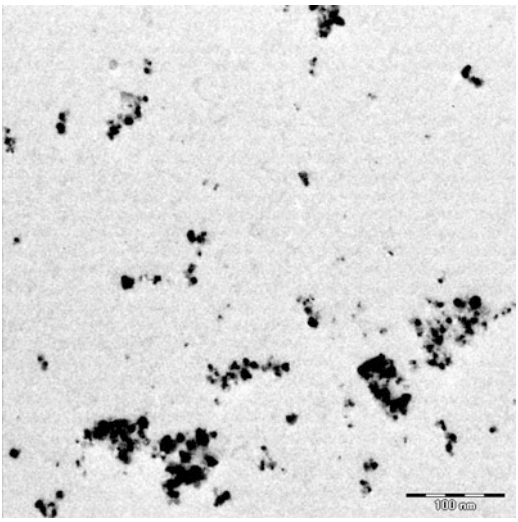

Fig. 11.4 Typical TEM micrograph of NCMC(Ti)

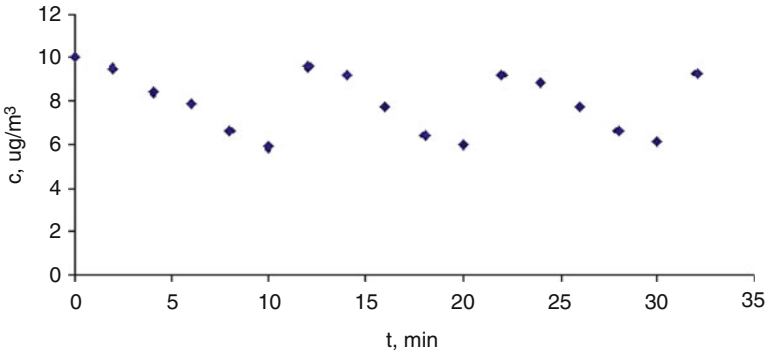

Fig. 11.5 Concentration changes of photocatalysts in the box as a function of time during the experiments

Benzene and toluene were chosen to study the processes of the destruction of aromatic hydrocarbons by UV irradiation and under sunlight in the presence of a NCMC (Ti) nanophotocatalyst at absolute air humidities of about 7 and 14 g/m^3. Results of measurements are given in Figs. 11.7 and 11.8. Degradation efficiencies of 90–99% are reached after 15–20 min and 2–2.5 h by UV irradiation and under sunlight, respectively. Previous research conducted by Hong [9] regarding photodegradation of benzene with prepared TiO_2 aerogel and commercially available TiO_2 photocatalysts and four 40 W blacklights UV lamp obtained 60% degradation during 10 h and observed reaction products such as phenols, 1,4-benzoquinone and hydroquinone. The photocatalytic degradations of toluene led to formation of methyl groups and benzyl radicals. However, in our studies based on using a NCMC(Ti) nanophotocatalyst we did not detect reaction products like phenols, 1,4-benzoquinone, hydroquinone, etc. This indicates that the concentration of

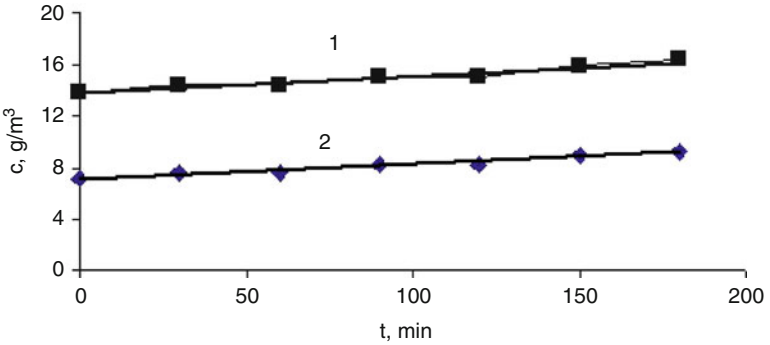

Fig. 11.6 Concentration changes of air humidity in the box as functions of time during the experiments for initial absolute humidities of 14 g/m^3 (*1*) and 7 g/m^3 (*2*)

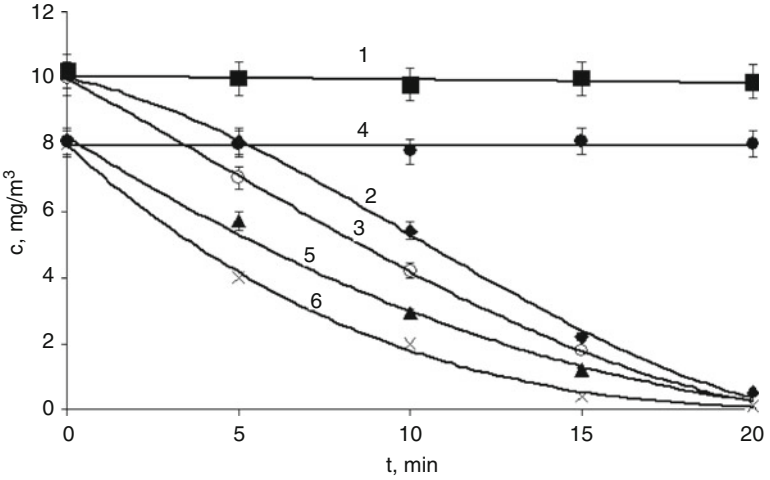

Fig. 11.7 Benzene (*1, 2, 3*) and toluene (*4, 5, 6*) destruction by UV irradiation at absolute air humidity of about 7 g/m^3 (*2, 3*) and 14 g/m^3 (*5, 6*), and without UV irradiation (*1, 4*)

possible secondary products is very low (less than 0.1 mg/m^3). Apparently, not only OH radicals but all active groups on the surface of carbon nanoparticles participate in the VOC degradation process. Possible reaction pathways for the photocatalytic degradation of benzene and toluene can be written as follows:

$$C_6H_6 + 15/2O_2 \rightarrow 6CO_2 + 3H_2O,$$
$$C_6H_5CH_3 + 9O_2 \rightarrow 7CO_2 + 4H_2O$$

Our studies have shown an influence of the water molecule concentration on photocatalytic reactions at least in the absolute humidity interval of 7–14 mg/m^3

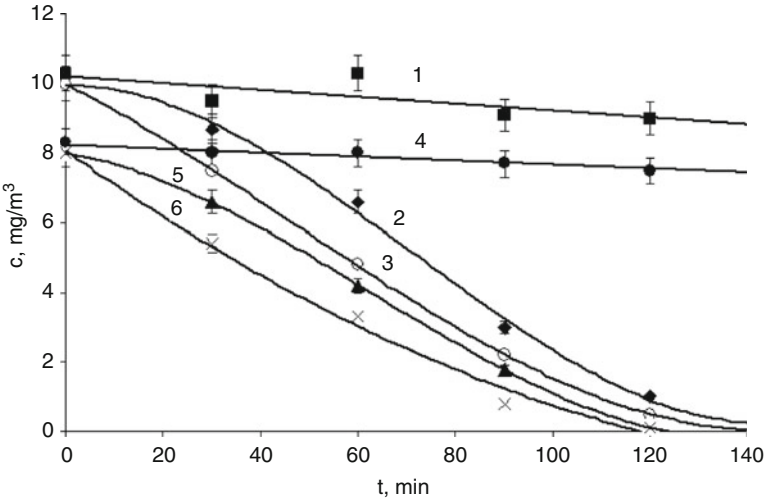

Fig. 11.8 Benzene (*1, 2, 3*) and toluene (*4, 5, 6*) destruction by sunlight irradiation at initial air humidity of about 7 g/m^3 (*2, 3*) and 14 g/m^3 (*5, 6*), and without sunlight irradiation (*1, 4*)

(Figs. 11.7 and 11.8). Thios confirms that the photooxidation requires the photogenerated holes to be scavenged by adsorbed water or hydroxyl radicals. This result also indicates that the product of this reaction is the hydroxyl radical, which can then initiate oxidation through hydroxylation of the aromatic ring. As the reaction proceeds, hydroxyl radicals and water molecules are involved in further reaction steps that lead to the eventual opening of the ring.

Trichloroethene (TCE), *cis*-dichloroethene and *trans*-dichloroethene (DCE) were chosen to study the processes of destruction of chlorinated hydrocarbons by UV irradiation and under sunlight in the presence of a NCMC (Ti) nanophotocatalyst. The results of the measurements are given in Figs. 11.9 and 11.10. Degradation efficiencies of 90–95% are reached after 20–25 min and 2.5–3.0 h by UV irradiation and under sunlight, respectively.

Oki et al. [22] studied the TCE and DCE degradation processes with TiO_2 photocatalyst prepared by the sol-gel method and 4 W blacklights UV lamp at ambient temperature. They obtained more than 95% degradation of TCE, *cis*-1,2-DCE and *trans*-1,2-DCE during 40, 170 and 120 min, respectively. It has been shown that the degradation of TCE produces dichloroacethyl chloride (DCAC), CO, HCl and phosgene ($COCl_2$). In addition to this, further irradiation during 400 min causes the decomposition of DCAC into CO, HCl and $COCl_2$. The species of the photocatalytic degradation for *trans*1,2-DCE are *cis*-1,2-DCE, DCAC, CO, HCl and $COCl_2$. Concentrations of DCAC, CO, and HCl increased simultaneously with UV irradiation time, and reached their maximum at around 160 min. The concentration of $COCl_2$ increased until around 200 min with UV irradiation time. These results show that a part of *trans*-1,2-DCE isomerizes to *cis*-1,2-DCE and forms DCAC, and then it decomposes to CO, HCl and $COCl_2$.

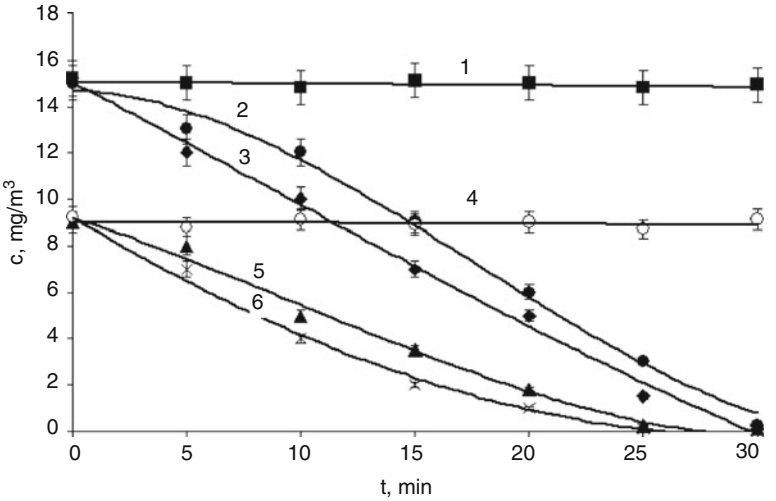

Fig. 11.9 TCE (*1, 2, 3*) and DCE (*4, 5, 6*) destruction by UV irradiation at absolute air humidity of about 7 g/m^3 (*2, 3*) and 14 g/m^3 (*5, 6*), and without UV irradiation (*1, 4*)

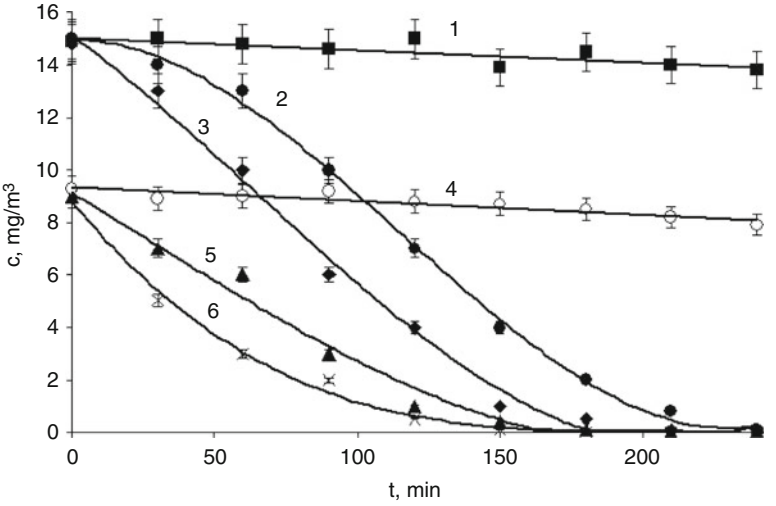

Fig. 11.10 TCE (*1, 2, 3*) and DCE (*4, 5, 6*) destruction by sunlight irradiation at absolute air humidity of about 7 g/m^3 (*2, 3*) and 14 g/m^3 (*5,6*), and without sunlight irradiation (*1, 4*)

In contrast to results obtained by Oki et al. [22] in our studies based on using a NCMC (Ti) nanophotocatalyst, we did not detect reaction products like DCAC and phosgene. This indicates that the concentration of possible secondary products is very low (less than 0.1 mg/m^3). Apparently, not only OH radicals but all active groups on

the surface of the carbon nanoparticles participate in the VOC degradation process. Possible reaction pathways for the photocatalytic degradation of TCE can be written as follows:

$$C_2HCl_3 + 3/2O_2 + H_2O \rightarrow 2CO_2 + 3HCl$$

$$C_2H_2Cl_2 + 2O_2 \rightarrow 2CO_2 + 2HCl$$

An influence of the water molecule concentration on the photocatalytic degradation of TCE and DCE was studied. Hong [9] indicates that water vapor strongly inhibits the oxidation of TCE when a TiO_2 photocatalyst and UV irradiation are used. In contrast to these results our measurements conducted with a NCMC(Ti) nanophotocatalyst have shown that an increase of the water molecule concentration enhances the decomposition of TCE and DCE at least in the absolute humidity interval of 7–14 mg/m^3 (Figs. 11.9 and 11.10). This result indicates that hydroxyl radicals participate in the degradation process.

11.5 Conclusion

The technology of NCMC (Ti) nanophotocatalysts synthesis is based on an electrolysis process in a cell with titanium and graphite electrodes. Active functional groups such as carbonyl (>C = O), hydroxyl (−OH), carboxyl (−COOH), and a photocatalytic group –Ti(OH)–O–Ti(OH)– are formed on the surface of carbon nanoparticles. For the destruction of VOCs an aqueous colloidal solution of NCMC (Ti) nanophotocatalysts is sprayed into the air and under natural solar radiation the nanocompositions form hydroxyl radicals in the presence of water molecules of aqueous solution drops or natural moisture. These radicals and active groups on the surface of nanoparticles react with VOC molecules and degrade them. Degradation efficiencies of 90–99% for benzene, toluene, TCE and DCE have been reached during 15 min irradiation of air by a UV lamp in an experimental box. Two to three hours were necessary to reach this degradation efficiency with irradiation of the box by sunlight. Concentrations of secondary products from the VOC degradation process were at least less than the detectable level. Taking into account the high efficiency of the NCMC (Ti) nanophotocatalysts, investigations of VOC destruction mechanism will be conducted in the nearest future.

References

1. Bakar WAWA, Ali R, Othman MY (2010) Photocatalytic degradation and reaction pathway studies of chlorinated hydrocarbons in gaseous phase. Trans C Chem Chem Eng 17(1):1–14
2. Bertram AK, Ivanov AV, Hunter M, Molina LT, Molina MJ (2001) The reaction probability of OH on organic surfaces of tropospheric interest. J Phys Chem A 105:9415–9421

3. Bryan CS, Michael OW (2005) Metal nanoparticle – conjugated polymer nanocomposites. Chem Commun 27:3375–3384
4. Claeys M, Graham B, Vas G, Wang W, Vermeylen R, Pashynska V, Cafmeyer J, Guyon P, Andreae MO, Artaxo P, Maenhaut W (2004) Formation of secondary organic aerosols through photooxidation of isoprene. Science 303(5661):1173–1176
5. George IJ, Abbatt JPD (2010) Chemical evolution of secondary organic aerosol from OH-initiated heterogeneous oxidation. Atmos Chem Phys Discuss 10:3265–3300
6. George IJ, Vlasenko A, Slowik JG, Broekhuizen K, Abbatt JPD (2007) Heterogeneous oxidation of saturated organic aerosols by hydroxyl radicals: uptake kinetics, condensed phase products, and particle size change. Atmos Chem Phys 7:4187–4201
7. Gross S, Iannone SX, Xiao S, Bertram AK (2009) Reactive uptake studies of NO_3 and N_2O_5 on alkenoic acid, alkanoate, and polyalcohol substrates to probe nighttime aerosol chemistry. Phys Chem Chem Phys 11:7792–7803
8. Holzinger R, Millet DB, Williams B, Lee A, Kreisberg N, Hering SV, Jimenez J, Allan JD, Worsnop DR, Goldstein AH (2007) Emission, oxidation, and secondary organic aerosol formation of volatile organic compounds as observed at Chebogue Point, Nova Scotia. J Geophys Res 112:D10S24. doi:10.1029/2006JD007599
9. Hong I (2006) VOCs degradation performance of TiO_2 aerogel photocatalyst prepared in SCF drying. J Ind Eng Chem 12(6):918–925
10. Hsu WK, Terrones M, Hare JP, Terrones H, Kroto HW, Walton DRM (1996) Electrolytic formation of carbon nanostructures. Chem Phys Lett 262:161–166
11. Jiang D, Zhao H, Zhang S, John R (2006) Comparition of photocatalytic degradation kinetic characteristics of different organic compounds at anatase TiO_2 nanoporous film electrodes. J Photochem Photobiol A Chem 177(2–3):253–260
12. Khaydarov RR, Khaydarov RA, Gapurova O (2009) Remediation of contaminated groundwater using nano-carbon colloids. In: Linkov I (ed) Nanomaterials: risk and benefits, NATO science for peace and security series C: environmental security. Springer, Dordrecht, pp 219–224
13. Khaydarov RA, Khaydarov RR, Gapurova O (2010) Water purification from metal ions using carbon nanoparticle-conjugated polymer nanocomposites. Water Res 44(6):1927–1933
14. Kim YB, Ziemann PJ (2009) Chemistry of secondary organic aerosol formation from OH radical-initiated reactions of linear, branched, and cyclic alkanes in the presence of NO_x. Aerosol Sci Technol 43:604–619
15. Kim SB, Cha WS, Hong SC (2002) Photocatalytic degradation of gas-phase methanol and toluene using thin-film TiO_2 photocatalyst. Kinetic study for the effect of initial concentration and photon flux. J Ind Eng Chem 8(2):162–167
16. Kim SB, Hwang HT, Hong SC (2002) Photocatalytic degradation of volatile organic compounds at the gas–solid interface of a TiO_2 photocatalyst. Chemosphere 48(4):437–444
17. Kim D, Hwang Y, Cheong SI, Lee JK, Hong D, Moon S, Lee JE, Kim SH (2005) Production and characterization of carbon nano colloid via one-step electrochemical method. J Nanopart Res 10(7):1121–1128
18. Kleindienst TE, Lewandowski M, Offenberg JH, Jaoui M, Edney EO (2009) The formation of secondary organic aerosol from the isoprene + OH reaction in the absence of NO_x. Atmos Chem Phys 9:6541–6558
19. Kroll JH, Seinfeld JH (2008) Chemistry of secondary organic aerosol: formation and evolution of low-volatility organics in the atmosphere. Atmos Environ 42:3593–3624
20. Kroll JH, Ng NL, Murphy SM, Flagan RC, Seinfeld JH (2005) Secondary organic aerosol formation from isoprene photooxidation under high-NO_x conditions. Geophys Res Lett 32: L18808. doi:10.1029/2005GL023637
21. Kroll JH, Smith JD, Che DL, Kessler SH, Worsnop DR, Wilson KP (2009) Measurement of fragmentation and functionalization pathways in the heterogeneous oxidation of oxidized organic aerosol. Phys Chem Chem Phys 11:8005–8014

22. Oki K, Tsuchida S, Nishikiori H, Tanaka N, Fujii T (2003) Photocatalytic degradation of chlorinated ethenes. Int J Photoenergy 5:11–15
23. Peckett JW, Trens P, Gougeon RD, Poppl A, Harris RK, Hudson MJ (2000) Electrochemically oxidised graphite: characterisation and some ion exchange properties. Carbon 38:345–353
24. Presto AA, Hartz KEH, Donahue NM (2005) Secondary organic aerosol production from terpene ozonolysis. Effect of NO_x concentration. Environ Sci Technol 39:7046–7054
25. Smith JD, Kroll JH, Cappa CD, Che DL, Liu CL, Ahmed M, Leone SR, Worsnop DR, Wilson KR (2009) The heterogeneous reaction of hydroxyl radicals with sub-micron squalane particles: a model system for understanding the oxidative aging of ambient aerosols. Atmos Chem Phys 9:3209–3222
26. Sopyan I (1996) An efficient TiO_2 thin-film photocatalyst: photocatalytic properties in gas-phase acetaldehyde degradation. J Photochem Photobiol A Chem 98(1–2):79–86
27. Tang WZ, An H (1995) UV/TiO2 photocatalytic oxidation of commercial dyes in aqueous solutions. Chemosphere 31:4157–4171
28. Tuazon EC, Atkinson R (1990) A product study of the gas-phase reaction of methacrolein with the OH radical in the presence of NO_x. Int J Chem Kinet 22:591–602
29. Vlasenko A, George IJ, Abbatt JPD (2008) Formation of volatile organic compounds in the heterogeneous oxidation of condensed-phase organic films by gas-phase OH. J Phys Chem A 112:1552–1560
30. Volkamer R et al (2006) Secondary organic aerosol formation from anthropogenic air pollution: rapid and higher than expected. Geophys Res Lett 33:L17811
31. Yu H, Zhang K, Rossi C (2007) Theoretical study on photocatalytic oxidation of VOCs using nano-TiO_2 photocatalyst. J Photochem Photobiol A Chem 188:65–73

Chapter 12
Production of the Atmospheric Oxidant Radicals OH and HO_2 from the Ozonolysis of Alkenes

William J. Bloss, M.S. Alam, A.R. Rickard, M. Camredon, K.P. Wyche, T. Carr, and P.S. Monks

Abstract The reactions of ozone with alkenes are of importance within atmospheric chemistry as a non-photolytic source of the oxidant radicals OH, HO_2 and RO_2. While OH yields are relatively well constrained, few data exist for production of HO_2 or RO_2. We report direct measurements of total radical yields from a range of small (C_2–C_5) alkenes, using LIF and PERCA techniques within large simulation chamber experiments. OH yields are found to be consistent with established understanding, while HO_2 yields are substantially smaller than previous measurements suggest, but in good agreement with those assumed within current atmospheric chemical mechanisms.

Keywords Troposphere • Alkenes • Ozonolysis • OH • HO_2

12.1 Introduction

Alkenes, unsaturated hydrocarbons, are emitted to the atmosphere from a range of natural and anthropogenic sources, notably biogenic emissions of isoprene, C_5H_8, and the isoprenoid terpenes (C_{10}) and sesquiterpenes (C_{15}). Alkenes can contribute up to 30% of the total OH sink in urban regions, and a higher proportion forested environments; atmospheric degradation of alkenes contributes to the production of ozone in the presence of nitrogen oxides, and leads to the production of substituted and/or oxygenated degradation products, which may act as precursors to, or contribute to the formation of, secondary organic aerosol (SOA). In addition to degradation driven by reaction with OH and NO_3, alkene oxidation may be initiated by reaction with ozone, a process which leads to the dark, non-photolytic production of

W.J. Bloss (✉) • M.S. Alam • A.R. Rickard • M. Camredon • K.P. Wyche • T. Carr • P.S. Monks
School of Geography, Earth & Environmental Sciences, University of Birmingham, Birmingham B15 2TT, UK
e-mail: w.j.bloss@bham.ac.uk

I. Barnes and K.J. Rudziński (eds.), *Disposal of Dangerous Chemicals in Urban Areas and Mega Cities*, NATO Science for Peace and Security Series C: Environmental Security,
DOI 10.1007/978-94-007-5034-0_12,

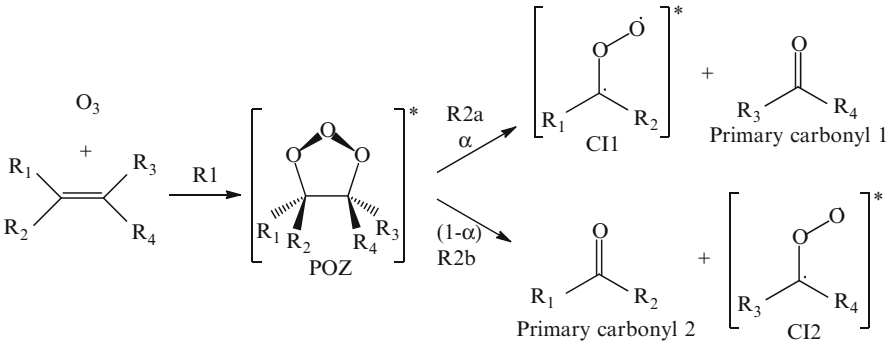

Fig. 12.1 Cycloaddition of ozone across the alkene double bond and subsequent decomposition of the POZ – The "Criegee Mechanism"

radical intermediates; detailed analyses of measurements from atmospheric field campaigns have shown ozonolysis to account for up to 30% of the total OH radical production. Understanding the yields of OH, HO_2 and RO_2 radicals, and their dependence upon atmospheric conditions, is essential to quantify this important contribution to atmospheric oxidising capacity.

Gas-phase alkene ozonolysis is believed to proceed *via* the Criegee mechanism [7], illustrated in Fig. 12.1. Ozonolysis is highly exothermic, initiated by the electrophilic cycloaddition of ozone across the C=C double bond to form an unstable 1,2,3-trioxolane (hereafter referred to as a primary ozonide, POZ) (R1). This intermediate is high in energy and rapidly decomposes at the central C–C bond and one of the O–O bonds. Given that the O–O bond can break at two different sites, a pair of carbonyl oxides (hereafter referred to as Criegee Intermediates, CIs) and stable carbonyl molecules can be formed (R2a and R2b).

The CI and carbonyl co-product produced from the exothermic decomposition of the POZ possess a significant amount of vibrational excitation. This energy enables further unimolecular reactions of the excited CI to occur but is not sufficient for the decomposition of the carbonyl molecule [6] – Fig. 12.2. The distribution of decomposition products of the POZ is dependent upon the substitution of the alkene. Different CIs behave as distinct chemical entities as demonstrated by the range of detected experimental products, dependent upon the extent of the substitution of the CI and distribution of energy following decomposition of the POZ. Substituted CIs can be formed in a *syn* (*i.e.* with the alkyl substituent on the same side of the CI as the terminal O atom) configuration or *anti* configuration, with a substantial barrier to interconversion between them. Briefly, *syn*- and di-substituted CIs are thought to predominantly decompose through isomerisation via a five-membered transition state to give an excited hydroperoxide species which subsequently decomposes to give OH and a vinoxy radical (the "hydroperoxide mechanism" – e.g. [17] and references therein). The proportion of the vibrationally excited CI that does not isomerise/decompose is suggested to be collisionally stabilised and can therefore undergo bimolecular reactions [25]. In general, at low pressures, energy rich

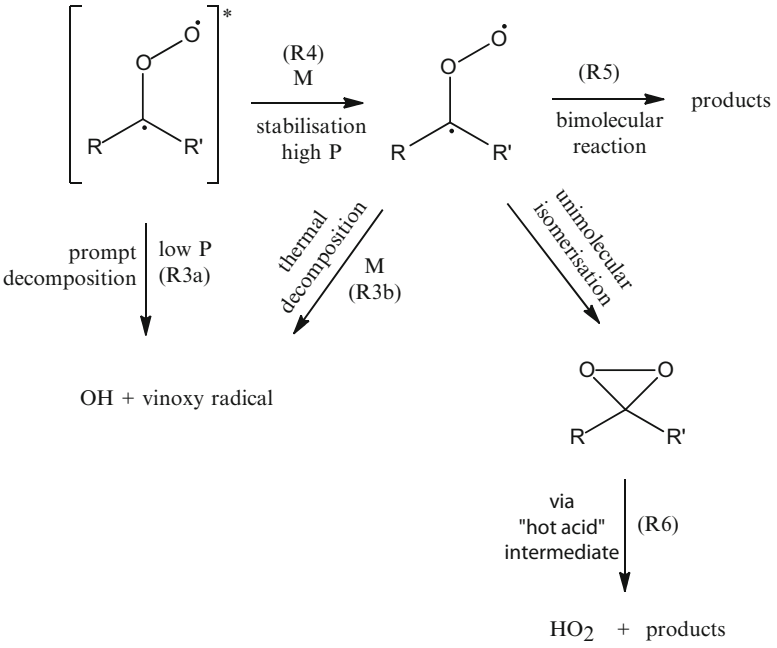

Fig. 12.2 Potential fates of the Criegee intermediate

CIs undergo prompt decomposition to yield OH and a vinoxy radical, which subsequently reacts near-instantaneously with O_2 to form a peroxy radical [9]. At higher pressures (*i.e.* under boundary layer conditions) the CI may be collisionally stabilised (Fig. 12.2, R4) and can thermally decompose to generate OH and a vinoxy radical (R3b) or undergo rearrangement through a dioxirane structure. The dioxirane structure can decompose to various products including HO_2 (R6), *via* a 'hot' acid intermediate.

The vinoxy radical formed alongside OH (Fig. 12.2) will react with oxygen in the atmosphere to form an excited β-oxo peroxy radical, which may be stabilised or undergo decomposition forming CO, a (secondary) stable carbonyl species and OH [19]. However, this pathway to OH formation is only thought to be significant if an aldehydic hydrogen is present. The stabilised β-oxo peroxy radical may then undergo self- or cross-reaction with other peroxy radicals to form stable species such as glyoxal, glycolaldehyde, peroxides and secondary carbonyls.

The fate of the *anti*-CI and of the CH_2OO CI formed from terminal alkenes is discussed in detail elsewhere [1]. Briefly, the *anti*-CI (and CH_2OO) can undergo rearrangement through a dioxirane structure, which can decompose to various products including OH, HO_2, CO, CO_2, H_2O and alkyl molecules *via* a 'hot' acid/ester intermediate (*e.g.* [6]). The *syn* and *anti*-CIs can also undergo stabilisation followed by bimolecular reaction, but studies suggest that stabilisation is a minor process for di-substituted and *syn* mono-substituted CIs, as their lifetime with respect to the vinyl hydroperoxide mechanism is thought to be substantially shorter than the time required for bimolecular processes to occur [10, 26]. Collisional

stabilisation is therefore more likely to occur for the *anti*-CI (for which the hydroperoxide route is unavailable), potentially enabling bimolecular reactions to proceed with many atmospherically relevant species such as H_2O, NO_2, SO_2 and CO [6, 13, 18]. In this article we review the results of a detailed study of the ozonolysis of a series of small-chain alkenes (ethene – isoprene), with a focus upon the production of the radical species OH an HO_2, and their dependence upon experimental conditions (e.g. humidity).

12.2 Experimental Approach

The experimental work was performed in the European Photoreactor (EUPHORE) in Valencia, Spain, coupled with detailed chemical box modelling analysis for data interpretation. The EUPHORE facility comprises two large scale atmospheric simulation chambers, used for studying the mechanisms of atmospheric processes. Briefly, each chamber consists of a 197 m^3 hemispherical reactor, formed from fluorine-ethene-propene (FEP) Teflon foil (127 μm thickness), and fitted with housings which exclude ambient sunlight. Detailed descriptions of the chambers and their instrumentation are given elsewhere [3]. In this study a range of analytical instrumentation was used, including traditional monitors (O_3, CO, HCHO, H_2O), Fourier transform infrared spectroscopy (FTIR) and chemical ionisation reaction time-of-flight mass-spectrometry (CIR-TOF-MS – [34]) for the detection of precursor and product species, including oxygenated derivatives. Radical species were monitored using laser induced fluorescence (LIF – [4, 32]) and peroxy radical chemical amplifier (PERCA – [12]) for the detection of OH/HO_2 and $HO_2 + \Sigma RO_2$ respectively.

All ozonolysis experiments were performed with the chamber housings closed to exclude ambient light/photochemical effects ($j(NO_2) < 2 \times 10^{-6}$ s^{-1}), at near atmospheric pressure and at ambient temperature (294–298 K). All experiments were conducted under NO_x-free conditions. In the absence of NO_x and sunlight, chamber wall radical production has been shown to be negligible [35]. For "dry" experiments, the relative humidity was low (in simulation chamber terms: <1% RH). The experimental procedure, starting with a clean flushed chamber (NMHC < 0.2 ppbV, CH_4 = ambient *i.e.* 1,800 ppbV, NO_y < 1 ppbV), was to add SF_6 (as a dilution tracer), followed by ozone (50–500 ppbV) and in certain cases an OH scavenger (CO or cyclohexane, in concentrations such that ≥95% of any OH produced was scavenged rather than reacting with the precursor alkene) was introduced prior to ozone injection. To initiate the reaction, a known aliquot of alkene (20–500 ppbV) was injected into the chamber and the evolution of reactants and products monitored over timescales of 1–3 h, at a time resolution ranging from seconds (e.g. LIF) to 10 min (FTIR scan time). For "wet" experiments, where the relative humidity was increased to *ca.* 30%, water was added to the chamber through a nebuliser prior to the addition of the reactants.

The EUPHORE data was analysed using a detailed chemical box model, based upon the Master Chemical Mechanism (MCM: http://mcm.leed.ac.uk/MCM) version 3.1 [5, 15, 31], incorporating an extended and updated version of the ozonolysis mechanism of interest (*c.f.* [1]). Within the model, the POZ and CI were assumed to decompose rapidly (compared with the timescale of the subsequent chemistry) to form radical products and stable species, or stabilised CIs, and were therefore not assigned individual rate constants. Rate constants for the bimolecular reactions of the SCI were taken directly from the MCM. The cyclohexane photo-oxidation mechanism, extracted from MCMv3.1, was also updated and extended as outlined in Alam et al. [1]. Simulations were initialised at the time point at which the maximum measured alkene mixing ratio was observed. Temperature, relative humidity and dilution rates were averaged over the duration of each experiment, as the variation in these parameters on the experimental timescale was minimal. Four analytical stages were performed, in each case to determine the *overall* yields of specific products from the *overall* fast ozonolysis reaction (i.e. the CI formation/decomposition chemistry). Briefly, alkene/O_3 reaction rate coefficients were optimised for experiments performed in the presence of a radical scavenger, followed by the optimisation of the branching ratios of the POZ decomposition, forming the respective pairs of carbonyl products (and CIs). Overall carbonyl yields were derived using model optimisation, by minimising the sum of squares of residuals between the simulated and observed concentrations, and classically, by (dilution corrected) mass balance calculations; both methods were in excellent agreement. Finally, HO_x radical yields were determined by optimising the branching ratio for the isomerisation/decomposition of the *syn*-CI to minimise the sum of squares of residuals between simulated and observed OH/HO_2 concentrations. The OH yield from the ozonolysis of ethene (0.17; [1]) was applied to the decomposition of the CH_2OO CI formed in all terminal alkene systems. The model optimization process accounted for further reactions of OH and HO_2, and for secondary formation processes. It is important to note that the overall HO_x yields obtained through this approach, relative to flux through each alkene-ozone reaction, are reasonably absolute and independent of the HO_x production route implemented in the model, but their attribution to specific reaction pathways of the ozonolysis system (*e.g.* Criegee decomposition branching ratios) is dependent upon the assumed mechanism. In the discussion below we draw inferences regarding the likely mechanistic origin of the observed OH and HO_2, from the variation in yields with co-products and experimental conditions.

12.3 OH Production

Figure 12.3 shows a typical temporal profile of the OH steady state concentration as measured by the LIF system, and model simulation comparisons for cis-2-butene ozonolysis. The data illustrate that MCMv3.1 overestimates (in the case of cis-

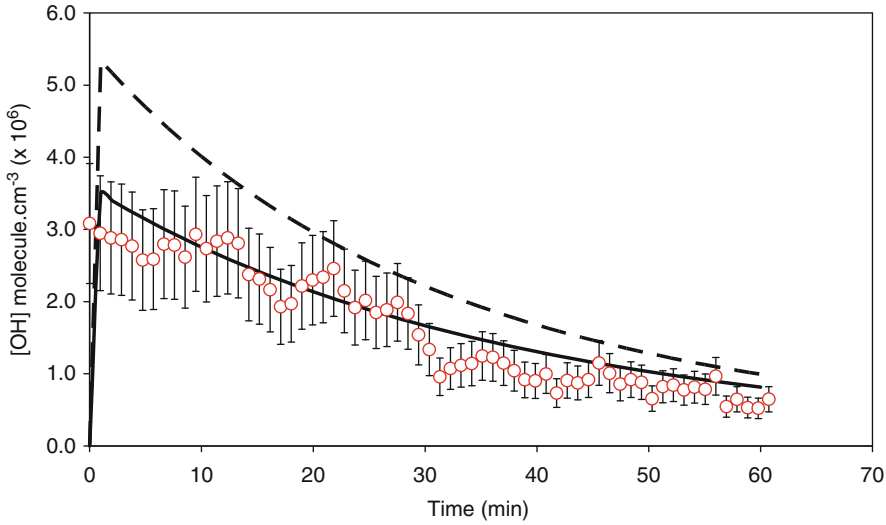

Fig. 12.3 *cis*-2-Butene ozonolysis. Temporal profile of OH (*circles*) plus model simulations before (*dashed line*, base case standard MCMv3.1 chemistry) and after (*solid line*) optimising the OH yield

2-butene) the OH yield, compared to the present work. (In this instance it is likely that this arises from the assumed 50:50 split of the *syn*/*anti* CIs in the MCM 3.1 mechanism – the lower yield obtained here (and in other studies – [14]) suggests that the *anti*-conformer of the CI is preferentially formed (alongside acetaldehyde) from the primary ozonide decomposition in this system – [29]).

Figure 12.4 shows the OH yields obtained for ethene, propene, 1-butene, 2-methylpropene, cis-2-butene, trans-2-butene and 2,3-dimethyl-2-butene, compared to those from other studies [2, 23, 24, 27, 28, 30] plotted as a function of the equivalent IUPAC recommendations for OH yields [14]. The uncertainties in the results from this work represent the combined (2σ) statistical uncertainty from repeated determinations propagated with the corresponding OH measurement calibration uncertainty (27%; [4]). The results are well correlated with the IUPAC values; as the literature studies mainly exploit indirect methods to detect OH, by the use of OH scavenger (*e.g.* [2]) and tracer (*e.g.* [30]) techniques, or indirect observation by matrix-isolation electron spin resonance [24] and PERCA [28] the agreement with the direct OH observations in this work is encouraging. The results are consistent with the isomerisation/decomposition of a given CI to a vinyl hydroperoxide and OH; the basis of the OH yield structure activity relationship (SAR) of Rickard et al. [30].

These OH production *yields* (Y_{OH}) correspond to the formation of OH via the (fast) direct decomposition/isomerisation of the CI, after taking secondary sources into account within the model; for example OH formation via $HO_2 + O_3$, from decomposition of the excited β-oxo peroxy radical [19] and the reactions of acyl peroxy radicals + HO_2 [8, 16].

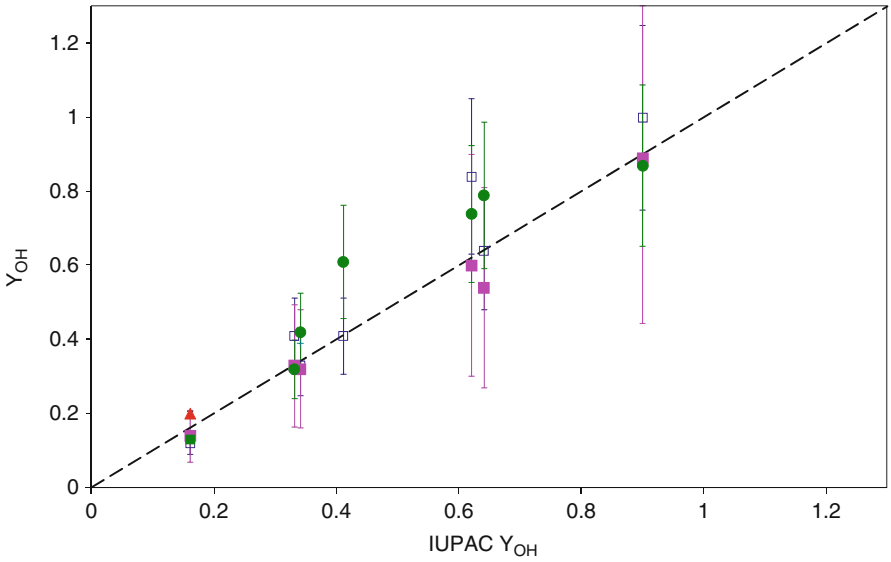

Fig. 12.4 Comparison of the OH yields from this work and literature studies, with the current [14] OH yield recommendations (abscissa). *Filled circles*: this work; *filled squares*: Rickard et al. [30]; *open squares*: Atkinson et al. [2]; *filled triangle*: Mihelcic et al. [24]. The *dashed line* shows the 1:1 correlation

12.4 HO_2 Production

The yields of HO_2 (Y_{HO2}) for the alkenes studied were found to be significantly larger in the absence of OH radical scavengers (specifically, carbon monoxide) – particularly for the 2-methylpropene and 2,3-dimethyl-2-butene ozonolysis systems, where "Y_{HO2}" values were found to be significantly greater than unity (1.51 and 1.74 respectively). It is likely that in the absence of radical scavengers the retrieved HO_2 concentrations are in fact biased high due to interference from the decomposition of β-hydroxyalkyl peroxy radicals, formed from the OH + alkene reactions, within the LIF instrument [11]. We therefore disregard the HO_2 observations/yields obtained in the absence of added CO, and focus upon the data recorded with excess CO present in the following. The OH yields previously obtained were employed within the model to distinguish direct HO_2 formation from indirect production via the OH + CO reaction. Figure 12.5 shows the temporal profile of HO_2 measured by LIF in a propene ozonolysis experiment, along with the HO_2 model results. The first stage of the experiment illustrates the β-hydroxyalkyl peroxy radical HO_2 interference effect noted above – the HO_2 levels are overestimated. Following addition of CO, the observed HO_2 increases slightly (increased through the conversion of OH to HO_2, offset by removal of the interferant RO_2 species) – this part of the experiment represents the base case scenario for retrieval of the HO_2 yield. In the third part of the experiment, water is added to increase the relative humidity to *ca.* 30%, and the observed HO_2 levels (shown corrected for the LIF system calibration humidity

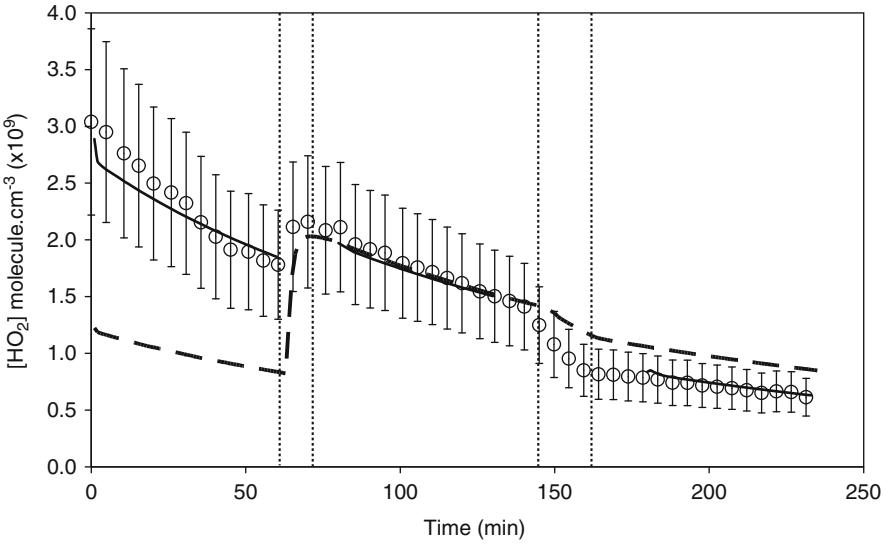

Fig. 12.5 HO_2 production in the ozonolysis of propene (section 1) and its response to the addition of CO (section 2; 62 min +) and H_2O (section 3; 144 min +). Data show the observed concentrations of HO_2 (*open circles*) plus model simulations with direct HO_2 yields of 0.61, 0.09 and 0.02 for sections 1–3 of the experiment respectively (*solid lines*), and for a single fixed yield of 0.09 throughout (*dashed lines*) for a propene ozonolysis

dependence) decrease. The dashed line in Fig. 12.5 represents the modelled HO_2 using an overall yield of 0.09, while the solid lines in sections 1, 2 and 3 show the individually optimized yields of 0.61, 0.09 and 0.02, respectively. The inference from Fig. 12.5 then is that interference effects increase the retrieved "HO_2" in the absence of CO (section 1); the HO_2 yield in the absence of H_2O is 9% (section 2), and upon addition of H_2O, the HO_2 levels decrease, to a greater extent than can be accounted for by the humidity dependence of the HO_2 recombination reaction (which is included in the model), corresponding to a reduction in the HO_2 yield from propene ozonolysis with increasing humidity (section 3).

The dry yields of HO_2 obtained here are compared with those from other studies in Fig. 12.6. The overestimate of the "HO_2 yield" obtained in the absence of CO, from the RO_2 interference, is clearly apparent (filled squares) – these data are not considered further. Our measured yields are in good agreement with measurements for ethene and propene obtained by PERCA, and for isoprene by direct observation by LIF, in the absence of an OH scavenger [22]. The yields obtained in this work are substantially smaller than those reported by Wegener et al. [33] – these values were obtained indirectly from analysis of alkene and ozone turnover in the course of long-duration experiments in the SAPHIR chamber. It is difficult to directly account for the difference between these studies – while the turnover approach is in principle independently sensitive to the HO_x (OH and HO_2) levels present, the sensitivity within the alkene and ozone decays is small (compared with reaction and dilution), reflected in the uncertainty of these values. The HO_2 yields obtained here,

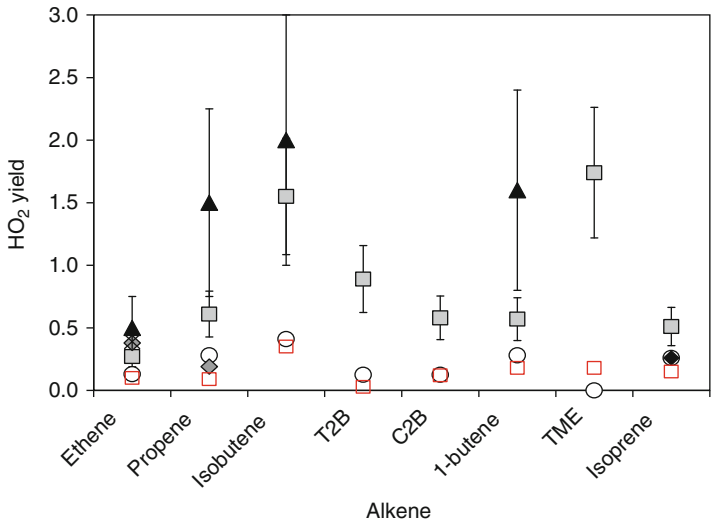

Fig. 12.6 Comparison of HO_2 yields for small chain alkenes investigated during this study with literature values. The abbreviations *T2B*, *C2B* and *TME* are trans-2-butene, cis-2-butene and 2,3-dimethyl-2-butene respectively. *Filled squares* – this work, no CO present (values overestimated due to RO_2 interference). *Open squares* – this work, excess CO experiments (valid HO_2 data); *filled triangles* – Wegener et al. [33]; *light filled diamonds* (ethene, propene) – Qi et al. [27, 28]; *dark filled diamond* (isoprene) – Malkin et al. [22]; *star* (ethene) – Mihelcic et al. [24] and *open circles* – model yields, MCMv3.1

and by Qi et al. [28] and Malkin et al. [22], are in good agreement with those implemented within the MCMv3.1, at least under dry conditions.

The humidity dependence of OH production was not studied in this work; the majority of previous studies have found no evidence for any variation with water vapour (*e.g.* [17] and references therein), although some indications of variations with H_2O have been reported (*e.g.* [33]). As noted above, HO_2 yields decreased upon addition of water vapour for the propene – ozone system (0.09 ± 0.02 to 0.02 ± 0.01). Reductions in HO_2 yields upon addition of water were also observed for ethene (0.10 ± 0.03 to 0.05 ± 0.01 – [1]) and *cis*-2-butene (albeit from a low starting point: 0.03 ± 0.01 to 0.00 ± 0.01), but interestingly not to any significant extent for 2-methyl propene (0.36 ± 0.10 to 0.38 ± 0.10). These data suggest that water vapour is able to intercept (at least part of) the HO_2 formation chemistry in (at least some) alkene ozonolysis reactions. The trend is consistent with the reduction in HO_2 yields observed with increasing humidity by Wegener et al. [33] – where yield reductions of *ca.* 20% were observed for ethene, propene and isobutene (but not for 1-butene) when going from dry conditions to ca. 10 mbar H_2O, albeit with considerable (≈50%) uncertainty. Recently, Leather et al. [20] have reported an increase in the yield of formic acid formation from ethene ozonolysis with increasing humidity, attributed to H_2O reacting with the (stabilized) Criegee intermediate in this system. Together, these studies indicate that the yield of HO_2 from alkene ozonolysis may vary with humidity, implying that competition may occur within the mechanism between radical production through decomposition, and

bimolecular reaction, of the stabilized Criegee intermediate (most likely, through decomposition of the "hot" acid intermediate which results from isomerisation of the *anti*-CI and/or CH_2OO).

12.5 Atmospheric Implications

A constrained zero-dimensional box model was used to quantify the role of alkene ozonolysis to radical production, under ambient conditions observed during the TORCH (Tropospheric Organic Chemistry) field experiment performed in a suburban location to the North-East of London during July and August 2003. This period coincided with an air pollution event and heatwave, leading to elevated ozone and VOC levels compared with the mean for the location and season [21]. The model was constrained to observed levels of long-lived species (NO_x, O_3, H_2O, VOCs, HCHO), meteorological parameters and photolysis rates, and used to calculate the relative contribution of the different (primary) OH and HO_2 production channels, employing the HO_x yields derived from the experiments described above. For OH, ozonolysis was found to account for 29% of primary production (dominated by $O_3 + h\nu/O(^1D) + H_2O$), while for HO_2 ozonolysis accounted for 8% of primary production, which was dominated by aldehyde, particularly HCHO, photolysis (this simple calculation neglects the nested contribution of ozonolysis to the aldehyde loading). Three caveats apply to these values – *total* OH production was dominated by radical cycling, with the reactions of HO_2 with NO and O_3 accounting for 88% of the total flux into OH; HONO photolysis was not included, as HONO observations were unavailable, and is likely to make a substantial contribution, and the ozonolysis radical yields used from this work were those obtained under dry conditions. If, as hypothesised above, radical yields are reduced in the presence of water vapour, and hence potentially other reaction partners (*e.g.* NO), these figures for the importance of ozonolysis in the atmosphere may be regarded as upper limits.

12.6 Conclusions

The production of OH and HO_2 radicals from the ozonolysis of a range of small alkenes has been studied through a simulation chamber approach using the EUPHORE facility, including direct observations of OH and HO_2 via laser-induced fluorescence, with the data obtained analysed in conjunction with a detailed chemical box model to obtain radical yields. OH yields are in agreement with previous measurements, and are consistent with the dominant mechanistic source being the rapid isomerisation and decomposition of *syn*-CIs (Criegee Intermediates) via the hydroperoxide mechanism. Yields of HO_2 were lower than those inferred in some other recent studies, but were in good agreement with those implemented in the Master Chemical Mechanism (version 3.1) under dry conditions. Analysis of atmospheric field data confirmed ozonolysis as a significant source of OH and HO_2 radicals in

the summertime semi-polluted continental boundary layer. Evidence for a reduction in HO_2 yield with increasing humidity was observed for ethene, propene and *cis*-2-butene, implying that these and other similar calculations may overestimate HO_x production from alkene ozonolysis under ambient humidity conditions.

Acknowledgements The contributions of the staff at EUPHORE is gratefully acknowledged, in particular Paco Alacreu, Mónica Vázquez, Mila Rodenas, Amalia Muñoz, and Teresa Vera Espallardo. This work was funded by the UK Natural Environment Research Council (NERC) as part of the TRAPOZ – Total Radical Production from Alkene Ozonolysis project, Grant Ref. NE/E016081/1.

References

1. Alam MS, Camredon M, Rickard AR, Carr T, Wyche KP, Hornsby KE, Monks PS, Bloss WJ (2011) Total radical yields from tropospheric ethene ozonolysis. Phys Chem Chem Phys 13:11002–11015
2. Atkinson R (1997) Gas-phase tropospheric chemistry of volatile organic compounds: 1. alkanes and alkenes. J Phys Chem Ref Data 26:215–290
3. Becker KH (1996) EUPHORE: final report to the European Commission. contract EV5V-CT92-0059. Bergische Universität Wuppertal, Germany
4. Bloss WJ, Lee JD, Bloss C, Heard DE, Pilling MJ, Wirtz K, Martin-Reviejo M, Siese M (2004) Evaluation of the Calibration of a laser-induced fluorescence instrument for the measurement of OH radials in the atmosphere. Atmos Chem Phys 4:571–583
5. Bloss C, Wagner V, Jenkin ME, Volkamer R, Bloss WJ, Lee JD, Heard DE, Wirtz K, Martin-Reviejo M, Rea G, Wenger JC, Pilling MJ (2005) Development of a detailed chemical mechanism (MCMv3. 1) for the atmospheric oxidation of aromatic hydrocarbons. Atmos Chem Phys 5:641–664
6. Calvert JG, Atkinson R, Kerr JA, Madronich S, Moortgat GK, Wallington TJ, Yarwood G (2000) The mechanism of atmospheric oxidation of the alkenes. Oxford University Press, New York
7. Criegee R (1975) Mechanism of ozonolysis. Angew Chem 14:745–752
8. Dillon TJ, Crowley JN (2008) Direct detection of OH formation in the reactions of HO_2 with $CH_3C(O)O_2$ and other substituted peroxy radicals. Atmos Chem Phys 8:4877–4889
9. Donahue NM, Drozd GT, Epstein SA, Presto AA, Kroll JH (2011) Adventures in ozoneland: down the rabbit-hole. Phys Chem Chem Phys 13:10848–10857
10. Fenske JD, Hasson AS, Ho AW, Paulson SE (2000) Measurement of absolute unimolecular and bimolecular rate constants for CH_3CHOO generated by the *trans*-2-butene reaction with ozone in the gas phase. J Phys Chem A 104:9921–9932
11. Fuchs H, Bohn B, Hofzumahaus A, Holland F, Lu KD, Nehr S, Rohrer F, Wahner A (2011) Detection of HO_2 by laser-induced fluorescence: calibration and interferences from RO_2 radicals. Atmos Meas Tech 4:1209–1225
12. Green TJ, Reeves CE, Fleming ZL, Brough N, Rickard AR, Bandy BJ, Monks PS, Penkett SA (2006) An improved dual channel PERCA instrument for atmospheric measurements of peroxy radicals. J Environ Monit 8:530–536
13. Hatakeyama S, Akimoto H (1994) Reactions of Criegee intermediates in the gas phase. Res Chem Intermed 20:503–524
14. IUPAC (2009) International union of pure and applied chemistry subcommittee on gas kinetic data evaluation. http://www.iupac-kinetic.ch.cam.ac.uk/
15. Jenkin ME, Saunders SM, Pilling MJ (1997) The tropospheric degradation of volatile organic compounds: a protocol for mechanism development. Atmos Environ 31:81–104

16. Jenkin ME, Hurley MD, Wallington TJ (2007) Investigation of the radical product channel of the $CH_3C(O)O_2$ + HO_2 reaction in the gas phase. Phys Chem Chem Phys 9:3149–3162
17. Johnson D, Marston G (2008) The gas-phase ozonolysis of unsaturated volatile organic compounds in the troposphere. Chem Soc Rev 37:699–716
18. Johnson D, Lewin AG, Marston G (2001) The effect of Criegee-intermediate scavengers on the OH yield from the reaction of ozone with 2-methylbut-2-ene. J Phys Chem A 105:2933–2935
19. Kuwata KT, Hasson AS, Dickinson RV, Petersen EB, Valin LC (2005) Quantum chemical and master equation simulations of the oxidation and isomerization of vinoxy radicals. J Phys Chem A 109:2514–2524
20. Leather KE, McGillen MR, Cooke MC, Utembe SR, Archibald AT, Jenkin ME, Derwent RG, Shallcross DE, Percival CJ (2011) Acid-yield measurements of the gas-phase ozonolysis of ethene as a function of humidity using Chemical Ionisation Mass Spectrometry (CIMS). Atmos Chem Phys Discuss 11:25173–25204
21. Lee JD, Lewis AC, Monks PS, Jacob M, Hamilton JF, Hopkins JR, Watson NM, Saxton JE, Ennis C, Carpenter LJ, Carslaw N, Fleming Z, Bandy BJ, Oram DE, Penkett SA, Slemr J, Norton E, Rickard AR, Whalley LK, Heard DE, Bloss WJ, Gravestock T, Smith SC, Stanton J, Pillin MJ, Jenkin ME (2006) Ozone photochemistry and elevated isoprene during the UK heatwave of August 2003. Atmos Environ 40:7598–7613
22. Malkin TL, Goddard A, Heard DE, Seakins PW (2010) Measurements of OH and HO_2 yields from the gas phase ozonolysis of isoprene. Atmos Chem Phys 10:1441–1459
23. McGill CD, Rickard AR, Johnson D, Marston G (1999) Product yields in the reactions of ozone with Z-but-2-ene, E-but-2-ene and 2-methylbut-2-ene. Chemosphere 38:1205–1212
24. Mihelcic D, Heitlinger M, Kley D, Musgen P, Volz-Thomas A (1999) Formation of hydroxyl and hydroperoxy radicals in the gas-phase ozonolysis of ethene. Chem Phys Lett 301:559–564
25. Niki H, Maker PD, Savage CM, Breitenbach LP, Hurley MD (1987) FTIR spectroscopic study of the mechanism for the gas-phase reaction between ozone and tetramethylethylene. J Phys Chem 91:941–946
26. Olzmann M, Kraka E, Cremer D, Gutbrod R, Andersson S (1997) Energetics, kinetics, and product distributions of the reactions of ozone with ethene and 2, 3-dimethyl-2-butene. J Phys Chem A 101:9421–9429
27. Qi B, Sato K, Imarnura T, Takami A, Hatakeyama S, Ma Y (2006) Production of the radicals in the ozonolysis of ethene: a chamber study by FT-IR and PERCA. Chem Phys Lett 427:461–465
28. Qi B, Yang B, Wang ZQ, Yang HY, Liu L (2009) Production of radicals in the ozonolysis of propene in air. Sci China B Chem 52:356–361
29. Rathman WCD, Claxton TA, Rickard AR, Marston G (1999) A theoretical investigation of OH formation in the gas-phase ozonolysis of E-but-2-ene and Z-but-2-ene. Phys Chem Chem Phys 1:3981–3985
30. Rickard AR, Johnson D, McGill CD, Marston G (1999) OH yields in the gas-phase reactions of ozone with alkenes. J Phys Chem A 103:7656–7664
31. Saunders SM, Jenkin ME, Derwent RG, Pilling MJ (2003) Protocol for the development of the Master Chemical Mechanism, MCM v3 (Part A): tropospheric degradation of non-aromatic volatile organic compounds. Atmos Chem Phys 3:161–180
32. Siese M, Becker KH, Brockmann KJ, Geiger H, Hofzumahaus A, Holland F, Mihelcic D, Wirtz K (2001) Direct measurement of OH radicals from ozonolysis of selected alkenes: a EUPHORE simulation chamber study. Environ Sci Technol 35:4660–4667
33. Wegener R, Brauers T, Koppmann R, Bares SR, Rohrer F, Tillmann R, Wahner A, Hansel A, Wisthaler A (2007) Simulation chamber investigation of the reactions of ozone with short-chained alkenes. J Geophys Atmos 112. doi:10.1029/2006JD007531
34. Wyche KP, Blake RS, Ellis AM, Monks PS, Brauers T, Koppmann R, Apel EC (2007) Technical note: performance of chemical ionization reaction time-of-flight mass spectrometry (CIR-TOF-MS) for the measurement of atmospherically significant oxygenated volatile organic compounds. Atmos Chem Phys 7:609–620
35. Zador J, Turanyi T, Wirtz K, Pilling MJ (2006) Measurement and investigation of chamber radical sources in the European Photoreactor (EUPHORE). J Atmos Chem 55:147–166

Chapter 13
Theoretical Investigation of the NO_3 Initiated Reaction of VOCs

Solvejg Jørgensen

Abstract We have studied the reaction mechanism for the NO_3 radical initiated atmospheric oxidation of three cresol isomers, *p*-cresol, *m*-cresol and *o*-cresol, in the presence of NO_2. We have focused on the reaction mechanism leading to the ring retaining products, methyl-nitrophenol isomers and methyl-benzoquinone isomers. Geometries of the reactants, intermediates, transition states, and products have been optimized at the DFT-B3LYP level of theory with the 6-311 + G(d,p) basis set. The single point energy calculations have been carried out at the CCSD(T) level of theory with the cc-pVDZ basis set. The reaction path where the NO_3 and NO_2 radicals are added ipso and ortho to the OH group of the cresol isomer, respectively, has the lowest energy barrier.

Keywords Nitrate radical • Cresol isomers • Reaction mechanism • Methyl-nitrophenol isomers • Methyl-benzo quinone isomers

13.1 Introduction

Monocyclic aromatic compounds are emitted to the atmosphere through the use of fossil fuel and solvent use. Toluene is the most abundant aromatic compound in urban air of the observed non-methane hydrocarbons. Toluene reacts mainly with the hydroxyl radial (OH) leading to cresol isomers (*p*-cresol, *m*-cresol and *o*-cresol) with the yield about 20% [2, 3, 17, 22]. The yield depends on the concentration of NO_x. In the OH initiated reaction of toluene the yield of the cresol isomers increases with increasing NO_x concentration [23].

During daytime, cresol isomers are oxidized mainly by OH radicals, whereas NO_3 radicals are the dominant oxidant at night. The rate coefficients of cresol

S. Jørgensen (✉)
Department of Chemistry, University of Copenhagen, Universitetsparken 5,
DK-2100 Copenhagen, Denmark
e-mail: solvejg@chem.ku.dk

I. Barnes and K.J. Rudziński (eds.), *Disposal of Dangerous Chemicals in Urban Areas and Mega Cities*, NATO Science for Peace and Security Series C: Environmental Security,
DOI 10.1007/978-94-007-5034-0_13,

isomers have been reported in the literature for the reaction with OH radical [1, 2, 4, 7, 13, 20] and NO_3 radicals [4, 6, 19]. Furthermore, the products of the reactions have been determined in a number of the experimental studies. For the NO_3 initiated reaction, the ring retaining products are methyl-nitrophenol and methyl-benzoquinone isomers. The yield of 4-methyl-2-nitrophenol accounts for about 40–90% of the total molar yield in the NO_3 initiated reaction of *p*-cresol [4, 6, 19]. The yield of methyl-nitrophenol isomers is greater for *p*-cresol than for *m*-cresol and *o*-cresol. Most of the reported experiments are preformed under high concentrations of NO_x and they may not be representative of the reaction mechanism in the troposphere.

Here, we review the reaction mechanism for the NO_3 initiated reaction of *p*-cresol, *m*-cresol and *o*-cresol in the presence of NO_2. We are using quantum mechanical calculations for the kinetic study. Earlier, a systematic theoretical study of the NO_3 and OH initiated reaction of the cresol isomers has been carried out to understand the multiple channel reaction mechanism [15, 16]. We have only focused here on the reaction mechanism leading to the ring-retaining products; methyl-nitrophenol isomers and methyl-benzoquione.

13.2 Computational Detail

All calculations are performed using the Gaussian 03 program [10]. The DFT-B3LYP level of theory [5, 18] with the 6-311 + G(d,p) basis set [9, 14] was used to optimize the geometries. Vibrational frequencies were calculated at the same level of theory, they are used to compute the zero point vibrational energy as well as characterize the stationary point (local minima or transition state). The intrinsic reaction coordinate calculations [11, 12] were carried out to ensure that the transition state structure connects the desired intermediates (local minima). Single-point energy calculations at the optimized geometries were performed using CCSD(T) [21] with the cc-pVDZ basis set [8]. The CCSD(T) energies are corrected with the zero point vibrational energies from the B3LYP/6-311 + G(d,p) calculations. Below, we refer to the CCSD(T) energy corrected for the zero point vibrational energy. Spin contamination is not considered to be severe.

13.3 Results

We will focus on the reaction mechanism leading to ring retaining products; methyl-nitrophenol isomers and methyl-benzoquinone isomers. The methyl-nitrophenol isomers are formed by either an addition-elimination or hydrogen abstraction reaction mechanism. In the addition-elimination reaction mechanism there are three steps; first, the NO_3 radical adds to the aromatic ring at various positions; second, the NO_2 radical adds to one of carbon atoms; and third, nitric acid (HNO_3) is eliminated. The hydrogen abstraction reaction mechanism consists of three steps; first, the NO_3

radical abstracts the hydrogen atom from the –OH group leading to a methyl-phenoxy radical; second, the NO_2 radical adds to one of carbon atoms; and third, there is a structural rearrangement leading to one of the methyl-nitrophenol isomers. The formation of methyl-benzoquinone is possible when molecular oxygen reacts with the methyl-phenoxy radical. The formation of methyl-benzoquinone is only possible for *m*-cresol and *o*-cresol.

We denote the carbon atom with the OH group as the C1 position. In *p*-cresol, *m*-cresol and *o*-cresol the methyl substituted carbon is denoted as the C4, C3, and C2 position, respectively. For *p*-cresol nitration can only occur at the C2 and C3 positions, the nitration could also occur at the C6 and C5 positions but they are equivalent to the C2 and C3 positions. For *m*-cresol nitration can occur at C2, C4, C5, and C6 whereas the C3, C4, C5, C6 positions could be nitrated in *o*-cresol.

All the reported energies are relative to the individual reactants. The relative energies of all the species involved in the studied reactions are calculated at the CCSD(T)/cc-pVDZ//B3LYP/6−311 + G(d,p) level of theory.

13.3.1 Addition-Elimination Reaction Mechanism

In the addition-elimination reaction mechanism, there are several sites of attack for the NO_3 radical that leads to different adducts denoted IMX, where X refers to the CX position of the addition. The adduct IMX reacts with an NO_2 radical via a barrierless addition to form the intermediates IMX-Y, where Y indicates the CY position, where NO_2 is added. HNO_3 is eliminated from IMX-Y passing through a transition state TSX-Y leading to methyl-nitrophenol isomers. The energy profile for the addition-elimination reaction for the *p*-cresol, when NO_3 is added to the C1 position and NO_2 to the C2 position, is shown in Fig. 13.1.

The addition of the NO_3 radical to the cresol isomers is either barrierless or with a barrier less than 5 kcal/mol. The energy of the IM1 adducts is given in Table 13.1. For all the three cresol isomers, the adduct IM1, where NO_3 has been added to the carbon with the –OH group, is better stabilized than any of the other addition adducts. The better stabilization of the IM1 adducts are due to a H-bond between one of the oxygen atoms in the $–ONO_2$ group and the hydrogen atom in the –OH group. The length of the hydrogen bond ranges from 2.08 to 2.10 Å; it is shortest in *p*-cresol and longest in *m*-cresol.

In the second step, the NO_2 radical is added to the same side of the ring (e.g. cis conformer) or to the opposite side of the carbon ring (e.g. trans conformer) as the added NO_3 group. If the NO_3 radical has been added to the carbon with the –OH group (C1 position) then the NO_2 radical can be added to the C2, C4 or C6 position. The energy barrier associated with the elimination of HNO_3 from the cis conformer of IMX-Y is much greater than one associated with the trans conformer of IMX-Y. For *p*-cresol, the energy of the cis conformer of transition state, TS1-2, is 60 kcal/mol above the energy of the trans conformer (see Fig. 13.1). From an energetic point of view the cis-elimination would not play a major role due to the high activation energies compared to the trans-elimination. Therefore, we only report

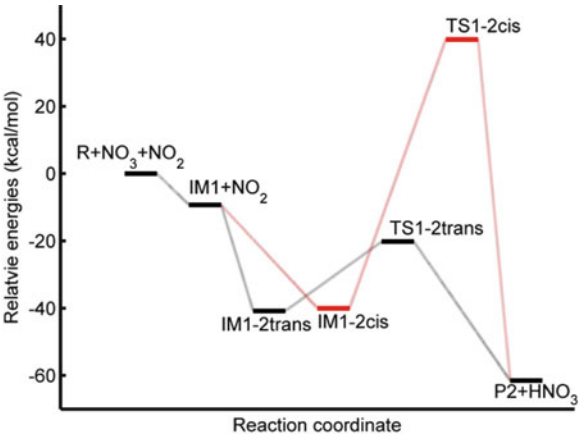

Fig. 13.1 The energy profile for the addition-elimination reaction mechanism of *p*-cresol obtained at CCSD(T)/cc-pVDZ//B3LYP/6-311 + (d,p) level of theory. The reaction path is shown for addition of NO_3 to C1 position. R and P2 refer to *p*-cresol and 4-methyl-2-nitrophenol, respectively

Table 13.1 Energetic of the addition-elimination reaction mechanism for NO_3 initiated reaction of the three cresol isomers (in kcal/mol) with respect to the individual reactants

	Y	IM1 + NO_2	IM1-Y	TS1-Y	PY+HNO_3	PY
p-cresol	2	−9.3	−40.8	−20.2	−61.5	4-methyl-2-nitrophenol
m-cresol	2	−8.6	−41.1	−11.1	−51.4	3-methyl-2-nitrophenol
m-cresol	4	−8.6	−40.8	−13.3	−56.6	3-methyl-4-nitrophenol
m-cresol	6	−8.6	−41.2	−28.8	−61.7	5-methyl-2-nitrophenol
o-cresol	4	−9.6	−35.1	−14.0	−58.3	2-methyl-4-nitrophenol
o-cresol	6	−9.6	−41.5	−21.3	−61.6	6-methyl-2-nitrophenol

NO_3 is added to the C1 position where NO_2 is added to the CY position. The products, PY, methyl-nitrophenol isomers are formed. The reaction products, PY, are listed for each reaction path. CCSD(T)/cc-pVDZ single point energy at B3LYP/6-311 + G(d,p) optimized geometry corrected with B3LYP/6-311 + G(d,p) zero point vibrational energy

the energy for the trans conformer of IMX-Y and TSX-Y. The molecular structures of IM1-2 and TS1-2 for *p*-cresol are shown in Fig. 13.2.

The relative energies of the intermediates, IM1-Y, and TS1-Y are tabulated in Table 13.1. For *m*-cresol, the three IM1-Y structures have almost the same energies whereas there is an energy difference for the two IM1-Y structures for *o*-cresol. The transition states TS1-Y are best stabilized if the NO_2 has been added ortho to the –OH group (e.g. at C2 or C6 position). For *m*-cresol the transition state, TS1-6, is better stabilized than TS1-2, this may indicate that addition to C6 is preferential compared to C2 addition. The energy barrier associated with the 1,4-elimination of HNO_3 from carbon atoms located at opposite side of the carbon ring like IM1-4 is greater than the one associated with the 1,2-elimination of HNO_3 from adjacent carbon atoms like IM1-2 or IM1-6. It is more favorable for 1,2-elimnation than 1,4-eliminations.

The following methyl-nitrophenol isomers are formed in the NO_3 initiated reaction; 4-methyl-2-nitrophenol for *p*-cresol, and 5-methyl-2-nitrophenol (major product), 3-methyl-2-nitrophenol and 3-methyl-4-nitrophenol for *m*-cresol, and 2-methyl-4-nitrophenol for *o*-cresol.

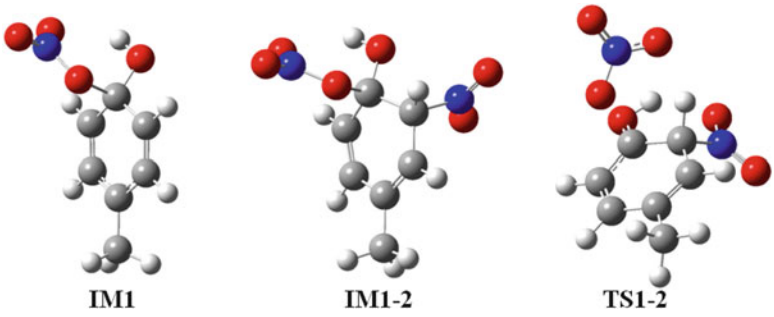

Fig. 13.2 The B3LYP/6-311 + G(d,p) optimized geometries for the addition–elimination reaction path of *p*-cresol where the NO_3 and NO_2 radical are added to the C1 and C2 positions. Both IM1-2 and TS1-2 are the trans conformer

The rate determining step for the addition-elimination reaction channel is the addition of NO_3 to the aromatic ring. The energies of the transition states describing the addition are 7 kcal/mol or less above the individual reactants.

13.3.2 Hydrogen Abstraction Reaction Mechanism

The energetic of the hydrogen abstraction reaction mechanism is given in Table 13.2. In the hydrogen abstraction reaction mechanism the NO_3 radical abstracts the hydrogen atom from the OH-group of the cresol isomer leading to methyl-phenoxy radical (IMabs1). We observed that the energies of the intermediates, IMabs1 and HNO_3, are ~15 kcal/mol below the individual reactants for all three cresol isomers. We have not been able to locate a transition state describing the hydrogen abstraction, either the hydrogen abstraction is barrierless or the NO_3 radical is first added to the aromatic ring and then it abstracts the hydrogen atom from the OH-group. The optimized structures of IMabs1, IMabs2, TSabs2 and P2 for the hydrogen abstraction reaction path of *p*-cresol are shown in Fig. 13.3.

After the formation of IMabs1, the NO_2 radical is added to the CY position leading to IMabsY. This is a barrierless addition. The energy of IMabsY is 38 kcal/mol below the individual reactants. The IMabs2 and IMabs6 conformers could also be formed by elimination of HNO_3 from IM1-2 or IM1-6 conformers, respectively. The energy barriers for elimination are roughly 15 kcal/mol.

After the addition of NO_2, there is a structural rearrangement leading to the product PY, where the hydrogen atom from the CY atom, where NO_2 is added, is transferred to the oxygen atom on the C1 position through a transition state (TSabsY). The energy barriers of the structural rearrangement are above 50 kcal/mol for all three cresol isomers. Furthermore, the energy of the transition states TSabsY are ~15 kcal/mol above the individual reactants for all the three cresol isomers. Therefore, the rate-determining step for the hydrogen abstraction reaction channel is the structural rearrangement of IMabsY via TSabsY to the methyl-nitrophenol isomers.

Table 13.2 Energetic of the hydrogen abstraction reaction mechanism for NO_3 initiated reaction of the three cresol isomers (in kcal/mol) with respect to the individual reactants

	Y	IMabs1 $+NO_2 + HNO_3$	IMabs2 $+HNO_3$	TSabsY $+HNO_3$	PY $+HNO_3$	PY
p-cresol	2	−15.9	−37.4	15.5	−61.5	4-methyl-2-nitrophenol
m-cresol	2	−14.9	−38.1	14.9	−51.4	3-methyl-2-nitrophenol
m-cresol	6	−14.9	−37.5	14.2	−61.7	5-methyl-2-nitrophenol
o-cresol	6	−16.4	−37.6	15.1	−61.6	6-methyl-2-nitrophenol

NO_3 is added to the C1 position and NO_2 is added to the CY position. The products, PY, methyl-nitro-phenol isomers are formed. The reaction products, PY, are listed for each reaction path. CCSD(T)/cc-pVDZ single point energy at B3LYP/6-311 + G(d,p) optimized geometry corrected with B3LYP/6-311 + G(d,p) zero point vibrational energy

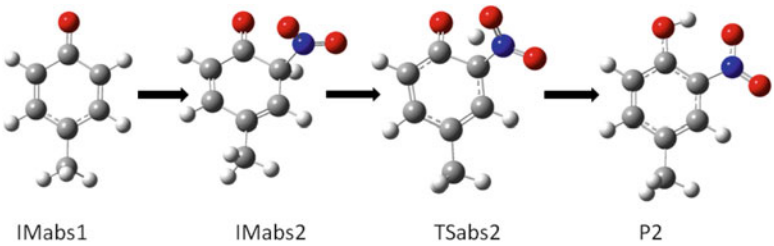

Fig. 13.3 The B3LYP/6-311 + G(d,p) optimized geometries for the hydrogen abstraction reaction path of *p*-cresol leading to 4-methyl-2-nitrophenol (P2)

13.3.3 Formation of Methyl-Benzoquinone Isomer

For *m*-cresol and *o*-cresol, methyl-1,4-benzoquinone can be formed from the methyl-phenoxy radical (IMabs1). First, the molecular oxygen is added to the C4 position forming IMO2. Second, the NO and IMO2 formed a pre-reactive complex, IMO2NO. Third, NO abstracts one of the oxygen atoms leading to IMO and NO_2 through a transition state TSO2, the abstraction is associated with a low energy barrier. Fourth, the molecular oxygen abstracts the hydrogen atom at the C4 position leading to methyl-1,4-benzoquinone and HO_2 via a transition state TSO. The energy barrier for hydrogen abstraction is approximately 20 kcal/mol. The energy profile for the formation of methyl-1,4-benzoquione from *m*-cresol is shown in Fig. 13.4. The one for *o*-cresol is similar. The structures of the intermediates along the reaction path are shown in Fig. 13.5. The energy of all the intermediates along the reaction path is below the energy of the individual reactants.

The methyl-phenoxy radical (IMabs1) is also the intermediate in the hydrogen abstraction reaction mechanism leading to methyl-nitrophenol isomers. If the methyl-phenoxy radial is formed from *m*-cresol or *o*-cresol, it is most likely that

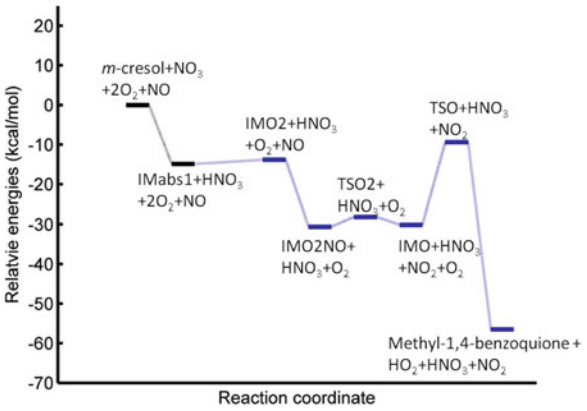

Fig. 13.4 The energy profile for the formation of methyl-1,4-benzoquione from the individual reactants, *m*-cresol + NO_3 + $2O_2$ + NO. The relative energies are computed at CCSD(T)/cc-pVDZ//B3LYP/6-311 + G(d, p) level of theory

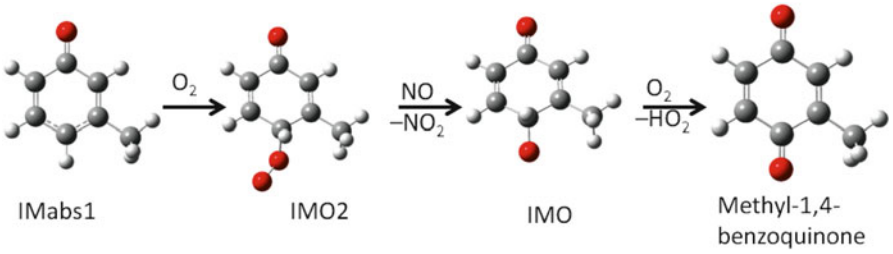

Fig. 13.5 The B3LYP/6-311 + G(d,p) optimized geometries for the reaction path of *m*-cresol leading to methyl-1,4-benzoquinone

they are transferred into methyl-benzoquinone than into methyl-nitrophenol, since the energy of the rate determining step of the hydrogen abstraction mechanism is much greater than one for the formation of methyl-benzoquinone. Furthermore, in the atmosphere the concentration of molecular oxygen is much greater than the concentration of NO_2; it is therefore more likely that methyl-phenoxy radical reacts with molecular oxygen than with NO_2.

13.4 Conclusion

We have investigated the reaction of the gas phase NO_3 initiated oxidation of the three cresol isomers, *p*-cresol, *m*-cresol and *o*-cresol, in the presence of NO_2. We have only focused here on the reaction mechanisms leading to the ring retaining products, methyl-nitrophenol isomers and methyl-benzoquinone isomers.

The methyl-nitrophenol isomers can be formed by either an addition-elimination or hydrogen abstraction reaction mechanism. The rate determining step in the addition-elimination reaction is the addition of the NO_3 radical to the carbon ring,

this addition is either barrierless or with a very low barrier (a few kcal/mol). The rate determining step in the hydrogen abstraction mechanism is the rearrangement of the IMabs2. At the CCSD(T)/cc-pVDZ//B3LYP/6-311 + G(d,p) level of theory, the energy of the transition state is located approximately 16 kcal/mol above the energy of the individual reactants. We would therefore expect that the formation of methyl-nitrophenol isomers proceed through the addition-elimination reaction.

Earlier, Atkinson et al. [4] have suggested that the NO_3 initiated nitration occurs through an addition of NO_3 to the ring and then elimination of HNO_3 leading to the methyl-phenoxy radical. This is equivalent to the reaction path IM1 through TSabs1 to IMabs1. But after the addition of NO_2 leading to IMabs2 the structural rearrangement is associated with a large barrier. It would therefore be more favorable to add both NO_3 and NO_2 before elimination of HNO_3, e.g., the addition-elimination reaction channels.

For *m*-cresol and *o*-cresol, the methyl-phenoxy radical (IMabs1) can be transferred into either the methyl-nitrophenol isomers or the methyl-benzoquinone. Since the energy of rate determining step of the formation of methyl-benzoquinone is much lower than the one associated with the formation of methyl-nitrophenol isomers, we would expect that methyl-phenoxy radical leads to methyl-benzoquinone rather than methyl-nitrophenol isomers.

References

1. Atkinson R, Aschmann SM (1990) Rate constant for the gas-phase reactions of the OH radical with the cresols and dimethylphenol at 296 ± 2K. Int J Chem Kinet 22:59–67
2. Atkinson R, Darnall KR, Pitts JN (1978) Rate constant for the reactions of OH radicals and ozone with cresols at 300 ± 1K. J Phys Chem 82:2759–2761
3. Atkinson R, Aschmann SM, Arey J, Carter WPL (1989) Formation of ring-retaining products from the OH radical-initiated reactions of benzene and toluene. Int J Chem Kinet 21:801–827
4. Atkinson R, Aschmann SM, Arey J (1992) Reaction of OH and NO_3 radicals with phenol, cresols, and 2-nitrophenol at 296 ± 2 K. Environ Sci Technol 26:1397–1403
5. Becke AD (1993) Density-functional thermochemistry. III. The role of exact exchange. J Chem Phys 98:5648–5653
6. Carter WPL, Winer AM, Pitts JN (1981) Major atmospheric sink for phenol and the cresols: reaction with the nitrate radical. Environ Sci Technol 15:829–831
7. Coeur-Tourneur C, Henry F, Janquin M-A, Brutier L (2006) Gas-phase reaction of hydroxyl radicals with *m*-, *o*-, *p*-cresol. Int J Chem Kinet 38:553–562
8. Dunning TH (1989) Gaussian-basis set for use in correlated molecular calculations. 1. The atoms boron through neon and hydrogen. J Chem Phys 90:1007–1023
9. Frisch MJ, Pople JA, Binkley JS (1984) Self-consistent molecular-orbital methods. 25 supplementary function for Gaussian-basis sets. J Chem Phys 80:3265–3269
10. Frisch MJ et al (2004) GAUSSIAN 03, Revision C.02. GAUSSIAN Inc, Wallingford
11. Gonzalez C, Schlegel HB (1989) An improved algorithm for reaction-path following. J Chem Phys 90:2154–2161
12. Gonzalez C, Schlegel HB (1990) Reaction-path following in mass-weighted internal coordinates. J Phys Chem 94:5523–5527
13. Grosjean D (1984) Atmospheric reactions of ortho cresol: gas phase and aerosol products. Atmos Environ 18:1641–1652

14. Hehre WJ, Ditchfield R, Pople JA (1972) Self-consistent molecular-orbital methods. 12 further extensions of Gaussian – type basis set for use in molecular-orbital studies of organic-molecules. J Chem Phys 56:2257–2261
15. Jessen CE, Gross A, Kongsted J, Jørgensen S (2011) A theoretical investigation of gas phase NO_3 initiated nitration of p-cresol. Chem Phys 389:39–46
16. Jørgensen S (2012) Gas-phase oxidation of cresol isomers initiated by OH and NO_3 radicals in the presence of NO_2. Int J Chem Kinet 44:165–178
17. Klotz B, Barnes I, Becker KH (1998) New results on the atmospheric photooxidation of simple alkylbenzenes. Chem Phys 231:289–301
18. Lee C, Yang W, Parr RG (1998) Development of the Colle-Salvetti correlation-energy formula into a functional of the electron density. Phys Rev B 37:785–789
19. Olariu RI (2001) Atmospheric oxidation of selected aromatic hydrocarbons. PhD thesis, University of Wuppertal, Wuppertal
20. Olariu RI, Klotz B, Barnes I, Becker KH, Macanu R (2002) FT-IR study of the ring-retaining products from the reaction of OH radical with phenol, *o*-, *m*-, *p*-cresol. Atmos Environ 36:3685–3697
21. Pople JA, Head-Gordon M, Raghavachar K (1987) Quadratic configuration-interaction a general technique for determining electron correlation energies. J Chem Phys 87:5968–5975
22. Smith DF, McIver CD, Kleindienst TE (1998) Primary product distribution from the reaction of hydroxyl radicals with toluene at ppb NO_x mixing ratio. J Atmos Chem 30:209–228
23. Volkamer R, Uecker J, Wirtz K, Platt U (2002) OH-radical initiated oxidation of BTXM: formation and atmospheric fate of phenol-type compounds in the presence of NO_x. In: Midgley PM, Reuther M (eds) Transport and chemical transformation in the troposphere, proceedings of EUROTRAC symposium 2002. Margraf-Verlag, Wiekersheim, pp 1–5

Chapter 14
Measurements of Trace Gases at Saint-Petersburg State University (SPbSU) in the Vicinity of Saint-Petersburg, Russia

Yury Timofeyev, Dmitry Ionov, Maria Makarova, Yana Virolainen, Anatoly Poberovsky, Alexander Polyakov, Hamud Imhasin, Sergey Osipov, Anton Rakitin, and Marina Kshevetskaya

Abstract An overview of atmospheric trace gas measurements made using various spectroscopic ground-based instrumentation and measurement techniques at the Department of Physics of Atmosphere, St. Petersburg State University is given. The SPbSU trace-gas retrievals have been compared to independent ground-based and satellite measurements as well as to models. Temporal variations (from diurnal cycles to long-term trends) of trace-gases have been studied on the basis of experimental data.

Keywords Ground-based measurements • Atmospheric trace gases • Fourier-spectrometer Bruker

14.1 Introduction

Atmospheric trace gases play an important role in forming the radiative characteristics of the atmosphere and ozonosphere and accordingly effect global climate [20]. Therefore measurements of the variability of climate influencing atmospheric gases by different local and remote methods are performed very intensively and continuously all over the world. At St. Petersburg State University (Atmospheric Physics Department) ground-based spectroscopic measurements of trace gases started in the early 1990s at Old Peterhof, approximately 35 km southwest from the center of St.-Petersburg (59°88′ N, 29°83′S, 20 m asl.). Measurements of IR solar radiation spectra by SIRS-spectrometer with middle resolution [3] were first performed at SPbSU but have subsequently been augmented by other remote methods for measuring the atmospheric trace gases.

Y. Timofeyev (✉) • D. Ionov • M. Makarova • Y. Virolainen • A. Poberovsky • A. Polyakov • H. Imhasin • S. Osipov • A. Rakitin • M. Kshevetskaya
Department of Atmospheric Physics, Saint-Petersburg State University, Ulyanovskaya, 1, St. Petersburg-Petrodvorets 198504, Russia
e-mail: tim@troll.phys.spbu.ru; Yana.Virolainen@JV14952.spb.edu

I. Barnes and K.J. Rudziński (eds.), *Disposal of Dangerous Chemicals in Urban Areas and Mega Cities*, NATO Science for Peace and Security Series C: Environmental Security,
DOI 10.1007/978-94-007-5034-0_14,

14.2 Instrumentation and Measurement Techniques

At first stage of the investigation (beginning in 1991), ground-based spectroscopic measurements of CH_4 and CO total column amounts (TCA) have been performed using a Solar IR Spectrometer (SIRS). SIRS is a low resolution (0.4−0.6 cm^{-1}) grating spectrometer which was designed at the Department for observations of solar IR radiation in the 3.15−4.55 μm wave-range. The gas TCA retrieval algorithm is based on the optimal estimation method [17]. CH_4 and CO TCA time series have been analyzed to reveal variability of different time scales (long-term trends, annual and interannual variability etc.) of the gases for the St. Petersburg region [4, 5].

Trace gas remote determinations have been carried out also by measurements of zenith scattered solar radiation in the UV and visible spectral ranges. For performing the measurements, an automated spectral complex based on a grating spectrometer (KSVU instrument) developed at SPbSU which allowed registration of a spectrum of scattered radiation in the range of 428−515 nm with 1.3 nm resolution has been used [11]. The NO_2 vertical column amount has been retrieved from twilight solar scattered visible radiation measurements using the DOAS (Differential Optical Absorption Spectroscopy) method [9]. Beginning with 2004, the measurements have been carried out by means of the KSVU instrument (later, since 2008 – by an OceanOptics spectrometer). The interpretation of this kind of ground-based measurements is performed using the standard techniques developed for the international network of stations NDACC (formerly NDSC) (http://www.ndacc.org) and SAOZ [15] (WinDOAS, [1]). Since 2008, determination of the ozone vertical profiles at the 20−80 km altitude region have begun using measurements of downward thermal radiation in the microwave ozone absorption lines [2].

Since January 2009, combined determination of atmospheric gas composition has been started using ground-based measurements of IR direct solar radiation by Fourier-spectrometer Bruker IFS-125 with a high spectral resolution (up to 0.002 cm^{-1}). An original sun-tracking system for the Bruker IFS125 HR was designed at the Atmospheric Physics Dept. of Saint-Petersburg State University. It makes possible the measurement of more than 20 greenhouse and reactive gases in the atmosphere over St. Petersburg [6, 7, 10, 12–14, 18, 19, 21]. In Table 14.1 short descriptions of the ground-based devices and measurement methods used at SPbSU are given.

14.3 Trace Gases Measurements Near St. Petersburg

Simultaneous measurements which were performed by SIRS (original retrieval algorithm [8]) and Bruker (SFIT2 retrieval algorithm [16]) during 2009–2010 allowed us to harmonize the CH_4 time series obtained by two spectrometers (Fig. 14.1). The systematic difference between the Bruker IFS125 HR and SIRS measurements totals 1.8%.

Long-term trends in the CH_4 TCA were estimated using SIRS and Bruker IFS125 HR observations (Fig. 14.2). The increase rate for 2005−2010 is

Table 14.1 Instruments and measurement techniques used by SPbSU for trace gases measurements

Device	Start	Retrieval algorithm	Method and spectral range	Measured gases	Comments
Spectrometer SIRS-2	1991	Original code (optimal estimation) [8]	Direct Sun radiation 3.15–4.55 μm	CO, CH_4, H_2O	Spectral resolution 0.2–0.5 cm^{-1}
Fourier-spectrometer Bruker IFS-125	2009	SFIT2 v. 3.9× (optimal estimation) [16]	Direct Sun radiation 1–16 μm	~20 gases	Spectral resolution – up to 0.002 cm^{-1}
UV-VIS-NIR spectrometers		WinDOAS [1]	Zenith scattered solar radiation	O_3, NO_2, O_2-O_2	Spectral resolution:
Visible-NIR-KSVU	2004		420–520 nm		1.3 nm
OCEAN OPTICS HR4000 UV HR4000 visible	2008		280–420 nm 400–610 nm		0.4 nm 0.6 nm
MW-ozonometer	2008	Original code (optimal estimation) [2]	MW atmospheric radiation 110 GHz	O_3	Vertical profile (25–60 km)

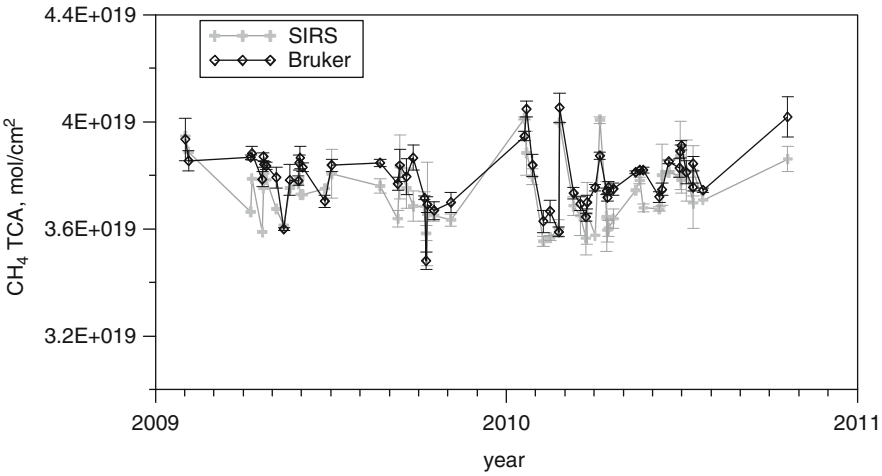

Fig. 14.1 Results of simultaneous measurements of the CH_4 TCA

(1.0 ± 0.4)% per year. The linear trend of CH_4 (near Saint-Petersburg) for the whole measurement period (1991−2010) amounts to (0.16 ± 0.1)% per year.

In Fig. 14.3 data on the stratospheric O_3 column retrieved from ground-based OceanOptics UV (top) and stratospheric NO_2 column retrieved from ground-based KSVU and OceanOptics VIS (bottom) measurements near Saint-Petersburg are compared with collocated satellite (Aura OMI instrument) and Envisat SCIAMACHY

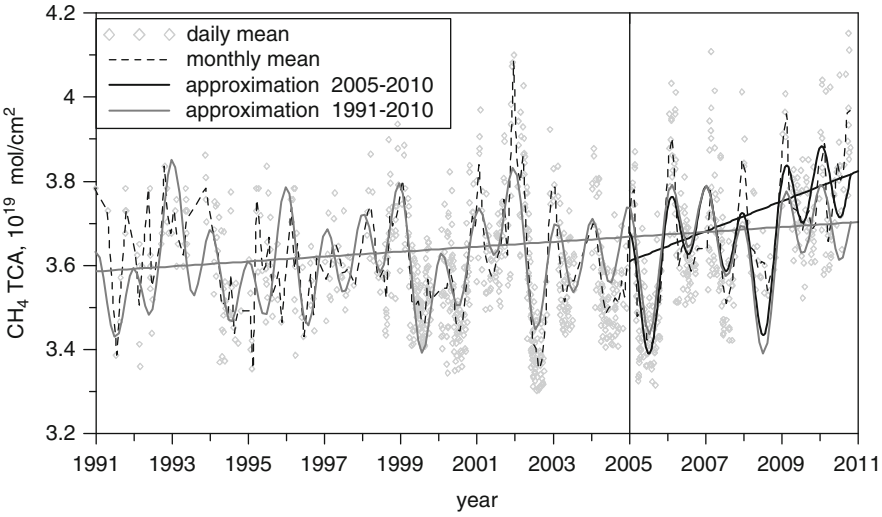

Fig. 14.2 Long-term trends in the CH_4 TCA near Saint-Petersburg

measurements, respectively. Reasonable agreement between the two types of data for both measurements is evident – the relative difference is +2.4 ± 4.3% for O_3 and 2 ± 48% for NO_2.

In Fig. 14.4 ground-based measurements of the NO_2 tropospheric column (KSVU) are compared with calculations using the HYSPLIT dispersion model and the correlative satellite OMI data in winter–spring 2006. There is qualitative agreement between the simulated (HYSPLIT) and measured (KSVU, OMI) tropospheric NO_2 variations. Currently, NO_2 can also be measured with a DOAS mobile device.

14.4 Combined Measurements of Atmospheric Trace Gases with a High Spectral Resolution

Since 2009 combined measurements of atmospheric trace gases have been performed using the Fourier-spectrometer Bruker IFS-125 with a high spectral resolution. In Table 14.2 the spectral windows used for the retrieved TCA of different gases and retrieval errors are given.

The spectral intervals used for trace gas retrieval are obtained from the recommendations of NDACC stations for such kinds of measurements as well as from preliminary analysis of measured and calculated spectra (e.g., Virolainen et al. [19]).

In Table 14.3 the annual-average N_2O TCA near Saint-Petersburg measured by a Fourier spectrometer (SPbSU) is compared with the same values for a number of NDACC stations.

One can see that the mean values and annual variability of N_2O TCA is very similar for all of the listed stations (mid and high latitudes).

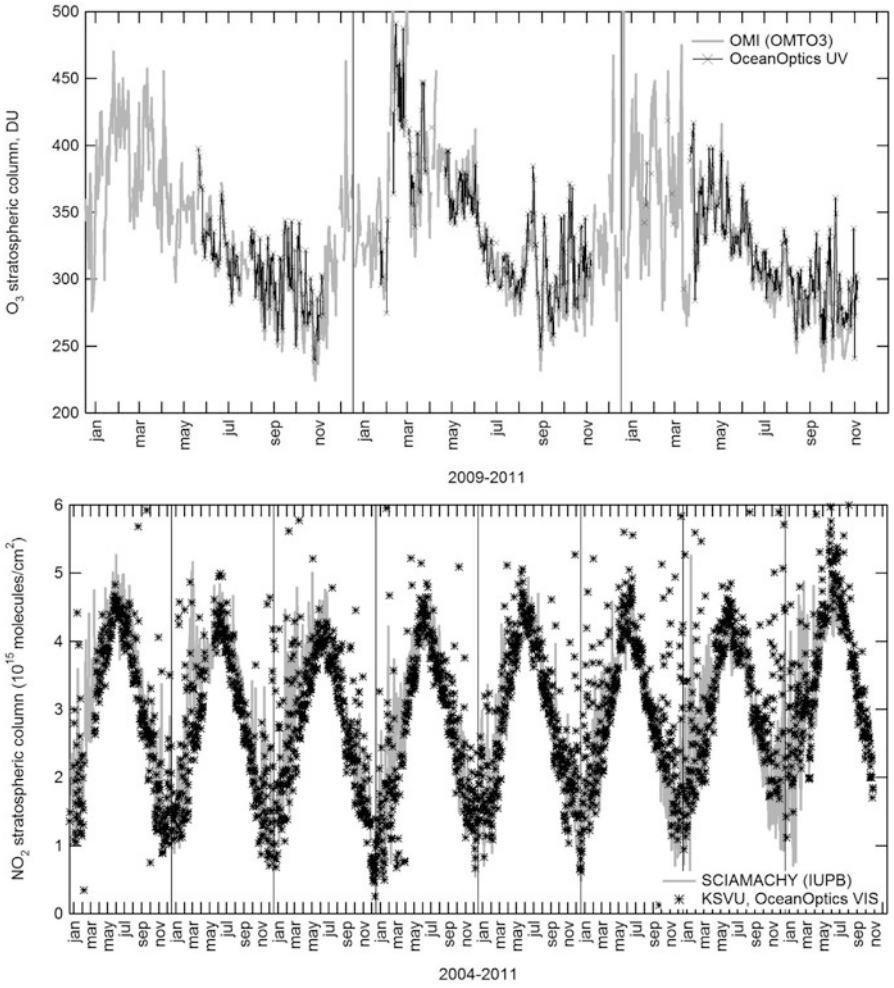

Fig. 14.3 Comparison of ground-based and satellite stratospheric O_3 (*top*) and NO_2 (*bottom*) column measurements

The results of ozone TCA ground-based measurements by Fourier spectrometer, Dobson spectrometer, ozonometer M-124 and satellite OMI measurements near Saint-Petersburg are compared in Fig. 14.5. Measurements by the Dobson spectrophotometer and M-124 filter ozonometer were carried out at the Main Geophysical Observatory in Voeikovo (50 km to the north-east of Peterhof), satellite measurements are collocated in space to ground-based measurements within about 100 km.

It is clearly evident that the different types of measurements are in good qualitative coincidence. The amplitude of ozone TCA changes obtained by Bruker spectrometer data are slightly less than by the OMI or M-124 data, especially in the early spring period of measurements, when the TCA values are sufficiently large (around 400 DU). In addition, one can see that the Bruker spectrometer data for August 2009 at small TCA values (less than 300 DU) are somewhat overestimated in comparison with the other probes.

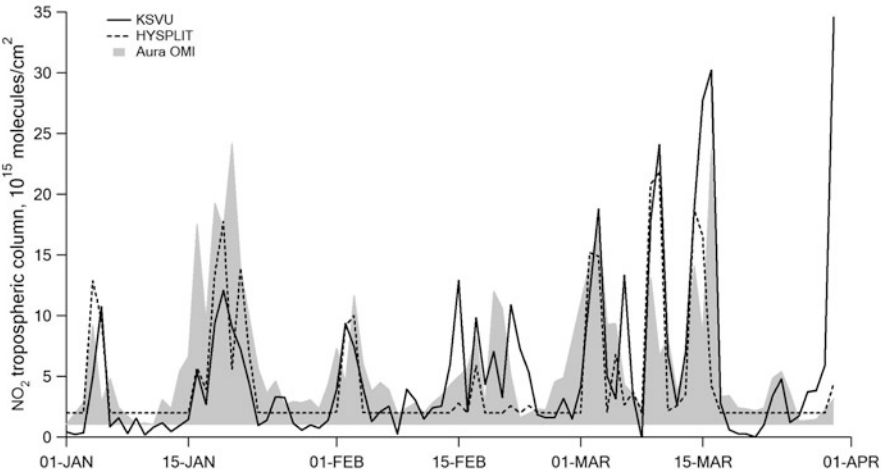

Fig. 14.4 NO_2 tropospheric column measurements at St. Petersburg compared to HYSPLIT dispersion model and satellite OMI data in winter–spring 2006

Table 14.2 Measured gases and random retrieval errors

Measured gases	Spectral windows, cm^{-1}	Random error for single measurement, %	Influenced gases
CO_2	2,626.3–2,627.0	1.0	CH_4, HDO
CH_4	2,613.70–2,615.40	1.0	HDO, CO_2, NO_2
	2,650.60–2,651.30		
	2,835.50–2,835.80		
	2,903.60–2,904.03		
CO	2,057.70–2,058.00	1.5	O_3, CO_2, OCS, N_2O, H_2O
	2,069.56–2,069.76		
	2,157.50–2,159.15		
HF	4,038.0–4,039.7	1–5	H_2O, CH_4
N_2O	2,551.435–2,552.400	1.1	CH_4
NO_2	2,914.590–2,914.707	8.2	CH_4, HDO
C_2H_6	2,976.6–2,977.1	4.0	O_3, H_2O, CH_4
HCl	2,925.75–2,926.0	1.7	CH_4, H_2O
O_3	six windows in 773–1,044	1	H_2O, CO_2
CCl_3F	830–870	13	H_2O, HNO_3, O_3
HNO_3	867.5–870.1	1–9	H_2O, CO_2, OCS

The results of numerical pair-wise comparison of different O_3 TCA measurements are given in Table 14.4. The period of comparison dates to 2009, from early spring to late fall, 52 sunny days of simultaneous measurements in total. The measurements under consideration use a F3 filter allocating the spectral range from 650 to 1,400 cm^{-1}. The spectral resolution of the measurements in the chosen spectral ensemble was 0.005–0.008 cm^{-1}. The average and rms errors, as well as the

Table 14.3 Comparison of N_2O TCA near Saint-Petersburg with that from NDACC stations

Station	Annual N_2O TCA, 10^{-18} mol/cm^2	Annual variability, %
SPbSU	6.53	12
Bremen	6.46	9
Toronto	6.49	17
Harestua	6.58	16
St. Danis	6.6	6

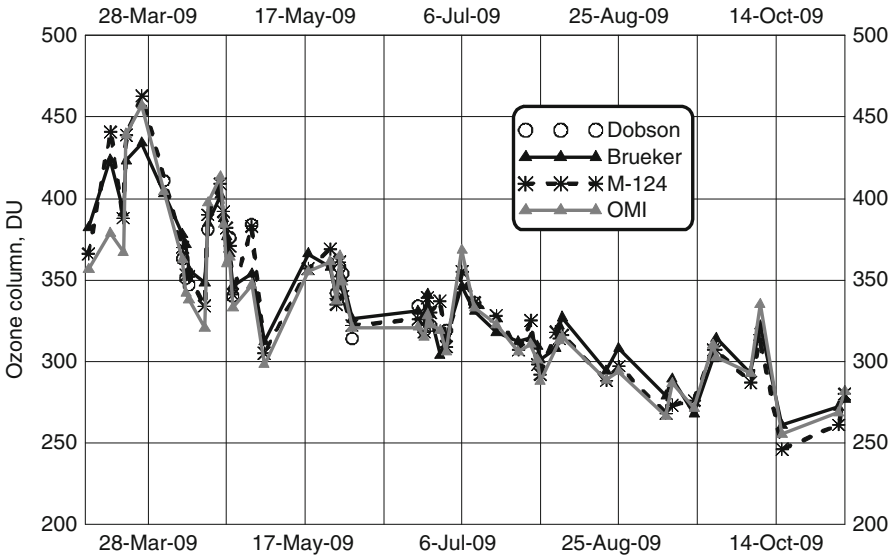

Fig. 14.5 Comparison of ground-based and satellite ozone TCA (in DU) measurements near Saint-Petersburg

Table 14.4 Comparison of O_3 TCA measurements

Measuring devices	Number of comparisons	Mean difference	RMS difference	Correlation coefficient
Bruker−Dobson	17	0.7 DU (0.3 %)	11.4 DU (3.2 %)	0.90
Bruker−OMI	51	5.3 DU (1.7 %)	14.2 DU (4.1 %)	0.95
Bruker−M124	51	0.6 DU (0.4 %)	11,7 DU (3.4 %)	0.97
M124−Dobson	16	−0.2 DU (−0.06 %)	6.8 DU (2.0 %)	0.99
M124−OMI	50	4.6 DU (1.3 %)	13.5 DU (3.8 %)	0.96
OMI−Dobson	17	−5.5 DU (−1.7 %)	12.2 DU (3.5 %)	0.91

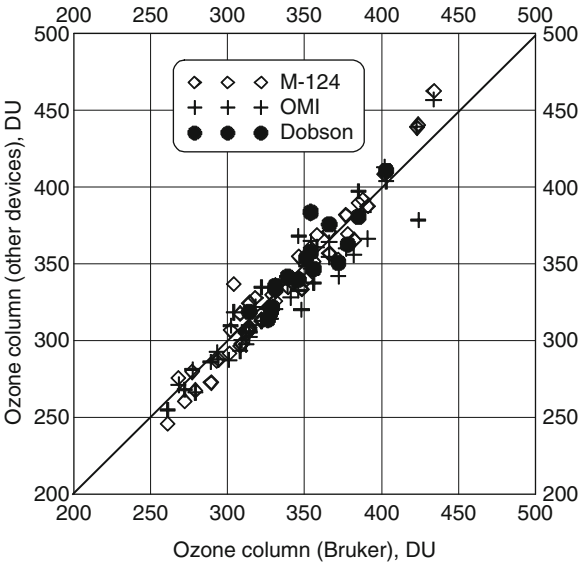

Fig. 14.6 Correlation between the ozone TCA obtained from different devices (mean: 0.3–1.7 %, RMS: 3–4 %) near Saint-Petersburg

coefficients of correlation between measurements by different probes, are presented. The correlation coefficients are close to unity with a maximum value of 0.97 for the Bruker–M-124 pair.

Analyzing the rms error, it can be seen that the maximum (4%) is observed between the ground-based measurements by the Bruker spectrometer and the results of the OMI satellite measurements. The rms between TOC measurements with the help of OMI and M_124 probes is also close to 4%. The rms error between the Peterhof and Voeikovo measurements is 3–3.5%. These errors can be explained by both the errors of the measurements themselves and the spatial and temporal variations of ozone.

In addition to the correlations shown in Table 14.4, Fig. 14.6 demonstrates the rate of consistency between the measurement results depending on the ozone TCA value. The average TCA value over all ensembles is around 330 DU; the rms value is around 45 DU (around 15%). It can be seen from Fig. 14.6 that the M-124 and Dobson spectrophotometer data are very linear (this is also because there are no shifts between these data); at the same time, the comparison between OMI and Bruker spectrometer data reveals that the TCA values for OMI are slightly higher. This is more apparent for ozone TCA values of around 340–400 DU (i.e., above average).

Measured monthly average values of the CO_2 TCA near Saint-Petersburg in 2009−2011 and their variations are given in Table 14.5.

It is seen that the maximum in CO_2 variability is observed in April 2009–2010, in July 2009 and during the summer months ion 2011 (more than 10 ppm and, consequently, more than 3% of mean values). The observed means of CO_2 TCA refer to 2010.

Ground-based measurements of the HF TCA by Fourier-spectrometer Bruker IFS-125 were carried out during April 2009−April 2010. The random and

Table 14.5 Monthly average values (in ppm) of CO_2 TCA and its variations (Δ) in 2009–2011

Year/month	2009	Δ	N	2010	Δ	N	2011	Δ	N
April	397.0	14.6	9	393.4	10.5	9	390.7	6.7	11
May	390.5	8.2	7	395.7	4.8	7	391.3	8.7	10
June	389.3	3.9	6	390.8	6.2	7	392.8	12.6	13
July	387.6	11.3	9	395.9	7.1	9	393.6	11.4	12
August	387.0	5.0	6	–	–	–	388.3	10.9	10
September	389.0	8.8	3	–	–	–	390.1	2.6	4

N – number of measurement days

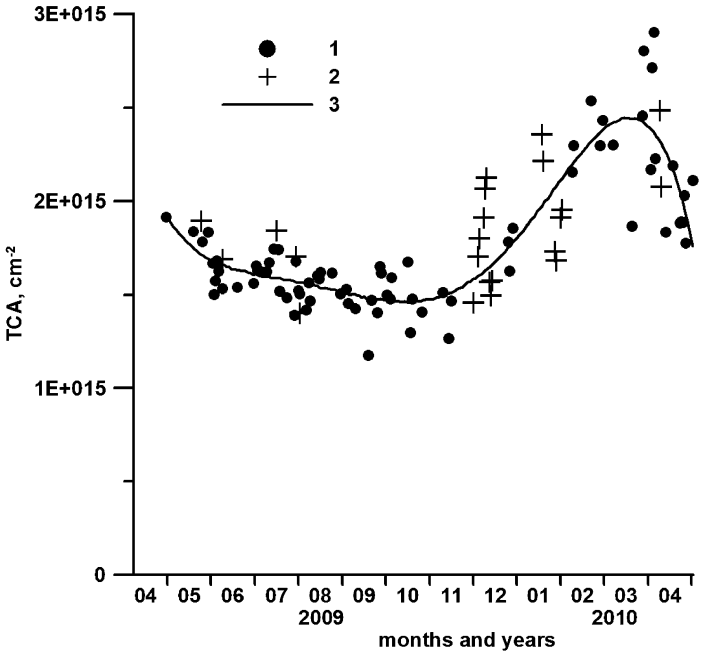

Fig. 14.7 Comparison of SPbSU ground-based (1) and satellite (calculated using profiles of HF mixing ratio measured by ACE-FTS) (2) HF TCA measurements for April 2009–April 2010 (3) – an approximation of HF TCA by a fifth-degree polynomial

systematical errors of the HF TCA measurement are 1–5% and 5–6%, respectively. The mean values and rms variations of the HF TCA are 1.77×10^{15} cm^{-2} and 21%, respectively. The results are in good agreement with other ground-based (NDACC data) and satellite (ACE-FTS) measurements (Fig. 14.7).

The numerical values of this comparison of ground-based (Bruker) and satellite (ACE experiment) measurements are presented in Table 14.6. The columns refer to 500 and 1,000 km distance coincidence of the considered measurements. One can see that the mean difference in both ensembles totals 8%, rms – 11 and 15% for 500 and 1,000 km, respectively.

Table 14.6 Statistical characteristics for a comparison of satellite and ground-based HF TCA measurements

Distance, km	500	1,000
Number of comparisons	9	43
Mean for Saint-Petersburg (SP), mol/cm^2	1.62×10^{15}	1.70×10^{15}
Mean for ACE-FTS	1.75×10^{15}	1.84×10^{15}
RMS HF for SP, % of the natural variability	16	16
RMS HF for ACE-FTS, % of the natural variability	8	13
Mean difference, %	8	8
RMS difference, %	11	15
Standard deviation, %	7	13

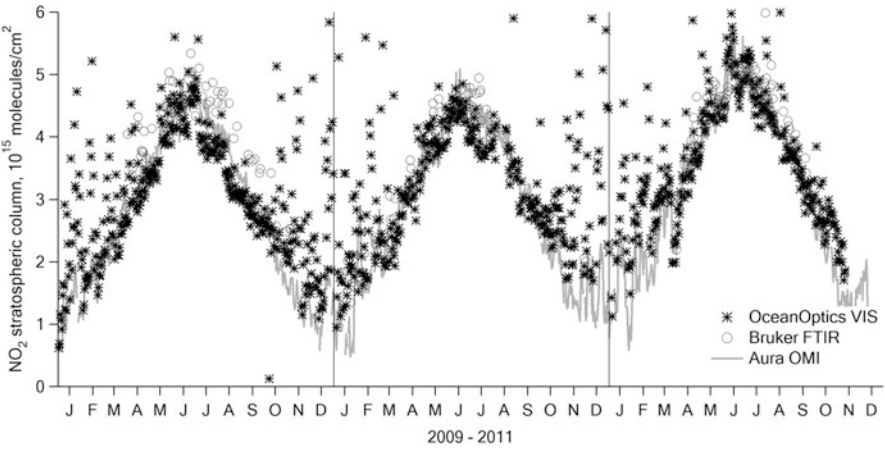

Fig. 14.8 Bruker NO_2 TCA measurements compared to ground-based (OceanOptics VIS and IR Bruker) and satellite data (OMI)

Results from a comparison of the NO_2 TCA ground-based (using DOAS method to zenith scattered solar radiation measurements and measurements of direct Sun spectra by Fourier-spectrometer Bruker IFS-125) and satellite measurements (Aura OMI instrument) are shown in Fig. 14.8.

One can see that the Bruker measurements of the NO_2 TCA are in good quantitative agreement with the OMI data (a little bit higher in summer maximum). The OceanOptics results have a larger spread of measurement values.

14.5 Summary

1. A large number of atmospheric trace gases are being measured since the early 1990s by different ground-based devices using different interpretation methods at SPbSU.

2. Currently, NO_2 is measured with a DOAS mobile device. In the near future other gases will be measured with the mobile FTIR spectrometer.
3. Temporal variations (from diurnal cycles to long-term trends) of trace gases are studied on the basis of experimental data.
4. Trace gases measurements are being used for validation of satellite data.
5. Further development of techniques for retrieving profiles of trace gases and increasing the number of retrieved trace gases are planned.

Acknowledgements In this work, measurements of The Atmospheric Chemistry Experiment (ACE), supported by Canada Space Agency and National Center for Scientific and Engineering Research, were used. The work was partly supported by the Ministry of Education and Science of Russian Federation in the frame of Federal special-purpose program "Scientific and Educational Manpower of Innovative Russia" (contracts No 969 of 27.05.2010 and No 16.740.11.0048 of 31.08.2010) and by SPSU (research projects 11.31.547.2010 and 11.37.28.2011).

References

1. Fayt C, Van Roozendael M (2009) WinDOAS 2.1 software user manual. http://UV-vis.aeronomie.be/software/WinDOAS
2. Kostsov VS, Poberovsky AV, Osipov SI, Timofeyev YM (2012) Integrated method of interpretation of ground-based microwave spectral measurements in the problem of ozone vertical profile retrieval. Atmos Ocean Opt 25:354–360
3. Makarova MV, Poberovskii AV, Timofeev YM (2001) Spectroscopic measurements of the total methane content in the atmosphere over St. Petersburg, Izv. Atmos Ocean Phys 37:61–66
4. Makarova MV, Poberovskii AV, Timofeev YM (2004) Temporal variability of total atmospheric carbon monoxide over St. Petersburg, Izvestiya. Atmos Ocean Phys 40:313–322
5. Makarova MV, Poberovskii AV, Visheratin KN, Polyakov AV (2009) Time variability of the total methane content in the atmosphere over the vicinity of St. Petersburg, Izv. Atmos Ocean Phys 45:723–730
6. Makarova MV, Poberovskii AV, Osipov SI (2011) Time variations of the total CO content in the atmosphere near St. Petersburg, Izv. Atmos Ocean Phys 47:739–746
7. Makarova MV, Rakitin AV, Ionov DV, Poberovskii AV (2011) Analysis of variability of the CO, NO_2, and O_3 contents in the troposphere near St. Petersburg, Izv. Atmos Ocean Phys 47:468–479
8. Mironenkov AV, Poberovskii AV, Timofeev YM (1996) Interpretation of infrared solar spectra for quantification of the column content of atmospheric gases. Izv. Atmos Ocean Phys 36:191–198
9. Platt U, Stuz J (2008) Differential optical absorption spectroscopy (DOAS), principles and applications. Springer, Berlin, 597 pp. ISBN 978-3-540-21193-8
10. Poberovskii AV (2010) High-resolution ground measurements of the IR spectra of solar radiation. Atmos Ocean Opt 23:161–163
11. Poberovskii AV, Shashkin AV, Ionov DV, Timofeev YM (2007) NO_2 content variations near St. Petersburg as inferred from ground-based and satellite measurements of scattered solar radiation. Izv. Atmos Ocean Phys 43:505–513
12. Poberovskii AV, Makarova MV, Rakitin AV, Ionov DV, Timofeev YM (2010) Variability of the total column amounts of climate influencing gases obtained from ground-based high resolution spectroscope. Dokl Earth Sci 432:656–658

13. Poberovskii AV, Polyakov AV, Timofeev YM (2010) Measurements of the hydrogen fluoride total column amount in the atmosphere over the vicinity of St. Petersburg, Izv. Atmos Ocean Phys 46:261–263
14. Polyakov AV, Timofeev YM, Poberovskii AV, Yagovkina IS (2011) Seasonal variations in the total content of hydrogen fluoride in the atmosphere. Izv. Atmos Ocean Phys 47:760–765
15. Pommereau J-P, Goutail F (1988) O_3 and NO_2 ground-based measurements by visible spectrometry during arctic winter and spring. Geophys Res Lett 15(1988):891–894
16. Rinsland CP, Jones NB, Connor BJ et al (1998) Northern and southern hemisphere ground-based infrared spectroscopic measurements of tropospheric carbon monoxide and ethane. J Geophys Res 103:28197–28217
17. Rodgers CD (2000) Inverse methods for atmospheric sounding: theory and practice. Series on atmospheric, oceanic and planetary physics, vol 2. World Scientific Publishing Co Pte Ltd, Hackensack, 238 pp. ISBN 981-02-2740-X
18. Virolainen YA, Timofeyev YM (2010) Complex method for determining ozone vertical profiles to validate satellite measurements. Earth Res Space 4:61–66 (In Russian)
19. Virolainen YA, Timofeev YM, Ionov DV, Poberovskii AV, Shalamyanskii AM (2011) Ground-based measurements of total ozone content by the infrared method, Izv. Atmos Ocean Phys 47:480–490
20. WMO, Scientific Assessment of Ozone Depletion: 2006 (2007) Global ozone research and monitoring project-report no. 50, Geneva, Switzerland, 572 pp
21. Yagovkina IS, Polyakov AV, Poberovskii AV, Timofeev YM (2011) Spectroscopic measurements of total CFC-11 freon in the atmosphere near St. Petersburg, Izv. Atmos Ocean Phys 47:186–189

Chapter 15
Nitro- and Nitro-Oxy-Compounds in Multiphase Particle Chemistry: Field and Analytical Studies

Yoshiteru Iinuma and Hartmut Herrmann

Abstract Recent field evidence shows the presence of nitro-phenolic compounds in biomass burning influenced secondary organic aerosol. The results from laboratory and smog chamber experiments suggest that these compounds likely form from the reaction of gas-phase phenolic compounds originating from biomass burning in the presence of NO_x. These compounds contribute as much as 3.8% to the organic carbon fraction of wintertime aerosols collected in a rural German village, indicating that they are important secondary organic aerosol constituents during the winter months.

Keywords Biomass burning • Nitroaromatics • Monoterpenes • HPLC • MS

15.1 Introduction

The atmospheric oxidation of volatile organic compounds (VOCs) leads to the formation of polar low-volatile organic compounds that form Secondary Organic Aerosol (SOA) through nucleation and/or condensation. Amongst a number of atmospherically relevant VOCs, the SOA formation from isoprene and monoterpene has been intensively studied in the past due to their high global emissions and reactivity towards atmospheric oxidants (e.g. see review by Hallquist et al. [10]). More recently, VOCs originating from biomass burning have been receiving attention for their SOA formation potential [3, 8, 9, 12, 17]. Depending on the approaches, the estimates for global SOA fluxes vary dramatically from 50–90 TgC $year^{-1}$ to 510–910 TgC $year^{-1}$ [6, 10] though all studies agree that SOA contributes significantly to the organic mass found in atmospheric fine particles.

Y. Iinuma (✉) • H. Herrmann
Leibniz-Institut für Troposphärenforschung, Permoserstr. 15, D-04318 Leipzig, Germany
e-mail: yoshi@tropos.de

I. Barnes and K.J. Rudziński (eds.), *Disposal of Dangerous Chemicals in Urban Areas and Mega Cities*, NATO Science for Peace and Security Series C: Environmental Security,
DOI 10.1007/978-94-007-5034-0_15,

Atmospheric organic particles are complex mixtures containing thousands of different compounds. Among various compound classes present in the particles, carboxylic acids and carbonyl compounds have been identified as SOA compounds in the past field and laboratory studies. More recent studies have shown that SOA compounds are not only made of carbon, oxygen and hydrogen atoms, but they also contain sulfur and nitrogen atoms in the molecules. In particular, organosulfates have been identified as an important class of compounds that originate from biogenic VOCs (BVOCs). It has been reported that organosulfates can account a significant fraction of the total particulate bound sulfate and OM, ranging up to 30% [14, 15, 18]. The fractions of other heteromolecular compounds in the particulate organic matter are not well known though nitrogen-containing species are likely as important as organosulfates in atmospheric fine organic aerosol. Two classes of nitrogen containing SOA species reported so far are nitroaromatic compounds from the oxidation of biomass burning VOCs and nitro-oxy- and nitro-oxy-organosulfate compounds from the oxidation of isoprene and monoterpenes [1, 2, 11–13, 18]. These nitrogen containing SOA species likely form when the emissions from anthropogenic pollution react with SOA precursor VOCs that originate from biogenic or anthropogenic sources.

In the present study, we report the occurrence of nitroaromatic SOA compounds originating from the oxidation of biomass burning VOCs and nitro-oxy-organosulfates from the oxidation of monoterpenes in the ambient PM10 samples collected during winter 2007–2008 and summer 2008 at a rural site in Germany. The samples are analysed using high-performance liquid chromatography (HPLC) equipped with an electrospray ionisation time-of-flight mass spectrometer (ESI-TOFMS). Both the nitroaromatic compounds and nitro-oxy organosulfates represent important fractions of the total polar organic SOA compounds determined using the HPLC/ESI-TOFMS technique.

15.2 Experimental

The ambient wintertime PM10 samples were collected between 22 October 2007 and 30 March 2008 at the rural village of Seiffen, Saxony, Germany (647 m above mean sea level). The village is surrounded by coniferous forest and the sampling site was located in a residential area. The village was significantly influenced by the emissions from domestic wood combustion during the sampling period. The samples were collected every 4 days on a quartz fibre filter with a Digitel DHA-80 high volume sampler (Digitel, Elektronik AG, Hegnau, Switzerland). The sampling duration was 24 h from midnight to midnight (720 m^3 total sampling volume).

A part of the sampled filter (3 × 2 cm diameter punches) was spiked with an internal standard (*trans*-cinnamic d_7 acid, 98 atom % D, Sigma-Aldrich, St. Louis, MO, USA) and ultrasonicated in 1 mL of LC-MS grade methanol for 30 min. The extracts were filtered through a syringe filter to remove nonsoluble materials (0.2 μm, PTFE Acrodisc, Pall, NY) and dried under a gentle stream of nitrogen at 10°C. The dry residue was reconstituted in 200 μL of a methanol/water solution (50/50, v/v) for the analysis.

The extracts were analysed using an Agilent 1100 series HPLC coupled with a Bruker micrOTOF mass spectrometer equipped with an electrospray ionization source (HPLC/(-)ESI-TOFMS). The separation was performed on an Agilent Zorbax SB-C18 column (150 × 3 mm, 5 µm, 80 Å). The mobile phase composition used for the separation was (A) 0.1% acetic acid in water and (B) methanol. The mobile phase gradient was programmed as follows: the mobile phase B was increased from 10 to 90% in 20 min, held constant for 15 min, and then re-equilibrated at 10% for 10 min. The mobile phase flow rate was 0.5 mL min^{-1}. The following parameters were applied for the analysis using micrOTOF: ion polarity, negative; ESI nebulizer (N_2), 1.5 bar; dry gas (N_2), 10 L min^{-1}; capillary voltage, 4.5 kV; end plate offset, −0.5 kV; ion source temperature, 200°C; and scan rage, *m*/*z* 50–1,200. The quantification of nitroaromatic compounds and nitro-oxy-organosuflates were achieved by running a series of standard solutions (0.05–6.25 mg L^{-1}, 8 points, quadratic fitting, $R^2 > 0.998$) containing 1.6 mg L^{-1} *trans*-cinnamic d_7 acid as an internal standard. The standard compounds used for the quantification were 4-nitrophenol, 4-nitrocatechol, 4-methyl-5-nitrocatechol (Sigma-Aldrich), 3-methyl-6-nitrocatechol (synthesized, [12]). As no standard compounds were available for monoterpene originating nitro-oxy-organosulfates, β-pinene organosulfates were used for the tentative quantification instead (synthesized, [11]).

15.3 Results

15.3.1 Nitroaromatic Compounds in Biomass Burning SOA

In our previous study [12], a series of methyl-nitrocatechols (3-methyl-5-nitrocatechol, 4-methyl-5-nitrocatechol, and 3-methyl-6-nitrocatechol) have been identified as possible marker compounds for biomass burning originating SOA. The sum of their concentration was as high as 29 ngm^{-3} when the sampling site was significantly impacted by the biomass burning emission. In addition to methyl-nitrocatechols, 4-nitrocatechol is detected at significant levels in these PM_{10} samples. Figure 15.1 shows a typical chromatogram highlighting the

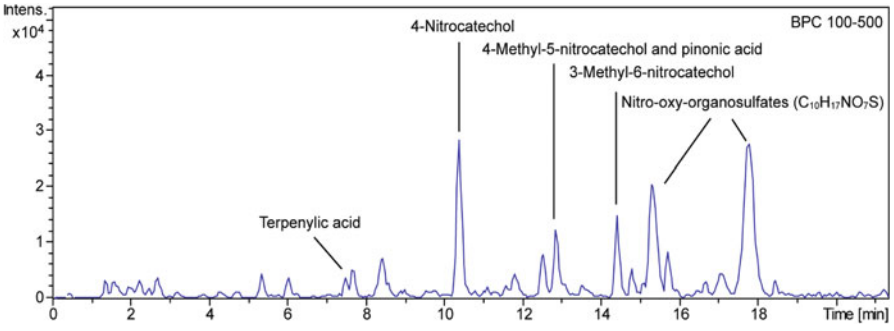

Fig. 15.1 A base peak ion chromatogram (BPC) of PM10 sample collected on 25 December 2007. Other PM10 samples showed similar chromatograms

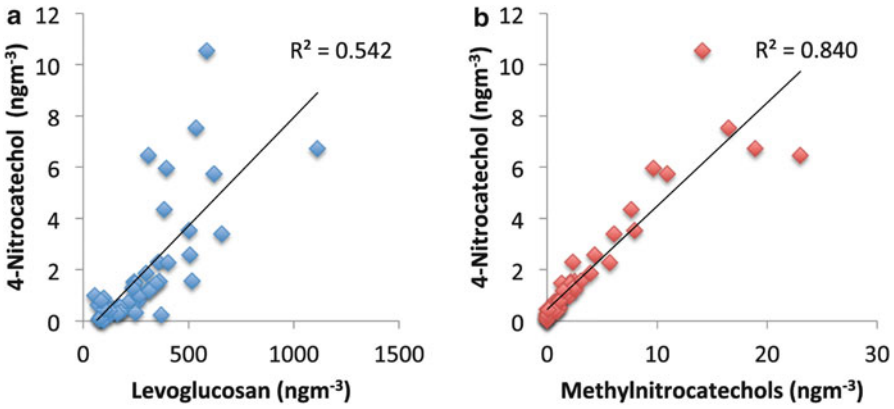

Fig. 15.2 Correlations between (**a**) 4-nitrocatechol and levoglucosan, and (**b**) 4-nitrocatechol and the sum of methylnitrocatechol isomers

abundance of nitroaromatic compounds in these samples. The concentration range of 4-nitrocatechol was from 0.02 to 10.5 ngm^{-3} with the average concentration of 1.9 ng m^{-3}. These values are comparable to the concentrations found for 4-methyl-5-nitrocatechol and 3-methyl-6-nitrocatechol [12]. The concentrations of 4-nitrocatechol, levolgucosan and methyl-nitrocatechols correlated well with each other, indicating the same source for these compounds, i.e. biomass burning (Fig. 15.2). In particular, 4-nitrocatechol correlated very well with methyl-nitrocatechol with R^2 value greater than 0.8. Considering the structural similarity of 4-nitrocatechol and methyl-nitrocatechols, the formation mechanisms for 4-nirocatechol is likely analogous to those of methyl-nitrocatechol. In our earlier study [12], we have proposed that methyl-nitrocatechols form from the photooxidation of *m*-cresol in the presence of NO_x based on a series of aerosol chamber experiments.

In the case of 4-nitrocatechol, phenol likely serves as a precursor for its formation. Phenol is emitted at significant levels from domestic wood combustion, and its emission factor is comparable or higher than the sum of cresol isomers [16]. Schauer et al. [16] have reported that the emission factor of phenol from the fireplace combustion of pinewood is about 525 mg kg^{-1}, and the emission factor for the sum of three cresol isomers is about 470 mg kg^{-1}. In their study, the emission factors of cresol isomers vary from wood type to wood type, with pinewood being the highest followed by oak and eucalyptus. Unlike cresols, the emission factor of phenol is relatively consistent regardless of the wood types. The similar concentrations found for both 4-nitrocatechol and methyl-nitrocresols are reasonable considering the fact that the sampling site was subject to significant influence of domestic and industrial coniferous wood combustion during the sampling period. The gas-phase reaction of phenol with OH largely forms catechol [4] that is further nitrated to form 4-nitrocatechol in the particle phase (Fig. 15.3, upper

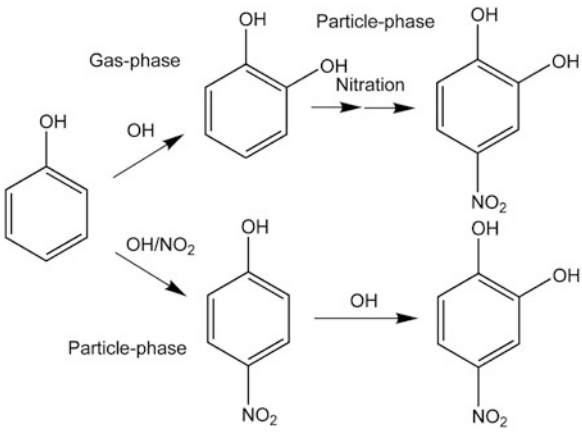

Fig. 15.3 Feasible formation pathways for 4-nitrocatechol from phenol oxidation in the presence of NO_2

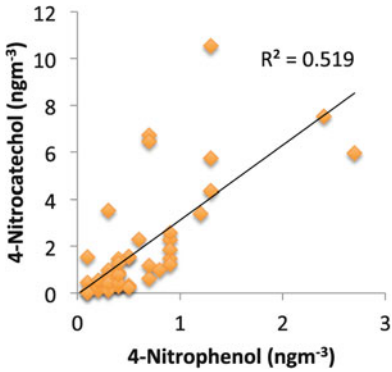

Fig. 15.4 A correlation between 4-nitrocatechol and 4-nitrophenol detected in the PM_{10} samples

pathway). Alternatively, the particle phase phenol can react with OH to form 4-nitrophenol in the presence of NO_2 and acidity [5]. 4-Nitrophenol further reacts with OH forming 4-nitrocatechol (Fig. 15.3, lower pathway). Indeed, 4-nitrophenol has been detected in these samples, and it correlated reasonably well with 4-nitrocatechol with R^2 value of about 0.5 (Fig. 15.4). Although the concentrations of nitroaromatic compounds were much lower than that of levoglucosan, they were comparable to SOA compounds originating from monoterpene oxidation such as terpenylic acid and pinic acid, indicating that SOA originating from biomass burning VOCs were as important as SOA originating from biogenic VOCs in these samples.

15.3.2 Nitro-Oxy Organosulfates in Biogenic SOA

The presence of monoterpene originating nitro-oxy-organosulfates (Fig. 15.5) has been reported in the ambient SOA samples [7, 11, 13, 18, 19] and laboratory produced SOA [18]. In the samples collected in the present study, a series of

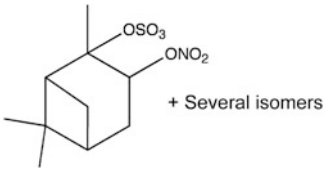

Fig. 15.5 A suggested structure for a-pinene originating nitro-oxy-organosulfate

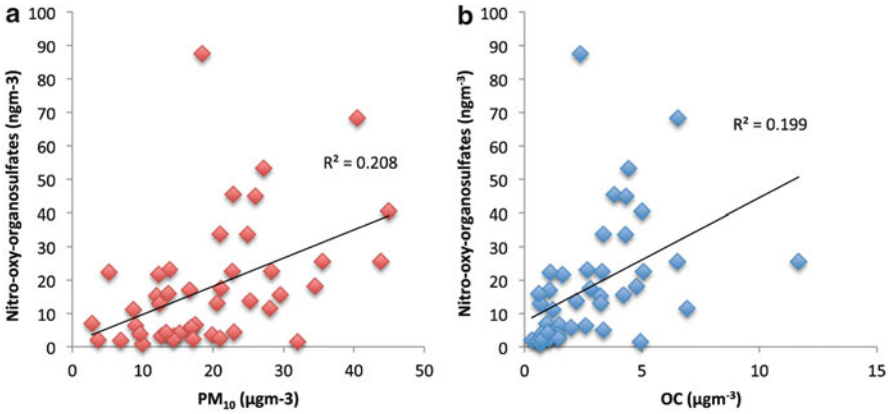

Fig. 15.6 Correlations between nitro-oxy-organosulfates and (**a**) PM_{10}, and (**b**) OC

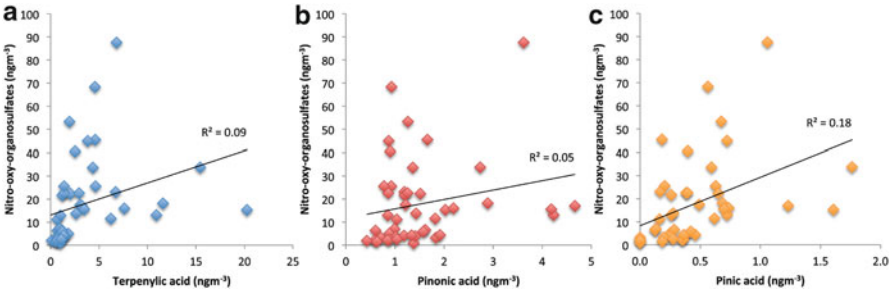

Fig. 15.7 Correlations between nitro-oxy-organosulfates and (**a**) terpenylic acid, (**b**) pinonic acid, and (**c**) pinic acid

nitro-oxy-organosulfates were detected at substantial levels (Fig. 15.1). Nitro-oxy-organosulfates were neither correlated with biomass burning tracer compounds nor inorganic ions, PM_{10} and OC (Fig. 15.6), though the time series was similar to that of OC (Fig. 15.7). The estimated concentrations for the sum of nitro-oxy-organosulfates were the highest between all biomass burning and biogenic SOA compounds detected in the samples, ranging up to 90 ng m^{-3}. In contrast, the concentrations of terpenoic acids were much lower than the nitro-oxy-organosulfates with terpenylic aicd, which is one of the most abundant SOA compounds in laboratory α-pinene oxidation experiments, being the highest with

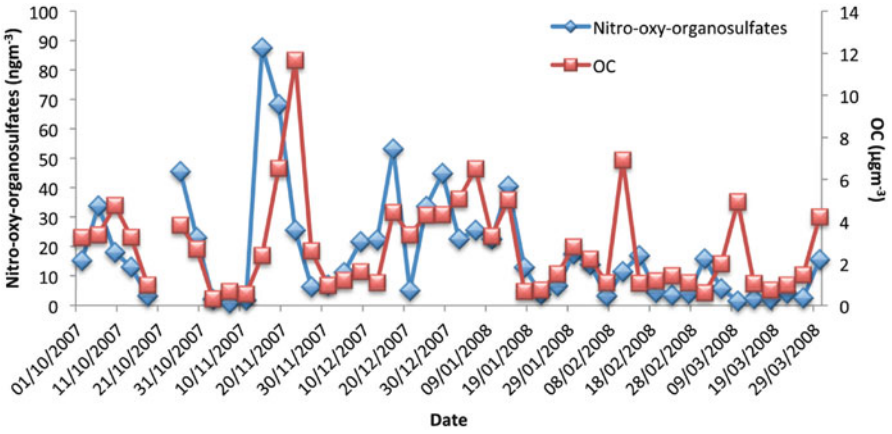

Fig. 15.8 Time series for nitro-oxy-organosulfates and OC

maximum concentration of 20 ng m^{-3}. Interestingly, nitro-oxy organosulfates did not correlate with terpenylic acid, pinonic acid and pinic acid, indicating that the formation of nitro-oxy-organosulfates likely requires conditions that are different from these for terpenolic acids (Fig. 15.7).

The exact formation mechanisms of nitro-oxy-organosulfates are still not well understood to this date. Surratt et al. [18] has reported these nitro-oxy-organosulfates likely arise from the photooxidation and/or nitrate radical initiated oxidation of monoterpenes in the presence of NO_x and extremely acidic seed particles based on a series of aerosol chamber experiments. The result from field study indicates that the formation mechanisms likely involve nighttime chemistry, as they were more abundant in the samples collected during the night [11]. It is noted that levels of nitro-oxy-organosulfates were relatively high even during the period with the lowest photochemical activity, pointing to a prominent role of non-photochemical biogenic SOA formation mechanisms at the sampling site (Fig. 15.8).

15.4 Conclusions

In the present study, we presented the field evidence for the formation of biomass burning originating SOA. Biomass burning originating VOCs, especially phenolic compounds, can be oxidized to form nitrated compounds in the presence of NO_x. These compounds are sufficiently low volatile to form SOA, especially during the wintertime when the temperature is low. The contribution of detected nitro-aromatic compounds (three isomers of methyl-nitrocatechols, 4-nitrocatechol and 4-nitrophenol) to the OC was about 0.5% on average with a maximum of 3.8%. Although this is about a factor of 10 smaller than the value found for levoglucosan, they contribute non-negligibly to the local wintertime PM.

It has been shown in this study that non-negligible amounts of biogenic SOA compounds were present in the wintertime PM samples. In particular, nitro-oxy-organosulfates originating from monoterpenes represent an important fraction of biogenic SOA. The contribution of nitro-oxy-organosulfates to the OC ranged from 0.01 to 1.5% with the average value of 0.3%. These values are comparable to those of nitroaromatic SOA compounds from biomass burning. The nitro-oxy-organosulfates did not show correlations with terpenolic acids, indicating that the formation of nitro-oxy-organosulfates requires different atmospheric conditions from those for terpenolic acids. Further study is warranted to elucidate the formation mechanisms of nitro-oxy-organosulfates, in particular the role of night-time chemistry for their formation.

References

1. Altieri KE, Turpin BJ, Seitzinger SP (2009) Composition of dissolved organic nitrogen in continental precipitation investigated by ultra-high resolution FT-ICR mass spectrometry. Environ Sci Technol 43:6950–6955
2. Altieri KE, Turpin BJ, Seitzinger SP (2009) Oligomers, organosulfates, and nitrooxy organosulfates in rainwater identified by ultra-high resolution electrospray ionization FT-ICR mass spectrometry. Atmos Chem Phys 9:2533–2542
3. Anastasio C, Sun J (2009) SOA formation via aqueous reactions of phenols from wood combustion. Geochim Cosmochim Ac 73:A39
4. Atkinson R, Aschmann SM, Arey J (1992) Reactions of OH and NO_3 radicals with phenol, cresols, and 2-nitrophenol at 296-K+-2-K. Environ Sci Technol 26:1397–1403
5. Barzaghi P, Herrmann H (2002) A mechanistic study of the oxidation of phenol by OH/NO_2/NO_3 in aqueous solution. Phys Chem Chem Phys 4:3669–3675
6. Goldstein AH, Galbally IE (2007) Known and unexplored organic constituents in the earth's atmosphere. Environ Sci Technol 41:1514–1521
7. Gómez-González Y, Surratt JD, Cuyckens F, Szmigielski R, Vermeylen R, Jaoui M, Lewandowski M, Offenberg JH, Kleindienst TE, Edney EO, Blockhuys F, Van Alsenoy C, Maenhaut W, Claeys M (2008) Characterization of organosulfates from the photooxidation of isoprene and unsaturated fatty acids in ambient aerosol using liquid chromatography/(-) electrospray ionization mass spectrometry. J Mass Spectrom 43:371–382
8. Grieshop AP, Donahue NM, Robinson AL (2009) Laboratory investigation of photochemical oxidation of organic aerosol from wood fires 2: analysis of aerosol mass spectrometer data. Atmos Chem Phys 9:2227–2240
9. Grieshop AP, Logue JM, Donahue NM, Robinson AL (2009) Laboratory investigation of photochemical oxidation of organic aerosol from wood fires 1: measurement and simulation of organic aerosol evolution. Atmos Chem Phys 9:1263–1277
10. Hallquist M, Wenger JC, Baltensperger U, Rudich Y, Simpson D, Claeys M, Dommen J, Donahue NM, George C, Goldstein AH, Hamilton JF, Herrmann H, Hoffmann T, Iinuma Y, Jang M, Jenkin ME, Jimenez JL, Kiendler-Scharr A, Maenhaut W, McFiggans G, Mentel TF, Monod A, Prevot ASH, Seinfeld JH, Surratt JD, Szmigielski R, Wildt J (2009) The formation, properties and impact of secondary organic aerosol: current and emerging issues. Atmos Chem Phys 9:5155–5236
11. Iinuma Y, Müller C, Berndt T, Böge O, Claeys M, Herrmann H (2007) Evidence for the existence of organosulfates from β-pinene ozonolysis in ambient secondary organic aerosol. Environ Sci Technol 41:6678–6683

12. Iinuma Y, Böge O, Gräfe R, Herrmann H (2010) Methyl-nitrocatechols: atmospheric tracer compounds for biomass burning secondary organic aerosols. Environ Sci Technol 44:8453–8459
13. Kristensen K, Glasius M (2011) Organosulfates and oxidation products from biogenic hydrocarbons in fine aerosols from a forest in North West Europe during spring. Atmos Environ 45:4546–4556
14. Lukács H, Gelencsér A, Hoffer A, Kiss G, Horváth K, Hartyáni Z (2009) Quantitative assessment of organosulfates in size-segregated rural fine aerosol. Atmos Chem Phys 9:231–238
15. Maenhaut W, Raes N, Chi XG, Cafmeyer J, Wang W (2008) Chemical composition and mass closure for PM2.5 and PM10 aerosols at K-puszta, Hungary, in summer 2006. X-Ray Spectrom 37:193–197
16. Schauer JJ, Kleeman MJ, Cass GR, Simoneit BRT (2001) Measurement of emissions from air pollution sources. 3. C-1-C-29 organic compounds from fireplace combustion of wood. Environ Sci Technol 35:1716–1728
17. Sun YL, Zhang Q, Anastasio C, Sun J (2010) Insights into secondary organic aerosol formed via aqueous-phase reactions of phenolic compounds based on high resolution mass spectrometry. Atmos Chem Phys 10:4809–4822
18. Surratt JD, Gomez-Gonzalez Y, Chan AWH, Vermeylen R, Shahgholi M, Kleindienst TE, Edney EO, Offenberg JH, Lewandowski M, Jaoui M, Maenhaut W, Claeys M, Flagan RC, Seinfeld JH (2008) Organosulfate formation in biogenic secondary organic aerosol. J Phys Chem A 112:8345–8378
19. van Pinxteren D, Bruggemann E, Gnauk T, Iinuma Y, Muller K, Nowak A, Achtert P, Wiedensohler A, Herrmann H (2009) Size- and time-resolved chemical particle characterization during CAREBeijing-2006: different pollution regimes and diurnal profiles. J Geophys Res [Atmos] 114. doi:10.1029/2008JD010890

Chapter 16
Heterogeneous and Liquid-Phase Reactions of BVOCs with Inorganic Pollutants in the Urban Atmosphere

Krzysztof J. Rudziński

Abstract This paper tries to say that urban air pollutants, which definitely are dangerous chemicals, can be efficiently removed from urban atmospheres by reactions with biogenic volatile organic compounds emitted by urban vegetation. It briefly recollects several ideas concerning a profitable coexistence of anthropogenic and green urban spaces in contemporary cities, and reviews recent achievements in the chemistry of BVOC-pollutant interactions arbitrarily considered important by the author.

Keywords Urban air quality • Urban atmosphere • BVOC • Isoprene

16.1 Introduction

Urbanisation is an inevitable future of human civilisation. Since 2008, more people live in the cities than elsewhere, and this proportion is continuously increasing. Some say that successful and sustainable development of urban environments is a key to the success of human civilisation [14]. Among numerous social, administrative and technical problems of maintaining a city, one of the most important is securing good air quality. Good air quality means better health of the city population, and less damage to buildings and constructions [8, 40].

Urban environments are composed of anthropogenic and green spaces arranged in various ways. Old epitome was a stone city surrounded by seas of vegetation, like Urbino, Italy is now. Such cities were ventilated fairly well with clean rural air. Industrial cities of the nineteenth century were larger, hardly green and poorly ventilated. The air quality thereof was poor as well. Contemporary cities tend to be interlaced spaces, containing a reasonable proportion of managed vegetation including city forests and parks, street alleys of plants, gardens and even the

K.J. Rudziński (✉)
Institute of Physical Chemistry PAS, Kasprzaka str. 44/52, 01-224 Warszawa, Poland
e-mail: kjrudz@ichf.edu.pl

I. Barnes and K.J. Rudziński (eds.), *Disposal of Dangerous Chemicals in Urban Areas and Mega Cities*, NATO Science for Peace and Security Series C: Environmental Security,
DOI 10.1007/978-94-007-5034-0_16,

ornamental or medicinal plants we keep at homes. Anthropogenic spaces comprise municipal and industrial facilities, household constructions, machinery and fleets of vehicles. Air quality in contemporary cities is an open matter.

Anthropogenic spaces generally spoil air quality. They produce a vast number of primary pollutants, both inorganic and organic, which originate from fuel burning, technological processes and household activities. Green spaces are believed to improve the air quality, among many other services they provide for urban ecosystems [12, 43]. They are best known for the capacity to absorb a commonly recognised greenhouse gas – carbon dioxide – and to turn it by the virtue of photosynthesis into carbon fixed in the molecules of plant tissues. Moreover, plants can absorb some pollutants, like sulphur dioxide or nitric oxide. On the other hand, pollutants which deposit to plant surfaces or enter their organisms through stomata, can harm the plants or even kill them [2].

Plants produce 100,000 chemical substances for their own purposes, such as inter and intra-species communication or fighting thermal, water, herbivore or chemical stresses. About 1,700 of these substances are biogenic volatile organic compounds (BVOCs) [10, 26]. It is worth to bear in mind that humans and animals also emit volatile organic compounds, endogenic or digestive by nature, which, methane excluded, are rather poorly quantified and difficult to classify since their sources are partially anthropogenic. Inevitably, pollutants and BVOCs meet in the cities and react together chemically or photochemically if sunlight is available. The outcome of these reactions are new organic compounds, volatile, semivolatile or non-volatile by nature, secondary organic aerosol (SOA) and more inorganic compounds. Some of these products are inert, but others are more or less harmful, so they are considered secondary pollutants.

Thus, we know plants help us to reduce air pollution and have some profits and much trouble from this, so that sometimes they retaliate and emit pollutants or induce secondary pollution. Plants are sort of socially intelligent, as they know how to communicate with insects, how to cool themselves by inducing aerosol, and how to induce nutrient formation. They appear valuable neighbours in our cities, so we should attempt to: (i) enhance our cooperation with plants and increase the mutual profits; (ii) understand how to manage the urban and sub-urban flora; (iii) find the ways to protect plants from pollution and land-greedy developers; and (iv) understand how to protect ourselves from adverse influences of plants.

Research space for these efforts is diverse in nature and scale. It spans from the sky down to the earth's surface and even below. The atmosphere is a huge multiphase photoreactor with much gas phase, some water droplets, i.e. clouds and rains, and distributed solid phase of atmospheric particulate matter. Below, there are buildings, constructions, machinery and vehicles which offer interesting sources of reactants and surfaces for heterogeneous transformations. Then, there are living things, including humans, animals, plants and microorganisms, who offer both surfaces and rich multiphase interiors of their bodies. At the bottom, there are natural waters and soils, which also can be penetrated into. A reasonable part of this space and related research efforts are assigned to us – the atmospheric chemists.

This mini-review aims to present some recent developments in pollutant – BVOCs chemistry arbitrarily considered important by the author. It also refers to the ARW objectives listed in the Preface to this volume: sources of HO_2 radicals, influence of HONO on atmospheric chemistry, and reactions of nitroaromatics. The leitmotiv of the talk is isoprene which I know well and consider a very important atmospheric constituent.

16.2 Aqueous Phase Chemistry

Aqueous phase reactions of BVOCs, and other trace constituents of the atmosphere were reviewed in the EUROTRAC volumes [36, 37, 47], followed by extensive journal reviews [17, 18]. Recent works were described in the following sections arranged after the reactants and most important products.

16.2.1 Isoprene

The aqueous-phase chemistry of isoprene was reviewed in the proceedings of two previous ARW meetings [32, 33]. Since then, only a few laboratories continued the work. Nozière repeated the experiments carried out by Claeys et al. [6] to show the aqueous-phase reactions of isoprene, H_2O_2 and H_2SO_4 produced racemic mixtures of methyl tetrols [30]. Using more data from smog chamber experiments and from the analyses of ambient aerosol from Aspverten, Sweden, these authors claimed that the stereochemical speciation of aerosol components could indicate the primary or secondary origin thereof. Consequently, they argued that 2-methyltetrols were not necessarily the tracers for the photochemical transformation of isoprene in the atmosphere.

Simple cuvette experiments on isoprene photo-oxidation in concentrated aqueous solutions of ammonium and sodium sulphates showed that the radical-initiated transformation produced organosulphates and surface active compounds [29]. However, the chemical mechanism involved has not been sufficiently elucidated.

The reaction of isoprene with OH radicals was studied in a 2.1 l aqueous-phase photoreactor with a minimal gas headspace [20]. The experiments were carried out at 10 °C and pH = 7 or 4, the latter probably adjusted with H_2SO_4. The authors used ion chromatography and ion-trap mass spectrometry with electrospray ionisation to identify many reaction products – several carbonyls: methacrolein (MACR, 10.9 ± 1.1%), methyl vinyl ketone (MVK, 24.1 ± 0.8%), formaldehyde, acetaldehyde, glyoxal (GL) and methylglyoxal (MG); organic acids: formic, acetic, propionic, pyruvic and oxalic; as well as high molecular weight (HMW) products with regular patterns of m/z differences: 12, 14 and 16 amu. The carbon balance of the products equalled 50% of consumed isoprene, HMW excluded. Using a competitive-kinetics method with salicylic acid as a reference compound, Huang

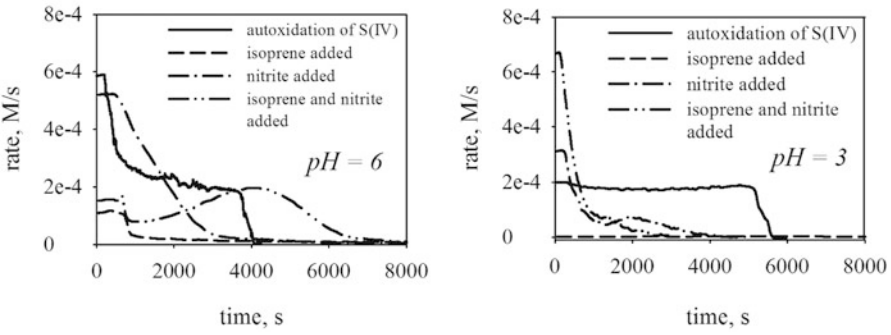

Fig. 16.1 Influence of isoprene and sodium nitrite on the rate of S(IV) autoxidation catalysed by $MnSO_4$ in a stirred batch reactor, at 25 °C and for different initial pH of solutions; initial concentrations of reactants were: 1 mM S(IV) (Na_2SO_3/$NaHSO_3$); 0.25 mM O_2; 0.01 mM $MnSO_4$; 0.1 mM C_5H_8; 0.1 mM $NaNO_2$; initial acidity of solutions was adjusted using sodium pyrosulphite and sulphuric acid

and co-workers determined a relative rate constant for the reaction of isoprene with OH radicals: $1.2(\pm 0.2) \times 10^{10}$ M^{-1} s^{-1}, using a rate constant for salicylic acid with OH of 1.6×10^{10} M^{-1} s^{-1}. They proposed a plausible chemical mechanism and run some box model simulations to test it.

From our own laboratory came the study of kinetic influence of HONO/$NaNO_2$ on the aqueous-phase reaction of isoprene with sulphate radicals formed in situ by the Mn-catalysed autoxidation of sulphite [22]. We found that nitrite and nitrous acid accelerated the autoxidation both in the presence or absence of isoprene (Fig. 16.1). The conclusion directly pertains to one of the objectives of this ARW.

We analysed the products of the aforementioned reactions using offline mass spectrometry with electrospray ionisation in negative mode (ESI/MS and ESI/MS/MS) to identify organosulphates similar to those formed in the absence of nitrite and HONO [35]. Failure to observe organonitrates and mixed S-N organic compounds might result from inadequate analytical procedures used. The chemical mechanism involved may not be simple, as it combines the oxidation of inorganic sulphites and nitrites, or SO_2 and HONO, with the oxidation of isoprene. Already a convolution of two relatively simple inorganic oxidations appears quite complicated, as shown in Fig. 16.2, presented here without literature references [34]:

I would also like to recall one of our older works because it matches one of the ARW objectives – the recycling of HO_2 radicals. A mechanism describing reactions of isoprene in aqueous solutions which are initiated by sulphoxy radical-anions [35] includes a split in which a sulphate or sulphite substituted alkoxy radical reacts either with dissolved oxygen to produce a substituted aldehyde and HO_2, or with a sulphite ion to produce a substituted alcohol and a sulphoxy radical:

The branching shown in Scheme 16.1 is quantitatively controlled by the proportion of sulphite to oxygen, the latter enhancing the HO_2 production.

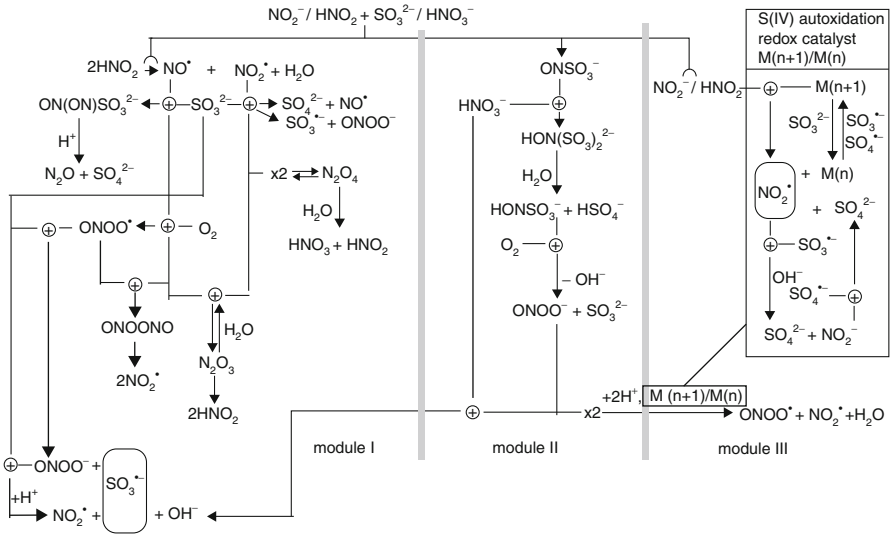

Fig. 16.2 Plausible chemical reactions involved in the oxidation of inorganic sulphites and nitrites in aqueous solutions; some steps in the scheme may require special conditions to proceed, such as high acidity or presence of transition metal catalysts (M)

Scheme 16.1 Formation of HO_2 radicals during aqueous-phase oxidation of isoprene

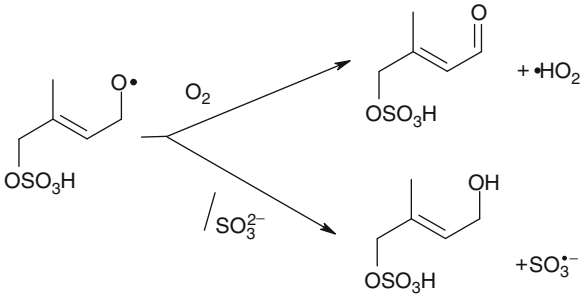

16.2.2 Primary Products of Isoprene Oxidation

Organosulphates and surface active compounds were obtained from the photooxidation of MVK and MACR in cuvette experiments analogous to those for isoprene [29]. Reactions were enhanced by concentrated ammonium and sodium sulphates.

Zhang and coworkers studied the reactions of MVK and MACR with OH radicals obtained by the photolysis of H_2O_2 [49]. The experimental setup and procedures were similar to those described above for isoprene [20], but the acidity of solutions (pH = 4) was not varied. The authors identified the following products: formaldehyde, methylglyoxal, formic acid, acetic acid, pyruvic acid, oxalic acid and High Molecular Weight products (m/z = 150–300). For MVK, glyoxal and

malonic acid were also identified. Zhang also proposed a chemical mechanism for each transformation. The product findings were generally consistent with those from another laboratory [25]. Relative rate constants for reactions of MACR and MVK with OH radicals were determined later at 10 °C by a competitive method described above for isoprene [20]: $(1.3 \pm 0.2) \times 10^{10}$ M^{-1} s^{-1} and $(1.2 \pm 0.1) \times 10^{10}$ M^{-1} s^{-1}, respectively. The rate constant for MACR obtained from stirred tank experiments at 6 °C, with 1-propanol as a reference compound was slightly lower: $(5.8 \pm 0.9) \times 10^{9}$ M^{-1} s^{-1} [25]. The rate constants obtained in another laboratory using a Laser Flash Photolysis – Long Path Laser Absorption method with thiocyanate as a reference [44] compared well for MACR: $(9.6 \pm 1.3) \times 10^{9}$ M^{-1} s^{-1}; and were slightly lower for MVK: $(5.3 \pm 0.5) \times 10^{9}$ M^{-1} s^{-1}. The latter work provided a comprehensive set of rate constants for reactions of OH radicals with MACR, MVK, methacrylic acid (MAA) and methacrylate ions (MAA^{-}) in the form of Arrhenius equations [44]. We also showed that the reactions of MAA and MAA^{-} were fully controlled by diffusion, while other reactions were close to the diffusion limit (Table 16.1).

Reactions of MACR and MVK with ozone were studied at 4–40 °C in a dark 500 ml aqueous-phase reactor [5]. The acidity of reacting solutions varied from pH = 3–7. Reaction products were analysed using high performance liquid chromatography preceded by derivatisation of carbonyl analytes, or appended with post column derivatisation in the case of peroxide analytes. Organic acids were determined with ion-chromatography. Ozone concentration in solution was measured using the indigo disulphonate spectrometry. Molar yields of the products were practically independent of pH and temperature. Ozonolysis of MACR produced hydroxylmethyl hydroperoxide (HMHP, molar yield of ~70%), formaldehyde (~32%) and methylglyoxal (~99%), while MVK turned into HMHP (~69%), HCHO (~13%), methylglyoxal (~75%) and pyruvic acid (~24%). Carbon balance closed at 99.6 ± 6.3% for MACR, and at 95.4 ± 9.7% for MVK. The authors proposed chemical mechanisms for the reactions considered.

The reaction of MACR with H_2O_2 in aqueous solutions of pH = 2–7 was found rather slow. The upper limit of the second-order rate constant was 0.13 M dm^{-3} s^{-1} at 298 K; as determined from experiments with ozonolysis of α-pinene [48]. Our own on-going ISOMASSKIN project deals with aqueous-phase reactions of MACR, MVK and MAA with sulphate radicals SO_4^{-}. Preliminary results indicate formation of organosulphates. The reactions are generally slower than the corresponding reactions with hydroxyl radicals.

16.2.3 Terpenes

Organosulphates and surface active compounds were obtained from the photooxidation of α-pinene in cuvette experiments analogous to those for isoprene [29]. Reactions were also enhanced by concentrated ammonium and sodium sulphates.

Aqueous reactions of α-pinene and β-pinene with ozone were studied using the methodology and conditions described above for MACR and MVK work by Chen

Table 16.1 Rate constants and Arrhenius parameters for reactions of isoprene oxidation products with OH radicals; observed (k_{obs}) and corrected for diffusional limitation (k_{corr}), valid for 5–45°C; after [42]

				MAA	
		MACR	MVK	pH = 3	pH = 7
$k_{25\ obs}$	$M^{-1}\ s^{-1}$	$(1.02 \pm 0.08) \times 10^{10}$	$(7.4 \pm 0.7) \times 10^{9}$	$(1.17 \pm 0.11) \times 10^{10}$	$(1.20 \pm 0.10) \times 10^{10}$
A_{obs}	$M^{-1}\ s^{-1}$	$(7.11 \pm 5.90) \times 10^{11}$	$(8.96 \pm 2.35) \times 10^{11}$	$(1.16 \pm 0.47) \times 10^{12}$	$(2.13 \pm 1.45) \times 10^{12}$
E_{obs}	$kJ\ M^{-1}$	10.00 ± 2.05	11.90 ± 0.64	11.45 ± 1.00	12.90 ± 1.68
$k_{25\ cor}$	$M^{-1}\ s^{-1}$	$(4.4 \pm 0.4) \times 10^{10}$	$(1.7 \pm 0.9) \times 10^{10}$	$(1.66 \pm 0.12) \times 10^{11}$	$(2.61 \pm 0.23) \times 10^{11}$
A_{cor}	$M^{-1}\ s^{-1}$	$(4.75 \pm 13.4) \times 10^{13}$	$(2.62 \pm 1.32) \times 10^{13}$	–	–
E_{cor}	$kJ\ M^{-1}$	18.35 ± 6.96	18.20 ± 1.22	–	–

[48]. Analysis of the reaction products showed that, irrespectively of temperature and solution acidity, H_2O_2 was formed with high yield from both pinenes, MACR was formed only from α-pinene, and HCHO – only from β-pinene. The authors suggested chemical mechanisms matching the product distributions observed.

The hope is growing as well as evidence that reactions on aqueous surfaces in the atmosphere can significantly increase our understanding of formation and composition of secondary organic aerosol. In a very interesting study, Enami and coworkers examined the early stages of ozone reaction with β-carophyllene (β-C) in a spraying chamber of an electrospray ionisation mass spectrometer. A few ppm of ozone were introduced in the stream of a flushing gas (nitrogen), while 4.4 mM β-C was added to acetonitrile/water solutions (4:1 by volume) sprayed into the chamber [11]. Contact time for the reactions was 10 μs; the reaction products were ejected to the gas phase and mass-detected within 1 ms. Basing on the MS spectra, the authors suggested the structures of carboxylic acids produced as well as novel reaction mechanisms involved. They also showed that reactions at aqueous interfaces can be significantly faster than processes based on the equilibrium partitioning of reactants to the aqueous phase commonly used in atmospheric models.

16.2.4 Various Organics

Reaction of glyoxal with OH radicals generated by photolysis of H_2O_2 was studied at room temperature in a simple 1 dm^3 photoreactor [23]. Initial concentrations of reactants were 3 and 13.3 mM, respectively. Each experiment lasted 5 h. The reacting solution was continuously sampled, atomised, dried and analysed with an Aerodyne time-of-flight Aerosol Mass Spectrometer. Additional samples of solutions were analysed offline using an ionic chromatograph with conductivity detector and a Total Organic Carbon analyser. The products identified included oxalic acid, glyoxylic acid and formic acid. Concentration vs. time profiles of these products and of glyoxal were presented. The authors suggested a chemical mechanism of the reaction, which can be used in atmospheric modelling.

Tan et al. studied the aqueous-phase reaction of methylglyoxal (30–3,000 μM) with OH radicals (~4×10^{-12} M) generated by the photolysis of H_2O_2, with and without H_2SO_4 added [46]. They used a 1 dm^3 batch reactor at 25°C. The acidity of reacting solutions varied from pH = 6.7–2.1. Ion chromatography supported occasionally with ESI-MS detection was used to identify and quantify several organic acids produced: pyruvic, acetic, formic, glyoxylic, glycolic, malonic, succinic and oxalic. Production of larger carboxylic acids (> C4) and high molecular weight products increased at higher initial concentrations of methylglyoxal. Selected samples of reacting solutions were analysed for total organic carbon. The authors used a dilute aqueous chemistry model for methylglyoxal – OH reaction to accurately reproduce the experimental time profiles of pyruvic acid, oxalic acid and TOC.

Chemical transformation of (i) 0.2 M formaldehyde, (ii) 2 M formaldehyde/methylglyoxal (MG) mixtures, (iii) 0.5 M acetaldehyde/MG mixtures and (iv) 2 M acetaldehyde/MG mixtures in 3.1 M solutions of ammonium sulphate were followed

using Aerosol Chemical Ionisation Mass Spectrometry [24]. The pH of solutions was 2.7–3.1. Another aim of the work was to measure the surface tension depression in transforming systems, as several products were expected to be surface active. The solutions were prepared and stored in ampules for 24 h, then diluted with water and nebulised for ACIMS analysis. Products identified in the experiments included respectively:

(i) formic acid, formaldehyde hemiacetals and hemiacetal oligomers, and hemiacetal sulphate;
(ii) formic acid, formaldehyde hemiacetal oligomers, MG aldol and hemiacetal, formaldehyde/MG hemiacetal oligomers, and cyclic formaldehyde acetals;
(iii) hydrated acetaldehyde, formic, pyruvic, glyocylic, glycolic acids, acetaldehyde and MG aldols, acetaldehyde aldol oligomers, acetaldehyde/MG aldol, MG hemiacetal;
(iv) hydrated A, formic, acetic, and crotonic acids, acetaldehyde and MG hemiacetals, MG and MG/A aldols.

The authors concluded that VOCs constitute a secondary source of surface-active organic components of atmospheric aerosol.

Direct photolysis of phenolic compounds (phenol, quaiacol and syringol) in aqueous solutions as well as reactions thereof with OH radicals generated by photolysis of H_2O_2 were studied in a series of cuvette experiments [41]. The solutions of pH = 5–7 were illuminated with simulated sunlight and monitored with HPLC/UV-VIS until half of the initial phenol was consumed. Then, part of the solutions was blown to dryness with nitrogen at room temperature. The solid residue was dissolved in water, nebulised into aerosol, dried and analysed using a high-resolution aerosol mass spectrometer. In addition, small inorganic and organic acids were determined with ion chromatography. Identified products included oxalic acid and other small acids not identified, as well as dimers and oligomers of phenolic compounds.

Since atmospheric chemistry of nitroaromatics is another objective of this ARW, I would like to remind an older work showing that nitrophenols reacted promptly with sulphate radical-anions in aqueous solutions [51]. The rate constants of these reactions were determined. They were generally smaller than the corresponding rate constants determined for chlorophenols [50]. However, all the constants fitted well a logarithmic-linear correlation against the strength of phenolic OH bond (Fig. 16.3).

16.2.5 Organosulphates and Organonitrates

Organosulphates and organonitrates are still a hot research topic among the aerosol community. Utilising developments in mass spectrometric techniques, researchers continue to discover these compounds in the free-troposphere aerosol [13], in field samples of ambient aerosol [15, 16, 21], and in aerosol produced in laboratory experiments [28]. It was shown that hydroxyepoxides formed by the OH-induced

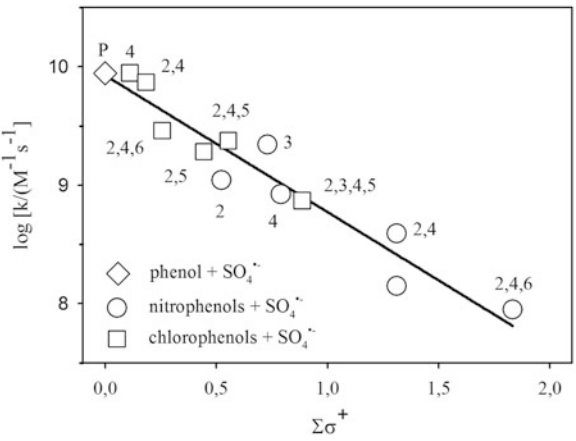

Fig. 16.3 Rate constants for reactions of chlorophenols and nitrophenols with sulphate radical-anions (25°C) correlated well against the strength of the phenolic OH bond

photoxidation of isoprene in the gas phase at low NO_x conditions [31] partitioned to the aerosol phase undergoing acid-catalysed ring opening followed by nucleophilic addition of inorganic sulphate, which produced a hydroxyl sulphate ester [42]. The mechanism involved included the addition of water, 2-methyltetrols and hydroxyl sulphate esters, if present, leading to C_5-alkane triols, 2-methyltetrols, as well as dimers and higher oligomers of tetrols and hydroxyl sulphate esters. On the other hand, a mechanism of organonitrate formation proposed for high-NO_x conditions included gas phase photoxidtation of isoprene to methacrolein, methacrylolperoxynitrate and C_4-hydroxynitrate peroxyacyl nitrate. The latter product partitioned to the aerosol phase and decomposed into 2-methylglyceric acid and its nitrate ester, which eventually formed higher oligomers [42].

Reactions of inorganic nitrates and sulphates with hydroxyepoxides produced by gas-phase photooxidation of isoprene were studied in the bulk aqueous solutions using NMR techniques [9]. Products observed included primary and tertiary organosulphates and organonitrates. Primary organonitrates and primary organosulphates were resistant to hydrolysis (i.e. nucleophilic substitution of nitrate or sulphate groups by OH from water). On the other hand, tertiary organonitrates underwent fast nucleophilic substitution with water or sulphate ions, which was much faster than the hydrolysis of tertiary organosulphates. The observation may explain why organonitrates occur in the atmosphere more rarely than organosulphates. The NMR work was continued [19], to determine the rates of the hydrolysis reactions and, in some cases, the corresponding thermodynamic data. Calculation of electronic structures was also carried out to determine the enthalpy of hydrolysis for these species, and for the previously studied isoprene-derived species. The results suggest that while organonitrates and organosulphates are thermodynamically unstable with respect to the corresponding alcohols at standard state, only the tertiary organonitrates (and perhaps some tertiary organosulphates) are able to efficiently hydrolyse on SOA timescales and acidities.

The reader is referred to chapter by Rafal Szmigielski in this book to read more on organosulphates and organonitrates in urban atmospheres.

16.3 Heterogeneous Glimpses

Reactive uptake of isoprene on films of concentrated H_2SO_4 (78–93 wt.%) and on surfaces of bulk solutions of the acid (60–85 wt.%) was studied at 220–260 K, using respectively a high vacuum Knudsen reactor (10^{-7}–10^{-4} Torr) and an infrared gas cell (0.1–50 Torr) [7]. Concentration of gaseous isoprene was monitored with a quadrupole mass spectrometer with electron ionisation and a FTIR spectrometer, respectively. The uptake coefficient increased with the concentration of the acid from 10^{-7} at 60% to 10^{-5} at 85%, and from 10^{-4} at 78% to 10^{-3} at 93%. Products of isoprene reactions with H_2SO_4 in the Knudsen reactor were identified online using FTIR-RAS (reflectance absorbance spectroscopy). In addition, the products were extracted both from the film and bulk samples with methylene chloride, derivatised and analysed using offline GC/MS, Yellow/red coloured monoterpenes and cyclic sesquiterpenes were tentatively identified, while organosulphate compounds were not observed. Interestingly, the terpenes partitioned back to the gas phase when water was added to post-reaction solutions containing 85% H_2SO_4. It is worth to remind that H_2SO_4 has power to increase the heterogeneous conversion of isoprene into 2-methyltetrols and related oxygenated products such as 4-hydroxy-1,3-dioxo-2-methylbutane [6, 45].

The Merriam Webster [27] says grime is all accumulated dirtiness and disorder. Accordingly, the urban grime is a mixture of all possible organic and inorganic components that covers city surfaces. It contains everything, from metals and inorganic sulphates and nitrates up to PAHs. Chemistry of urban grime has been largely unexplored, but is expected to influence urban air quality [1]. These authors studied heterogeneous reactions of NO_2 on solid films consisting of pyrene, a model PAH compound, and KNO_3. They used a flow tube photoreactor (300–420 nm) to pass air-NO_2 mixtures (30–120 ppbv) over the film at 288 K. NO_2 and gaseous reaction products were monitored with a chemiluminescent analyser and a carbonate denuder. The film products were analysed offline using gas chromatography with mass spectrometric detection and ionic chromatography. Steady-state reactive uptake coefficient increased linearly with the intensity of the irratiation, revealing a photoinduced nature of the process. Gaseous products of the reaction included NO and HONO, while the film products were nitrite and traces of 1-nitropyrene. The post-reaction films irradiated in NO_2-free atmosphere released gaseous HONO. The results indicated urban grime can be a HONO source, and consequently the OH source in the urban atmosphere.

The last heterogeneous work mentioned here dealt with the analysis of laboratory aerosols and SOA surfaces by titrating the surface-embedded functional groups with several probe gases [38], a technique well known in the field of heterogeneous catalysis [3, 39]. The authors used a Knudsen flow reactor equipped with effusive molecular-beam phase sensitive mass spectrometric detector with electron ionisation. The probe gases included trimethylamine

(which shows Brønsted and Lewis acid sites), hydroxylamine (carbonyl groups of aldehydes and ketones), hydrochloric acid and trifluoroacetic acid (Lewis base sites), nitrogen dioxide and ozone (reduced sites). The advantage of the analysis is that it reveals the potential reactivity of aerosol surfaces, which pertains not only to atmospheric chemistry, but also to the health effects of inhaled particles.

16.4 Conclusions

Sound understanding of BVOCs interaction with inorganic, and possibly organic pollutants in urban atmospheres can be one of the key factors essential for successful attempts to improve the urban air quality using urban vegetation. The interaction processes take place in the atmosphere, as well as on surfaces and inside plant organisms which, on the other hand, constitute a main source of BVOCs. Tackling such a complex problem requires interdisciplinary cooperation of scientist ranging from molecular biologists to atmospheric chemists and meteorologists. Although such cooperation has already been initiated through several programmes, namely EUROTRAC, EUROTRAC2, Accent, Accent Plus, Introp, Vocbas and Eurovol, it still needs further enhancement.

Several recent works by atmospheric chemists reviewed here indicated plausible areas of common research. They included studies on aqueous-phase chemistry of isoprene and terpenes, as well as gas-phase oxidation products thereof, which involved both radical initiated reactions and direct reactions with inorganic acids and salts. The importance of reactions that take place at water-air interfaces has been emphasised, especially in the case of less soluble volatiles, which can react with the aqueous phases faster and more efficiently than is predicted from the equilibrium solubility relations.

Organosulphates and organonitrates derived from isoprene continue to be intriguing products of atmospheric chemistry. A recently preferred mechanism involves direct nucleophilic substitution of inorganic ions in products of decomposition of dissolved hydroxyepoxides, while radical substitution at double bonds has not been ruled out.

Objectives of this workshop were addressed by showing that: the aqueous phase oxidation of isoprene in the presence of dissolved sulphites is a source of HO_2 radicals; the relatively simple aqueous-phase oxidation of sulphur dioxide is significantly complicated by the involvement of nitrite ions or HONO; simple nitrophenols react in the aqueous phase with sulphate radical-anions, also affecting the oxidation of S(IV).

Future directions of research may include:

(i) increased involvement in aqueous-phase chemistry (poorly soluble reactant BVOCs; more pollutants, including organics; fast reactions at water-air interfaces);

(ii) enhanced heterogeneous kinetic studies;
(iii) reactions of BVOCs and pollutants on plant surfaces and inside plant structures;
(iv) field campaigns extended beyond sampling to constitute the open laboratory experiments, the idea originally brought to my attention by [5].

Acknowledgements The author gratefully acknowledges the financial support of this research work by the European Commission through the Marie Curie European Reintegration Grant (ISOMASSKIN project), and by Polish Ministry of Science and Higher Education through the science funds 2011–2012 granted for the realisation of the international co-financed project.

References

1. Ammar R, Monge ME, George C, D' Anna B (2010) Photoenhanced NO_2 loss on simulated urban grime. Chem Phys Chem 11(18):3956–3961
2. Bell JNB, Treshow M (2002) Air pollution and plant life. Wiley, Chichester
3. Bonarowska M, Malinowski A, Karpiński Z (1999) Hydrogenolysis of C–C and C–Cl bonds by Pd–Re/Al_2O_3 catalysts. Appl Catal Gen 188(1–2):145–154
4. Calfapietra C (2010) Private communication
5. Chen ZM, Wang HL, Zhu LH, Wang CX, Jie CY, Hua W (2008) Aqueous-phase ozonolysis of methacrolein and methyl vinyl ketone: a potentially important source of atmospheric aqueous oxidants. Atmos Chem Phys 8:2255–2265
6. Claeys M, Wang W, Ion AC, Kourtchev I, Gelencsér A, Maenhaut W (2004) Formation of secondary organic aerosols from isoprene and its gas-phase oxidation products through reaction with hydrogen peroxide. Atmos Environ 38(25):4093–4098
7. Connelly BM, Tolbert MA (2010) Reaction of isoprene on thin sulfuric acid films: kinetics, uptake, and product analysis. Environ Sci Technol 44(12):4603–4608
8. Costa D (2011) Air quality in a changing climate. Environ Health Perspect 119:4
9. Darer AI, Cole-Filipiak NC, O'Connor AE, Elrod MJ (2011) Formation and stability of atmospherically relevant isoprene-derived organosulfates and organonitrates. Environ Sci Technol 45(5):1895–1902
10. Dicke M, Loreto F (2010) Induced plant volatiles: from genes to climate change. Trends Plant Sci 15(3):115–117
11. Enami S, Hoffmann MR, Colussi AJ (2010) Prompt formation of organic acids in pulse ozonation of terpenes on aqueous surfaces. J Phys ChemLett 1(15):2374–2379
12. Escobedo FJ, Kroeger T, Wagner JE (2011) Urban forests and pollution mitigation: analyzing ecosystem services and disservices. Environ Pollut 159(8–9):2078–2087
13. Froyd KD, Murphy SM, Murphy DM, de Gouw JA, Eddingsaas NC, Wennberg PO (2010) Contribution of isoprene-derived organosulfates to free tropospheric aerosol mass. Proc Natl Acad Sci USA 107(50):21360–21365
14. Glaser E (2011 Sept) Cities: engines of innovation. Scientific American
15. Gómez-González Y, Surratt JD, Cuyckens F, Szmigielski R, Vermeylen R, Jaoui M, Lewandowski M, Offenberg JH, Kleindienst TE, Edney EO, Blockhuys F, Van Alsenoy C, Maenhaut W, Claeys M (2008) Characterization of organosulfates from the photooxidation of isoprene and unsaturated fatty acids in ambient aerosol using liquid chromatography/(-) electrospray ionization mass spectrometry. J Mass Spectrom 43(3):371–382
16. Hatch LE, Creamean JM, Ault AP, Surratt JD, Chan MN, Seinfeld JH, Edgerton ES, Su Y, Prather KA (2011) Measurements of isoprene-derived organosulfates in ambient aerosols by aerosol time-of-flight mass spectrometry – part 2: temporal variability and formation mechanisms. Environ Sci Technol 45(20):8648–8655

17. Herrmann H (2003) Kinetics of aqueous phase reactions relevant for atmospheric chemistry. Chem Rev 103(12):4691–4716
18. Herrmann H, Hoffmann D, Schaefer T, Bräuer P, Tilgner A (2010) Tropospheric aqueous-phase free-radical chemistry: radical sources, spectra, reaction kinetics and prediction tools. Chemphyschem 11(18):3796–3822
19. Hu KS, Darer AI, Elrod MJ (2011) Thermodynamics and kinetics of the hydrolysis of atmospherically relevant organonitrates and organosulfates. Atmos Chem Phys 11(16):8307–8320
20. Huang D, Zhang X, Chen ZM, Zhao Y, Shen XL (2011) The kinetics and mechanism of an aqueous phase isoprene reaction with hydroxyl radical. Atmos Chem Phys 11(15):7399–7415
21. Kristensen K, Glasius M (2011) Organosulfates and oxidation products from biogenic hydrocarbons in fine aerosols from a forest in North West Europe during spring. Atmos Environ 45(27):4546–4556
22. Kuznietsova I, Rudzinski K, Szmigielski R, Gmachowski L (2011) Influence of nitrite ions and nitrous acid on reactions of isoprene with sulfoxy radical anions. Paper presented at the 3rd Urbino symposium, Urbino
23. Lee AKY, Zhao R, Gao SS, Abbatt JPD (2011) Aqueous-phase OH oxidation of glyoxal: application of a novel analytical approach employing Aerosol Mass Spectrometry and complementary off-line techniques. J Phys Chem A 115(38):10517–10526
24. Li Z, Schwier AN, Sareen N, McNeill VF (2011) Reactive processing of formaldehyde and acetaldehyde in aqueous aerosol mimics: surface tension depression and secondary organic products. Atmos Chem Phys 11(22):11617–11629
25. Liu Y, El Haddad I, Scarfogliero M, Nieto-Gligorovski L, Temime-Roussel B, Quivet E, Marchand N, Picquet-Varrault B, Monod A (2009) In-cloud processes of methacrolein under simulated conditions – Part 1: aqueous phase photooxidation. Atmos Chem Phys 9(14): 5093–5105
26. Loreto F, Schnitzler J-P (2010) Abiotic stresses and induced BVOCs. Trends Plant Sci 15(3): 154–166
27. Merriam-Webster: Merriam Webster online dictionary (2012) http://www.merriam-webster.com/
28. Nguyen TB, Laskin J, Laskin A, Nizkorodov SA (2011) Nitrogen-containing organic compounds and oligomers in secondary organic aerosol formed by photooxidation of isoprene. Environ Sci Technol 45(16):6908–6918
29. Nozière B, Ekström S, Alsberg T, Holmström S (2010) Radical-initiated formation of organosulfates and surfactants in atmospheric aerosols. Geophys Res Lett 37(5):L05806
30. Nozière B, González NJD, Borg-Karlson A-K, Pei Y, Redeby JP, Krejci R, Dommen J, Prevot ASH, Anthonsen T (2011) Atmospheric chemistry in stereo: a new look at secondary organic aerosols from isoprene. Geophys Res Lett 38(11):L11807
31. Paulot F, Crounse JD, Kjaergaard HG, Kürten A, St Clair JM, Seinfeld JH, Wennberg PO (2009) Unexpected epoxide formation in the gas-phase photooxidation of isoprene. Science 325(5941):730–733
32. Rudziński KJ (2006) Heterogeneous and aqueous-phase transformations of isoprene. In: Barnes I, Rudziński KJ (eds) Environmenatl simulation chambers: application to atmospheric chemical processes. Springer, Dordrecht, pp 261–278
33. Rudziński KJ (2008) Undiscovered chemistry – is it important for mechanisms and models? In: Barnes I, Kharytonov M (eds) Simulation and assessment of chemical processes in a multiphase environment. Springer, Dordrecht, pp 232–253
34. Rudziński KJ, Ziajka J, Szeremeta E, Ulejczyk M (2005) Cross-activation of atmospheric pollutants – reactions coupled with S(IV) autoxidation. Institute of Physical Chemistry PAS, Warsaw, pp 1–16
35. Rudziński KJ, Gmachowski L, Kuznietsova I (2009) Reactions of isoprene and sulphoxy radical-anions – a possible source of atmospheric organosulphites and organosulphates. Atmos Chem Phys 9(6):2129–2140
36. Schurath U, Neumann K-H (eds) (2003) CMD chemical mechanism development. Forschungszentrumc, Karlsruhe

37. Schurath U, Peeters J, Wayne RP, Moortgat GK, Grgic I, George C, Herrmann H, Poppe D (2003) Chemical mechanism development: overview of subproject CMD. In: Midgley PM, Reuther M (eds) Towards cleaner air for Europe – science, tools and applications, Part 2. Overviews from the final reports of the EUROTRAC-2 subprojects. Margraf Verlag, Weikersheim
38. Setyan A, Sauvain J-J, Demirdjian MB, Rossi MJ (2010) Probing functional groups at the gas–aerosol interface using heterogeneous titration reactions: a tool for predicting aerosol health effects? Chemphyschem 11(18):3823–3835
39. Skotak M, Karpiński Z, Juszczyk W, Pielaszek J, Kępiński L, Kazachkin DV, Kovalchuk VI, d'Itri JL (2004) Characterization and catalytic activity of differently pretreated Pd/Al_2O_3 catalysts: the role of acid sites and of palladium–alumina interactions. J Catal 227(1):11–25
40. Solomon PA (2011) Air pollution and health: bridging the gap from sources to health outcomes. Environ Health Perspect 119(4)
41. Sun YL, Zhang Q, Anastasio C, Sun J (2010) Insights into secondary organic aerosol formed via aqueous-phase reactions of phenolic compounds based on high resolution mass spectrometry. Atmos ChemPhys 10(10):4809–4822
42. Surratt JD, Chan AWH, Eddingsaas NC, Chan M, Loza CL, Kwan AJ, Hersey SP, Flagan RC, Wennberg PO, Seinfeld JH (2010) Reactive intermediates revealed in secondary organic aerosol formation from isoprene. Proc Natl Acad Sci USA 107(15):6640–6645
43. Susca T, Gaffin SR, Dell'Osso GR (2011) Positive effects of vegetation: urban heat island and green roofs. Environ Pollut 159(8–9):2119–2126
44. Szeremeta E, Barzaghi P, Böge O, Herrmann H, Gmachowski L, Rudzinski KJ (2009) Aqueous-phase reactions of isoprene oxidation products with hydroxyl radicals. In: Sandro F, Michela M (eds) Secondary aqueous-phase reactions of isoprene oxidation products with hydroxyl radicals. Proceedings of second ACCENT symposium. ARACNE editrice, Rome, pp 1–4 (CD)
45. Szmigielski R, Vermeylen R, Dommen J, Metzger A, Maenhaut W, Baltensperger U, Claeys M (2010) The acid effect in the formation of 2-methyltetrols from the photooxidation of isoprene in the presence of NO_x. Atmos Res 98(2–4):183–189
46. Tan Y, Carlton AG, Seitzinger SP, Turpin BJ (2010) SOA from methylglyoxal in clouds and wet aerosols: measurement and prediction of key products. Atmos Environ 44(39): 5218–5226
47. Warneck P (ed) (1996) Heterogeneous and liquid phase processes. Springer, Berlin/Heidelberg
48. Zhang X, Chen Z, Wang H, He S, Huang D (2009) An important pathway for ozonolysis of alpha-pinene and beta-pinene in aqueous phase and its atmospheric implications. Atmos Environ 43(29):4465–4471
49. Zhang X, Chen ZM, Zhao Y (2010) Laboratory simulation for the aqueous OH-oxidation of methyl vinyl ketone and methacrolein: significance to the in-cloud SOA production. Atmos Chem Phys 10(19):9551–9561
50. Ziajka J, Rudzinski KJ (2007) Autoxidation of SIV inhibited by chlorophenols reacting with sulfate radicals. Environ Chem 4(5):355–363
51. Ziajka J, Rudzinski K (2009) Reactions of chloro- and nitrophenols with sulphate radicals. In: Fuzzi S, Maione M (eds) Secondary reactions of chloro- and nitrophenols with sulphate radicals. Proceedings second ACCENT symposium 2007. Aracne editrice, Rome, pp 1–3 (CD)

Chapter 17
Chemistry of Organic Sulfates and Nitrates in the Urban Atmosphere

Rafal Szmigielski

Abstract The paper overviews the current state of knowledge regarding the origin, formation mechanisms, properties and atmospheric implications of organic sulfates (organosulfates, OS) and organic nitrates (organonitrates, ON). Based on field measurements and smog chamber experiments, these esters have been proved to be relevant components of ambient atmospheric aerosols. Despite the fact that chemical knowledge on esters of sulfuric and nitric acids with simple alcohols has been well documented since the advent of classical organic chemistry (a second part of the nineteenth century), it has been only a recent decade since the discovery of these species in the airborne particulate matter attracted attention of the atmospheric community owing to their enhanced polarity and hydrophilic properties. The advances in the field of analytical instrumentations, chiefly in mass spectrometry, made it possible to provide a detailed characterization of organo-sulfates/nitrates at the molecular level. The composition of aerosol samples collected from various field campaigns showed clearly that organosulfates/nitrates may serve as excellent molecular tracers for anthropogenically affected aerosol sources, as it is the case of urban atmosphere.

Keywords Organosulfates (OS) • Organonitrates (ON) • Inorganic pollutants • Ambient Aerosol • Urban air quality • Atmospheric sciences • Mass spectrometry

17.1 Introduction

The atmosphere of urbanized regions is a complex system where numerous physico-chemical dark and/or light-induced transformations take place. On one side, the living vegetation introduces to the atmosphere a number of biogenic

R. Szmigielski (✉)
Laboratory of Environmental Chemistry, Institute of Physical Chemistry, Polish Academy of Sciences (PAS), Kasprzaka 44/52 St., 01-224 Warsaw, Poland
e-mail: ralf@ichf.edu.pl

I. Barnes and K.J. Rudziński (eds.), *Disposal of Dangerous Chemicals in Urban Areas and Mega Cities*, NATO Science for Peace and Security Series C: Environmental Security,
DOI 10.1007/978-94-007-5034-0_17,

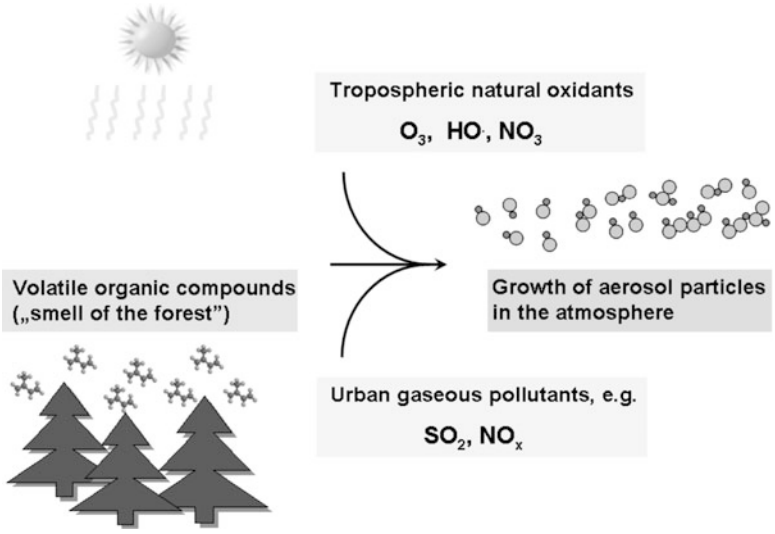

Fig. 17.1 Schematic representation of the atmospheric aerosol network. The network rationalizes the formation of organosulfates and organonitrates – key components of urban SOA – through biogenic and anthropogenic processes

volatile compounds (BVOCs), of which isoprenoid hydrocarbons, i.e., isoprene (C_5H_8), monoterpenes ($C_{10}H_{16}$) and sesquiterpenes ($C_{15}H_{24}$) are the most ubiquitous. Depending on the weather conditions and the emitting source, the emission rate of isoprene ranges from 500 to 750 TgC year^{-1} [22], whereas monoterpenes – from 100 to 127 TgC year^{-1} [2] and sesquiterpenes – from 12 to 100 TgC year^{-1} [21, 45]. This process is schematically shown in Fig. 17.1 as an indisputably relevant part of a complex atmospheric aerosol network.

The BVOC family plays a major role in air quality shaping, secondary organic aerosol (SOA) formation and carbon sequestration. Once emitted to the atmosphere, BVOCs enter a chain of dark and/or sunlight-stimulated chemical reactions with atmospheric oxidants, such as ozone, HO and NO_x (x = 1–3) radicals as well as sulfur-centered radical-anions, leading to a less volatile oxygenated products. In the majority of cases these products are more reactive than initial hydrocarbons (i.e., the C=C double bond turns into the far more polar and reactive C=O double bond), and consequently are prone to further chemical processes, such as oxidation, oligomerization, esterification, condensation etc. As a result, an estimated number of 10,000–100,000 different organic compounds can be formed in the atmosphere [16], most of which belong to the aerosol phase.

The situation is further complicated by the increasing urbanization and industrialization processes that contribute to the release of inorganic pollutants, such as sulfur dioxide and nitrogen oxides, to the atmosphere. In the context of environmental sciences, SO_2 and NO_x are the major anthropogenic pollutants with their global emission rates of 65–90 Tg year^{-1} [35] and 122 Tg year^{-1} [41], respectively.

Numerous studies reported their adverse effects on the biosphere and its habitants with their strong influence on the SOA budget in the highly urbanized regions. Indeed, the recent smog chamber photo-oxidation study on the isoprene SOA formation revealed the enhancement of SOA yield onto acidic particles. In a series of experiments, in which gaseous isoprene oxidation products were passed over a sulfuric acid treated and non-treated quartz-fiber filters, Szmigielski an co-workers have observed the significant enhancement of the organic carbon and 2-methyltetrol amounts on the sulfuric acid-treated filter as compared to non-treated ones [64]. The observation is in line with previous laboratory data [42]. On the other hand, an increased level of nitrogen oxides, which is a typical signature of urban-impacted environments, gives rise to an elevated ozone concentration via a complex reaction chain. Although a clear progress has been recently made in identifying key biogenic and anthropogenic SOA components, significant gaps still remain in our scientific knowledge on the formation, properties and environmental implications of organosulfates and organonitrates – key components of the urban aerosol particles. The objective of this paper is to give a short overview on the significance of these species in the context of atmospheric chemistry.

17.2 A Bit of Statistics

The advances in the analytical instrumentation over last 10 years have opened up new horizons to conduct the identification and quantification of organic components of ambient aerosols at greater signal-to-noise ratios (i.e., with a higher sensitivity). Hyphenated off-line mass spectrometry techniques with a prior GC x GC or UPLC separation along with on-line screening methods such as proton transfer reaction mass spectrometry (PTR-MS) and aerodyne aerosol mass spectrometry (AMS) allow to identify novel components of aerosol samples, ranging from highly polar low-molecular mass compounds, such as OS and ON to amphiphilic (i.e., both hydrophilic and hydrophobic) oligomers, all these species otherwise undetectable with conventional approaches. Comprehensive review papers on this subject have been recently published elsewhere [23, 27, 50, 51].

An eye glimpse on the papers from the last decade dealing with the chemistry of the Earth's atmosphere clearly demonstrates that both organic nitrates and organic sulfates are in the limelight of the research community. In order to clarify this issue I addressed a simple literature query using the two renowned research platforms: SciFinder® (operated by the American Chemical Society; https://scifinder.cas.org/scifinder) and Web of Knowledge® (operated by Thomson Reuters; http://wokinfo.com). In each case the following word phrases were entered and screened in term of a number of papers released between 1946 and 2012: "organosulfate", "organosulfate & atmosphere" and "organosulfate & aerosol" as well as "organonitrate", "organonitrates & atmosphere" and "organonitrates & aerosol". The outcome of the query is summarized in Table 17.1.

Table 17.1 The output from a literature query obtained with SciFinder® and Web of Knowledge® – the two powerful web engines

		Number of papers	
Entry	Searched phrase	SciFinder®	Web of Knowledge®
1	Organosulfate	106	53
2	Organosulfate & aerosol	53	22
3	Organosulfate & atmosphere	33	7
4	Organonitrate	54	21
5	Organonitrate & aerosol	23	14
6	Organonitrate & atmosphere	13	4

The survey covers the time between the onset of 1946 and the end of 2011

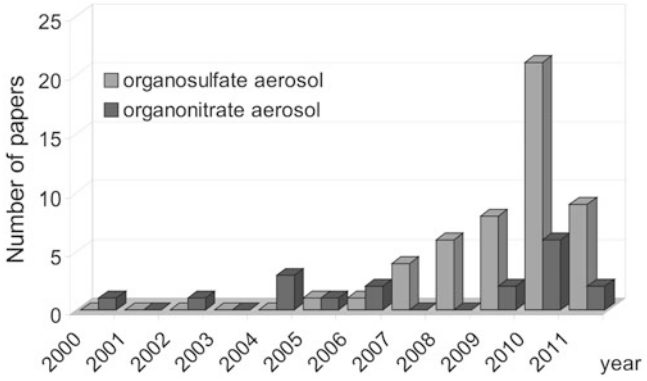

Fig. 17.2 The number of scientific papers released between 2000 and 2011 on organosulfates and organonitrates in the context of atmospheric aerosols obtained with the SciFinder® platform

The comparison of the data implies a certain statistical regularity and thus leads to the following conclusions:

1. Organic sulfates and organic nitrates have become undoubtedly an important research target in the framework of the atmospheric studies;
2. The existence of a regular discrepancy in the data distribution is strongly depended upon the type of a search engine used;
3. The application of the Web of Knowledge engine gives rise to the systematic underestimation.

Regardless the searching method used, one is to take all precautions while looking up the literature since a deployment of a single Internet engine may lead to a painful loss of data.

In the last decade, an increasingly growing number of papers have been observed that dealt with the chemistry of OS and ON in the context of atmospheric aerosols (Fig. 17.2). This trend could be rationalized in terms of specific properties of OS and ON, i.e., their enhanced chemical reactivity and increased affinity to the aqueous phase, both underlying the microphysics of ambient particle growth.

The breakthrough in the research was made during the period of 2005–2007 by a few international research groups. The first evidence was provided by Romero [53] and Reemtsma [52] who reported organosulfates as a new component of ambient aerosols capable of forming humic-like substances (HULIS). HULIS are macromolecular substances containing polysaccharidic and aliphatic residues that have dark yellow to brown color and strongly absorb UV and VIS light. The latter species constitute the major fraction of water-soluble particular matter enhancing the capability of aerosols to act as cloud condensation nuclei (CNN) [18]. However, according to Romero and Reemtsma, the sources and source processes of OS remained unclear. Surratt and co-workers reported organosulfates and nitrooxy-organosulfates as key components of smog chamber generated isoprene SOA [61, 62]. Interestingly, major OS formed from isoprene SOA were detected under ambient conditions at numerous sites in the southeastern U.S. and Europe [1, 15, 17, 24, 34, 59]. These include among others derivatives of polyalcohols (i.e., the 2-methyltetrols), aldehydes (i.e., glyoxal, methylglyoxal) and hydroxycarboxylic acids (i.e., 2-methylglyceric acid, 2-/3-hydroxyglutaric acid, glycolic acid and lactic acid).

The outbreak of data concerning the organosulfates and organonitrates from alpha-/beta-pinene SOA stems from laboratory and field measurements conducted independently by Liggio and Iinuma. In the laboratory experiments Liggio and co-workers [36] noted that pinonaldehyde is rapidly taken up on acid sulfate aerosols, resulting in the formation of the sulfated pinonaldehyde (a molecular weight 266). The latter compound exhibits rather high vapor pressure, so it is effectively transported into the condensed phase. A number of sulfated components from the photo-oxidation of alpha-/beta-pinene were identified in the smog chamber generated SOA [60]. Some of these species were present in ambient aerosol samples from Germany [29], and later on – from the U.S. [62], to mentioned a few: nitrooxy organosulfate with a 2,10-dihydroxypinane residue (a molecular weight of 295) and sulfated 10-hydroxypinonic acid (a molecular weight 280). Based on the laboratory experiments, both derivatives were suggested to form according to the night-time NO_3 chemistry.

The formation of organosulfates and organonitrates in the airborne particulate matter and/or in tropospheric cloud droplets along with their further chemical processing requires a thorough understanding of the underlying chemistry. The next paragraph is concerned with this issue in more detail.

17.3 Organosulfates and Organonitrates – Underlying Chemistry

Organosulfates (OS) and organonitrates (ON), recognized also in the literature as alkylsulfuric acids and alkyl nitrates, respectively, are intrinsically connected classes of organic compounds with the following structural cores: R–O–SO_3H and

R–O–NO_2, where R stands for any organic residue, e.g., isoprene-related moieties. All OS and ON are thus esters of organic alcohol and strong inorganic acid, i.e., sulfuric acid and nitric acid, respectively. The electronic structure calculations for a number of OS and ON revealed their increased chemical reactivity, both in the gas- and condensed phases. However, it should be noted that the chemical reactivity of OS and ON differs considerably being strongly depended upon the architecture of the bonding system.

As far as OS are concerned, these compounds readily enter nucleophilic substitution at the carbon center through the R–O bond cleavage. Comprehensive kinetic and thermodynamic studies carried out in the context of atmospheric sciences on the hydrolysis reaction of isoprene-derived organosulfates showed that the efficiency of hydrolysis of these OS increases in the order: primary > secondary > tertiary [28]. Therefore, at relevant ambient SOA acidities (pH > 0) and lifetimes (several days), primary and secondary OS are likely to be stable, and thus become measurable at the molecular level in the aerosol phase. On the contrary, tertiary OS are by far unstable, particularly at elevated relative humidities, with lifetimes significantly shorter (0.019–0.67 h) than typical SOA timescale. However, in the light of experiments it was evidenced that the presence of the adjacent OH group in the molecule of isoprene-derived OS decreases the rate of hydrolysis for tertiary OS making these species convert more slowly to the corresponding alcohol. These findings are in line with previously published data [10] providing a potential explanation for the fact that organosulfates are more commonly detected in ambient SOA than organonitrates.

The presence of the weak C–O single bond in the OS structure, in which two OH groups of sulfuric acid are simultaneously substituted by the RO residue (i.e., RO–SO_2–OR, where R denotes any alkyl group), explains another relevant OS behavior that is typical of the condensed-phase chemistry: a simple alkyl group transfer (R = methyl, ethyl), from OS to any nitrogen-, oxygen- or sulfur-centered nucleophiles. This alkyl transfer is typically assumed to occur via an S_N2 reaction and as such is widely used in the preparative organic chemistry for the facile synthesis of alkyl esters of carboxylic acids or quaternary ammonium salts [57].

The analysis of the gas-phase chemistry of OS clearly demonstrates that the presence of the weak C–O single bond triggers the most characteristic fragmentation pattern leading to the diagnostic bisulfate ion (*m*/*z* 97) in the negative-ion atmospheric-pressure-ionization mass spectrometry [(-)API-MS/MS]. Figure 17.3 shows a representative API product ion mass spectrum recorded for the quasi-molecular ion of the atmospherically-relevant organosulfate with a C-5 skeleton. Recently, this species has been structurally identified as the major product of the aqueous-phase reaction of isoprene with sulfate radical mono-anions generated through the sulfur(IV) autoxidation chain in the aqueous bulk solution [56]. The formation of the *m*/*z* 97 ion could be explained through the heterogeneous six-centered-mediated cleavage of the C–O bond in the molecule. Consequently, the fragmentation process can be represented as a concerted *syn*-elimination (Fig. 17.3) similar to the mechanism for the Cope elimination and other gas-phase pyrolytic processes [57]. Mass spectrometry study with the application of deuterium labeling

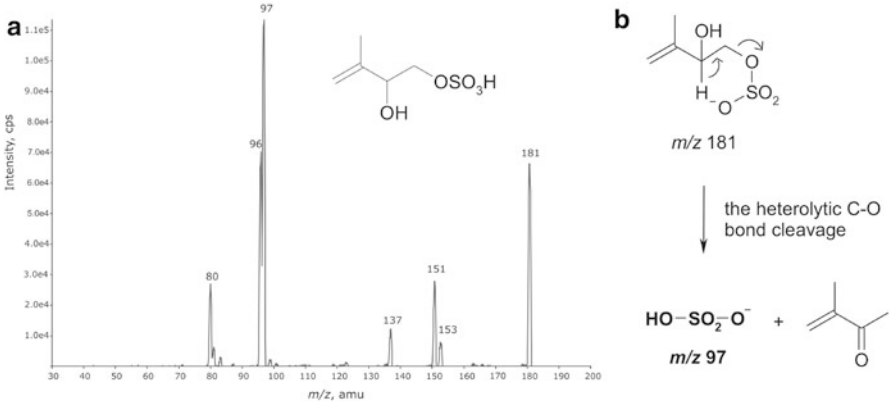

Fig. 17.3 (**a**) (-)Electrospray-triple quadrupole product ion mass spectrum recorded for the $[M–H]^-$ ion (*m*/*z* 181) of isoprene-related organosulfate at the collision energy of 30 V; (**b**) plausible fragmentation pathway leading to the bisulfate ion (*m*/*z* 97), which serves as a diagnostic peak for the qualitative and quantitative analysis of the organosulfate family

techniques revealed that an important requirement for facile HSO_4^- elimination is the ability of the resulting neutral product to accommodate a double bond between C-1 and C-2 [3]. However, organosulfates bearing hydroxyl groups proximal to the sulfate moiety may produce bisulfate ion (*m*/*z* 97) along alternative reaction channels.

The analysis of the structure-reactivity relationship for organonitrates leads to the conclusion that in contrast to organosulfates the underlying chemistry of organic nitrates follows different rules. In principle, diverse chemical properties of organic nitrates can be attributed to the labile O–N single bond that is the site of chemical reactivity. The activation energy for the cleavage of the O–N bond of ethyl nitrate, $C_2H_5O–NO_2$, to form two radicals ($C_2H_5O^*$ and $^*NO_2$) ranges from 36.0 to 41.2 kcal/mol depending on the study [14]. More data can be found in the comprehensive review by Boschan and co-workers [6]. Interestingly, the activation energy for thermal fragmentation and unimolecular, homolytic cleavage of the O–O bond in ethyl hydroperoxide to form two radicals ($C_2H_5O^*$ and $^*OH$) is approximately 37 kcal/mol [14]. The comparison of these values allows to conclude that in terms of the chemical reactivity organic nitrates are similar to hydroperoxides. Once formed in the sunlight-induced tropospheric processes, the alkoxy and NO_2 radicals can engage in secondary reactions in the gas- or condensed phases with other molecules that ultimately generate more stable products such as carbonyl compounds (aldehydes, ketones, and carboxylic acids) and nitro compounds. Higher molecular weight organic nitrates may also generate simpler ones within the particulate phase or aqueous bulk solution, delivering new intermediates for further source processes. Kinetic studies revealed that very high acid concentration (i.e., $>55\%_{w/w}$) is required to initiate the effective hydrolysis of primary and secondary organonitrates. However, the aforementioned conditions are rather too far from these of ambient SOA [28]. In contrast, tertiary organonitrates were shown

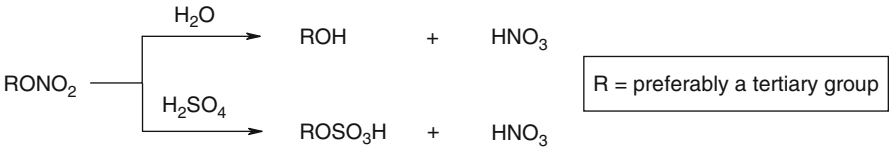

Fig. 17.4 Favorable reaction channels for tertiary organonitrates

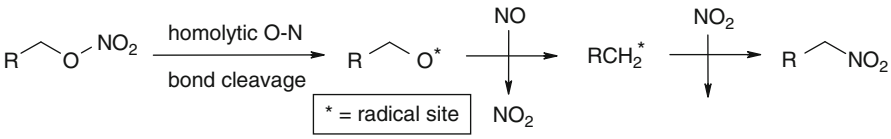

Fig. 17.5 Heterogeneous transformations of organonitrates to the corresponding alkyl nitrates requires a homolytic O–N bond fission

to be highly unstable under typical SOA acidities and lifetimes, and thus readily enter nucleophilic substitution reactions with either water or a sulfate anion to form alcohol and organosulfate, respectively (Fig. 17.4).

It is noteworthy that the hydrolysis proceeds even at neutral pH values following the S_N1-type mechanism. In this respect the chemical behavior of tertiary organonitrates resembles that of organosulfates. However, alkaline aerosol surfaces such as Sahara mineral dust particles [5] may serve as an excellent environment for the heterogeneous transformation of organonitrates into the corresponding nitro derivatives (Fig. 17.5).

To my knowledge, this chemical transition, formally regarded as electrophilic substitution with respect to the OS carbon, has not been incorporated in the atmospheric models, although it does represent a relevant sink of tropospheric NO_x.

17.4 Organosulfates and Organonitrates – Atmospheric Implications

Taking into account the enhanced chemical reactivity of organosulfates and organonitrates, it should be emphasized that these species are likely behind mechanisms for new SOA particle formation and growth in the atmosphere via a number of heterogeneous and in-cloud processes.

Ambient and laboratory measurements with state-of-the art analytical techniques, including aerosol mass spectrometry (AMS), capillary gas chromatography with either electron capture detection (GC/ECD) or negative ion chemical ionization mass spectrometry (GC/NCI) and Fourier transform infrared spectroscopy (FTIR) allowed to identify and quantify a series of C-3 to C-12 organonitrates [33]. The argument was raised that ON with a backbone containing less than 20 carbon atoms would preferably occupy the gas-phase acting as a relatively stable NO_x reservoir. In that sense short-chain organonitrates play an important role in dissemination of

atmospheric pollution through long-range transport of sequestered NO_x from highly polluted regions to forest-impacted environments. On the other hand, a number of ON has been recently detected in secondary organic aerosol from the oxidation of isoprene [38] and alpha-/beta-pinene [13, 38, 39], which proves the capacity of ON to easily partition to the condensed phases. Organonitrates have been shown to comprise 10–20% of carbonaceous aerosol mass at urban locations with maximum loadings in submicron-sized particles [11]. Most organonitrates in the atmosphere are produced either by photochemical (i.e., OH-initiated) or nocturnal (i.e., NO_3-initiated) oxidation reactions of volatile organic compounds (VOC) of either the biogenic (e.g., isoprene) or anthropogenic (e.g., benzene) origin. It is estimated that OH/NO_3 production pathways account for *ca.* 50/50% of isoprene nitrates [38]. In contrast, industrial emissions constitute a minor fraction of atmospheric ON. Interestingly, the surface layer of ocean waters pump into the atmosphere a high load of methyl and ethyl nitrates, although the mechanism of their formation still remains unclear [4].

A few attempts were undertaken to quantify the individual ON originated from isoprene and alpha-pinene in the aerosol phase. The quantification of isoprene ON with calibrated FTIR and AMS instrumentation showed that they can account for almost 10% of organic matter in particles produced from urban combustion emissions [11, 13]. In addition, the relatively short lifetimes of these species, which range from ca. 1–2 h, imply that they may act rather as intermediate products in the formation of less reactive dinitrates and carbonyl nitrates [10, 38]. Conversely, the lifetimes of alpha-pinene-derived ON are in the order of hours to days, making it possible for them to contribute significantly to the aerosol mass [39]. It was asserted that tertiary ON from alpha-pinene can further react in the aerosol phase with other reactive species, e.g., with sulfate radical-anions [43].

Organosulfates and nitrooxy-organosulfates pose a remarkable coupling of anthropogenic air pollution with the formation of SOA from biogenic VOCs. To date, several mechanisms have been proposed to rationalize the formation of OS in atmospheric aerosols and rainwater. The following concepts are commonly accepted by the atmospheric community, although the lively discussion continues to take place:

1. **Acid-catalyzed alcohol esterification.**
   This concept is historically the oldest one and arises from the fact that acidic sulfated seeds significantly enhance SOA yield [32]. Recent chamber photo-oxidation studies with isoprene, alpha-pinene, limonene, beta-pinene, pinonaldehyde and glyoxal in the presence of acidic particles have confirmed that organosulfates constitute a relevant fraction of generated SOA [29, 30, 36, 37, 61–63]. The formation of organosulfates through the esterification of hydroxyl groups or keto groups (after gem-diol formation) with sulfuric acid was also evidenced in the laboratory framework through the aqueous-phase reactions of photo-oxidation products from biogenic VOCs, i.e., from unsaturated fatty acids [17] and cyclic alkenes [49]. However, recently the esterification mechanism has been argued to be kinetically limited and not likely to proceed in the ambient atmosphere [40, 43].

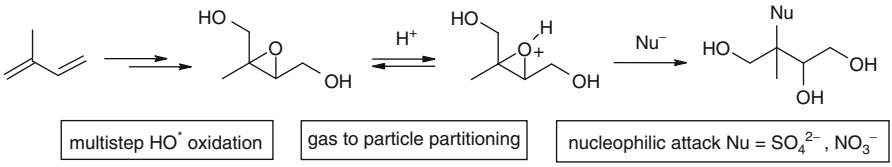

Fig. 17.6 Epoxydiol-mediated conversion of isoprene to the corresponding organosulfates and organonitrates

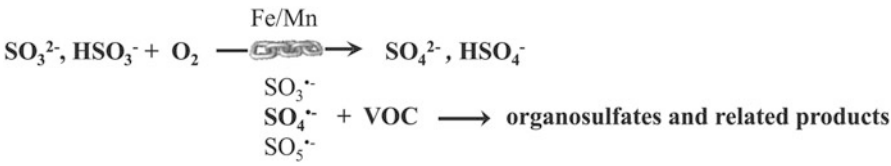

Fig. 17.7 The organosulfate formation through the heterogeneous S(IV) autoxidation chain

2. **Acid-catalyzed ring-opening of epoxydiol.**
   For the first time Paulot and co-workers demonstrated that isoprene photooxidation under low-NO_x conditions generates large concentrations of gas-phase epoxydiols that can easily partition to the aerosol phase [48]. Based on gas chromatography-mass spectrometry approaches, it was evidenced that mass concentration of isoprene epoxydiols in ambient fine aerosols can range from 1 to 24 ng/m^3 [8]. Several laboratory and field studies have demonstrated the role of epoxides in the formation of the major SOA organic components [8, 10, 15, 63]. Owing to the reactive nature (triggered by the highly strained 3-membered ring), epoxydiols undergo efficient hydrolysis on SOA particles to form relevant aerosol tracers, such as the 2-methyltetrols, the C5-alkenetriols (isoprene SOA tracers) and pinenediol (alpha-pinene SOA tracer) [31]. On the other hand, epoxydiols are susceptible to react with other nucleophilic species, including inorganic anions (SO_4^{2-}, NO_3^-) that prevail the inorganic fraction of ambient particulate matter (Fig. 17.6). Thus, the latter processes provide a rational explanation for the existence of organosulfates and organonitrates in the SOA bulk.

   The nucleophilic addition of sulfates and nitrates to the epoxide system can be accomplished either in the gas phase with the concomitant gas-to-particle conversion or in cloud droplets. The atmospheric fate of epoxy intermediates largely depends upon aerosol pH and liquid water content [12].
3. **Addition of sulfate radical to the C=C double bond.**
   This concept invokes, on one side, the mechanism of atmospheric acid rain formation, and on the other hand, technology of cleaning of industrial waste-gases or waste-waters [55]. Regardless the context, the underlying chemistry follows the same scheme and relies on the autoxidation process of S(IV)-containing compounds, such as SO_2, SO_3^- and HSO_3^- leading to the corresponding S(VI) species, such as H_2SO_4, SO_4^{2-} and HSO_4^- (Fig. 17.7).

The process engages a complex matrix of radical-based transition-metal catalyzed simple reactions, albeit conceptually can be recognized as a continuous pump of sulfoxy radicals, mainly SO_4^- radicals, in the water solution [7]. A few research groups have spent a lot of effort to investigate the role of SO_4^- radical in the aqueous-phase reactions with organic constituents that might be important in tropospheric chemistry of carbonaceous aerosols and cloud water [19, 20, 25, 26, 46, 47]. However, it has been only Rudzinski and co-workers who first provided an experimental evidence, based on the UV/VIS and MS measurements, that the addition of sulfate radicals to the C=C double bond of isoprene in the aquatic system results in the formation of organosulfates with the preserved C-5 backbone [54, 56]. More details can be found in Dr. Rudzinski's paper that is presented as an independent chapter of this book.

The interesting approach, based on the SO_4^- radical addition to the C=C double bond, was proposed by Noziere and co-workers to explain the formation of atmospheric organosulfates [43]. The starting point in their research was an observation that atmospheric aerosols contain both organic compounds and inorganic material, and as such, the molecular cocktail is capable of yielding a row of organosulfates through the mutual organic-inorganic chemical interactions under photochemical conditions. Based on the API-type mass spectrometry, it was shown that UV irradiated (280–320 nm) aqueous solutions, each containing sulfate (ammonium and sodium sulfate; concentration of ca. 4 mol/L) and biogenic VOC (isoprene, alpha-pinene, methyl vinyl ketone/methacrolein) produces the same organosulfates as previously identified in aerosols and rainwater. The formation of OS in the aqueous aerosols and clouds from glycoaldehyde and photo-chemically-generated SO_4^- radicals was evidenced by laboratory study by Perri and co-workers [49].

Despite the chemical mechanisms, our knowledge in the atmospheric chemistry of organosulfates is still far from being completed. As mentioned above, OS have been detected in numerous field campaigns and in smog-chamber experiments, and proposed to contribute to the aerosol growth. However, the unambiguous structural identification and quantitation of OS has been constrained owing to a lack of authentic standards. A very limited number of studies were undertaken to determine the concentrations of OS in aerosol. Studies with a synthesized beta-pinene-derived organosulfate [29, 30] demonstrated that the concentration of beta-pinene organosulfates in ambient SOA from a spruce forest ranged up to 23 ng/m^3 and as such was higher than the sum of the known alpha-pinene oxidation products. The application of a laboratory-synthesized authentic standard allowed for the quantitation of isoprene-derived 2-methyltetrols OS in both downwind Atlanta and rural location in Georgia (5–65 ng/m^3) [8]. The quantitation analysis of hydroxycarboxylic acid-derived OS in the ambient particular matter ($PM_{2.5}$) collected in urban locations in the U.S., Mexico City and Pakistan using lactic acid sulfate and glycolic acid sulfate, as authentic standards, showed the concentrations of OS ranged from 0.4 to 3.8 ng/m^3 and from 1.9 to 11.3 ng/m^3, respectively [44]. The authors pointed out that glycolic acid sulfate may represent a versatile standard for quantitation of atmospheric processes that form OS in ambient particulate matter. The other semi-quantitative approach using liquid chromatography (LC) hyphened to the API-type

tandem mass spectrometry (MS/MS) and commercially available surrogate standards was shown to be an alternative method of choice to assess the rough concentrations of OS in ambient SOA samples. The most deployable turned out to be the following commercially available surrogate standards: (1S)-(+)-camphor-10-sulphonic acid (e.g., Refs. [9, 34]), galactoze sulfate (e.g., Ref. [59]) and isotopically-labeled magnesium sulfate [58]. Additional studies used methods to measure the functional groups and elemental composition of organic aerosols to estimate the quantitative contribution of OS. Overall, the aforementioned approaches gain insights into the quantitative contribution of organosulfates to SOA, however the additional effort is needed to obtain novel quantitative protocols with the application of additional authentic standards. Not only is there a room for analytical chemists but also for synthetic organic specialists.

17.5 Conclusions and Future Directions

The topics discussed in this paper demonstrate an increasing significance of organonitrates (ON) and organosulfates (OS) in the context of the urban atmosphere where biogenic and anthropogenic effects are getting overlapped (e.g., big cities, overpopulated regions). The paper provides a broad overview on the origin, formation mechanisms, properties and environmental implications of these compounds through the lens of the organic chemistry.

Both ON and OS are highly polar and reactive species and thus can greatly enhance the hydrophilic properties of atmospheric aerosols. The strong affinity to the aqueous phase makes OS and ON important intermediates on the route to the formation of higher molecular mass components of ambient secondary organic aerosols, such as HULIS. These in-cloud transformations are by far poorly quantified and thus deserve further scientific effort. A detailed analysis of the structure-reactivity relationship indicates a profound discrepancy in the chemical reactivity between ON and OS. More specifically, the chemistry of OS is driven by the weak C–O bonding system, whereas the behavior of ON could be explain through the labile O–N molecular residue.

On the other hand, ON and OS act in the polluted atmosphere as masked carriers of NO_x and SO_2, respectively, providing a rational explanation for their unprecedented role in a tropospheric long-range transport of the major inorganic pollutants. Despite a large number of experimental data from field observations and smog chamber simulations, a lot of uncertainties appears regarding the novel mechanisms leading to ON and OS in the urban atmosphere. A particular scientific effort is needed in regard to the understanding of the in-cloud transformations of biogenic VOC under dark and photochemical conditions. These two processes are poorly explored and thus deserve a detailed characterization.

Since the onset of the 1990s, the advances in analytical instrumentations, chiefly in mass spectrometry, have made it possible to detect and identify a row of organosulfates and organonitrates, both in the gas-phase samples as well as in the ambient

and/or smog-chamber generated SOA samples. However, in many cases the unambiguous structural identification and quantitation of organosulfates, and to a lower extent of organonitrates, has been hampered owing to a lack of authentic standards. Therefore, further research is warrant to elaborate new analytical methods for screening of these molecular species with a higher resolution power.

Acknowledgment The research of Dr. Rafal Szmigielski at the Institute of Physical Chemistry, Polish Academy of Sciences was allowed through the funding from a Marie Curie Reintegration fellowship of the European Community's Seventh Framework Programme ([FP7/2007–2013]) under grant agreement n° PERG05-GA-2009-249160. The author would like to acknowledge the invitation from Dr. Ian Barnes, Prof. Alia Shakour and Dr. Krzysztof Rudzinski to the NATO symposium on *disposal of dangerous chemicals in urban areas and mega cities: oxides and acids of nitrogen – their role in the oxidation capacity of urban areas and mega cities* and the opportunity to present a plenary lecture.

References

1. Altieri KE, Turpin BJ, Seitzinger SP (2009) Composition of dissolved organic nitrogen in continental precipitation investigated by ultra-high resolution FT-ICR mass spectrometry. Environ Sci Technol 43(18):6950–6955
2. Arneth A, Monson RK, Schurgers U, Niinemets G, Palmer PI (2008) Why are estimates of global terrestrial isoprene emissions so similar (and why is this not so for monoterpenes)? Atmos Chem Phys 8:4605–4620
3. Attygalle AB, García-Rubio S, Ta J, Meinwald J (2001) Collisionally-induced dissociation mass spectra of organic sulfate anions. J Chem Soc Perkin Trans 2:498–506
4. Ballschmiter K (2002) A marine source for alkyl nitrates. Science 297:1127–1128
5. Beine HJ, Amoroso A, Esposito G, Sparapani R, Ianniello A, Georgiadis T, Nardino M, Bonasoni P, Cristofanelli P, Dominé F (2005) Deposition of atmospheric nitrous acid on alkaline snow surfaces. Geophys Res Lett 32:L10808
6. Boschan R, Merrow RT, Van Dolah RW (1955) The chemistry of nitrate esters. Chem Rev 55:485–510
7. Buxton GV, Salmon GA, Williams JE (2000) The reactivity of biogenic monoterpenes towards OH and SO_4-radicals in de-oxygenated acidic solution. J Atmos Chem 36:111–134
8. Chan MN, Surratt JD, Claeys M, Edgerton ES, Tanner RL, Shaw SL, Zheng M, Knipping EM, Eddingsaas NC, Wennberg PO, Seinfeld JH (2010) Characterization and quantification of isoprene-derived epoxydiols in ambient aerosol in the Southeastern United States. Environ Sci Technol 44(12):4590–4596
9. Claeys M, Wang W, Vermeylen R, Kourtchev I, Chib X, Farhat Y, Surratt JD, Gómez-González Y, Sciare J, Maenhaut W (2010) Chemical characterisation of marine aerosol at Amsterdam Island during the austral summer of 2006–2007. Aerosol Sci 41:13–22
10. Darer AI, Cole-Filipiak NC, O'Connor AE, Elrod MJ (2011) Formation and stability of atmospherically relevant isoprene-derived organosulfates and organonitrates. Environ Sci Technol 45(5):1895–1902
11. Day DA, Liu S, Russell LM, Ziemann PJ (2010) Organonitrate group concentrations in submicron particles with high nitrate and organic fractions in coastal southern California. Atmos Environ 44(16):1970–1979
12. Eddingsaas NC, VanderVelde DG, Wennberg PO (2010) Kinetics and products of the acid-catalyzed ring-opening of atmospherically relevant butyl epoxy alcohols. J Phys Chem A 114:8106–8113

13. Farmer DK, Matsunaga A, Docherty KS, Surratt JD, Seinfeld JH, Ziemann PJ, Jimenez JL (2010) Response of an aerosol mass spectrometer to organonitrates and organosulfates and implications for atmospheric chemistry. Proc Natl Acad Sci USA 107:6670–6675
14. Francisco MA, Krylowski J (2005) Chemistry of organic nitrates: thermal chemistry of linear and branched organic nitrates. Ind Eng Chem Res 44:5439–5446
15. Froyd KD, Murphy SM, Murphy DM, de Gouw JA, Eddingsaas NC, Wennberg PO (2010) Contribution of isoprene-derived organosulfates to free tropospheric aerosol mass. Proc Natl Acad Sci USA 107(50):21360–21365
16. Goldstein AH, Galbally I (2007) Known and unexplored organic constituents in the Earth's atmosphere. Environ Sci Technol 41:1514–1521
17. Gomez-Gonzalez Y, Surratt JD, Cuyckens F, Szmigielski R, Vermeylen R, Jaoui M, Lewandowski M, Offenberg JH, Kleindienst TE, Edney EO, Blockhuys F, Van Alsenoy C, Maenhaut W, Claeys M (2008) Characterization of organosulfates from the photooxidation of isoprene and unsaturated fatty acids in ambient aerosol using liquid chromatography/(-) electrospray ionization mass spectrometry. J Mass Spectrom 43(3):371–382
18. Graber ER, Rudich Y (2006) Atmospheric HULIS: how humic-like are they? A comprehensive and critical review. Atmos Chem Phys 6:729–753
19. Grgic I, Dovzan A, Bercic G, Hudnik V (1998) The effect of atmospheric organic compounds on the Fe-catalyzed S(IV) autoxidation in aqueous solution. J Atmos Chem 29:315–337
20. Grgic I, Losno R, Pasiuk-Bronikowska W (2003) EUROTRAC – II final report: chemical mechanism development (CMD). Springer, Munich, p 49
21. Guenther A, Hewitt C, Erickson D, Fall R, Geron C, Graedel T, Harley P, Klinger L, Lerdau M, Mckay WA, Pierce T, Scholes B, Steinbrecher R, Tallamraju R, Taylor J, Zimmerman P (1995) A global model of natural volatile organic compound emissions. J Geophys Res 100: 8873–8892
22. Guenther A, Karl T, Harley P, Wiedinmyer C, Palmer PI, Geron C (2006) Estimates of global terrestrial isoprene emissions using MEGAN (Model of Emissions of Gases and Aerosols from Nature). Atmos Chem Phys 6:3181–3210
23. Hallquist M, Wenger JC, Baltensperger U, Rudich Y, Simpson D, Claeys M, Dommen J, Donahue NM, George C, Goldstein AH, Hamilton JF, Herrmann H, Hoffmann T, Iinuma Y, Jang M, Jenkin ME, Jimenez JL, Kiendler-Scharr A, Maenhaut W, McFiggans G, Mentel TF, Monod A, Prevot ASH, Seinfeld JH, Surratt JD, Szmigielski R, Wildt J (2009) The formation, properties and impact of secondary organic aerosol: current and emerging issues. Atmos Chem Phys 9:5155–5236
24. Hatch LE, Creamean JM, Ault AP, Surratt JD, Chan MN, Seinfeld JH, Edgerton ES, Su Y, Prather KA (2011) Measurements of isoprene-derived organosulfates in ambient aerosols by aerosol time-of-flight mass spectrometry – Part 1: Single particle atmospheric observations in Atlanta. Environ Sci Technol 45(12):5105–5111
25. Herrmann H (2003) Kinetics of aqueous phase reactions relevant for atmospheric chemistry. Chem Rev 103:4691–4716
26. Herrmann H, Hoffmann D, Schaefer T, Bruer P, Tilgner A (2010) Tropospheric aqueous-phase free-radical chemistry: radical sources, spectra, reaction kinetics and prediction tools. Eur J Chem Phys Phys Chem 11:3796–3822
27. Hoffmann T, Huang RJ (2011) Atmospheric analytical chemistry. Anal Chem 83:4649–4664
28. Hu KS, Darer AI, Elrod MJ (2011) Thermodynamics and kinetics of the hydrolysis of atmospherically relevant organonitrates and organosulfates. Atmos Chem Phys 11(16):8307–8320
29. Iinuma Y, Muller C, Berndt T, Boge O, Claeys M, Herrmann H (2007) Evidence for the existence of organosulfates from beta-pinene ozonolysis in ambient secondary organic aerosol. Environ Sci Technol 41(19):6678–6683
30. Iinuma Y, Muller C, Boge O, Gnauk T, Herrmann H (2007) The formation of organic sulfate esters in the limonene ozonolysis secondary organic aerosol (SOA) under acidic conditions. Atmos Environ 41:5571–5583

31. Iinuma Y, Boege O, Kahnt A, Herrmann H (2009) Laboratory chamber studies on the formation of organosulfates from reactive uptake of monoterpene oxides. Phys Chem Chem Phys 11(36):7985–7997
32. Jang M, Czoschke NM, Lee S, Kamens RM (2002) Heterogeneous atmospheric aerosol production by acid-catalyzed particle-phase reactions. Science 298:814–817
33. Koppman R (2007) Volatile organic compounds in the atmosphere. Wiley/Wiley-Blackwell, Chichester
34. Kristensen K, Glasius M (2011) Organosulfates and oxidation products from biogenic hydrocarbons in fine aerosols from a forest in North West Europe during spring. Atmos Environ 45:4546–4556
35. Levin Z, Cotton WR (2009) Aerosol pollution impact on precipitation: a scientific review. Springer, Dordrecht
36. Liggio J, Li SM (2006) Organosulfate formation during the uptake of pinonaldehyde on acidic sulfate aerosols. Geophys Res Lett 33(13):L13808
37. Liggio J, Li SM, McLaren R (2005) Reactive uptake of glyoxal by particulate matter. J Geophys Res 110:D10304. doi:10310.11029/12004JD005113
38. Lockwood AL, Shepson PB, Fiddler MN, Alaghmand M (2010) Isoprene nitrates: preparation, separation, identification, yields, and atmospheric chemistry. Atmos Chem Phys 10:6169–6178
39. Ma SX, Rindelaub JD, McAvey KM, Gagare PD, Nault BA, Ramachandran PV, Shepson PB (2011) α-Pinene nitrates: synthesis, yields and atmospheric chemistry. Atmos Chem Phys 11: 6337–6347
40. Minerath EC, Casale MT, Elrod MJ (2008) Kinetics feasibility study of alcohol sulfate esterification reactions in tropospheric aerosols. Environ Sci Technol 42:4410–4415
41. Muller JF (1992) Geographical distribution and seasonal variation of surface emissions and deposition velocities of atmospheric trace gases. J Geophys Res 97:3787–3804
42. Ng NL, Kwan AJ, Surratt JD, Chan AWH, Chhabra PS, Sorooshian A, Pye HOT, Crounse JD, Wennberg PO, Flagan RC, Seinfeld JH (2008) Secondary organic aerosol (SOA) formation from reaction of isoprene with nitrate radicals (NO_3). Atmos Chem Phys 8:4117–4140
43. Noziere B, Ekstrom S, Alsberg T, Holmstrom S (2010) Radical-initiated formation of organosulfates and surfactants in atmospheric aerosols. Geophys Res Lett 37:L05806
44. Olson CN, Galloway MM, Yu G, Hedman CJ, Lockett MR, Yoon T, Stone EA, Smith LM, Keutsch FN (2011) Hydroxycarboxylic acid-derived organosulfates: synthesis, stability, and quantification in ambient aerosol. Environ Sci Technol 45(15):6468–6474
45. Ormeño E, Gentner DR, Fares S, Karlik J, Hoo Park J, Goldstein AH (2010) Sesquiterpenoid emissions from agricultural crops: correlations to monoterpenoid emissions and leaf terpene content. Environ Sci Technol 44:3758–3764
46. Pasiuk-Bronikowska W, Bronikowski T, Ulejczyk M (2003) Inhibition of the S(IV) Autoxidation in the atmosphere by secondary terpenic compounds. J Atmos Chem 44:97–111
47. Pasiuk-Bronikowska W, Bronikowski T, Ulejczyk M (2003) Synergy in the autoxidation of S(IV) inhibited by phenolic compounds. J Phys Chem A 107:1742–1748
48. Paulot F, Crounse JD, Kjaergaard HG, Kürten A, Clair JM, Seinfeld JH, Wennberg PO (2009) Unexpected epoxide formation in the gas-phase photooxidation of isoprene. Science 325:730–733
49. Perri MJ, Lim YB, Seitzinger SP, Turpin BJ (2010) Organosulfates from glycolaldehyde in aqueous aerosols and clouds: laboratory studies. Atmos Environ 44(21–22):2658–2664
50. Pratt KA, Prather KA (2012) Mass spectrometry of atmospheric aerosols – recent developments and applications. Part II: On-line mass spectrometry techniques. Mass Spectrom Rev 31:17–48
51. Pratt KA, Prather KA (2012) Mass spectrometry of atmospheric aerosols – recent developments and applications. Part I: Off-line mass spectrometry techniques. Mass Spectrom Rev 31:1–16
52. Reemtsma T, These A, Venkatachari P, Xia X, Hopke PK, Springer A, Linscheid M (2006) Identification of fulvic acids and sulfated and nitrated analogues in atmospheric aerosol by electrospray ionization Fourier transform ion cyclotron resonance mass spectrometry. Anal Chem 78:8299–8304

53. Romero F, Oehme M (2005) Organosulfates – a new component of humic-like substances in atmospheric aerosols? J Atmos Chem 52:283–294
54. Rudzinski KJ (2004) Degradation of isoprene in the presence of sulphoxy radical anions. J Atmos Chem 48:191–216
55. Rudzinski KJ (2006) Heterogeneous and Aqueous-Phase Transformations of Isoprene. Environmental simulation chambers: application to atmospheric chemical processes NATO science series: IV. Earth Environ Sci 62:261–277
56. Rudzinski KJ, Gmachowski L, Kuznietsova I (2009) Reactions of isoprene and sulphoxy radical-anions – a possible source of atmospheric organosulphites and organosulphates. Atmos Chem Phys 9:2129–2140
57. Smith MB, March J (2007) March's advanced organic chemistry: reactions, mechanisms, and structure. Wiley-Interscience/Wiley, Hoboken
58. Stone EA, Hedman CJ, Sheesley RJ, Shafer MM, Schauer JJ (2009) Investigating the chemical nature of humic-like substances (HULIS) in North American atmospheric aerosols by liquid chromatography tandem mass spectrometry. Atmos Environ 43:4205–4213
59. Stone EA, Yang L, Yu LE, Rupakheti M (2012) Characterization of organosulfates in atmospheric aerosols at Four Asian locations. Atmos Environ 47:323–329
60. Surratt JD (2010) Analysis of the chemical composition of atmospheric organic aerosols by mass spectrometry. PhD thesis, California Institute of Technology
61. Surratt JD, Kroll JH, Kleindienst TE, Edney EO, Claeys M, Sorooshian A, Ng NL, Offenberg JH, Lewandowski M, Jaoui M, Flagan RC, Seinfeld JH (2007) Evidence for organosulfates in secondary organic aerosol. Environ Sci Technol 41:517–527
62. Surratt JD, Gomez-Gonzalez Y, Chan AWH, Vermeylen R, Shahgholi M, Kleindienst TE, Edney EO, Offenberg JH, Lewandowski M, Jaoui M, Maenhaut W, Claeys M, Flagan RC, Seinfeld JH (2008) Organosulfate formation in biogenic secondary organic aerosol. J Phys Chem A 112(36):8345–8378
63. Surratt JD, Chan AWH, Eddingsaas NC, Chan MN, Loza CL, Kwan AJ, Hersey SP, Flagan RC, Wennberg PO, Seinfeld JH (2010) Reactive intermediates revealed in secondary organic aerosol formation from isoprene. Proc Natl Acad Sci USA 107:6640–6645
64. Szmigielski R, Vermeylen R, Dommen J, Metzger A, Maenhaut W, Baltensperger U, Claeys M (2010) The acid effect in the formation of 2-methyltetrols from the photooxidation of isoprene in the presence of NO_x. Atmos Res 98:183–189

Chapter 18
Tracers for Biogenic Secondary Organic Aerosol from α-Pinene and Related Monoterpenes: An Overview

Magda Claeys, Rafal Szmigielski, Reinhilde Vermeylen, Wu Wang, Mohammad Safi Shalamzari, and Willy Maenhaut

Abstract In this review, we first address the terpenoid composition of ambient fine rural aerosol to give a report on the current state of knowledge in regard to the molecular characterisation of biogenic secondary organic aerosol tracers. The major known, recently elucidated, and still unknown tracers, which can be detected at a significant relative abundance, are listed and briefly discussed. In a second part, we provide a historic account on the discovery of 3-methyl-1,2,3-butanetricarboxylic acid, which involved a long search with several failures and a final success, and propose a revised formation pathway. Finally, we present some brief conclusions and perspectives.

Keywords Alpha-pinene • Ambient fine aerosol • 3-Methyl-1,2,3-butanetricarboxylic acid • Molecular Characterisation • Secondary Organic Aerosol • Terpenylic Acid

18.1 Introduction

Biogenic secondary organic aerosol (SOA) from the oxidation of monoterpenes such as α-pinene is a dynamic and complex mixture [19, 22, 23]. As the SOA evolves or ages due to oxidation reactions, which involve ozone and/or OH or NO_3

M. Claeys (✉) • R. Vermeylen • W. Wang • M.S. Shalamzari • W. Maenhaut
Department of Pharmaceutical Sciences, University of Antwerp, Universiteitsplein 1, BE-2610 Antwerp, Belgium
e-mail: magda.claeys@ua.ac.be

R. Szmigielski
Laboratory of Environmental Chemistry, Institute of Physical Chemistry, Polish Academy of Sciences (PAS), Kasprzaka 44/52 St., 01-224 Warsaw, Poland
e-mail: ralf@ichf.edu.pl

I. Barnes and K.J. Rudziński (eds.), *Disposal of Dangerous Chemicals in Urban Areas and Mega Cities*, NATO Science for Peace and Security Series C: Environmental Security,
DOI 10.1007/978-94-007-5034-0_18,

radical-initiated reactions, more oxygenated products are formed with increased hydrophilic properties, enhancing the capability of the aerosol to act as cloud condensation nuclei (for a review, see Ref. [10]). On the other hand, oxidation reactions of semi-volatile precursors in the gas phase may also result in fragmentation to smaller molecules. In addition to gas-phase oxidation reactions, heterogeneous reactions occurring in the particle phase have to be considered; these reactions include esterification with sulfuric acid of hydroxyl- or epoxy-containing SOA products [14, 15, 33–35], esterification of pinic acid with hydroxyl-containing terpenoic acids [4, 28, 38], and OH-initiated oxidation reactions [5].

Despite the fact that biogenic SOA is rather complex, it contains single components at a significant relative abundance that are suitable as molecular markers or tracers for the characterisation of ambient fine aerosol and allow one to gain insights into biogenic volatile organic compound (BVOC) precursors and aerosol formation processes. Since the lifetime of ambient fine aerosol is variable and may be from a few hours to a few days it is useful to have tracers which reflect fresh (unaged) and aged biogenic SOA. Well-established tracers that are known for a long time for fresh α-pinene SOA are pinonic and *cis*-pinic acids (e.g., Refs. [1, 6, 11–13, 41]). However, during the past decade, significant progress has been made with respect to the chemical characterisation of additional α-pinene SOA tracers, including tracers for fresh as well as aged SOA. For example, a novel tracer for fresh α-pinene SOA is terpenylic acid [3], while 3-methyl-1,2,3-butanetricarboxylic acid (MBTCA) is a tracer for aged α-pinene SOA [36].

18.2 Monoterpene SOA Tracer Composition of Ambient Fine Rural Aerosol

Figure 18.1 shows selected chromatographic data [base peak chromatogram (BPC) and extracted ion chromatograms (EICs)] for a methanolic extract of K-puszta fine aerosol (PM2.5; particulate matter with an aerodynamic diameter <2.5 μm), which can be regarded as representative for a biogenic SOA-rich aerosol [20]. The extract was obtained from a pooled aerosol sample comprising portions of 5-day- and night-time samplings of the warm period of the 2006 summer campaign [27] and contains fresh as well as aged SOA. The data were obtained using liquid chromatography coupled to negative ion electrospray ionisation mass spectrometry [LC/(-)ESI-MS], following a published procedure [39].

The major tracers that could be detected at a significant relative abundance were:

1. the known α-pinene SOA tracers, *cis*-pinonic acid (MW 184), *cis*-pinic acid (MW 186), and 10-hydroxypinonic acid (MW 200), and related isomers from the oxidation of Δ^3-carene: at *m*/*z* 183, *cis*-pinonic acid [retention time (RT) 23.3 min], and caronic acid (RT 23.9 min); at *m*/*z* 185, *cis*-pinic acid (RT 22.3 min) and caric acid (RT 23.2 min); and at *m*/*z* 199, 10-hydroxypinonic acid (RT 20.7 min) (e.g., Refs. [1, 6, 7, 11–13, 26, 40, 41]). With regard to the

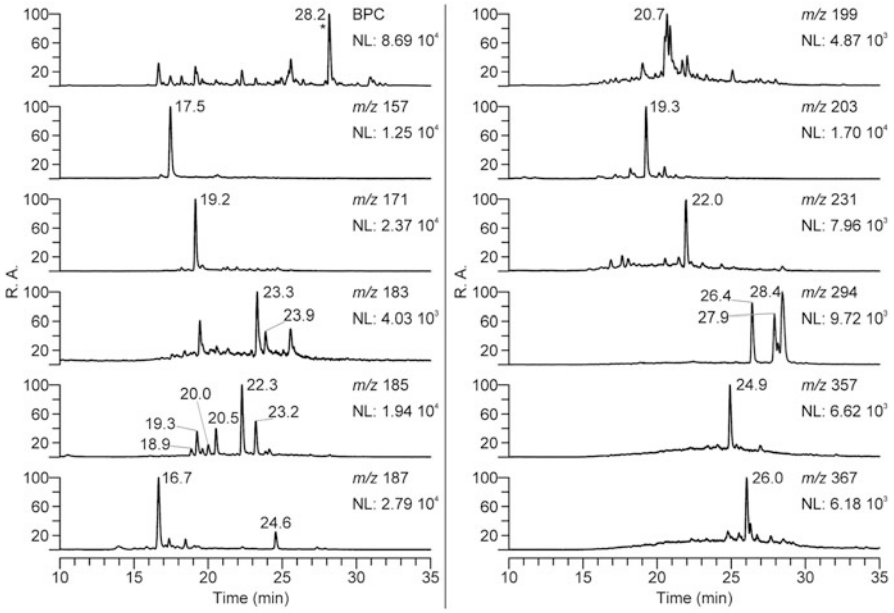

Fig. 18.1 Selected LC/(-)ESI-MS chromatographic data [base peak chromatogram (BPC) and extracted ion chromatograms (EICs)] for a methanolic extract of K-puszta PM2.5 aerosol, containing fresh and aged biogenic SOA. The peak denoted with an *asterisk* in the BPC was also present in the field blank. Abbreviation: *NL* normalisation level (in arbitrary units)

m/*z* 199 compounds, it can be seen that there are additional isomers eluting close to 10-hydroxypinonic acid (RT 20.7 min); these isomers remain to be elucidated.

2. lactone-containing terpenoic acids, terebic (MW 158) and terpenylic acid (MW 172), both α-pinene SOA tracers, and a homologue, homoterpenylic acid (MW 186) from the oxidation of β-pinene: at *m*/*z* 157, terebic acid (RT 17.5 min); at *m*/*z* 171, terpenylic acid (RT 19.2 min); and at *m*/*z* 185, homoterpenylic acid (RT 20.5 min) [3, 38].
3. a C_8-tricarboxylic acid (MW 204), a tracer for aged α-pinene SOA: at *m*/*z* 185 and 203: MBTCA (RT 19.3 min) [36].
4. a still unknown α-pinene SOA tracer: at *m*/*z* 187, tentatively characterised as a C_8-hydroxydicarboxylic acid (RT 16.7 min) [39].
5. diaterpenylic acid acetate, a 1,8-cineole and α-pinene SOA tracer: at *m*/*z* 231 (RT 22.0 min) [3, 16].
6. pinanediol-related MW 295 nitrooxy organosulfates: at *m*/*z* 294 (RTs 26.4, 27.9, and 28.4 min) [8, 15, 21, 34].
7. di-esters formed between pinic acid and a hydroxyl-containing terpenoic acid: at *m*/*z* 357 (RT 24.9 min, hydroxyl-containing terpenoic acid = diaterpenylic acid) [4, 38]; and at *m*/*z* 367 (RT 26.0 min, hydroxyl-containing terpenoic acid = 10-hydroxypinonic acid) [28].

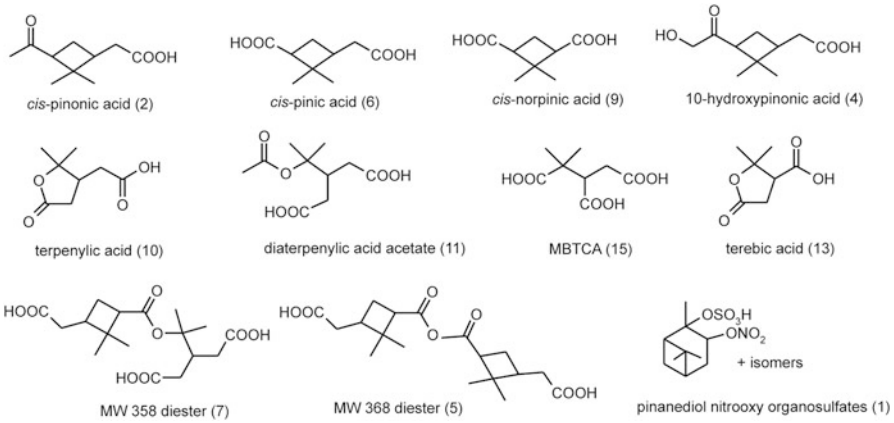

Fig. 18.2 Chemical structures of α-pinene SOA tracers. The numbers between *parentheses* refer to the numbers used in Fig. 18.4

Additional information on the *m*/*z* 185 compounds with RTs 18.9 and 19.6 min, identified as ketolimononic and limonic acids, respectively, and the *m*/*z* 187 compound with RT 24.6 min, identified as the C_9-dicarboxylic acid azelaic acid, can be found in Yasmeen et al. [39].

The chemical structures of the α-pinene SOA tracers that are mentioned above and can be readily detected using LC/(−)ESI-MS is given in Fig. 18.2. These α-pinene SOA tracers should not be regarded as complete; additional minor tracers, for example, are the di-ester formed between *cis*-pinic acid and diaterebic acid [38], and the organosulfates derived from 3-hydroxyglutaric acid and 10-hydroxypinonic acid [34].

Compared to previous work that resorted to GC/MS with prior trimethylsilylation (e.g., Ref. [20]), the number of biogenic SOA tracers that can be readily detected using LC/(−)ESI-MS has increased; a possible reason for this increase is that some of the tracers are not stable (e.g., esters) during the trimethylsilylation procedure and are detected as the corresponding monomers. In addition, some of the organic species such as the lactone-containing terpenoic acids have escaped detected by GC/MS with prior trimethylsilylation.

The tracers listed above, except 10-hydroxypinonic acid and the di-esters, were measured in PM2.5 aerosols that were collected during a 2007 summer campaign at Brasschaat, Belgium, a forest site that is severely impacted by urban pollution [9]. This study showed that the highest atmospheric concentrations of MBTCA and the lowest ones of *cis*-pinonic acid were found during the first five days of the campaign that were characterised by maximum temperatures >22 °C. This is consistent with MBTCA being a tracer for aged biogenic SOA and *cis*-pinonic acid serving as its intermediate precursor. In addition, the unknown MW 188 ($C_8H_{12}O_5$) terpenoic acid revealed the same time series as MBTCA, suggesting that it is also a potential tracer for aged biogenic SOA. Some of the tracers reflected day-time oxidation

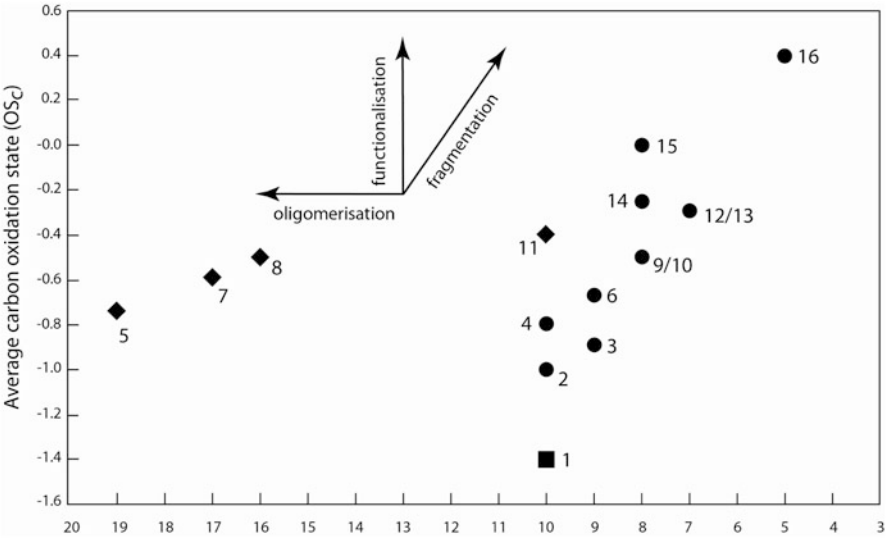

Fig. 18.3 Location of known, recently elucidated, and still unknown α-pinene SOA tracers in the average oxidation framework, developed by Kroll et al. [23]. The di-esters are denoted with ◆, the terpenoic acids with ●, and the pinanediol nitrooxy organosulfates with ■. Note that 3-hydroxy-2,2-dimethylglutaric acid (*11*), terebic acid (*12*), the unknown MW 188 compound (*13*), MBTCA (*14*) and 3-hydroxyglutaric acid (*15*) are located in the *upper right corner*, consistent with tracers for aged α-pinene SOA. *1* pinanediol (nitrooxy organosulfates), *2* pinonic acid, *3* norpinonic acid, *4* hydroxypinonic acid, *5* pinic acid/hydroxypinonic acid, *6* pinic acid, *7* pinic acid/diaterpenylic acid, *8* pinic acid/diaterebic acid, *9* norpinic acid, *10* terpenylic acid, *11* diaterpenylic acid acetate, *12* 3-hydroxy-2,2-dimethylglutaric acid, *13* terebic acid, *14* unknown MW 188, *15* MBTCA, *16* 3-hydroxyglutaric acid

processes (e.g., *cis*-pinonic, terpenylic, and terebic acids, MBTCA, and diaterpenylic acid acetate), while others pointed to night-time aerosol formation processes (e.g., *cis*-pinic, caric, and limonic acids, and the pinanediol-related MW 295 nitrooxy organosulfates). Furthermore, it could be confirmed that MBTCA, in contrast to *cis*-pinonic acid, shows a strong Arrhenius-type temperature relationship, as first documented in a German field study by Zhang et al. [42].

In order to describe the processes of α-pinene SOA formation, which are very complex and dynamic, a useful framework has recently been proposed by Kroll et al. [23]. In this system, the aerosol is presented in terms of the average carbon oxidation state [$OS_C \approx 2(O:C)–H:C$], a quantity that increases with oxidation and is readily measured by a technique such as high-resolution MS (e.g., Refs. [30–32]). As the SOA evolves, it will functionalise, fragment, or oligomerise, with the first two processes affecting the oxidation state. Figure 18.3 places the α-pinene SOA tracers, mentioned above, as well as some additional ones that were reported in the literature, in the average oxidation framework. The latter tracers include norpinonic acid (e.g., Ref. [17]), norpinic acid (e.g., Ref. [6]), 3-hydroxyglutaric acid [2], and 3-hydroxy-2,2-dimethylglutaric acid [2].

18.3 Historic Account on the Discovery of MBTCA: A Search with Failures

The structure elucidation of MBTCA presented an analytical challenge, mainly because the dimethylcyclobutane ring of α-pinene was not retained during its formation. Two approaches can be taken when dealing with the structural elucidation of unknown compounds. A first approach is to isolate the unknown compound in pure form and sufficient quantity, and to elucidate its structure using NMR techniques. A second approach is to synthesise the proposed compound and to compare the chromatographic and mass spectrometric behaviours of the unknown compound with those of the synthesised one. As the first approach was not feasible in the case of a very complex mixture such as α-pinene SOA, the second approach was finally followed.

Our research dealing with MBTCA goes back to 1998, about 2 years before we published an article on "Carbonaceous aerosol characterization in the Amazon basin, Brazil: novel dicarboxylic acids and related compounds" [24]. In the latter study, we focused on the structural characterisation of unknown organic acids that were present in aerosols collected from the Amazon basin, Brazil, during the wet season, and, therefore, were most likely from biogenic origin and not due to biomass burning (taking place in the dry season). These organic acids were found to be enriched in the fine size fraction, suggesting that they were biogenic SOA products formed by gas-to-particle conversion. For the characterisation and structure elucidation of the unknowns, we employed fractionation by solid-phase extraction of the dichloromethane extracts, various types of derivatisations in combination with gas chromatography/mass spectrometry (GC/MS), and detailed interpretation of the electron ionisation (EI) mass spectra. Among the unknowns, a C_8-tricarboxylic acid was identified as 3-carboxyheptanedioic acid (MW 204). However, this identification was tentative since an authentic compound was not available and the identification was only based on the interpretation of mass spectral data. It later turned out that the unknown MW 204 compound was a branched isomer of 3-carboxyheptanedioic acid, i.e., MBTCA. The biogenic precursor of the novel identified compound could not be pinpointed at that time, but we hypothesised that it was most likely a monoterpene or an unsaturated fatty acid. Incidently, the BVOC precursor for the unknown C_8-tricarboxylic acid was later established as the monoterpene α-pinene [18]. A reference compound was still not available, implying that the identification as 3-carboxyheptanedioic acid was still tentative. In a subsequent study [2], the latter structure was questioned because the linear structure of 3-carboxyheptanedioic acid could not be linked to α-pinene, an alternative structure was proposed, i.e., 2-hydroxy-4-isopropyladipic acid, and the proposed compound was synthesised. The EI mass spectral behaviour of its ethyl ester trimethylsilyl ether derivative matched rather well but not completely with that of the unknown MW 204 compound. Its chromatographic retention time

deviated slightly from that of the unknown compound, leading to the conclusion that the synthesised compound was likely a diastereoisomer, which, unfortunately, still turned out not to be the right structure. Accurate mass measurements using high-resolution (−)ESI-MS revealed an elemental composition of $C_8H_{11}O_6$ for the deprotonated molecule of the MW 204 a-pinene SOA tracer, which finally led us to revise the structure as MBTCA [36]. A synthetic effort was undertaken by synthesising the proposed compounds, i.e., MBTCA and another positional isomer (i.e., 2-methyl-4-carboxyadipic acid), which were analysed using GC/MS with prior trimethylsilylation and with LC/(−)ESI-MS. The unknown MW 204 α-pinene SOA tracer was unambiguously elucidated as MBTCA because its chromatographic and mass spectral behaviours perfectly agreed with those of the synthesised compound. In this study, *cis*-pinonic acid was proposed as a gas-phase intermediate in the OH radical-initiated formation of MBTCA, a hypothesis which was recently confirmed in an environmental chamber study [29].

18.4 Formation Pathway of MBTCA and Related α-Pinene SOA Tracers

With regard to formation pathways, a route starting with hydrogen abstraction at the C-10 position (relating to the pinane structure [25]) was proposed by Szmigielski et al. [36], while several additional routes were formulated by Müller et al. [29] taking into account that hydrogen abstraction by the OH radical preferentially occurs at certain positions, i.e., the C-1 and C-7 positions [37]. It has to be kept in mind that mechanisms are always to some extent speculative and hard to proof experimentally, and that the initial site where the radical is created due to hydrogen abstraction by the OH radical may migrate. In this regard, evidence has been obtained for the migration of the initial radical site upon OH radical-initiated oxidation of α-pinene in the presence of NO and highly acidic sulfuric acid-containing seed particles; more specifically, upon formation of the MW 295 nitrooxy organosulfates the initial radical site on the cyclohexane ring migrates to a ring position and the methyl group of the dimethylcyclobutane ring [34]. Figure 18.4 proposes a revised mechanistic route to MBTCA starting with hydrogen abstraction at the favoured C-4 position (C-2 position of *cis*-pinonic acid). As in the case of the initial OH radical attack on *cis*-pinonic acid, the attack of an OH radical on intermediate (d) may proceed through an initial attack at another carbon atom. It can be noted that the formation of MBTCA starting from *cis*-pinonic acid requires two molar OH radical equivalents.

The route proposed in Fig. 18.4 has the merit that it also allows one to explain the formation of several other known and more recently elucidated α-pinene SOA tracers, i.e., *cis*-pinic acid (e.g., Refs. [7, 41]), 10-hydroxypinonic acid [6, 40], 3-hydroxyglutaric acid [2], and 3-hydroxy-2,2-dimethylglutaric acid [2] (Fig. 18.5).

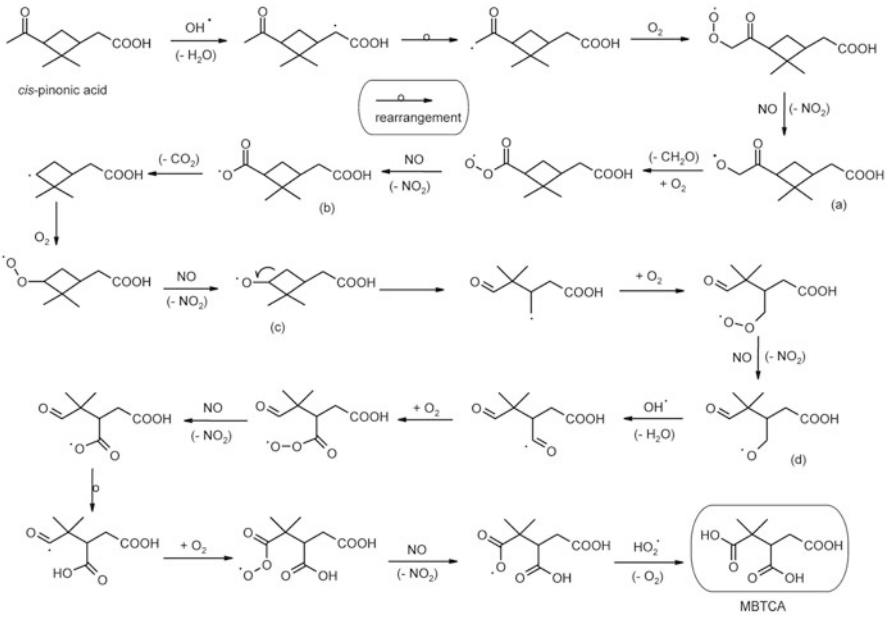

Fig. 18.4 Proposed revised mechanistic pathway leading to MBTCA

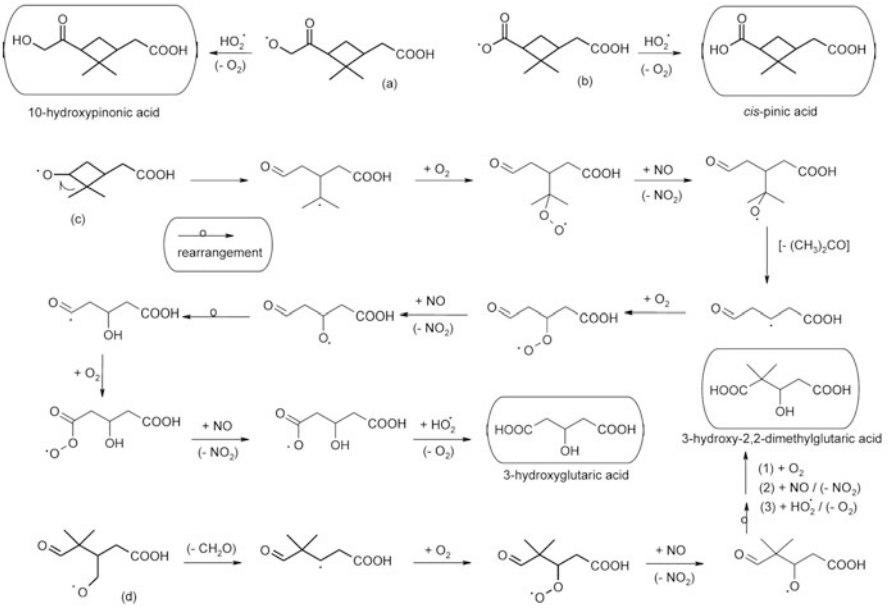

Fig. 18.5 Proposed revised mechanistic pathway leading to known and recently elucidated α-pinene SOA tracers, i.e., *cis*-pinic, 10-hydroxypinic, 3-hydroxyglutaric, and 3-hydroxy-2, 2-dimethylglutaric acids. For the route leading to intermediates (*a–d*), see Fig. 18.4

18.5 Conclusions and Perspectives

Significant progress has been made during the last decade with the structural characterisation of α-pinene and related monoterpene (i.e., β-pinene, *d*-limonene, and Δ^3-carene) SOA tracers. Hence, we have now reached the stage where the major terpenoids in ambient fine forest aerosol that is enriched in biogenic SOA have been identified. A major terpenoic acid from the photo-oxidation of α-pinene, however, which shows a high relative abundance in ambient fine forest aerosol but remains to be fully identified, is the $C_8H_{12}O_5$ hydroxydicarboxylic acid. Since it is a potential tracer for aged biogenic SOA, its structural elucidation would be warranted. Another class of SOA tracers that have only been partially explored and for which suitable analytical methods still have to be developed are the organosulfates. These tracers have a mixed biogenic/anthropogenic origin since their formation involves the participation of sulfuric acid which is of anthropogenic origin. Furthermore, more detailed insights are required on the time evolution of oxygenated and processed (e.g., esterified) products during laboratory irradiation experiments under simulated atmospheric conditions to better constrain their suitability as tracers for photochemical and other ageing processes.

Characterisation of α-pinene and related monoterpene SOA tracers at the molecular level using a chromatographic technique (GC or LC) hyphenated to a mass spectrometric technique and detailed interpretation of MS fragmentation data can be analytically challenging, as was the case for MBTCA which had not retained the dimethylcyclobutane ring of α-pinene. It was a search with several failures in which we experienced that nature does not reveal its secrets all at once. However, it was worth the efforts since it resulted in the structural elucidation of a major tracer for aged biogenic SOA that is useful for ambient fine aerosol characterisation.

An emerging analytical technique for the detailed characterisation of biogenic SOA, including minor components, is high-resolution MS such as Fourier Transform Ion Cyclotron Resonance MS (FT-ICR MS). This technique enables the accurate measurement of the numerous molecular masses present in a complex SOA mixture and as such their O:C ratio (and their average carbon oxidation state) which increases upon photochemical ageing. It allows for a detailed characterisation of biogenic SOA that is complementary to that achieved with GC- or LC-based MS techniques and interpretation of MS fragmentation data.

Acknowledgements Research at the Universities of Antwerp and Ghent was supported by the Belgian Federal Science Policy Office, the Research Foundation – Flanders (FWO), and the Special Research Funds of the Universities of Antwerp and Ghent. Rafal Szmigielski was supported by a Marie Curie Intra-European fellowship. We also acknowledge the close collaboration during the past several years with Tad Kleindienst, Ed Edney, and coworkers, at the US Environmental Protection Agency (Research Triangle Park, NC, USA), Jason Surratt, John Seinfeld, and coworkers, at the California Institute of Technology (Pasadena, CA, USA), and Yoshi Iinuma, Hartmut Herrmann, and coworkers, at the Leibniz-Institute for Tropospheric Research (Leipzig, Germany).

References

1. Christoffersen TS, Hjorth J, Horie O, Jensen NR, Kotzias D, Molander L, Neeb P, Ruppert L, Winterhalter R, Virkkula A, Wirtz K, Larsen BR (1998) cis-Pinic acid, a possible precursor for organic aerosol formation from ozonolysis of α-pinene. Atmos Environ 32:1657–1661
2. Claeys M, Szmigielski R, Kourtchev I, Van der Veken P, Vermeylen R, Maenhaut W, Jaoui M, Kleindienst TE, Lewandowski M, Offenberg JH, Edney EO (2007) Hydroxydicarboxylic acids: novel markers for secondary organic aerosol from the photooxidation of α-pinene. Environ Sci Technol 41:1628–1634
3. Claeys M, Iinuma Y, Szmigielski R, Surratt JD, Blockhuys F, Van Alsenoy C, Böge O, Sierau B, Gómez-González Y, Vermeylen R, Van der Veken P, Shahgholi M, Chan AWH, Herrmann H, Seinfeld JH, Maenhaut W (2009) Terpenylic acid and related compounds from the oxidation of α-pinene: implications for new particle formation and growth above forest. Environ Sci Technol 43:6976–6982
4. Gao Y, Hall WA IV, Johnston MV (2010) Molecular composition of monoterpene secondary organic aerosol at low mass loading. Environ Sci Technol 44:7897–7902
5. George IJ, Abbatt JPD (2010) Chemical evolution of secondary organic aerosol from OH-initiated heterogeneous oxidation. Atmos Chem Phys 10:5551–5563
6. Glasius M, Duane M, Larsen BR (1999) Determination of polar terpene oxidation products in aerosols by liquid chromatography-ion trap mass spectrometry. J Chromatogr A 833:121–135
7. Glasius M, Lahaniati M, Calogirou A, Di Bella D, Jensen NR, Hjorth J, Duane M, Kotzias D, Larsen BR (2000) Carboxylic acids in secondary aerosols from oxidation of cyclic monoterpenes by ozone. Environ Sci Technol 34:1001–1010
8. Gómez-González Y, Surratt JD, Cuyckens F, Szmigielski R, Vermeylen R, Jaoui M, Lewandowski M, Offenberg JH, Kleindienst TE, Edney EO, Blockhuys F, Van Alsenoy C, Maenhaut W, Claeys M (2008) Characterization of organosulfates from the photooxidation of isoprene and unsaturated fatty acids in ambient aerosol using liquid chromatography/(-) electrospray ionization mass spectrometry. J Mass Spectrom 43:371–382
9. Gómez-González Y, Wang W, Vermeylen R, Chi X, Neirynck J, Janssens IA, Maenhaut W, Claeys M (2012) Chemical characterization of atmospheric aerosols during a 2007 summer field campaign at Brasschaat, Belgium: sources and source processes of biogenic secondary organic aerosol. Atmos Chem Phys 12:125–138
10. Hallquist M, Wenger JC, Baltensperger U, Rudich Y, Simpson D, Claeys M, Dommen J, Donahue NM, George C, Goldstein AH, Hamilton JF, Herrmann H, Hoffmann T, Iinuma Y, Jang M, Jenkin ME, Jimenez JL, Kiendler-Scharr A, Maenhaut W, McFiggans G, Mentel TF, Monod A, Prévôt ASH, Seinfeld JH, Surratt JD, Szmigielski R, Wildt J (2009) The formation, properties and impact of secondary organic aerosol: current and emerging issues. Atmos Chem Phys 9:5155–5236
11. Hatakeyama S, Izumi K, Fukuyama T, Akimoto H (1989) Reactions of ozone with alpha-pinene and beta-pinene in air – yields of gaseous and particulate products. J Geophys Res Atmos 94:13013–13024
12. Hoffmann T, Odum JR, Bowman F, Collins D, Klockow D, Flagan RC, Seinfeld JH (1997) Formation of organic aerosols from the oxidation of biogenic hydrocarbons. J Atmos Chem 26:189–222
13. Hoffmann T, Bandur R, Marggraf U, Linscheid M (1998) Molecular composition of organic aerosols formed in the α-pinene/O_3 reaction: implications for new particle formation processes. J Geophys Res Atmos 103:25569–25578
14. Iinuma Y, Müller C, Böge O, Gnauk T, Herrmann H (2007) The formation of organic sulfate esters in the limonene ozonolysis secondary organic aerosol (SOA) under acidic conditions. Atmos Environ 41:5571–5583
15. Iinuma Y, Müller C, Berndt T, Böge O, Claeys M, Herrmann H (2007) Evidence for the existence of organosulfates from beta-pinene ozonolysis in ambient secondary organic aerosol. Environ Sci Technol 41:6678–6683

16. Iinuma Y, Böge O, Keywood M, Gnauk T, Herrmann H (2009) Diaterebic acid acetate and diaterpenylic acid acetate: atmospheric tracers for secondary organic aerosol formation from 1,8-cineole oxidation. Environ Sci Technol 43:280–285
17. Jang M, Kamens RM (1999) Newly characterized products and composition of secondary aerosols from the reaction of α-pinene and ozone. Atmos Environ 33:459–474
18. Jaoui M, Kleindienst TE, Lewandowski M, Offenberg JH, Edney EO (2005) Identification and quantification of aerosol polar oxygenated compounds bearing carboxylic or hydroxyl groups: 2 organic tracer compounds from monoterpenes. Environ Sci Technol 39:5661–5673
19. Jimenez JL, Canagaratna MR, Donahue NM, Prévôt ASH, Zhang Q, Kroll JH, DeCarlo PF, Allan JD, Coe H, Ng NL, Aiken AC, Docherty KS, Ulbrich IM, Grieshop AP, Robinson AL, Duplissy J, Smith JD, Wilson KR, Lanz VA, Hueglin C, Sun YL, Tian J, Laaksonen A, Raatikainen T, Rautiainen J, Vaattovaara P, Ehn M, Kulmala M, Tomlinson JM, Collins DR, Cubison MJ, Dunlea EJ, Huffman JA, Onasch TB, Alfarra MR, Williams PI, Bower K, Kondo Y, Schneider J, Drewnick F, Borrmann S, Weimer S, Demerjian K, Salcedo D, Cottrell L, Griffin R, Takami A, Miyoshi T, Hatakeyama S, Shimono A, Sun JY, Zhang YM, Dzepina K, Kimmel JR, Sueper D, Jayne JT, Herndon SC, Trimborn AM, Williams LR, Wood EC, Middlebrook AM, Kolb CE, Baltensperger U, Worsnop DR (2009) Evolution of organic aerosols in the atmosphere. Science 326:1525–1529
20. Kourtchev I, Copolovici L, Claeys M, Maenhaut W (2009) Characterization of atmospheric aerosols at a forested site in Central Europe. Environ Sci Technol 43:4665–4671
21. Kristensen K, Glasius M (2011) Organosulfates and oxidation products from biogenic hydrocarbons in fine aerosols from a forest in North West Europe during spring. Atmos Environ 45:4546–4556
22. Kroll JH, Seinfeld JH (2008) Chemistry of secondary organic aerosol: formation and evolution of low-volatility organics in the atmosphere. Atmos Environ 42:3593–3624
23. Kroll JH, Donahue NM, Jimenez JL, Kessler SH, Canagaratna MR, Wilson KR, Altieri KE, Mazzoleni LR, Wozniak AS, Bluhm H, Mysak ER, Smith JD, Kolb CE, Worsnop DR (2011) Carbon oxidation state as a metric for describing the chemistry of atmospheric organic aerosol. Nat Chem 3:133–139
24. Kubátová A, Vermeylen R, Claeys M, Cafmeyer J, Maenhaut W, Roberts G, Artaxo P (2000) Carbonaceous aerosol characterization in the Amazon basin, Brasil: novel dicarboxylic acids and related compounds. Atmos Environ 34:5037–5051
25. Larsen BR, Lahaniati M, Calogirou A, Kotzias D (1998) Atmospheric oxidation products of terpenes: a new nomenclature. Chemosphere 37:1207–1220
26. Larsen BR, Di Bella D, Glasius M, Winterhalter R, Jensen NR, Hjorth J (2001) Gas-phase OH oxidation of monoterpenes: gaseous and particulate products. J Atmos Chem 38:231–276
27. Maenhaut W, Wang W, Chi X (2011) Semivolatile behaviour and filter sampling artifacts for dicarboxylic acids during summer campaigns at three forested sites in Europe. Boreal Environ Res 16:273–287
28. Müller L, Reinnig M-C, Warnke J, Hoffmann T (2008) Unambiguous identification of esters as oligomers in secondary organic aerosol formed from cyclohexene and cyclohexene/α-pinene ozonolysis. Atmos Chem Phys 8:1423–1433
29. Müller L, Reinnig M-C, Naumann KH, Saathoff H, Mentel TF, Donahue N, Hoffmann T (2011) Formation of 3-methyl-1,2,3-butanetricarboxylic acid via gas phase oxidation of pinonic acid – a mass spectrometric study of SOA aging. Atmos Chem Phys Discuss 11: 19443–19476
30. Nizkorodov SA, Laskin J, Laskin A (2011) Molecular chemistry of organic aerosols through the application of high resolution mass spectrometry. Phys Chem Chem Phys 13:3612–3629
31. Putman AL, Offenberg JH, Fisseha R, Kundu S, Rahn TA, Mazzoleni LR (2012) Ultrahigh-resolution FT-ICR mass spectrometry characterization of α-pinene ozonolysis SOA. Atmos Environ 46:164–172
32. Reinhardt A, Emmenegger C, Gerrits B, Panse C, Dommen J, Baltensperger U, Zenobi R, Kalberer M (2007) Ultrahigh mass resolution and accurate mass measurements as a tool to characterize oligomers in secondary organic aerosols. Anal Chem 79:4074–4082

33. Surratt JD, Kroll JH, Kleindienst TE, Edney EO, Claeys M, Sorooshian A, Ng NL, Offenberg JH, Lewandowski M, Jaoui M, Flagan RC, Seinfeld JH (2007) Evidence for organosulfates in secondary organic aerosol. Environ Sci Technol 41:517–527
34. Surratt JD, Gómez-González Y, Chan AWH, Vermeylen R, Shahgholi M, Kleindienst TE, Edney EO, Offenberg JH, Lewandowski M, Jaoui M, Maenhaut W, Claeys M, Flagan RC, Seinfeld JH (2008) Organosulfate formation in biogenic secondary organic aerosol. J Phys Chem A 112:8345–8378
35. Surratt JD, Chan AWH, Eddingsaas NC, Chan MN, Loza CL, Kwan AJ, Hersey SP, Flagan RC, Wennberg PO, Seinfeld JH (2010) Reactive intermediates revealed in secondary organic aerosol formation from isoprene. Proc Natl Acad Sci USA 107:6640–6645
36. Szmigielski R, Surratt JD, Gómez-González Y, Van der Veken P, Kourtchev I, Vermeylen R, Blockhuys F, Jaoui M, Kleindienst TE, Lewandowski M, Offenberg JH, Edney EO, Seinfeld JH, Maenhaut W, Claeys M (2007) 3–methyl-1,2,3–butanetricarboxylic acid: an atmospheric tracer for terpene secondary organic aerosol. Geophys Res Lett 34:L24811. doi:10.1029/2007GL031338
37. Vereecken L, Peeters J (2002) Enhanced H-atom abstraction from pinonaldehyde, pinonic acid, pinic acid, and related compounds: theoretical study of C–H bond strengths. Phys Chem Chem Phys 4:467–472
38. Yasmeen F, Vermeylen R, Szmigielski R, Iinuma Y, Böge O, Herrmann H, Maenhaut W, Claeys M (2010) Terpenylic acid and related compounds: precursors for dimers in secondary organic aerosol from the ozonolysis of α- and β-pinene. Atmos Chem Phys 10:9383–9392
39. Yasmeen F, Szmigielski R, Vermeylen R, Gómez-González Y, Surratt JD, Chan AWH, Seinfeld JH, Maenhaut W, Claeys M (2011) Mass spectrometric characterization of isomeric terpenoic acids from the oxidation of α-pinene, β-pinene, *d*-limonene, and Δ3-carene in fine forest aerosol. J Mass Spectrom 46:425–442
40. Yu JZ, Flagan RC, Seinfeld JH (1998) Identification of products containing –COOH, –OH, and –C=O in atmospheric oxidation of hydrocarbons. Environ Sci Technol 32:2357–2370
41. Yu JZ, Cocker DR III, Griffin RJ, Flagan RC, Seinfeld JH (1999) Gas-phase ozone oxidation of monoterpenes: gaseous and particulate products. J Atmos Chem 34:207–258
42. Zhang YY, Müller L, Winterhalter R, Moortgat GK, Hoffmann T, Pöschl U (2010) Seasonal cycle and temperature dependence of pinene oxidation products, dicarboxylic acids and nitrophenols in fine and coarse air particulate matter. Atmos Chem Phys 10:7859–7873

Chapter 19
An Ionization Method Based on Photoelectron Induced Thermal Electron Generation: capillary Atmospheric Pressure Electron Capture Ionization (cAPECI)

Valerie Derpmann, Iustinian Bejan, Hendrik Kersten, Klaus J. Brockmann, Ian Barnes, Jörg Kleffmann, Thorsten Benter, Hannah Sonderfeld, and Ralf Koppmann

Abstract A novel method for atmospheric pressure ionization of compounds with high electron affinity (e.g., nitroaromatic compounds) or gas phase acidity (e.g., phenols) is reported. The method is based on the generation of thermal electrons by the photoelectric effect, followed by electron capture of oxygen in air or, within pure nitrogen, of the analyte itself. In the presence of oxygen, ionization of the analyte is accomplished via charge transfer or proton abstraction by the strong gas phase base O_2^-. In terms of least invasive sample structure, the interaction of UV-light with metals represents a very clean method for the generation of thermal electrons at atmospheric pressure. This leads to a soft and selective ionization method, generating exclusively negative ions. The implementation of the ionization stage within a fast flowing gas system additionally reduces the retention time of the ionized sample within the high pressure region of the mass spectrometer. Therefore ion transformation processes are reduced and the mass spectrum corresponds more closely to the neutral analyte distribution than for ionization methods operating in conventional ion sources.

Keywords Nitroaromatic • Photoelectric effect • Explosive detection • Mass spectrometry • electron capture • Ionization • cAPECI

V. Derpmann • I. Bejan • H. Kersten • K.J. Brockmann • I. Barnes • J. Kleffmann • T. Benter (✉)
FB C – Physical & Theoretical Chemistry, University of Wuppertal, Gaussstraße 20, 42119 Wuppertal, Germany
e-mail: v.derpmann@uni-wuppertal.de; kleffman@uni-wuppertal.de; tbenter@uni-wuppertal.de

H. Sonderfeld • R. Koppmann
FB C – Physics Department, University of Wuppertal, Gaussstraße 20, 42119 Wuppertal, Germany

I. Barnes and K.J. Rudziński (eds.), *Disposal of Dangerous Chemicals in Urban Areas and Mega Cities*, NATO Science for Peace and Security Series C: Environmental Security,
DOI 10.1007/978-94-007-5034-0_19,

19.1 Introduction

19.1.1 Nitroaromatic Compounds

Nitroaromatic compounds, predominantly monoaromatics and especially nitrophenols, are an important class of volatile aromatic compounds in the atmosphere, because of their phytotoxic and mutagenic properties [17, 28, 29]. Direct emission to the atmosphere occurs by combustion processes and the production of dyes, explosives and drugs [13]. Additionally these substances are formed in situ as degradation products of organic hydrocarbons via reaction with OH-radicals (daytime) in the presence of NO_2 or NO_3-radicals (nighttime) [1, 3, 10, 27]. Nitroaromatics have been found in air at concentration levels of ng/m^3 [11, 13]. Investigations by Lüttke et al. [25], Voznakova et al. [32] and Kawamura and Kaplan [18] revealed significant concentrations of this compound class in clouds, soil, rain and snow, as well. Furthermore the photolysis of ortho-nitrophenols seems to be a potentially important photolytic source of nitrous acid (HONO) in the atmosphere [2, 15], a vital precursor for the generation of OH-radicals.

In addition it is well known that nitroaromatic compounds form the basis for most explosives (e.g. trinitrotoluene, RDX). The salient challenge in terms of detection and hence in terms of security reasons as, e.g., in airports is the low vapor pressure of these substances, which renders their detection very difficult and highlights the need for sensitive and reliable analytical instrumentation for their detection.

19.1.2 Detection of Nitroaromatic Compounds

As mentioned, both applications, investigation of chemical processes in the atmosphere and the detection of explosives, require a selective, sensitive, robust and reliable detection method. Currently Ion Mobility Spectroscopy (IMS) is the most widely used technique for the detection of explosives [7], whereas in atmospheric chemistry Proton Transfer Reaction Mass Spectrometry (PTR-MS) has become an important method in the past years [23].

For ionization in IMS fast electrons generated by the β-decay of ^{63}Ni [7] and for mass spectrometric detection of explosives atmospheric pressure chemical ionization (APCI) [5, 12] is widely established. The electrons ionize matrix compounds like N_2 leading to a thermodynamically equilibrated distribution of protonated water clusters, $[H(H_2O)_n]^+$. Simultaneously, negative reactant ions are formed. Both positive and negative reactant ions can ionize analytes by charge transfer and proton transfer or proton abstraction, respectively. This type of chemical ionization leads to complex ion mobility and mass spectra, which are difficult to reproduce due to the low selectivity of the ionization method, the existence of oppositely charged ions in the ion source and the high dependence of the reactant ion distribution on the conditions inside the ion source such as relative humidity or temperature.

In contrast to IMS, mass spectrometry allows identification of the analyte by its mass to charge ratio, however, an unselective ionization method, such as APCI, produces high background noise which renders the interpretation of the resulting mass spectra more difficult. The use of a discharge ionization source as used in APCI inevitably produces vast amounts of highly reactive neutral radicals, beneath N_2^+. These drive a rich chemistry within the ionization source affecting the resulting mass spectra with spurious signal artifacts due to subsequent neutral radical-ion molecule reactions [19, 31]. Indeed, these artifacts are a major drawback of this well established method.

In PTR-MS the reagent ions H_3O^+ and $[H(H_2O)_n]^+$-cluster are generated with a hollow cathode discharge operated in a water vapor saturated environment. Exclusively positively charged ions enter the drift tube (approx. 3 mbar) where the analyte gas is introduced. The ionization mechanism proposed for PTR is the so called "ligand switching mechanism" [21]. An analyte molecule approaches the protonated water cluster, while water molecules are ejected.

$$M + H^+(H_2O)_n \rightarrow MH^+(H_2O)_m + \text{n-m } H_2O \tag{19.1}$$

An electrical field gradient inside the drift tube of several hundred volts is applied to dissociate the protonated analyte water clusters towards protonated analyte molecules. However, the applied electrical field strength inside the drift tube is high enough for significant collision induced dissociation processes of the protonated analyte molecules, rendering the analysis of the recorded mass spectra more difficult. The limits of detection for many different compound classes are in the pptV-regime, which is a decisive advantage of PTR-MS and thus explains its wide spread use, e.g., in atmospheric chemistry [9].

An ionization method for IMS that utilizes the high electron affinities of most nitroaromatic compounds is based on thermal electron generation with the photoelectric effect and subsequent electron capture by oxygen and chemical ionization of the analyte [14]. For the electron generation a thin gold film is vapor deposited on a quartz window, pulsed UV-light impinges the surface at an angle that is smaller than the critical angle of total internal reflection, so that electrons are produced, but the light does not enter into the ion source, therefore photo induced dissociation of the analytes is avoided. The electrons are immediately thermalized by collisions with buffer gas and are then captured by oxygen, followed by charge or proton transfer. Although the method is very selective for compounds with high electron affinities, it has not yet found its way into practical applications.

As mentioned above most mass spectra derived from standard atmospheric pressure ionization methods do not represent the neutral analyte distribution correctly, but are changed by ion transformation processes, e.g., ion-molecule/neutral radical reactions or fragmentation of analyte ions. These processes are enhanced by high reactant ion and neutral radical concentrations inside the ion source, long transfer times of the analyte ions from the ion source to the nearly collision free high vacuum region of the mass spectrometer and by high electrical field gradients. In negative ion mass spectrometry similar reaction cascades are described for different ionization methods even though the primary ion generation is

very different [26]. This means any ionization method operated at atmospheric pressure is most likely affected by fragmentation or ion-molecule reactions often reported for negative ion mass spectrometry. The only way to shift the mass spectra closer to the neutral analyte distributions is to shorten the time between ion generation and entrance into the collision free region and to reduce the radical and oppositely charged ion concentrations in the ionization region.

In this work we introduce a novel atmospheric pressure ionization method, which is based on the photoelectric effect. To reduce the dwell times of the ions in the high pressure region, ionization is located in the transfer capillary, which is used for pressure reduction from atmospheric pressure inside the ion source to approx. 4 mbar in the first differential pumping stage of the mass spectrometer. The flow inside the transfer capillary is characterized as fully turbulent [20]. Inside the transfer capillary dwell times lower than 1 ms are achieved [4]. The generation of solely negatively charged particles avoids fast reactions of the analyte ions with oppositely charged particles inside the ion source. Basically three different pathways can lead to the ionization of analytes: (1) direct electron capture by the analyte, (2) electron capture by a primary charge carrier present in excess, e.g., O_2, with subsequent charge transfer to the analyte or (3) with subsequent proton abstraction from the analyte. Hence, compounds with high electron affinities and/or high gas phase acidities are amenable to this method (e.g., nitrocompounds, phenols, quinones). To express the ionization principle and emphasize the specific position of ionization it is termed "capillary Atmospheric Pressure Electron Capture Ionization" (cAPECI). Due to the fact that dwell times of the generated ions within the high pressure region are reduced this method is hardly affected by ion transformation processes. Furthermore, detection limits in the lower ppbV range have been achieved. In the following cAPECI is characterized and is then compared with the established ionization method PTR-TOF-MS.

19.2 Experimental Section

19.2.1 Chemicals

All chemicals were purchased from Sigma Aldrich in the highest purity available and were used without further purification. Synthetic air and nitrogen were purchased from Gase.de, Sulzbach, Germany, with a stated purity of 99.999 % vol.

19.2.2 Ion Source

For cAPECI a quartz capillary of 18 cm length with an inner diameter of 0.5 mm and an outer diameter of 4 mm was modified with one half of the capillary channel chemically coated with silver. The custom capillary was built into the mass

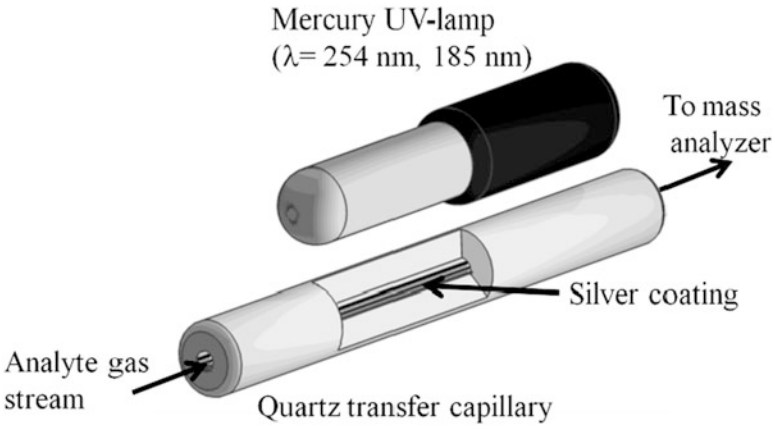

Fig. 19.1 Schematic of the cAPECI capillary with light source

spectrometer replacing the conventional transfer capillary used as the pressure reduction stage between the atmospheric pressure and the low pressure side (approximately 4 mbar) in the first differential pumping stage. As the work function of silver ranges between 4.25 and 4.74 eV [22] radiation with a minimum wavelength of 261 nm is necessary to generate photoelectrons. A low pressure mercury lamp (LSP035, LOT-Oriel GmbH & Co. KG, Darmstadt, Germany) was used to provide light at mainly 254 nm and to a lesser extent 185 nm. The cAPECI setup is shown schematically in Fig. 19.1.

19.2.3 Instrumentation

cAPECI measurements were performed with an esquire6000 quadrupole ion trap (Bruker Daltonik GmbH, Bremen, Germany) and for PTR-MS measurements a PTR-HRTOF-MS (Ionicon Analytik GmbH, Innsbruck, Austria) was used. The ion source used for cAPECI is described in Sect. 19.2.2. The PTR-MS was used without further modifications.

The gas phase concentrations of the analytes were determined simultaneously to the mass spectrometric measurements by a Fourier-Transform Infrared-Spectrometer (FT-IR) Nicolet Nexus (Thermo Scientific), in a 10 l measurement cell containing a multiple reflection gold coated mirror system operated at a total optical path length of 32.8 m. For the delivery of precise mixing ratios a minor gas flow of synthetic air was saturated with the vapor pressure of the solid analyte at room temperature and then added to a main synthetic air carrier gas. Both gas flows were regulated with mass flow controllers (Mass Flo Controller, MKS Instruments, Andover, MA, USA).

19.3 Results and Discussion

19.3.1 Ionization Mechanism

Under high vacuum conditions with clean electrode surfaces the mechanism of the photoelectric effect is fairly well understood. In a typical ion source environment at ambient pressure, however, surfaces are more likely covered with layers of different types of molecules, primarily water. The impact of these layers on the electrode characteristics in terms of electron liberation into the gas phase is not yet understood. Mechanisms allowing for permanent negative charging of these layers with the generated photo electrons followed by intensive interaction with the analyte should also be taken into account. Nevertheless some general mechanistic remarks can already be made from several experiments.

In cAPECI thermal electrons are generated by the photo electric effect with a low pressure mercury UV-lamp as the light source. The kinetic energy of the emitted electrons can be calculated from the difference of the work function of the metal and the wavelength of the photons. In this case, the interaction of UV-light (254 and 185 nm) with silver (work function 4.74 eV) results in electron kinetic energies of 0.14 and 1.96 eV, respectively. However, the free electrons are readily thermalized via collisions with the surrounding buffer gas (mainly N_2) down to E_{kin} ~ 0.02 eV. Once thermalized the electrons are captured by molecules with high electron affinities, followed by collisions with the buffer gas to transfer the excess energy. Depending on the matrix constituents the dominating species for the electron capturing process might either be the analyte itself or, e.g., O_2 to form O_2^-. In most cases the latter is very fast and thus the predominant process since, firstly, oxygen is often present in excess and, secondly, the third order rate constant with $k = 2 \times 10^{-30}$ cm^6 s^{-1} [30] is high. The generated superoxide reacts with a neutral analyte molecule M by charge transfer to form the M^- if the electron affinity of the analyte exceeds the electron affinity of oxygen or by proton abstraction if the gas phase basicity of O_2^- is higher than the gas phase basicity of the deprotonated analyte anion $[M - H]^-$. It is currently under investigation if O_2^- water clusters are formed and if so what role they play for ionization of the analyte. Table 19.1 gives an overview of electron affinities and gas phase acidities of some analytes and

Table 19.1 Calculated electron affinities and gas phase acidities (basicity in case of O_2^-)

Analyte	Electron affinity [eV]	Gas phase acidity [eV]	Observed signal
Oxygen	0.61 (0.45[a])	14.89 (basicity of O_2^-)	–
1,4-Benzoquinone	2.22 (1.85−1.99[a])	15.89	M^-
4-Methylphenol	−0.45	13.77	$[M\text{-}H]^-$
2-Nitrophenol	1.12	15.07	$[M\text{-}H]^-$
1-Nitro-2-isopropylbenzol	1.29	–	M^-
Sulfur hexafluoride	1.15 (1.07−1.2[a])	–	M^-

[a]Literature values [24]

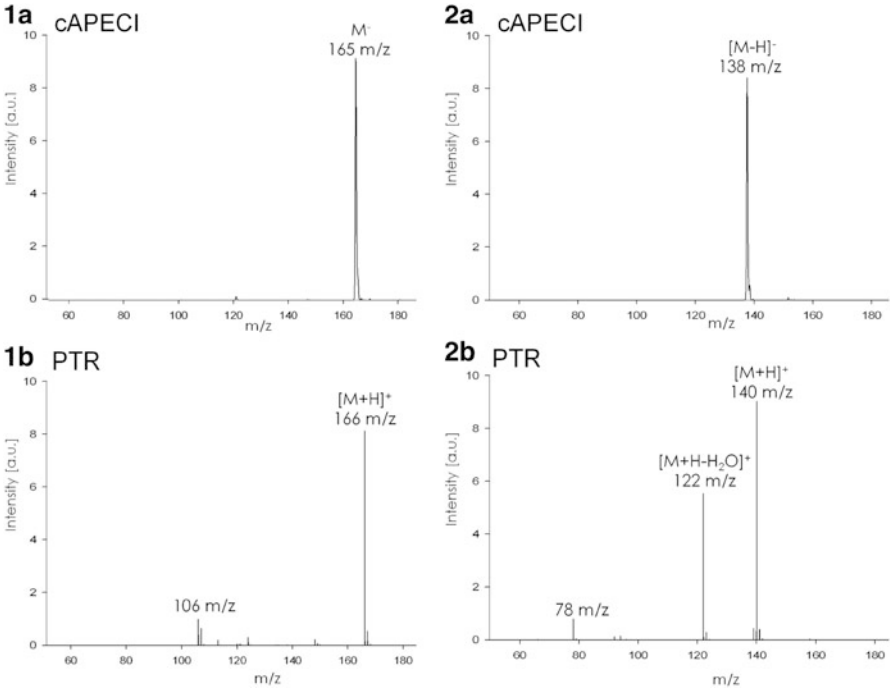

Fig. 19.2 Comparison of the mass spectra of (*1*) 2-nitroisopropylbenzene and (*2*) 2-nitrophenol recorded upon ionization with (**a**) cAPECI and (**b**) PTR

the signal type in the cAPECI mass spectra. For oxygen the gas phase basicity of O_2^- is given instead of the gas phase acidity. Both the electron affinities and gas phase acidities were calculated using the density functional theory (DFT) with the Becke-3-Parameter-Lee-Yang-Parr functional (B3LYP) and the 6-31++G(d,p) doubly-diffuse and doubly-polarized split-valence basis set, with the Gaussian program [8] and the graphical user interface GaussView [6]. Literature values are additionally given where available.

Analytes with high electron affinity tend to generate the radical anion M^- signal in cAPECI mass spectra. In case of analytes containing hydroxyl groups the deprotonated analyte anion $[M - H]^-$ is the prevailing detected species.

19.3.2 Comparison of cAPECI with PTR-MS

While cAPECI is a very selective method for the negative ion mode, PTR offers ionization of a very broad analyte spectrum, but only in the positive ion mode. Figure 19.2 shows a comparison of the mass spectra of 2-nitroisopropylbenzene (molecular weight 165 g/mol) and 2-nitrophenol (molecular weight 139 g/mol)

obtained with both ionization methods. The mass spectra were measured simultaneously from the same sample.

In the cAPECI mass spectrum of 2-nitro-isopropylbenzene and other nitro-alkylbenzenes only one signal, the M^-, is obtained (cf. Fig. 19.2 1a). PTR also shows one main signal related to the analyte, the $[M + H]^+$ at 166 m/z (cf. Fig. 19.2 1b). There are other signals at around 106 m/z which could not be identified. The mass spectrum of 2-nitrophenol obtained with cAPECI shows only one signal assigned to the deprotonated form of the analyte (cf. Fig. 19.2 2a). The most abundant signal in the PTR-MS mass spectrum (cf. Fig. 19.2 2b) is assigned to the protonated species $[M + H]^+$, followed by a fragment ion at m/z 122, corresponding to the loss of water of the protonated species. The third signal appearing at m/z 78 has not yet been identified.

For comparison of the performance of PTR and cAPECI the lower limit of detection (LOD) for 3-methyl-2-nitrophenol was estimated following the procedure described by Kaiser and Specker, (3σ) [16]. With the PTR-TOF-MS a LOD of 250 pptV with an acquisition time of 30 s was obtained. For cAPECI in combination with the ion trap a LOD of 1 ppbV was obtained, however with an acquisition time less than 1 s.

19.4 Conclusion

With cAPECI a selective ionization method for analytes with high electron affinity or gas phase acidity is introduced. Its principle of operation is based on the generation of thermal electrons via the photoelectric effect with subsequent electron capture. The high selectivity results in very good signal-to-noise ratios and thus in low detection limits. For 3-methyl-2-nitrophenol a limit of detection of around 1 ppbV with an ion trap acquisition time below 1 s was determined. For comparison, PTR-MS needs an acquisition time of 30 s to achieve a detection limit of 250 pptV for the same compound. Gas samples can be directly analyzed by cAPECI without any sample preparation. The major advantage of cAPECI is that unwanted fragmentation and ion transformation processes are virtually absent; hence the obtained mass spectra are close to the neutral analyte distribution. The radical anions M^- or the deprotonated species $[M - H]^-$ of the analytes are the predominant mass signals. For comparison, PTR-MS often shows more than one signal per analyte, in particular for hydroxyl and nitro groups containing compounds extensive fragmentation occurs.

19.5 Future Work

The cAPECI capillary ion source has some disadvantages such as an inhomogeneous silver surface inside the capillary or the appearance of charging effects due to the material quartz. Hence we are working on a new ion source design which avoids

these problems and allows the use of metals other than silver. Additionally, a homogeneous metal surface will result in an improved sensitivity. With this ion source measurements relevant for atmospheric chemistry like photo-oxidation and product studies will be performed.

References

1. Atkinson R, Aschmann SM, Arey J (1992) Reactions of hydroxyl and nitrogen trioxide radicals with phenol, cresols, and 2-nitrophenol at 296 ± 2 K. Environ Sci Technol 26: 1397–1403
2. Bejan I, Abd El Aal Y, Barnes I, Benter T, Bohn B, Wiesen P, Kleffmann J (2006) The photolysis of ortho-nitrophenols: a new gas phase source of HONO. Phys Chem Chem Phys 8:2028–2035
3. Bolzacchini E, Bruschi M, Hjorth J, Meinardi S, Orlandi M, Rindone B, Rosenbohm E (2001) Gas-phase reaction of phenol with NO_3. Environ Sci Technol 35:1791–1797
4. Brockmann KJ, Wissdorf W, Hyzak L, Kersten H, Mueller D, Brachthaeuser Y, Benter T (2010) Fundamental characterization of ion transfer capillaries used in atmospheric pressure ionization sourced. In: 58th ASMS conference on mass spectrometry and allied topics, Salt Lake City, UT, USA
5. Covey TR, Thomson BA, Schneider BB (2009) Atmospheric pressure ion sources. Mass Spectrom Rev 28:870–897
6. Dennington R, Keith T, Millam J (2007) GaussView; 4.1. Semichem, Inc, Shawnee Mission
7. Ewing RG, Atkinson DA, Eiceman GA, Ewing GJ (2001) A critical review of ion mobility spectrometry for the detection of explosives and explosive related compounds. Talanta 54: 515–529
8. Frisch MJ et al (2003) Gaussian 03W; revision C.02. Gaussian, Inc, Wallingford
9. Graus M, Müller M, Hansel A (2010) High resolution PTR-TOF: quantification and formula confirmation of VOC in real time. J Am Soc Mass Spectrom 21:1037–1044
10. Grosjean D (1984) Atmospheric reactions of ortho cresol: gas phase and aerosol products. Atmos Environ 18:1641–1652
11. Grosjean D (1991) Ambient levels of formaldehyde, acetaldehyde and formic acid in southern California: results of a one-year baseline study. Environ Sci Technol 25:710–715
12. Gross M, Caprioli RM (eds) (2007) The encyclopedia of mass spectrometry, vol 6. Elsevier, Oxford/Großbritannien
13. Harrison MAJ, Barra S, Borghesi D, Vione D, Arsene C, Olariu RI (2005) Nitrated phenols in the atmosphere: a review. Atmos Environ 39:231–248
14. Hong F (2004) Photoemission applied to ion mobility spectrometry to detect explosives at ambient pressure and room temperature. Dissertation, North Dakota State University
15. Jagiella S, Zabel F (2007) Reaction of phenylperoxy radicals with NO_2 at 298 K. Phys Chem Chem Phys 9:5036–5051
16. Kaiser H, Specker H (1956) Bewertung und Vergleich von Analysenverfahren. Fresenius J Anal Chem 149:46–66
17. Kawai A, Goto S, Matsumoto Y, Matsushita H (1987) Mutagenicity of aliphatic and aromatic nitro compounds. Industrial materials and related compounds. Jpn J Ind Health 29:34–54
18. Kawamura K, Kaplan IR (1986) Biogenic and anthropogenic organic compounds in rain and snow samples collected in southern california. Atmos Environ 20:115–124
19. Kersten H, Funcke V, Lorenz M, Brockmann KJ, Benter T, O'Brien R (2009) Evidence of neutral radical induced analyte ion transformations in APPI and near-VUV APLI. J Am Soc Mass Spectrom 20:1868–1880

20. Kersten H, Derpmann V, Barnes I, Brockmann K, O'Brien R, Benter T (2011) A novel APPI-MS setup for in situ degradation product studies of atmospherically relevant compounds: capillary Atmospheric Pressure Photo Ionization (cAPPI). J Am Soc Mass Spectrom. doi:10.1007/s13361-011-0212-y
21. Liang C-W, Lee YT, Chen C-H, Wang Y-S (2010) Ionizing nonvolatile samples using laser desorption proton-transfer reaction with cluster reagent ions. Int J Mass Spectrom 291:61–66
22. Lide DR (ed) (2007–2008) CRC handbook of chemistry and physics, 88tth edn. CRC Press, Boca Raton
23. Lindinger W, Hansel A, Jordan A (1998) On-line monitoring of volatile organic compounds at pptv levels by means of proton-transfer-reaction mass spectrometry (PTR-MS) medical applications, food control and environmental research. Int J Mass Spectrom 173:191–241
24. Linstrom PJ, Mallard WG (eds) (2011) National Institute of Standards and Technology, Gaithersburg, MD. http://webbook.nist.gov. Retrieved 21 Dec 2011
25. Lüttke J, Scheer V, Levsen K, Wünsch G, Neil Cape J, Hargreaves KJ, Storeton-West RL, Acker K, Wieprecht W, Jones B (1997) Occurrence and formation of nitrated phenols in and out of cloud. Atmos Environ 31:2637–2648
26. McEwen CN, Larsen BS (2009) Ionization mechanisms related to negative ion APPI, APCI, and DART. J Am Soc Mass Spectrom 20:1518–1521
27. Olariu RI, Klotz B, Barnes I, Becker KH, Mocanu R (2002) FT-IR study of the ring-retaining products from the reaction of OH radicals with phenol, o-, m-, and p-cresol. Atmos Environ 36:3685–3697
28. Purohit V, Basu AK (2000) Mutagenicity of nitroaromatic compounds. Chem Res Toxicol 13:673–692
29. Rippen G, Zietz E, Frank R, Knacker T, Klöpffer W (1987) Do airborne nitrophenols contribute to forest decline? Environ Tech Lett 8:475–482
30. Shimamori H, Fessenden RW (1981) Thermal electron attach ment to oxygen and van der Waals molecules containing oxygen. J Chem Phys 74:453–466
31. Song L, Wellman AD, Yao H, Bartmess JE (2007) Negative ion-atmospheric pressure photoionization: electron capture, dissociative electron capture, proton transfer, and anion attachment. J Am Soc Mass Spectrom 18:1789–1798
32. Voznakova Z, Podehradska J, Kohlickova M (1996) Determination of nitrophenols in soil. Chemosphere 33:285–291

Chapter 20
NO_x in Chinese Megacities

Jun Liu and Tong Zhu

Abstract In the past 30 years, China has undergone great economic improvements, the urbanization rate is increasing, megacities and city clusters are expanding, leading to the development of China's economy and society. However, the city expansion has resulted in a series of environmental problems, such as increasing energy consumption and consequently emission of pollutants, as well as deterioration in urban air quality. In spite of many measures taken by the Chinese government, air pollution from nitrogen oxides ($NO_x = NO + NO_2$) is still serious and the NO_x concentration is increasing. This article analyses NO_x pollution and its trends in Chinese megacities from three aspects, authoritative routine reports, campaign based research observations, and satellite observations. The article also discusses the main sources of NO_x in Chinese Megacities. The discussion is based on a review of research papers on the China NO_x emission inventory.

Keywords Nitrogen oxides (NO_x) • Megacity • NO_x concentrations • NO_x sources

20.1 Introduction

Since 2000, the annual growth rate of the gross domestic product (GDP) in China was about 10%. In 2010, the GDP in China ranked No. 2 across the world, accounting for 9.5% of the GDP in the whole world [10]. With rapid development of the economy, the urbanization rate is increasing faster. The number of cities has increased from 208 in 1961 to 654 in 2010 (Fig. 20.1). In 2010, 231 prefecture (and higher) level cities had over one million residents and nine cities had over ten million residents (Fig. 20.2). From 1960 to 2010, the urban population percentage

J. Liu • T. Zhu (✉)
State Key Laboratory for Environmental Simulation and Pollution Control,
College of Environmental Sciences, Peking University, Beijing, China
e-mail: tzhu@pku.edu.cn

I. Barnes and K.J. Rudziński (eds.), *Disposal of Dangerous Chemicals in Urban Areas and Mega Cities*, NATO Science for Peace and Security Series C: Environmental Security,
DOI 10.1007/978-94-007-5034-0_20,

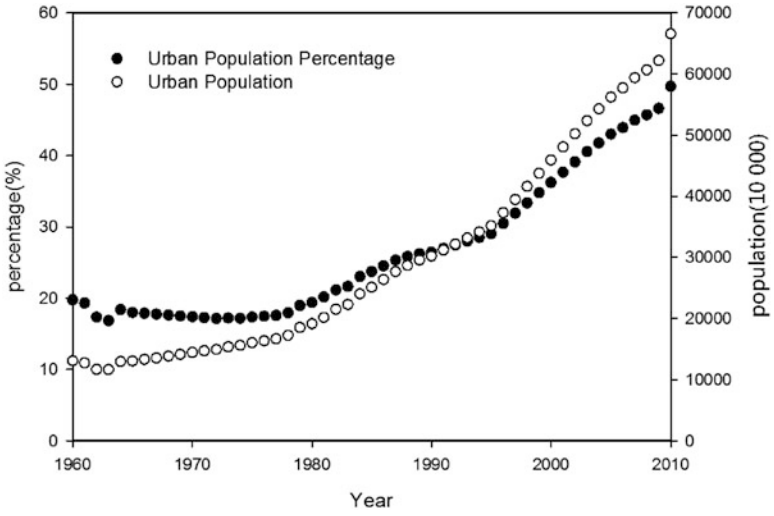

Fig. 20.1 The urban population and urban population proportion trend in China since 1960 (China Statistical Yearbook 2011)

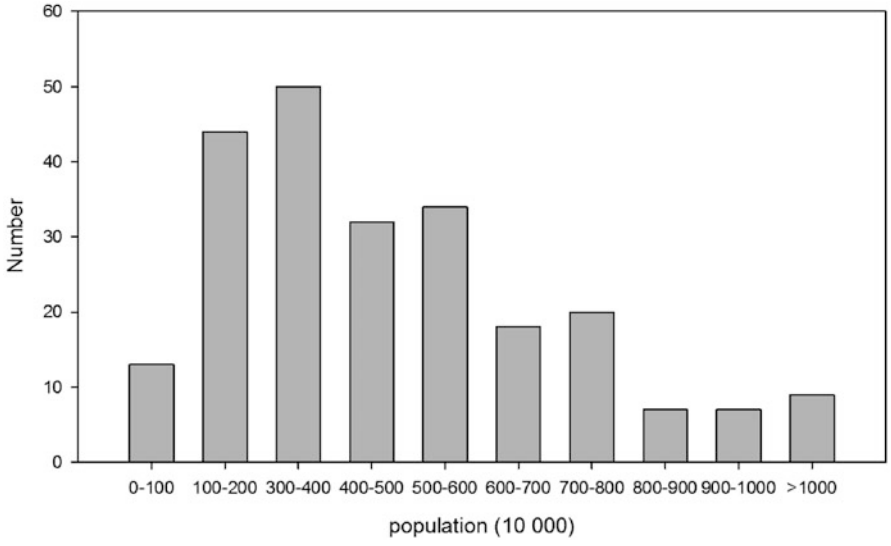

Fig. 20.2 Prefecture (and higher) level city size in China in 2010 [10]

in China increased from 19.7 to 49.7% (Fig. 20.1). In 2010, the urban population reached 665.6 million [10].

Figure 20.3 shows that, since 2000, the total energy consumption rate in China has been increasing, and in 2010, the total energy consumption was equivalent to 3.25 billion tons of coal, which is 2.2 times the amount consumed in 2000 [8]. Because China does not have large oil and natural gas resources, it was the largest

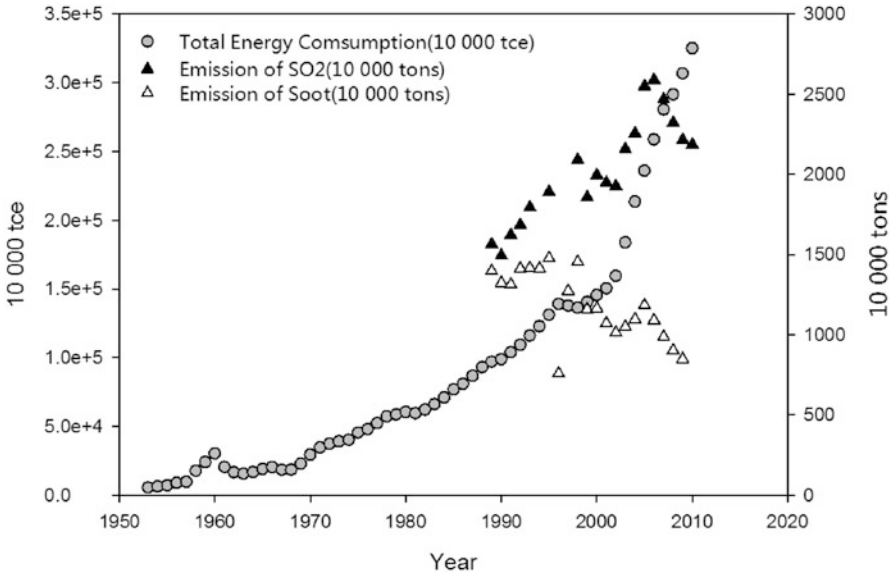

Fig. 20.3 Annual total energy consumption and pollutants emission in China [6, 8, 9]

coal consuming country in the world, and in 2010, the use of coal accounted for 74% of the country's total energy consumption [7]. However, the quality of the coal resources in China is poor, often with a low desulfurization ratio; therefore coal-burning processes was accompanied with large SO_2, soot and NO_x emissions, which led to serious air pollution problems. Since the first official SO_2 emission data was reported in 1989, SO_2 emissions in China substantially increased over the years [9], until 2006. In 2006 the National Eleventh Five-year Plan issued SO_2 emission reduction requirements, after which SO_2 emissions in China began to decrease [48]. At the same time, the number of motor vehicles in Beijing, Shanghai, Guangzhou and other megacities significantly increased. By the end of June 2011, the number of motor vehicles in China reached 217 million, of which the number of automobiles and motorcycles was 98.5 million and 102 million, respectively. There were 11 cities in China, including Beijing, Shenzhen, Shanghai, Chengdu and Tianjin, which have more than one million automobiles [30]. Motor vehicle emissions of NO_x, VOCs and other pollutants in megacities have exacerbated the air pollution problems in China.

To deal with the serious air pollution problems, the Chinese government implemented a series of control measures. In 1998, the State Council approved Acid Rain Control Zones and SO_2 Pollution Control Zones, and SO_2 was treated as one of the major environmental protection indicators in the National Eleventh FIVE-year Plan, which was expected to achieve the target of 10% reduction of emissions compared to 2005 [48]. Based on strict control standards, SO_2 emissions in China decreased by 13.14% during 2005–2009, 82.5% of the cities had SO_2 annual concentrations below the Grade-II standard in 2008 [33].

While SO_2 control achieved significant improvements, NO_x control has not kept pace with the rate of energy consumption. With the accelerated process of urbanization, the populations in Megacities kept growing, the number of motor vehicles increased rapidly, and NO_x pollution became more and more common in megacities. Akimoto, [1] has compared NO_x emission trends in North America, Europe and Asia. He found that NO_x emissions in Asia have increased rapidly since the 1970s and that they surpassed those in North America and Europe in the mid-1990s. Akimoto speculated that the trend would continue for decades. The NO_x seriously polluted areas in China are mainly in the megacities with high population density [28], thus health effects induced by NO_x pollution should be one of the top environmental concerns in the development of many Chinese megacities. Recently, the Chinese government began to pay attention to the NO_x problem in the country. The National Twelfth Five-year Plan approved in 2010 ranked NO_x as one of the major environmental protection indicators for the first time, and set a 10% reduction target in NO_x emissions during the period of 12th 5-year plan [49].

By combining three aspects of pollution data, including authoritative reports, campaign based research observations, and satellite observations, the article analyzes NO_x pollution in Chinese megacities. The article will also discuss the main sources of NO_x emissions in Megacities to provide scientific support for reasonable control measures. The discussion is based on a review of research papers on the China NO_x emission inventory.

20.2 NO_2 Pollution Situation

20.2.1 Routine Monitoring Network

In 1996, the revised Chinese National Ambient Air Quality Standards (CNAAQS) included NO_2 as a Routine Monitoring species. In 2000, NO_2 replaced the original Monitoring indicator NO_x [3]. Table 20.1 presents the concentration limits for NO_2 in the CNAAQS (GB3095-1996). Since then, most cities in China have begun to monitor NO_2 and publish information on the pollutant's concentration.

Seven Chinese megacities in regions with the highest tropospheric column amounts of NO_2 (Beijing, Shanghai, Tianjin, Chongqing, Guangzhou, Shenzhen and Chengdu) have been selected as typical representatives, Table 20.2 shows the basic conditions of the seven megacities (except City District Population, other indexes are based on data for the whole city).

Figure 20.4 presents trends of the NO_x annual concentrations in each city since 1999. In 1999–2010, the NO_x annual concentrations of the seven megacities were all below the Grade-II standard 80 $\mu g/m^3$, but exceeded the Grade-I standard 40 $\mu g/m^3$. NO_x concentrations in the megacities have a gradually decreasing trend during the 12 years; the average concentration of the seven megacities (referred to as Average in Fig. 20.4) decreased from 0.06 mg/m^3 in 1999 to 0.049 mg/m^3 in 2010, i.e. a decrease of 21.2%. In 2004, the NO_2 concentrations in most southern

Table 20.1 Concentration limits for NO_2 in the Chinese National Ambient Air Quality Standards (CNAAQS) (mg/m^3) [3]

Pollutants	Averaging time	Concentration limits		
		Grade-I[a]	Grade-II[a]	Grade-III[a]
Nitrogen dioxide (NO_2)	Annual	0.04	0.08	0.08
	Daily	0.08	0.12	0.12
	Hourly	0.12	0.24	0.24

[a] According to the National Ambient Air Quality Standards, ambient air quality functional areas are divided into three categories: first category areas are nature reserves, scenic spots and other areas requiring special protections; second category areas are residential areas, commercial traffic and residential mixing areas, cultural areas, generally industrial areas and rural areas; third category areas are specific industrial areas. Ambient air quality is divided into three grades: first category areas follow Grade-I concentration limits; second category areas follow Grade-II concentration limits; third category areas follow Grade-III concentration limits

Table 20.2 Basic conditions of the seven megacities in 2009 (except city district population, other indexes are based on data for the whole city)

City	Lat-Lon	GDP (billion)	City district population (10,000)	Total energy consumption (10,000 tce)	Number of civil vehicles owned (1,000)
Beijing	E116°28′ N39°54′	1,215.3[a]	1,164.5[d]	6,570[e]	3,681[a]
Shanghai	E121°29′ N31°14′	1,504.6[a]	1,326.7[d]	1,0367[e]	1,471[a]
Tianjin	E117°11′ N39°09′	752.2[a]	798.4[d]	5,874[e]	1,300[a]
Chongqing	E106°32′ N29°32′	653.0[a]	1,426.3[d]	7,030[e]	908.9[a]
Chengdu	E104°05′ N30°39′	405.3[b]	515.5[d]	–	2,359[g]
Guangzhou	E113°15′ N23°08′	913.8[c]	650.3[d]	5,586.4[f]	1,341[c]
Shenzhen	E114°04′ N22°37′	820.1[c]	884.3[d]	–	1,419[c]

[a] China Statistical Yearbook 2010. National Bureau of Statistics of China, China Statistics Press
[b] Sichuan Statistical Yearbook 2010. Sichuan Provincial Bureau of Statistics, National Bureau of Investigation Corps in Sichuan, China Statistics Press
[c] Guangdong Statistical Yearbook 2010. Guangdong Provincial Bureau of Statistics, National Bureau of Investigation Corps in Guangdong, China Statistics Press
[d] China City Statistical Yearbook 2010. National Bureau of Urban Social and Economic Survey Division, China Statistics Press
[e] China Energy Statistical Yearbook 2010, National Bureau of Statistics Energy Statistics Division, China Statistics Press
[f] Guangzhou Statistical Yearbook 2010, Guangzhou Municipal Bureau of Statistics, National Bureau of Investigation Team in Guangzhou, China Statistics Press
[g] China Statistical Yearbook of regional economy 2010. National Bureau of Comprehensive Statistics Division, China Statistics Press

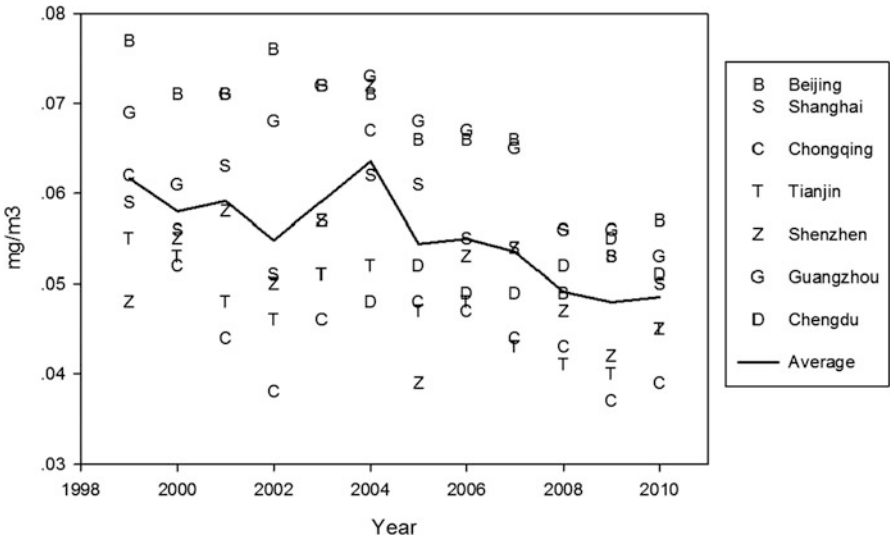

Fig. 20.4 Trends of NO_2 annual concentrations of seven megacities in 1999–2010 [31, 32, 34–38]

cities substantially increased compared to 2003, increasing by 45.7, 26.3 and 8.8% in Chongqing, Shenzhen and Shanghai respectively. However, the NO_2 concentrations in the northern cities showed no significant increase; the change rate was 1.9 and −1.3% in Beijing and Tianjin respectively. Chan and Yao [5] reported that O_3 and $NO_2 + O_3$ annual concentrations in Shenzhen increased in 2004, and other pollutants also showed significant increases in concentrations in Hong Kong, possibly linked to the low rainfall in the south. From late 2008 to 2009, due to the global financial crisis, economic depression brought improvements in the environment quality, which may also result in decreases in NO_2 concentrations.

During 1999–2007, the NO_2 annual concentrations in Beijing were almost the highest among the seven megacities. Before and during the 2008 Olympic Games, Beijing and surrounding areas implemented strict emission reduction measures, including reducing on-road motor vehicles, freezing construction activities, relocating heavy polluters and introducing strict vehicular emissions standards [54]. Through these measures the air quality in Beijing was significantly improved, the NO_2 annual concentration decreased from 0.066 mg/m^3 in 2007 to 0.049 mg/m^3 in 2008, i.e. by 25.8%. However, after 2008, with fewer control measures, increasing energy consumption led to larger emissions, and the NO_2 concentrations began to rise. In 2010 the NO_2 annual concentration was 0.057 mg/m^3, i.e. 14% higher than that in 2008. The annual trend of NO_2 in Shanghai was similar to the average of the seven cities; in the period 1999–2007 the NO_2 annual concentrations in Shanghai decreased by 15.3%.

Guangzhou and Shenzhen are two megacities located in the Pearl River Delta in China. Geographically, Guangzhou is close to Shenzhen, but the NO_2 annual concentration trend in Guangzhou was 10.9–74.3% higher than that in Shenzhen.

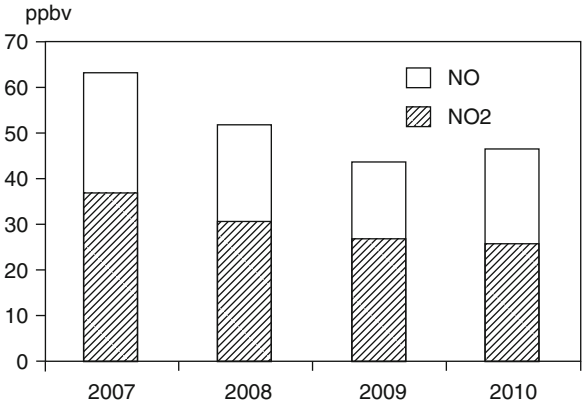

Fig. 20.5 Annual variations of NO and NO_2 concentrations observed in Peking University during 2007–2010

This was not only because of higher NO_x emissions in Guangzhou [65], more importantly, Guangzhou which is located in the heart of the Pearl River Delta region, is affected by emissions from Foshan, Dongguan and other surrounding cities and has thus become the centre of regional air pollution in Pearl River Delta. Shenzhen, on the other hand, is adjacent to the South China Sea in the south, and the prevailing sea and land breezes promote diffusion and transmission of the air pollution, thus resulting in lower NO_2 concentrations in Shenzhen.

Chengdu is the Capital city of Sichuan province, located in the western Sichuan Basin and surrounded by mountains with two main rivers (Min and Tuo river) passing through the city. It's also the economic center and an important communications hub of Southwest China. In 2009, the number of vehicles in Chengdu exceeded 2.35 million [63]. Due to the special basin meteorological conditions, Chengdu is frequently foggy, with low wind speeds, high humidity and thick tropospheric cloud cover, all of which are not good for the diffusion of pollutants. So far, there have been no peer reviewed research articles reporting the air pollution in Chengdu, but some Chinese journal articles have reported an increasing trend in the observed NO_x concentrations in the city district [56], which are ascribed to emissions from the increasing number of motor vehicles in Chengdu [42, 56, 63]. In our study, Chengdu was the only megacity with a continuous increasing trend in the NO_2 annual concentrations, and even during the 2008–2009 financial crisis period, the NO_2 concentration still increased. In 2009, the NO_2 annual concentration in Chengdu reached the highest concentration of 0.055 mg/m^3.

20.2.2 NO_x Concentrations Based on Research Campaigns

There are many scientific papers reporting NO_x concentrations based on ground research campaigns [11, 13, 14, 16, 29, 40, 46, 47, 60, 66]. This article uses NO_x observational data from the environmental monitoring platform on the Science Building of Peking University (Referred to PKU) as an example. Figures 20.5 and

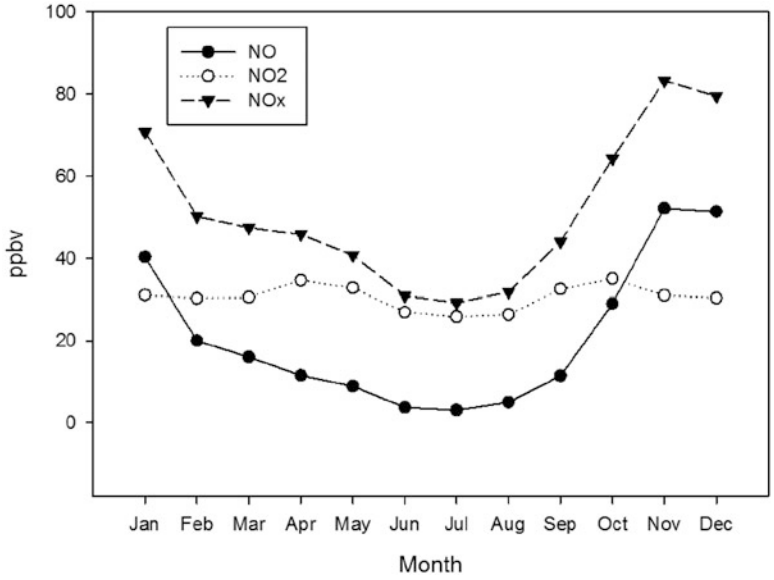

Fig. 20.6 Monthly variations of NO and NO_2 concentrations observed in Peking University from July in 2006 to December in 2010

20.6 show the annual and monthly variations of NO, NO_2 and NO_x concentrations observed in PKU from July in 2006 to December in 2010. As can be seen in Fig. 20.5, there was an obviously decreasing trend in the NO_2 annual concentration during 2007–2010, and in 2010 the annual concentration of NO_2 was 25.4 ppbv. During the observation period, NO_x concentrations first gradually decreased, and then began to increase in 2010. With respect to monthly variations, the NO and NO_x concentrations showed distinct seasonal variations with the highest concentrations in the winter (October–December) and the lowest concentrations in the summer (June–August). There were no obvious seasonal variations for NO_2 which fluctuated around a relatively stable concentration of 30 ppbv.

In the winter, the measured NO_x reached a maximum resulting from higher NO_x emissions, lower mixing layer and removal rates. Beijing begins domestic heating in November, and NO emissions increase due to higher energy consumption. At the same time, lower reaction rates at lower temperatures, lower OH concentrations due to lower actinic flux, and lower vertical dispersion due to a shallower boundary layer all result in lower dilution and removal rates of NO_x. The situation in the summer is opposite. Similar annual variations were detected in observational studies of other megacities in China [29]. Unlike NO, NO_2 in the ambient air was mainly produced from NO. Hence NO_2 concentrations were determined by many factors, such as NO concentrations, NO reaction rate, and boundary layer height. The combined effects of these factors led to a relatively stable NO_2 concentration all around the year. There have been many studies observing NO_x diurnal variations in Beijing, Shanghai and other megacities, which show an obvious double peak of

Table 20.3 Tropospheric NO_2 vertical columns over megacities in China [59]

City	Mean concentration NO_2 in 1997(10^5 molec/cm^2)	Linear trend in NO_2 (10^5 molec/cm^2 a^{-1})	Growth (% year^{-1}) (reference year 1997)
Beijing	12.7	2.3	18
Tianjin	13	2	20
Shanghai	10.1	1.7	13.1
Guangzhou	10.7	0.9	16.4
Chengdu	3.8	0.7	19.1
Chongqing	3.7	0.7	19
Background (86°E × 40°N)	0.6	−0.03	−5.2

NO and NO_2 during the day [29, 47], with the highest concentrations in the morning and evening rush hours and the lowest concentrations between 14:00 and 16:00 in the afternoon, and the NO_2 peak lagging behind the NO peak. This behavior is in line with motor vehicle exhaust emissions being an important source of NO_x in megacities in China.

20.2.3 Trends of Tropospheric NO_2: Satellite Observations

In recent years, many studies have focused on the trend and seasonal variations of tropospheric NO_2 over east Asia or China on the basis of measurements from the satellite instruments GOME and SCIAMACHY [17, 18, 23–25, 39, 41, 51, 57, 59].

Richter et al. [39] studied the global tropospheric column density of NO_2 retrieved from GOME and SCIAMACHY, and found evidence for large increases over industrial areas of China (30°N, 110°E to 40°N, 123°E), with a significant increase of about 50% during the period 1996–2004. Based on GOME and SCIAMACHY satellite data, van der et al. [51] found a large growth of tropospheric NO_2 over eastern China, especially over Shanghai with the highest linear increase in NO_2 columns of 20% ± 6% per year (reference year 1996) in the period 1996–2005. Similarly, Zhang et al. [59] analyzed tropospheric NO_2 over China during 1997–2006: from the spatial distribution, the average tropospheric NO_2 vertical column density over eastern (110–123°E,30–40°N) and western (80–100°E, 30–40°N) China is 9.3×10^5 and 0.6×10^5 molec/cm, respectively. The concentration was especially high in the Jingjinji region, the Yangtze delta region, the Pearl River Delta region and Sichuan Basin; from the temporal distribution, there was a distinct increase in tropospheric NO_2 over eastern China during 1997–2006 and no obvious change in western China. Table 20.3 shows tropospheric NO_2 vertical columns over megacities in China.

Since 2008, the trend of tropospheric NO_2 over China has changed. In 2008, because of the Olympic Games, Beijing and surrounding areas implemented several measures to improve air quality; concentrations of PM_{10}, SO_2, NO_x and other pollutants in Beijing were dramatically decreased, and the satellite data also showed

a significant reduction in the tropospheric NO_2 vertical column density [25, 57, 62]. From late 2008 to 2009, the global financial crisis resulted in an improvement of environmental air quality, and the tropospheric NO_2 over eastern China decreased in 2008. However, with the economic recovery, tropospheric NO_2 began to rise again in 2010 [17, 23].

20.3 NO_x Emission Sources

20.3.1 NO_x Emission Trend in China

Kato and Akimoto [22] developed an inventory of anthropogenic emissions of NO_x based on fuel consumption and emission factors, and the calculated NO_x emission in China was about 45% of the whole emissions of Asia. Similarly, on the basis of the bottom-up method, several other studies have calculated China's NO_x emissions in the 1990s [2, 15, 43, 44, 50]. In 2003, Streets et al. [45] developed an anthropogenic emission inventory for a variety of species for Aisa in 2000, in which the NO_x emissions in China were 11.4 Tg/year, and accounted for 42.5% of the whole the emissions of Asia. Wang et al. [52] used a constrained method in conjunction with aircraft and ground station observations during the TRACE-P field campaign to evaluate China's TRACE-P NO_x emissions. Richter et al. [39] analyzed the tropospheric NO_x column density retrieved from GOME and SCIAMACHY and found a significant increase in tropospheric NO_x over the industrial areas of China, higher than that calculated from the bottom-up method. After that, several studies compared emission inventories estimated from bottom-up and top-down constrained methods [21, 53, 55, 58], and found the former is lower than the latter. Possible explanations for these discrepancies included: (1) The bottom-up method may under-estimate the soil NO_x emitting process and NO_x emission factors in winter [58, 59]; (2) Top-down constraints are affected by seasonal emission variations, variability of the meteorology, NO_x injection height, and the increasing trend of sulfate aerosols [58]. Both methods had advantages and disadvantages. To support the Intercontinental Chemical Transport Experiment-Phase B (INTEX-B), [61] developed a new air pollution inventory in Asia with a series of improved methodologies, the estimated anthropogenic NO_x emission in China in 2006 was 20.8 Tg, accounting for 56.7% of the total emissions in Asia.

We have summarized research on China's NO_x emission inventory over the last 20 years and obtained annual NO_x emissions in China. In Fig. 20.7, the three hollow symbols (○ [21]; △ [52]; ◇ [64]) come from top-down constrained studies, the other data are from bottom-up methods, and emissions in 2010 and 2020 are estimates based on current conditions. Since 1975, there has been an increasing trend in China's NO_x emissions and the emission growth rate accelerated after 2000. The China NO_x emission estimated in the INTEX-B mission in 2006 was 20.8 Tg, and China's official emission data [4] was 16.4 Tg, which was lower than literature reports but had a consistent trend with other research efforts. On the basis of satellite data, NO_x emissions in 2000 [21], 2001 [52] and 2007

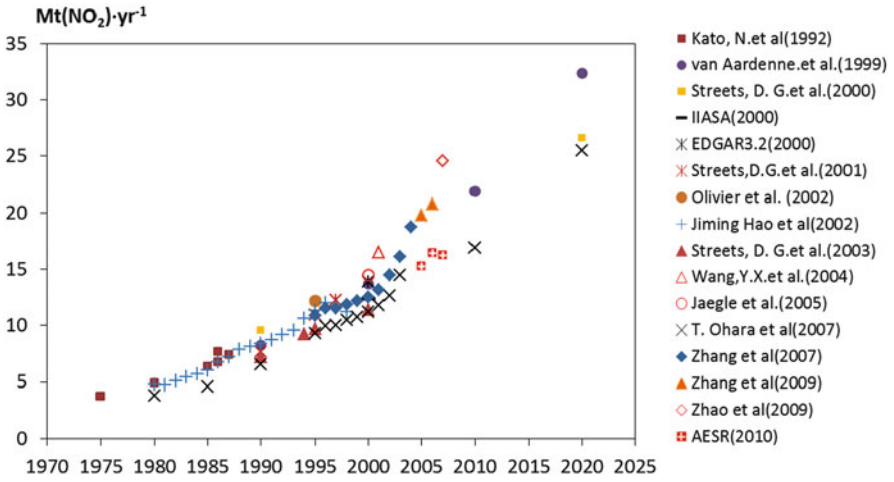

Fig. 20.7 NO_x annual emissions in China($Mt(NO_2)/year^{-1}$) [4, 12, 15, 19, 21, 22, 26, 27, 43–45, 50, 52, 58, 61, 64]

Table 20.4 NO_x emissions in four Chinese municipalities in 2006 by sector [20]

Unit: Gg of NO_2					
Year: 2006	Power	Industry	Residential	Transportation	Total
Beijing	101.5	64.5	30.4	130.2	326.7
Shanghai	232.2	239.7	43.7	128.3	643.9
Tianjin	128.1	99.8	15.6	121.2	364.8
Chongqing	94.5	108.2	29.5	93.8	326.1

[64] derived from top-down constrained methods were significantly higher that those in other emission inventories. The discrepancy is attributed to differences in the research methods.

20.3.2 NO_x Emissions in Megacities

Table 20.4 presents NO_x emissions in four Chinese municipalities in 2006 by sector. In 2006, NO_x emissions in Shanghai ranked top in the four municipalities, and industry had the highest emissions, accounting for 37.2% of total emissions. In Shanghai, Tianjin and Chongqing, power plants or industry was the largest contributor, but in Beijing, Transportation contributed most, accounting for 39.9% of the total emissions. Emissions from power plants contributed significantly in the four megacities, emissions from industry were large in all the cities except Beijing, emissions from transportation were large in all the cities, and residential emissions contributed the least in the four cities, not more than 10%.

20.4 Conclusions

With the rapid economic development in China, air quality has been deteriorating in Chinese megacities. Despite the many measures taken by the Chinese government, the NO_x pollution is still a big concern for the country. According to official data in seven typical megacities Beijing, Shanghai, Tianjin, Chongqing, Guangzhou, Shenzhen and Chengdu, there has been a downward trend in NO_2 concentrations, especially during the economic recession period 2008–2009 the NO_2 concentrations decreased significantly. However, with the economic recovery, the concentration has begun to rise again. A similar trend was detected by means of NO_x ground observations in PKU and satellite data. Interestingly, over the past 10 years, satellite data and emission inventory data all indicate an obvious upward trend in China's NO_x emissions, but the NO_x concentrations observed in megacities are decreasing. The reasons for the discrepancy are unclear and need further study.

From the aspect of NO_x pollution sources, major sources of NO_x emissions in Chinese megacities include power plants, industry, transportation, and residential, with power plants being the largest contributor and industry and transportation accounting for large proportions of the emissions. By applying control measures on power plants, industry and transportation, future emission control in China should be able to make good progress.

Acknowledgement This study was supported by China National Science Foundation Committee (41121004, 21190051), and the Chinese Ministry of Environmental Protection (201009032).

References

1. Akimoto H (2003) Global air quality and pollution. Science 302(5651):1716
2. Akimoto H, Narita H (1994) Distribution of SO_2, NO_x and CO_2 emissions from fuel combustion and industrial activities in Asia with 1-degrees-X 1-degrees resolution. Atmos Environ 28(2):213–225
3. Ambient Air Quality Standards (2000) Ministry of Environmental Protection of the People's Republic of China. http://kjs.mep.gov.cn/hjbhbz/bzwb/dqhjbh/dqhjzlbz/199612/t19961206_67502.htm. Accessed 4 Sep 2012
4. Annual Environmental Statistical Report (2010) Ministry of Environmental Protection of the People's Republic of China. http://www.mep.gov.cn/zwgk/hjtj/nb/. Accessed 4 Sep 2012
5. Chan CK, Yao X (2008) Air pollution in mega cities in China. Atmos Environ 42(1):1–42
6. China Compendium of Statistics (1949–2008) Department of comprehensive statistics of national bureau of statistics. China Statistics Press, Beijing
7. China Energy Statistical Yearbook (2010) National bureau of statistics energy statistics division. China Statistics Press, Beijing
8. China Statistical Yearbook (1990–2010) National bureau of statistics of China. China Statistics Press, Beijing
9. China Statistical Yearbook of Environment (2010) National bureau of statistics of China. China Statistics Press, Beijing
10. China Statistical Yearbook (2011) National bureau of statistics of China. China Statistics Press, Beijing

11. Chou CCK, Tsai CY, Shiu CJ, Liu SC, Zhu T (2009) Measurement of NO(y) during Campaign of Air Quality Research in Beijing 2006 (CAREBeijing-2006): implications for the ozone production efficiency of NO(x). J Geophys Res Atmos 114
12. EDGAR (2000) Emission Database for Global Atmospheric Research(EDGAR). http://themasites.pbl.nl/tridion/en/themasites/edgar/emission_data/edgar_32ft2000/index-2.html. Accessed 4 Sep 2012
13. Geng FH, Tie XX, Xu JM, Zhou GQ, Peng L, Gao W, Tang X, Zhao CS (2008) Characterizations of ozone, NO_x, and VOCs measured in Shanghai, China. Atmos Environ 42(29): 6873–6883
14. Han SQ, Bian H, Feng YC, Liu AX, Li XJ, Zeng F, Zhang XL (2011) Analysis of the Relationship between O(3), NO and NO(2) in Tianjin, China. Aerosol Air Qual Res 11(2): 128–139
15. Hao JM, Tian HZ, Lu YQ (2002) Emission inventories of NO_x from commercial energy consumption in China, 1995–1998. Environ Sci Technol 36(4):552–560
16. Hao N, Zhou B, Chen D, Sun Y, Gao S, Chen LM (2006) Measurements of NO_2, SO_2, O_3, benzene and toluene using differential optical absorption spectroscopy (DOAS) in Shanghai, China. Annali Di Chimica 96(7–8):365–375
17. Hao N, Valks P, Loyola D, Cheng Y, Zimmer W (2011) Space-based measurements of air quality during the World Expo 2010 in Shanghai. Environ Res Lett 6:044004
18. He Y, Uno I, Wang Z, Ohara T, Sugirnoto N, Shimizu A, Richter A, Burrows JP (2007) Variations of the increasing trend of tropospheric NO_2 over central east China during the past decade. Atmos Environ 41(23):4865–4876
19. IIASA (2000) Scenarios of world anthropogenic emissions of air pollutants and methane up to 2030. http://www.iiasa.ac.at/rains/global_emiss/global_emiss1.html. Accessed 4 Sep 2012
20. INTEX-B (2006) The intercontinental chemical transport experiment phase B (INTEX-B). http://www-air.larc.nasa.gov/missions/intex-b/intexb.html. Accessed 4 Sep 2012
21. Jaegle L, Steinberger L, Martin RV, Chance K (2005) Global partitioning of NO_x sources using satellite observations: relative roles of fossil fuel combustion, biomass burning and soil emissions. Faraday Discuss 130:407–423
22. Kato N, Akimoto H (1992) Anthropogenic emissions of SO_2 and NO_x in Asia: emission inventories. Atmos Environ Part A Gen Top 26(16):2997–3017
23. Lin J, Nielsen CP, Zhao Y, Lei Y, Liu Y, McElroy MB (2010) Recent changes in particulate air pollution over China observed from space and the ground: effectiveness of emission control. Environ Sci Technol 44(20):7771–7776
24. Ma J, Richter A, Burrows JP (2006) Comparison of model-simulated tropospheric NO_2 over China with GOME-satellite data. Atmos Environ 40(4):593–604
25. Mijling B, van der RJA, Boersma F, Van Roozendael M, De Smedt I, Kelder HM (2009) Reductions of NO_2 detected from space during the 2008 Beijing Olympic Games. Geophys Res Lett 36(13):L13801
26. Ohara T, Akimoto H, Kurokawa J, Horii N, Yamaji K, Yan X, Hayasaka T (2007) An Asian emission inventory of anthropogenic emission sources for the period 1980–2020. Atmos Chem Phys 7(16):4419–4444
27. Olivier J, JJm GJB, Peters JAHW, Bakker J, Visschedijk AJH, Bloos JPJ (2002) Applications of EDGAR emission database for global atmospheric research. RIVM report 773301001/NRP report 410 200 051. National Institute of Public Health and the Environment
28. Parrish DD, Zhu T (2009) Clean air for megacities. Science 326(5953):674–675
29. Ran L, Zhao CS, Geng FH, Tie XX, Tang X, Peng L, Zhou GQ, Yu Q, Xu JM, Guenther A (2009) Ozone photochemical production in urban Shanghai, China: analysis based on ground level observations. J Geophys Res Atmos 114:D15301
30. Report from the Ministry of Public Security (2011) Chinanews. http://www.chinanews.com/auto/2011/07-18/3189951.shtml. Accessed 4 Sep 2012
31. Report on the State of the Environment in Beijing (1999–2010) Beijing Municipal Environmental Protection Bureau. http://www.bjepb.gov.cn/portal0/tab181/. Accessed 4 Sep 2012

32. Report on the State of the Environment in Chengdu (2005–2010) Chengdu Environmental Protection Bureau. http://www.cdepb.gov.cn/Lm.asp?tc=784&cc=652. Accessed 4 Sep 2012
33. Report on the State of the Environment in China (2008) Ministry of Environmental Protection of the People's Republic of China. http://jcs.mep.gov.cn/hjzl/zkgb/. Accessed 4 Sep 2012
34. Report on the State of the Environment in Chongqing (1999–2010) Chongqing Environmental Protection Bureau. http://www.cepb.gov.cn/zlkz/hjzkgb/default.htm. Accessed 4 Sep 2012
35. Report on the State of the Environment in Guangzhou (1999–2010) Guangzhou Environmental Protection Bureau. http://www.gzepb.gov.cn/zwgk/hjgb/. Accessed 4 Sep 2012
36. Report on the State of the Environment in Shanghai (1999–2010) Shanghai Environmental Protection Bureau. http://www.sepb.gov.cn/fa/cms/shhj/shhj2072/shhj2144/index.shtml. Accessed 4 Sep 2012
37. Report on the State of the Environment in Shenzhen (1999–2010) Shenzhen Environmental Protection Bureau. http://www.szhec.gov.cn/xxgk/xxgkml/xxgk_7/xxgk_7_1/. Accessed 4 Sep 2012
38. Report on the State of the Environment in Tianjin (1999–2010) Tianjin Environmental Protection Bureau. http://www.tjhb.gov.cn/tabid/184/Default.aspx. Accessed 4 Sep 2012
39. Richter A, Burrows JP, Nuss H, Granier C, Niemeier U (2005) Increase in tropospheric nitrogen dioxide over China observed from space. Nature 437(7055):129–32
40. Shao M, Zhang YH, Zeng LM, Tang XY, Zhang J, Zhong LJ, Wang BG (2009) Ground-level ozone in the Pearl River Delta and the roles of VOC and NO(x) in its production. J Environ Manage 90(1):512–518
41. Shi C, Fernando H, Wang Z, An X, Wu Q (2008) Tropospheric NO_2 columns over East Central China: comparisons between SCIAMACHY measurements and nested CMAQ simulations. Atmos Environ 42(30):7165–7173
42. Song DL, Zhou LD, Chai FH, Zhang P (2010) Analysis of concentration contribution of vehicle emission in Chengdu urban area. In: Chengdu science and technology conference – air environmental pollution prevention and control symposium of the Modern Garden City in the World, pp 103–109 (In Chinese)
43. Streets DG, Waldhoff ST (2000) Present and future emissions of air pollutants in China: SO_2, NO_x, and CO. Atmos Environ 34(3):363–374
44. Streets DG, Tsai NY, Akimoto H, Oka K (2001) Trends in emissions of acidifying species in Asia, 1985–1997. Water Air Soil Pollut 130(1):187–192
45. Streets DG, Bond TC, Carmichael GR, Fernandes SD, Fu Q, He D, Klimont Z, Nelson SM, Tsai NY, Wang MQ, Woo JH, Yarber KF (2003) An inventory of gaseous and primary aerosol emissions in Asia in the year 2000. J Geophys Res Atmos 108(D21)
46. Su H, Cheng YF, Cheng P, Zhang YH, Dong S, Zeng LM, Wang X, Slanina J, Shao M, Wiedensohler A (2008) Observation of nighttime nitrous acid (HONO) formation at a non-urban site during PRIDE-PRD2004 in China. Atmos Environ 42(25):6219–6232
47. Tang G, Li X, Wang Y, Xin J, Ren X (2009) Surface ozone trend details and interpretations in Beijing, 2001–2006. Atmos Chem Phys 9(22):8813–8823
48. The 11th Five-year Plan (2006) Xinhuanet. http://news.xinhuanet.com/ziliao/2006-01/16/content_4057926.htm. Accessed 4 Sep 2012
49. The 12th Five-year Plan (2011) Xinhuanet. http://news.xinhuanet.com/politics/2011-03/16/c_121193916.htm. Accessed 4 Sep 2012
50. van Aardenne JA, Carmichael GR, Levy H, Streets D, Hordijk L (1999) Anthropogenic NO_x emissions in Asia in the period 1990–2020. Atmos Environ 33(4):633–646
51. van der ARJ, Peters DHMU, Eskes H, Boersma KF, Van Roozendael M, De Smedt I, Kelder HM (2006) Detection of the trend and seasonal variation in tropospheric NO_2 over China. J Geophys Res Atmos 111(D12)
52. Wang YXX, McElroy MB, Wang T, Palmer PI (2004) Asian emissions of CO and NO_x: constraints from aircraft and Chinese station data. J Geophys Res Atmos 109(D24)

53. Wang YX, McElroy MB, Martin RV, Streets DG, Zhang Q, Fu TM (2007) Seasonal variability of NO_x emissions over east China constrained by satellite observations: implications for combustion and microbial sources. J Geophys Res Atmos 112(D6)
54. Wang M, Zhu T, Zheng J, Zhang RY, Zhang SQ, Xie XX, Han YQ, Li Y (2009) Use of a mobile laboratory to evaluate changes in on-road air pollutants during the Beijing 2008 Summer Olympics. Atmos Chem Phys 9(21):8247–8263
55. Wang X, Zhang Y, Hu Y, Zhou W, Lu K, Zhong L, Zeng L, Shao M, Hu M, Russell AG (2010) Process analysis and sensitivity study of regional ozone formation over the Pearl River Delta, China, during the PRIDE-PRD2004 campaign using the Community Multiscale Air Quality modeling system. Atmos Chem Phys 10(9):4423–4437
56. Yan J, Wang WC, Yang Z, Jiang YL (2010) Analysis of the effects of increasing vehicle population on atmospheric NO_2 concentrations in Chengdu. In: The eleventh environmental monitoring symposium in Sichuan, pp 103–106 (In Chinese)
57. Yu H, Wang PC, Zong XM, Li X, Lu DR (2010) Change of NO(2) column density over Beijing from satellite measurement during the Beijing 2008 Olympic Games. Chin Sci Bull 55(3): 308–313
58. Zhang Q, Streets DG, He K, Wang Y, Richter A, Burrows JP, Uno I, Jang CJ, Chen D, Yao Z (2007) NO_x emission trends for China, 1995–2004: the view from the ground and the view from space. J Geophys Res 112:18
59. Zhang XY, Zhang P, Zhang Y, Li XJ, Qiu H (2007) The trend, seasonal cycle, and sources of tropospheric NO_2 over China during 1997–2006 based on satellite measurement. Sci China Ser D Earth Sci 50(12):1877–1884
60. Zhang Y, Su H, Zhong L, Cheng Y, Zeng L, Wang X, Xiang Y, Wang J, Gao D, Shao M (2008) Regional ozone pollution and observation-based approach for analyzing ozone-precursor relationship during the PRIDE-PRD2004 campaign. Atmos Environ 42(25):6203–6218
61. Zhang Q, Streets DG, Carmichael GR, He KB, Huo H, Kannari A, Klimont Z, Park IS, Reddy S, Fu JS, Chen D, Duan L, Lei Y, Wang LT, Yao ZL (2009) Asian emissions in 2006 for the NASA INTEX-B mission. Atmos Chem Phys 9(14):5131–5153
62. Zhang XY, Wang YQ, Lin WL, Zhang YM, Zhang XC, Gong S, Zhao P, Yang YQ, Wang JZ, Hou Q, Zhang XL, Che HZ, Guo JP, Li Y (2009) Changes of atmospheric composition and optical properties over Beijing 2008 olympic monitoring campaign. Bull Am Meteorol Soc 90(11):1633+
63. Zhang P, Zhou LD, Wang ZY (2010) Characteristics and sources of atmospheric NO_x pollution in the urban ambient air in the central urban area of Chengdu. In: Chengdu science and technology conference – air environmental pollution prevention and control symposium of the Modern Garden City in the World, pp 96–102 (In Chinese)
64. Zhao C, Wang Y (2009) Assimilated inversion of NO_x emissions over east Asia using OMI NO_2 column measurements. Geophys Res Lett 36
65. Zheng J, Zhang L, Che W, Zheng Z, Yin S (2009) A highly resolved temporal and spatial air pollutant emission inventory for the Pearl River Delta region, China and its uncertainty assessment. Atmos Environ 43(32):5112–5122
66. Zheng JY, Zhong LJ, Wang T, Louie PKK, Li ZC (2010) Ground-level ozone in the Pearl River Delta region: analysis of data from a recently established regional air quality monitoring network. Atmos Environ 44(6):814–823

Chapter 21
Urban and Global Effects of Megacity Pollution

Tim Butler

Abstract Megacities and other large urban areas can often be associated with poor air quality. In the developed world, stricter emissions control legislation has resulted in dramatic improvements in urban air quality. Future emissions scenarios project that this will also spread to the developing world. A result of this will be that air quality in urban areas will become more influenced by emissions from outside of these areas.

Keywords Ozone • Modelling • Megacities

21.1 Introduction

Ozone (O) in the troposphere is a harmful pollutant, which contributes to radiative forcing of the climate system and has detrimental effects on plant and animal health. Ozone is not emitted to any significant degree by natural or anthropogenic processes, but is instead formed via chemical reactions in the atmosphere involving the emitted precursor species oxides of nitrogen (NO and NO, collectively referred to as NO) and Volatile Organic Compounds (VOC, e.g. Refs. [1, 18, 30], and references therein). Ozone production due to anthropogenic emissions of these precursor species is the third highest contributor to enhanced radiative forcing of the climate system behind carbon dioxide and methane, and the single largest cause of pollution- induced reduction of the yields of agricultural crops [32].

Since 1900, anthropogenic emissions of these ozone precursor species have increased by approximately a factor of 6 [19], associated with increases in human population and economic activity. Much of the increase in population has occured in urban areas. It is estimated that in 2008, the urban population of the world

T. Butler (✉)
Institute for Advanced Sustainability Studies, Berliner Str. 130, 14467 Potsdam, Germany
e-mail: tim.butler@iass-potsdam.de

I. Barnes and K.J. Rudziński (eds.), *Disposal of Dangerous Chemicals in Urban Areas and Mega Cities*, NATO Science for Peace and Security Series C: Environmental Security,
DOI 10.1007/978-94-007-5034-0_21,

exceeded the rural population for the first time in history, with this trend expected to continue [33]. Part of this trend is a growth in the number of so-called "megacities", which are generally regarded as cities with more than about ten million inhabitants. The movement of human populations and their associated emissions of tropospheric ozone precursor species into such geographically small regions creates "hotspots" of air pollution, which not only have serious consequences for the inhabitants of these megacities, but also have the potential to influence air quality on regional and even global scales through their effects on the atmospheric budgets of particles, reactive nitrogen, and tropospheric ozone.

The high population density in urban areas can lead to energy efficiencies which have the potential to reduce the per capita emissions of their inhabitants [13], with potential consequences for global air quality. In the developed world, there have been very strong recent improvements in air pollutant emissions due to strengthening of legislation. Despite substantial increases in population and vehicle traffic, air quality in North American megacities has increased substantially over the last five decades [27]. Between 1990 and 2008, total emissions of toxic pollutants in the USA declined by 41% [11]. Efforts to reduce emissions in urbanised areas of the developed world have been so successful that many studies now indicate a strong influence of regional and long range transport of ozone and its precursors on ozone air quality in these areas [17, 26, 37]. The developing world has yet to catch up to these standards; air quality in the megacities of the developing world can be especially poor [15].

21.2 Global Effects of Megacity Emissions

So far there have been few studies examining the effects of megacity emission hotspots on atmospheric chemistry at the global scale, and none examining the extent to which megacities are influenced by external pollution sources using global modelling frameworks. Mayer et al. [24] incorporated a parameterised form of urban photochemistry into a global, two dimensional climate model with background tropospheric photochemistry in order to study the effects of urban emissions processing on global atmospheric composition. They did not specifically investigate the contribution of megacities, but rather studied the effects of urban areas in general, finding that incorporation of the effects of urban chemistry in their model reduced the amount of tropospheric ozone compared to model runs in which the effects of urban chemistry were not included.

Taking a different approach, Lawrence et al. [21] used a global, three dimensional transport model to investigate the transport of pollutants away from megacities and other large population centres. Their model did not include any atmospheric chemistry, but rather employed tracers with fixed lifetimes of 1, 10, and 100 days. They found large differences in the regional pollution potentials of the various megacities, and that differences in the amount of vertical transport from megacities play a large role in determining the local dilution of emissions in the vicinity of megacities as well as the extent of the transport of pollutants away from megacities.

Butler and Lawrence [3] used a global, three dimensional transport model with interactive NMHC chemistry in order to investigate the effects of emissions from megacities on global atmospheric composition. They employed an "annihilation" methodology, in which the emissions from a set of pre-identified megacity grid cells were removed from the model emission inventory, altering the total global emissions of ozone precursor species. Comparing their annihilation run with a control run using the unaltered emission inventory, Butler and Lawrence [3] showed that the influence of megacities on tropospheric ozone was disproportionately small compared to their share of the total global emission of ozone precursors.

Butler et al. [5] performed a similar study to that of Butler and Lawrence [3], making use of the four updated emissions projections ("Representative Concentration pathways", RCP) for the upcoming IPCC AR5 report [25, 34]. In addition to the annihilation methodology employed by Butler and Lawrence [3], the study of Butler et al. [5] also used a novel method of redistributing emissions from megacities throughout their host countries, ensuring that the total global emissions of ozone precursor species remained unchanged, and thus allowing the investigation of the effects of megacity emissions on the local urban air quality within the megacities themselves.

All four of the RCP emissions projections include declining anthropogenic emissions of ozone precursor species throughout the twenty-first century, due to similarities in their assumptions about future changes in emissions control legislation [34]. In all cases, emissions control legislation is assumed to become stricter as per- capita income increases, similarly to the changes in emissions already seen in the United States of America, as noted above. In the case of the "buisness as usual" scenario (RCP-8.5 [28]), these emissions reductions associated with more stringent emissions control legislation are assumed to occur primarly in urban regions. This leads to the interesting result from Butler et al. [5] that future megacity air quality under this scenario becomes less influenced by local emissions within the urban areas themselves, and more dependant on the background ozone mixing ratio, which can be due to emissions large distances away. The study of Butler et al. [5] should be interpreted with some care, as they use a global model with a grid resolution of $2.8^\circ \times 2.8^\circ$. This grid resolution approaches the size of some of the larger urban agglomorations, but their results must still be reproduced using more highly resolved models. Additionally, as in all global models of tropospheric chemistry, the chemical mechanism used in their study was substantially simplified for computational reasons.

21.3 Urban Effects of Megacity Emissions

Ozone is formed in the troposphere during the oxidation of VOC in the presence of NO (oxides of nitrogen, NO and NO). The formation of ozone by VOC oxidation is related to the number of transformations of NO to NO by peroxy radicals occurring during the oxidation process (e.g. Refs. [18, 30]). In the presence of oxygen, VOC

can react with hydroxyl radicals (OH) forming organic peroxy radicals (RO) and hydroperoxy radicals (HO). These peroxy radicals can then convert NO to NO, which can then photolyse, ultimately forming O.

The organic products thus formed (R'CHO) can undergo further oxidation reactions, yielding more peroxy radicals, and thus additional NO to NO conversions to form O [1]. As the size of the RO radicals increases, reaction with NO increasingly yields radical-terminating alkyl nitrates (R'NO) at the expense of alkoxy radicals [2]. Due to these, and other differences in the structure and reactivity of individual VOC species, and the number of intermediate species involved in their degradation, each VOC has a different effect on NO, and therefore also on ozone. Under conditions of high NO, the production of ozone is limited by the availability of VOC, while under conditions of high VOC, the production of ozone is limited by the availability of NO (e.g. Refs. [18, 30]).

In many cases it can be desirable to have knowledge of the differing abilities of individual VOC to influence the production of ozone (the Ozone Production Potential, or OPP). These OPP can be used to make estimates of the potential of an airmass to produce ozone based on speciated measurements of VOC [10]. They also have policy applications through the design of reactivity-based substitution strategies for air quality control; Capps et al. [6] for example, investigated the effects of substituting emissions of high-OPP VOC with lower-OPP VOC. Another application of OPP is in model development. For reasons of computational efficiency, most air quality models must employ highly simplified chemical mechanisms, which usually do not treat VOC oxidation explicitly, based on the current best understanding of the chemical kinetics from laboratory studies, but rather lump whole classes of VOC together in the model in some way. This lumping can be done according to structural similarity, the number of carbon atoms in the molecule, the rate constant for initial attack by OH, or by some measure of the OPP of each of the VOC [36].

Early attempts to quantify the OPP of individual VOC species involved hanging strips of vulcanised rubber in irradiated flasks containing mixtures of VOC and NO and measuring the total depth of cracks in the rubber thus formed [16]. Experiments performed in smog chambers have been used to guide emission control strategies [9]. More recently, photochemical models have been employed using incremental reactivity techniques [7, 8] to assess the varying impacts of different VOC on tropospheric ozone. Using these incremental reactivity techniques, several runs of a photochemical model are performed, each with a slight perturbation to the amount of a particular target VOC. The change, or increment, in the amount of ozone produced by the model in response to the incremental change in VOC is then used to determine the ozone production potential of each VOC under consideration.

Derwent et al. [8] used an incremental reactivity technique to calculate their Photochemical Ozone Creation Potentials (POCP) using a model setup applicable to a 5 day trajectory under Western European conditions. Using a more idealised approach, Carter [7] did not attempt to model any specific location or trajectory, but instead calculated generic incremental reactivity scales by adjusting the emissions

of NO in their model relative to each VOC to give the desired effect on ozone. In this way, Carter [7] calculated two different reactivity scales: the "Maximum Incremental Reactivity" (MIR) scale; and the "Maximum Ozone Incremental Reactivity" (MOIR) scale. The MIR scale is calculated at NO concentrations such that an incremental change in the concentration of each VOC produces the largest incremental change in O; Carter [7] gives no information about the actual O concentrations which result. The MOIR, on the other hand, is calculated at the NO concentrations which yield the largest concentrations of O. The MOIR is calculated at lower NO than the MIR.

When a forecast of the ozone production in a particular region at a particular time is desired, there is no substitute for direct modelling of that particular situation, including any locally relevant transport characteristics (e.g. Ref. [31]). On the other hand, if one is interested in the inherent ozone production potentials of VOC themselves, it may be more appropriate to perform more idealised experiments with a photochemical model (e.g. Ref. [7]). According to Luecken and Mebust [23], the various incremental reactivity approaches tend to produce results which correlate well with each other. They also show that the MOIR scale may be more appropriate to larger areas of the USA which are subject to high rates of ozone formation than the MIR scale. This can have the effect of exaggerating the effect on ozone of VOC with higher OPP, relative to VOC with lower OPP. Capps et al. [6] show that reactivity-based substitution efforts to reduce ozone using the MIR can actually lead to increased ozone concentrations due to this exaggeration. Capps et al. [6] show that such reactivity-based emission substitution may be more effective when using the MOIR, which does not exaggerate the OPP of highly ozone- producing VOC under the most common conditions.

Incremental reactivity techniques do not give any mechanistic information about the OPP of VOC (for example, which oxidation intermediates are responsible to which degree for converting NO to NO). When different VOC have different OPP, or when different chemical oxidation mechanisms differ in their predictions of OPP for the same VOC, it can be difficult to understand exactly why this is.

Butler et al. [4] describe a method for calculating the OPP of VOC without using incremental reactivity techniques, and which is able to provide more information about the mechanism of ozone production. The method is based on the principle of "tagging" the degradation sequence of each of the VOC present in the model. Tagging of chemical tracers in three dimensional models of atmospheric chemistry has been previously used to trace the advection of airmasses from different origins [20], to trace the contribution of different sources of NO to the formation of tropospheric ozone [12, 22], to trace the composition of aerosol particles [35], and to trace isotopic composition through chemical transformations [14]. Butler et al. [4] use tagging to trace the chemical evolution of VOC oxidation intermediates in order to track their effect on the peroxy radicals (HO and RO) which convert NO to NO, thus calculating the ozone production potential of these VOC.

Using this tagging approach combined with the detailed chemical mechanism MCM-3.1 (Master Chemical Mechanism [29]), Butler et al. [4] were able to identify systematic differences between the timing of ozone production due to the

oxidation of aromatic species such as toluene and xylenes, which produce ozone rapidly, and similarly sized alkanes, such as heptane and octane, which produce ozone slowly. These differences were found to be related to the speed at which these large VOC molecules react to form smaller fragments, such as CHO radicals. It is these smaller fragments which are primarily responsible for the NO to NO conversions which ultimately lead to ozone formation. These differences in timing have implications for emission control strategies. Alkanes, previously regarded as less reactive (e.g. Ref. [7]) could potentially be significant sources of ozone during stagnant meteorological conditions, or have large effects on ozone production downwind of source regions.

21.4 Conclusions

Enhanced production of tropospheric ozone due to emissions from anthropogenic activity has significant effects on both radiative forcing of the climate system and air quality, especially for the growing number of people living in large urban regions. Current projections of anthropogenic emissions throughout the rest of the twenty-first century suggest that stricter emissions controls will lead to a shift in the emission sources responsible for urban ozone pollution; emission sources outside of large urban regions are predicted to play an increasing role in urban air quality. With an increasing potential for ozone production from long range transport of emissions, the role of emissions of alkane species, which have previously been regarded as less reactive must be reassessed.

References

1. Atkinson R (2000) Atmospheric chemistry of VOCs and NO_x. Atmos Environ 34:2063–2101
2. Atkinson R (2007) Rate constants for the atmospheric reactions of alkoxy radicals: an updated estimation method. Atmos Environ 41:8468–8485
3. Butler TM, Lawrence MG (2009) The influence of megacities on global atmospheric chemistry: a modelling study. Environ Chem 6:219–225
4. Butler TM, Lawrence MG, Taraborrelli D, Lelieveld J (2011) Multi-day ozone production potential of volatile organic compounds calculated with a tagging approach. Atmos Environ 45:4082–4090
5. Butler TM, Stock ZS, Russo MR, van der Gon Denier HAC, Lawrence MG (2012) Megacity ozone air quality under four alternative future scenarios. Atmos Chem Phys Discuss 12:129–163
6. Capps SL, Hu Y, Russell AG (2010) Assessing near-field and downwind impacts of reactivity-based substitutions. J Air Waste Manage Assoc 60:316–327
7. Carter W (1994) Development of ozone reactivity scales for volatile organic compounds. J Air Waste Manage Assoc 44:881–899
8. Derwent R, Jenkin M, Saunders S, Pilling M (1998) Photochemical ozone creation potentials for organic compounds in northwest Europe calculated with a master chemical mechanism. Atmos Environ 32:2429–2441

9. Dimitriades B (1977) Oxidant control strategies 1 urban oxidant control strategy derived from existing smog chamber data. Environ Sci Technol 11:80–88
10. Duan J, Tan J, Yang L, Wu S, Hao J (2008) Concentration, sources and ozone formation potential of volatile organic compounds (VOCs) during ozone episode in Beijing. Atmos Res 88:25–35
11. EPA (2010) Our nation's air: status and trends through 2008. Technical report EPA-454/R-09-002. U.S. Environmental Protection Agency, Office of air quality planning and standards, Research Triangle Park, North Carolina, USA
12. Grewe V (2004) Technical note: a diagnostic for ozone contributions of various NO_x emissions in multi-decadal chemistry-climate model simulations. Atmos Chem Phys 4:729–736
13. Grimm NB, Faeth SH, Golubiewski NE, Redman CL, Wu J, Bai X, Briggs JM (2008) Global change and the ecology of cities. Science 319:756–760
14. Gromov S, Jöckel P, Sander R, Brenninkmeijer CAM (2010) A kinetic chemistry tagging technique and its application to modelling the stable isotopic composition of atmospheric trace gases. Geosci Model Dev 3:337–364
15. Gurjar BR, Butler TM, Lawrence MG, Lelieveld J (2008) Evaluation of emissions and air quality in megacities. Atmos Environ 42:1593–1606
16. Haagen-Smit AJ, Fox MM (1956) Ozone formation in photochemical oxidation of organic substances. Ind Eng Chem 48:1484–1487
17. Jacob D, Logan J, Murti P (1999) Effect of rising Asian emissions on surface ozone in the United States. Geophys Res Lett 26:2175–2178
18. Kleinman L, Daum P, Lee J, Lee Y, Nunnermacker L, Springston S, Newman L, WeinsteinLloyd J, Sillman S (1997) Dependence of ozone production on NO and hydrocarbons in the troposphere. Geophys Res Lett 24:2299–2302
19. Lamarque JF, Bond TC, Eyring V, Granier C, Heil A, Klimont Z, Lee D, Liousse C, Mieville A, Owen B, Schultz MG, Shindell D, Smith SJ, Stehfest E, Van Aardenne J, Cooper OR, Kainuma M, Mahowald N, McConnell JR, Naik V, Riahi K, van Vuuren DP (2010) Historical (1850–2000) gridded anthropogenic and biomass burning emissions of reactive gases and aerosols: methodology and application. Atmos Chem Phys 10:7017–7039
20. Lawrence MG, Rasch PJ, von Kuhlmann R, Williams J, Fischer H, de Reus M, Lelieveld J, Crutzen PJ, Schultz M, Stier P, Huntrieser H, Heland J, Stohl A, Forster C, Elbern H, Jakobs H, Dickerson RR (2003) Global chemical weather forecasts for field campaign planning: predictions and observations of large-scale features during MINOS, CONTRACE, and INDOEX. Atmos Chem Phys 3:267–289
21. Lawrence MG, Butler TM, Steinkamp J, Gurjar BR, Lelieveld J (2007) Regional pollution potentials of megacities and other major population centres. Atmos Chem Phys 7:3969–3987
22. Lelieveld J, Dentener F (2000) What controls tropospheric ozone? J Geophys Res 105:3531–3551
23. Luecken DJ, Mebust MR (2008) Technical challenges involved in implementation of VOC reactivity-based control of ozone. Environ Sci Technol 42:1615–1622
24. Mayer M, Wang C, Webster M, Prinn RG (2000) Linking local air pollution to global chemistry and climate. J Geophys Res 105:22869–22896
25. Moss RH, Edmonds JA, Hibbard KA, Manning MR, Rose SK, van Vuuren DP, Carter TR, Emori S, Kainuma M, Kram T, Meehl GA, Mitchell JFB, Nakicenovic N, Riahi K, Smith SJ, Stouffer RJ, Thomson AM, Weyant JP, Wilbanks TJ (2010) The next generation of scenarios for climate change research and assessment. Nature 463:747–756
26. Parrish DD, Aikin KC, Oltmans SJ, Johnson BJ, Ives M, Sweeny C (2010) Impact of transported background ozone inflow on summertime air quality in a California ozone exceedance area. Atmos Chem Phys 10:10093–10109
27. Parrish DD, Singh HB, Molina L, Madronich S (2011) Air quality progress in North American megacities: a review. Atmos Environ 45:7015–7025
28. Riahi K, Rao S, Krey V, Cho C, Chirkov V, Fischer G, Kindermann G, Nakicenovic N, Rafaj P (2011) RCP 8.5 – a scenario of comparatively high greenhouse gas emissions. Clim Change 109:33–57

29. Saunders SM, Jenkin ME, Derwent RG, Pilling MJ (2003) Protocol for the development of the master chemical mechanism, MCM v3 (Part A): tropospheric degradation of non-aromatic volatile organic compounds. Atmos Chem Phys 3:161–180
30. Sillman S (1999) The relation between ozone, NO and hydrocarbons in urban and polluted rural environments. Atmos Environ 33:1821–1845
31. Song J, Lei W, Bei N, Zavala M, de Foy B, Volkamer R, Cardenas B, Zheng J, Zhang R, Molina LT (2010) Ozone response to emission changes: a modeling study during the MCMA-2006/MILAGRO Campaign. Atmos ChemPhys 10:3827–3846
32. UNEP (2011) Integrated assessment of black carbon and tropospheric ozone: summary for decision makers. Technical report UNEP/GC/26/INF/20. United Nations Environment Program
33. UNFPA (2007) State of world population 2007: Unleashing the potential of urban growth, UNFPA, New York, USA. ISBN 978-0-89714-807-8
34. van Vuuren D, Edmonds J, Kainuma M, Riahi K, Thomson A, Hibbard K, Hurtt G, Kram T, Krey V, Lamarque J-F, Masui T, Meinshausen M, Nakicenovic N, Smith S, Rose S (2011) The representative concentration pathways: an overview. Clim Change 109:5–31
35. Wang ZS, Chien CJ, Tonnesen GS (2009) Development of a tagged species source apportionment algorithm to characterize three-dimensional transport and transformation of precursors and secondary pollutants. J Geophys Res 114:D21206
36. Watson LA, Shallcross DE, Utembe SR, Jenkin ME (2008) A Common Representative Intermediates (CRI) mechanism for VOC degradation. Part 2: Gas phase mechanism reduction. Atmos Environ 42:7196–7204
37. Yoshitomi M, Wild O, Akimoto H (2011) Contributions of regional and intercontinental transport to surface ozone in the Tokyo area. Atmos Chem Phys 11:7583–7599

Chapter 22
Temporal Concentration Variation of Gaseous Pollutants and Ionic Species in Mansoura City, Egypt

Alia A. Shakour, Sayed S. Abd El Rehim, Inas A. Saleh, and Mohammed Abd El-Samea Ali El-Hashemy

Abstract Measurements of gaseous air pollutants and water soluble ions (SO_4^{2-}, NO_3, Cl^-, NH_4^+) were performed at four sites in the urban area of Mansoura city and surroundings and at another background site in a rural area near the city. The results showed that concentrations of gaseous air pollutants undergo seasonal variations characterized by winter maximum levels for SO_2 (41.95 μg/m^3), and H_2S (21.46 μg/m^3), autumn maximum levels for NO_2 (72.21 μg/m^3) and summer maximum levels for total photochemical oxidants (332.33 μg/m^3). Higher concentrations of SO_4^{2-} followed by NH_4^+, Cl^- and NO_3^-, respectively were found in the total water soluble ions (TWSI). These major ions also showed seasonal variations with maximum concentration in summer/autumn for SO_4^{2-}, NO_3^- and NH_4^+ and spring for Cl^-. A statistical analysis of long term measurement data for the measured pollutants indicated strong correlations. It can be concluded that the industrial and residential activities beside the traffic emission are the major sources of air pollutants in the atmosphere of this investigated area. Also the existence of these pollutants in the presence of sun light causes the formation of secondary pollutants, like ozone.

Keywords Air pollutants • Water-soluble ions • Seasonal variation • Mansoura city

22.1 Introduction

Urban air quality in Egypt like all developing countries has deteriorated gradually because of rapid urbanization, population growth and industrialization [26]. The pollutants are added to the environment through various natural processes as

A.A. Shakour (✉) • I.A. Saleh
Air Pollution Department, National Research Center, Dokki, Cairo, Egypt
e-mail: aliashakour@gmail.com

S.S.A. El Rehim • M.A.E.-S.A. El-Hashemy
Chemistry Department, Faculty of Science, Ain Shams University, Cairo, Egypt
e-mail: mohammed_elhashmy@yahoo.com

I. Barnes and K.J. Rudziński (eds.), *Disposal of Dangerous Chemicals in Urban Areas and Mega Cities*, NATO Science for Peace and Security Series C: Environmental Security,
DOI 10.1007/978-94-007-5034-0_22,

well as anthropogenic sources, industrial processes, autoexhaust and domestic sources [11]. The air pollutants are categorized as particulate matter and gases and their associated forms. Inorganic gaseous pollutants represent an important class of air pollutant that can greatly affect the ambient air quality. Gaseous pollutants monitored in this study are sulphur dioxide, nitrogen dioxide, total oxidant, hydrogen sulphide and ammonia.

Sulphur dioxide is important air pollutant that has been closely associated with urban air quality problems. It is usually emitted during the combustion of fossil fuels and is often one of the most prevalent air pollutants in cities, and contributes to the formation of sulphate aerosols. Nitrogen oxide emissions originate from the burning of fossil fuel, nitrification processes in soil, lightning discharges and combustion processes. Road traffic and energy production are the primary sources of atmospheric nitrogen oxides. However, the most deleterious effects tend to be from NO_2. Effects include a number of respiratory disorders. Extended exposures can cause damage to vegetation, effect materials include fading of certain dyes, deterioration of selected fabrics, and metal corrosion [5].

Ozone has been established as the principle gas found among a range of photochemical oxidants [10]. It is formed as a secondary air pollutant from the oxidation of the primary pollutants NO_x and volatile organic compounds (VOC) under bright sunlight [30]. The effects of ozone are widespread and are the result of its characteristics as a high-strength oxidizing chemical. Human health [31], materials [29] and vegetation [2] are all subject to adverse impacts as a function of ozone concentration and contact time.

Hydrogen sulphide is used as a reagent and intermediate in industrial processes. It is a degradation product of human and animal waste, and it is created naturally under certain environmental conditions. Hydrogen sulphide has a relatively short lifetime (4.4 days) in the atmosphere, being rapidly converted to SO_2 and to sulphates [10]. Although the concentration of H_2S in ambient air is not commonly so high to cause any health effects, it is necessary to monitor its concentration in certain locations since the presence of this gas has been one of the possible causes of casualties among people who work in sewers and similar environments [28].

Ammonia is the third most abundant nitrogen compound and the most important alkaline gas in the atmosphere and its role in the neutralisation of atmospheric acids is of primary relevance [20]. Particulate species formed by the reaction between ammonia and acid gases contribute significantly to the long-range transport of acidic pollutants since the atmospheric lifetime of ammonia is no longer than a few days while ammonium salts have a lifetime of the order of a few weeks [1]. The impact of ammonia and ammonium salts on the ecosystem has many effects, ranging from the acidification and eutrophication of the environment to the modification of the global radiative balance of the atmosphere and the reduction of atmospheric visibility, through light scattering. Ammonium salts are among the more corrosive salts in atmospheric aerosols [15]. This complex role of ammonia makes the identification of its manifold emission sources a significant task in the field of atmospheric pollution.

Water-soluble inorganic ions, such as sulphate, nitrate, ammonium and chloride, are of great concern in urban air pollution problems; they control the degree of acidity of the particles and their effect on environmental acidification. Nitrate, sulphate and ammonium are the most common components of secondary particles in the atmosphere [9].

22.2 Experimental

22.2.1 Description of Study Area

The city of Mansoura (31°03′00″N, 31°23′00″E) has 480,494 inhabitants and a land area of 371 km^2 [4]. It is situated in the Nile River Delta region of Egypt. It is about 120 km northeast of Cairo and far from Mediterranean Sea in the north by about 60 km as shown in Fig. 22.1. Mansoura city is the capital of the Dakahlia Governorate and represents an urban area surrounded by major industrial and agricultural activities. The main industrial activities include textile, cotton ginning, resins, oil and soap plants besides fertilizer and electric power plants. Most of the heavy industry land use is located at the north and the eastern south part of the city at Talkha city and in the Sandoub suburbs, respectively. Fertilizer plant and electric power plants are located at Talkha city. Textile, resin, oil and soap plants are located in the Sandoub suburbs. Rice and cotton ginning mills are located in the middle eastern part of the city.

22.2.2 Samples Collection and Analysis

The monitoring stations used for the measurements of gaseous and particulate pollutants are located at four sites (urban) in Mansoura city (see Fig. 22.2) and a rural site located in Miniut Samanoud village far from Mansoura city by about 17 km.

Fig. 22.1 Location of Mansoura city

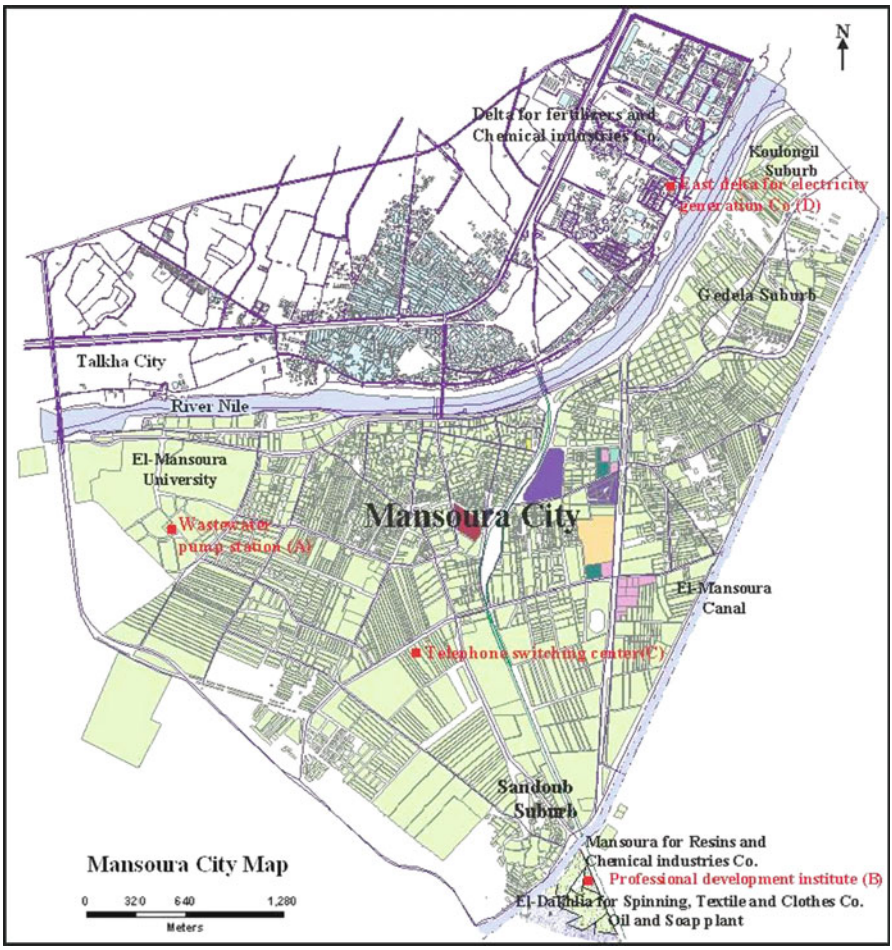

Fig. 22.2 Sampling sites in Mansoura City and surroundings

These sites are the following:

1. Wastewater pump station (A)
2. Professional development institute (B)
3. Telephone switching centre (C).
4. Control building in the East delta for electricity generation Co. (D).
5. A house in Miniut Samanoud village (E).

All air-samplers were installed on the roofs of the buildings (10 m above ground level). These five sampling sites were classified into three categories, as presented in Table 22.1.

The absorption method was used for collecting the gaseous samples on a 24-h basis at the five monitoring stations twice weekly from 1 December 2005 to 31 November 2007. The sampling equipment consisted of gas bubblers through which

Table 22.1 Classification of the investigated sampling sites

Sites		Classification	
El-Mansoura city	Wastewater pump station (A)	Urban – residential	Characterized by pumping waste water
	Professional development institute (B)	Urban – industrial	Characterized by high traffic density and adjacent to: – El Mansoura for resins and chemical industries Co. – El Dakhlia for spinning, textile and clothes Co. – Open air waste burning area – Sandoub sewage canal in the south direction
	Telephone switching centre (C)	Urban – residential	Present near El-Mansoura city centre with its high traffic density
	East delta for electricity generation Co. (D)	Urban – industrial	Adjacent to Delta for fertilizers and chemical industries Co.
Miniut Sammanoud village	Miniut Sammanoud village (E)	Rural – residential	Near to the main road connecting the eastern and western banks of river Nile with its high traffic density and brick making factories

the gas sample was drawn, calibrated vacuum pump with flow rate set at 1 l/min. and dry gas-meter. The pararosaniline hydrochloride colorimetric method was used to measure the SO_2 levels [12], the naphthylethylenediamine method was used to measure the NO_2 levels [25], the alkaline potassium iodide method was used to measure the total oxidants levels [12] which are expressed in terms of O_3, the Nesslerization method was used to measure NH_3 levels [19] and the methylene blue method was used to measure the H_2S levels [12].

Water soluble ions were extracted from particulate matter by ultrasonic agitation in 50 ml of doubly distilled water for a period of 20 min. These extracts were filtered through a filter paper (Whatman No. 42) into pre-cleaned polypropylene bottles. These were refrigerated at 4°C and used for the analysis of major inorganic ions [17]. SO_4^{2-} was measured by turbidimetry as barium sulfate [12], Cl^- was measured by turbidimetry as silver chloride [25], NO_3^- was measured colorimetrically by the salicylate method [16] and NH_4^+ was measured by the Nesslerization method [19]. All chemicals used were of analytical reagent grade and solutions were prepared in doubly distilled water.

22.2.3 Meteorological Data

The meteorological data including temperature, relative humidity (RH), wind speed, precipitation, etc. were obtained from the Central Laboratory for Agricultural Climate The average temperature during summer season was 26.7°C and

during winter season was 15.6°C during the study period. The rain fall time start generally on November and gradually increased until reach the top in winter months and then gradually decrease until almost finished in summer months. The variation of RH was not so distinct in Mansoura city. The wind was mostly blowing from the north-west and north in Mansoura city all the year, but west wind blowing more than north-west wind specially in winter. Figure 22.3 shows the wind frequency distribution during the study period seasons.

22.3 Results and Discussion

22.3.1 Sulphur Dioxide

Table 22.2 gives the annual and the seasonal average concentrations of SO_2 during the study period. The urban areas had higher concentrations of SO_2 than in rural area (E). The maximum annual average concentration of SO_2 was detected at site (B). This may be attributed to the presence of chemical industries and an open-air waste burning area near to this site, beside mobile sources, which play an important role in increasing the SO_2 concentration.

The annual average concentrations of SO_2 ranged from 15.93 μg/m^3 at site (E) to 25.90 μg/m^3 at site (B). The data show that the concentrations were less than the Egyptian air quality limit for SO_2 concentration (60 μg/m^3) [7] and the USA ambient air quality standard (80 μg/m^3) [13]. However, these values were similar to values found in different cities all over the world such as 18.9 μg/m^3 in SaoPaulo, Brazil in 1996–1998 [24], 17.7 μg/m^3 in Hong Kong, China in 1995–1997 [32] and 23.7 μg/m^3 in London, Great Britain in 1992–1994 [32]. However, SO_2 concentrations were higher than those recorded before in Mansoura city by the Egyptian Environmental Affairs Agency [6]: 12 μg/m^3 in 2000, 14 μg/m^3 in 2002 and 15 μg/m^3 in 2003.

The seasonal variation of SO_2 concentrations showed an increase in the winter season. This may be due to the need of burning of more fuels, the lower dispersion and lower photochemical reactions during the colder months leading to increasing SO_2 emissions. The higher dispersion and higher photochemical reactions during warm months lead to a decrease in SO_2 concentrations in the summer season.

22.3.2 Nitrogen Dioxide

The annual average concentrations of NO_2 ranged from 42.70 μg/m^3 at site (E) to 59.04 μg/m^3 at site (B) as shown in Table 22.2. These values were higher than that given in the WHO air quality guideline for annual average NO_2 concentration (40 μg/m^3) [13] but they were less than the US ambient air quality standard

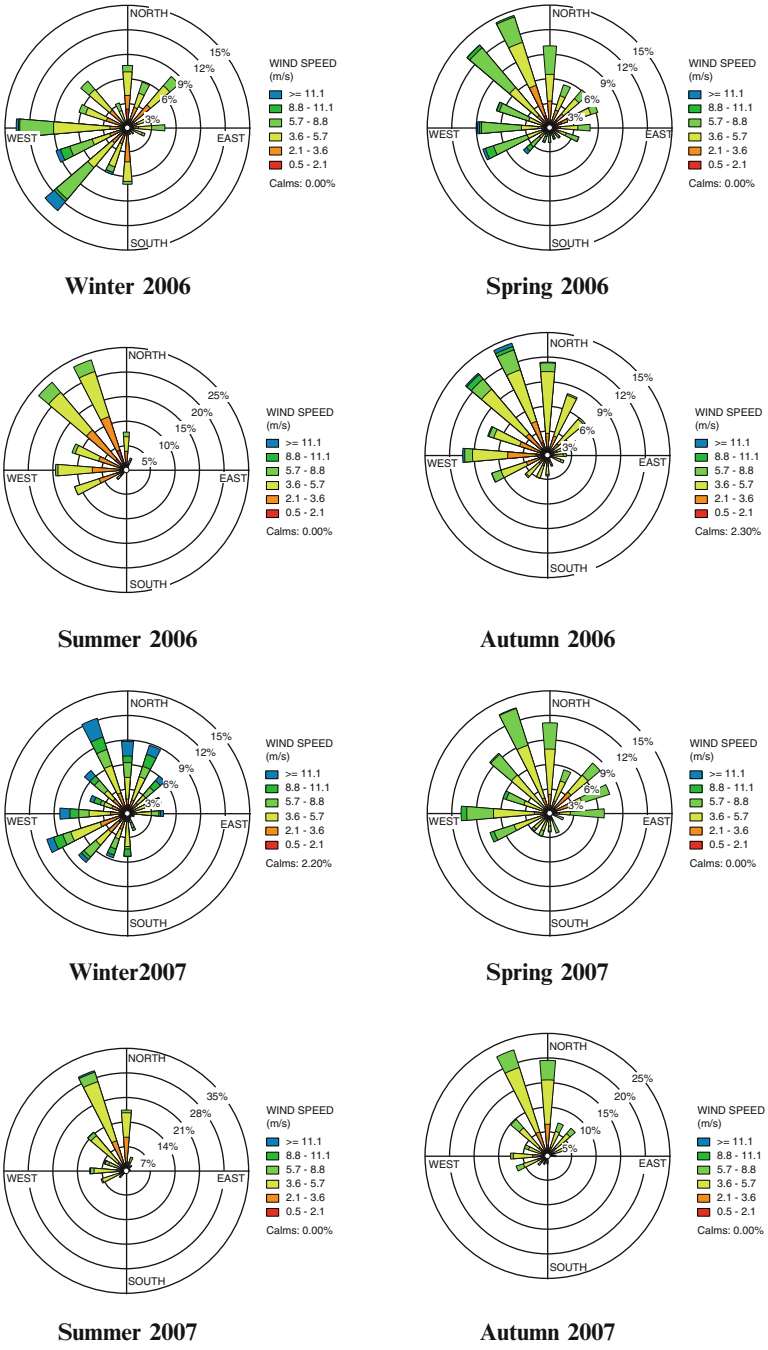

Fig. 22.3 Wind rose distribution measured at Mansoura city during four seasons in 2006 and 2007

Table 22.2 Average annual and seasonal concentrations (± sd) of gaseous pollutants (μg/m^3) during the periods of study

		First year (Dec. 2005–Nov. 2006)					Second year (Dec. 2006–Nov. 2007)				
	Season	Site (A)	Site (B)	Site (C)	Site (D)	Site (E)	Site (A)	Site (B)	Site (C)	Site (D)	Site (E)
SO_2	Winter	30.15 ± 8.28	41.95 ± 7.07	23.00 ± 2.53	30.19 ± 6.09	20.63 ± 5.94	33.48 ± 4.70	28.95 ± 15.29	21.40 ± 4.57	28.25 ± 15.45	21.03 ± 8.28
	Spring	19.22 ± 7.59	24.55 ± 13.87	14.69 ± 7.26	14.74 ± 4.58	12.71 ± 7.54	23.84 ± 1.90	24.42 ± 1.76	19.61 ± 6.62	23.48 ± 0.91	18.61 ± 2.24
	Summer	14.73 ± 8.23	10.06 ± 4.34	13.22 ± 6.15	15.56 ± 9.07	14.55 ± 4.95	11.53 ± 4.46	12.83 ± 1.96	11.42 ± 4.95	12.97 ± 4.5	10.33 ± 3.49
	Autumn	20.22 ± 12.86	19.06 ± 9.68	16.88 ± 2.29	19.48 ± 1.23	15.84 ± 7.04	26.58 ± 8.15	23.78 ± 7.80	18.75 ± 1.49	23.60 ± 20.82	14.57 ± 2.49
	Annual	21.08 ± 12.17	25.90 ± 12.84	16.95 ± 5.81	19.99 ± 8.19	15.93 ± 6.29	23.86 ± 9.44	22.50 ± 9.65	17.79 ± 5.69	22.08 ± 12.66	16.13 ± 5.90
NO_2	Winter	41.14 ± 11.30	60.68 ± 16.15	39.61 ± 6.98	43.30 ± 3.25	41.39 ± 3.96	36.57 ± 6.99	56.00 ± 11.12	38.37 ± 3.95	46.72 ± 6.96	56.56 ± 8.35
	Spring	42.07 ± 2.68	60.67 ± 26.12	39.71 ± 6.54	43.94 ± 5.40	35.08 ± 12.27	40.86 ± 5.65	49.79 ± 3.06	37.43 ± 5.11	48.65 ± 1.27	36.54 ± 6.77
	Summer	40.41 ± 24.30	42.60 ± 31.55	41.66 ± 14.84	48.74 ± 0.29	37.21 ± 9.74	42.36 ± 5.76	43.67 ± 5.12	38.04 ± 8.09	50.83 ± 7.45	36.55 ± 8.37
	Autumn	65.49 ± 28.11	72.21 ± 40.91	60.63 ± 5.36	68.67 ± 13.78	57.11 ± 8.97	64.95 ± 10.68	68.87 ± 11.26	63.13 ± 1.15	67.04 ± 25.60	59.03 ± 5.27
	Annual	47.53 ± 19.82	59.04 ± 27.91	45.40 ± 12.12	51.17 ± 12.57	42.70 ± 11.97	46.19 ± 13.21	54.58 ± 12.12	44.25 ± 12.23	53.31 ± 14.47	47.17 ± 12.76
Total oxidants	Winter	28.99 ± 8.50	58.44 ± 15.60	37.22 ± 23.21	41.83 ± 2.34	23.61 ± 12.05	26.27 ± 5.25	51.65 ± 7.27	29.61 ± 0.91	31.48 ± 0.75	13.61 ± 3.06
	Spring	86.37 ± 34.16	132.14 ± 40.83	79.34 ± 38.22	92.60 ± 53.26	80.16 ± 19.25	77.55 ± 2.81	117.14 ± 27.19	92.35 ± 27.44	113.86 ± 11.60	75.87 ± 7.64
	Summer	201.62 ± 79.84	332.33 ± 98.83	219.89 ± 97.28	271.81 ± 119.69	177.77 ± 45.17	187.85 ± 24.85	316.72 ± 51.96	215.56 ± 72.22	291.22 ± 3.71	184.33 ± 15.03
	Autumn	108.15 ± 78.78	149.21 ± 81.02	115.33 ± 36.70	125.99 ± 66.19	99.71 ± 60.68	85.04 ± 53.92	129.38 ± 20.71	118.24 ± 21.57	121.42 ± 33.58	97.51 ± 30.53
	Annual	106.28 ± 82.04	168.03 ± 120.01	112.94 ± 85.57	133.06 ± 109.08	95.31 ± 66.77	94.18 ± 66.30	153.72 ± 106.43	113.94 ± 77.83	139.59 ± 99.70	92.83 ± 65.59
NH_3	Winter	37.77 ± 11.08	44.43 ± 10.41	31.09 ± 4.27	40.81 ± 7.06	28.44 ± 1.12	40.27 ± 3.10	50.34 ± 7.23	35.39 ± 4.21	39.22 ± 1.68	30.01 ± 4.31
	Spring	34.11 ± 6.38	40.87 ± 10.77	36.64 ± 9.13	41.64 ± 3.12	36.87 ± 10.42	34.73 ± 1.84	30.29 ± 2.65	36.64 ± 5.26	45.96 ± 1.44	33.48 ± 5.60
	Summer	39.80 ± 9.78	51.13 ± 3.24	42.32 ± 8.04	51.51 ± 5.62	36.85 ± 5.51	32.28 ± 11.54	49.36 ± 8.49	42.09 ± 7.69	51.12 ± 4.90	41.51 ± 9.13
	Autumn	33.35 ± 5.34	44.15 ± 12.54	38.57 ± 23.08	56.11 ± 27.54	33.18 ± 7.95	28.38 ± 4.27	39.12 ± 1.51	33.85 ± 0.87	47.72 ± 1.83	30.04 ± 4.38
	Annual	36.26 ± 7.74	45.15 ± 9.30	37.155 ± 12.04	47.52 ± 14.17	33.84 ± 7.07	33.91 ± 7.08	42.28 ± 9.88	36.99 ± 5.45	46.01 ± 5.13	33.76 ± 7.19
H_2S	Winter	21.46 ± 2.54	0.41 ± 0.01	0.38 ± 0.05	0.42 ± 0.16	0.72 ± 0.04	15.30 ± 0.87	0.51 ± 0.17	0.13 ± 0.04	0.08 ± 0.01	0.40 ± 0.25
	Spring	16.61 ± 8.69	0.20 ± 0.03	0.14 ± 0.01	0.24 ± 0.13	0.41 ± 0.06	13.60 ± 2.02	0.41 ± 0.10	0.13 ± 0.03	0.06 ± 0.04	0.12 ± 0.03
	Summer	6.38 ± 3.14	1.12 ± 0.97	0.09 ± 0.04	0.11 ± 0.07	0.26 ± 0.08	2.79 ± 1.08	1.56 ± 0.58	0.15 ± 0.03	0.11 ± 0.02	0.19 ± 0.05
	Autumn	5.26 ± 2.85	0.14 ± 0.11	0.09 ± 0.04	0.06 ± 0.01	0.06 ± 0.05	10.72 ± 8.16	0.20 ± 0.01	0.09 ± 0.02	0.11 ± 0.01	0.23 ± 0.06
	Annual	12.43 ± 8.32	0.47 ± 0.58	0.17 ± 0.13	0.21 ± 0.17	0.36 ± 0.26	10.60 ± 6.19	0.67 ± 0.61	0.13 ± 0.04	0.09 ± 0.03	0.24 ± 0.16

(100 μg/m^3) [13] and the Egyptian ambient air quality standards (60 μg/m^3). Compared with the limits of the daily average NO_2 concentration (150 μg/m^3) of the Egyptian air quality[7], only 6.25, 4.08 and 2.13% of the daily average measured NO_2 concentration at sites (B), (A) and (D) respectively, were higher than the requirement.

However, these values were similar to values found in different cities all over the world as 55.9 μg/m^3 in Hong Kong, China in 1995–1997[32] and 42.5 μg/m^3 in Aarau, Switzerland in 1991[18]. Moreover, these measured NO_2 concentrations were higher than those recorded before in Mansoura city by Egyptian Environmental Affairs Agency [6]: 39 μg/m^3 in 2001 and 35 μg/m^3 in 2003.

The seasonal average concentrations of nitrogen dioxide listed in Table 22.2 showed that the maximum NO_2 concentration was recorded during the autumn season. This may be due to rice straw open burning during this season. Moreover, the lower concentration in the summer season than in the winter season may be due to the lower fuel combustion and greater photochemical reaction of NO_2 in summer season. The NO_2 concentrations were also affected also by wind direction and wind speed especially at site (D), where north winds carried the NO_2 emissions from the fertilizer plant to site (D). As a result, the NO_2 concentration at site (D) decreased in the winter season due to the decrease in the north wind direction percentage as shown in Fig. 22.3.

22.3.3 Total Oxidants

Photochemical oxidants are produced in the atmosphere as a result of chemical reactions involving sunlight, NO_x, O_2, and a variety of hydrocarbons. Photochemical oxidants produced from such reactions include O_3, NO_2, PAN, odd hydrogen compounds (HO, HO_2, H_2O_2, etc.), and RO_2 [10]. Ozone has been established as the principal gas found in photochemical oxidants [23].

The annual mean concentrations of total oxidants at the different sites ranged from 92.83 μg/m^3 at site (E) to 168.03 μg/m^3 at site (B) as shown in Table 22.2. Most of these values were less than the US ambient air quality standard for a 1-h average O_3 concentration (235 μg/m^3) [13], and also the Egyptian air quality limit for average O_3 concentration for 1 h measurements (180 μg/m^3) [7]. The high photochemical oxidant concentration at site (B) may be attributed to the accumulation of high concentrations of NO_2 and hydrocarbons emitted from the chemical industries present near to this site and from combustion of fuels in motor vehicles.

The seasonal mean concentrations of total oxidant listed in Table 22.2 showed that maximum seasonal concentrations were detected during the summer season at all the investigated sites; while the minimum concentrations were detected during the winter season at all the sites. The seasonal variations may be attributed to the meteorological conditions such as high temperature, clear skies, and high solar radiation intensity which are very important factors affecting the photochemical formation of photochemical oxidants. The higher concentrations of photochemical oxidants during the summer season may be due to higher temperature and sunny

days that characterize the summer season in Egypt, which increase photochemical reactions and so their formation. On the other hand, the relative absence of sunlight, the presence of clouds and rain, and the small amount of solar radiation reaching the surface of the ground during winter, cause a decrease in the photochemical formation of photochemical oxidants. Generally there is a positive correlation between total oxidant concentration and temperature [23].

22.3.4 Ammonia

The annual average of ammonia concentrations ranged from 33.76 μg/m^3 at site (E) to 47.52 μg/m^3 at site (D) as presented in Table 22.2. These concentrations were less than the annual average of the ambient level set by the US EPA (100 μg/m^3) (WHO). The maximum annual average concentration of NH_3 was detected at site (D). This may be attributed to the presence of a nitrogenous fertilizer plant near to this site. Table 22.2 also gives the seasonal mean concentrations of ammonia, which shows that the maximum NH_3 concentration was recorded during the summer season. It seems that the ammonia concentration is highly affected by meteorological factors such as temperature, wind direction and rainfall.

Ammonia gas is very soluble in water and therefore it dissolves readily in rainwater causing a reduction of the gas during the winter. While the stable conditions and absence of rain during summer cause the accumulation of the gas in the atmosphere besides the emission from biological processes, which increase with increasing temperature. Thus, temperature is the major factor influencing the level of atmospheric ammonia, besides wind speed and rainfall [22, 23]. The wind direction especially at site (D) affects NH_3 concentrations, where north west winds carry the NH_3 emissions from the ammonia production tower at the fertilizer plant and then increase the concentration over site (D). Consequently, the NH_3 concentration at site (D) decreases in winter seasons due to the decrease in the north west wind direction percentage as can be seen in Fig. 22.3.

22.3.5 Hydrogen Sulphide

The annual mean concentrations of hydrogen sulphide at the different sites ranged from 0.09 μg/m^3 at site (D) to 12.43 μg/m^3 at site (A) as presented in Table 22.2. Most of these values were less than the recent WHO recommended value for avoiding odour annoyance of 7 μg/m^3 [30] except at site (A) where high hydrogen sulphide concentrations were detected because H_2S is the predominant odorant associated with sewage [3, 27].

The seasonal average concentrations of hydrogen sulphide listed in Table 22.2 showed that the maximum seasonal concentrations were detected during the winter season especially at site (A) because the waste water entering the pumping station usually has a high organic load, and under conditions of reduced vertical mixing of

the water column the bottom might become hypoxic or anoxic. Bottom anoxia might then lead to the emission of reduced sulphur compounds from the decomposition of sulphur-containing organic waste [14]. This occurs mainly in winter because the amount of wastewater entering the pumping station decreases in the winter season.

22.3.6 Water Soluble Ionic Species

Water-soluble ions comprise a large part of atmospheric particles and play an important role in the atmosphere. The concentrations of the most abundant ionic species followed the order $SO_4^{2-} > NH_4^+ > Cl^- > NO_3^-$ in most of the investigated sites. The sum of these major ions contribution to the total soluble ion concentrations in atmospheric particles ranged between 72.72% at site (C) and 84.19% at site (B) as shown in Table 22.4.

Table 22.3 shows that the annual average concentrations ranged between 15.15 $\mu g/m^3$ at site (A) and 24.95 $\mu g/m^3$ at site (B) for water-soluble sulphates, 2.52 $\mu g/m^3$at site (A) and 4.06 $\mu g/m^3$ at site (C) for water-soluble nitrates, 2.85 $\mu g/m^3$at site (A) and 4.67 $\mu g/m^3$ at site (E) for water-soluble chlorides and 3.16 $\mu g/m^3$at site (B) and 7.79 $\mu g/m^3$ at site (E) for ammonium salts.

22.3.7 Temporal Variations of Ionic Species

Temporal variations of the major water soluble ionic species of the atmospheric particles were shown in Tables 22.3 and 22.4. The seasonal variation of the water-soluble sulphate concentrations ranged between 11.12 $\mu g/m^3$ in spring season at site (A) and 30.86 $\mu g/m^3$ in autumn season at site (B). High water-soluble sulphate percentage concentrations in the total water-soluble ions over the investigated sites were recorded during the autumn and summer seasons. While the low percentage was recorded during winter season, this confirmed that sulphates might be formed in the atmosphere through atmospheric chemical reactions between SO_2 and alkaline species that increased in warm months [21].

The seasonal variation of the water-soluble nitrate concentrations ranged between 0.99 $\mu g/m^3$ in the winter season at site (C) and 5.87 $\mu g/m^3$ in the autumn season at site (D). Nitrates show a marked seasonal variation with maximum values occurring during the autumn and summer seasons for most of the sites. This may be because the high rate of chemical transformation of nitrogen oxides to nitrates depends on the degree of photochemical reactions. This hardly takes place during in rainy and dusty atmospheres.

The seasonal variation of the water-soluble chloride concentrations ranged between 1.21 $\mu g/m^3$ in the winter season at sites B and C and 6.25 $\mu g/m^3$ in the spring season at site C. The maximum percentage concentration of chlorides over most of the investigated sites was during the spring and summer seasons. The high

Table 22.3 Average annual and seasonal concentrations (± standard deviation) of major ionic soluble species (μg/m^3) during the periods of study

		First year (Dec., 2005 –Nov., 2006)					Second year (Dec., 2006 – Nov., 2007)				
	Season	Site (A)	Site (B)	Site (C)	Site (D)	Site (E)	Site (A)	Site (B)	Site (C)	Site (D)	Site (E)
SO_4^{2-}	Winter	11.95 ± 7.35	12.50 ± 4.96	13.10 ± 5.38	13.32 ± 2.40	22.69 ± 23.55	14.43 ± 1.57	21.75 ± 6.25	12.98 ± 1.80	13.89 ± 8.05	19.41 ± 1.49
	Spring	11.12 ± 1.31	17.42 ± 7.52	12.83 ± 0.23	15.14 ± 3.96	14.03 ± 12.59	13.70 ± 4.21	19.24 ± 2.71	20.31 ± 2.29	13.90 ± 1.04	11.17 ± 1.75
	Summer	20.34 ± 8.19	25.93 ± 1.86	18.73 ± 8.94	18.94 ± 9.70	17.04 ± 8.50	21.97 ± 7.59	31.20 ± 6.05	25.65 ± 7.69	18.14 ± 2.89	27.05 ± 6.83
	Autumn	17.18 ± 4.36	30.86 ± 6.91	25.81 ± 3.02	28.48 ± 1.94	19.53 ± 6.06	24.27 ± 5.06	27.59 ± 4.23	27.85 ± 3.82	27.24 ± 8.07	24.69 ± 5.94
	Annual	15.15 ± 6.44	21.68 ± 8.94	17.62 ± 7.21	18.97 ± 7.69	18.32 ± 12.67	18.59 ± 6.48	24.95 ± 6.52	21.70 ± 7.12	18.29 ± 7.60	20.58 ± 7.51
NO_3^-	Winter	1.14 ± 1.05	2.23 ± 0.40	0.99 ± 0.47	1.57 ± 0.35	3.95 ± 4.91	2.26 ± 0.49	4.35 ± 0.75	2.20 ± 1.52	4.73 ± 3.18	2.56 ± 0.81
	Spring	1.60 ± 0.31	2.42 ± 1.29	1.82 ± 0.13	2.09 ± 0.86	2.28 ± 0.74	2.29 ± 0.13	2.90 ± 1.38	4.47 ± 1.84	2.63 ± 1.32	3.97 ± 1.98
	Summer	3.38 ± 0.78	3.32 ± 0.27	2.93 ± 0.78	2.99 ± 0.23	2.89 ± 0.53	2.62 ± 0.97	4.30 ± 0.66	5.65 ± 1.05	3.02 ± 0.83	3.87 ± 0.66
	Autumn	3.97 ± 1.04	5.14 ± 0.40	4.66 ± 0.64	5.87 ± 1.87	3.60 ± 0.42	3.23 ± 1.09	2.29 ± 0.98	3.92 ± 1.28	3.72 ± 1.32	3.01 ± 2.14
	Annual	2.52 ± 1.43	3.28 ± 1.35	2.60 ± 1.51	3.13 ± 1.95	3.18 ± 2.24	2.60 ± 0.77	3.46 ± 1.26	4.06 ± 1.79	3.53 ± 1.81	3.35 ± 1.46
Cl^-	Winter	2.07 ± 2.00	1.21 ± 0.85	1.54 ± 0.82	1.53 ± 0.64	8.09 ± 10.26	2.72 ± 1.10	2.95 ± 1.65	1.21 ± 0.94	2.28 ± 1.99	3.99 ± 4.01
	Spring	2.83 ± 0.81	3.40 ± 1.21	3.07 ± 0.88	3.62 ± 0.18	3.99 ± 0.96	2.97 ± 0.36	3.41 ± 0.39	6.25 ± 2.24	3.83 ± 0.62	4.55 ± 1.46
	Summer	4.21 ± 1.63	5.60 ± 0.89	4.85 ± 0.24	4.59 ± 0.77	4.51 ± 0.87	1.74 ± 1.35	4.33 ± 1.74	6.01 ± 1.69	3.53 ± 0.57	3.94 ± 0.95
	Autumn	2.33 ± 1.85	3.75 ± 2.04	3.40 ± 2.27	2.84 ± 2.19	2.09 ± 2.12	3.95 ± 1.16	3.64 ± 1.84	3.52 ± 2.69	2.70 ± 1.26	2.86 ± 1.45
	Annual	2.86 ± 1.64	3.49 ± 1.99	3.21 ± 1.65	3.14 ± 1.56	4.67 ± 5.04	2.85 ± 1.22	3.58 ± 1.40	4.25 ± 2.74	3.09 ± 1.25	3.84 ± 2.07
NH_4^+	Winter	2.18 ± 1.32	2.28 ± 0.47	3.53 ± 0.39	7.15 ± 1.94	16.12 ± 8.16	3.50 ± 0.19	4.08 ± 0.59	4.64 ± 1.01	5.69 ± 0.68	3.83 ± 1.33
	Spring	3.03 ± 0.95	1.97 ± 0.83	2.61 ± 1.06	3.27 ± 1.02	1.98 ± 1.52	3.15 ± 1.65	4.04 ± 1.13	4.92 ± 1.54	3.93 ± 1.06	4.19 ± 1.69
	Summer	4.14 ± 1.49	3.16 ± 0.79	3.33 ± 0.83	5.95 ± 1.05	4.70 ± 3.61	3.86 ± 0.85	4.35 ± 2.08	6.75 ± 1.24	4.57 ± 0.64	6.34 ± 0.89
	Autumn	4.95 ± 0.64	5.24 ± 0.21	5.82 ± 0.27	8.70 ± 1.03	8.38 ± 0.91	5.01 ± 0.70	4.34 ± 0.36	6.92 ± 0.38	5.78 ± 1.17	6.30 ± 1.51
	Annual	3.58 ± 1.47	3.16 ± 1.43	3.82 ± 1.40	6.27 ± 2.36	7.79 ± 6.77	3.88 ± 1.12	4.21 ± 1.06	5.81 ± 1.44	4.99 ± 1.12	5.17 ± 1.70

Table 22.4 Percentage of the annual and seasonal average concentration of the major ionic species in the total soluble fraction of SPM

		First year (Dec. 2005–Nov. 2006)					Second year (Dec. 2006–Nov. 2007)				
	Season	Site (A)	Site (B)	Site (C)	Site (D)	Site (E)	Site (A)	Site (B)	Site (C)	Site (D)	Site (E)
SO_4^{2-}	Winter	43.58	43.16	43.49	43.81	35.17	48.70	52.24	43.04	42.00	54.39
	Spring	43.96	49.73	38.70	43.93	40.57	48.07	54.29	47.04	42.73	33.25
	Summer	50.21	56.54	46.16	45.26	43.51	59.78	62.00	48.80	50.12	53.86
	Autumn	46.24	57.61	54.72	53.96	48.09	55.17	59.18	54.17	57.67	54.13
	Annual	46.00	51.76	45.77	46.74	41.84	52.93	56.93	48.26	48.13	48.91
NO_3^-	Winter	4.19	7.18	3.89	5.32	4.75	7.93	12.07	8.11	13.19	7.25
	Spring	6.87	7.11	6.18	6.69	8.72	8.39	7.83	9.65	8.03	11.30
	Summer	8.97	7.46	7.91	7.84	8.17	7.12	8.49	10.98	8.34	7.82
	Autumn	12.37	10.19	9.79	10.74	9.02	8.05	5.69	8.00	7.83	6.20
	Annual	8.10	7.99	6.94	7.65	7.66	7.87	8.52	9.19	9.35	8.14
Cl^-	Winter	7.03	3.73	5.71	5.17	9.42	9.03	8.18	4.75	7.40	9.77
	Spring	11.65	9.72	10.48	12.34	13.72	10.89	9.63	13.70	11.95	13.22
	Summer	10.51	12.36	13.96	11.83	12.74	4.88	8.48	11.48	9.77	8.03
	Autumn	5.84	7.08	7.13	5.32	4.73	9.63	7.87	7.25	5.88	6.59
	Annual	8.76	8.22	9.32	8.66	10.15	8.61	8.54	9.30	8.75	9.40
NH_4^+	Winter	8.14	8.05	13.09	24.17	30.36	12.09	11.03	16.46	19.50	10.99
	Spring	12.18	5.85	8.50	10.84	6.05	10.71	11.13	10.94	12.74	12.18
	Summer	11.13	6.80	8.80	15.27	11.52	10.82	8.41	13.23	12.64	12.87
	Autumn	15.93	10.07	12.40	16.35	21.63	12.11	10.04	14.52	12.78	14.38
	Annual	11.85	7.69	10.69	16.66	17.39	11.43	10.15	13.79	14.41	12.61
Total percentage of annual contribution		74.71	75.66	72.72	79.71	77.04	80.84	84.14	80.54	80.64	79.06

concentration in spring might be caused by strong winds in this season, which could carry particulate matter such as sea salts from Northern side areas to Mansoura city and surroundings.

The seasonal variation of the ammonium salts concentrations ranged between 1.97 μg/m^3 in the spring season at site B and 16.12 μg/m^{3}in winter season at site E. Higher ammonium concentrations over the investigated sites were recorded during the autumn and summer seasons. Furthermore, the lower concentration of ammonium was recorded during the winter season. However, high ammonium concentrations were notable in the winter season at site D. This is due to the fact that ammonium nitrate, the most likely formed at this site, is a relatively stable compound in winter but decomposes with the increase in the temperature through the other seasons so that ammonium in the atmosphere is highly affected by the weather conditions [8]. A high ammonium concentration also was notable in the winter season at site E during the first year of the study. This was due to a shortage in infrastructure leading to continuous leakage of wastewater from collector sewers in streets during this period.

22.3.8 Statistical Analysis and Discussion

The correlation matrix for long-term data for gaseous air pollutants, major ionic species of SPM and climatic parameters (ambient temperature) is shown in Table 22.5. It is important to note that temperature correlated with most of the air pollutants especially total oxidants which referred to their formation by photochemical reactions. Strongly positive correlations between atmospheric NH_4^+ salts and both SO_4^{2-} and NO_3^- salts at sites A, B and C indicates the formation of ammonium nitrate and ammonium sulphates. The positive correlation between H_2S and NH_3 concentrations may be because they are emitted from the same source at sites A and B. A positive correlation between NH_4^+, NH_3, $NO_3^-$and NO_2 concentrations are found because they may be emitted from the same source (fertilizer production plant) which is the main point source of nitrate and ammonia. The positive correlation between the ammonia concentration and temperature stems from the production of ammonia by thermal decomposition of organic wastes.

22.4 Conclusions

The five study sites located at Mansoura city, Egypt (urban area) and a rural area near to the city exhibited different levels of pollution. The measurements of gaseous and soluble ions species were performed during the period December 2005 to November 2007. The average concentrations of gaseous pollutants (SO_2, NO_2, NH_3 and total oxidants) in urban areas exhibited higher levels than in rural area.

The concentrations of gaseous and water soluble ions showed a marked seasonal trend characterized by winter maximum levels for SO_2 (42.19 μg/m^3), H_2S (21.48 μg/m^3) and SPM (392.32 μg/m^3), autumn maximum levels for NO_2 (77.70 μg/m^3) and smoke (72.01 μg/m^3) and summer maximum levels for total oxidants (324.76 μg/m^3) and NH_3 (52.08 μg/m^3). The sum of the total water-soluble ions ranged between 24.69 and 35.96% of the atmospheric particulates and showed clear seasonal variation with maximum concentrations in the summer and autumn seasons due to the increase of atmospheric reactions during the warm months leading to the formation of soluble species such as SO_4^{2-}, NO_3^- and NH_4^+ salts. SO_4^{2-} was the most abundant of all of the species in SPM and NH_4^+ was the second highest ion followed by Cl^- and NO_3^-. The contribution of the sum of these ions to the total ranged between 72.72 and 84.19% at the sites investigated in the study. These major ions showed seasonal variations with maximum concentration in summer / autumn for SO_4^{2-}, NO_3^- and NH_4^+ and spring for Cl^-. A statistical analysis of long term data for these measured pollutants indicated strong correlations.

Table 22.5 Correlation matrix (Person correlation) of long term data for gaseous pollutants, ionic species of SPM and temperature

Site (A)	NH_4^+									
NH_4^+	1.00	SO_4^-								
SO_4^-	0.76*	1.00	NO_3^-							
NO_3^-	0.91**	0.70	1.00	Cl^-						
Cl^-	0.40	0.34	0.48	1.00	SO_2					
SO_2	−0.23	−0.37	−0.31	0.21	1.00	NO_2				
NO_2	0.86**	0.59	0.68	0.39	−0.06	1.00	Total oxidant			
Total oxidant	0.40	0.62	0.54	0.11	−0.90**	0.11	1.00	NH_3		
NH_3	−0.63	−0.55	−0.35	−0.05	0.39	−0.72*	−0.28	1.00	H_2S	
H_2S	−0.73*	−0.74*	−0.77*	−0.03	0.74	−0.39	−0.84**	0.49	1.00	Temperature
Temperature	0.66	0.81*	0.68	0.20	−0.82	0.47	0.92**	−0.59	−0.89**	1.00
Site (B)	NH_4^+									
NH_4^+	1.00	SO_4^-								
SO_4^-	0.81*	1.00	NO_3^-							
NO_3^-	0.71*	0.70	1.00	Cl^-						
Cl^-	0.24	0.60	0.14	1.00	SO_2					
SO_2	−0.44	−0.78*	−0.42	−0.81*	1.00	NO_2				
NO_2	0.40	0.19	0.19	−0.29	0.18	1.00	Total oxidant			
Total oxidant	0.13	0.62	0.24	0.88**	−0.77*	−0.45	1.00	NH_3		
NH_3	−0.16	0.23	0.34	0.26	−0.14	−0.26	0.47	1.00	H_2S	
H_2S	−0.01	0.38	0.24	0.59	−0.48	−0.76*	0.83*	0.62	1.00	Temperature
Temperature	0.42	0.81*	0.26	0.83*	−0.82*	−0.07	0.88**	0.21	0.55	1.00
Site (C)	NH_4^+									
NH_4^+	1.00	SO_4^-								
SO_4^-	0.88**	1.00	NO_3^-							
NO_3^-	0.83**	0.91**	1.00	Cl^-						
Cl^-	0.34	0.56	0.73*	1.00	SO_2					
SO_2	−0.29	−0.48	−0.62	−0.68	1.00	NO_2				

(continued)

Table 22.5 (continued)

NO_2	0.50	0.60	0.33	−0.17	−0.01	1.00	Total oxidant			
Total oxidant	0.36	0.65	0.69	0.77*	−0.84**	0.08	1.00	NH_3		
NH_3	0.00	0.27	0.46	0.66	−0.87**	−0.18	0.83**	1.00	H_2S	
H_2S	−0.30	−0.44	−0.52	−0.34	0.49	−0.44	−0.44	−0.54	1.00	Temperature
Temperature	0.51	0.81*	0.76*	0.69	−0.78	0.38	0.95*	0.70	−0.53	1.00
Site (D)	NH_4^+									
NH_4^+	1.00	SO_4^-								
SO_4^-	0.58	1.00	NO_3^-							
NO_3^-	0.57	0.53	1.00	Cl^-						
Cl^-	−0.54	−0.14	−0.16	1.00	SO_2					
SO_2	0.31	−0.38	−0.01	−0.63	1.00	NO_2				
NO_2	0.56	0.94**	0.66	−0.26	−0.16	1.00	Total oxidant			
Total oxidant	−0.08	0.30	−0.07	0.67	−0.77*	0.05	1.00	NH_3		
NH_3	0.33	0.69	0.23	0.41	−0.63	0.48	0.85**	1.00	H_2S	
H_2S	−0.03	−0.40	−0.72*	−0.35	0.27	−0.54	−0.26	−0.40	1.00	Temperature
Temperature	0.10	0.66	0.11	0.48	−0.79*	0.44	0.90**	0.93**	−0.36	1.00
Site (E)	NH_4^+									
NH_4^+	1.00	SO_4^-								
SO_4^-	0.38	1.00	NO_3^-							
NO_3^-	0.30	0.08	1.00	Cl^-						
Cl^-	0.70	−0.07	0.17	1.00	SO_2					
SO_2	0.30	−0.31	−0.07	0.43	1.00	NO_2				
NO_2	−0.01	0.36	−0.28	−0.47	0.31	1.00	Total oxidant			
Total oxidant	−0.22	0.36	0.21	−0.29	−0.87**	−0.36	1.00	NH_3		
NH_3	−0.32	0.26	0.24	−0.29	−0.77*	−0.52	0.86**	1.00	H_2S	
H_2S	0.53	−0.03	−0.45	0.74*	0.49	−0.13	−0.55	−0.49	1.00	Temperature
Temperature	−0.16	0.49	0.27	−0.41	−0.87**	−0.11	0.94**	0.72*	−0.65	1.00

**Correlation is significant at the 0.01 level; *Correlation is significant at the 0.05 level

References

1. Aneja VP, Chauhan JP, Walker JT (2000) Characterisation of atmospheric ammonia emissions from swine waste storage and treatment lagoons. J Geophys Res 105:11535–11545
2. Ashmore MR (2005) Assessing the future global impact of ozone on vegetation. Plant Cell Environ 28:949–964
3. Bonnin C, Laborie A, Paillard H (1990) Odor nuisances created by sludge treatment: problems and solutions. Water Sci Technol 22:65–74
4. CAPMAS (Central Agancy for Public Mobilization and Statistics) (2007) Primary results for the public mobilization of inhabitants, housing and buildings: El-Dakahlia governorate 2006, Egypt, pp 1–25 (In Arabic)
5. Corbitt RA (1999) Standard hand book of environmental engineering, 2nd edn. McGraw-Hill Companies, Inc., New York, pp 4.4–4.8
6. EEAA (Egyptian Environmental Affair Agency) (2008) Air quality in Egypt: annual reports. (2000–2007), Internet: http://www.eeaa.gov.eg/english/info/report_search.asp. last accessed 4 Sep 2012
7. EEAA (Egyptian Environmental Affair Agency) (2011) Environmental Protection Law No. 4 (1994) and its regulation, Egypt, p 41
8. EMPH (Egyptian Minister of Public Health) (1971) Order No. 470 for the year
9. Fang GC, Wu YS, Chen JC, Rau JY, Huang SH, Lin CK (2006) Concentrations of ambient air particulates (TSP, $PM_{2.5}$ and $PM_{2.5-10}$) and ionic species at offshore areas near Taiwan Strait. J Hazard Mater B132:269–276
10. Godish T (1997) Air quality, 3rd edn. CRC Press LLC, Boston, pp 207–208
11. Goyal P, Sidhartha (2003) Present scenario of air quality in Delhi: a case study of CNG implementation. Atmos Environ 37:5423–5431
12. Harrison RM, Perry R (1986) Handbook of air pollution analysis, 2nd edn. Chapman and Hall, London/New York, pp 280–295
13. Katsouyanni K (2003) Ambient air pollution and health. Br Med Bull 68:143–156
14. Kourtidis K, Kelesis A, Petrakakis M (2008) Hydrogen sulfide (H_2S) in urban ambient air. Atmos Environ 42:7476–7482
15. Manahan SE (2000) Environmental chemistry, 7th edn. CRC Press LLC, Boca Raton, pp 175–183
16. Monteiro MIC, Ferreira FN, de Oliveira NMM, Avila AK (2003) Simplified version of the sodium salicylate method for analysis of nitrate in drinking waters. Anal Chim Acta 477:125–129
17. Mouli CP, Mohan VS, Reddy JS (2003) A study on major inorganic ion composition of atmospheric aerosols at Tirupati. J Hazard Mater B96:217–228
18. Oglesby L, Künzli N, Monn C, Schindler C, Ackermann-Liebrich U, Leuenberger P, The SAPALDIA Team (2000) Validity of annoyance scores for estimation of long term air pollution exposure in epidemiologic studies. Am J Epidemiol 152:75–83
19. Patnaik P (1997) Handbook of environmental analysis: chemical pollutants in air, water, soil, and solid wastes. CRC Press LLC, Boca Raton, pp 277–279
20. Perrino C, Catrambone M, Di Menno Di Bucchianico A, Allegrini I (2002) Gaseous ammonia in the urban area of Rome, Italy and its relationship with traffic emissions. Atmos Environ 36:5385–5394
21. Shakour AA (1992) Evaluation of dust deposited over urban and rural areas in Egypt. TESCE 18(1):86–106
22. Shakour AA, El-Taieb NM (1992) Study of gaseous pollutants in new urban center in Cairo. In: Proceedings of 5th International conference on environmental contamination, Morges, Switzerland, September, pp 207–209
23. Shakour AA, El-Taieb NM, Mohamed SK, Zakey AS (1998) Investigation of air quality in industrial area north Cairo. Cent Europ J Occup Environ Med 4(2):192–204

24. Sharovsky R, Cesar LA, Ramires JA (2004) Temperature, air pollution, and mortality from myocardial infarction in Sao Paulo, Brazil. Braz J Med Biol Res 37:1651–1657
25. Stern AC (1986) Air pollution, vol I, 3rd edn. Academic Press. Inc, NewYork, pp 211–219
26. Turalioğlu FS, Nuhoğlu A, Bayraktar H (2005) Impacts of some meteorological parameters on SO_2 and TSP concentrations in Erzurum, Turkey. Chemosphere 59:1633–1642
27. Vincent A, Hobson J (1998) Odour control, CIWEM monographs on best practice No. 2. Chartered Institution of Water and Environmental Management, Terence Dalton Publishing, London
28. Volkan M, Eroğlu T, Eroğlu AE, Ataman OY, Mark HB (1998) A novel sorbent tube for ambient hydrogen sulfide determination. Talanta 47:585–593
29. Weatherley NS, Timmis RJ (2001) The atmosphere in England and Wales: an environmental management review. Atmos Environ 35:5567–5580
30. WHO (2000) Air quality guidelines for Europe, 2nd edn, WHO Regional Publications, European Series No. 91. WHO Regional Office for Europe, Copenhagen
31. WHO (2004) Health aspects of air pollution: Results from the WHO project "Systematic review of health aspects of air pollution in Europe". World Health Organisation, Geneva
32. Wong CM, Atkinson RW, Anderson HR, Hedley AJ, Ma S, Chau PYK, Lam TH (2002) A tale of two cities: effects of air pollution on hospital admissions in Hong Kong and London compared. Environ Health Perspect 110:67–77

Chapter 23
Remote and Ground-Based Sensing of Air Polluted by Nitrogen Dioxide in the Dnepropetrovsk Region (Ukraine)

Mykola M. Kharytonov, Valentina M. Khlopova, Sergey A. Stankevich, and Olga V. Titarenko

Abstract Data of atmospheric remote sensing in Dnepropetrovsk region have been obtained for different periods (2001, 2004, 2005, 2006 and 2010) from five points located within the Dnepropetrovsk region. Current ground-based stationary research has been carried out at three observation laboratories controlling air pollution during the last 15 years. This paper analyzes the annual mean of the NO_2 concentration, on a regional (south east of Ukraine) scale. A tendency for increased nitrogen dioxide concentrations in the air around cities such as Dnepropetrovsk, Dneprodzerzhinsk and Krivoy Rog is found. The average nitrogen dioxide concentrations registered at all these cities' observation stations have exceeded the maximum permissible concentration values by as much as three to four times during the last decade.

Keywords Air pollution • Nitrogen dioxide • Remote and ground based sensing • Monitoring

23.1 Introduction

Urbanization development, industrial growth and the continuous increase of city public transport in metropolises has led to a series of negative phenomena such as the accumulation of different contaminating gases and vaporized pollutants

M.M. Kharytonov (✉)
Soil Science and Ecology Department, Dnipropetrovsk State Agrarian University, Dnipropetrovsk 49027, Ukraine
e-mail: mykola_kh@yahoo.com

V.M. Khlopova
Dnipropetrovsk Hydrometeorological Center, Dnipropetrovsk 49600, Ukraine
e-mail: lnza@yandex.ru

S.A. Stankevich • O.V. Titarenko
Scientific Centre for Aerospace Research of the Earth, Kiev, Ukraine
e-mail: olgatitarenko@casre.kiev.ua

I. Barnes and K.J. Rudziński (eds.), *Disposal of Dangerous Chemicals in Urban Areas and Mega Cities*, NATO Science for Peace and Security Series C: Environmental Security,
DOI 10.1007/978-94-007-5034-0_23,

as well as acid rain formation [1, 2]. The leaves and petals of flowers are damaged by rain acid which results in a decrease in field and vegetable crops. Acid rains damage the process of plant breathing resulting in decreasing pH levels of soils and surface and underground waters [3]. Emissions from high temperature fuel combustion (exhaust gases from cars and airplanes, emissions of industrial enterprises and thermal power stations) are the main sources of nitrogen and sulfur oxides to the atmosphere. Nitrogen dioxide stands out taking into consideration its level of concentration in the air compared with all other pollutants [4]. Nitrogen oxides in combination with ultraviolet solar radiation and hydrocarbons form many different products in photochemical reactions [5]. In Ukraine, emissions mainly take place in the cities of Krivoy Rog, Dneprodzerzhinsk and Dnepropetrovsk because of the high density of harmful industries located in these cities. The main pollution sources are the facilities of metallurgy, power industry, mining, chemical and petrochemical industries. The metallurgical sector accounts for 64 % of the total regional emission growth (about 530,000 tons per year) with NO_2 input up to 20,000 tons per year. To meet the demands for energy, 11 thermal power stations have been built in the Dnepropetrovsk region. The thermal power industries contribute to NO_2 air pollution (around 50,000 tons per year) [6]. The goal of our research is to estimate the dynamics of nitrogen dioxide emissions made by different sources located in the Dnepropetrovsk region within the last decade.

23.2 Materials and Methods

The data of remote atmospheric sensing in Dnepropetrovsk region have been obtained for different periods (2001, 2004, 2005, 2006 and 2010). The data have been obtained at five points located within the Dnepropetrovsk region. Continual spectrometric recordings carried out using the Envisat/SCIAMACHY sensor permit to obtain daily recordings worldwide concerning the NO_2 concentration (density: 10^{15} molec/cm^2). The monthly data (on a planetary level and on geographic regions) are archived as cartographic representations on the website: www.temis.nl/airpollution [8]. The tropospheric column n/S, [molec/cm^2] conversion to NO_2 concentration C [mg/m^3] was recalculated using the formula:

$$C = 10^7 \frac{n}{S} \frac{m_{NO_2}}{h\, N_A}, \tag{23.1}$$

where $m_{NO2} = 46{,}005.6$ mg/mol is the molar mass of NO_2, $N_A = 6.022 \times 10^{23}$ mol^{-1} is the Avogadro constant and $h \approx 12 \times 10^3$ m is the approximate troposphere depth.

Current ground-based stationary research is carried out at three observation laboratories controlling air pollution. These laboratories were created to provide background monitoring in the cities of Dnepropetrovsk (DP), Dneprodzerzhinsk (DZ) and Krivoy Rog (KR). Forecasting and comparison with actual pollution levels and the development of activities aimed at air pollutant migration were the

objectives and reasons for the creation of the station networks on the territories of these cities in this industrial region. Information on the pollution content of the air is gathered systematically at specially equipped stations. The number and locations of the stationary observation stations are varied. There are six stationary and two mobile stations in Dnepropetrovsk, five stations are located in Krivoy Rog, and Dneprodzerzhinsk has four.

To evaluate air pollution methods such as laboratory, express and automatically control ones are used. The background monitoring data of the investigated substances in the atmosphere, obtained on a daily, monthly and/or annual basis, are compared with the maximum permissible concentrations. Comparative analyses of air polluted with nitrogen dioxide for cities in the Dnepropetrovsk region were carried out.

The calculation of the air pollution index (API) was performed using the formula [8]:

$$API = \sum_{i=1}^{n} (C_i - A_i)^k, \tag{23.2}$$

where n is the number of substances needed to calculate API; C_i is the substance concentration; A_i is the index of substance aggressivity; and $A_i = 1/MPC_i$; k is the index depending on the substance safety category: for the first category it is equal 1.7; for the second category it is equal 1.3; for the third category it is equal 1.0; and for the fourth category it is equal 0.9. If API value ≤ 5, then the level of air pollution is below average, if $5 < API \leq 8$ then it is estimated as average; if $8 < API \leq 15$ then it is above average, and if $API > 15$ then it is considerably as high.

23.3 Results and Discussion

The paper is focused on the situation with the NO_2 concentration in the troposphere during the last decade and its distribution in South-Eastern Ukraine. The data on NO_2 tropospheric column density in two industrial regions Prydneprovye and Donbas are presented in the satellite image shown in Fig. 23.1. The NO_2 concentration for most parts of the study area was within the limits of 8–11 $\times$ 10^{15} molec/cm^2 in January, 2011. A slightly larger nitrogen dioxide concentration of (15–18 $\times$ 10^{15} molec/cm^2) was observed in the atmosphere over the industrial region of Donbas in December, 2010 [9].

The monthly average of the NO_2 tropospheric column density, obtained from remote sensing data smoothing using five point measurements within the period of 2004, 2005, 2006 и 2010 years is presented in Fig. 23.2.

On average, the highest concentrations of NO_2 were fixed from October till December for the 4 years. NO_2 concentrations in February, March and from May till August were three to four times lower than those as the end of each year. The ground based data on the NO_2 concentration for the years 2004, 2005, 2006 and 2010 for two industrial cities are presented in Table 23.1. The NO_2 concentration varied in the range 0.05–0.09 in Dneprodzerzhinsk, from 0.03 to 0.08 mg/m^3 in

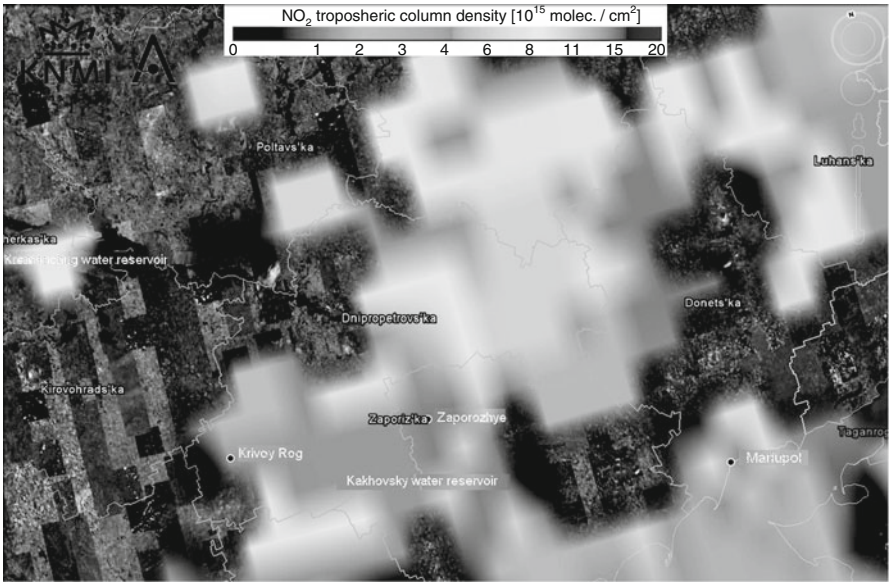

Fig. 23.1 The data on NO_2 tropospheric column density in South-Eastern Ukraine

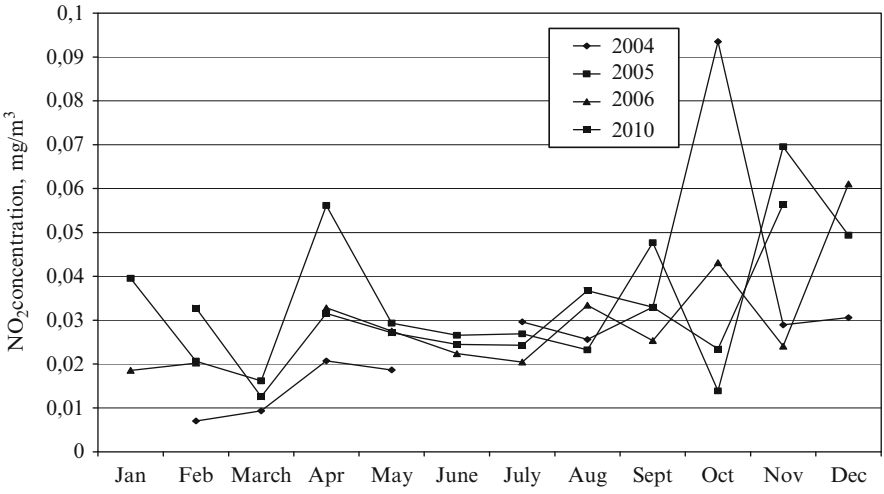

Fig. 23.2 Monthly average of the NO_2 concentration (mg/m^3) in the Dnepropetrovsk region for the years 2004, 2005, 2006 and 2010

Krivoy Rog. Data to carry out a comparison of the monthly average nitrogen dioxide concentration in the air of Dnepropetrovsk with the maximum permissible concentration are pointed out in Fig. 23.3. The comparison is carried out taking into consideration the values of maximum permissible concentration, the quantity of days with maximum level of air pollution and still air display in 2006.

Table 23.1 NO_2 air pollution (mg/m^3) in the cities of Dneprodzerzhinsk and Krivoy Rog

	Year							
	2004		2005		2006		2010	
Month	DZ	KR	DZ	KR	DZ	KR	DZ	KR
Jan	0.08	0.05	0.07	0.04	0.06	0.04	0.06	0.03
Feb	0.06	0.05	0.06	0.04	0.07	0.05	0.06	0.05
March	0.05	0.05	0.06	0.04	0.06	0.05	0.07	0.05
Apr	0.06	0.04	0.09	0.06	0.08	0.06	0.07	0.06
May	0.08	0.04	0.08	0.06	0.07	0.04	0.07	0.05
June	0.07	0.04	0.07	0.04	0.07	0.05	0.07	0.05
July	0.06	0.05	0.07	0.05	0.07	0.05	0.07	0.05
Aug	0.06	0.05	0.09	0.05	0.08	0.06	0.07	0.06
Sept	0.05	0.05	0.08	0.05	0.07	0.05	0.07	0.05
Oct	0.06	0.04	0.06	0.05	0.09	0.06	0.08	0.05
Nov	0.07	0.04	0.06	0.06	0.08	0.05	0.08	0.08
Dec	0.05	0.04	0.05	0.05	0.08	0.05	0.06	0.06

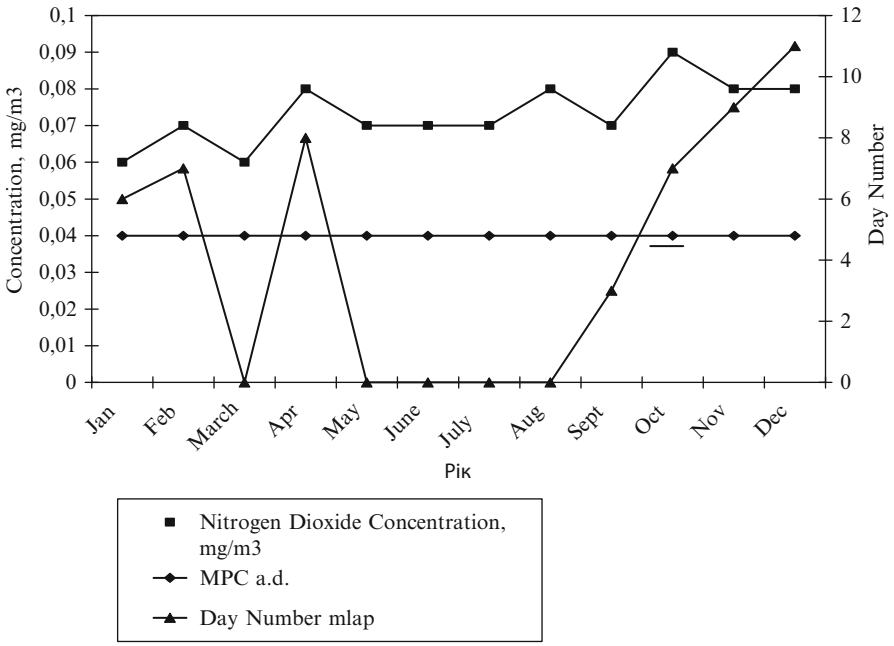

Fig. 23.3 Maximum permissible concentration and the quantity of days with maximum level of air pollution (mlap)

In accordance with the data presented in Fig. 23.3 the monthly average nitrogen dioxide concentration in the air of Dnepropetrovsk is 1.5–2.25 times higher than the maximum permissible concentration.

Comparison of the data shows that increased nitrogen dioxide concentration levels in the air occurred for the months having the lowest air flow velocity (Fig. 23.4).

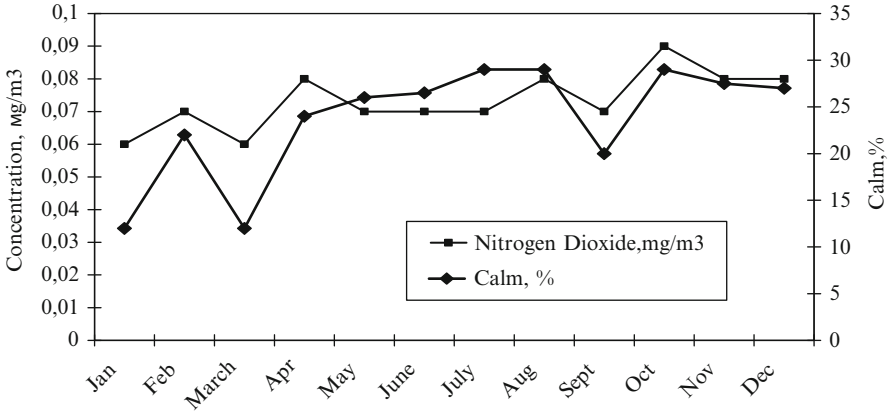

Fig. 23.4 Monthly average nitrogen dioxide concentration in the air of Dnepropetrovsk with regard to still air data for 2006

It is established that the nitrogen dioxide concentration in the lowest atmospheric layer has a clear daily variability. Maximum concentrations are registered at the pollution observation stations during the early morning and afternoon hours (transport peaks). During warm seasons maximum concentrations are registered more often during the early morning and evening time within warm seasons [10]. These periods are characterized by intensive convective mass transfer of air in the lowest atmospheric layer.

Dwellings and high industrial buildings form erratic uneven surfaces. Such erratic surfaces become an obstacle for the free movement of air masses and result in alteration of the structure of the lowest atmospheric layers. Taking into account the fact that a city's surface is more built up and developed than a rural area of the same *size*, phenomenon such as urban heat island (UHI) occur. As a result, higher solar energy absorption during the day and its consequent conservation for prolonged periods at night occur in the city. Hence, powerful flows of warm air masses rise into the highest atmospheric layers with taking with them pollutants. This flow then spreads in all directions and descends to the city's suburbs. Further, the flow in the lowest layer moves back to the city centre. Thus, a self-sustained air circulation is formed, which can be disturbed only by another powerful air current. Due to this, during still air days pollutant concentrations increase under the city's smoky dome.

The results from a comparison of background NO_2 data with maximum permissible concentration levels of nitrogen dioxide in the atmosphere are shown in Fig. 23.5 for a decade of observations.

The analysis of the data obtained shows the significant exceedance of the background nitrogen dioxide concentration (up to three to four times) over the established maximum permissible concentration values. The final results from calculations of the annual average values of Dnepropetrovsk's air pollution index for the period of 2001–2006 are shown in Fig. 23.6.

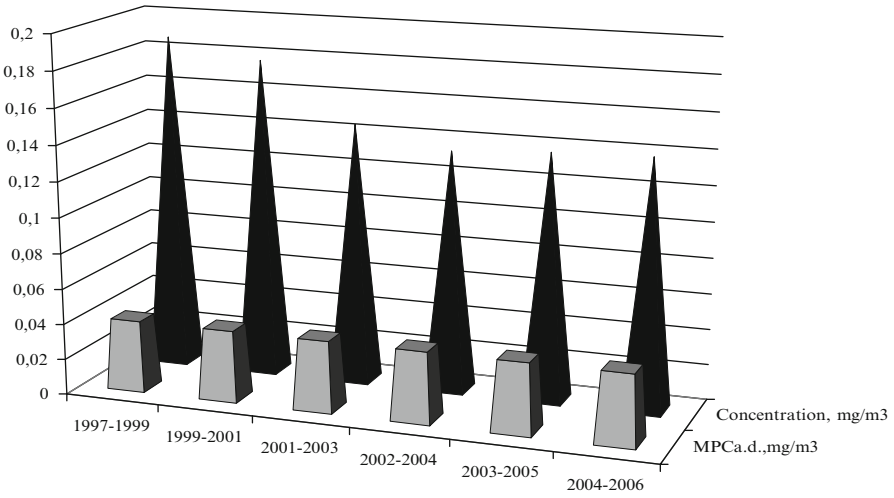

Fig. 23.5 Background pollutant concentrations with regard to the nitrogen dioxide content

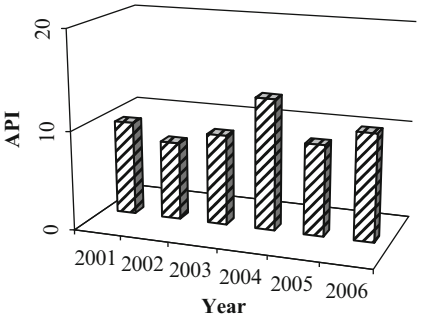

Fig. 23.6 Air pollution index

From a comparison of the values of the air pollution index for the 6 year period it can be seen that the value of API for the city of Dnepropetrovsk is above average.

23.4 Conclusions

Increased nitrogen dioxide concentration levels in the air of Dnepropetrovsk are observed in the months with the lowest air velocity. The average nitrogen dioxide concentrations registered at all the city observation stations in the study have been up to three to four times higher than the maximum permissible concentration values during the last decade. The value of the air pollution index is above average in the city of Dnepropetrovsk. A tendency for increased nitrogen dioxide concentrations in the air around such cities as Dnepropetrovsk, Dneprodzerzhinsk

and Krivoy Rog has been established which confirms the possible risk of acid rain fallout not only on the areas marked as industrial regions but also on adjacent suburban territories as well. Special scientific interest is connected with carrying out the estimation of technogenic land degradation and the degree of agricultural crop damage in places experiencing acid rain fallout.

References

1. Zaikov GE, Maslow SA, Rubaylo VL (1991) Acid rain and environment. Himiya, Moscow, 144 p (In Russian)
2. Kopach PI, Shapar AG, Shvartsman VM (2006) Technogenes and acid rains. Naukova dumka, Kiev, 173 p (In Russian)
3. Duccer WM, Ting IP (1970) Air pollution oxidants – their effects on metabolic processes in plants. Ann Rev Plant Physiol 21:215–234
4. Environmental Protection Agency (EPA) (2005) Acid rain program, 2004 progress report, EPA Report, EPA 430-R-05-012, Washington, DC
5. Crutzen PJ (1979) The role of NO and NO_2 in the chemistry of the troposphere and stratosphere. Annu Rev Earth Planet Sci 7:443–472
6. Babiy AP, Kharytonov MM, Gritsan NP (2003) Connection between emissions and concentrations of atmospheric pollutants. In: Melas D, Syrakov D (eds) Air pollution processes in regional scale, NATO science series, IV: Earth and environmental sciences. Kluwer Academic Publishers, Dordrecht, pp 11–19
7. Soloshenko OV (2008) Ecology: manual. Parus, Kharkov, 371 p (In Ukrainian)
8. www.temis.nl/airpollution/ Nitrogen dioxide (NO_2), tropospheric NO_2 from satellites
9. Loghin VD (2010) Atmospheric nitrogen dioxide monitoring by remote sensing. A special regarding at Europe and Romania. The annals of Valahia University of Târgovişte. Geographical series, Tome 10. Valahia University of Târgovişte, Romania, pp 93–96
10. Khlopova VM, Kharytonov MM (2011) Acid rains forming in metropolis. News of Dnipropetrovsk State Agrarian University, Dnipropetrovsk, No. 1, pp 8–14 (In Ukrainian)

Chapter 24
Atmosphere Pollution Problems in Urban Areas on the Territory of Georgia

Teimuraz Davitashvili

Abstract Air emissions from industrial facilities and motor vehicles and monitoring of the atmosphere quality in the most industrialized cities of Georgia, Tbilisi Rustavi, Qutaisi, Zestafoni and Batumi, are presented. Fuel consumption and emissions from the transport sector in Tbilisi have been investigated. Using mathematical simulation, the concentration distribution of harmful substances, NO_x, at Rustavely Avenue, the crossroad of King David Agmashenebeli and King Tamar Avenue, where traffic is congested, have been studied. Some results from the numerical calculations are presented.

Keywords Air pollution • Mathematical simulation • Emissions • Monitoring • Air quality

24.1 Introduction

Considerable technical developments have taken place in recent years with the emergence of advanced transportation systems. This has consequently increased the pollution burden on the environment. Nowadays the damages caused by air pollution in the world are large. It is estimated that as many as 2.4 million people die each year from diseases caused, or made worse, by atmospheric pollution. Unfortunately the main polluter of the Earth's atmosphere is man. At present atmospheric pollution by harmful substances of anthropogenic origination is several times greater than air pollution caused by natural phenomena such as: volcanic eruptions, forest fires, earthquakes, tornados, cyclones etc. Generally harmful substances having anthropogenic origin are mainly emitted from power plants

T. Davitashvili (✉)
I.Vekua Institute of Applied Mathematics, Tbilisi State University, 2 University Str., 0186 Tbilisi, Georgia
e-mail: tedavitashvili@gmail.com

I. Barnes and K.J. Rudziński (eds.), *Disposal of Dangerous Chemicals in Urban Areas and Mega Cities*, NATO Science for Peace and Security Series C: Environmental Security,
DOI 10.1007/978-94-007-5034-0_24,

and vehicle engines [2]. The same situation is observed on the territory of Georgia. Atmospheric air pollution has always been the environmentally most sensitive issue in Georgia. Georgia's most industrialized cities have been at the top of the list of most polluted cities of the former Soviet Union (NSoG [30]). In recent years the development of industry and transportation systems has strengthened the impact on the environment, i.e., on the biosphere and hydrosphere and particularly on the atmosphere on the territory of Georgia. All over the world the main source of atmospheric air pollution is the exhaust from motor-vehicle transport, which constitutes about 75% of the total pollution. In Georgia this value is higher and it is about 84% [37]. The point is that since 1991 economic activities have drastically decreased in Georgia; many industrial facilities stopped production due to loosing traditional channels for selling outputs in the markets of former Soviet Union. However, at the same time the role of transportation on the territory of Georgia has increased. Georgia holds a strategic location between Europe and Asia, among Russia, Turkey, Armenia and Azerbaijan. Since ancient times the route of the historical Silk Road has passed through territory of Georgia. At present, Georgia is once again becoming one of the most important transit countries. The European Union (EU) is one of the main sponsors and advocates of the transport corridor Europe-Caucasus-Asia (TRACECA). The EU considers Georgia as a partner in the development of the transport networks between the Black Sea and Central Asia because of its geopolitical position. Georgia participates in 21 from 35 projects elaborated by the regional program TRACECA [12]. Using railways, highways and oil-gas pipelines, oil, gas, coal, cotton, and metals are conveyed across Georgia from central Asia and Azerbaijan to the Black and Mediterranean Seas' coast. According to the experience of European transit countries the transit of strategic materials causes great losses regarding the ecological situation thus counteracting the intended political and economical benefits. In addition to ordinary pollution of the environment it is possible that extraordinary events like oil and gas pipeline leaks and explosions and auto traffic and railway accidents occur (also terrorist attacks may occur) and fires as a consequence. Thus, nowadays transportation systems have become the main sources of atmospheric pollution on the territory of Georgia and in Georgian's cities [18].

24.2 Material and Estimation Method

In Georgia hydro-meteorological field observations and investigations began in 1887, but the system of monitoring of atmospheric air quality began only in 1974, i.e. 33 observation stations allocated in 11 towns of Georgia began monitoring the air quality. Since 1992 there have some problems with the monitoring system arising from political and economical developments within the territory of Georgia. The number of observation stations has decreased, the functioning stations have not been upgraded with modern devices and instruments for monitoring, the data obtained were not processed by computers and at observation stations and standardized methodology for data analyses does not exist. Generally data observation and collection has also been fragmentary in character [28].

At present air quality monitoring is performed by the Georgian National Agency of Environment using seven observation stations distributed in the five cities of Georgia. In eastern Georgia they are located in Tbilisi and Rustavi and in western Georgia in Qutaisi, Zestafoni and Batumi. Each city has only one or two observation stations. It is obvious that this number of stations is not sufficient to make a proper assessment of the air quality over the territory of a town. In fact there is information of air quality only for separated regions of the town were the stations are located [36].

The following pollutants are monitored on the territory of Georgia: in Tbilisi (Capital city of Georgia)- dust, carbon monoxide, nitrogen monoxide and nitrogen dioxide, sulphur dioxide, and lead; in Kutaisi- dust, sulphur dioxide, nitrogen monoxide and nitrogen dioxide; in Batumi-dust, nitrogen and sulphur dioxides; and in Zestaphoni-dust, nitrogen dioxide, sulphur dioxide and manganese dioxide. Ground level ozone monitoring began in 2010 in Tbilisi and carbon monoxide in Kutaisi and Batumi [37].

For the determination of the degree of air pollution the measured concentrations of the pollutants are compared to the national standards of air quality which are called Maximum Allowed Concentrations (MAC) of harmful substances in ambient air that were established by the Ministry of Labor, Health and Social Protection of Georgia in 2003. The Maximum Allowed Concentration of a substance in ambient air represents the concentration (averaged for a specific time period) below which the substance does not affect human health or the environment over regular periodic or lifetime exposure [6]. Two types of MACs have been established: (a) Maximum one-time concentration (measured within 20–30 min, mg/m^3), (b) Mean daily concentrations (mg/m^3). Average annual concentrations are also measured based on the mean daily concentrations [28]. It should be noted that MACs for air pollutants formally established in Georgia are based on former Soviet standards of air quality and they, in some cases, differ from standards recommended by the World Health Organization (WHO) as well as standards adopted by the EU. All of the standards are considered in the evaluation.

24.3 Air Pollution Problems in the Period 1990–1996 on the Territory of Georgia

In the beginning of the 1990s Georgia was on the brink of war, critically endangered, collapse of political and economic policies. In 1991 Georgia won its independence but owing to an economic blockade by Russia Georgia's economic activities drastically decreased, many industrial plants stopped production. The energy supply to industry and households decreased to critical levels. In the period 1990–1994 Total Domestic Product (TDP) of Georgia was reduced by almost 65% [28].

Table 24.1 shows that TDP in Georgia from 1990 to 1994 has been reduced with a peak in 1992 of about −40%. After 1995 TDP began to grow. In 1992 there were only nine large industrial plants on the territory of Georgia. These nine large

Table 24.1 Dynamics of Georgia's total domestic product between 1990 and 1996

Years	1990	1991	1992	1993	1994	1995	1996
Change of GDP (%)	−15	−20.1	−39.7	−29.3	−12.1	+3.3	+11

industrial facilities were responsible for 80% (148,594 tonnes) of total emissions of harmful substances (185,816 tonnes) into the air [28]. Analyses of air pollution from traffic and industry in Georgia from 1985 to 1992 shows that the Georgian transport sector was a significant source of environmental stress. From 1985 to 1990 emissions from traffic were double the emissions from industry and it was only in 1992 that the values became almost equal. So the traffic was the main source of air pollution in Georgia. The reason is the large number of vehicles (750,000 units registered in 1990), as well as the use of the low quality fuel. In the years 1992–1994 the fuel shortage caused a considerable decrease in the emission levels in Georgian cities [30].

24.4 Air Pollution Problems Between 1995 and 2010 on the Territory of Georgia

Economic recovery in Georgia started in 1995 and was the result of the establishment of political stability in the country and initiated privatization processes which resulted in fast economic growth.

Table 24.2 shows that TDP started to increase between 2004 and 2007 with the growth rate amounting to 6–12%. Armed conflict with Russia in August 2008 and the global economic crisis severely affected Georgia's economic development. Real TDP growth rate reduced to 2.3% in 2008 and it was negative in 2009. Nevertheless, TDP grew by 6.4% in 2010 [28]. Due to the dynamics of Georgia's TDP the main atmospheric pollutants of the air in the main industrial cities of Georgia, Tbilisi, Kutaisi, Zestafoni and Batumi, had different character in the period 2005–2009. Analysis of the emissions of dust and Volatile Organic Compounds (VOCs) to the atmosphere, caused by the industrial, energy and auto-transport sectors, have shown that up to 2008 the main source of dust in air was industry, mainly the cement plants in Rustavi and Kaspi [28]. In 2009 those plants were equipped with modern air filters which significantly decreased their emissions and consequently from 2009 the picture changed. The main source of VOCs to air was the energy sector, mainly due to methane losses from gas distribution systems in Georgian cities. From 2005 to 2009 in all the considered cities the average annual concentrations of dust exceed the MAC value by factors of 2 or 3. Comparatively low values of dust concentrations (a little more than the MAC) were measured in Batumi and rather high values were found in Kutaisi and Tbilisi (three times higher than the MAC). Sulphur dioxide is emitted into ambient air from the combustion of sulphur containing fuel. From 2005 to 2009 in all the considered cities the average annual sulphur dioxide concentrations exceed the MAC value for the Georgian

Table 24.2 Dynamics of Georgia's Total Domestic Product (TDP) for the years 2005–2010

Years	2004	2005	2006	2007	2008	2009	2010
Change of GDP (%)	102.4	109.6	109.4	112.3	102.3	96.1	101.5

standard but for the European standard it is exceded only slightly in Qutaisi in Tbilisi (about 1.2 times) mainly caused by the exhaust gases from motor vehicles. Carbon monoxide emissions in the air increased from 2000 to 2008 about 2.5 times owing to the transport sector, while those from the industrial and energy sectors did not change. As for sulphur dioxide, emissions from the transport and energy sectors increased 1.8 and 2.1 times, respectively, from 2000 to 2008, but those from industry did not change for this period. Nitrogen dioxide and monoxide are the products of fuel combustion at a very high temperature in the presence of an abundance of oxygen. The main sources are motor vehicle exhausts, emissions from power stations and the burning of solid waste [21]. The main source of nitrogen dioxide in the air of Georgia is the transport sector, namely the exhaust gases of motor vehicles. However, it is important to note that for 2000–2008 contributions the energy and industrial increased by 1.5 and 2 times, respectively. Investigations have shown that from 2005 to 2009 in all the considered towns (Tbilisi, Kutaisi, Zestafoni and Batumi) the average annual nitrogen dioxide concentrations exceeded the Georgian MAC standard as well for the European standard (the MAC for nitrogen dioxide is the same in Georgian and the EU). The main sources of nitrogen dioxide to the atmosphere in Georgia are from the exhaust gases of vehicles, natural gas emissions, emissions from power stations and the burning of solid waste. It is known that manganese dioxide is a highly toxic substance which has an impact on the central nervous system [29]. The main source of manganese dioxide is the metallurgical industry. The source of the main pollutant in Zestaphoni, manganese dioxide, is considered to be the metal production company "Georgian Manganese Ltd". Regular monitoring of air quality revealed that the manganese dioxide mean annual concentration substantially exceeds the MAC (the MAC for manganese dioxide is the same in Georgian and the EU) about eight to nine times for the period 2005–2009 [28].

24.5 Air Pollution Problems in Tbilisi

The capital city of Georgia, Tbilisi, is located on both banks of the Kura River, stretches 33 km along the river and has a complex relief. The climate in Tbilisi is mild and warm, it is transitional from the steppe to mild humid subtropical. Winter is mild, not very cold and summer is mild, not very hot. The average annual temperature is 12.7 °C, in January 0.3 °C and in July 24.4 °C. The amount of precipitation per year is on average 560 mm. For the last 10-year period observations have been carried out in Tbilisi, at three posts, situated in different districts. There are only two meteorological observation posts in the central (highly polluted) part of Tbilisi (at the crossroad of the King Tamar and King David Agmashenebeli avenues

Table 24.3 Emissions of major pollutants from stationary sources in Tbilisi for the period 2005–2009 (Tonnes)

Major pollutants	2005	2006	2007	2008	2009
Particulate matter	66	89	57	66	59
Sulphur dioxide	96	89	51	3	3
Nitrogen oxides	30	21	13	15	14
Carbon monoxide	101	77	58	35	30
Hydrocarbons	36	18	12	36	7
Other pollutants	13	10	9	34	5
TOTAL	342	304	200	189	118

Source: Ministry of Environment of Georgia

Table 24.4 Emissions of selected pollutants from stationary sources and motor vehicles in Tbilisi (Tonnes, 2009)

Harmful substance	Carbon monoxide (CO)	Nitrogen dioxide (NO_2)	Sulphur dioxide (SO_2)	Hydrocarbons (ΣCH)	Particulate matter (PM)
Stationary sources	30	14	3	7	59
Motor vehicles	103,165	10,155	3,460	23,724	2,423

and in the Tsereteli avenue) and a third meteorological observation post is situated in Moscow Avenue which is quite far from the central part of Tbilisi. North and North-West winds dominate in Tbilisi, however, South-East winds often blow as well. In most of the territories of Tbilisi the average annual wind speed is 3–4 m/s, in some open areas of the city, such as Digomi, Samgori and Saburtalo, it is 6–7 m/s. The wind speed can exceed 40 m/s in some particular cases [33].

Table 24.3 shows that despite the growth of industrial production in Tbilisi for the period 2005–2009 significant reduction in emissions was observed: in sulphur dioxide about 30 times, iNtrogen oxides 2 times, carbon monoxide three times. The totally emissions of major pollutants from stationary sources in Tbilisi was reduced by a factor of about 2.89 for the period 2005–2009. Data provided by the Ministry of Environment on air emissions from 35 major stationary pollution sources suggests that 99% of total suspended particulates (TSP) resulting in industrial processes have been captured in filters and recycled. However, all the other pollutants such as SO_2, NO_x, CO and hydrocarbons in industrial processes were emitted into the environment because of a poor state or non-existence of respective filters at the industrial facilities [28].

The Georgian transport sector is a significant source of environmental pollution. The number of transport vehicles has doubled since 2000 while the number of busses and minibuses has tripled. It is important to note that number of vehicles at least has doubled from 2008 to 2011 and diesel fuel consumption increased five-fold. The distribution of public transport and a quantitative measure of GHG emissions by mini-buses in Tbilisi is assessed in Beglarashvili [3].

Table 24.4 shows that despite the revival of the industrial sector, air emissions from this sector have been significantly reduced and in contrast, air emissions from traffic have increased substantially due to increasing number of vehicles, from which 82% are more than 10 years old in Tbilisi [3].

There are no data on emissions from auto transport in Tbilisi. However, taking into account that the number of transport in Tbilisi constitutes 41% of all the transport in Georgia, it is possible to calculate emissions for Tbilisi based on emissions from transport in Georgia.

24.6 Mathematical Modelling of Air Pollution in Tbilisi Streets

The list of the polluting admixtures, exhausted by the motor-transport is long. It comprises more than 200 substances. The main polluting components exhausted by motor transport are: firm particles in the form of dust (mostly soot), carbon monoxide (CO), sulphur dioxide (SO_2), nitric oxides (NOx), formaldehyde (HCHO), stannous oxides (PbxOy). Among the most important components of air pollutants are acid constituents, namely nitric and sulphur acid are the main contributors to the acidity in rain. Thus, investigation of dispersion of exhaust gases in the main Tbilisi streets, by means of mathematical modelling is very important for human health, environmental management and future economic planning, including revisions of the street network and traffic management.

Models describing the dispersion and transport of air pollutants in the atmosphere can be distinguished: plumerise, Gaussian, Semi-empirical, Eulerian, Lagrangian, Chemical and Stochastic models. The model most widely used today for pollutant dispersion within urban street-canyons is an empirically derived Street-model [21, 22, 24, 25]. Sobottka and Leisen [34] describe a model with similar basic equations as the street-models but with improvements in the treatment of dispersion. These models have been developed by Liousse et al. [26] Huang and Drake [23]. In 1994, a Revised Version of the Nordic Computational Method was issued [4]. With this model they were able to study parameterisation of dispersion in the case of general street configurations, frequency of low wind speeds and chemical transformations. For some time, however, investigators have realized that non-Gaussian models better describe the dispersion of passive contaminants from the surface and elevated releases in the atmospheric boundary layer [7, 11, 15, 27]. At present Lagranjian and Eulerian meso-scale meteorological models and chemical transport models are widely used for simulation the transfer and conversion of harmful substances in the atmosphere. The models include about 120 gas phase reactions and 65 separate chemical species [43]. The models simulate gas phase ozone, various peroxides, NO_x and NOy compounds, hydroxyl radicals, and hydrocarbons, and are designed for regional-scale analyses [14, 16, 19, 39, 40] and investigations of the impact of dust on nitrate and ozone formation [42]. Also widely used are a sulphur transport Eulerian model and an atmosphere chemistry box model (STEM). The STEM comprehensive model has been developed to investigate the relationships between the emissions, atmospheric transport, chemical transformation, removal processes, and the resultant distribution of air pollutants and deposition patterns on meso and regional scales [9, 10, 39].

Also some interesting studies are concerned with environmental protection. Namely, with the purpose of enhancing fuel economy and reducing the exhaust emissions, a lean burn gasoline engine system is used for NOx emission after treatment [41] and new town planning for imbalanced development [32]. Analysis and evaluation of air pollution episodes in European cities, testing the quality of different operational meteorological forecasting systems for urban areas and implementation and demonstration of improved urban air quality information and forecasting systems is discussed in Baklanov and Rassmusen [2]. The Euler Box photochemical model approach is widely used in air pollution modeling [17, 31, 35, 43]. In Georgia the problems of exhaust gas dispersion in street canyons are examined at the Institute of Hydrometeorology [20]. However, these investigations are carried out using mainly empirical-statistical methods.

24.6.1 Problem Formulation

The amount of vehicle exhaust and the content of the main harmful substances in the gas, such as carbon monoxide (CO), nitric oxides (NO_x) and hydrocarbons (C_xH_x), depend on the traffic intensity, vehicle type and speed, road width and the number of traffic lines. On the given lengthwise layer in the given time unit, the exhaust amount is calculated using the following formula [1, 5, 8]:

$$\mathrm{M} = \mathrm{a} \sum \mathrm{Qi} * \Pi\mathrm{i} * \mathrm{Ni}, \tag{24.1}$$

where $\boldsymbol{M}$ is an exhaust emission of the harmful substance (g/s km) per 1 km; $\boldsymbol{a} = \boldsymbol{a^I}\ \rho$; ρ is the average density of the fuel (≈0.74 kg/l); $\boldsymbol{a^I}$ = 1,000 gh/(3,600 kg h); $\boldsymbol{a} \approx 0.2$; $\boldsymbol{N}$ is the traffic intensity (number of vehicles, passing the given lengthwise layer in given time unit (h^{-1})); $\boldsymbol{Q}$ is the amount of the petrol consumed by the vehicle per one km (l/km); $\boldsymbol{\Pi}$ is an un-dimensioned coefficient, expressing the correlation of the harmful exhaust to consumed petrol; n is the number of the cars of different types. If we pick out cars, buses, microbuses and lorries, then from (24.1) we will have:

$$\mathrm{M} = 0.2[(\mathrm{Q} * \Pi * \mathrm{N})_{\mathrm{cars}} + (\mathrm{Q} * \Pi * \mathrm{N})_{\mathrm{buses}} + (\mathrm{Q} * \Pi * \mathrm{N})_{\mathrm{micbuses}} + (\mathrm{Q} * \Pi * \mathrm{N})_{\mathrm{lorries}}],$$

where $Q_{\mathrm{cars}} = 0.11$, $Q_{\mathrm{buses}} = 0.35$, $Q_{\mathrm{mic\text{-}buses}} = 0.18$, $Q_{\mathrm{buses}} = 0.31$. N_{cars}, N_{buses}, $N_{\mathrm{mic\text{-}buses}}$, $N_{\mathrm{lor.}}$ are determined by experimental observations. As recommended by Berkovich et al. [4] $\Pi_{NOX} = 0.04$, $\Pi_{CXHX} = 0.1$, which don't depend on the speed. Π_{co} depends on the average speed, namely: $\Pi_{\mathrm{co}}(20) = 0.72$, $\Pi_{\mathrm{co}}(30) = 0.6$, $\Pi_{\mathrm{co}}(40) = 0.45$, $\Pi co(50) = 0.22$, $\Pi co(80) = 0.16$. The CO, and NO_x exhaust emissions from the cars with diesel engine are several times less than those from the cars with petrol engine, although it's difficult to determine for our conditions.

The existence of the crossroads has a definite influence on the concentration of the exhausted substance that can be represented by the following mathematical dependence:

$$C_{crossroad} = C_o(1 + N_2/N_1), \tag{24.2}$$

where C_o is the maximum concentration caused by the exhaust on the observed main arterial road. N_1 and N_2 indicate the intensity of the traffic for the given main and crossroads, respectively.

The fulfillment of the experimental activities, provided by the given method includes the following stages: (1) determining the average typical structure of the motor transport stream; (2) determining the intensity of the roads; (3) determining the average value of the intensity of the traffic by the formula:

$$N_{aver.} = 1/3\left(N_{morning} + N_{noon} + N_{evening}\right).$$

24.6.2 Mathematical Model

The method of researching atmospheric air pollution by motor transport is based on well-known and tested different physical and mathematical models [1, 11], which approximately represent the dynamics and mechanisms of such processes. Namely, this method is based on solving the system of three-dimensional differential equations of a non-stationary turbulent boundary layer together with harmful substances transference in the atmosphere which is described by a diffusion equation [13, 38]. The temperature and wind regime of the lower layer of the atmosphere, where the main mass of the polluting components lies, depends on synoptic scale processes (advection, vertical movements) as well as on boundary layer processes (turbulence, radiation). In our model the influence of the broad-scaled factors, were determined by means of the background meteorological fields (wind velocity, temperature and harmful substance concentrations). There is also an inflow of the harmful substances into the considered region. The available data, such as: background concentrations, geostrophical wind velocity, the vertical distribution of the wind, temperature, the coefficient of the vertical change, are used for investigation of the distribution of the harmful substance concentrations in the lower atmospheric layer. In this model we assume, that at the time of initiation the wind velocity is uniform on the horizontal plane (small sixes of the considered area) and it changes on height likewise density and pressure. When we examine the problem of transference and diffusion of adverse substances for the Tbilisi street network, since the landscape of Tbilisi is inhomogeneous, and the street network of the city is not all on the same plane it is necessary to take into consideration the relief. This is the way in which the numerical model takes into account the topography of the examined region of Tbilisi [13].

24.6.3 Results and Discussion

First of all we have investigated the air pollution problem of the main avenue of Tbilisi-Rustaveli Avenue by exhaust gases from motor transport. To determine the average value of the intensity of the traffic by the formula, $N_{aver.} = 1/3 (N_{morning} + N_{noon} + N_{evening})$, we have observed motor transport movement in the Rustaveli Avenue for a week. Our observations have shown that on average it was about 3,200 motor cars per hour during rush hours. Usually three kinds of motor transport are observed on the Rustaveli Avenue: passenger cars, microbuses and buses. During our study the transport means have had the following distribution of intensity: $N_{pass.} = 0.54$; $N_{mic.} = 0.26$; $N_{bus.} = 0.03$;

By means of the obtained data and (1), we have determined the mass of detrimental substance $M_{nox} = 0.936$ mg, where M_{Ox} is a corresponding mass fixed in time unit, unit of distance. According to Berlyand [5] and a given mass of M_{Ox} we have determined the initial values of the concentrations. By means of the obtained data and the mathematical model discussed above we have computed the distribution of the concentrations of the detrimental substance NO_x across the Ruistaveli Avenue. We have assumed that in the initial moment of time motor transport starts movement with an intensity of 3,200 car per hour and that the traffic maintained this movement intensity for 50 min. On the basis of the point of view that at the end of the motor transport movement, the function of the concentrations reaches its maximal value and in the numerical model the stationary movement after 50 min slows down noticeably. Also for the initial period of time (during 25 min) the wind vector was directed from the North-West to South-East across the axis Ox (wind velocity accelerated, in accordance with the height, from 0 to 5 m/s and reaches a maximal value at the height of Z = 600 m.). But further, after 25 min the wind changed direction and air currents were directed from the West to East. This kind of wind vector alteration is often observed in Tbilisi. Results of numerical calculations have shown that after 1 h of physical time values of the concentrations were about 1.3 times more than the initial values of the concentrations. Some of the results of the calculations are presented in Fig. 24.1.

Figure 24.1 shows that the maximum concentrations are observed at the central part of Rustaveli Avenue, which is due to traffic congestion in the central area of the Rustaveli Avenue (lateral arterial streets with intensive traffic join the Rustaveli Avenue). Besides probably it is caused by mutation of wind's direction (we have performed a calculation with constant wind direction during all the calculation period and the results of which have shown a more homogenous concentration distribution across the Rustaveli Avenue). Figure 24.1 also shows that very high concentrations are observed not. The point is that the Rustaveli Avenue is directed along the direction of the wind and the Rustaveli Avenue is well ventilated.

Further we have learnt spreading of harmful substances at the intersection of King Agmashenebeli and King Tamar Avenues as data of meteorological observations have shown that this place is highly contaminated. On Agmashenebeli Avenue the intensity of the traffic was approximately 3,000 cars per hour, and on King Tamar Avenue 3,600 cars per hour. The traffic intensity of the different

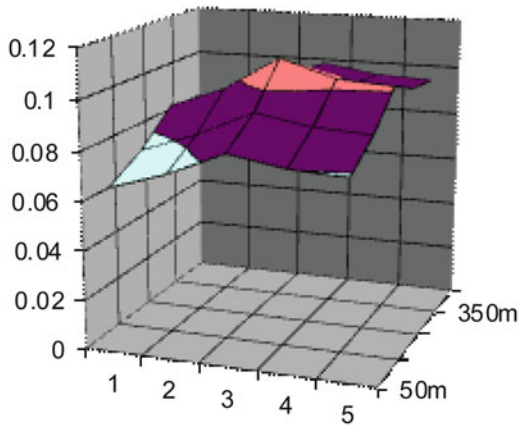

Fig. 24.1 Distribution of the NO_x (mg/m^3) concentration along the Rustaveli Avenue

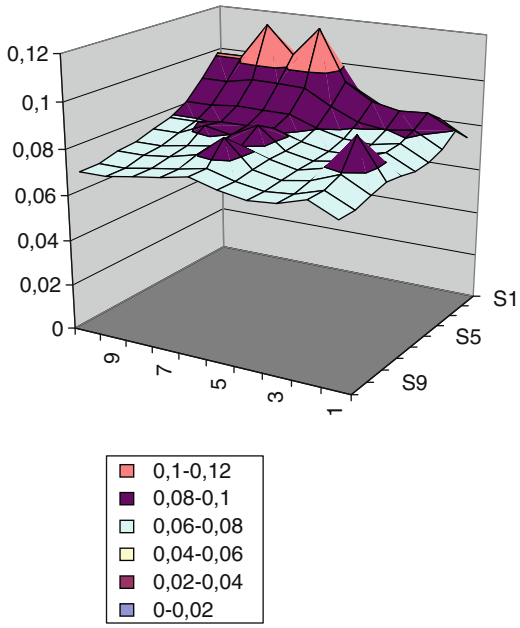

Fig. 24.2 Distribution of NO_x (mg/m^3) concentrations at the intersection of King Agmashenebeli and King Tamar Avenues

types cars on Agmashenebeli and King Tamar Avenues have been determined as follows: Agmashenebeli Avenue; $N_{pass.} = 0.38$; $N_{mic.} = 0.40$; $N_{bus.} = 0.05$ and for King Tamar Avenue; $N_{pass.} = 0.53$; $N_{mic.} = 0.38$; $N_{bus.} = 006$.

The results of numerical calculations have shown that the highest concentrations of harmful substances are observed at the street intersections, and have exceeded the average daily maximum permissible concentrations approximately 1.5 times – up to 0.12 mg/m^3 (here and henceforth concentrations of NO_x mg/m^3 is meant with harmful substances). With increasing distance from the crossroad along the streets, the amount of pollution falls (from 0.09 to 0.4). The concentrations were relatively low at the outskirt territories; from 0.02 to 0.03 mg/m^3 (Fig. 24.2). High

concentrations were observed in the neighborhood of the crossroad, at the south side of King Tamar Avenue and at the east side of Agmashenebeli Avenue. In addition, the results of the calculations have shown that after the motor transport was stopped for 10 min, the concentration distributions radically changed. The level of pollution increasess from 0.06 to 0.08 mg/m^3 from the south-east to north-west direction, because transfer of harmful substances was conditioned by the wind direction.

As the pollution level radically decreased, we may conclude that during 10 min the harmful substances were conditionally transferred out of the territory's borders.

We have also studied the influence of traffic light signals in the streets on the distribution of harmful substances. There are light-signals at each corner of the King Tamar and Agmashenebeli Avenues crossroad and the working cycle is 35 s. During this time, vehicles accumulate at the both sides of the avenues, which consequently leads to the growth of gas masses. The accumulation of cars reaches an average maximum distance of 50 m away from the intersection. Consequently, in this radius, the growth of unhealthy gas depends on the traffic intensity at the present moment in time. In our case the concentration increased approximately two times (0.19 g/m^3).

24.7 Conclusions

Despite the growth of industrial production in Georgia in recent years significant reduction of emissions of harmful substances is observed. For example, in Tbilisi, the total emissions of major pollutants from stationary sources for the period 2005–2009 were reduced by a factor of about 2.89. The transport sector is the main source of air pollution in Georgia. The main emissions are: carbon monoxide (CO), hydrocarbons (volatile organic compounds and methane), nitrogen oxides (NO_x), sulphur dioxide (SO_2), soot and carbon dioxide (CO_2). Accordingly, emissions of nitrogen oxides (NO_x) and sulphur dioxide (SO_2) are present in areas with intensive traffic such as big cities and transit roads. The most crucial situation is observed in Tbilisi. Numerical calculations have shown that the wind vector has an important influence on concentration distribution of harmful substances. The concentration distribution monotonously increases from the north-west to south-east direction in Tbilisi. Existence of traffic lights had a significant effect on the concentration distribution within a radius of 250–300 m from the Agmashenebeli and King Tamar intersection, at the places, where traffic is congested. As the distance from this point increases, the concentration gradually decreases. The existence of traffic lights also increased the concentration of harmful substances approximately two times. Taking as a basis the model calculation, we conclude that the growth of harmful substances wholly depends on the traffic intensity as well as on the placement of traffic lights and their working cycle.

References

1. Adrian G, Fiedler F (1991) Simulation of un-stationary wind and temperature fields over complex terrain and comparison with observations. Int J Beitr Phys Atmos 64:27–48
2. Baklanov A, Rassmusen A (2006) Integrated systems for forecasting urban meteorology, air pollution and population exposure, FUMAPEX:, EVK4-CT-2002-00097, Final report, including 3rd periodic report and 6th management report and a final T.I.P., Copenhagen, http://fumapex.dmi.dk. Accessed 5 Sep 2012
3. Beglarashvili N (2011) Quantitative measure of GHG emissions by mini-buses in Tbilisi. Trans Inst Hydrometeorol Georgian Tech Univ 117:140–142 (In Georgian)
4. Berkovich R, Hertel O, Niels N, Michelsen J (1994) Modeling air pollution from traffic in urban areas. In: Proceedings of IMA conference on flow and dispersion through groups of obstacles, University of Cambridge,Cambridge, pp 28–30
5. Berlyand ME (1975) Predication and regulation of air pollution. Gidrometeoisdat, Leningrad, p 387
6. Berlyand ME, GenikhovichI G IV, Gracheva I, Onikul K (1985) Physical and meteorological principles of establishing maximum permissible emissions into the atmosphere. J Main Geophys Obs 495:3–23
7. Brown M, Arya JSP, Snyder WH (1993) Vertical dispersion from surface and elevated releases: an investigation of non-Gaussian plume model. J Appl Meteor 32:490–504
8. Burenin N, Onikul N, Solomatina I (1999) On estimation of motor-transport emissions in to the atmosphere and air pollution near highways. J Main Geophys Obs 436:102–110 (In Russian)
9. Carmichael GR, Peters LK, Kitada TA (1986) Second generation model for regional scale transport/chemistry/deposition. Int J Atmos Environ 20:173–188
10. Carmichael GR, Peters LK, Saylor RD (1990) The STEM-II regional scale acid deposition and photochemical oxidant model – I. An overview of model development and applications. Int J Atmos Environ 25:2077–2090
11. Chang J, Brost R, Isaksen I, Madronich S, Middleton P, Stokwell W, Walcek C (1987) A three-dimensional Eulerian acid deposition model: physical concepts and formulation. Int J Geophys Res 12:14681–14777
12. Davitashvili T (2007) Oil infiltration into soil: problems of the Georgian section of TRACECA and their numerical treatment. In: Ebel A, Davitashvili T (eds) Air water and soil quality modelling for risk and impact assessment. Springer, Dordrecht, pp 247–258
13. Davitashvili T, Sichinava J (2002) Mathematical modeling of Tbilisi air pollution. Rep Enlarged Sessions VIAM 17:38–44
14. Doran JC, Fast JD, Barnard JC, Laskin A, Desyaterik Y, Gilles MK, Hopkins RJ (2008) Applications of Lagrangian dispersion modeling to the analysis of changes in the specific absorption of elemental carbon. Atmos Chem Phys 8(5):1377–1389
15. Elliot WP (1961) The vertical diffusion of gas from continuous source. Int J Air Water Pollut 4:33–46
16. Fast JD (2003) Forecasts of valley circulations using the terrain-following and step-mountain vertical coordinates in the Meso Eta model. Weather and Forecasting 18(6):1192–1206
17. Fay B, Glaab D, Jacobsen I, Scrodin R (1995) Evaluation of Eulerian and Lagranjian atmospheric transport models of the Deutscher Wetterdients using anatex surface tracer data. Atmos Environ 29:2485–2497
18. GEO-Cities Tbilisi: an integrated environment assessment of state and trends for Georgia's capital city (2011) 124. http://geocities-tbilisi.ge/failebi/5414-Introduction.pdf
19. Grossman-Clarke S, Liu Y, Zehnder JA, Fast JD (2008) Simulations of the urban planetary boundary layer in an arid metropolitan area. J Appl Meteorol Climatol 47(3):752–768
20. Gunia G (1992) Meteorological problems of urban area air pollution. Hydromet Press, 193 (in Russian)
21. Hertel O, Bekrovich R (1989) Modelling pollution from traffic in a street canyon, evaluation data and model development. DMU Luft A-136: 27

22. Hertel O, Bekrovich R, Larssen S (1990) The operational street pollution model (OSPM), In: 18th International meeting of NATO/CEMS on air pollution modelling and its application, Vancouver, Canada, pp 741–749
23. Huang CH, Drake RL (1997) Validation of Gaussian non-Gaussian diffusion models for a point source. In: Proceedings of international conference on applications of air pollution, Salt Lake City, pp 299–303
24. Hung-Lung Allen H (2005) Numerical weather prediction utilization of cloud affected radiances – progress so far. WSEAS Trans Environ Dev 1(1):124–132
25. Jonson WB, Ludwig FL, Dabbert WF, Allen RI (1973) An urban diffusion simulation model for carbon monoxide. J Air Pollut Control Assess 23:490–498
26. Liousse CJ, Penner E, Chuang C, Walton JJ, Eddleman H, Cachier H (1996) A three-dimensional model study of carbonaceous aerosols. J Geophys Res 101:19411–19432
27. Michael I, Brown MJ, Arya SP (1997) Plume descriptors derived from a Non-Gaussian concentration model. Atmos Environ 31(2):183–189
28. MoEPoG-(Ministry of Environment Protection of Georgia), State of the Environment Report for Georgia 2007–2009, Tbilisi 2011. http://soegeorgia.blogspot.com/p/english-version.html. Accessed 5 Sep 2012
29. MoH (Ministry of Labour, Health and Social affairs of Georgia). http://www.moh.gov.ge/
30. NSoG-(National Statistics Office of Georgia) (2009). http://www.geostat.ge/. Accessed 5 Sep 2012
31. Ortega S, Solar MR, Benetto J, Pino D (2004) Evaluation of two ozone air quality modeling systems. Atmos Chem Phys 4:1389–1398
32. Shokouhi MA (2005) New town planning and imbalanced development: the case of Stevenage. WSEAS Trans Environ Dev 1(1):79–87
33. Shotadze M (2003) Air pollution in Tbilisi – priority national problem. Georgian Center for Strategic Research and Development, Tbilisi, Georgia, vol 80, p 119
34. Sobottka H, Leisen P (1980) Vehicle exhaust gas emission in city streets abd model aspects. In: IMA conference on modelling of dispersion on transport pollution, Southend on Sea, England, pp 34–42
35. Sportisse B (2001) Box models versus Eulerian models in air pollution modeling. Atmos Environ 35:175–178
36. TCH-(Tbilisi City Hall) (2009) Tbilisi millennium development report, p 213
37. UNDP (2009) Second National Communication to the UNFCCC of the Ministry of Environment of Georgia, Tbilisi
38. Veltishcheva N (1975) Modeling of pollution of an urban atmosphere from a series of continuous elevated sources. Int J Meteorol Hydrol 9(in Russian):52–58
39. Walton JJ, Mac-Cracken MC, Ghan SJ (1998) A global-scale Lagrangian trace species model of transport, transformation, and removal processes. J Geophys Res 93:8339–8354
40. Whiteman CD, Zhong S, Bian X, Fast J, Doran J (2000) Boundary layer evolution and regional-scale diurnal circulations over the Mexico Basin and Mexican Plateau. J Geophys Res D (Atmos) 105(D8):10081–10102
41. Ye Z, Li Z, Mohamadian H (2007) Engine performance improvement on fuel economy and exhaust emissions using lean burn control technologies. WSEAS Trans Environ Dev 4(3): 45–56
42. Zhang Y, Sunwoo Y, Carmichael G, Kotamarthi V (1994) Photochemical oxidant processes in the presence of dust: an evaluation of the impact of dust on particulate nitrate and ozone formation. J Appl Meteorol 33:813–824
43. Zlatev Z (1989) The Danish Eulerian model. In: Environmental pollution monitoring programme, WMD, Geneva, Switzerland, vol 65, pp 30–38

Chapter 25
The Numeric Forecast of Air Pollution Caused by a Blasting Accident in the Enterprise Responsible for Rocket Fuel Utilization in Ukraine

Mykola M. Biliaiev and Mykola M. Kharytonov

Abstract A mathematical model which can take into account all the scenarios of accidents has been developed. The code *AIR-SIM* was worked out on the basis of the described difference schemes. This code was used to simulate the atmospheric pollution for different accidents on the territory of the Pavlograd Chemical Plant. In particular, a numerical model was used to predict the atmospheric pollution in the case of *HCN* emission from the opening at the roof of the building. During the numerical experiment the dynamic of the toxic dose in each room was determined for each case study. It was established that the hitting zone will be about 6 km.

Keywords Air pollution • Numeric forecast • Blasting accident • Rocket fuel

25.1 Introduction

The State Enterprise Research-Industrial Complex "Pavlograd Chemical Plant" (SE RIC PCP) was established in 1929 as a plant for the production of explosive materials and charging of ammunition for various purposes (artillery, aviation, navy, engineering etc.). During the last decade the State Enterprise Research-Industrial Complex "Pavlograd Chemical Plant" has participated in international and state programs on elimination of strategic armaments, stage-by-stage reduction and elimination of ICBM SS-24, a program on the disposal of solid propellant of ICBM SS-24, a program on the disposal of conventional types of ammunition unsuitable for further application and storage, a regional comprehensive program

M.M. Biliaiev (✉)
Department of Fluid Dynamics, Railway Transport University, Dnipropetrovsk 49000, Ukraine
e-mail: ecohous@ukr.net

M.M. Kharytonov
Department of Soil Science and Ecology, Dnipropetrovsk State Agrarian University, Dnipropetrovsk 49027, Ukraine
e-mail: mykola_kh@yahoo.com

I. Barnes and K.J. Rudziński (eds.), *Disposal of Dangerous Chemicals in Urban Areas and Mega Cities*, NATO Science for Peace and Security Series C: Environmental Security,
DOI 10.1007/978-94-007-5034-0_25,

on conversion of mining enterprises to use of environmentally safe and TNT-free explosives and the development of blasting science in Ukraine [1].

It is obvious that the Pavlograd Chemical Plant is the highest potential source of environment contamination in the case of an accident on its territory. The calculation of the hitting zone in the case of an accident at this plant was carried out using the empirical model at the Ministry of Emergency of Ukraine [2]. This model is used in Ukraine as the main tool to predict the pollution level caused by accidents at chemical plants, however, the results obtained were not satisfactory. The results could not be used to estimate the real scale of the danger of accidents at this plant. The model used could not predict the pollution dynamics in the merits of the plant territory, especially in the vicinity of the buildings. The model does not take into account different types of accidents, for example, the emission of the toxic gas from the partially destroyed building, the emission of the toxic gas through the roof of the building etc. The Representative of the Ministry of Emergency of Ukraine in Dnepropetrovsk Region set the problem to the authors of this paper to determine the level of pollution that would result from the different types of accidents which could take occur at the plant. Of special interest were pollution levels resulting from accidents with solid missile propellant. To solve the problem it was necessary to develop a mathematical model which could take into account all the possible accident scenarios which could occur at such a plant.

25.2 Materials and Methods

The Pavlograd Chemical Plant is situated 5 km to the west of Pavlograd City (Ukraine, Dnepropetrovsk Region). The nearest settlement (the so-called "workers village") is 2.5 km from this plant (Fig. 25.1).

Fig. 25.1 Location of the Pavlograd Chemical Plant near Pavlograd City

A distinct feature of this plant is the storage of a very large quantity of toxic substances at the site. The toxic substances at the plant can be divided on two classes: (a) "ordinary" chemical substances: HCl, HCN, etc. (b) solid missile propellant.

25.3 Mathematical Model of Pollutant Dispersion

To estimate the affected area, henceforth called "hitting zone", if an accident takes place at the chemical plant it is necessary to calculate the dispersion of toxic substances in the atmosphere. To simulate the dispersion process in the atmosphere the transport model is used

$$\frac{\partial C}{\partial t}+\frac{\partial uC}{\partial x}+\frac{\partial vC}{\partial y}+\frac{\partial (w-ws)C}{\partial z}+\sigma C=\frac{\partial}{\partial x}\left(\mu_x\frac{\partial C}{\partial x}\right)+\frac{\partial}{\partial y}\left(\mu_y\frac{\partial C}{\partial y}\right)+\frac{\partial}{\partial z}\left(\mu_z\frac{\partial C}{\partial z}\right)+\sum Q_i(t)\delta(x-x_i)\delta(y-y_i)\delta(z-z_i) \tag{25.1}$$

where C is the concentration of toxic gas; u, v, w are the wind velocity components; w_s is the rate of gravitional fallout; σ is a coefficient taking into account the process of pollutant decay or rain washout; $\mu = (\mu_x, \mu_y, \mu_z)$ are the diffusion coefficients; Q_i is the intensity of point source of ejection; $\delta(x-x_i)\delta(y-y_i)\delta(z-z_i)$ are Dirac's delta functions; $r_i = (x_i, y_i, z_i)$ are the coordinates of the ejection source.

In the numerical model developed the following approximations for the wind speed and diffusion coefficients are used [3]:

$$u = u_1\left(\frac{z}{z_1}\right)^n,$$

$$\mu_z = 0,11z \quad \mu_y = \kappa_0 u,$$

$$\mu_y = \mu_x$$

where u_1 is the wind speed at the height $z_1 = 10$ m; n = 0,15; k_0 is the empirical parameter [3].

25.4 Hydrodynamic Model

In the case of an accident the dispersion of pollutants will take place at first in the vicinity of buildings which are situated at the plant site. The simulation of the wind flow near buildings on the basis of *Navier – Stokes* equations and using different turbulent models needs a very refined mesh [4]. It would take days to obtain the results of the considered problem using computers which are currently in use in

Ukraine. To circumvent this problem the model of potential flow is used to simulate the *3D* wind flow at the chemical plant in the vicinity of buildings. In this case the governing equation is

$$\frac{\partial^2 P}{\partial x^2} + \frac{\partial^2 P}{\partial y^2} + \frac{\partial^2 P}{\partial z^2} = 0, \tag{25.2}$$

where P is the potential of velocity. The velocity components are calculated as follows:

$$u = \frac{\partial P}{\partial x}, \quad v = \frac{\partial P}{\partial y}, \quad w = \frac{\partial P}{\partial z}.$$

25.5 Numerical Model

The numerical integration of the governing Eqs. (25.1) and (25.2) is carried out using a rectangular grid. The main features of the difference schemes which are used are considered below. The time dependence derivative in Eq. (25.1) is approximated as follows:

$$\frac{\partial C}{\partial t} \approx \frac{C_{ijk}^{n+1} - C_{ijk}^{n}}{\Delta t}.$$

In a first step the convective derivatives are represented in the following way:

$$\frac{\partial uC}{\partial x} = \frac{\partial u^+ C}{\partial x} + \frac{\partial u^- C}{\partial x};$$

$$\frac{\partial vC}{\partial y} = \frac{\partial v^+ C}{\partial y} + \frac{\partial v^- C}{\partial y};$$

$$\frac{\partial wC}{\partial z} = \frac{\partial w^+ C}{\partial z} + \frac{\partial w^- C}{\partial z},$$

where $u^+ = \frac{u+|u|}{2}$; $u^- = \frac{u-|u|}{2}$, $v^+ = \frac{v+|v|}{2}$; $v^- = \frac{v-|v|}{2}$, $w^+ = \frac{w+|w|}{2}$; $w^- = \frac{w-|w|}{2}$

In a second step the convective derivatives are approximated as follows:

$$\frac{\partial u^+ C}{\partial x} \approx \frac{u^+_{i+1,j,k} C^{n+1}_{ijk} - u^+_{ijk} C^{n+1}_{i-1,j,k}}{\Delta x} = L_x^+ C^{n+1},$$

$$\frac{\partial u^- C}{\partial x} \approx \frac{u^-_{i+1,j,k} C^{n+1}_{i+1,j,k} - u^-_{ijk} C^{n+1}_{ijk}}{\Delta x} = L_x^- C^{n+1},$$

$$\frac{\partial v^+ C}{\partial y} \approx \frac{v^+_{i,j+1,k} C_{ijk} - v^+_{ijk} C_{i,j-1,k}}{\Delta y} = L^+_y C^{n+1};$$

$$\frac{\partial v^- C}{\partial y} \approx \frac{v^-_{i,j+1,k} C_{i,j+1,k} - v^-_{ijk} C_{ijk}}{\Delta y} = L^-_y C^{n+1};$$

$$\frac{\partial w^+ C}{\partial z} \approx \frac{w^+_{i,j,k+1} C_{ijk} - w^+_{ijk} C_{i,j,k-1}}{\Delta z} = L^+_z C^{n+1};$$

$$\frac{\partial w^- C}{\partial z} \approx \frac{w^-_{i,j,k+1} C_{i,j,k+1} - w^-_{ijk} C_{i,j,k}}{\Delta z} = L^-_z C^{n+1}.$$

The second order derivatives are approximated as follows:

$$\frac{\partial}{\partial x}\left(\mu_x \frac{\partial C}{\partial x}\right) \approx \tilde{\mu}_x \frac{C^{n+1}_{i+1,j,k} - C^{n+1}_{ijk}}{\Delta x^2} - \tilde{\mu}_x \frac{C^{n+1}_{i,j,k} - C^{n+1}_{i-1,j,k}}{\Delta x^2}$$
$$= M^-_{xx} C^{n+1} + M^+_{xx} C^{n+1},$$

$$\frac{\partial}{\partial y}\left(\mu_y \frac{\partial C}{\partial y}\right) \approx \tilde{\mu}_y \frac{C^{n+1}_{i,j+1,k} - C^{n+1}_{ijk}}{\Delta y^2} - \tilde{\mu}_y \frac{C^{n+1}_{i,j,k} - C^{n+1}_{i,j-1,k}}{\Delta y^2}$$
$$= M^-_{yy} C^{n+1} + M^+_{yy} C^{n+1},$$

$$\frac{\partial}{\partial z}\left(\mu_z \frac{\partial C}{\partial z}\right) \approx \tilde{\mu}_z \frac{C^{n+1}_{i,j,k+1} - C^{n+1}_{ijk}}{\Delta z^2} - \tilde{\mu}_z \frac{C^{n+1}_{i,j,k} - C^{n+1}_{ij,k-1}}{\Delta z^2}$$
$$= M^-_{zz} C^{n+1} + M^+_{zz} C^{n+1}.$$

In these expressions L^+_x, L^-_x, L^+_y, L^-_y, L^+_z, L^-_y, M^+_{xx}, M^-_{xx} are the difference operators. Using these expressions the difference scheme for the transport equation can be written as follows:

$$\frac{C^{n+1}_{ijk} - C^n_{ijk}}{\Delta t} + L^+_x C^{n+1} + L^-_x C^{n+1} + L^+_y C^{n+1}$$
$$+ L^-_y C^{n+1} + L^+_z C^{n+1} + L^-_z C^{n+1} + \sigma C^{n+1}_{ijk}$$
$$= \left(M^+_{xx} \tilde{N}^{n+1} + M^-_{xx} \tilde{N}^{n+1} + M^+_{yy} \tilde{N}^{n+1} + M^-_{yy} C^{n+1} + M^+_{zz} C^{n+1} + M^-_{zz} C^{n+1}\right)$$

The solution of the transport equation in the finite – difference form is split into four steps on the time step of integration dt:

- at the first step ($k = \frac{1}{4}$) the difference equation is:

$$\frac{C^{n+k}_{ij} - C^n_{ij}}{\Delta t} + \frac{1}{2}\left(L^+_x C^k + L^+_y C^k + L^+_z C^k\right) + \frac{\sigma}{4} C^k_{ijk}$$
$$= \frac{1}{4}\left(M^+_{xx} C^k + M^-_{xx} C^n + M^+_{yy} C^k + M^-_{yy} C^n + M^+_{zz} C^k + M^-_{zz} C^n\right); \qquad (25.3)$$

- at the second step ($k = n + \frac{1}{2};\ c = n + \frac{1}{4}$) the difference equation is

$$\frac{C^k_{ijk} - C^c_{ijk}}{\Delta t} + \frac{1}{2}\left(L^-_x C^k + L^-_y C^k + L^-_z C^k\right) + \frac{\sigma}{4} C^k_{ij}$$
$$= \frac{1}{4}\left(M^-_{xx} C^k + M^+_{xx} C^c + M^-_{yy} C^k + M^+_{yy} C^c + M^-_{zz} C^k + M^+_{zz} C^c\right); \tag{25.4}$$

- at the third step ($k = n + \frac{3}{4};\ c = n + \frac{1}{2}$) the expression (25.4) is used;
- at the fourth step ($k = n + 1;\ c = n + \frac{3}{4}$) the expression (25.3) is used.

At the fifth step (at this step the influence of the source of pollutant ejection is taken into account) the following approximation is used:

$$\frac{\overset{5}{C}{}^{n+1}_{i,j,k} - \overset{5}{C}{}^{n}_{i,j,k}}{\Delta t} = \sum_{l=1}^{N} \frac{q_l(t^{n+1/2})}{\Delta x\, \Delta y\, \Delta z}\ \delta_l$$

Function δ_l is equal to zero in all cells except the cells where the 'l' source of ejection is situated. This difference scheme is implicit and absolutely steady but the unknown concentration C is calculated using the explicit formulae at each step (the so-called "*method of running calculation*").

The approach to integrate Eq. (25.2) for the potential of velocity (Laplas equation) is as follows: instead of Laplas equation (25.2) the '*time-dependent*' equation for the potential of velocity is used

$$\frac{\partial P}{\partial \eta} = \frac{\partial^2 P}{\partial x^2} + \frac{\partial^2 P}{\partial y^2} + \frac{\partial^2 P}{\partial z^2}, \tag{25.5}$$

where η is the 'fictitious' time. For $\eta \to \infty$ the solution of this equation tends to the solution of the Laplas equation. To solve Eq. (25.5) A.A. Samarskii's change-triangle difference scheme is used [5]. According to this scheme the solution of the equation is split in two steps:

– *at the first step the difference equation is*

$$\frac{P^{n+1/2}_{i,j,k} - P^n_{i,j,k}}{0,5\Delta\eta} = \frac{P^n_{i+1,j,k} - P^n_{i,j,k}}{\Delta x^2} + \frac{-P^{n+1/2}_{i,j,k} + P^{n+1/2}_{i-1,j,k}}{\Delta x^2} + \frac{P^n_{i,j+1,k} - P^n_{i,j,k}}{\Delta y^2}$$
$$+ \frac{-P^{n+1/2}_{i,j,k} + P^{n+1/2}_{i,j-1,k}}{\Delta y^2} + \frac{P^n_{i,j,k+1} - P^n_{i,j,k}}{\Delta z^2} + \frac{-P^{n+1/2}_{i,j,k} + P^{n+1/2}_{i,j,k-1}}{\Delta z^2},$$

– *at the second step the difference equation is*

$$\frac{P^{n+1}_{i,j,k} - P^{n+1/2}_{i,j,k}}{0,5\Delta\eta} = \frac{P^{n+1}_{i+1,j,k} - P^{n+1}_{i,j,k}}{\Delta x^2} + \frac{-P^{n+1/2}_{i,j,k} + P^{n+1/2}_{i-1,j,k}}{\Delta x^2} + \frac{P^{n+1}_{i,j+1,k} - P^{n+1}_{i,j,k}}{\Delta y^2}$$
$$+ \frac{-P^{n+1/2}_{i,j,k} + P^{n+1/2}_{i,j-1,k}}{\Delta y^2} + \frac{P^{n+1}_{i,j,k+1} - P^{n+1}_{i,j,k}}{\Delta z^2} + \frac{-P^{n+1/2}_{i,j,k} + P^{n+1/2}_{i,j,k-1}}{\Delta z^2}.$$

From these expressions the unknown value P is determined using the explicit formulae at each step ("*method of running calculation*"). The calculation is completed if the condition

$$\left|P_{i,j,k}^{n+1} - P_{i,j,k}^{n}\right| \leqslant \varepsilon$$

is fulfilled (where ε is a small number, n is the number of iteration). The components of the velocity vector are calculated on the sides of computational cell as follows

$$u_{i,j,k} = \frac{P_{i,j,k} - P_{i-1,j,k}}{\Delta x},$$

$$v_{i,j,k} = \frac{P_{i,j,k} - P_{i,j-1,k}}{\Delta y},$$

$$w_{i,j,k} = \frac{P_{i,j,k} - P_{i,j,k-1}}{\Delta z}.$$

On the basis of the described difference schemes the *AIR-SIM* code was developed. This code was used to simulate the atmosphere pollution for the different accidents on the territory of the *Pavlograd Chemical Plant*. Some numerical results are given below.

25.6 Results and Discussion

25.6.1 Atmosphere Pollution in the Case of a Partially Destroyed Building

This problem deals with a solid missile propellant accident on the plant territory. This is the solid propellant of the three stage ballistic missile *RS-22"Scalpel"* (in Russian: '*МБРС-22*'). This missile was developed in the USSR to destroy targets at distances of *6,000 km* or more. The warhead of this missile had 10 nuclear loads. This missile was developed to be launched from the railway platforms used in freight trains (Fig. 25.2).

During the conversion these missiles were cut and their solid propellant was placed at the *Pavlograd Chemical Plant* (Figs. 25.3 and 25.4).

The prediction of air pollution caused by the ignition of the solid propellant is of particular interest. This problem of the air pollution resulting from the situation when the roof of the building, where the propellant is placed, has been destroyed is considered. The source of *HCl* ejection is situated inside the building (Fig. 25.5).

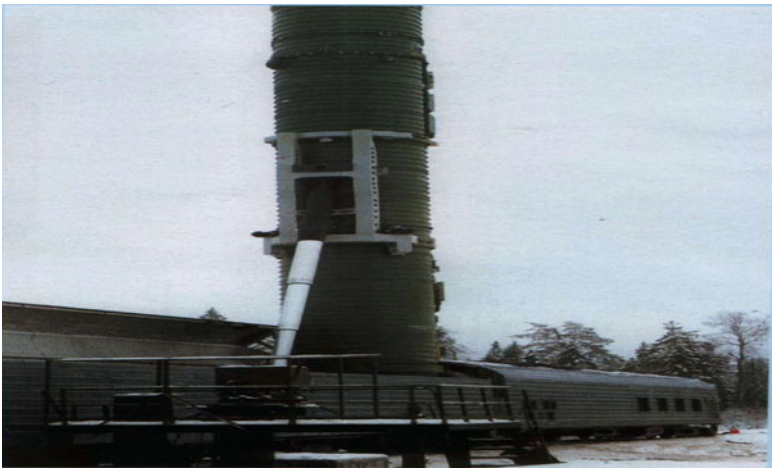

Fig. 25.2 The RS-22 missile in vertical position

Fig. 25.3 The first stage of RS-22 missile at the *Pavlograd Chemical Plant*

Figures 25.6, 25.7, 25.8, and 25.9 show very clearly the formation of an intensively contaminated area inside the building and the plume formation near the opening in the building. The HCl concentration as a function of the distance and time from the opening in the building is shown in Table 25.1. The high level of atmosphere pollution near the partially destroyed building is obvious.

Fig. 25.4 The third stage engine of the *RS-22* missile at the *Pavlograd Chemical Plant*

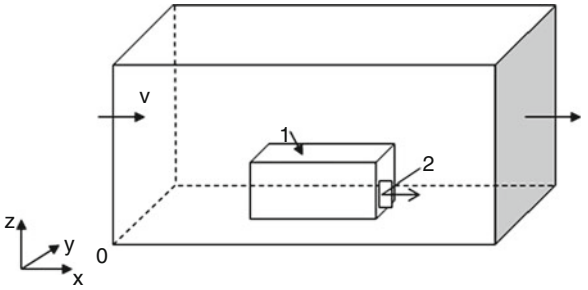

Fig. 25.5 Sketch of the computational domain: *1* partially destroyed building (no roof, the source of ejection is situated inside the building); *2* opening in the building

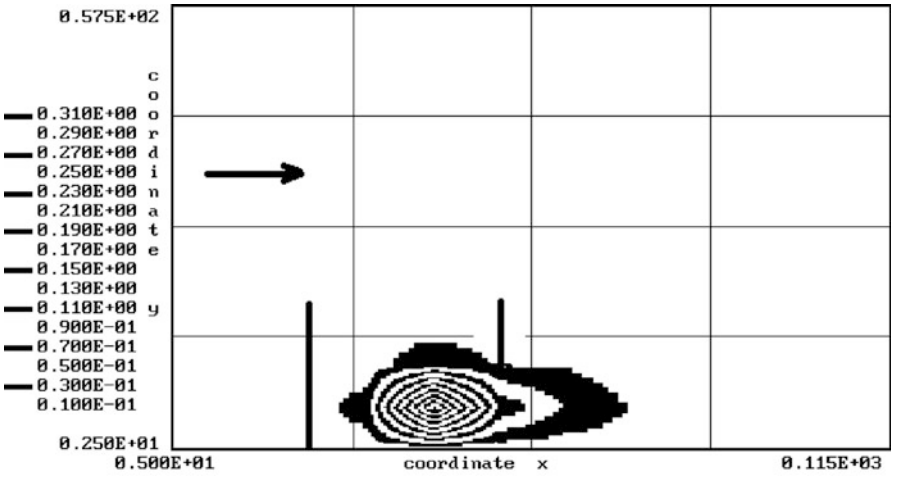

Fig. 25.6 Concentration of toxic gas near buildings for t = 3 s, (*side view*, section Y = 65 m)

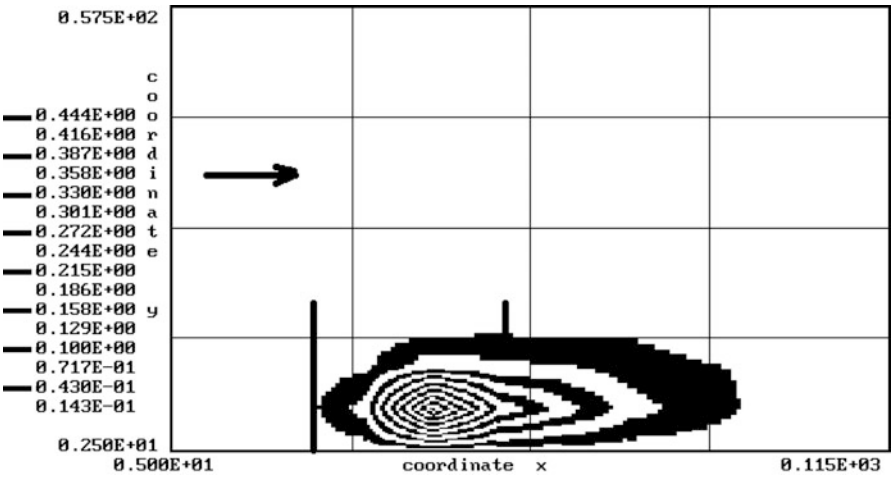

Fig. 25.7 Concentration of toxic gas near the building for t = 10 s, (*side view*, section y = 65 m)

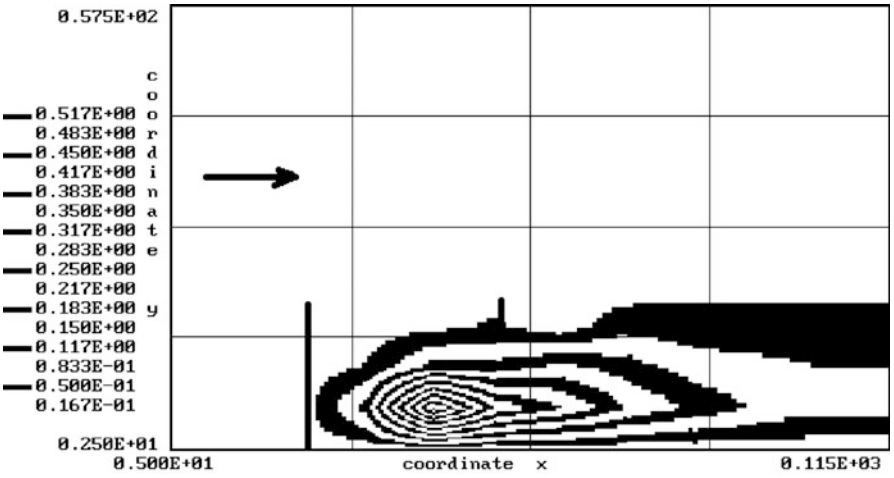

Fig. 25.8 Concentration of toxic gas near the building for time t = 40 s, (*side view*, section y = 65 m)

25.6.2 The Atmospheric Pollution Resulting from Toxic Gas Emission Through the Roof of the Building

This problem deals with an accident at the Chemical Plant when the toxic gas hydrogen cyanide (HCN) is emitted from an opening in the roof of the building. The aim of the mathematical simulation is the prediction of the level of the air pollution in two rooms which are situated in the second building (Fig. 25.10). The polluted air

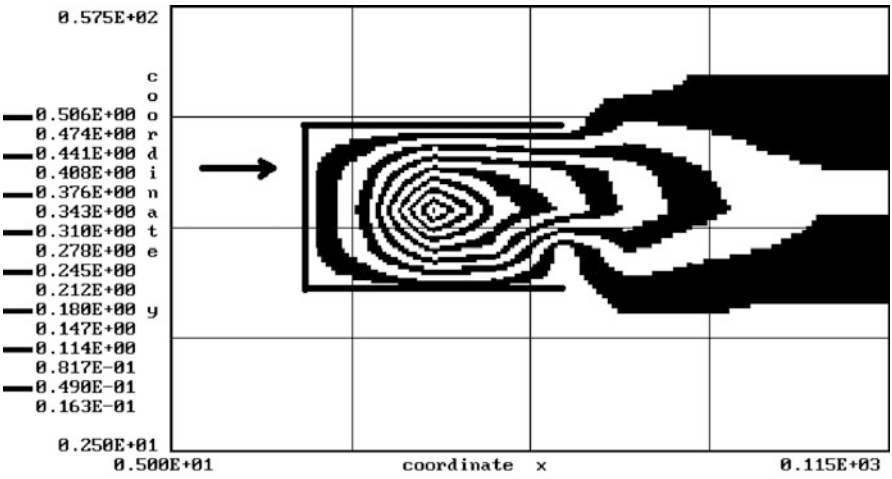

Fig. 25.9 Concentration of toxic gas near the building for time t = 30 s, (*top view*, section Y = 2.5 m)

Table 25.1 The atmospheric HCl concentration (level z = 2.5 m) at different distances from the opening in the building

t (s)	Distance from the opening, x = 10 m (g/m^3)	Distance from the opening, x = 20 m (g/m^3)
6	0.019	0.007
12	0.064	0.033
21	0.109	0.071
30	0.129	0.091
65	0.143	0.106

can flow through the ventilation system into the rooms. The inflow opening of the ventilation system of the first room is situated at the side wall of the second building (position1, Fig. 25.10) and the inflow opening of the ventilation system of the second room is situated on the front wall of the second building (position 2, Fig. 25.10).

To calculate the level of pollution in the room if the polluted air flows into the room through the ventilation system the following balance model was used

$$VdC_{room} = L \cdot C \cdot dt - L \cdot C_{room} \cdot dt \tag{25.6}$$

where V is the room volume; C_{room} is the concentration of the toxic gas at the outlet opening of the ventilation system; L (in m^3/s) is an air flow rate (the operating rate of the ventilation system); t is time; C is the concentration of the toxic gas in the inflow air (the concentration at the inflow opening of the ventilation system). A weakness of this model is that the concentration in the room is considered to be equal to the concentration of the toxic gas at the outlet opening of the room ventilation

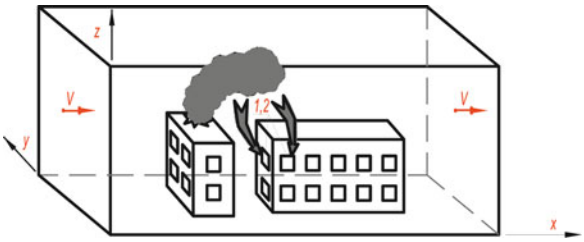

Fig. 25.10 Sketch of the computational domain used in the problem of the toxic gas emission from an opening in the roof of the building (*1* the position of the ventilation opening at the side wall of the second building, *2* the position of the ventilation opening at the front wall of the second building)

Table 25.2 The dynamics of the toxic dose in the first room

T (s)	TD (mg/l·min)
60	0.004
91	0.014
150	0.041
200	0.070
332	0.151

Table 25.3 The dynamics of the toxic dose in the second room

T (s)	TD (mg/l·min)
60	$0.14 \cdot 10^{-4}$
91	$0.41 \cdot 10^{-4}$
150	$0.19 \cdot 10^{-3}$
200	$0.21 \cdot 10^{-3}$
332	$0.5 \cdot 10^{-3}$

system; however, this model is widely used in practical cases in Ukraine. Equation (25.6) is solved together with Eq. (25.1). From Eq. (25.1) the concentration $C = f(x,y,z,t)$ at the inlet opening of the ventilation system is determined.

The developed numerical model was used to predict the atmosphere pollution in the event of *HCN* emission from the opening at the roof of the first building. The initial data is as follows: the wind speed is 2.5 m/s at a height of 10 m; the intensity of the gas emission is 500 g/s; the emission takes place during 10 s; the volume of each room in the second building is 200 m^3; the air flow rate in both rooms is 0.83 m^3/s.

For the numerical experiment the dynamics of the toxic dose in each room was determined using the following expression

$$TD = \int_0^t C dt,$$

The results of toxic dose calculation for both rooms are presented in Table 25.2 and Table 25.3.

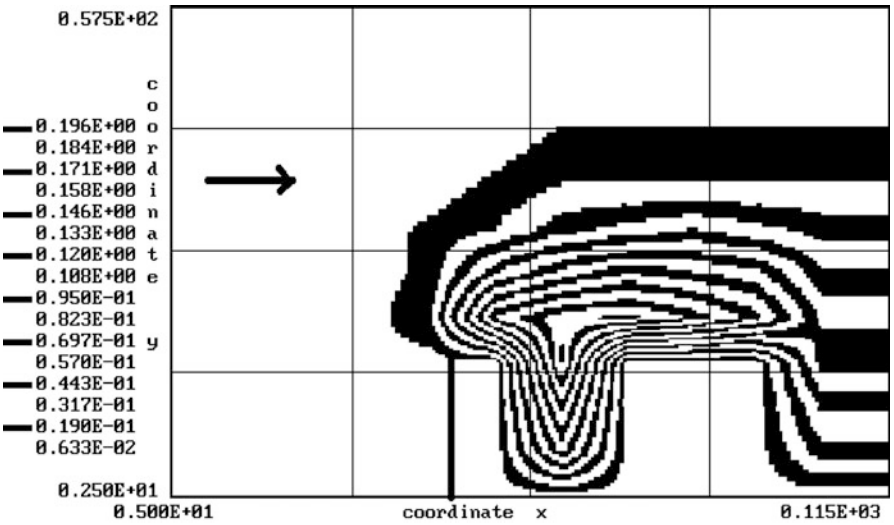

Fig. 25.11 Concentration of toxic gas near buildings for time t = 17 s, (*side view*, section Y = 60 m)

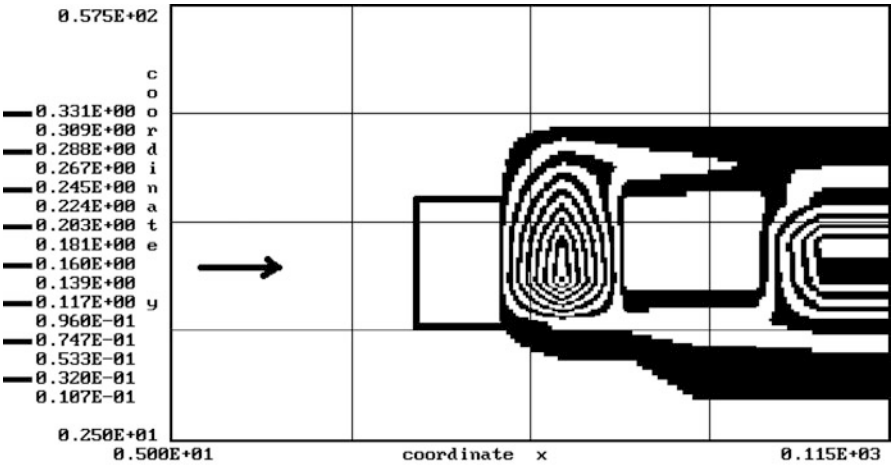

Fig. 25.12 Concentration of toxic gas near buildings for time t = 42 s, (*top view*, section z = 2.5 m)

In Figs. 25.11 and 25.12 the polluted area (concentration of *HCN) is* shown for different time periods after the accident and for the different sections. It is evident that between the buildings an intensive contaminated area is formed.

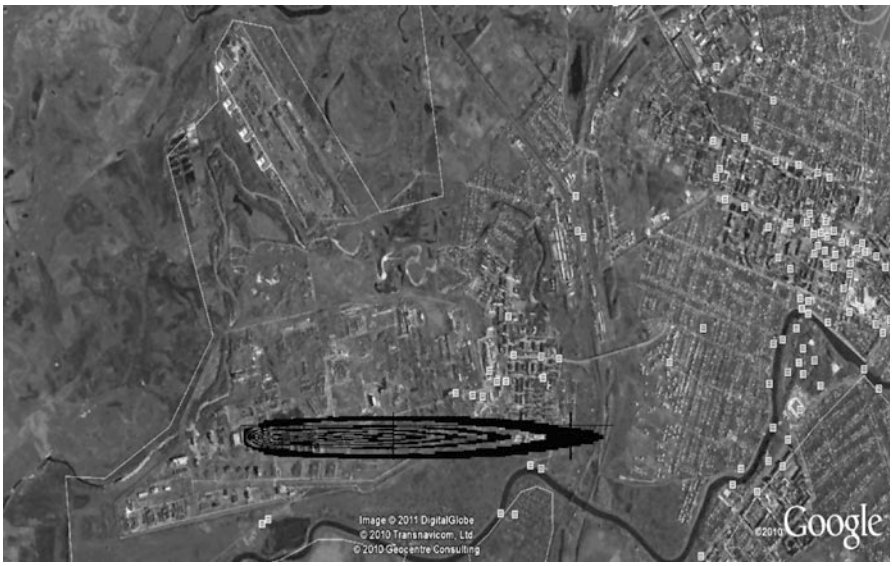

Fig. 25.13 Contaminated area (HCl, level z = 12 m, t = 20 min)

25.6.3 Calculation of Hitting Zone

At the third stage of this work calculations of the "hitting zone 2" were carried out using only Eq. (25.1). The calculations predict that the plume of toxic gases will reach the city site very quickly (Fig. 25.13).

The numerical experiment shows that the "hitting zone" will be about 6 km. This means that most parts of the city will be gravely affected by the accident.

25.7 Conclusions

The presented modeling study deals with the problems arising from an accident with solid missile propellant at a chemical plant. The solid propellant is that of the three stage ballistic missile *RS-22"Scalpel"*. The levels of pollution resulting from different types of accidents at the Pavlograd Chemical Plant have been modelled. In particular, air pollution problems resulting when the roof of the building where the propellant is stored has been destroyed were considered. To estimate the "hitting zone" if the accident takes place at the chemical plant it is necessary to calculate the dispersion of the toxic substances in the atmosphere. To simulate the dispersion process in the atmosphere a transport model was used. The initial data were different. The polluted area was predicted for different time periods after the accident and for different sections. The calculations show that the plume of toxic gases will reach the city site very quickly. Thus most of the city will be under the great danger.

References

1. State Enterprise Research-Industrial Complex "Pavlograd Chemical Plant" (SE RIC PCP), www.ric-phz.com.ua/index.php?pages=about&ln=en
2. Ministry of Emergency of Ukraine, http://www.mns.gov.ua/
3. Berlyand ME (1985) Prediction and control of the atmosphere pollution. Gidrometeoizdat Publishing House, Leningrad, p 273
4. Murakami S (1998) Overview of turbulence models applied in CWE – 1997. J Wind Eng Ind Aerodyn 74–76:1–24
5. Samarskii AA (1983) The theory of difference schemes. Science Publishing House, Moscow, p 616

Chapter 26
Deterministic and Probabilistic Potential Risk Analysis of Lead Contamination in an Urban Environment in Egypt

Nasser M. Abdel-Latif, George Shaw, and Mike Ashmore

Abstract A combined deterministic dynamic and probabilistic analysis using a multimedia spreadsheet model has been applied to model the environmental fate of deposited lead in different media of the Egyptian environment and consequent human exposure. The main aim was to provide evidence-based guidance on the magnitude of the contribution of atmospheric emissions, in relation to other environmental media, to human risk in Egypt. Uncertainty and sensitivity analysis approaches have been applied to assess the variation in the output function based on the collective and individual variation of the model inputs.

The dynamic steady state of lead accumulation in soil due to continuous deposition of lead from the atmosphere and irrigation water, and the length of time taken to reach a steady state was examined. Predictions of the model revealed that lead in greater Cairo is high enough to cause concern for the human population. Predicted deterministic and probabilistic human blood lead (Pb_B) levels in the urban environment exceed the guidance value of 10 μg dl^{-1} and pose a high potential risk for a significant percentage of the exposed population. Ingestion of lead-contaminated vegetables was found to be the most significant contributor to total Pb_B.

The current study reveals also that Pb from the atmosphere is the most significant source of lead contamination of vegetation, and all of the deposited lead, controlled by the rate of deposition, remains associated with food contamination with Pb either directly (uptake from air) or indirectly (uptake from soil). Direct foliar contamination is clearly the most important pathway in this concern, which is confirmed by the significant reduction in the contribution to total Pb_B by the application of washing factor. The model has provided a framework for multimedia risk assessment in Egypt and highlighted some uncertainties.

N.M. Abdel-Latif (✉) • G. Shaw • M. Ashmore
Air Pollution Department, National Research Centre, Dokki, Cairo, Egypt
e-mail: nabdellatif@gmail.com

I. Barnes and K.J. Rudziński (eds.), *Disposal of Dangerous Chemicals in Urban Areas and Mega Cities*, NATO Science for Peace and Security Series C: Environmental Security,
DOI 10.1007/978-94-007-5034-0_26,

26.1 Introduction

Quantitative Risk Assessment has been used for a few decades to evaluate the potential impacts of environmental pollutants on human health, as well as on the environment. Human Health Risk Assessment follows the four steps recommended by the United States National Academy of Science [16, 26, 33]: hazard identification; dose-response assessment; exposure assessment; and risk characterization. Humans are exposed, in general, to a multitude of potentially hazardous chemicals in air, food, soil and water. Consequently, assessing the total exposure of humans to a contaminant requires the identification of many factors, including: its concentration and sources, environmental media of exposure, transport through each exposure medium, chemical and physical transformation, routes of entry to the body and frequency of contact [25, 32].

Multimedia mathematical models have gained growing acceptance as a powerful tool to understand complex environmental processes and to assess human exposure risk from pollutants [35], as well as for estimating exposures in situations where measurements are unavailable [32]. These models are closely linked to the behaviour of pollutants and involve calculations related to the environmental distribution and fate of those pollutants [47]. They consequently require information on the sources, transport, transformation and fate of the contaminants. The atmosphere is the major initial recipient of lead pollution, from where it is then transported through to environmental media (soil, water, food), undergoing further exchange and transport between these media. Through these various possible routes in the environment, lead can reach humans by direct inhalation of air-borne particulate or by ingestion of lead in food, water, soil and dust.

A considerable quantity of lead has been emitted each year from different industrial and urban activities in Egypt since the 1960s, especially in the greater Cairo area. This lead ultimately ends up in a variety of environmental components. Elevated levels of lead have been recorded in air, soil, crops and the River Nile (the main source of drinking and irrigated water) during the last two decades, and these pose a potential risk to human health in Egypt.

By using a multimedia- multiple- pathway exposure model, the current study aims to assess human exposure to lead in Egypt from all potential pathways from the atmosphere based on data on deposition of atmospheric lead particulate, its transport through various environmental media and assumptions about lead intake rates. Possible exposure routes included are ingestion of food and water, inhalation, and dermal penetration.

The work presented here is partly from a PhD thesis carried out at Imperial College, London.

26.2 Materials and Methods

26.2.1 Model Description

A multimedia simulation model, PbMod Egypt, was constructed as a risk assessment tool to assess the transport of lead in the environment, and to predict the likely blood lead concentration for adults exposed to lead at the typical levels monitored

in different environmental media in Egypt. This model was written as a Microsoft® Excel workbook and coded as a multiple pathway exposure model. The main environmental components that comprise the model include air, soil, water, plants, and animals. Accordingly, the main lead intake routes are inhalation of polluted air, ingestion of foods, ingestion of water, ingestion of soil, and absorption through the skin. PbMod Egypt calculated the potential health risk to humans and operated on annual time-steps.

26.2.2 Model Parameterisation

26.2.2.1 Main Inputs

The physicochemical input parameters (Table 26.1) describe the deposition of particulate lead from the atmosphere to agricultural soil and onto the surface of vegetable crops, as well as the transfer of airborne lead to meat and dairy products as a result of food ingestion by farm animals. The concentration of trace metals in soil is a function of all inputs, outputs, sources and sinks in the ecosystem and therefore a function of time. To simulate the time taken to reach the steady state of lead in soil (the main basis of the exposure assessment) under the conditions of the current study, calculations in this model have been based on physical and chemical properties of soil (26.1, 26.2, 26.3, 26.4).

26.2.2.2 Human Inputs

Model inputs for human uptake include the average daily intake rate of foodstuffs, water, soil and dust, air and dermal absorption (Table 26.1). The aim of these parameters is to calculate the contribution of different media and exposure pathways to total blood lead of adults resulting from exposure to these media. In addition to intake rate, calculations were based on the concentration, contact rates and the pathway specific constants (Table 26.1). The latter are empirically determined ratios between intake and blood level [9].

26.3 Sensitivity and Uncertainty Analysis

The main advantage of probabilistic analysis is that it allows the characterization of a range of potential risks and their likelihood of occurrence instead of presenting a single point estimate of risk. Finley and Paustenbach [17] showed that probabilistic assessment is much more conductive to sensitivity and quantitative uncertainty analysis than point estimate analysis.

The Monte Carlo (MC) technique, used to assess the model uncertainty for the current model, has been implemented in many different areas of risk analysis, and

Table 26.1 Main and human input parameters of the model

Parameter description and dimension	Best Estimate	Range	*Ref.*
Main input			
C_a; Pb concentration in air (mg m^{-3})	2.0E-03	3.0E-04–4.0E-03	1–9
C_w; Pb concentration in irrigation water (mg m^{-3})	20.00	5.0–50.0	10, 11
V_g; Pb deposition velocity (m $year^{-1}$)	5.26E + 04	3.5E + 04–5.0E + 05	3, 6, 12, 13
F_a; Air interception fraction (−)	0.50	0.25–0.85	14
R_i; Irrigation water application Rate (m^3 m^{-2} $year^{-1}$)	3.0	2.0–4.0	15
k_u; Rate coefficient, plant uptake of Pb ($year^{-1}$)	6.0E-05	5.4E-05–6.6E-05	16
k_s; Rate coefficient, soil leaching of Pb ($year^{-1}$)	6.0E-04	1.0E-04–1.0E-02	17
R_f; Feeding rate of animals (kg day^{-1})	7.2	5.0–10.0	18
F_{mk}; feed-to-milk transfer coefficient (day l^{-1})	1.00E-04	9.0E-05–1.1E-04	18
F_{mt}; feed-to-meat transfer coefficient (day kg^{-1})	5.00E-04	1.0E-4–7.0E-4	18
M_p; Mass of plant tissue (kg m^{-2})	1.5	0.75–2.0	19
Δ_s; Soil Depth (m)	0.10	0.05–0.15	20
ρ; Soil bulk density (g ml^{-1})	1.30	1.0–2.0	21
ν; Soil moisture infiltration rate (m $year^{-1}$)	2.00	1.0–4.0	22
θ; Volumetric soil water content (ml ml^{-1})	0.30	0.2–0.5	23
K_d; Pb Solid–liquid distribution coefficient (ml g^{-1})	2.5E + 04	2.5E + 02–5.0E + 04	24
M_s; mass of soil (kg m^{-2})	130.0	50.0–300	25
ω; Washing factor (%)	75.0	25–85	26, 27
Human input parameters			
Dietary Intake			
R_V; Vegetable consumption rate (kg day^{-1})	0.500	0.450–0.550	28
R_{Mt}; Meat consumption rate (kg day^{-1})	0.060	0.054–0.066	28
R_{Mk}; Milk consumption rate (μg l^{-1})	0.100	0.900–0.110	28
R_W; Water consumption rate (μg l^{-1})	1.500	1.000–2.000	29, 30
K_{DA}; Dietary constant, adult (day dl^{-1})	0.040	_	31
Soil & Dust Ingestion Intake			
R_S; Soil ingestion rate (g day^{-1})	0.055	0.049–0.060	31
K_{SA}; Soil constant, adult (day dl^{-1})	0.018	_	31
Inhalation Intake			
K_{AA}; Inhalation constant, adult (m^3 dl^{-1})	1.64	_	31
Dermal absorption			
R_{Sk}; Dermal absorption rate (g day^{-1})	1.000	0.900–1.100	31
K_{Sk}; Dermal constant (day dl^{-1})	1.00E-04	_	31

(1) Abdel-Latif [1]; (2) Ali [3]; (3) Ali et al. [5]; (4) Hassanien et al. [20]; (5) Rizk et al. [36]; (6) Shakour and El-Taieb [42]; (7) Shakour and El-Taieb [41]; (8) Shakour and El-Taieb [43]; (9) Shakour and Hindy [44]; (10) Fahim et al. [15]; (11) Mohamed et al. [28]; (12) Buzorius et al. [8]; (13) personal communication; (14) Shaw [45]; (15) Adjustable; (16) pers. comm.; (17) Baes and Sharp [7]; (18) IAEA [22]; (19); (20) Adjustable; (21) Etherington [14]; (22) Calculated; (23) Qing [34]; (24) Ashmore et al. [6]; (25) Calculated; (26) Elnimr and Moharram [13]; (27) Ali and Nasralla [4]; (28) Abo El-Naga [2]; (29) WHO [51]; (30) McKone and Kastenberg [27]; (31) Carlisle and Wade [9]

involves the repeated generation of values of 'random' variables which are drawn from specified PDFs (triangular PDFs were used in the current study), and are within the predicted or common range of model parameters [46]. In this study probabilistic analysis was carried out using Crystal Ball®, an add-in program used in conjunction with Microsoft® Excel.

The statistics of the predicted variables (mean, standard deviation, median, etc.,) were calculated by Crystal Ball after 10,000 iterative calculations. The impact of parameter variance on the model prediction was assessed with uncertainty and sensitivity analysis.

26.4 Exposure Calculations

Lead concentrations in each of model components were calculated as follows:

$$\text{Soil Pb Input } \left(\text{mgm}^{-2}\text{year}^{-1}\right) : [(V_g C_a(1-F_a)) + (R_i C_w)] \tag{26.1}$$

$$\text{Soil Pb Output } \left(\text{mgm}^{-2}\text{year}^{-1}\right) : [C_s M_s(K_s + K_u)] \tag{26.2}$$

$$\text{Soil at the steady state}\left(\text{mgm}^{-2}\text{year}^{-1}\right) : [(V_g C_a(1-F_a)) + (R_i C_w)] = [C_s M_s(K_s + K_u)] \tag{26.3}$$

$$\text{Pb concentration in soil at the steady state}\left(\text{mgkg}^{-1}\right) : C_s = \frac{V_g C_a(1 - F_a) + R_i C_w}{M_s(K_s + K_u)} \tag{26.4}$$

$$\text{Soil leaching; } R_S; \left(\text{year}^{-1}\right) : (v/\theta)/(\Delta_s[1 + \{\rho \times K_d\}/\theta]) \tag{26.5}$$

$$\text{Lead intake by plant; } C_p; \left(\text{mgkg}^{-1}\right) : [V_g C_a F_a(0.33) + K_u C_s M_s(0.33)]/M_p \tag{26.6}$$

$$\text{Pb concentration in milk; } C_{mk;}\left(\text{mgl}^{-1}\right) : C_p \times R_f \times F_{mk} \tag{26.7}$$

$$\text{Lead concentration in meat; } C_{mt;}\left(\text{mgkg}^{-1}\right) : C_p \times R_f \times F_{mt} \tag{26.8}$$

$$\text{The contribution of each medium to human blood lead } \left(Pb_B, \mu\text{gdl}^{-1}\right) : Pb_{B\,(\text{Medium})} = (\text{Pb Concentration} \times \text{Intake Rate} \times \text{Intake Constant})_{(\text{Medium})} \tag{26.9}$$

26.5 Results and Discussion

There is no doubt that the prevailing conditions over the last decades and the resultant atmospheric metallic pollution in Egypt pose a direct hazard to human health through inhalation or an indirect threat through other environmental media polluted by metallic deposition. Soils and plants in the Egyptian urban environment are highly contaminated with lead due to urbanization and industrialization activities.

26.5.1 Deterministic Model Run (Single Point Estimate)

The main aim of the deterministic run was to examine the dynamic simulation for lead accumulation in soil and to determine the time which was likely to be taken to achieve steady state lead concentration in soil with continuous lead inputs to the soil from air and irrigation water. Dynamic solution calculations were carried out according to Eq. 26.3 over 100 years and with an initial Pb concentration in the soil of 15 mg kg^{-1}.

Steady state of lead in urban soil was reached after 50 years, while half of the steady state concentration was reached after about 10 years. Soil depth (Δ_s) and soil bulk density (ρ) are among those parameters which control the dynamics of Pb concentration in soil. Soil depth was assumed in the model to be 0.1 m, as the best average for the rooting zone depth of most vegetables. However, mixing of this surface layer (0.3–0.5 m), during preparation of agricultural lands for new crops, could slow down the dynamics of the uppermost soil layer. In another run of the model, soil depth was set at 0.3 m, and it was found that the steady state was achieved after 90 years. The time to reach half of the steady state concentration increased to 20–25 years.

Determination of Pb concentration in vegetation was the next step in the assessment of the transfer of Pb from atmosphere and soil to plant tissues. Pb concentration in seasonal vegetable crops tissue was calculated according to Eq. 26.6 and depended on the assumed Pb concentration in air (C_a) and its deposition velocity (V_g), in addition to the steady state Pb concentration in soil. Pb concentration in animal products (milk and meat) has also been calculated according to Eqs. 26.4 and 26.5, from the modeled plant Pb concentration at steady state.

The last step in the deterministic analysis was to determine the contribution of each medium, and related pathways, to total blood lead due to the exposure to those specific media. Calculation was carried out according to the equations described by Carlisle and Wade [9]. Table 26.2 shows the values of output parameters of the dynamic model solution. These results showed that the predicted concentrations of lead in soil and plant tissue were high due to the increased Pb concentration in air and irrigation water.

Table 26.2 Outputs of the deterministic model run at steady state for both scenarios

Parameter	Pb concentration
C_s; Pb concentration in soil (mg kg^{-1})	1,312
C_p; Pb concentration in plant tissue (mg kg^{-1})	13.8
C_{mk}; Pb concentration in milk (mg l^{-1})	0.01
C_{mt}; Pb concentration in meat (mg kg^{-1})	0.05

Table 26.3 Total deterministic blood lead (Pb_B) concentration (μg dl^{-1})

Parameter	(μg dl^{-1})
Pb concentration in blood (due to individual exposure pathways)	
Vegetable ingestion	69.12
Washing factor: 75%	138.24
Washing factor: 50%	
Meat ingestion	0.119
Milk ingestion	0.04
Water ingestion	1.20
Soil ingestion	1.295
Air inhalation	3.28
Dermal absorption	0.131
Total blood Pb (due to all exposure pathways)	
Washing factor: 75%	75.19
Washing factor: 50%	144.30

Deterministic total blood lead (Pb_B) due to exposure to different media is presented in Table 26.3, which shows the contribution of each individual medium to human Pb_B. The main contribution to total Pb_B is from vegetable ingestion, with a rough percentage of 92%. These results indicate clearly that the food intake pathway is the most significant route for lead deposition to human blood. This is consistent with the demonstration that crop consumption, with soil ingestion and inhalation of air, generally contributes at least 90% to the total exposure for all contaminants [48].

26.5.2 Washing Factor

Washing metal-contaminated particulate materials from vegetable surfaces in the field or during preparation for cooking is an important method of removing a significant part of deposited lead [19]. Foliar deposition of airborne lead was concluded to account for most of the lead in grasses and other plants having a high leaf surface per unit mass ([10]; in Ref. [49]). The percentage reduction of metal by washing processes varies according to the amount of water applied and depends on individual human behavior. Thornton [49] found that up to 75% of lead

Table 26.4 Monte Carlo analysis for key input and main output parameters

Parameter	Statistics (10,000 trials)				
	Mean	Median	SD	Variance	CV
Pb concentration in air (μg m^{-3})	2.10E-3	2.08E-3	7.5E-4	5.68E-7	0.36
Deposition velocity (m $year^{-1}$)	1.95E5	1.77E5	1.06E5	1.1E10	0.54
Pb concentration in water (μg m^{-3})	25.1	24.21	9.27	85.97	0.37
Irrigation water rate (mg l^{-1})	3.00	3.00	0.407	0.166	0.14
Pb concentration in soil (mg kg^{-1})	917.9	497.1	1,271	1,615,336	1.38
Pb concentration in plant (mg kg^{-1})	54.78	43.2	42.07	1,770	0.77
Pb voncentration in milk (mg l^{-1})	0.041	0.032	0.032	0.001	0.79
Pb concentration in meat (mg kg^{-1})	0.176	0.131	0.152	0.023	0.87

SD Standard deviation, *CV* Coefficient of variability

Table 26.5 Monte Carlo analysis for total blood lead and contribution of different exposure pathways to total Pb_B

Parameter (μg dl^{-1})	Statistics (10,000 trials)				
	Mean	Median	SD	Variance	CV
Total Pb_B	317	239.8	266.6	71074.1	0.84
Vegetable Pb_B	310.5	233	265.3	70399	0.85
Air Pb_B	3.44	3.41	1.24	1.53	0.36
Water Pb_B	1.505	1.43	0.602	0.36	0.4
Meat Pb_B	0.421	0.316	0.368	0.135	0.87
Milk Pb_B	0.162	0.127	0.129	0.017	0.79
Skin Pb_B	0.092	0.05	0.127	0.016	1.39

SD Standard deviation, *CV* Coefficient of variability

was removed from lettuce plants by washing. In Egypt, it has been reported that a percentage between 50 up to 75% of lead was removed from clover plants by washing [4]. It has reported that lead content of plants is primarily from external contamination, rather than from uptake from the soil (Englert 1986; cited in [13]). It can be noticed from Table 26.3 that the reduction of washing factor from 75 to 50% approximately doubled the contribution of vegetables to total blood Pb, which reflects the importance of this factor.

26.5.3 Probabilistic Model Run

Probabilistic run using Monte Carlo simulation statistics of the main input and output parameters, after 10,000 trials, are shown in Tables 26.4 and 26.5. These tables show the predicted variables for the probabilistic distribution (PDF) of all parameters. Distributions exhibit some degree of positive skewness, i.e. most of values are grouped toward the lower end of the distribution (*figures are not shown*). Skewness is often reported to be associated with hazardous waste sites [38]. The distribution asymmetry of the model parameters can also be indicated by the large difference between median and mean values.

26.5.4 Uncertainty Analysis

Frequency distributions and the corresponding statistics obtained from the probabilistic run of the model showed a similar trend to the deterministic run. The simulation details of the key input and main output parameters are presented in Table 26.4 and show that the mean values of simulated distributions of deposition velocity (V_g) and lead concentration in irrigated water (C_w) were higher than the assumed best estimate values for both scenarios (Table 26.1). By contrast, the simulated mean values of lead concentration in air (C_a) and application rate of irrigation water (R_i) were similar to the assumed values of the corresponding parameters, which can be attributed to the symmetrical triangular distribution for the input assumptions. On the other hand, both assumed and simulation mean values of C_a and V_g were lower than the corresponding calculated arithmetic mean values derived from the collected information. However, the simulated means of these parameters were close to the corresponding geometric mean values.

Uncertainty analysis showed that about 55% of probabilistic prediction of Pb concentrations in air was higher than the deterministic prediction. More than 90% of the probabilistic deposition velocities (V_g) were higher than the deterministic value (1.95E + 5 m year^{-1}), which reflect the higher uncertainty in deposition velocity due to data variability and the subsequent wide assumed range for this parameter.

The probabilistic means of lead concentration in the soil and plant output, resulting from all possible contributions, had different trends to the deterministic model run. The simulated mean of lead concentration in soil (C_s) was lower than the deterministic concentrations, in contrast to lead concentrations in plant (C_p) which were higher in the probabilistic simulation than in the deterministic run. Similarly, these results were higher than the corresponding measured concentrations in Egypt, and reflect the high uncertainty in the simulated Pb concentration outputs. The deterministic concentrations of lead in soil and plant are compared to the PDFs obtained from the probabilistic run (*figures not shown*). The deterministic means of 1,312 mg kg^{-1} (in soil) and 13.8 mg kg^{-1} (in plant) occur at around 81 and 9% of the PDF, respectively. The results of the Monte Carlo analysis in Table 26.4 show that the coefficient of variation (CV) for Pb concentration in soil was very high. This is a clear indication of the high variability in Pb concentration in soil as a direct result of the variable data of the parameters responsible for Pb accumulation in soil. The high variability in this forecast is indicated also by the large difference between the mean and the median, as well as by big standard deviation.

Table 26.5 shows that the predicted risk, in term of Pb_B, is very high (317 ± 266.6 μg dl^{-1}); this level accounts for the effect of washing at 75%. The range of Pb_B recorded in Egypt was between 12 and 69 μg dl^{-1} with a mean concentration of 38 ± 12 μg dl^{-1} [23, 30, 40]). The coefficient of variability (CV = standard deviation/mean) can be used to compare the variability of different forecasts since this statistic is independent of the units of parameters. The results indicate that the uncertainty of the simulated Pb_B risk is high due to high CV value (0.84).

Table 26.6 **Monte** Carlo sensitivity analysis and the percentage contributions of different input parameters to output Pb concentrations in soil, plant, milk and meat

Pb_B	C_a	V_g	C_w	M_p	K_s	F_a	M_s	R_f	F_{mt}
Cs	6.8	16.7	1.8		59.6	3.4	11		
Cp	24.7	62	0.1	4.9	0.1	8.1			
Cmk	23.9	60.3	0.1	4.7	0.2	8.1		2.4	
Cmt	20.4	51.5		4.1	0.1	7.2		2.1	14.4

Table 26.7 Monte Carlo sensitivity analysis and the percentage contributions of different input parameters to total Pb_B, vegetable Pb_B, air Pb_B and water Pb_B

Pb_B	C_a	V_g	C_w	F_a	Wash %	K_s	R_w	M_p
Total	21.4	53.8	0.1	7.1	12.6	0.2		4.3
Vegetable	21.3	53.7		7.2	12.7	0.1		4.3
Air	98.7							
Water			89.6				9.4	

Table 26.8 Monte Carlo sensitivity analysis and the percentage contributions of different input parameters to meat Pb_B, milk Pb_B, soil Pb_B and skin Pb_B

Pb_B	C_a	V_g	C_w	F_{mt}	F_a	K_s	M_s	M_p	R_f
Meat	20.5	51.2		14.3	7.1	0.1		4.1	201
Milk	23.8	60.2	0.1		8	0.2		4.7	2.4
Soil	6.8	16.8	1.7		3.5	59.3	11		
Skin	6.8	16.7	1.8		3.4	59.4	11		

The probabilistic mean of Pb_B is higher than the corresponding deterministic value. Moreover, the PDF of total Pb_B predicted that 90% of the population is expected to have Pb_B more than 75 μg dl^{-1}. The simulation results showed that vegetables contribute about 98% of total Pb_B, compared to 92% in the corresponding deterministic run.

26.5.5 Sensitivity Analysis

The purpose of sensitivity analysis in modeling is to evaluate the relative contribution of the different input parameters to the output parameters, and thus to determine those factors of most significance within the model. Tables 26.6, 26.7 and 26.8 show the relationship between the changes in the input parameters and the resulting changes in the model output (the percent of outcome variance attributable to specific input). In these tables, only the parameters with the highest contributions to variance are presented for each output.

This analysis shows the contribution of input parameters to Pb in soil (C_s), plant (C_p), human blood (Pb_B), and other output parameters. For example, Table 26.7 shows that the dominant contributor to blood lead level variance is the variability in deposition velocity (54% contribution to variance). The second most important contribution to variance in the urban scenario is the concentration of Pb in the atmosphere (C_a, 21% contribution to variance). Furthermore, C_a and V_g contribute to human Pb_B variance in Egypt with 75 and 48% (Table 26.7). These results confirm that the deposition of lead Pb to soil and vegetation is most likely to be

responsible for any shift in the magnitude and spread of risk distribution. In addition to V_g and C_a, washing dust-borne Pb off vegetable leaves is another significant factor, which contributes 13% of the variance.

The parameters identified as most significant for lead concentration in urban soil were lead leaching rate coefficient (K_s), lead deposition velocity (V_g), mass of soil (M_s), and lead concentration in air (C_a). Furthermore, the most significant parameters responsible for the variance in Pb concentration in vegetables are deposition velocity (V_g), and Pb concentration in air (C_a). In terms of Pb flux, V_g and C_a account for a total contribution of 87% to vegetation Pb. Moreover, the interception fraction (F_a) and mass of cultivated plants (M_p) make a considerable contribution to the variance in Pb concentration in vegetation.

26.6 Conclusions and Implications

Based on the results of the current study, lead is present at high enough levels in air, water, food and soil, particularly in the greater Cairo zone, to cause concern for the human population. Predicted deterministic and probabilistic human blood lead (Pb_B) levels in the current study, were found to exceed the guidance value of 10 μg dl^{-1} and to pose a high potential risk for a significant percentage of the exposed population. The probabilistic Pb_B level is higher than the range levels (14–28 μg dl^{-1}) reported for rural areas in Egypt by Ibrahim [23]. Despite that the deterministic Pb_B is higher also than this range levels, it is close to the highest levels measured for traffic policemen, 63 ± 16.6 μg dl^{-1} [30], and for workers, 69 ± 19.4 μg dl^{-1} [40].

In conjunction with the Monte Carlo analysis, two approaches have been used to assess the influence of parameter variance on model predictions; uncertainty analysis and sensitivity analysis. As demonstrated by Rood et al. [37], model prediction uncertainty may be attributed to errors in the scientific basis and physics of model formulation, errors in model input and concentration measurements, and uncertainty due to natural variability. The first type of uncertainty could be present in the current study by the dependence of Pb transport complex process in soil medium on many chemical and physical parameters, which, in turn, are site specific parameters. In the current model, soil parameter ranges were derived from international studies or selected based on personal judgement. Furthermore, errors in model input and concentration measurements may result from instrumentation and personal measurement error for any of the collected data (e.g. C_a, V_g). Mixing of soil, to aid growth of plants or to cover contaminated soil with new soil or dilute it with amendments [12], is another factor which potentially can affect Pb concentration in the upper soil layer and which can add to model uncertainty.

The model presented was intended to provide a first estimate for Pb concentration in soils and plants as a result of atmospheric Pb deposition in Egypt, and from these environmental media to calculate the human health risk associated with these levels of environmental contamination (lead in blood). Information concerning Pb in the Egyptian environment was derived from many different sources and research

work conducted for quite different purposes, other than risk assessment. The ranges assumed for C_a and V_g were chosen to be between the minimum value of the collected data and its calculated mean value, because the majority of data collected for these particular parameters were found to fall between these values. Furthermore, since few environmental data are available for rural areas, professional judgement was used to estimate C_a and V_g ranges for rural areas. Farm animals are assumed to be exposed to Pb contamination via ingestion of contaminated food which has previously been shown to be the main exposure route [47].

Since late 1960s, emissions of lead and other contaminants have increased in association with the vast development of industrialisation and urbanisation. By mid 1970s, attention was drawn to the higher increase in particulate emissions due to urban activities and the steadily increase in Pb concentration in the atmosphere since that time [31, 39]. Accordingly, the range of values of Pb concentration in soil reported in Egypt can be attributed to the accumulation of deposited lead from the atmosphere over the past years. This indicates that the steady state predicted by the deterministic model for Pb in soil (50 years) has not been reached yet, and about 10 years more of continuous Pb deposition at the assumed deposition, are needed to reach steady state for lead in soil. It has been reported that lead accumulation in soil is long-term process resulting from low-level deposition of lead over a prolonged period [11, 24]. Moreover, it has been shown that despite significant reductions of lead emission, concentrations of lead in soil remained practically constant during 5-year study [21] or decreased slightly over 11 years [50]. However, the fall in lead emission to the atmosphere was found to contribute to the progressive reduction of human risk from exposure to lead [50]. According to these, and to the results of the current model, the environmental plan undertaken to reduce the emissions from different sources in Egypt should decrease the risk to human by reducing deposited lead to vegetation and other media. In contrast, reduction of Pb concentration in the atmosphere, even to the lowest international guideline, may not reduce Pb concentration in soil for several decades.

The variance in the probabilistic Pb simulation for soils and plants, compared to the deterministic values, reveals the uncertainty in the simulation. These results are in accordance with the study of McKone and Ryan [28] who reported that the predicted value of exposure estimated from the Monte Carlo simulation can be significantly larger than the value obtained by using a single point estimate, in some exposure estimates.

The main finding of the current study was that the most significant contributor to the total Pb_B is the ingestion of contaminated vegetables, and the washing process is an important factor which can greatly reduce the ingested amount of lead. This is consistent with the demonstration that the largest portion of lead received by people is through food ingestion [52, 53]. This is also in agreement with the finding of [18] who found that ingestion is the significant route in exposure to Pb.

The current study reveals also that Pb from the atmosphere is the most significant source of lead contamination of vegetation. Moreover, direct foliar contamination was shown to be the most important pathway of food contamination with Pb which, in turn, was controlled by the rate of deposition of lead [52, 53]. In the current study, Pb concentration in the atmosphere (C_a) and deposition velocity (V_g) were found

to greatly influence almost all output forecasts such as C_s, C_p, and Pb_B, although to differing degrees. Physicochemical soil parameters, such as the soil leaching coefficient and soil mass were found to affect concentration of lead in soil (C_s), soil Pb_B and skin Pb_B. In accordance with the importance of direct deposition from atmosphere, washing factor was found to influence lead concentration in vegetable (C_p), vegetable Pb_B and total Pb_B.

In conclusion, as a multimedia risk assessment, the PbMod Egypt model provides a means of assessing potential risk of human lead exposure from environmental sources in Egypt. It can be shown from this study that all of the deposited lead remains associated with the plant either directly (uptake from air) or indirectly (uptake from soil): since vegetation contamination is so evidently important further study of the contamination processes is recommended.

As the first attempt, the current study indicates that Pb is a potential hazard to human blood through the contamination of many environmental media with atmospheric lead. The current assessment simulated the transfer of atmospheric lead to human blood and all environmental media, either directly or indirectly. Pb levels in all the media examined are clearly related to its concentration in atmosphere, and the priority should be given to improve and enhance reductions in emissions from industrial activities to international standards. Many steps have been taken over the last decade to reduce atmospheric pollution in the greater Cairo area, such as the use of natural gas in power stations, public transport and industrial activities. Such improvements should reduce the levels of lead accumulated by seasonal vegetables, and consequently, inputs of lead to human blood via food ingestion should be reduced significantly. Moreover, rural atmospheric pollution should be avoided in future, and attention should be given also to protect rural areas from any current point sources of lead pollution.

References

1. Abdel-Latif NMM (1993) An investigation on some combustion generated pollutants affected plant growth. MSc thesis, Faculty of Science, Botany Department, Zagazig University, Zagazig, Egypt
2. Abo El-Naga IN (1996) The possibility of calculating self sufficiency ratio of food on the national level using essential quantities of food needed. Alexandria J Agric Res 41:35–54
3. Ali EA (1993) Damage to plants due to industrial pollution and their use as bioindicators in Egypt. Environ Pollut 81:251–255
4. Ali EA, Nasralla MM (1986) Impact of motor vehicle exhausts on the cadmium and lead contents of clover plants grown around Egyptian traffic roads. Int J Environ Stud 28:157–161
5. Ali EA, Nasralla MM, Shakour AA (1986) Spatial and seasonal variation of lead in Cairo atmosphere. Environ Pollut 11B:205–210
6. Ashmore MR, Colgan A, Hill M, Pan G, Paton G, Rieuwerts J, Tipping E (2001) Modelling and microbial toxicity of pore-water free ion concentrations of metals in upland soils. In Curlik J (ed) Proceedings of UN/ECE Ad-hoc international expert group on effects based critical limits, Bratislava

7. Baes CF, Sharp RD (1983) A proposal for estimation of soil leaching and leaching constants for use in assessment models. J Environ Qual 12:17–28
8. Buzorius G, Rannik U, Makela JM, Vesela T, Kulmala M (1998) Vertical aerosol particle fluxes measured by eddy covariance technique using concentration particle counter. J Aerosol Sci 29:157–171
9. Carlisle JC, Wade MJ (1992) Predicting blood lead from environmental concentrations. Regul Toxicol Pharmacol 16:280–289
10. Chamberlain AC (1983) Fallout of lead and uptake by crops. Atmos Environ 17:693–706
11. Chaney RL, Mielke HW (1986) Standards for soil lead limitations in the United States. Trace Subst Environ Health 20:355–377
12. Chaney RL, Mielke HW, Sterrett SB (1988) Speciation, mobility and bioavailability of soil lead. In: Davies BE, Wixson BG (eds) Lead in soil: issues and guidelines. Supplement of vol 9 (1989) of Environmental geochemistry and health. Whistable Litho Printers Ltd., Whistable, pp 105–129
13. Elnimr T, Moharram BM (1994) Studies on human exposure to environmental lead in Tanta. Radioisotopes 43:197–203
14. Etherington JR (1982) Environment and plant ecology. Wiley, New York
15. Fahim FA, Abdllah AMA, Abdel Razek TAM (1995) Flow and accumulation of pollutants in an agro-industrial ecosystem. J Afr Earth Sci 20:297–301
16. Felter SP, Dourson ML, Patterson J (1998) Assessing risks to human health from chemicals in the environment. In: Calow P (ed) Handbook of environmental risk assessment and management. Blackwell Science, London, pp 9–23
17. Finley B, Paustenbach D (1994) The benefits of probabilistic exposure assessment: three case studies involving contaminated air, water, and soil. Risk Anal 14:53–73
18. Goodrum PE, Diamond GL, Hassett JM, Johnson DL (1996) Monte Carlo modeling of childhood lead exposure: development of a probabilistic methodology for use with the USEPA IEUBK model for lead in children. Human Ecol Risk Assess 2:681–708
19. Harrison RM, Laxen DPH (1981) Lead pollution causes and control. Chapman and Hall, London. ISBN 0412163608
20. Hassanien MA, Rieuwerts J, Shakour AA, Bitto A (2001) Seasonal and annual variations in air concentrations of Pb, Cd and PAHs in Ciro, Egypt. Int J Environ Health Res 11:13–27
21. Hršak J, Fugaš M, Vadjić V (2000) Soil contamination by Pb, Zn and Cd from a lead smeltery. Environ Monit Assess 60:359–366
22. IAEA (International Atomic Energy Agency) (1994) Handbook of parameter values for the prediction of radionuclide transfer in temperate environments, Technical reports series No. 364, Vienna
23. Ibrahim SH (1992) The extent of environmental pollution from motor vehicles and its biological indices, MD thesis, Cairo University, Cairo
24. Lin Z, Harsbo K, Ahlgren M, Qvarfort U (1998) The source and fate of Pb in contaminated soils at the urban area of Falun in centarl Sweden. Sci Total Environ 209:47–58
25. Lioy PJ (1990) Assessing total human exposure to contaminants. Environ Sci Technol 24:938–945
26. Loranger S, Courchesne Y (1997) Health risk assessment of an industrial site contaminated with polycyclic aromatic hydrocarbons using CalTox, an environmental fate/exposure model. SAR QSAR Environ Res 6:81–104
27. McKone TE, Kastenberg WE (1986) Application of multimedia pollutant transport model to risk analysis. In: Cohen Y (ed) Pollutants in a multimedia environment. Plenum Press, New York/London, pp 167–189
28. McKone TE, Ryan PB (1989) Human exposures to chemicals through food chains: an uncertainty analysis. Environ Sci Technol 23:1154–1163
29. Mohamed MAM, Osman MA, Potter TL, Levin RE (1998) Lead and cadmium in Nile River water and finished drinking water in greater Cairo, Egypt. Environ Int 24:767–772

30. Nasralla MM, Shakour AA, Said EA (1984) Effect of lead exposure on traffic policemen. Egypt J Ind Med 8:87–104
31. Nasralla MM, Abdel Salam MS, Ali EA (1985) Impact of industrial pollution sources on the environment of Shoubra El-Kheima. Egypt J Occup Med 9:115–130
32. NRC (1991) Human exposure assessment for airborne pollutants – advances and opportunities, Committee on Advances in Assessing Human Exposure to Airborne Pollutants. National Research Council, National Academy of Science, Washington, DC
33. NRC (1994) Science and judgment in risk assessment. National Research Council, National Academy of Science, Washington, DC
34. Qing H (1998) Migration and plant uptake of radionulides in laboratory columns lysimeters with contaminated water tables. PhD thesis, Centre for Analytical Research in the Environment, Imperial College at Silwood Park, Ascot
35. Renner R (1995) Predicting chemical risks with multimedia fate models. Environ Sci Technol 29:556–559
36. Rizk HFS, Shakour AA, Meleigy MI (1995) Concentration of surface ozone, total oxidants and heavy metals in urban areas downwind of industrial area in Cairo, Egypt. In: Wilken R-D, Förster J, Knöchel A (eds) International conference of heavy metals in the environment, vol. 1, Hamburg, pp 164–167
37. Rood AS, Killough GG, Till JE (1999) Evaluation of atmospheric transport models for use in phase II of the historical public exposures studies at the Rocky Flats Plant. Risk Anal 19:559–576
38. Schulz TW, Griffin S (1999) Estimating risk assessment exposure point concentrations when the data are not normal or lognormal. Risk Anal 19:577–584
39. Shakour AA (1982) Study on some pollutants in Cairo atmosphere. PhD thesis, Al-Azhar University, Cairo
40. Shakour AA (1995) Blood lead level in Egyptian works. In Wilken R-D, Forstner U, Knochel A (eds) International conference. Heavy metals in the environment, vol. 2, Hamburg, pp 209–212
41. Shakour AA, El-Taieb NM (1994) Effects of atmospheric lead exposure on urban children. Egypt J Occup Med 18:37–47
42. Shakour AA, El-Taieb NM (1995) Heavy metals in atmospheric particulate in the industrial area north Cairo, Egypt. In: Wilken R-D, Förster J, Knöchel A (eds) International conference of heavy metals in the environment, vol. 1, Hamburg, 172–175
43. Shakour AA, El-Taieb NM (1995) Lead deposition on a residential area in the vicinity of lead smelters in Cairo city. In: Wilken R-D, Förster J, Knöchel A (eds) International conference of heavy metals in the environment, vol 2, Hamburg, pp 213–216
44. Shakour AA, Hindy KT (1992) Study of atmospheric contamination in recently developed residential area in Cairo. In: Vernet J-P (ed) Environmental contamination. The 5th international conference, Morges, Switzerland, pp 200–203
45. Shaw GG (1997) Expert B – rationales and responses of expert panel on soil and plant transfer and process. In: Probabilistic accident consequence uncertainty analysis: food chain uncertainty assessment. US Nuclear Regulatory Commission and Commission of European Communities. NUREG/CR-6523, vol 2 (appendices), pp C17–C29
46. Shorter JA, Rabitz HA (1997) Risk analysis by the guided Monte Carlo technique. J Stat Comput Simul 57:321–336
47. Stevens JB, Swackhamer DL (1989) Environmental pollution: a multimedia approach to modeling human exposure. Environ Sci Technol 23:1180–1186
48. Swartjes FA (1999) Risk-based assessment of soil and groundwater quality in the Netherlands: standards and remediation urgency. Risk Anal 19:1235–1249
49. Thornton I (1991) Metal contamination of soils in urban areas. In: Bullock P, Gregory PJ (eds) Soils in the urban environment. Blackwell Scientific Publications, Oxford/London, pp 47–75
50. Wang Y, Thornton I, Farago M (1997) Changes in lead concentrations in the home environment in Birmingham, England over the period 1984–1996. Sci Total Environ 207:149–156

51. WHO (World Health Organization) (1996) Guidelines for drinking-water quality, vol 2: Health criteria and other supporting information, 2nd edn. WHP, Geneva
52. WHO/ECEH (1996) Update and revision of the WHO air quality guidelines for Europe, vol 2, Inorganics. World Health Organization, Regional Office for Europe, European Centre for Environment and Health, Bilthoven
53. WHO/ROE (1987) Air quality guidelines for Europe. European series no. 23. World Health Organization, Regional Office for Europe, WHO Regional Publications, Copenhagen

Index

I. Barnes and K.J. Rudziński (eds.), *Disposal of Dangerous Chemicals in Urban Areas and Mega Cities*, NATO Science for Peace and Security Series C: Environmental Security,
DOI 10.1007/978-94-007-5034-0,